IMPERIAL COLLEGE OF SCIENCE AND TECHNOLOGY

Department of Mechanical Engineering

Exhibition Road, London SW7 2BX

Measurements and calculations of velocity in small-diameter ducts; with particular application to blood flow in venules.

~~BLOOD FLOW IN SMALL DIAMETER~~

~~DUCTS; PARTICULARLY IN VENULES~~

by

Nicholas Spyro Vlachos

Dipl.Eng., M.Sc., D.I.C.

Thesis submitted for the degree of

Doctor of Philosophy

in the Faculty of Engineering

of the University of London

March 1977

ABSTRACT

The major motivation for the present work relates to the medical importance of the flow of blood in the vascular bed of man. Clinical, pathological and experimental evidence indicates that the initiation and growth of atherosclerotic plaques, and acute coronary and other thromboses, critically depends on the properties of the blood flowing in the vicinity of these lesions. Further progress in the understanding of the biochemical mechanisms underlying platelet aggregation requires information of the local velocity of blood flowing in small venules. The present investigation is, however, also relevant to a wide range of internal flow applications where knowledge of the flow characteristics downstream of bends, in the vicinity of axisymmetric constrictions and in pipe flows with three-dimensional obstacles, may assist the design of industrial devices.

The thesis describes theoretical and experimental contributions to the solution of the above problems. Numerical methods have been developed and used for the solution of two- and three-dimensional equations appropriate to the flow of Newtonian and non-Newtonian fluids at low Reynolds numbers in ducts with obstacles. In the experimental work, laser Doppler velocimetry has been developed and used for the measurement of water, saline, plasma and blood, with various haematocrit values, flowing in small diameter tubes.

Predicted values of velocity, pressure and shear stress distributions of laminar Newtonian flow downstream of a bend in a round tube and of the Newtonian and non-Newtonian flow in the vicinity of axisymmetric and three-dimensional obstacles are reported. The results are interpreted from the biological and engineering viewpoints in terms of the study of atherosclerosis, thrombosis, haemolysis and embolus formation and

engineering designs. Measurements of velocity are reported in the developing laminar water flow downstream of a bend in a round tube and the implications for blood flowing past arterial branchings are discussed. Experiments in small diameter glass capillaries allowed an appraisal of the problems associated with measurements *in vivo* and also contributed information of the constitutive equation for blood which was subsequently used in the calculations mentioned above. These calculations quantify, for example, the local shear stresses present in blood flow; they reveal high values which are capable of damaging red cells and regions of low values where atherosclerotic plaques and thrombi may be formed. Attempts to measure the local velocity of blood flow in living animals are also reported and allowed the formulation of the laser Doppler microscope design for future *in vivo* measurements.

ACKNOWLEDGEMENTS

It gives me great pleasure to express gratitude to my supervisor, Professor J.H. Whitelaw, for his guidance and constructive criticism throughout my research at Imperial College. His ability to define the optimum path of the research enabled me to carry through the experimental and computational investigation. His encouraging attitude and continuous interest in the work led me to the completion of this thesis.

I am indebted to Dr A.D. Gosman who, as a member of my thesis committee, was interested in my research and provided help with the understanding, development and application of the numerical schemes reported in this thesis.

Professor G.V.A. Born of Cambridge University was co-holder of the British Heart Foundation grant which supported much of this research; Professor P. Richardson of Brown University provided help with the understanding of the biomedical aspects of this work; Dr A. Atherton of the Imperial Cancer Research Institute assisted with the handling of blood flows; their continuous interest is much appreciated.

Mr J. Laker helped with the electronic problems, while Mr R.H. Church and Mr O. Vis constructed most parts for the experimental rigs; Mr J. Zeidler of Leitz Instruments (England) made available the microscope for the development of the laser Doppler microscope; the photographs in this thesis were processed by Mr J. Pilmer; I am thankful to them all.

My colleagues made the everyday College life most interesting and pleasant. In particular, my thanks are due to Dr D. Durao, Dr F. Durst, Dr J. McGuirk, Mr J. Humphrey, Dr A. Melling, Mr S. Syed, Mr. A. Taylor and Mr. A. P. Watkins for many valuable discussions on LDV and numerical schemes.

The financial support of the British Heart Foundation and the Ministry of Coordination of Greece (NATO grant) is acknowledged.

My thanks to Mrs. H. A. Bastin and Miss E. A. Quin who had the patience to go through every typing detail with great skill.

Finally, I would like to take this opportunity to extend my deepest gratitude to my family for their support and encouragement throughout my career.

N. S. Vlachos
March 1977

CONTENTS

LIST OF TABLES

LIST OF FIGURES

NOMENCLATURE

Symbol	Meaning
A	Area
A_i^j	Coefficient of finite-difference equation for the i location and j dependent variable
a^o	Obstacle half angle
C	Light speed
C_d	Orifice discharge coefficient
C_D, C_{D_p}, C_{D_τ}	Drag coefficients
C_i	Convection coefficient of finite-difference equation for the i cell face
C_p	Pressure coefficient
C_x	Pressure loss coefficient
D	Capillary or pipe diameter
D_i	Diffusion term of finite-difference equation for the i cell face
D_i^j	Pressure coefficient of finite-difference equation for the i cell face and j dependent variable
D_{ph}	Photomultiplier pinhole diameter
d	Beam waist diameter
d_a	Displacement of optical axis of receiving optics
d_p	Scattering particle diameter
d_{ph}	Control volume diameter viewed by the photomultiplier
dp/dx, $d\bar{p}/dx$	Pressure gradient
d_s	Diameter of LDV control volume for off-axis detection
E_i	Amplitude of electromagnetic field
F	Hydrodynamic drag force
f , f_D	Doppler signal frequency

Symbol	Meaning
f_i	Body force
f_s	Frequency shift
g_ϕ	Generation term of ϕ-property of fluid flow
H	Haematocrit
h	Plank's constant
I	Incident light intensity
I_1, I_2, I_3	Tensor invariants
I_s	Scattered light intensity
$J_{\phi,i}$	Diffusion flux of ϕ
k	Thermal conductivity
L	Total length of flow disturbance
l_c	Coherence length
l_e	Re-attachment length
l_m	Length of effective LDV control volume
l_s	Length of LDV control volume for off-axis detection
l_t	Length of interference pattern
M	Receiving optics magnification
m	Coefficient of viscosity power law
$\dot{m}$	Mass flow rate
N_{fr}	Number of fringes
n	Index of viscosity power law
P	Laser beam power
P_e	Peclet number
P_N	Noise power
P_S	Scattered light power
$P(x)$	Probability distribution function
p	Pressure

Symbol	Meaning
$\bar{p}$	Average pressure
p'	Pressure-correction
q_i	Heat flux vector
R	Capillary or pipe radius
R_a	Capillary apparent diameter
Re	Reynolds number
Re_N	Modified Reynolds number
Re_N'	Generalised Reynolds number
R_i	Capillary inside diameter
$R_{N,\phi}$	Normalising quantity of residual source of ϕ
R_o	Capillary outside diameter
$R(x)$	Radius of Gaussian beam wavefront
R_ϕ	Residual source of ϕ
r	Radial coordinate
r_i	Random number
r_p	Radius of plug flow (Casson's viscosity law)
S^j	Source term of j dependent variable
s_f	Sample deviation of f
T	Temperature
u	x-direction velocity component
u'	Correction of u
V	Fringe visibility
V_i	Velocity vector
v	y-direction velocity component
v'	Correction of v

Symbol	Meaning
w	z-direction velocity component
w'	Correction of w
x_i, y_i, z_i	Unit vectors
x, y, z	Coordinates

Greek Symbols

Symbol	Meaning
α	Relaxation factor
Γ_{ii}	Auto-correlation function
Γ_{ij}	Cross-correlation or mutual coherence function
γ	Shear rate
γ_{ij}	Normalised mutual coherence function
γ_{ϕ}	Diffusion coefficient of ϕ-property
Δf	Frequency bandwidth
Δ_{ij}	Tensor of rate of deformation
Δp, Δp_{th}	Pressure drops
Δt	Oscilloscope sweep delay time
ΔT_N	Doppler signal measurement time
ΔT_o	Width of measurement time pulse
Δx, Δy, Δz	Dimensions of the computational cell in the x, y, z-directions, respectively
Δx_w, Δx_a	Displacement of LDV control volume in water and air, respectively
δ_{ijk}	Kronecker delta
δT_1, δT_2	Interpolator measurement times

Symbol	Meaning
δx, δy, δz	Distances between variable locations in the x, y, z-directions, respectively
η	General viscosity
η_b, η_g, η_w	Refractive indices of blood, glass and water, respectively
η_q	Photodetector quantum efficiency
λ	Laser light wavelength
μ	Newtonian viscosity
μ_p, μ_s	Plasma and suspension viscosity, respectively
ν_i	Laser light frequency
ν_D	Doppler frequency
ρ	Density
σ	Standard deviation
T, T^-	Predicted maximum and minimum shear stresses
τ	Predicted wall shear stress
τ_{ij}	Shear stress tensor
τ_{max}	Maximum predicted shear stress
τ_w	Wall shear stress of fully developed laminar pipe flow
τ_y	Blood yield stress
τ_o	Coherence time
ϕ	Half beam incidence angle
ϕ_a, ϕ_w	Half beam incidence angle in air and water, respectively
ϕ_g	Beam refraction angle in glass
ϕ_s	Off-axis detection angle
ψ, ψ^-	Stream function
Ω	Solid angle of detection

Subscripts

Symbol	Meaning
D, E, N, P, S, U, W	Grid nodes
d, e, n, s, u, w	Cell faces
p	Pressure
ph	Photomultiplier
s	Off-axis detection
t	Transmitting optics
x, y, z	Orthogonal coordinates

Superscripts

Symbol	Meaning
p	Pressure-correction
u	u velocity component
v	v velocity component
w	w velocity component
ϕ	ϕ-property of flow

CHAPTER 1

GENERAL INTRODUCTION

1.1 OBJECTIVES

The major objective of this thesis is related to the medical importance of the flow of blood in the vascular bed of man. Clinical, pathological and experimental evidence indicates that the initiation and growth of atherosclerotic plaques, acute coronary and other thromboses, critically depend on the properties of the blood flowing at the site of these lesions. For further progress in the understanding of the biochemical mechanisms underlying platelet aggregation, it has become necessary to measure the velocity and associated shear of flowing blood in small venules. The purpose of this investigation was, therefore, to examine laser Doppler velocimetry and determine the extent to which it would allow measurements of this type to be obtained *in vitro* and *in vivo* without disturbance to the flow. The technique utilises the Doppler effect whereby the frequency shift of scattered laser light by moving particles is used to detect their velocity. Laser Doppler velocimetry offers the potential advantage of a non-invasive measuring method which is important for *in vivo* blood flows.

Although the initial motivation is physiological fluid mechanics, the present investigation is relevant to a wide range of internal flow applications where knowledge of the flow characteristics downstream of bends, in the vicinity of axisymmetric constrictions and in pipe flows with obstacles may be desirable in industrial designs. Understanding of the microscopic and macroscopic characteristics of these flows may assist the diagnosis and improvement of engineering designs as well as contribute to the explanation of biorheological phenomena such as atherosclerosis, thrombosis, haemolysis and embolus formation.

The experimental purpose might be extended to include the detailed velocity and stress characteristics of the flow around coagulations, other blockages, bifurcations, bends, etc. This would represent a very extensive task and consequently the solution of appropriate differential equations is examined on the grounds that it would reduce the number of required measurements. Indeed, for the laminar flow of a Newtonian fluid, it could obviate the need for measurements.

For the flows considered here, i.e. bends, axisymmetric and asymmetric pipe blockages, the appropriate forms of the Navier-Stokes equations are complex but can be solved by means of finite-difference numerical procedures. An existing algorithm has been extended for this purpose and calculated values of velocity and local shear are presented for a range of practically relevant flows with Newtonian stress-strain relationships. Similar calculations are also presented for blood flow and make use of a stress-strain relationship suggested by the literature and the present measurements.

From the above discussion, the following specific objectives may be extracted:

1. To measure the velocity characteristics of the flow downstream of a bend and to solve corresponding differential equations by numerical methods. This experimental programme was intended to provide experience of the measurement method. Comparison of the measurements and numerical calculations is intended to demonstrate the appropriateness of the numerical procedures.

2. To develop laser Doppler velocimetry for the measurement of the

velocity of blood flowing in small glass capillaries and in venules; to assess the precision of measurements, and to extract from them a stress-strain relationship for use in subsequent blood flow numerical computations.

3. To extend numerical methods to allow the solution of the form of the Navier-Stokes equations appropriate to the flow of water and blood (with the stress-strain relationship derived from paragraph 2) in the vicinity of axisymmetric obstructions in round pipes. To examine the consequent velocity and stress profiles and to make derivations of relevance to physiological and to engineering fluid mechanics.

4. To repeat the work of paragraph 3 for asymmetric blockages in round pipes, thus extending the numerical methods to three-dimensional Newtonian and non-Newtonian recirculating flows.

The nature of the present investigation, therefore, demands engineering and biorheological knowledge for both its theoretical and experimental parts. This is the subject matter of the following sections.

1.2 HISTORICAL BACKGROUND

1.2.1 Engineering Background

Many engineering designs for industrial applications and control systems involve flows past bends, axisymmetric constrictions and asymmetric obstacles in pipes. Examples of flows past bends are encountered in almost every pipeline system. Axisymmetric constrictions are design elements of orifices, valves and combustion chambers. Finally, asymmetric obstacles may be found in furnaces, valves and flows past buildings.

Non-Newtonian flows of fluids and particle suspensions, which form a subject of this investigation, are also encountered in many engineering applications. Typical examples are the flow of printing inks, cement, milk, glycerine, flour, slurries, etc.

Control systems, film cooling and fluid amplifiers may involve fluid flows in limited, microscale size channels. In addition, the study of turbulence generation and structure may demand measurements in the small laminar and transition sublayers.

The direct interest of laminar flows is limited since most practical flows are turbulent. However, the growing application of general computational procedures for the prediction of practical flow situations requires testing in physically simple laminar flows. Successful predictions of laminar flows provide confidence in the numerical procedures and stimulates their extension to turbulent and reacting flows of practical importance. On the other hand, experimental knowledge of the details of the flow may assist more efficient and universal modelling.

The flow configurations of objectives 1 and 3 have been studied theoretically and experimentally but only the general characteristics are available in the literature. The problem of asymmetric obstacles in round pipes is of a three-dimensional nature and has not so far been investigated. The reasons for this omission stem mainly from the fact that appropriate theoretical and experimental techniques were unavailable.

For the case of the flow through and past bends, the available general characteristics are reviewed, for example, by Detra (1953), Ward-Smith (1963) and Rowe (1970). The details of such flows have been studied both experimentally and numerically by Gosman, Vlachos and Whitelaw (1973) in the developing laminar water flow downstream of the bend. A similar three-dimensional parabolic flow computational procedure (see Patankar and Spalding (1972)) was applied by Patankar, Pratap and Spalding (1974) to laminar flows in helically coiled pipes.

Work is more extensive in the case of the axisymmetric constriction. Johansen (1930) and Tuve and Sprenkle (1933) measured the discharge coefficients of pipe orifices for low Reynolds numbers. The first numerical solution of axially symmetric flows was that for a creeping flow in a sudden expansion presented by Thom (1932). Later, numerical work on flows with axial symmetry has been reported by, among others, Jenson (1959), Gosman et al (1969), and Runchal (1969). Macagno and Hung (1967) studied, numerically, the characteristics of a captive annular eddy in a pipe with a sudden expansion. Numerical computations of laminar tube flow through an abrupt contraction have also been presented by Christiansen, Kelsey and Carter (1972). Predictions of pipe flow with axisymmetric constrictions have been reported by Mills (1968) and Greenspan (1973).

The numerical methods of the above paragraph employed the vorticity-stream function approach. The present numerical work used primitive variables, i.e. velocities and pressure, as dependent variables and is based on a recent numerical approach for solving in axisymmetric recirculating flows reported by Gosman and Pun (1974). However, a vorticity-stream function numerical method developed for a water filtration problem (Vlachos and Lekkas (1977)) produced similar results to the velocity-pressure method. The major advantage of the latter is the ease in the interpretation of the results and the implementation of the boundary conditions.

Computational and experimental research in non-Newtonian fluids is growing rapidly because of their direct relevance to practical problems. Work on this topic has been reported, for example, by Halmos, Boger and Cabelli (1975) on the behaviour of power law fluids through a sudden axisymmetric expansion and by Vlachopoulos and Stournaras (1975) on non-Newtonian jets. Laminar flows with non-Newtonian fluids represented by Casson's law of viscosity are being studied by Shah (1975).

The lack of measuring techniques for low speed flows has impaired the detailed experimental investigation of two- and three-dimensional laminar flows. This is mainly due to the fact that most available methods require the insertion of measuring probes which disturb the local characteristics of low speed flows. In addition, microscopic probes for miniature flows are difficult, if impossible, to construct. The non-invasive character of laser Doppler velocimetry offers a suitable technique to provide the experimental information needed.

With the advent of laser beams (Dicke (1958), Prokhorov (1958), and Schawlow and Townes (1958)) the engineering field of optics has been greatly expanded. Among the applications of coherent light beams, laser Doppler velocimetry has offered a new measuring technique in fluid mechanics.

Since Yeh and Cummins (1964) first demonstrated that measurements of local instantaneous velocities, as low as 0.07 mm/sec, could be obtained by use of coherent beams, laser Doppler velocimetry has expanded to cover many industrial and medical applications. Its fast development and wide application made it competitive and, in some cases, superior to other modern measuring techniques. It favourably compares with the hot wire anemometry method developed in the last two decades.

Since the first demonstration of the technique, research has been directed (Whitelaw (1975)) towards a better understanding of its principles and its application to a wider range of flow situations. The design of integrated optical units, the development of suitable Doppler signal processing systems, and the estimation of measurement errors have all progressed rapidly.

The principles of LDV have been described, for example, by Goldstein and Kreid (1967), Lading (1971), Durst and Whitelaw (1971a,1973), Blake and Jespersen (1972), Drain (1972), George and Lumley (1973), and Durst, Melling and Whitelaw (1976).

The capabilities of the method have been demonstrated by its wide application to a variety of industrial, medical and laboratory produced flows. Turbulent water flows have been measured, for example, by Goldstein and Hagen (1967), Greated (1970a,1970b), Berman and Dunning (1973), and Bedi and Thew (1973); turbulent air jets by Huffaker et al (1969), and Durao (1976); oscillatory water flows by Denison and Stevenson (1970); turbulent pipe flows of polymer solution by Rudd (1972). Supersonic flows have been measured by, among others, Jackson and Paul (1971), Yanta et al (1971), and Pfeifer and Vom Stein (1973); recirculating air flows by Durst, Melling and Whitelaw (1974); combusting flows by Baker Hutchinson and Whitelaw (1974), and Durao and Whitelaw (1974a). Measurements of laminar water flow in small glass tubes (ca. 5 mm) have been reported by Kawata et al (1971), and in glass capillaries (ca. 100 μm) by Vlachos and Whitelaw (1974).

Work on LDV optical configurations has been reported, for example, by Greated (1971), Durst and Whitelaw (1971b), Wang (1972), and Brayton, Kalb and Crosswy (1973).

Electronic signal processing systems for laser Doppler velocimetry have also been examined. For example, measurements with frequency analysis have been reported by Adrian and Goldstein (1971), and Asalor (1973); with frequency trackers by Mazumder (1972), Durao and Whitelaw (1974b), and Melling (1975a). Durrani and Greated (1974a) and Durrani, Greated and Wilmshurst (1973) have presented an analysis of LDV tracking systems. Work on frequency counting has been reported by Wilmshurst, Greated and Manning (1971), Brayton, Kalb and Crosswy (1973), Vlachos and Whitelaw (1974), and Durao (1976); and with photon correlators by Pike (1972). A statistical analysis of LDV measurements employing the photon correlation technique is given by Durrani and Greated (1974b).

Finally, work on error estimation has been presented by Edwards et al (1971), Greated and Durrani (1971), Goldstein and Adrian (1971), Adrian (1972), McLaughlin and Tiederman (1973), George and Lumley (1973), Hanson (1973), Kreid (1974), Vlachos and Whitelaw (1974), and Owen and Rogers (1975); statistical analyses of laboratory and computer simulated Doppler signals have been presented by Durrani and Greated (1973), and Durrani, Greated and Wilmshurst (1973).

However, there is not much work reported in the literature concerning flows in small size channels and, thus, much remains to be done to cover this field of LDV applications. The requirement of high measurement resolution demands an extensive investigation of the design and performance characteristics of the LDV suitable for miniature size channels. This is one of the tasks of the experimental work reported in this thesis.

1.2.2 Biorheological Background

The episodes of heart attacks, atheroscleroses, and thromboses, where malfunctions of the cardiovascular system seem to be the main cause, have reached high proportions today (Spain (1966)). One of the most important aspects of the complex human recirculatory system (Rodkiewicz and Roussel (1973)) is the flow of blood in the vascular tree and, thus, it has become desirable to understand qualitatively and quantitatively both its microscopic and macroscopic characteristics. For this reason, this introductory section reviews the known properties of blood flow and the subsequent phenomena which fall within the scope of the present investigation.

The engineering and physical sciences have substantially contributed to the understanding of the flow properties of biological fluids, especially blood, and a collaboration between engineers and medical scientists is essential for successful applications; the complexity of living organisms and biological fluids should always be considered when designing medical equipment or experiments involving physiological fluids.

The flow of blood in the vascular bed of man is reported to be of pulsatile particulate nature (Bugliarello and Sevilla (1970); Aroesty and Gross (1972)). However, in the remote sites of the vascular tree, blood may be considered to flow in a steady fashion. The flow in most situations is reported to be of laminar nature but there are regions where the local conditions may produce turbulence (Munter and Stein (1973)).

The properties of human blood are important to this investigation and relevant comments, therefore, follow. They are intended to assist the reader to understand related comments in later chapters and to appreciate the complexity of the fluid.

Human blood is a suspension of particles in a complex aqueous continuous phase called plasma which contains inorganic and organic molecules. Almost 97% of the particulate phase consists of red blood cells, the others being white blood cells and platelets. Red blood cells are biconcave in shape with a diameter between 7 - 8 μm and thickness of 2 - 3 μm. White blood cells are of spherical shape with a diameter of 8 - 11 μm. Platelets are amorphous and their dimensions range between 2 - 3 μm. In a normal human blood there are 5,000,000 red blood cells, 5,000 white cells and 250,000 platelets per mm^3. The volume fraction of red blood cells, called the haematocrit, is about 42 - 45%. They are also called erythrocytes and consist of a thin membrane with an interior filled with a complex aqueous solution, which is a saturated haemoglobin compound. The red blood cell membrane is basically unstretchable but it may show a certain degree of flexibility. In normal blood, erythrocytes tend to aggregate and form rouleaux under very low shear.

The immense variety and complexity of blood behaviour confronted the scientists with a real challenge. Poisseuille was the first to investigate the subject and his research was of fundamental importance in the establishment of the causes and effects of fluid flow. There is no experimental evidence that the rheological properties of blood are time or history dependent*. In addition, there are no normal stress effects demonstrated and the compressibility of blood has been found to be the same as that of distilled water and independent of haematocrit (Sacks and Tickner (1968)). Its average density is of the order of 1.055 and its average viscosity three times that of water. However, the viscosity of blood reduces with capillary radius for radii below 300 μm (Fahrheus and Lindqvist (1931)).

Considering its rheological properties, blood cannot be treated

---

* This may not be true for blood outside the living body.

as a continuum without loss of generality, especially when the diameter of the containing vessels is less than 50 - 100 times the cell diameter (Cokelet (1963)).

It has been reported that blood possesses Newtonian properties when flowing fast or in large vessels, and non-Newtonian when flowing slowly or in small venules (for example, Charm and Kurland (1974)). The range of vessel diameters considered in this thesis (60 - 250 μm) falls within the range where blood attains non-Newtonian behaviour. From the possible non-Newtonian laws reported in the literature for blood viscosity, a power-law is selected here and justification for this selection is described in Chapter 3 when it is used in the relevant calculations.

From all cardiovascular diseases, atherosclerosis and thrombosis seem to be the most determining for the healthy state of the recirculatory system of humans and animals. Contributions to the physical aspects of both can be made through the combined use of laser Doppler velocimetry and numerical solution methods.

Atherosclerosis involves various type of tissue changes. It mainly begins with the deposition of lipoids, such as cholesterol, from the blood stream on the inner layer of the arterial wall. By penetrating the layer, they form plaques which thicken the wall and thus narrow the blood channel. It becomes apparent that continuation of this process may lead either to a total blockage of the arteries or pieces of the plaques may break loose and block smaller arteries as they are carried downstream by the flowing blood. A blockage occurring in the coronary artery results in a heart attack; in the brain, in a cerebral stroke; in the terminal arteries, in a gangrene (Spain (1966)). Although atherosclerosis is under investigation, its aetiology is described by a few theses; these are reviewed, for example, by Constantinides (1965). High blood pressure and cholesterol concentration may result in the formation of artheromatic lesions. In addition, turbulence may also induce thrombosis and atherosclerosis (Wesolowski et al (1962)) and wall damage (Fry (1968)). Rodkiewicz (1975) postulated that the atherosclerotic formations of the aortic arch commence and develop at the locations where there are separation and stagnation points. Caro et al (1971) suggested that the distribution of early atheroma in man is coincident with those regions where the arterial wall shear stress is expected to be relatively low, while the development of lesions is inhibited or retarded in those regions where wall shear stress is expected to be relatively high.

Thrombosis involves that abnormality of the recirculating system where blood has the tendency to clot or form thrombi. The complex mechanism of blood clotting commences with protein deposition and platelet adhesion. It proceeds through many stages to build up a thrombus containing a protein network, platelets and trapped cells. Platelets form the basis for the development of thrombi and possible pathways may include:

- An abnormality in the platelets themselves
- Changes in the endothelial wall of the blood vessels
- Changes in plasma composition
- Changes in blood viscosity
- Changes in the flow of blood

In healthy humans and animals, formed blood elements tend to separate from each other and do not stick in healthy normal endothelium. Red cells from a healthy animal are known to carry a small negative electric charge and, *in vivo*, repel each other (Kniseley (1965)).

The complete occlusion of a vessel by a thrombus implies that blood is not delivered to the corresponding tissues; subsequently, degenerative processes occur (Mason-Guest (1965)). If a thrombus is formed in the major vessel supplying a vital organ, death results from failure of that organ to perform its function. However, many thrombi are not the cause of fatal processes and the organism can copy with the circulatory defect. However, some reversible or irreversible changes occur to the tissues affected; these depend upon the extent of the defect and the regenerative processes.

Understanding of the mechanism by which platelets form adhesive aggregates at sites of damage, whether through disease or injury, is increasing rapidly (Begent and Born (1970); Atherton and Born (1972,1973)). In addition, the discovery that the reactivity of platelets can be inhibited by specific chemical agents in low concentrations formed the basis for chemical trials of drugs for the prevention or treatment of thrombosis.

Platelet aggregation is also a major problem in the design and use of artificial organs. Thus, acute rejection episodes after renal transplants are due to blockage of the small arteries supplying the grafts by platelet aggregates. Similar problems are encountered in the design of artificial oxygenators. Clinically, there is evidence indicating that platelets, as well as plasma constituents, are deposited at sites where local velocity changes are such that laminar flow becomes turbulent.

Embolism may be a consequence of thrombosis, where a thrombus detaches and is carried downstream to a new location. Most venous emboli lodge in the pulmonary vascular bed where a progressive decrease of the vessel diameter is observed. Embolism in the more peripheral vessels is less critical than in the pulmonary vessels. The latter may result in a decrease of the blood supply to the heart to critical levels.

Recirculation of blood elements, lipoids and colloids may be the result of reduction of blood flow or complete stasis; the decrease or absence of shearing forces may allow the formation of aggregates. Thus, slowing of the circulation has been considered to be an important thrombogenetic cause, especially in the venous system. Adhesion to blood vessels and losses through wall permeability changes may alter the local cell concentration and affect their flow and aggregation characteristics.

Another abnormality of the recirculatory system of relevance to the present investigation is haemolysis. The term haemolysis implies the escape of a considerable portion of the intracellular contents of the red cells into the bloodstream. This may occur as a result of disease or may be triggered by haemodynamic forces exerted on the cell membrane. The intracellular contents, mainly haemoglobin, may form deposits on the kidney tubules and restrain the urine passage (Green (1968)). Thus, haemolysis is considered dangerous because of the deleterious effect of haemoglobin outside the red cell.

So far, there has been no exact quantitative analysis of the above phenomena, mainly because, until recently, there were no available theoretical and experimental methods. It seems likely that the flow properties of blood cause damage to the circulating blood elements (erythrocytes, leucocytes and platelets) as well as to the vascular endothelium. However, there have been no experimental means for testing these assumptions.

This state of affairs is now changing with the availability of delicate methods for observing damages to blood constituents. Platelet thrombogenesis can be measured by the technique of iontophoresis of a thrombogenetic stimulus (mainly ADP: adenosine diphosphate) to the outside of normal blood vessels (Begent and Born (1970); Atherton and Born

(1972,1973)).

The obstruction of arteries and veins caused by physiological and pathological processes can, in many circumstances, cause flow separation and stagnation and consequently affect the rheological properties of blood. The problem becomes more complicated if account is taken of the fact that the blood vessels are not rigid but possess the ability to expand or contract according to the dynamic load imposed on them within the heart cycle. The elasticity of the vessels is greatly reduced by atherosclerotic formations.

With the availability of numerical methods for flow computations, the above phenomena may be investigated and qualitative and quantitative conclusions drawn. However, the modelling of blood flow requires a detailed knowledge of its rheological properties, which are not, at present, fully explored. Most of the information has been obtained from *in vitro* experiments and it remains to determine whether the *in vitro* biorheological properties of blood (for example, the formation of platelet thrombi (Begent and Born (1970)) account for *in vivo* blood flows. It becomes apparent, therefore, that measurements are necessary both *in vitro* and *in vivo* to allow the determination of the stress-strain relationship as a function of haematocrit and other blood properties. The magnitude of the local stress, in the vicinity of coagulations and bifurcations, is also required since high values can damage the cells and promote coagulations. In general, the present approach is to attempt to determine the stress-strain relationship from measurements and to use it in the conservation equation appropriate to the relevant flow configurations, which are solved numerically.

Computational work on fluid-dynamical contributions to atherosclerosis in arterial branchings have been reported by Lynn, Fox and Ross (1972). Their results may explain the migration of suspended particles to the outer wall of the branching.

Measurements on model stenoses and thrombi in laminar and turbulent flows have been reported by Young and Tsai (1973). They showed that the flow is strongly influenced by the geometry, size and shape of the stenoses.

In vitro measurements of blood flow have been carried out in the past using optical methods. For example, Bugliarello and Hayden (1962) and Goldsmith (1967) used high speed microcinephotography to study the flow of blood in glass capillaries and Bugliarello and Sevilla (1970) extended it to pulsatile blood flows. They reported a blunt profile for low shear rates and a parabolic profile for high shear. A radial migration of red blood cells towards the axis of the capillary and a cell depleted zone near the wall were also observed*. Bennet (1968) observed with a microscopic interferometer the near wall continuous velocity profile of blood flowing in small glass capillaries. However, these methods required considerable time to extract the velocity information.

The simplicity and non-invasive character of laser Doppler velocimetry offered a challenge for its application to blood flows in small channels, both *in vitro* and *in vivo*. The flow of ghost red blood cells has been investigated with LDV by Kreid and Goldstein (1971) and DiGiovanni and Einav (1974) who reported a blunt velocity profile. Measurements of diluted and whole blood flow in small glass capillaries has been reported by Vlachos and Whitelaw (1974), Mishina, Asakura and Nagai (1974), Born, Vlachos and Whitelaw (1975), and Einav et al (1975a).

Early *in vivo* blood flow work involved the measurement of the

---

* This is in agreement with similar observations of Segré & Silberberg (1962).

bulk velocity by the use of thermodilution, thin film gauges, isotopes, electromagnetic meters and ultrasonics. Monro (1964) and Berman and Fuhro (1969) used a rotating prism positioned at the optical axis of a microscope to observe the flow of blood in arterioles of the hamster cheek pouch.

The possibility of obtaining Doppler signals from *in vivo* blood flows was demonstrated by Durst (1972). Riva, Ross and Benedek (1972) obtained Doppler spectra in glass capillaries with whole blood and a characteristic Doppler spectrum in the retinal arteries of the rabbit. Mishina, Asakura and Nagai (1974) and Mishina, Koyama and Asakura (1975) obtained Doppler spectra in blood vessels of 70 μm in diameter, and a representative Doppler spectrum in 10 μm capillaries in the web of a frog, which indicated the response of the heart to various stimuli. *In vivo* measurements have also been reported by Einav et al (1975a,b) in blood vessels of the order of 65 - 95 μm in the hamster cheek pouch.

In spite of the measurements reported in the literature, much remains to be done to develop an LDV suitable for these flows. The purpose of the experimental work reported in this thesis is to quantify the extent of measurement localisation that can be achieved by LDV, to determine and quantify related problems, and to propose a potential design for *in vivo* blood flows.

1.3 OUTLINE OF THESIS

The rest of the thesis is divided into three chapters. The computational investigation of the problems outlined in this introduction are described in Chapter 2. In section 2.2, the governing flow equations of three-dimensional parabolic, two- and three-dimensional recirculating flows are presented in forms appropriate to the present purposes. Non-Newtonian fluids are included and a constitutive equation for blood is established. This equation is based on past experimental and theoretical work as well as experimental work reported in this thesis. The numerical aspects of three-dimensional parabolic flows are presented and discussed in section 2.3; those for two-dimensional recirculating flows in section 2.4; and for three-dimensional recirculating flows in section 2.5. Computational results, for the flows under consideration, are presented and discussed in section 2.6. The results are examined and interpreted from the engineering and biorheological viewpoint, in terms of the useful information for engineering designs and the study of atherosclerosis, haemolysis, thrombosis, and embolus formation.

In Chapter 3, the experimental investigation is described. First, a brief introduction to laser Doppler velocimetry, as a velocity measuring technique, is presented in section 3.2. Measurements in medium size channels are presented and discussed in section 3.3. The experimental work on the laminar water flow past a 15^{o} bend in a round pipe is presented and discussed in this section. A Doppler signal processing system employing a computing counter to record the frequency of the burst and a numerical procedure to estimate the size of the control volume and the broadening due to velocity and concentration gradients are also presented and discussed.

A study of the design and operation parameters of laser Doppler velocimeters, especially those resulting in a miniature control volume, is also described in section 3.4. Measurements of glass capillary flows of water, plasma, diluted and whole blood are presented and discussed in section 3.5. Various problems pertinent to the application of the technique to flow measurements in small channels are analysed, and recommendations for their solution based on experience with the technique are given. A derivation of an appropriate blood viscosity law for the numerical computations is presented in section 3.6.

A proposal for a laser Doppler velocimeter incorporated into a microscope is followed through its stages in section 3.7; design aspects are discussed. Attempts to measure the flow of blood in the venules of living animals are described in section 3.8.

Finally, in Chapter 4 a general discussion and evaluation of the present work, from both the engineering and biorheological viewpoint, is presented and conclusions are drawn. Recommendations for further work form a brief closure to this thesis.

CHAPTER 2

COMPUTATIONAL INVESTIGATION

2.1 INTRODUCTION

2.1.1 Objectives

The fundamental laws governing the transfer of matter, momentum and heat of a fluid flowing in a confined or free space may be described by partial differential equations. In principle, the velocity, pressure and local stress characteristics of any fluid flow configuration can be determined from the solution of the governing equations together with the appropriate boundary conditions. In many cases, reduced forms of the Navier-Stokes equations can adequately represent the flow under consideration and can be solved more readily and easily than the complete set of equations. In this chapter, reduced forms of the Navier-Stokes equations are used to represent the flow in the neighbourhood of three geometric arrangements, corresponding to the steady laminar developing flow of a fluid downstream of a bend and through round tubes with axisymmetric and asymmetric blockages. The partial differential equations appropriate to these flows are, respectively, three-dimensional parabolic, two-dimensional elliptic and three-dimensional elliptic in form* and are solved numerically.

In flows where a linear stress-strain relationship does not apply, an appropriate form must be obtained and the flow equations adjusted accordingly. The equations corresponding to the two blockage problems mentioned in the previous paragraph and to a non-Newtonian stress-strain

---

* For the classification of partial differential equations see, for example, Richtmyer (1957), Forsythe and Wasow (1960), Smith (1965) or Ames (1969).

relationship, determined with the assistance of the experiments of Chapter 3, have also been solved and are relevant to the flow of blood in small tubes and venules. For the parabolic flow problem, the equations are intended to include non-Newtonian fluids.

The geometrical arrangements considered here, and the corresponding flow boundary conditions, necessitate the use of numerical solution procedures based on finite-difference methods. Those used for the solution of three-dimensional parabolic and two-dimensional elliptic flow equations are based on the previous work of Patankar and Spalding (1972) and of Gosman and Pun (1974), respectively. The procedure used for the solution of three-dimensional elliptic flow equations was developed specifically for this purpose although it has features in common with the two-dimensional method of Gosman and Pun (1974).

The flows considered in this thesis are of engineering importance, since they are encountered in many practical designs. From the biorheological viewpoint, their importance is related to the flow of blood in the vascular bed, where knowledge of the characteristics of the flow in arterial branchings, aortic stenoses and vascular thrombi may assist the understanding of atherosclerotic plaque formation and thrombi growth.

The objectives of the work described in this chapter may, therefore, be stated as follows:

1. To modify and apply an existing calculation procedure for the prediction of the flow of Newtonian fluids downstream of a 15^{o} bend in a round tube; to compare the predicted results with the experiments of Chapter 3, and to assess the validity of the numerical method; to extend the procedure to cover flows of non-Newtonian fluids, such as blood; to determine

the maximum and minimum values of local shear stress in the flow.

2. To modify and apply an existing numerical scheme for the prediction of the flow in round tubes with axisymmetric blockages of different shapes; to extend the numerical scheme to flows of fluids with a non-Newtonian stress-strain relationship; to determine the influence of non-Newtonian fluid flows corresponding to the blood flow of Chapter 3; and to predict the overall drag force on the blockage and the maximum and minimum values of local shear stress in the flow.
3. To develop and apply a calculation procedure for the solution of the flow in a round tube with asymmetric blockages of different shapes; to extend the procedure and determine the influence of a non-Newtonian stress-strain relationship corresponding to the blood flow of Chapter 3; and to determine the overall drag force on the blockage and the maximum and minimum values of local shear stress in the flow.

In each of the above three purposes, the ability of the numerical schemes to produce economic, grid-independent solutions will be demonstrated and the engineering significance of the results discussed. In all three objectives, the implications of the results for the flow of blood in vessels are of particular interest.

The three numerical procedures reported here have common features regarding the numerical approximation, solution of the resulting matrix equations, convergence criteria, economy and accuracy of the solution, etc. These are reviewed in the following section to avoid repetition when the numerical aspects of the procedures are treated separately.

2.1.2 Outline of Chapter

The rest of this chapter is divided into five major sections. The general flow equations and the numerical method used for their solution are presented in section 2.2. In section 2.3, the numerical procedures for the prediction of parabolic flows are presented. The numerical schemes for the calculation of axisymmetric steady recirculating flows are described in section 2.4. A three-dimensional numerical scheme for recirculating flows is discussed in detail in section 2.5.

Finally, section 2.6 presents numerical computations and discussions of the following fluid flows:

(a) Laminar developing water flow downstream of a 15^{0} bend in a round tube.

(b) Laminar water flow in a round pipe with an axisymmetric constriction.

(c) Laminar non-Newtonian blood flow in the vicinity of an aortic stenosis.

(d) Laminar water flow in a round pipe with an asymmetric obstacle.

(e) Laminar non-Newtonian blood flow in the vicinity of a thrombus in a venule.

2.2 THE MATHEMATICAL PROBLEM

2.2.1 Introduction

Before the general form of the flow equations is introduced, it is necessary to state the basic concepts and assumptions used for their derivation:

It is common practice in science and engineering to consider matter, in this case the fluid undergoing flow, as a continuum, i.e. a hypothetical structureless substance to which, at any point, kinematical or dynamical variables are assigned.

In order to accommodate the observed phenomena, a number of coefficients must be inserted into the equations derived by the continuum method. In general, these coefficients can be derived from the molecular theory of matter. In practice, however, they are usually obtained from observed phenomena.

It is obvious that there are conditions under which any flow modelling, based on a continuum hypothesis, will be grossly incorrect. This may be true especially in the case of blood flowing in small diameter vessels where it is possible for the continuum approach to fail, because the particulate nature of blood cannot be neglected completely. Although the phenomena observed here are due to the particulate rather than the molecular structure of blood, their explanations are based on the same reasoning. The relatively small size of the vessels, however, does not allow blood to be treated as structureless without limitations.

In the case of Newtonian fluids, the continuum approach has long been accepted as adequate. For non-Newtonian fluids, like blood, the proper coefficients may be derived from experimental observations and the necessary limitations of the present model may be stated.

The constitutive equation of a fluid, i.e. the relationship between its dynamical state at some instant, the kinematical state at the same instant and perhaps its kinematical state in the past, which is also called the rheological equation of state, is influenced by its thermodynamic state. For example, viscosity, a typical coefficient appearing in the constitutive equation of a fluid, is a function of temperature and pressure.

To derive the flow governing equations, three of the basic concepts of fluid mechanics are used, namely, mass, linear momentum and enthalpy conservation for a closed system. There are two basic representations for the equations of hydrodynamics, namely, the Langragian and Eulerian representations. In the first, for each fixed element of the fluid, the equations are solved to obtain the velocity, acceleration, and position of the element, pressure, density, energy, etc., as a function of time. There are certain difficulties in the solution of flow problems using the Langragian method of representation, especially when the fluid undergoes violent distortion as in the cases of recirculating or turbulent flows. Thus, the present work makes use of the Eulerian approach for the determination of the state of the flow. Here, the governing equations are solved for the velocity, acceleration, pressure, density, energy, etc., for fixed positions of the coordinate system of Euclidean space.

2.2.2 The General Flow Equations

For any given point,P,in a steady laminar flow, the flow properties may be determined by simultaneous solution of the mass and linear momentum conservation equations. These equations may be expressed, in tensor form, as follows:

Mass conservation equation:

$$\nabla \cdot \rho V_i = 0 \qquad (2.2.2\text{-}1)$$

where ρ is the density and V_i is the velocity vector of the flowing fluid at the point P.

Momentum conservation equation:

$$\nabla \cdot \rho V_i V_j = - \nabla \cdot \tau_{ij} - \nabla p + f_i \qquad (2.2.2\text{-}2)$$

where τ_{ij} is the stress tensor, p the static pressure, and f_i any acting body force.

The symbols $\nabla.\rho V_i V_j$ and $\nabla.\tau_{ij}$ in equation (2.2.2-2) are not single divergences because of the diadic and tensorial form of $\rho V_i V_j$ and τ_{ij}. They are given by relationships of the following form, for cartesian coordinates (see Bird et al (1960)or Vavra (1960)):

$$\nabla \cdot \rho V_i V_j = \sum_i \sum_j \left[\frac{\partial}{\partial x_i} (\rho V_i V_j) \cdot x_i\right] \qquad (2.2.2\text{-}3)$$

and:

$$\nabla \cdot \tau_{ij} = \sum_i \sum_j \left[\frac{\partial}{\partial x_i} (\tau_{ij}) \cdot x_i\right] \qquad (2.2.2\text{-}4)$$

where x_i are the unit vectors of the coordinate system.

Similarly, the general property ϕ, which can be convected and diffused, may be determined by simultaneous solution, with the previous equations, of the general ϕ-property conservation equation, written as follows:

$$\nabla \cdot \rho V_i \phi = - \nabla \cdot J_{\phi,i} + g_\phi \qquad (2.2.2\text{-}5)$$

where $J_{\phi,i}$ = the diffusion flux of ϕ

g_ϕ = generation of ϕ

In this equation, ϕ can represent enthalpy, species concentration, etc. Although scalar fields are not predicted in the present work, reference to equation (2.2.2-5) is made here to demonstrate its similarity to equation (2.2.2-2). This similarity allows for the extension of the numerical procedures reported here to include the equations for scalar properties.

The reduced form of these equations appropriate to the three flow configurations, referred to in section 2.1, needs to be established in order to provide a starting point for the numerical integration procedures to be discussed in the following sections. These are as follows:

(a) Three-dimensional boundary-layer flows

A flow is referred to as boundary-layer (or parabolic) if its nature allows the following assumptions to be made:

1. A predominant direction of the flow exists, i.e. there is no reverse flow in this direction.
2. The diffusion of mass, momentum, heat, etc., is negligible in this direction.
3. The downstream pressure field has little or no influence on the upstream flow conditions.

Under these assumptions, the reduced forms of the general flow equations, for a cartesian coordinate system, may be written as follows:

Mass conservation equation:

$$\frac{\partial}{\partial x}(\rho u) + \frac{\partial}{\partial y}(\rho v) + \frac{\partial}{\partial z}(\rho w) = 0 \qquad (2.2.2\text{-}6)$$

u-momentum conservation equation:

$$\underbrace{\frac{\partial}{\partial x}(\rho u u) + \frac{\partial}{\partial y}(\rho v u) + \frac{\partial}{\partial z}(\rho w u)}_{\text{convection terms}} - \underbrace{\left[\frac{\partial}{\partial y}\left(\eta \frac{\partial u}{\partial y}\right) + \frac{\partial}{\partial z}\left(\eta \frac{\partial u}{\partial z}\right)\right]}_{\text{diffusion terms}} =$$

$$\underbrace{-\frac{\partial \bar{p}}{\partial x}}_{\text{pressure force}} + \underbrace{f_x}_{\text{body force}} \qquad (2.2.2\text{-}7)$$

v-momentum conservation equation:

$$\frac{\partial}{\partial x}(\rho uv) + \frac{\partial}{\partial y}(\rho vv) + \frac{\partial}{\partial z}(\rho wv) - \left(\frac{\partial}{\partial y}(\eta\,\frac{\partial v}{\partial y}) + \frac{\partial}{\partial z}(\eta\,\frac{\partial v}{\partial z})\right) =$$

$$-\frac{\partial p}{\partial y} + f_y + \left[\frac{\partial \eta}{\partial y}\cdot\frac{\partial v}{\partial y} + \frac{\partial \eta}{\partial z}\cdot\frac{\partial w}{\partial y}\right] \qquad (2.2.2\text{-}8)$$

w-momentum conservation equation:

$$\frac{\partial}{\partial x}(\rho uw) + \frac{\partial}{\partial y}(\rho vw) + \frac{\partial}{\partial z}(\rho ww) - \left(\frac{\partial}{\partial y}(\eta\,\frac{\partial w}{\partial y}) + \frac{\partial}{\partial z}(\eta\,\frac{\partial w}{\partial z})\right) =$$

$$-\frac{\partial p}{\partial z} + f_z + \left[\frac{\partial \eta}{\partial y}\cdot\frac{\partial v}{\partial z} + \frac{\partial \eta}{\partial z}\cdot\frac{\partial w}{\partial z}\right] \qquad (2.2.2\text{-}9)$$

ϕ-property conservation equation:

$$\frac{\partial}{\partial x}(\rho u\phi) + \frac{\partial}{\partial y}(\rho v\phi) + \frac{\partial}{\partial z}(\rho w\phi) - \left(\frac{\partial}{\partial y}(\gamma_\phi\,\frac{\partial \phi}{\partial y}) + \frac{\partial}{\partial z}(\gamma_\phi\,\frac{\partial \phi}{\partial z})\right) = g_\phi \qquad (2.2.2\text{-}10)$$

In these equations, the viscosity η is variable and may be Newtonian or non-Newtonian. If the viscosity η were constant, the terms in $\left[\ \right]$ brackets vanish. The coefficient γ_ϕ of equation (2.2.2-10) is the diffusion coefficient of ϕ. The axis x is aligned with the dominant direction of the flow, and axial diffusion has been neglected since there are no second order derivative terms in the x-direction. Furthermore, it is recognised that there is no flow reversal and no transmission upstream of downstream influences. The latter implies that the pressure gradient in the x-momentum equation may be taken as uniform over the cross-section and this is why the overbar has been used in the pressure term of the u-momentum differential equation.

These simplifications suggest that the governing differential equations of the flow are rendered parabolic with respect to the dominant direction x. It becomes possible, therefore, to employ a solution procedure of the forward-marching kind, which commences from a given set of initial conditions in the cross-stream plane and advances downstream in the dominant x-direction. This procedure will be discussed in section 2.3.

(b) Axisymmetric recirculating flows

The reduced form of the differential equations describing an axisymmetric, recirculating (elliptic) flow may be written as follows:

Mass conservation equation:

$$\frac{1}{r}\left[\frac{\partial}{\partial x}(r\rho u) + \frac{\partial}{\partial y}(r\rho v)\right] = 0 \qquad (2.2.2\text{-}11)$$

u-momentum conservation equation

$$\underbrace{\frac{1}{r}\left[\frac{\partial}{\partial x}(r\rho uu) + \frac{\partial}{\partial y}(r\rho vu)\right]}_{\text{convection terms}} - \underbrace{\frac{1}{r}\left[\frac{\partial}{\partial x}\left(r\,\eta\,\frac{\partial u}{\partial x}\right) + \frac{\partial}{\partial y}\left(r\,\eta\,\frac{\partial u}{\partial y}\right)\right]}_{\text{diffusion terms}} =$$

$$\underbrace{-\frac{\partial p}{\partial x}}_{\text{pressure term}} + \underbrace{f_x}_{\text{body force term}} + \underbrace{\left[\frac{\partial \eta}{\partial x}\cdot\frac{\partial u}{\partial x} + \frac{\partial \eta}{\partial y}\cdot\frac{\partial v}{\partial x}\right]}_{\text{extra variable-viscosity diffusion terms}} \qquad (2.2.2\text{-}12)$$

v-momentum conservation equation:

$$\frac{1}{r}\left[\frac{\partial}{\partial x}(r\rho uv) + \frac{\partial}{\partial y}(r\rho vv)\right] - \frac{1}{r}\left[\frac{\partial}{\partial x}(r\ \eta\ \frac{\partial v}{\partial x}) + \frac{\partial}{\partial y}(r\ \eta\ \frac{\partial v}{\partial y})\right] =$$

$$-\frac{\partial p}{\partial y} + f_y + \left[\frac{\partial \eta}{\partial x}\cdot\frac{\partial u}{\partial y} + \frac{\partial \eta}{\partial y}\cdot\frac{\partial v}{\partial y}\right] - \left\{\frac{\eta\ .\ v}{r^2}\right\} \qquad (2.2.2\text{-}13)$$

ϕ-property conservation equation:

$$\frac{1}{r}\left[\frac{\partial}{\partial x}(r\rho u\phi) + \frac{\partial}{\partial y}(r\rho v\phi)\right] - \frac{1}{r}\left[\frac{\partial}{\partial x}(r\ \gamma_\phi\ \frac{\partial \phi}{\partial x}) + \frac{\partial}{\partial y}(r\ \gamma_\phi\ \frac{\partial \phi}{\partial y})\right] = g_\phi \qquad (2.2.2\text{-}14)$$

where x is the axial coordinate and r and y refer to the radial coordinate. If r is taken as unity, and the term $\{\eta.v/r^2\}$ vanishes, the equations relate to a two-dimensional plane flow and the independent variables relate to rectangular cartesian coordinates.

For constant viscosity fluids, the extra variable-viscosity terms $\left[\partial\eta/\partial x.\partial u/\partial x + \partial\eta/\partial y.\partial v/\partial x\right]$ and $\left[\partial\eta/\partial x.\partial u/\partial y + \partial\eta/\partial y.\partial v/\partial y\right]$ vanish. The numerical procedure for the solution of these kinds of equations will be discussed in section 2.4.

(c) Three-dimensional recirculating flow

The differential equations describing a three-dimensional laminar recirculating (elliptic) flow may be written in a general form as follows:

Mass conservation equation:

$$\frac{1}{r}\left[\frac{\partial}{\partial x}(\rho u) + \frac{\partial}{\partial y}(r\rho v) + \frac{\partial}{\partial z}(r\rho w)\right] = 0 \qquad (2.2.2\text{-}15)$$

u-momentum conservation equation:

$$\frac{1}{r}\left[\frac{\partial}{\partial x}(\rho uu) + \frac{\partial}{\partial y}(r\rho vu) + \frac{\partial}{\partial z}(r\rho wu)\right]$$

convection term

$$-\frac{1}{r}\left[\frac{\partial}{\partial x}(\eta\,\frac{\partial u}{r\,\partial x}) + \frac{\partial}{\partial y}(\eta\, r\,\frac{\partial u}{\partial y}) + \frac{\partial}{\partial z}(\eta\, r\,\frac{\partial u}{\partial z})\right] \quad = \quad -\frac{\partial p}{r\,\partial x} \quad + \quad f_x$$

diffusion terms — pressure force — body force

$$+ \quad \left\{\frac{2\eta}{r^2}\cdot\frac{\partial v}{\partial x} - \frac{\eta u}{r^2}\right\} \quad - \quad \left\{\frac{\rho vu}{r}\right\}$$

extra diffusion terms (for cylindrical coordinates) — Coriolis force (for cylindrical coordinates)

$$+ \left[\frac{\partial\eta}{r\,\partial x}\left(\frac{\partial u}{r\,\partial x} + \left\{\frac{2\,v}{r}\right\}\right) + \frac{\partial\eta}{\partial y}\left(\frac{\partial v}{r\,\partial x} - \left\{\frac{v}{r}\right\}\right) + \frac{\partial\eta}{\partial z}\left(\frac{\partial w}{r\,\partial x}\right)\right] \qquad (2.2.2\text{-}16)$$

extra variable-viscosity diffusion terms

v-momentum conservation equation:

$$\frac{1}{r}\left[\frac{\partial}{\partial x}(\rho uv) + \frac{\partial}{\partial y}(r\rho vv) + \frac{\partial}{\partial z}(r\rho wv)\right]$$

$$-\frac{1}{r}\left[\frac{\partial}{\partial x}(\eta\,\frac{\partial v}{r\,\partial x}) + \frac{\partial}{\partial y}(\eta\, r\,\frac{\partial v}{\partial y}) + \frac{\partial}{\partial z}(\eta\, r\,\frac{\partial v}{\partial z})\right] = -\frac{\partial p}{\partial y} + f_y + \left\{\frac{\rho u^2}{r}\right\}$$

$$-\left\{\frac{\eta v}{r^2} - \frac{2\eta}{r^2}\cdot\frac{\partial u}{\partial x}\right\} + \left[\frac{\partial\eta}{r\,\partial x}\left(\frac{\partial u}{\partial y} - \left\{\frac{u}{r}\right\}\right) + \frac{\partial\eta}{\partial y}\left(\frac{\partial v}{\partial y}\right) + \frac{\partial\eta}{\partial z}\left(\frac{\partial w}{\partial y}\right)\right] \qquad (2.2.2\text{-}17)$$

w-momentum conservation equation:

$$\frac{1}{r}\left\{\frac{\partial}{\partial x}(\rho u w) + \frac{\partial}{\partial y}(r \rho v w) + \frac{\partial}{\partial z}(r \rho w w)\right\}$$

$$-\frac{1}{r}\left\{\frac{\partial}{\partial x}(\eta \frac{\partial w}{r\,\partial x}) + \frac{\partial}{\partial y}(\eta\, r \frac{\partial w}{\partial y}) + \frac{\partial}{\partial z}(\eta\, r \frac{\partial w}{\partial z})\right\} = -\frac{\partial p}{\partial z} + f_z$$

$$+\left[\frac{\partial \eta}{r\,\partial x}(\frac{\partial u}{\partial z}) + \frac{\partial \eta}{\partial y} \cdot \frac{\partial v}{\partial z} + \frac{\partial \eta}{\partial z} \cdot \frac{\partial w}{\partial z}\right] \qquad (2.2.2\text{-}18)$$

ϕ-property conservation equation:

$$\frac{1}{r}\left\{\frac{\partial}{\partial x}(\rho u \phi) + \frac{\partial}{\partial y}(r \rho v \phi) + \frac{\partial}{\partial z}(r \rho w \phi)\right\}$$

$$-\frac{1}{r}\left\{\frac{\partial}{\partial x}(\gamma_\phi \frac{\partial \phi}{r\,\partial x}) + \frac{\partial}{\partial y}(\gamma_\phi\, r \frac{\partial \phi}{\partial y}) + \frac{\partial}{\partial z}(\gamma_\phi\, r \frac{\partial \phi}{\partial z})\right\} = g_\phi \qquad (2.2.2\text{-}19)$$

Again, if a rectangular cartesian system of coordinates is required, r may be set to unity. Then, u, v, w are the velocity components in the x, y, z-directions and the terms in $\{\ \}$ brackets vanish. When cylindrical coordinates are used:

u = circumferential velocity component (x-direction)

v = radial velocity component (y-direction)

w = axial velocity component (z-direction)

When fluids with linear stress-strain relationships are considered, the coefficient η is the Newtonian viscosity. If constant viscosity fluids are considered, the terms in $[\ ]$ brackets vanish. The numerical procedure developed for these kinds of flows is discussed in section 2.5.

2.2.3 Boundary and Initial Conditions

(a) Boundary conditions

The application of the differential equations (2.2.2-1), (2.2.2-2) and (2.2.2-5) to a flow problem necessitates the specification of the boundary conditions. When these equations are elliptic, the boundary conditions need to be specified on all sides of the boundary, while for parabolic equations, there is no need for these conditions to be specified on the forward boundary. Either the value of the variable or its normal gradient must be specified on the boundary.

The boundaries encountered in the present situations can be accommodated in the following categories: inlet sections, outlet sections, solid walls and axes or planes of symmetry. For these categories of boundaries, the conditions may be summarised as follows:

1. Inlet sections: In general, the conditions of the fluid at the inlet are supplied as part of the problem specification. For example, the velocity, pressure and temperature of the entering fluid may be given. Thus, if the independent variables are given at the inlet boundary, the dependent variables are calculated from these.

2. Outlet sections: For parabolic types of flows, the marching nature of the solution procedure does not require the outlet fluid conditions to be known. For elliptic flows, however, a boundary condition for each variable must be specified. In the problems considered here, the flow tends to be of boundary-layer nature in the downstream region and the corresponding boundary conditions do not, therefore, have a strong influence on the upstream flow. As a consequence, it is possible to specify zero or constant axial gradient conditions at a

downstream location and to show that their upstream influence is negligible.

3. Solid walls: For a solid impermeable wall, the no-slip condition implies that the tangential and normal components of the velocity must be zero. This may not be strictly true for blood flows where a slip velocity on the vessel wall has been reported.

4. Axes or planes of symmetry: By recognising that there will be no transfer of matter, momentum or heat along an axis or plane of symmetry, the appropriate boundary condition may be deduced. Thus, the normal component of velocity and the normal fluxes must be zero.

(b) Initial conditions

For the solution procedures of the type described in this thesis, it may be necessary to specify the initial conditions. Thus, for a parabolic type of flow solved by means of a forward-marching non-iterative numerical scheme, the inlet conditions of the fluid serve as initial conditions.

For an elliptic flow, the iterative nature of the solution procedure does not, in general, require the initial conditions to be specified. In practice, however, a close guess of the variable field becomes an advantage in that it enhances the convergence.

2.2.4 Auxilliary Information and Non-Newtonian Behaviour of Blood

The constitutive equation of the fluid must be known to complete the formulation of the equations of conservation of momentum. For a Newtonian fluid, this may be written as:

$$\tau_{ij} = \mu \cdot \Delta_{ij} \tag{2.2.4-1}$$

where μ is independent of the rate of strain Δ_{ij}. For the energy equation, the corresponding information may be supplied by Fourier's law:

$$q_i = k \cdot \nabla T \tag{2.2.4-2}$$

where k is the thermal conductivity of the fluid, q_i is the heat flux vector, and T the fluid temperature.

In the case of blood, a fluid of particular importance to the present work, the Newtonian viscosity law applies, except for flows in small diameter tubes. In section 3.6, a review of the known and relevant properties of blood is given. For the purposes of this chapter, it suffices to state that from all the reported viscosity laws for blood flow in small diameter tubes, the power viscosity law is selected. This law may be written as:

$$\tau_{ij} = m \cdot \Delta_{ij}^{n} \tag{2.2.4-3}$$

where m and n are independent of the rate of strain Δ_{ij}.

The derivation of the constitutive equation of blood, following the power viscosity law, may be summarised as follows (see Bird et al (1960)):

Consider blood to be a general Newtonian fluid with the following rheological relationship:

$$\tau_{ij} = \eta \cdot \Delta_{ij} \tag{2.2.4-4}$$

where the general viscosity η is a function of the rate of deformation Δ_{ij} as well as of temperature and thermodynamic pressure.

In this thesis the general viscosity η is treated as an isotropic property of the fluid. It appears, therefore, that η should be a scalar expressed as a function of the invariants of Δ_{ij}, so that it remains constant under rotation of the coordinate system.

The invariants of the tensor Δ_{ij} are:

$$I_1 = \Sigma_i \Delta_{ii} \qquad (2.2.4\text{-}5)$$

$$I_2 = \Sigma_i \Sigma_j \Delta_{ij} \Delta_{ji} \qquad (2.2.4\text{-}6)$$

$$I_3 = \Sigma_i \Sigma_j \Sigma_k \delta_{ijk} \Delta_{1i} \Delta_{2j} \Delta_{3k} \qquad (2.2.4\text{-}7)$$

where the Kronecker delta is defined as:

$\delta_{ijk} = 1$ if ijk = 123, 231, 312

$\delta_{ijk} = -1$ if ijk = 321, 132, 213

$\delta_{ijk} = 0$ if any two indices are alike

For an incompressible fluid, like blood, the invariant I_1 is zero:

$$I_1 = 2\nabla \cdot V_i = 0 \qquad (2.2.4\text{-}8)$$

and it is commonly assumed that I_3 is not very important in most of the flows. Therefore, it may be concluded that the general viscosity η is a function of only I_2:

$$\eta = f\,(I_2)$$

For these reasons, Bird et al (1960) proposed the following general constitutive equation for power law fluids:

$$\tau_{ij} = -m \cdot \left|\sqrt{I_2}\right|^{n-1} \cdot \Delta_{ij} \qquad (2.2.4\text{-}9)$$

Thus, the general viscosity η is given by the relationship:

$$\eta = m \cdot \left|\left(\tfrac{1}{2}\,\Delta_{ij} : \Delta_{ij}\right)\right|^{(n-1)/2} \qquad (2.2.4\text{-}10)$$

where m and n are independent of Δ_{ij}, and $|a|$ is the modulus of a.

For axisymmetric flows, equation (2.2.4-10) may be rewritten as follows:

$$\eta = m \cdot \left\{2\left[\left(\frac{\partial u}{\partial x}\right)^2 + \left(\frac{\partial v}{\partial y}\right)^2 + \left\{\frac{v}{r}\right\}^2\right] + \left(\frac{\partial u}{\partial y} + \frac{\partial v}{\partial x}\right)^2\right\}^{(n-1)/2} \qquad (2.2.4\text{-}11)$$

Again, the term $\{v/r\}^2$ vanishes for cartesian coordinates and x, y are the axial and radial coordinates for a cylindrical frame of reference, respectively.

For a three-dimensional flow, equation (2.2.4-10) may be written as follows:

$$\eta = m \cdot \left\{2\left[\left(\frac{\partial u}{r\,\partial x} + \left\{\frac{v}{r}\right\}\right)^2 + \left(\frac{\partial v}{\partial y}\right)^2 + \left(\frac{\partial w}{\partial z}\right)^2\right] + \left[\left(\frac{\partial v}{r\,\partial x}\right) + \left(\frac{\partial u}{\partial y}\right) - \left\{\frac{u}{r}\right\}\right]^2\right.$$
$$\left. + \left[\left(\frac{\partial w}{r\,\partial x}\right) + \left(\frac{\partial u}{\partial z}\right)\right]^2 + \left[\left(\frac{\partial w}{\partial y}\right) + \left(\frac{\partial v}{\partial z}\right)\right]^2\right\}^{(n-1)/2} \qquad (2.2.4\text{-}12)$$

where r is equal to unity and the terms in { } brackets vanish for cartesian coordinates. x, y, z are the circumferential, radial and axial coordinates for a cylindrical system, respectively.

✓ 2.2.5 The Numerical Approximation Methods

The three numerical schemes employed in this thesis make use of velocity and pressure as dependent variables which describe the hydrodynamic field, and the solution algorithms are based on Chorin's (1968) earlier suggestion.

The principle of finite-difference methods is to replace the differentials of a variable by the difference taken over finite intervals. It becomes necessary, therefore, to replace the continuous domain of interest by a system of grid lines covering the whole domain. To derive the finite-difference form of the differential equations, the following general rules are applied:

(a) A grid (in this case, an orthogonal grid) is specified to cover the whole duct. On the corresponding grid nodes, fluid properties are assigned or calculated by means of physical hypotheses or experimental observations. For example, viscosity, in the case of blood, is calculated through the relationships of the previous section.

(b) For each variable, the differentials are calculated by taking the differences over the surrounding grid intervals.

(c) The variation of properties and variables is assumed linear between successive locations.

(d) A semi-integral approach is applied here assuming a finite control volume surrounding each location and thus the body forces, heat sources, etc., in general called source terms, are incorporated by use of the linearised source term method of Patankar and Spalding (1972).

Each variable is assumed constant inside the control volume.

The linear variation of properties and variables leads to a "central-difference" scheme* of expressing the various differentials appearing in the governing equations. Past practice has shown that numerical procedures for the solution of fluid flow problems based on "central-difference" schemes are not always successful. Thus, Thom (1933), and Greenspan (1967), experienced difficulties with Reynolds numbers of more than 500. These difficulties resulted from the non-linearity of the differential equations and the strong influence of the convection terms. Thus, an "upwind-difference" or "donor cell" scheme has been introduced by some workers (see, for example, Greenspan (1967), Runchal and Wolfshtein (1969)) to overcome the problem of divergence at high Reynolds numbers. According to this scheme, the various differentials are evaluated by always taking differences based on the upstream side values of the convected fluid property under consideration, i.e. it is always assumed that the property convected into the control volume ("cell") has the upstream value.

However, this practice is not always the most satisfactory and an alternative approximation which is a hybrid of the "central-difference" and "upwind-difference" schemes may be employed. The basic philosophy of the "hybrid-difference" scheme is that diffusion is neglected when the flow is highly convective and "upwind-difference" formulae are employed to express the differentials. On the other hand, when diffusion is comparable with convection, the former is taken into account by employing "central-difference" numerical schemes. The required magnitude of diffusion to justify consideration may be determined by a simple one-dimensional combined convection and diffusion

* For a classification of these schemes, see Spalding (1972).

flow problem. Thus, Spalding (1972) proposed the following:

Use of "central-difference" scheme if $|Pe| \leq 2$

and

Use of "upwind-difference" scheme if $|Pe| > 2$

where the Peclet number of the flow at the site is:

$$Pe = \frac{\text{convection}}{\text{diffusion}}$$

Runchal (1972) performed numerical experiments based on this proposal and found it to be superior to the other two schemes and unconditionally stable.

The present numerical work makes use of the "hybrid-difference" scheme whenever there exists a need to evaluate the relative importance of convection and diffusion in the transformation of the differential equations to finite-difference form.

2.2.6 The Solution Procedures

The finite difference equations may be solved by a single non-iterative "marching" sweep (parabolic flows) from one end of the integration domain to the other; alternatively, an iterative procedure may be used (elliptic flows). The idea of solving large systems of linear equations by iterative methods dates back at least to Gauss, and Southwell made use of them to solve problems of physics and engineering. Modern matrix iterative analysis starts with the introduction of high speed digital computers and it is concerned with the efficient solution of matrix equations arising from discrete approximations to partial differential equations. These matrix equations are generally sparse, i.e. a large percentage of their entries are zero. In addition, the non-zero entries occur in a regular pattern.

It is possible to use direct methods of solving this set of equations and on the other extreme, a point-by-point iterative method of the Gauss-Seidel type (see Varga (1962), and Westlake (1968)). In practice, however, most iterative procedures pertinent to fluid flows make use of intermediate methods involving the tri-diagonal matrix algorithm (TDMA), as in the alternating-direction implicit method of Peaceman and Rachford (1955). A tri-diagonal matrix algorithm (TDMA)* was employed for the solution of the matrix equations resulting from the finite-difference representation of the conservation equations over the grid, and it may be described as follows:

The general form of the finite-difference flow equations of this thesis may be written as follows:

$$\phi_P = \sum_{i=N,S,E,W} A_i^{\phi}\, \phi_i + S^{\phi} \qquad (2.2.6\text{-}1)$$

or:

$$\phi_P = A_N^{\phi}\, \phi_N + A_S^{\phi}\, \phi_S + \left[A_E^{\phi}\, \phi_E + A_W^{\phi}\, \phi_W + S^{\phi}\right] \qquad (2.2.6\text{-}2)$$

where N, S, E, W are the neighbouring locations of P, and S^{ϕ} a constant. With the aid of the known boundary conditions, it is possible to solve for all ϕ_P's along a grid line, assuming the quantity in brackets is known. Once the values at a grid line are obtained, the solution of the ϕ_P's at the next line is sought following the same procedure. Thus, the whole domain is swept from one side of the boundary to the other. This sweeping may be repeated as many times as it is practically necessary. Alternatively, a double sweep along the normal direction may be employed. For this reason, equation (2.2.6-1) is rewritten in the form:

---

* For a description of the TDMA, see Appendix A.

$$\phi_P = A_E^\phi \phi_E + A_W^\phi \phi_W + \left(A_N^\phi \phi_N + A_S^\phi \phi_S + S^\phi\right) \qquad (2.2.6\text{-}3)$$

and thus a traverse is performed from one side of the boundary to the other. Again, it is a matter of numerical experiment to establish the optimum number of single or double sweeps which give the best convergence for the flow problem under consideration.

2.2.7 Solution Accuracy, Economy, Convergence and Under-Relaxation

The prediction of the flow field is not only a matter of obtaining an adequate numerical scheme of solving the governing differential equations. These equations must themselves express satisfactorily the significant features of the physics of the flow. Thus, a significant error may be introduced in the numerical predictions which is inherent to the hypotheses used to describe the physics of the phenomena to be predicted. It is obvious that this error is difficult to assess and only comparison between numerical solutions and experimental data can reveal its relative importance.

The difference between the numerical solution of the finite-difference equations and the exact solution of the differential equations is defined as the overall numerical error. The replacement of the continuous expressions by discrete ones introduces an error, called the discretisation error. It is obvious that when these discrete equations are solved by iterative methods, an additional error, called the iterative error, may occur. Furthermore, it has been established that all digital computers have a certain degree of accuracy of number representation, and thus an additional error, called the round-off error, is introduced.

The grid size affects the discretisation and iterative errors in the opposite sense. The first decreases as the mesh size decreases, while the second generally increases, and for this reason it is not always certain that refining the grid will result in increased accuracy. However, in order to obtain an accurate and economic procedure, both the total computing time and the accuracy of the solution have to be considered.

In the present computations, the requirements are that: A solution has converged if, at any point, the predicted values do not alter more than a pre-specified percentage between successive iterations. This is set in such a way as to leave four significant figures unaltered. At the same time, the sums of the absolute residuals for momentum, mass, etc., are monitored in order to establish whether they converge to small quantities. A mathematical expression for the latter convergence criterion may be stated as follows:

$$\frac{R_\phi^i}{R_{N,\phi}} < \varepsilon \qquad (2.2.7\text{-}1)$$

where ε is a small quantity (usually 10^{-4}), R_ϕ^i is the sum of the absolute residuals of ϕ at the ith iteration, and $R_{N,\phi}$ is a normalising quantity, e.g. the mass flow rate, the inlet fluid momentum, the inlet fluid enthalpy, etc. Once these criteria are satisfied, the computation is stopped and the solution is said to be converged.

In almost all problems involving iterative procedures, there is a lack of adequate initial conditions. When the guessed values are grossly incorrect, considerable instability problems may result. In order to avoid instabilities of the solution procedure, it has become common practice to under-relax the newly calculated variable fields. The under-relaxation scheme employed in the present numerical computations may be summarised as follows:

Consider that ϕ_{i-1} is the value of the variable ϕ at the *(i-1)*th iteration and ϕ_i^* is the newly calculated value at the *i*th iteration. The final value of ϕ at the *i*th iteration is obtained from the following formula:

$$\phi_i = \alpha \cdot \phi_i^* + (1 - \alpha)\, \phi_{i-1} \qquad (2.2.7\text{-}2)$$

where α is the under-relaxation factor ($0 < \alpha < 1$). However, when $\alpha > 1$, the solution is said to be over-relaxed. Under-relaxation was applied only in the elliptic procedures reported in this chapter, since the nature of the parabolic procedure did not require iterations. Numerical experiments with different under-relaxation factors proved that the optimum value of α for the velocity field was of the order of 0.5. There was no under-relaxation applied to the pressure field ($\alpha = 1.0$).

2.2.8 Closing Remarks

In this section, the theoretical foundations of the flow problems considered have been described. Reduced forms of the Navier-Stokes equations applicable to the three flow configurations under study have been given and the general features of the numerical methods employed for their solution have been outlined. With the aid of this introductory material, the specific numerical procedures applied for the present Newtonian and non-Newtonian flows may now be described. This is the subject matter of the following sections.

2.3 NUMERICAL ASPECTS OF THREE-DIMENSIONAL PARABOLIC FLOWS

2.3.1 Problem Statement

The purpose of this section is to describe the numerical procedures employed to predict flows with boundary-layer features. In section 2.2.2, it was mentioned that the nature of the differential equations describing a parabolic flow allows a forward marching numerical procedure to be employed. This is the main feature of the procedure discussed here. It is mainly based on a similar procedure developed by Patankar and Spalding (1972) for boundary layers. In order to arrive at the finite-difference equations and their solution, all the general rules laid down in section 2.2 are applied. Thus, a finite control volume is assumed to surround a point, and by integration of the differential equations over the control volume, their finite-difference form may be derived as shown in section 2.3.3. This requires a grid to be specified, together with the locations of fluid properties and dependent variables.

2.3.2 The Grid

Figures 2.3.2-1 and 2.3.2-2 illustrate the grid, the "cell" arrangement, and the locations of the dependent variables and fluid properties.

The u-velocity component, pressure, ϕ-property and fluid properties are stored at the intersection of the grid lines (grid nodes) and the lateral velocities v and w are placed midway between nodes. Thus, a typical node P for u-velocity, pressure or ϕ-property "cell" has five close neighbours; the in-plane ones labelled N, S, E, W and the upstream neighbour labelled U. Similarly, v and w-velocity "cells" may be formed.

2.3.3 The Finite-Difference Equations

Finite-difference counterparts of the differential equations (2.2.2-6) to (2.2.2-10) are obtained by integrating the latter over control volumes surrounding each variable to give equations of the form*:

Mass conservation equation:

$$\left[(\rho uA)_U - (\rho uA)_P\right] = \left[(\rho vA)_n - (\rho vA)_s\right] + \left[(\rho wA)_e - (\rho wA)_w\right] \qquad (2.3.3\text{-}1)$$

u-momentum equation:

$$A^u_P\, u_P = A^u_N\, u_N + A^u_S\, u_S + A^u_E\, u_E + A^u_W\, u_W + S^u + D^u \left(\frac{dp}{dx}\right) \qquad (2.3.3\text{-}2)$$

v-momentum equation:

$$A^v_P\, v_P = A^v_N\, v_N + A^v_S\, v_S + A^v_E\, v_E + A^v_W\, v_W + S^v + D^v\, (p_S - p_P) \qquad (2.3.3\text{-}3)$$

w-momentum equation:

$$A^w_P\, w_P = A^w_N\, w_N + A^w_S\, w_S + A^w_E\, w_E + A^w_W\, w_W + S^w + D^w\, (p_W - p_P) \qquad (2.3.3\text{-}4)$$

ϕ-property equation:

$$A^\phi_P\, \phi_P = A^\phi_N\, \phi_N + A^\phi_S\, \phi_S + A^\phi_E\, \phi_E + A^\phi_W\, \phi_W + S^\phi \qquad (2.3.3\text{-}5)$$

In these equations, A and D are areas of the surfaces of the control volume

---

* For a derivation of these formulae, refer to Appendix B.

and A_i are coefficients combining both the convective and diffusive effects of the flow. These are calculated from the geometry and upstream values of the properties and dependent variables. The quantities S incorporate any existing source terms and in the present work, for reasons of numerical stability, are expressed in a linearised form as follows:

$$S^{\phi} = S_p \cdot \phi + S_u \qquad (2.3.3\text{-}6)$$

where S_p and S_u are quantities calculated from geometrical data, upstream properties and dependent variables, and for this reason are independent of the variable ϕ.

2.3.4 The Solution Procedure

The solution procedure may now be described in terms of the necessary operations required to calculate the unknown values of the dependent variables at the plane downstream from the known ones. These may be either the inlet conditions or those newly calculated at the upstream section. This sequence may be summarised as follows:

1. Assume that the velocities u and pressures p^* are known at the downstream plane. Intermediate values of the velocities v^* are obtained by simultaneous solution of the set of equations (2.3.3-3).
2. Similarly, intermediate values of velocities w^* are obtained by solving equation (2.3.3-4).
3. An axial pressure gradient $(d\bar{p}/dx)^*$ is assumed and intermediate values of the velocities u^* are obtained by simultaneous solution of the set of equations (2.3.3-2).

These velocities satisfy the momentum equation but do not, in general, satisfy overall continuity.

4. Thus, a correction $(d\bar{p}/dx)'$ to the guessed pressure gradient is obtained by requiring that the velocities obtained from the relationship:

$$u_P = u_P^* + u_P' = u_P^* + D^u \left(\frac{dp}{dx}\right)' \tag{2.3.4-1}$$

should satisfy the overall continuity relationship:

$$\sum_{all\ nodes} (\rho u A) = \dot{m} \tag{2.3.4-2}$$

where A is the cross-sectional area of the control volume, and $\dot{m}$ is the mass flow rate through the duct. Once $(d\bar{p}/dx)'$ has been calculated from equation (2.3.4-2), the new velocities u may be obtained from equation (2.3.4-1).

5. Then, a field of pressure-corrections p' is obtained by introducing relations of the form:

$$v_P = v_P^* + v_P' = v_P^* + D^v (p_S' - p_P') \tag{2.3.4-3}$$

$$w_P = w_P^* + w_P' = w_P^* + D^w (p_W' - p_P') \tag{2.3.4-4}$$

$$p_P = p_P^* + p_P' \tag{2.3.4-5}$$

into the local continuity equation (2.3.3-1). This yields, for each node, a pressure-correction equation of the form*:

$$p'_P = \sum_{i=N,S,E,W} A_i^p \, p'_i + S^p \qquad (2.3.4\text{-}6)$$

where the summation is performed over the cell faces and the coefficients A^p are derived from the corresponding equations. The solution of the set of simultaneous equations represented by equation (2.3.4-6) yields a pressure-correction field p'. Finally, the new v's, w's and new pressures p are obtained from equations (2.3.4-3), (2.3.4-4) and (2.3.4-5), respectively.

6. The set of equation (2.3.3-6) is solved simultaneously to obtain the new ϕ's.
7. A new step is taken and the procedure is repeated at the downstream station.

The equation for the pressure-correction allows only adjustments of the cross-stream velocities, i.e. local continuity is implemented by adjusting the cross-sectional velocities alone. For the main flow direction velocity field u, the pressure gradient is either presumed known (for a free boundary flow) or else (for a confined flow) a uniform pressure gradient correction is applied, as discussed, in order to satisfy overall continuity. Thus, u-momentum equations are "uncoupled" from v- and w-momentum equations. This "uncoupling" is realistic and necessary (Spalding (1974)).

---

* For a derivation of this equation, see Appendix B.

2.3.5 Modifications for Irregular Boundaries

The algorithm described above may be applied to flow problems with boundary conditions appropriate to rectangular ducts. However, in many practical situations, such as those discussed by McGuirk (1975), irregular boundaries are involved. This is the case when the prediction of a circular duct flow is sought by employing a rectangular mesh as in the present application.

Figure 2.3.5-1 illustrates the grid used for the calculation of the flow in circular cross-sectioned ducts with the present algorithm. It is recognised that there are three different kinds of cells:

1. Cells with all neighbours inside the circular boundary.
2. Cells with all neighbours outside the boundary.
3. Cells with neighbours on both sides of the boundary.

The special treatment employed here may be summarised as follows:

1. Cells of the first kind are treated as before.
2. Cells of the second kind are assigned zero values of the variables. This is done as follows: The finite-difference equation (2.3.3-5) is rewritten as:

$$A_P^{\phi}\, \phi_P = \sum_{i=N,S,E,W} A_i^{\phi}\, \phi_i + (S_p \cdot \phi_P + S_u) \qquad (2.3.5\text{-}1)$$

   By assigning values of $S_p = -10^N$ and $S_u = 0$, where N is a large integer (for example, 30), the value of ϕ_P is forced to zero.
3. The cross-sectional areas of the cells adjacent to the boundary (cells of the third kind) are computed beforehand so

that the proper mass flow rate may be established at all downstream stations.

4. The proper wall shear stress is evaluated by means of the Couette flow equation (Schlichting (1968)):

$$\tau_w = \mu \left(\frac{u}{h} - \frac{h}{2\mu} \left(\frac{\partial \overline{p}}{\partial x}\right)\right) \quad (2.3.5\text{-}2)$$

where h is the shortest distance from the node point to the curved boundary. The calculation of the wall shear stresses by equation (2.3.5-2) is only applied in the u-velocity momentum balance. This is reasonable since the u-velocity component is parallel to the tube wall at any time, while the lateral velocity components resolve to small, negligible components parallel to the wall in most of the cases.

The modifications discussed above introduce certain inaccuracies in the solution procedure, for they take account only of the main direction of the flow. However, the boundary layer nature of the flow justifies this treatment in practice, as is shown by the predicted results of section 2.6.

2.3.6 Closing Remarks

It is recognised that the laminar water flow downstream of a 15^0 bend in a pipe is of a parabolic nature. Experiments (see Gosman, Vlachos and Whitelaw (1973)) have shown that there is no reverse flow in the pipe. Thus, the present numerical procedure has been applied to predict this flow. Results of the computations, test cases, and problems associated with the economy and accuracy of the procedure are presented and discussed in section 2.6. Implications of the influence of non-Newtonian particulate flows relevant to blood flows in bends and bifurcations are also discussed.

2.4 NUMERICAL ASPECTS OF AXISYMMETRIC RECIRCULATING FLOWS

2.4.1 Problem Statement

The purpose of this section is to describe the main features of the numerical scheme developed to predict Newtonian and non-Newtonian axisymmetric elliptic flows referred to in the introduction of this chapter. The recirculating nature of the flow does not allow a forward marching procedure to be employed as in the boundary layer flows. Thus, the main feature of the solution scheme outlined here is its iterative nature. The numerical scheme described here is based on a similar scheme developed by Gosman and Pun (1974) for recirculating flows. Again, a finite control volume is assumed to surround a point, and by integration of the differential equations over the control volume, their finite-difference form may be derived as shown in section 2.4.3. Thus, a grid needs to be specified together with the locations of the fluid properties and dependent variables.

2.4.2 The Grid

Figures 2.4.2-1 and 2.4.2-2 illustrate the grid, the cell arrangement and the location of fluid properties and dependent variables. The fluid properties, such as density, viscosity, thermal conductivity, etc., are stored on the grid nodes as well as pressure and the ϕ-property. The velocity components u and v are stored midway between grid nodes. Thus, any point P has four neighbours labelled E, W, N and S, as shown in Figure 2.4.2-2. In many cases, a non-uniform grid is required to facilitate better predictions with increased accuracy and economy. This is essential in the case of flows with obstacles as in the present applications. Thus, the grid shown in these Figures is a general, unevenly spaced one. The latter implies that special arrangement and treatment of the cells has to be employed in order to counterbalance the fact that properties and mass fluxes are not available at the cell faces. The facility of uneven grids forms the main difference of this procedure from that of Gosman and Pun (1974) regarding the finite-difference equations to be described below.

2.4.3 The Finite-Difference Equations

Finite-difference counterparts of the differential equations (2.2.2-11) to (2.2.2-14) are obtained by integration of the latter over control volumes surrounding each variable. They may be written as follows*:

Mass conservation equation:

$$\left[(\rho u A)_e - (\rho u A)_w\right] + \left[(\rho u A)_n - (\rho u A)_s\right] = 0 \tag{2.4.3-1}$$

u-momentum equation:

$$A_P^u\, u_P = A_N^u\, u_N + A_S^u\, u_S + A_E^u\, u_E + A_W^u\, u_W + S^u + D^u\, (p_W - p_P) \tag{2.4.3-2}$$

v-momentum equation:

$$A_P^v\, v_P = A_N^v\, v_N + A_S^v\, v_S + A_E^v\, v_E + A_W^v\, v_W + S^v + D^v\, (p_S - p_P) \tag{2.4.3-3}$$

ϕ-property equation:

$$A_P^\phi\, \phi_P = A_N^\phi\, \phi_N + A_S^\phi\, \phi_S + A_E^\phi\, \phi_E + A_W^\phi\, \phi_W + S^\phi \tag{2.4.3-4}$$

---

* For a derivation of these equations, refer to Appendix C.

In these equations, A and D are areas of the surfaces of the control volume, while A_i are coefficients combining the convection and diffusion effects of the flow and are calculated from the geometry, properties and dependent variable values at the previous iteration. Again, the quantities S incorporate any existing source terms and are expressed in a linearised form as below:

$$S^{\phi} = S_p \cdot \phi + S_u \qquad (2.4.3\text{-}5)$$

where, again, the quantities S_p and S_u are independent of ϕ and are calculated from geometrical data, fluid properties and dependent variable values of the previous iteration.

2.4.4 The Solution Procedure

The necessary steps for the solution of the above finite-difference equations, which are coupled and therefore cannot be solved independently, may be summarised as follows:

1. Guessed values of the velocities u and v, pressures p, and property ϕ are established at the beginning of the iteration procedure.
2. The u-momentum equation (2.4.3-2) is solved to obtain intermediate velocities u^*.
3. Similarly, intermediate values v^* are obtained for the v-velocity field by simultaneous solution of the set of equations (2.4.3-3).
4. The new velocity fields u^* and v^* satisfy the momentum equations (2.4.3-2) and (2.4.3-3) but do not necessarily

satisfy local continuity. Thus, a correction, p', of the pressure field is sought in order to satisfy local continuity by introducing relationships of the form:

$$u_P = u_P^* + u_P' = u_P^* + D^u \, (p_W' - p_P') \qquad (2.4.4\text{-}1)$$

$$v_P = v_P^* + v_P' = v_P^* + D^v \, (p_S' - p_P') \qquad (2.4.4\text{-}2)$$

$$p_P = p_P^* + p_P' \qquad (2.4.4\text{-}3)$$

Substituting these relationships into equation (2.4.3-1) yields the pressure-correction equation with the following form*:

$$A_P^p \, p_P' = A_N^p \, p_N' + A_S^p \, p_S' + A_E^p \, p_E' + A_W^p \, p_W' + S^p \qquad (2.4.4\text{-}4)$$

The simultaneous solution of equation (2.4.4-4) yields a pressure correction field p'. Then, the new values of velocities u and v and pressure p are obtained via equations (2.4.4-1), (2.4.4-2) and (2.4.4-3), respectively.

5. The set of equations (2.4.3-4) is solved simultaneously to yield a new field for the general ϕ-property.
6. The newly calculated values of velocities u and v, pressure p, and property ϕ are used as guessed values for the new iteration and the procedure is repeated until a specified degree of convergence is achieved.

---

* For a derivation of this equation, see Appendix C.

2.4.5 Closing Remarks

The presence of an axisymmetric obstruction in a round pipe flow renders it an axisymmetric elliptic flow in the vicinity of the obstruction. As a consequence, the numerical procedure described here is applied to predict this kind of flow.

Results of these computations, test cases and problems associated with the economy and accuracy of the procedure are presented and discussed in section 2.6. Results for non-Newtonian fluid flows, relevant to blood flow in an aortic stenosis, are also presented and discussed. The results are reviewed in both the engineering and biorheological context.

2.5 NUMERICAL ASPECTS OF THREE-DIMENSIONAL RECIRCULATING FLOWS

2.5.1 Problem Statement

This section describes the numerical scheme developed specifically for the prediction of laminar Newtonian and non-Newtonian three-dimensional elliptic flows. Again, the recirculating nature of the flow does not allow a forward marching procedure to be employed and thus an iterative procedure is utilised. Although this procedure covers a wider range of flows, it has common features with both the axisymmetric recirculating flow scheme and the parabolic procedure described in the previous two sections. Thus, it may be said that it is a natural extension of the scheme of Gosman and Pun (1974) to cover the third coordinate. As in the previous two numerical schemes, a finite control volume is assumed to surround a point, and by integration of the differential equations of the flow over the control volume, their finite-difference form is derived as shown in section 2.5.3. Thus, it becomes necessary to define a grid together with the locations of the various fluid properties and dependent variables.

2.5.2 The Grid

Figures 2.5.2-1 and 2.5.2-2 show a typical grid and cell arrangement used in the present numerical scheme. As in the case of axisymmetric elliptic flows, the grid is unevenly spaced. This facilitates better grid usage when flows with obstacles are encountered, as in the present applications. The three velocity components u, v and w are stored midway between grid nodes. Pressure, ϕ-property and fluid properties, such as density, viscosity, thermal conductivity, etc., are stored on the grid nodes.

Thus, any point P has six surrounding points labelled E, W, N, S, D and U as shown in Figure 2.5.2-2.

2.5.3 The Finite-Difference Equations

By integration of each of equations (2.2.2-15) to (2.2.2-19) over control volumes surrounding each variable and application of the numerical methods described in section 2.2, the finite-difference equations may be obtained. These equations have the following forms*:

Mass conservation equation:

$$\left[(\rho uA)_e - (\rho uA)_w\right] + \left[(\rho vA)_n - (\rho vA)_s\right] + \left[(\rho wA)_d - (\rho wA)_u\right] = 0 \qquad (2.5.3\text{-}1)$$

u-momentum equation:

$$A^u_P u_P = A^u_E u_E + A^u_W u_W + A^u_N u_N + A^u_S u_S + A^u_D u_D + A^u_U u_U + S^u + D^u\,(p_W - p_P) \qquad (2.5.3\text{-}2)$$

v-momentum equation:

$$A^v_P v_P = A^v_N v_N + A^v_S v_S + A^v_E v_E + A^v_W v_W + A^v_D v_D + A^v_U v_U + S^v + D^v\,(p_S - p_P) \qquad (2.5.3\text{-}3)$$

w-momentum equation:

$$A^w_P w_P = A^w_N w_N + A^w_S w_S + A^w_E w_E + A^w_W w_W + A^w_D w_D + A^w_U w_U + S^w + D^w\,(p_U - p_P) \qquad (2.5.3\text{-}4)$$

ϕ-property equation:

$$A^\phi_P\,\phi_P = A^\phi_E\,\phi_E + A^\phi_W\,\phi_W + A^\phi_N\,\phi_N + A^\phi_S\,\phi_S + A^\phi_D\,\phi_D + A^\phi_U\,\phi_U + S^\phi \qquad (2.5.3\text{-}5)$$

---

* See Appendix D for full details.

Again, in these equations, A and D are areas of the surfaces of the control volume, while the coefficients A_i combine both the convection and diffusion effects of the flow. The quantities S incorporate any existing source terms in a linearised form as follows:

$$S^{\phi} = S_p \cdot \phi + S_u \qquad (2.5.3\text{-}6)$$

where the coefficients S_p and S_u are independent of ϕ and are calculated from geometrical data, fluid properties and dependent variables from the previous iteration.

2.5.4 The Solution Procedure

There are various ways by which the finite-difference equations (2.5.3-1) to (2.5.3-5) can be solved by iterative procedures. It seems natural that the coefficients A_i should be calculated for all points and then the equations solved simultaneously. However, this practice would involve three-dimensional computer storage for the coefficients A_i thus imposing a limitation to the computer storage space.

The algorithm used in the present work employs the following steps:

1. Guessed values of u, v, w velocities, pressure p, ϕ-property, and fluid properties are imposed, wherever not known.
2. The set of equations (2.5.3-2) is solved simultaneously from plane to plane to obtain intermediate values of velocities u^*.
3. Equation (2.5.3-3) is solved simultaneously from plane to plane to yield an intermediate velocity field v^*.
4. Similarly, equation (2.5.3-4) is solved to obtain intermediate values of the velocities w^*.

5. The calculated velocities u^*, v^*, w^* satisfy the momentum equation but do not, in general, satisfy local continuity. Thus, a pressure-correction field p' is sought via relationships of the form:

$$u_P = u_P^* + u_P' = u_P^* + D^u (p_W' - p_P') \tag{2.5.4-1}$$

$$v_P = v_P^* + v_P' = v_P^* + D^v (p_S' - p_P') \tag{2.5.4-2}$$

$$w_P = w_P^* + w_P' = w_P^* + D^w (p_U' - p_P') \tag{2.5.4-3}$$

$$p_P = p_P^* + p_P' \tag{2.5.4-4}$$

which will enable the velocities u, v and w to satisfy local continuity as well. Substitution of relationships (2.5.4-1) to (2.5.4-3) into the local continuity equation (2.5.3-1) yields the pressure-correction equation with the following form*:

$$A_P^p p_P' = A_E^p p_E' + A_W^p p_W' + A_N^p p_N' + A_S^p p_S' + A_D^p p_D' + A_U^p p_U' + S^p \tag{2.5.4-5}$$

The plane by plane simultaneous solution of the set of equation (2.5.4-5) yields the pressure-correction field throughout the flow domain. Then, the new velocities u, v and w and the new pressures p are obtained via the relationships (2.5.4-1) to (2.5.4-4).

6. The set of equations (2.5.3-5) is solved simultaneously to yield the new values of ϕ-property.

---

* See Appendix D for full details.

7. The newly calculated values of velocities, pressures and ϕ-properties are used as guessed values for the new iteration and the procedure is repeated until a specified degree of convergence is achieved.

The above procedure implies that the pressure correction p' and the pressure coefficients D must be three-dimensional arrays. An alternative procedure requiring only two-dimensional storage for these variables may be outlined as follows:

1. Assuming guessed values of velocities, pressures, ϕ-properties and fluid properties, if necessary, the set of equations (2.5.3-2) is solved at a plane to obtain intermediate values of velocity u^*.
2. Similarly, intermediate values of velocities v^* are obtained at the same plane by solving equation (2.5.3-3).
3. At the same plane, the set of equations (2.5.3-4) is solved to obtain intermediate values of velocities w^*.
4. Then, the set of pressure-correction equations (2.5.4-5) is solved, at the same plane, and the new velocities and pressures are obtained.
5. The ϕ-property equation (2.5.3-5) is solved simultaneously to obtain the new ϕ's.
6. Steps 1 to 5 are repeated throughout the whole calculation domain obtaining the velocities, pressures and ϕ-property everywhere.
7. These newly calculated values are used as initial values for the new iteration and the procedure is repeated until a

specified degree of convergence is reached.

This algorithm, although less demanding in computer space, may produce slower convergence under certain conditions. The present computations have been carried out on the basis of the first of the two algorithms outlined above. However, since the latter employs a forward marching procedure within an iteration, it has common features with the algorithm described for parabolic flows, and thus it has been used as the basis for a new parabolic scheme developed by Gosman, Lockwood & Syed (1976).

2.5.5 Closing Remarks

An asymmetric obstruction in a flow renders it three-dimensional and elliptic in its vicinity. Therefore, a numerical procedure similar to that described here may be employed to predict such a flow.

Results of these computations, test cases, and problems associated with economy and accuracy of the solution procedure are presented and discussed in section 2.6. Results of non-Newtonian fluid flows relevant to blood flow in a venule with a thrombus are also presented. The engineering and biorheological relevance of these results are also discussed.

2.6 COMPUTATIONAL RESULTS AND DISCUSSION

2.6.1 Introduction

The numerical procedures outlined in sections 2.3, 2.4 and 2.5 have been tested against existing computational and experimental results. These tests are described briefly in section 2.6.2. The procedures are then applied to the prediction of the following flow situations:

(a) Laminar Newtonian flow downstream of a 15^0 bend in a round pipe.

(b) Laminar Newtonian flow in the vicinity of an axisymmetric constriction in a round pipe.

(c) Laminar non-Newtonian blood flow in the vicinity of an axisymmetric aortic stenosis.

(d) Laminar Newtonian flow in the vicinity of an asymmetric constriction in a round pipe.

(e) Laminar non-Newtonian blood flow in the vicinity of an asymmetric thrombus in a venule.

For each application of the numerical procedures, the grid employed, initial and boundary conditions, solution convergence and computer economy are discussed in turn. The results are viewed from both the engineering and biorheological point and attempts are made to interpret the behaviour of blood in the vascular system.

2.6.2 Test Cases

All three numerical procedures were tested, whenever possible, before their final application to the specific problems mentioned in the previous section. Results of these tests are reviewed as follows:

(a) Three-dimensional parabolic flows

The parabolic algorithm described in section 2.3 has been tested, in the form of a computer program by Patankar and Spalding (1972), and Curr, Sharma and Tatchell (1972). Their predictions of a developing square duct flow with or without a moving wall support the validity of the numerical procedure for the present purposes. Preliminary tests with the present numerical procedure on the same flows produced similar to their results.

However, the application of the present algorithm employing a rectangular mesh on a round pipe flow was tested against the analytical solution of fully developed pipe flow. The results showed an agreement better than 1% between the predicted and analytical values of both the velocity profiles and the pressure gradient.

(b) Axisymmetric elliptic flows

The axisymmetric elliptic procedure outlined in section 2.4 was tested, in the form of a computer program, against fully developed laminar Newtonian and non-Newtonian pipe flow and the flow between parallel walls. The results of these tests showed that the maximum deviation between predicted and analytical velocity profiles was of the order of: 1% for Newtonian pipe flow, 1.5% for non-Newtonian (power law) pipe flow, 1% for Newtonian parallel flow, and 2% for non-Newtonian (power law) parallel flow. The discrepancy is mainly due to the 22 x 12 grid used. Predictions of Newtonian and non-Newtonian pipe flow with a 22 x 17 grid showed an agreement of better than 0.5%. Predictions of annular Newtonian and non-Newtonian flow also produced satisfactory agreement with the analytical fully developed profiles.

The entrance lengths for developing pipe flow are of interest because they provide an indication of the behaviour of viscous flow at low Reynolds numbers. This was used to determine the inlet and outlet pipe lengths for the flows with the constriction. The entrance lengths are plotted in Figure 2.6.2-1 as a function of the generalised Re'_N for power law fluids. The generalised Reynolds number is defined as follows (see Bird et al (1960)):

$$Re'_N = Re_N \cdot \frac{2^{3-n}}{(3 + \frac{1}{n})^n} \qquad (2.6.2\text{-}1)$$

where n is the index of the power law and the modified Reynolds number Re_N applied to power law fluids is obtained from the relationship:

$$Re_N = \frac{\rho \cdot D^n \cdot \bar{u}^{2-n}}{m} \qquad (2.6.2\text{-}2)$$

where m is the constant of the power viscosity law. It can readily be deduced from Figure 2.6.2-1 that there exists an agreement better than 1% when the generalised Reynolds number is used to correlate entrance lengths of Newtonian (n = 1) and non-Newtonian (n = 2/3) fluids. The asymptotic value of 0.070 for the dimensionless entrance length le/DRe'_N compares favourably with the value of 0.065 of Boussinesq and 0.057 of Langhaar (Shapiro et al. (1954)).

The non-Newtonian version of the axisymmetric elliptic procedure has also been tested against the Newtonian version by simply defining the power law equal to unity (n = 1) for a pipe flow. Thus the viscosity law in both versions was effectively the same Newtonian one, but there was a difference in the expression of the viscous terms between the Newtonian and non-Newtonian procedures. The former made use of the momentum equations (2.2.2-12) to (2.2.2-13) without the extra variable-viscosity terms, while the latter employed their full form.

The results of both the Newtonian and non-Newtonian versions of the numerical procedure were identical on all velocity components and pressures, which confirmed the validity of the non-Newtonian procedure.

(c) Three-dimensional elliptic flows

The three-dimensional elliptic numerical procedure has been tested, in the form of a computer program, against the axisymmetric elliptic procedure on laminar Newtonian and non-Newtonian pipe flows with or without a constriction. The results of these computations were numerically identical and this supported, to a first degree, the validity of both the Newtonian and non-Newtonian three-dimensional elliptic procedures.

Next, the developing laminar square duct flow has been predicted with the present elliptic algorithm. Figure 2.6.2-2a shows the development of the average pressure along the duct together with predictions of Curr et al (1972) and experimental results of Beavers et al (1970). The solutions of Han (1960) and Wiginton and Dalton (1970) are also plotted for comparison. Figure 2.6.2-2b presents the development of the centre line axial velocity. On the same graph are plotted the predictions of Curr et al (1972) and experimental results of Goldstein and Kreid (1967) for comparison. It is evident that a grid of $20 \times 20 \times 22$ produces fair agreement between the results of the present scheme, that of Patankar and Spalding (see Curr et al (1972)), and the available experimental results.

However, the present numerical procedure has been developed for the purpose of predicting recirculating flows and thus its iterative nature renders it expensive when applied to parabolic flows where forward marching numerical algorithms are more economic.

The present algorithm has also been tested against the developing laminar square duct flow with a moving wall. Figure 2.6.2-3a presents results of these computations where the development of the maximum axial velocity is plotted. The fully developed lateral velocity profile at the centre plane is plotted in Figure 2.6.2-3b. Results of Curr et al (1972) and the analytical solution of Burggraf (1966) are also plotted for comparison. The deviation observed is mainly due to the coarse grid (12 × 12 × 22) used for the present predictions, which effectively was half the grid size used by Curr et al (1972).

The above summary of preliminary tests provides evidence of the validity of the procedures to be used in the following subsections.

2.6.3 Laminar Newtonian Flow Downstream of a 15^{o} Bend in a Round Pipe

The flow downstream of a 15^{o} bend in a round pipe was examined experimentally by Gosman, Vlachos and Whitelaw (1973) (see also Chapter 3), who demonstrated that the flow is boundary-layer in nature. This justified the use of the three-dimensional boundary-layer approach. Figure 2.6.3-1 shows the 17 × 17 rectangular grid employed for the prediction of this flow. The modifications mentioned in section 2.3.5 have been applied here for the treatment of the curved boundary.

The computations started from five (5) pipe diameters downstream of the bend centre and marched downstream until a fully developed flow was attained. The initial velocity profile required for the start of the computation was obtained by laser Doppler velocimetry as described in section 3.3.2. For this reason, the axial velocity profiles on six (6) diameters 30^0 apart were measured and are shown in Figure 2.6.3-2.

The forward step was initially taken to be 0.1% of the pipe diameter. Then, as the calculation procedure moved downstream, the step was increased with a ratio 1.1 until it reached the value of 5% of the pipe diameter remaining constant thereafter.

Initial calculations were performed with three grids of 11×11, 17×17 and 20×20. The results of these computations are shown in Figure 2.6.3-3 where the velocity profiles in the plane of the bend and in the normal plane are plotted for a downstream station x/D of 2. It can be seen that the two finer grids produced a maximum deviation of the order of 0.5%, while a deviation of the order of 10% was observed with the coarse grid. The final calculations were performed with the 17×17 grid for economic reasons. The computer time required for these computations was approximately 200 seconds on a CDC 6600 computer.

Figures 2.6.3-4 and 2.6.3-5 present the development of the velocity profiles in the plane of the bend and in the normal plane. The experimental velocity profiles obtained by laser Doppler Velocimetry in section 3.3.2 are plotted in the same graphs for comparison. The general agreement is satisfactory with the maximum deviation on the centre line, of the order of 4%, occurring between two and five diameters downstream of the inlet station. This deviation may be explained to be the result of, firstly a rectangular grid with a limited number of grid nodes, and secondly the presence of secondary flows. The latter have been neglected in the initial conditions used to start the marching calculation procedure. In an effort to determine the influence of these secondary flows, the computed cross-stream velocities at x/D of 0.5 were input as initial conditions at x/D of 0 and the calculation procedure was repeated; this practice reduced the maximum deviation to 3%.

The calculations presented in Figures 2.6.3-4 and 2.6.3-5 confirmed that the velocity profiles in the plane of the bend were asymmetric, while they attain symmetry in the plane normal to the bend. The flow was fully developed parabolic at about fifteen (15) diameters downstream of the initial station. Thus, the flow had acquired its fully developed parabolic shape within twenty (20) diameters downstream of the centre of the bend for a Reynolds number of 300, which was equal to that used in the experiments.

The axial development of the average pressure gradient, average pressure and centre line velocity were also calculated and are presented in Figure 2.6.3-6. The pressure gradient converges to a correct value at around x/D of 0.25 and grows towards the fully developed pipe flow value; this value was not attained at x/D of 15 but the deviation was less than 0.5%. Similarly, the average pressure drops non-linearly in the first five diameters and then adjusts to an almost linear drop. The centre line velocity starts from its initial value and grows towards the fully developed value of twice the average velocity at around x/D of 15 with a 0.5% discrepancy.

The inner and outer wall shear stresses have also been calculated and are plotted in Figure 2.6.3-6. The outer wall shear stresses were higher than those of the inner wall. The maximum value on the outer wall was 40% in excess, and the minimum on the inner wall was 20% less than the fully developed value. This occurred in the plane of the bend and at x/D of 0. The difference between maximum and minimum values will become more pronounced as the angle of the bend is increased and in the immediate vicinity of the bend.

For flows of non-Newtonian fluids such as blood, the three-dimensional constitutive equation (2.2.4-12) may be used to calculate the local viscosity and then, the momentum equations (2.2.2-7), (2.2.2-8) and (2.2.2-9) in their full form, without cancellation of the extra diffusion terms, may be solved to obtain the flow characteristics.

In the light of the above observations, one may deduce the phenomena likely to occur in blood flow downstream of bends and bifurcations of the recirculatry system of man. The presence of local shear stress values 40% in excess of the fully developed flow value may become significant for the breakdown of cells in the region of the outer wall*. On the other hand, local shear stresses 20% less than the fully developed flow value may facilitate the adherence on the vessel wall of platelets and blood lipoids to form atherosclerotic plaques (Caro et al (1971)).

The pressure drop from the initial station to the fully developed flow region at, for example, x/D of 15 is of the order of 7% in excess of the pressure drop in a straight pipe with the same length. Thus, a pressure increase is required to maintain the proper flow rate necessary for the blood to carry on with its tissue nutrition duties. This may effectively lead to two consequences. Firstly, an increased pressure will increase the vessel wall permeability and decrease its elasticity. The result of this may be an upset of the balance of the biological function of the vessel as well as its dynamic properties. Secondly, the increased pressure requirements may result in increased work of the heart to maintain the proper blood flow rate.

It becomes evident from both the engineering and biorheological viewpoint that bends in a recirculatory system introduce extra pressure losses (see Ward-Smith (1963)). These may readily be

---

* For haemolysis see Champion et al. (1971), Blackshear (1972) and Sutera and Mehrjandi (1975).

predicted for, at least, the developing flow downstream of the bend with the present numerical procedure.

2.6.4 Laminar Newtonian Flow in the Vicinity of an Axisymmetric Constriction in a Pipe

The presence of an axisymmetric constriction in a pipe renders the flow in its vicinity axisymmetric and elliptic. Thus, the numerical procedure outlined in section 2.4 has been applied for the prediction of these kinds of flows. The grid used for the present calculations is shown in Figure 2.6.4-1. It is a 22×17 grid covering half the diametral section of the pipe since the flow is axisymmetric and needs to be computed only in one half. This reduces the storage requirement and allows more economic computation. In the radial direction, the grid is evenly spaced. In the axial direction and in the entrance portion of the pipe, the grid is contracting, then half way along the constriction is expanding, along the other half is contracting, and in the outlet portion of the pipe it expands again.

The inlet velocity profile was assumed fully developed parabolic, while the outlet pipe length was taken to be long enough for the flow to have acquired its boundary-layer nature far away from the recirculating zone at the downstream side of the constriction. These two assumptions required that the lengths of the inlet and outlet portions of the pipe were long enough to implement their validity. Thus, the calculations started with assumed inlet and outlet lengths and a number of iterations was allowed until a fair degree of convergence was achieved and the results were temporarily stored. The inlet and outlet boundary conditions were then checked. If the inlet and outlet lengths were too short or too long, a readjustment was made and the stored data served as initial conditions for the continuation of the iterative procedure. This practice, though laborious, produced more economic and optimised results. The time spent on the CDC 6600 for the present computations varied between 100 to 200 seconds. In cases where the geometry or the Reynolds number allowed it, results of a previous set of calculations were used as initial conditions. This reduced further the required time for the present computations.

There were three initial calculations performed with a Reynolds number of 100, constriction diameter 40% of the pipe diameter and constriction width 20% of the pipe diameter. The corresponding grids were 12 × 7, 16 × 12 and 22 × 17, the first number being the number of grid lines in the axial direction and the second in the radial. Figure 2.6.4-2 shows the results of these computations where axial velocity profiles are plotted for two stations, one before and one after the re-attachment point. A maximum deviation of 5% was observed with the two finer grids while the coarse grid yielded a maximum deviation of 20%. Thus, grid 22 × 17 was chosen for the final computations, which involved various Reynolds numbers, constriction diameters and widths as shown in Table 2.6.4-1*.

Results of these computations are shown in Figures 2.6.4-3 to 2.6.4-9 where the axial and radial velocity profiles, the stream lines and the local shear stress contours are plotted for the geometries and Reynolds numbers shown in Table 2.6.4-1**. It is evident from inspection of the graphs that the

---

* The Reynolds number of interest is of the order of 100 for aortic stenosis flow.

** These graphs have been prepared by computer aided plotting routines developed for this purpose. See footnote over.

higher the Reynolds number, the more the flow is disturbed. This can be seen from the extension of the recirculation zone downstream of the constriction. The same happens when the constriction diameter is decreasing. The variation of the constriction width does not play such an important rôle, and it is obvious that beyond a width that the flow along the constriction becomes fully developed, the length of the recirculation zone becomes independent of the width of the constriction. Thus, radial constriction variations have a stronger effect than axial ones. The imposed flow rate drastically influences the flow pattern. By inspection of the shear stress contours for different Reynolds numbers, one can see that the originally broad zone of high shear stresses contracts towards the leading edge of the constriction. This is in accordance with the theory of potential flow (equivalent to viscous flow with very high *Re*) that at this point there exists a singularity. Inspection of the axial velocity profiles reveals that the profile at the

---

[§] The scales of the vectors and the velocity profiles are given in the graphs. The contours are plotted with values expressed in % of the maximum and minimum values observed in the field. Thus, for streamlines, the maximum ψ value appears at the axis of the duct and the wall value is zero. The recirculation zone has negative values with their maximum absolute value appearing on the top of the graph as ψ^-.

For the shear stresses, the maximum negative and positive values appear on the top of the contour graphs marked T^- and T. The contours are then marked as a percentage of T^- or T, e.g. 0.02^- is the contour 0.02 T^- and 0.10 is the contour 0.10 T.

The same rules apply to all streamline and shear stress contours presented in this thesis.

entrance of the constriction becomes more blunt as the Reynolds number increases, while the recirculation zone downstream of the constriction increases with Re, the small recirculation zone upstream of the constriction at Re of 1 contracts towards the upstream wall of the constriction and vanishes for Re of 100. Similarly, the point where the flow starts being disturbed by the presence of the constriction contracts towards the constriction with increasing Re. The total extent of the disturbance of the flow is evaluated in terms of the length between the points of fully developed flow before and after the constriction. Thus, the extent of the disturbance is longer for higher Re or for smaller constriction diameter.

The above observations are summarised quantitatively in Table 2.6.4-2, where the length of re-attachment, the maximum shear stress* observed in the field and the total length of the disturbance are shown.

The pressure coefficient defined by the following relationship:

$$C_p = \frac{\Delta p}{\frac{1}{2}\rho u^2} \tag{2.6.4-1}$$

where Δp is the pressure drop between the points of fully developed flow before and after the constriction, is also evaluated and presented in Table 2.6.4-2 together with the pressure loss coefficient defined as follows:

$$C_x = \frac{\Delta p - \Delta p_{th}}{\Delta p_{th}} \tag{2.6.4-2}$$

where Δp_{th} is the theoretical pressure drop for fully developed flow in the pipe without the constriction.

Both these coefficients increase as the Re and the constriction diameter decrease, while the influence of constriction width

---

* These stresses are normalised by those of fully developed pipe flow.

is less important. Thus, relative pressure losses are higher for lower Re and narrower constrictions.

The constriction may be thought of as an orifice and therefore it is of interest to calculate its discharge coefficient. The discharge coefficients presented here are based on pressure corner tappings and are calculated from the relationship (see British Standard, BS 1042):

$$\dot{m} = C_d \cdot S_o \cdot \sqrt{\frac{2\rho \ \Delta p}{1 - (S_o/S)^2}} \qquad (2.6.4\text{-}3)$$

where $\dot{m}$ = mass flow rate

C_d = discharge coefficient

S_o = orifice cross-sectional area

S = pipe cross-sectional area

ρ = fluid density

and Δp = the pressure difference between the tappings

The results of the predicted discharge coefficients are also shown in Table 2.6.4-2. For comparison, experimental discharge coefficients measured by Johansen (1930), and those predicted by Mills (1968) are presented in the same Table.

The values calculated by the present work show a maximum deviation of approximately 11% for Johansen's and 14% for Mills' results. The discrepancy stems mainly from the fact that the width of the orifices was broader in the present work.

The total drag force is computed and presented in the form of the drag coefficient defined by the following relationship (see Hoerner (1965)):

$$C_D = \frac{F}{\frac{1}{2} \rho \ u^2 \ A} \qquad (2.6.4\text{-}4)$$

where F is the total drag force in the axial direction, A the cross-sectional area of the constriction and $\frac{1}{2}\rho u^2$ the dynamic pressure. The force F is the sum of the pressure and shear forces acting in the axial direction. The pressure force F_p was computed by the relationship:

$$F_p = \int_A p \, dA \tag{2.6.4-5}$$

where p is the static pressure and A is the area of the constriction normal to the axial direction. The shear force F_τ was calculated as follows:

$$F_\tau = \int_S \tau \, dS \tag{2.6.4-6}$$

where τ is the shear stress acting on the tangential plane and in the axial direction.

Thus, the coefficient C_D is the sum of the pressure drag coefficient C_{Dp} and the shear drag coefficient $C_{D\tau}$.

All three coefficients have been calculated and are presented in Table 2.6.4-2.

Inspection of these values reveals the following:

(a) The drag coefficient decreases as the flow rate increases, but the drag force increases.

(b) Decrease of the constriction diameter results in an increase of the drag coefficient as well as the drag force.

(c) The influence of constriction width is less important as one may see from the slow increase of the drag coefficient with increasing constriction width.

The relative importance of the pressure and shear drag may be assessed from the values of C_{Dp} and $C_{D\tau}$ in the Table. Thus, the influence of the shear force decreases when the Reynolds number increases, the constriction becomes narrower and thinner.

The axial centre-line velocity development for all computed cases is presented in Figure 2.6.4-10. The centre-line velocity starts from its theoretical value of twice the average velocity, increases as the fluid passes through the constriction and drops asymptotically towards the theoretical value. The centre-line velocity rises earlier for lower *Re* and reaches its theoretical value further downstream for higher *Re*.

The centre-line pressure development is plotted in Figure 2.6.4-11. The pressure drops according to the theoretical value before the obstruction, then there is a high pressure drop around it, due to the acceleration of the fluid, as shown in the previous Figure, and after some recovery it adjusts again to the theoretical linear drop of a fully developed pipe flow shown in the Figure.

2.6.5 Laminar Non-Newtonian Blood Flow in the Vicinity of an Aortic Stenosis

A power viscosity law fluid (power index, $\eta = 2/3$) has been assumed to simulate blood as discussed in sections 2.2.4 and 3.6. The same grid size as that of the previous section, i.e. 22 × 17, was employed here, and the profile at the inlet of the venule was taken to be that of a fully developed pipe flow of a fluid obeying the power viscosity law, i.e. given by the relationship:

$$u = \bar{u} \cdot \frac{3n + 1}{n + 1} \cdot \left[1 - \left(\frac{r}{R}\right)^{(n+1)/n}\right] \qquad (2.6.5\text{-}1)$$

where $\bar{u}$ is the average velocity, r the radial coordinate, R the venule radius and n the index of the power law.

The same practices applied for the computations of the Newtonian flows in the pipe with the constriction are applied here. Because of the exponentials involved in the computation of the local viscosity, the non-Newtonian procedure is more expensive in computing time. The time spent on a CDC 6600 varied between 120 to 300 seconds for each flow configuration. However, the use of previously computed results as initial conditions, where appropriate, reduced the required computing time considerably.

The results of these computations have been plotted by the use of the same computer aided plotting routines as in the case of Newtonian flows. Figure 2.6.5-1 to Figure 2.6.5-7 present plots of the axial and radial velocity profiles, streamlines and shear stress contours for the flow rates and geometries shown in Table 2.6.5-1. Qualitatively, the same conclusions may be drawn as in the case of Newtonian flows. Quantitative results of these computations are summarised in Table 2.6.5-2, where the re-attachment length, the maximum shear stress observed in the field, and the total length of flow disturbance, as defined in the previous section, are shown. The values of re-attachment and total lengths are higher than those corresponding to Newtonian flows, but the maximum shear stresses normalised by the wall shear stress of fully developed flow are lower.

The pressure coefficients C_p and pressure loss coefficients C_x defined by equations (2.6.4-1) and (2.6.4-2), respectively, have also been evaluated and shown in the Table. These coefficients are smaller in comparison to those for Newtonian flows. The discharge coefficients C_d have been evaluated and are also shown in the Table. They are higher than the corresponding coefficients for Newtonian flows.

The total drag coefficient C_D and its two components C_{Dp} and $C_{D\tau}$ are also presented in the Table. Similar conclusions may be drawn for the effect of Re, constriction diameter and width as in the case of Newtonian fluid flows. However, the coefficients appear to be smaller in this case although the relative importance of the pressure and shear drag forces is similar to that of Newtonian flows.

The development of the axial velocity at the centre-line of the venule is plotted in Figure 2.6.5-8 for all computed cases. The velocity starts with its theoretical value of 1.8 times the average velocity, increases as the fluid passes through the constriction and then drops asymptotically towards the fully developed value again. As in the case of Newtonian flows, the centre-line velocity rises earlier for low Re_N and reaches its theoretical value at the centre-line further downstream of the constriction for higher Re_N.

Figure 2.6.5-9 shows the development of the centre-line pressure for the computed cases. The pressure drops first linearly, then there is a high pressure drop near the stenosis and after some recovery in the recirculation region downstream of the stenosis, it adjusts again to the theoretical pressure drop given by the slope of the theoretical pressure drop shown in the Figure.

The above qualitative and quantitative observations reveal two hydrodynamic phenomena of biorheological importance. Firstly, there exists a region of high shear stresses appearing at the leading edge of the stenosis. Thus, one may explain the haemolysis of blood occurring in aortic stenoses as due to the cell breakdown under the high shearing in this region (Champion et al (1971), Blackshear (1972)).* In addition, there is a possibility of thrombus detachment with the dangerous consequence of embolus formation and total blockage of the venule as this embolus is carried downstream by the flowing blood.

Secondly, in the corners formed by the stenosis with the venule wall, there appears to be a low shear stress region. Cells or platelets inside these regions may adhere on the venule or stenosis wall. It is known today that platelet adhering is caused by the release of active adhesive agents at the site of thrombotic lesions (Begent and Born (1970)). The adhering of platelets and cells will cause further release of these agents in a feedback process. At the same time, the blood cell concentration will drop and thus its viscous characteristics will be altered. This, in turn, may disturb the stability of the annular eddy and new cells will enter the recirculation zone to assist in maintaining its dynamic balance. Thus, complex stability of the flow pattern may be expected around the stenosis which stems from biological processes still under investigation as well as from the particulate nature of blood.

A consequence of these observations is that under the acting shearing forces, due to the flow, and the adhesion of platelets and cells, due to biological processes, the shape of a stenosis is most likely to deform into that shown in Figure 2.6.5-10, which is a shape commonly observed in aortic stenoses.

2.6.6 Laminar Newtonian Flow in the Vicinity of an Asymmetric Obstacle in a Round Pipe

It is clear from the previous axisymmetric flow calculations

---

* shear stresses higher than $\sim 2000\ dyn/cm^2$ may cause cell breakdown

that an asymmetric blockage in a pipe, as shown in Figure 2.6.6-1, will cause a three-dimensional recirculating flow in its near vicinity. A three-dimensional numerical elliptic procedure is therefore required to predict such a flow. The numerical scheme described in section 2.5 and tested in section 2.6.2 has been used here to investigate these kinds of recirculating flows.

Because of symmetry, and for economic reasons, half the cross-section is considered. The grid employed for the present purpose is three-dimensional with even spacing in the radial and circumferential directions, as shown in Figure 2.6.6-1. The grid is unevenly spaced in the axial direction and it is basically similar to that used for axisymmetric flows.

The inlet velocity profile was taken to be that of a fully developed pipe flow, while the length of the outlet portion of the pipe was assumed long enough for the flow to have acquired its boundary-layer nature, i.e. far away from the recirculation zone.

It was necessary to ensure that both the inlet and outlet portions of the pipe were adequately long for the inlet and outlet boundary conditions to be valid. The same practices of storing the results and checking the boundary conditions at the inlet and outlet applied for the axisymmetric flows were used here.

A preliminary computational experiment was carried out to establish the best combination of the number of sweeps of the TDMA for the solution of the finite-difference equations described in section 2.4. Fast convergence is important, particularly with three-dimensional elliptic procedures where their iterative nature renders them expensive in terms of computer time and space. The outcome of this test is shown in Figure 2.6.6-2 where the normalised sums of residual mass and axial momentum are plotted against the number of iterations for different combinations of number of sweeps of the momentum and pressure-correction equations. It appears that a double sweep of pressure-correction and a single sweep of the momentum equations is likely to produce good rates of convergence and economic results.

The FTN compiler was used to create the object code. Although the compilation time was considerably longer than using the MNF compiler, the object code was twice as fast. Where possible, results of previous computations were used as initial conditions for a new set of flow and geometry characteristics, which effectively reduced the time required for the computations.

The time spent on the CDC 6600 machine to compute a flow configuration varied between 300 and 600 seconds, depending on the flow configuration.

Three initial calculations were performed to establish the appropriate grid size for the final calculations. Thus, for a Reynolds number* of 10, a constriction/pipe diameter ratio of 0.40, width ratio of 0.40 and half angle α^o of 72^0 was used with grids of $7 \times 7 \times 12$, $12 \times 12 \times 12$ and $12 \times 12 \times 22$. Results of these computations are shown in Figure 2.6.6-3, where the velocity profile in the symmetry plane and at a station z/D of 0.25 downstream of the trailing edge of the constriction, and the development of the centre-line axial velocity are plotted. The two former grids produced a maximum deviation of 3%, while there was a discrepancy of 10% for the coarse grid. Thus, the grid with $12 \times 12 \times 22$ lines was chosen for the final computations with

---

* The Reynolds number is defined in terms of the average velocity and the diameter of the pipe.

the flow rates and geometries given in Table 2.6.6-1*. Results of these computations, corresponding to Re = 10, d/D = 0.40, l/D = 0.40 and $\alpha = 72^0$, are shown in Figures 2.6.6-4 to 2.6.6-11** where velocity vector fields, velocity profiles and shear stress contours are plotted for different planes, as shown in the Figures.

Inspection of the graphs reveals that the flow is disturbed and retarded around the obstacle with a small recirculation zone on the downstream side. There is a high shear stress region on the edges of the constriction and regions of low shear stresses in the corners formed between the side walls of the constriction and the pipe wall. The flow starts deviating from the fully developed flow upstream of the constriction, then accelerates as it passes through it and starts developing again after the obstacle.

A summary of the results obtained for different flow configurations is given in Table 2.6.6-2, where the length of re-attachment, the total length of flow disturbance and the maximum shear stress observed in the field are shown.

The recirculation zone increases with increasing Reynolds number and constriction angle. The same conclusions may be drawn for the total length of the disturbance zone and the maximum shear stress observed in the field.

The pressure coefficients C_p and the pressure loss coefficient C_x, defined by equations (2.6.4-1) and (2.6.4-2), respectively, have also been calculated and presented in the Table. Both coefficients increase with decreasing Reynolds number and increasing obstacle

---

* The Reynolds number of interest is of the order of 10 which is closer to blood flow in venules.

** These graphs have, again, been prepared by the use of computer aided plotting routines developed for this purpose.

angle. Thus, the relative pressure losses are higher for wider obstacle angles and lower Reynolds numbers.

The total drag force in the axial direction has been evaluated and expressed in the form of the total drag coefficient C_D as defined by equation (2.6.4-3). This force now consists of three components. The two ones calculated via equations (2.6.4-4) and (2.6.4-5) and an extra component due to the shear forces acting on the side diametral planes. Thus, the total drag coefficient C_D consists of three components, C_{Dp}, $C_{D\tau_I}$, $C_{D\tau_{II}}$, attributed to pressure forces, circumferential shear forces, and radial shear forces acting in the axial direction, respectively.

The total drag coefficient C_D and its three components, C_{Dp}, $C_{D\tau_I}$ and $C_{D\tau_{II}}$ are shown in Table 2.6.6-2. All four coefficients increase with decreasing Re and increasing constriction angle. The influence of the shear forces is higher for low Reynolds numbers.

Figure 2.6.6-12 shows the development of the axial velocity along the centre-line of the pipe for different computed flow configurations. The centre-line velocity starts with its fully developed value, rises as the fluid passes through the constriction and then falls asymptotically towards the fully developed value of twice the average velocity. The value of the maximum velocity increases as the constriction angle increases.

The centre-line pressure, shown in Figure 2.6.6-13 for all computed cases of Table 2.6.6-1, drops linearly before the constriction, then there is a high drop around the obstacle and, after some recovery, it begins to drop linearly again and parallel to the theoretical drop for a fully developed flow without an obstacle. The pressure drop around the constriction increases as the angle is increasing.

2.6.7 Laminar Non-Newtonian Blood Flow in the Vicinity of an Asymmetric Thrombus in a Venule

The comparison of results of Newtonian and non-Newtonian axisymmetric flows revealed a general similarity of the flow in the vicinity of the constriction. Results of the three-dimensional recirculating flows near an asymmetric obstacle presented in the previous section showed the effect of both the flow rate and the angle of the obstacle on the flow pattern and its characteristics. This section presents computational results of the flow with the same three-dimensional configuration but employs a fluid with a non-Newtonian (power law) constitutive equation similar to that attributed to blood flowing in narrow glass capillaries or blood vessels at low Reynolds numbers.

The grid used for the Newtonian flows was also used here. The velocity profile at the inlet of the venule before the thrombus was taken to be that of a fully developed blood flow in a venule obeying the power law calculated from equation (2.6.5-1). The length of the venule after the thrombus was taken to be much longer than the recirculation zone and the condition that the flow is of a boundary-layer nature was imposed at the outlet. It was necessary, therefore, to check that both the inlet and outlet lengths are adequate for these two conditions to be valid. Thus, previous practices of storing the results of a number of iterations and checking the validity of these conditions were repeated here.

Because of the exponentials involved in the computation of the local viscosity via equation (2.2.4-12), the time required to predict a non-Newtonian flow configuration was longer than for a corresponding Newtonian flow. Thus, the time spent for the prediction of the non-Newtonian flow of Table 2.6.7-1 was 1200 seconds on a CDC 6600 machine, and is twice that for the same flow of a Newtonian fluid.

Results of these predictions for one non-Newtonian fluid flow, corresponding to a Reynolds number of 10, venule/thrombus diameter ratio of 0.40, width ratio of 0.40 and half angle of 72^{0} are shown in Figures 2.6.7-1 to 2.6.7-8 , where velocity vector fields, velocity profiles and shear stress contours are presented for the planes shown in the Figures. A similarity of the flow field with the Newtonian flow may be readily deduced.

Quantitative results of these computations are presented in Table 2.6.7-2 where the re-attachment length, total disturbance length, maximum shear stress* observed in the field, pressure coefficients Cp and Cx, and the drag coefficients C_D , C_{Dp}, $C_{D\tau_I}$ and $C_{D\tau_{II}}$ are shown.

The two lengths are longer than in the corresponding Newtonian flow configuration but all the other values of the Table are lower than for the Newtonian case. However, the contribution of the shear drag coefficients $C_{D\tau_I}$ and $C_{D\tau_{II}}$ to the total drag coefficient C_D is similar to that for the Newtonian flow.

The centre-line axial velocity and pressure development are shown in Figures 2.6.7-9 and 2.6.7-10, respectively. Similar conclusions to those drawn for Newtonian flows may be drawn here. Thus, the velocity at the centre-line starts with its fully developed value of 1.8 times the average velocity, rises as the blood passes through the thrombus and then falls asymptotically towards the fully developed value. The pressure, on the other hand, falls linearly before the thrombus, there is a high pressure drop around the thrombus and after some recovery, the pressure settles to a linear drop parallel to the theoretical drop for flows without a thrombus shown in the Figure.

From the biorheological viewpoint, it is recognised that

---

* This stress is normalised by that on the wall of fully developed pipe flow.

there exist regions of high shear stresses, mainly around the circumferential surface of the thrombus, and regions of low shear stresses appearing in the corners formed by the radial surfaces of the thrombus and the wall of the venule. It appears, therefore, that the conclusions drawn for the aortic stenosis problem may be applied here as well.

Although the values of shear stresses and drag coefficients of Table 2.6.5-2, which refer to the stenosis problem, are higher than those of the present Table, qualitatively the flow may produce the same effects on the thrombus.

Thus, the high shear stresses may result in a cell breakdown and haemolysis may be observed around the thrombus. When the drag forces exceed the adhesive forces of the thrombus structure, one may expect that either parts of the thrombus detach or the whole thrombus is detached and becomes an embolus carried downstream by the flowing blood. On the other hand, in the low shear stress regions, one expects that the biological adhesive agents released at the site of the thrombus will attract more platelets and blood cells. The thrombus, therefore, is expected to grow in these sites of low shear stress.

The overall stability of the eddies in the downstream side of the thrombus is expected to be of a complex nature since blood corpuscles will enter the recirculation zone to assist its hydrodynamic balance disturbed by the adherence of platelets, blood cells and lipoids on the walls of the thrombus and the venule.

As an outcome of these observations, one may expect that the thrombus will, under the action of the shear forces of the flow and adhesive forces of the released biological active agents, deform to the shape given in Figure 2.6.7-11.

2.7 CLOSURE

The predictions presented in this chapter demonstrated the capability of the numerical schemes to produce detailed characteristics of Newtonian and non-Newtonian flows. The study of the detailed characteristics of the flow configurations considered revealed important features for the design of industrial and medical equipment. In addition, it was demonstrated that the results may contribute to the explanation of the phenomena of atherosclerosis, thrombosis, haemolysis and embolism occurring in the cardiovascular system of man.

The geometries studied were designed to demonstrate the capability of the procedures and other configurations may be handled. The parabolic procedure was tested against experimental results obtained with laser Doppler velocimetry and a good agreement was found. Experimental work is needed to demonstrate the validity of the two elliptic procedures and to allow more accurate viscosity laws for blood to be obtained. Laser Doppler velocimetry may be used for this purpose; its suitability is demonstrated in the following chapter.

CHAPTER 3

EXPERIMENTAL INVESTIGATION

3.1 INTRODUCTION

3.1.1 Objectives

The main purpose of the present experimental investigation was to develop a laser Doppler velocimeter capable of measuring in small ducts, and particularly in venules. This chapter, therefore, reviews laser Doppler velocimetry as a method for the measurement of instantaneous local velocity and describes an investigation of the design parameters and resulting performance of a LDV. Various methods of achieving a measuring control volume of small dimensions and a signal processing system, based on frequency counting techniques, are described and have been applied in various flow configurations.

Measurements in flows of air, water and diluted or whole blood in small glass capillaries are reported. Experiments *in vivo* using live mice are also described and the results are interpreted in terms of the present limitations of the technique and the necessary steps required to allow the precise measurement of the velocity profile in the small venules of living animals.

As a consequence of the experimental programme, a laser Doppler velocimeter, embodied in a microscope, was designed and its advantages and disadvantages as a velocity measuring device for small channel flows, and especially blood flow in venules, are discussed.

Measurements of laminar flows in small size ducts are carried out with a control volume of finite dimensions and, as a consequence of spatial velocity fluctuations, the results have to be interpreted appropriately; a method of correcting for velocity fluctuations due to velocity gradient broadening is reported. In the case of blood flow, concentration gradient broadening is also considered and a method for its correction is described.

3.1.2 Outline of Chapter

The remainder of this chapter is divided into eight sections. Section 3.2 introduces laser Doppler velocimetry as a local velocity measuring technique. In section 3.3, measurements in medium size channels (≈ 10 mm) are reported and discussed. Various arrangements intended to minimise the control volume are described in section 3.4, while in section 3.5, measurements of velocity in water, diluted and whole blood flowing in small glass capillaries are presented and discussed. A derivation of a blood viscosity law, based on available information in the literature and the present glass capillary experiments, is presented in section 3.6. A laser Doppler velocimeter design, combined with a microscope, for miniature flows is presented and discussed in section 3.7. Attempts to measure *in vivo* blood flow in the mouse mesentery are reported in section 3.8. Finally, in section 3.9, concluding remarks are presented.

3.2 LASER DOPPLER VELOCIMETRY

3.2.1 Introduction

Laser Doppler velocimetry is based on the principle that light scattered by a moving particle has a shifted frequency which is proportional to the velocity of the moving particle. The application of the technique in fluid mechanics, therefore, requires a knowledge of the principles of the Doppler frequency shift of light scattered by small moving particles, the properties of laser light and its propagation through various optical components, light detecting devices and electronic Doppler signal processing systems. These subjects have been considered, for example, by Durst, Melling and Whitelaw (1976) and only a brief review of the basic phenomenon of the Doppler shift and frequency response equations of a laser Doppler velocimeter are presented here.

3.2.2 Doppler Signal Generation and Interpretation

Consider a light beam of frequency ν and wave length λ propagating in the direction x_i and incident on a small particle moving with velocity V_i, as shown in Figure 3.2.2-1a. An observer moving with the particle will record a light frequency ν_P, which is Doppler shifted and is given by the relationship:

$$\nu_P = \nu \cdot \left(1 - \frac{V_i \cdot x_i}{C}\right) \tag{3.2.2-1}$$

where C is the light speed.

The moving particle transmits light with a frequency ν_P and thus a stationary observer in the direction y_i at A will record a frequency ν_A, which is again Doppler shifted and given as follows:

$$\nu_A = \frac{\nu_P}{1 - \frac{V_i \cdot y_i}{c}} = \nu \cdot \frac{1 - \frac{V_i \cdot x_i}{c}}{1 - \frac{V_i \cdot y_i}{c}} \tag{3.2.2-2}$$

The original light beam of frequency ν, having been scattered by the moving particle, is received at A with a Doppler shifted frequency ν_A given by equation (3.2.2-2). In general, the shifted frequency ν_A could be recorded and, from the geometry of the system, the velocity of the moving particle determined. However, a light detection device cannot respond to the high frequency of light ($\approx 5 \times 10^{14}$ Hz) and thus convenient ways have to be introduced to record the Doppler shift of the frequency of the light beam.

By mixing light from the stationary source of frequency ν with light scattered from the moving particle and received at A with Doppler shifted frequency ν_A, the frequency difference can be determined and the particle velocity calculated from the relationship:

$$\nu_D = \nu_A - \nu = \frac{1}{\lambda} \cdot V_i \cdot (y_i - x_i) \tag{3.2.2-3}$$

Frequency-velocity response of an LDV

There are three basic modes of operation of a laser Doppler velocimeter: Doppler mode, reference beam mode, and fringe mode. The general layout of these configurations is shown in Figure 3.2.2-1. In the Doppler mode (Figure 3.2.2-1b), a laser beam of frequency ν propagating in the direction z_i, is focused by the lens L_1 to its waist P within the flow. Light is collected by the lens L_2 in the directions x_i and y_i and focused onto the photomultiplier pinhole. Light scattered by a particle with velocity V_i at P and collected at A has a frequency:

$$\nu_A = \nu \cdot \frac{1 - \dfrac{V_i \cdot z_i}{c}}{1 - \dfrac{V_i \cdot x_i}{c}} \tag{3.2.2-4}$$

Similarly, the frequency of light received at B is given by:

$$\nu_B = \nu \cdot \frac{1 - \dfrac{V_i \cdot z_i}{c}}{1 - \dfrac{V_i \cdot y_i}{c}} \tag{3.2.2-5}$$

Thus, the frequency difference recorded after photomixing on the photodetector is given by the relationship:

$$\nu_D = \nu_B - \nu_A = \frac{\nu}{c} \cdot \frac{1 - \dfrac{V_i \cdot z_i}{c}}{\left(1 - \dfrac{V_i \cdot x_i}{c}\right)\left(1 - \dfrac{V_i \cdot y_i}{c}\right)} \cdot V_i \cdot (y_i - x_i) \tag{3.2.2-6}$$

Because $V_i << c$ in most practical cases, this equation may be rewritten as follows:

$$\nu_D = \frac{1}{\lambda} \cdot V_i \cdot (y_i - x_i) \tag{3.2.2-7}$$

In the <u>reference beam mode</u>, shown in Figure 3.2.2-1c, the laser beam is split up into two beams I and II and focused by the lens L_1 into their waists at the crossing point P inside the flow. Light is collected by the lens L_2 in the forward direction x_i of beam I from the point P and focused onto the pinhole of the photodetector. A particle with velocity V_i at P scatters light from beam I propagating in the direction x_i, which is collected by the lens L_2 with frequency ν_I given by the relationship:

$$\nu_I = \nu \cdot \frac{1 - \frac{V_i \cdot x_i}{C}}{1 - \frac{V_i \cdot x_i}{C}} = \nu \tag{3.2.2-8}$$

Similarly, light from the beam II, propagating in the direction y_i, is scattered by the moving particle P and collected by the lens L_2 in the direction x_i with frequency ν_{II}, which is given by the formula:

$$\nu_{II} = \nu \cdot \frac{1 - \frac{V_i \cdot y_i}{C}}{1 - \frac{V_i \cdot x_i}{C}} \tag{3.2.2-9}$$

The recorded frequency difference on the photodetector is then given as follows:

$$\nu_D = \nu_{II} - \nu_I = \frac{\nu}{C} \cdot \frac{1}{1 - \frac{V_i \cdot x_i}{C}} \cdot V_i \cdot (y_i - x_i) \tag{3.2.2-10}$$

and since $V_i << C$ for most flows:

$$\nu_D = \frac{1}{\lambda} \cdot V_i \cdot (y_i - x_i) \tag{3.2.2-11}$$

Finally, in the case of fringe mode, shown in Figure 3.2.2-1d, a laser beam is split into two beams I and II focused by the lens L_1

into their waists at the crossing point P inside the flow. Light is collected by the lens L_2 and focused onto the photodetector pinhole. A particle at P with velocity V_i scatters light from beam I propagating in the direction x_i, which is collected in the direction z_i of the lens L_2 with a frequency ν_I given as follows:

$$\nu_I = \nu \cdot \frac{1 - \dfrac{V_i \cdot x_i}{C}}{1 - \dfrac{V_i \cdot z_i}{C}} \tag{3.2.2-12}$$

Similarly, light from beam II scattered by the moving particle at P is collected by the lens with a frequency ν_{II} given by:

$$\nu_{II} = \nu \cdot \frac{1 - \dfrac{V_i \cdot y_i}{C}}{1 - \dfrac{V_i \cdot z_i}{C}} \tag{3.2.2-13}$$

The frequency beat recorded by the photodetector is then given by the relationship:

$$\nu_D = \nu_I - \nu_{II} = \frac{V_i \cdot (y_i - x_i)}{1 - \dfrac{V_i \cdot z_i}{C}} \tag{3.2.2-14}$$

and, since $V_i << C$:

$$\nu_D = \frac{1}{\lambda} \cdot V_i \cdot (y_i - x_i) \tag{3.2.2-15}$$

An alternative but less comprehensive approach in the establishment of the response equation of the fringe mode of an LDV may be summarised as follows:

Two coherent light beams I and II with plane wavefronts and wavelength λ combined at P form an interference pattern of stationary planar fringes parallel to the bisector of the two beams (Collier et al (1971), Lading (1971)). The fringe spacing is given by the relationship:

$$\Delta x = \frac{\lambda}{2 \sin \phi} \tag{3.2.2-16}$$

where ϕ is the half angle of incidence of the two light beams. Thus, a particle travelling with velocity V_i will scatter light with a frequency of the order of the light frequency modulated by the frequency of the crossing of the fringes:

$$\nu_D = \frac{V_i \cdot n_i}{\Delta x} = \frac{V_i \cdot (y_i - x_i)}{\lambda} \tag{3.2.2-17}$$

where n_i is the unit vector normal to the fringes.

It appears, therefore, from equations (3.2.2-7), (3.2.2-11) and (3.2.2-15) or (3.2.2-17) that the three modes of operation of an LDV have the same frequency-velocity response equation, which depends on the light wavelength and the geometry of the system. Thus, for a given laser beam wavelength λ and angle 2ϕ, as shown in Figure 3.2.2-1, the velocity component u normal to the bisector of the angle 2ϕ is related to the Doppler shift via the relationship:

$$\nu_D = \frac{2\, u \,.\, \sin \phi}{\lambda} \tag{3.2.2-18}$$

which is common for the three modes. The advantages and disadvantages of the three modes are discussed later.

Scattering of light by small particles

The operation of an LDV is based upon the detection of Doppler shifted light scattered by small particles in the flow. Light scattering by particles much smaller than the light wavelength is dealt with by the Rayleigh theory of scattering. In most LDV applications, however, the size of the particles is of the order of the wavelength and thus Mie light scattering theory is applied (see Van de Hulst (1957), Kerker (1969)).

In Mie scattering, a plane electromagnetic wave incident upon a particle induces forced oscillations in its charges with the same frequency. The intensity distribution of the scattered light depends on the refractive index and the size of the particle.

Particle scattering for LDV has been treated by, among others, Berman (1972,1973), Melling (1971) and Durst (1972), and here only the two major selection criteria are mentioned. These are, firstly, that the particles should follow the flow without disturbing it in order to represent it and, secondly, they should possess good scattering qualities in order to produce Doppler signals of good quality.

Considering the first requirement, Melling (1971) suggested an upper limit (of d_p = 1 μm) for the diameter of the liquid droplets used as scattering centres in gas flows. In terms of the optimum signal quality of an LDV operating in the fringe mode with fringe spacing Δx, Durst (1972) proposed the following criterion:

$$d_p \simeq \frac{\Delta x}{4} \tag{3.2.2-18a}$$

However, this cannot serve as a strict criterion for the selection of either the fringe spacing or the particle size. For example, an experiment with a rotating wire of 10 μm diameter and fringe spacing of

≈ 0.6328 μm was conducted prior to the blood flow tests. The signals thus obtained were of good quality and this showed that similar quality signals could be expected from blood cells. Furthermore, Doppler signals obtained in the present work from red blood cells as scattering centres were of good quality, although the cell size-to-fringe spacing ratio was as high as 20.

Figure 3.2.2-2 shows the aximuthal distribution of scattered light intensity computed by Durst (1972) and based on van de Hulst's (1957) equations. It is clear that scattering is stronger in the forward direction for larger particles. However, if the particles become very large ($d_p >> \lambda$), then the laws of reflection are applied rather than Mie scattering.

Photomixing and photodetectors

The mixing of light waves has been treated by Forrester et al (1955), Forrester (1956, 1961), Corcoran (1965) and Drain (1972) made an analysis of coherent and non-coherent detection methods, as applied to LDV. When two waves of slightly different frequencies combine, they produce a wave with an average frequency which is modulated by the difference frequency. This may be used to mix light waves, provided that they are coherent. Thus, if a beam with a Doppler frequency shift ν_D is mixed with the original beam, the output of the photodetector will contain the Doppler frequency ν_D, provided that ν_D is within the frequency response of the detector. The frequency response of photomultiplier tubes is of the order of several hundred megaHertz and thus the average frequency of the two signals is not usually observed.

Most photodetectors are square law devices where the output current I_o is related to the input electric field E_i by the equation:

$$I_o = K_o \cdot E_i^2 \qquad (3.2.2\text{-}19)$$

where K_o is a constant. For two beams with amplitudes E_1 and E_2, mixing on the photodetector:

$$E_i = E_1 \cos 2\pi \nu_1 t + E_2 \cos 2\pi \nu_2 t \qquad (3.2.2\text{-}20)$$

and thus:

$$I_o = K_o \Big[E_1^2 \cos^2 2\pi \nu_1 t + E_2^2 \cos^2 2\pi \nu_2 t + E_1 E_2 \cos 2\pi (\nu_1 + \nu_2) t + E_1 E_2 \cos 2\pi (\nu_1 - \nu_2) t\Big] \qquad (3.2.2\text{-}21)$$

By taking the time average, the output current may be expressed as follows:

$$I(t) = K \cdot \left[\left(\frac{E_1^2 + E_2^2}{2}\right) + E_1 E_2 \cos 2\pi \nu_D t\right] \qquad (3.2.2\text{-}22)$$

where K is a constant. Thus, the output signal is a combination of a DC signal:

$$I_{dc} = K \cdot \frac{E_1^2 + E_2^2}{2} \qquad (3.2.2\text{-}23)$$

and the Doppler signal:

$$I_D = K \cdot E_1 E_2 \cos 2\pi \nu_D t \qquad (3.2.2\text{-}24)$$

It becomes apparent, therefore, from equation (3.2.2-24) that the Doppler shift ν_D can be detected if light beams with this frequency difference are optically mixed on the photodetector. Photodiodes and photomultipliers may be used as light detecting devices in laser Doppler velocimetry. A limitation for the photomixing process is the signal-to-noise ratio. For this reason, photodiodes are limited in terms of frequency response for most practical flow situations and thus photomultipliers are preferred.

Comparison of the three LDV modes

When more than one particle is present in the control volume, the scattered light received in the photodetector must be in phase, otherwise a signal cancellation may occur and the result will be a drop of the signal strength. The analysis of Forrester et al (1955), Corcoran (1965) and Drain (1972) showed that under multiple scattering conditions, light should be detected coherently. The coherent detection condition may be stated as follows (Ross (1966) and Lading (1971)):

$$A < \frac{\lambda^2}{\Omega} \qquad (3.2.2\text{-}25)$$

where A is the area of the detector and Ω is the solid angle by which the detector views the scattering control volume.

Wang and Snyder (1974) have shown that there is a specific concentration of particles for which the signal-to-noise ratio becomes maximum for each of the three modes of LDV operation. Their results showed that this concentration is smaller for the Doppler mode and higher for the reference beam mode. However, increasing the particle concentration further than these values results in a rapid decrease of the signal strength.

These results bear an importance to measurements in blood flow where red blood cells, used as light scatterers, have a high concentration. It seems reasonable therefore to use coherent detection methods to achieve optimum signal quality. These problems are discussed in the blood flow measurements section.

Experience with the three LDV modes has shown that the best quality of signal-to-noise ratio is achieved with the fringe mode and thus this mode has been selected for the present experiments.

3.2.3 The LDV Control Volume

The fringe mode of LDV operation has been used for all the experiments reported in this thesis and thus the control volume considerations of this section are referred to this mode.

The properties of laser beams are first considered and then the fringe visibility is discussed in relation to the temporal and spatial coherence of the beams. Finally, theoretical relationships for the estimation of the size and shape of the control volume are described.

✓ Laser beams

The theory of laser operation, a necessary component of laser Doppler velocimetry, is discussed by Lamb (1964). In general, a laser consists of an optical resonator formed by two coaxial mirrors and some laser gain medium. Optical resonators are described by Kogelnik (1965) and Kogelnik and Li (1966), but historically the origin is traced back to when Dicke (1958), Prokhorov (1958) and Schawlow and Townes (1958) independently proposed the use of Fabry-Perrot interferometers as laser resonators. The frequency band over which laser oscillation occurs is determined by the frequency region over which the gain of the laser medium exceeds the losses of the resonator (Smith (1970)). The total output of a laser, as a function of time, depends on the amplitudes, frequencies and relative phases of all the resonator oscillating modes falling within this band. If the oscillating modes maintain a constant frequency spacing and fixed phase relationship, the output will be well-defined and the laser will be "mode-" or "phase-locked". The form of the output beam will then depend on which laser modes are oscillating and what phase relationship is maintained.

Auston (1968) showed that the output of a traverse mode-locking (TEM_{00}) laser beam has a Gaussian intensity distribution. The He-Ne and Argon lasers used in the present experiments operated in the TEM_{00} mode and produced Gaussian beams.

Properties of Gaussian beams

Kogelnik (1965) has shown that a Gaussian beam expands as it propagates through space (see Figure 3.2.3-1a), according to the law:

$$d^2 = d_w^{\,2} \left[1 + \left(\frac{4\lambda x}{\pi d_w^{\,2}}\right)^2 \right] \tag{3.2.3-1}$$

where d is the diameter of the beam at the $1/e^2$ intensity level at distance x from the beam waist, where the beam has its minimum diameter d_w. The radius of curvature of the wave front at x is given by the relationship:

$$R(x) = x \cdot \left[1 + \left(\frac{\pi d_w^{\,2}}{4\lambda x}\right)^2 \right] \tag{3.2.3-2}$$

When a Gaussian beam passes through a thin lens, a new beam waist is formed and the parameters of the expansion law are changed (Figure 3.2.3-1b). Focusing of Gaussian beams by lenses is treated by Kogelnik (1965) and covers many lens configurations. Here, only the simple focusing function of a thin lens is treated. Consider a parallel Gaussian beam with intensity distribution:

$$I(r) = I_o \cdot e^{-8r^2/D^2} \tag{3.2.3-3}$$

where I_o is the maximum intensity of the beam and D is the beam diameter at the $1/e^2$ intensity level.

The beam will be focused at its new waist with a diameter given as follows:

$$d = \frac{4 \lambda f}{\pi D} \tag{3.2.3-4}$$

where f is the focal length of the lens and λ is the wavelength of the parallel beam.

The intensity distribution of the beam will be Gaussian given by equation (3.2.3-3). Assuming a total power P, the maximum intensity of the beam may be calculated from the expression:

$$P = \int_o^{d/2} I_o \, e^{-8r^2/d^2} \, 2\pi \, r \, dr = \frac{\pi I_o d^2}{8} \tag{3.2.3-5}$$

and thus:

$$I_o = \frac{8P}{\pi d^2} \tag{3.2.3-6}$$

It is possible, therefore, for the case of blood flow, to select the laser power from equation (3.2.3-6) when the maximum intensity before cell breakdown or burning is known.

Coherence and fringe visibility

Temporal or spatial coherence is of importance in the formation of a fringe pattern with high fringe contrast, which in turn gives rise to good quality Doppler signals. Laser beams are said to be both temporally and spatially coherent. When two electromagnetic fields of light E_1 and E_2 combine at a point P, they produce a total intensity which may be expressed as follows (Fowles (1968)):

$$I = \lim_{T\to\infty} \int_0^T (E_1 + E_2)\ (E_1^* + E_2^*)\ dt \qquad (3.2.3\text{-}7)$$

where E_1^* and E_2^* are the complex conjugates of E_1 and E_2, respectively. If the two fields are assumed to be stationary and equally polarised, their vectorial form can be ignored and equation (3.2.3-7) rewritten in the form:

$$I = I_1 + I_2 + 2\ Re \left[\lim_{T\to\infty} \int_0^T (E_1 \cdot E_2^*)\ dt\right] \qquad (3.2.3\text{-}8)$$

where the intensities I_1 and I_2 are given by:

$$I_1 = |E_1|^2 \quad \text{and} \quad I_2 = |E_2|^2$$

The integral term in this equation is called the "interference term" because it causes intensity variations and, as a result, fringe formation*. Although the two beams originate from the same laser, they might not travel equal pathways. Assuming that there is a time difference τ between the two beams from the source until they combine at P, equation (3.2.3-8) may be rewritten as:

$$I = I_1 + I_2 + 2\ Re\ \Gamma_{12}\ (\tau) \qquad (3.2.3\text{-}9)$$

where: $$\Gamma_{12}\ (\tau) = \lim_{T\to\infty} \int_0^T E_1\ (t) \cdot E_2^*\ (t+\tau)\ dt \qquad (3.2.3\text{-}10)$$

---

* When the beams are orthogonally polarised, there are no fringes formed.

is called the correlation or mutual coherence functions (Lee (1960)). The auto-correlation functions of E_1 and E_2 for $\tau = 0$ are the light intensities I_1 and I_2, respectively, i.e. $\Gamma_{11}\ (0) = I_1$ and $\Gamma_{22}\ (0) = I_2$. Usually, the correlation functions of E_1 and E_2 are expressed in a normalised form as follows:

$$\gamma_{12}\ (\tau) = \frac{\Gamma_{12}\ (\tau)}{\sqrt{\Gamma_{11}\ (0)\ .\ \Gamma_{22}\ (0)}} = \frac{\Gamma_{12}\ (\tau)}{\sqrt{I_1\ I_2}} \qquad (3.2.3\text{-}11)$$

Equation (3.2.3-~~10~~9) may be expressed, then, as:

$$I = I_1 + I_2 + 2\ \sqrt{I_1\ I_2}\ .\ Re\ (\gamma_{12}\ (\tau)) \qquad (3.2.3\text{-}12)$$

In general, $\gamma_{12}\ (\tau)$ is a periodic function of τ and the value of $|\gamma_{12}\ (\tau)|$ characterises the degree of coherence. Thus, when $|\gamma_{12}\ (\tau)| = 1$, the beams are said to be completely coherent; if $0 < |\gamma_{12}\ (\tau)| < 1$, the beams are partially coherent, and finally if $|\gamma_{12}\ (\tau)| = 0$, the beams are said to be completely incoherent.

The fringe visibility in a fringe pattern is defined as:

$$V = \frac{I_{max} - I_{min}}{I_{max} + I_{min}} \qquad (3.2.3\text{-}13)$$

where the maximum and minimum intensities are given by:

$$I_{max} = I_1 + I_2 + 2\ \sqrt{I_1\ I_2}\ |\gamma_{12}\ (\tau)| \qquad (3.2.3\text{-}14)$$

$$I_{min} = I_1 + I_2 - 2\ \sqrt{I_1\ I_2}\ |\gamma_{12}\ (\tau)| \qquad (3.2.3\text{-}15)$$

Equations (3.2.3-13), (3.2.3-14) and (3.2.3-15) may be combined to yield:

$$V = \frac{2\sqrt{I_1 I_2} \cdot |\gamma_{12}(\tau)|}{I_1 + I_2} \qquad (3.2.3\text{-}16)$$

From this equation it can be deduced that, for a certain degree of coherence, the optimum fringe visibility is obtained when the beam intensities are equal, i.e. $V = |\gamma_{12}(\tau)|$. Then, for completely coherent beams, the fringe visibility is maximised, i.e. $V = 1$, and for completely incoherent beams, the visibility is zero and fringes are not formed.

A useful quantity, when coherence is concerned, is the coherence time, i.e. the time interval when the phase of the emitted light waves remains constant. For quasi-monochromatic light beams of coherence time τ_o, the normalised coherence function is:

$$\begin{aligned} \gamma_{12}(\tau) &= 1 - \frac{\tau}{\tau_o} \qquad \text{for} \qquad \tau < \tau_o \\ \gamma_{12}(\tau) &= 0 \qquad \text{for} \qquad \tau \geq 0 \end{aligned} \qquad (3.2.3\text{-}17)$$

Because the fringe visibility has been shown to be proportional or equal to $|\gamma_{12}(\tau)|$, it becomes apparent that the fringe visibility drops to zero when the two beams travel pathways with time difference greater than the coherence time. This implies that the difference in the light paths of the two beams should not exceed the value:

$$l_c = C\,\tau_o \qquad (3.2.3\text{-}18)$$

where l_c is referred to as the "length of coherence" and C the light speed.

The coherence length of the He-Ne and Argon lasers used in the present experiments is of the order of several metres. However, care has been taken to avoid large differences of light paths, which were always of the order of several centimetres. Light path equalisers can be used (Durst (1972)), but this was found unnecessary for the present purposes. Apart from time coherence, spatial coherence, longitudinal or lateral, is of importance in the coherent detection of light scattered by more than one particle present in an extended control volume. Spatial coherence is treated by Born and Wolf (1964) and Collier et al (1971).

✓ Control volume shape and dimensions

Figure 3.2.3-2a shows an LDV operating in the fringe mode. The two parallel Gaussian beams I and II of wavelength λ originate from the same laser and, provided that the light path difference is small compared to the coherence length, they are coherent. The beams are focused to their waists at the measuring point P by the lens L_1 of focal length f. The diameter of the waists may be calculated from equation (3.2.3-4); the beam intensity distribution from equation (3.2.3-3); and the maximum intensity from equation (3.2.3-6). Equation (3.2.2-16) may be used to calculate the fringe spacing and the frequency-velocity response is represented by equation (3.2.2-18).

Due to the Gaussian intensity distribution of the laser beams and their parallel wavefronts near their waists, the intensity distribution of the fringe pattern, which is formed at their crossing region, is a three-dimensional Gaussian of the following form (Kreid (1974)) (Figure 3.2.3-2b):

$$I\ (x,y,z) = I_o \cdot \left\{ exp \left[- \frac{(x-x_o)^2}{X} - \frac{(y-y_o)^2}{Y} - \frac{(z-z_o)^2}{Z} \right] \right\} \cdot sin^2 \left(\pi \frac{x}{\Delta x} \right) \quad (3.2.3\text{-}19)$$

where I_o is the maximum intensity at the centre of the control volume

(x_o, y_o, z_o). X, Y, Z are the semi-axes of the ellipsoidal at the e^{-2} intensity level.

The axes of the ellipsoidal, which forms the scattering volume at the e^{-2} intensity level, and the number of fringes are given by:

$$\begin{aligned} 2X &= d_t = d/\cos\phi \\ 2Y &= l_t = d/\sin\phi \\ 2Z &= d \\ N_{fr} &= \frac{d_t}{\Delta x} \end{aligned} \qquad (3.2.3\text{-}20)$$

When a particle passes through the control volume at the centre (x_o, y_o, z_o) with constant velocity $V_i = (u,v,w)$, the intensity of the resulting scattered light is given by:

$$\begin{aligned} I_s(t) &= I_{s_o} \cdot \exp\left[-\left(\frac{ut}{X}\right)^2 - \left(\frac{vt}{Y}\right)^2 - \left(\frac{wt}{Z}\right)^2\right] \cdot \sin^2\left[\pi \cdot \left(\frac{ut}{\Delta x}\right)\right] \\ &= I_{s_o} \cdot \exp\left[-\left(\frac{ut}{X}\right)^2 - \left(\frac{vt}{Y}\right)^2 - \left(\frac{wt}{Z}\right)^2\right] \cdot \left[\frac{1 - \cos 2\pi\nu_D t}{2}\right] \end{aligned} \qquad (3.2.3\text{-}21)$$

where I_{s_o} is the maximum scattered intensity at the centre (x_o, y_o, z_o), and $\nu_D = 2\, u^{*} \sin\phi/\lambda$ is the Doppler frequency of equation (3.2.2-18).

It appears, therefore, that the frequency of the scattered light depends only on the fringe spacing and the u-velocity component. In order to measure another velocity component, the control volume should be rotated so that the fringes are normal to this component.

Since most photodetectors are square law devices, it can be assumed that the electrical signal from the photomultiplier is of similar shape as the scattered light intensity given by equation (3.2.3-21). In practice, however, the particles are randomly dispersed in the flow and pass randomly through the control volume. The output of the photo-

---

*where u is normal to the fringes

detector, therefore, will be of similar shape to the light intensity distribution along the particle path within the scattering volume.

So far, the transmitting optical components have determined a potential scattering control volume at the e^{-2} light intensity level with dimensions given by equation (3.2.3-20). The Doppler burst is determined by the intensity distribution of equation (3.2.2-18) and the scattering characteristics of the particles dispersed in the flow.

The dimensions of the measuring control volume are also dependent on the arrangement of the optical components which observe the Doppler signal and transmit it to the photodetector. These consist of a light collecting lens and a pinhole located in front of the photodetector. The diameter of the lens influences the signal quality through the cone angle of the collected light; an increased angle can improve the signal quality and, at the same time, reduce the dimensions of the control volume. The pinhole of the photomultiplier enhances the signal quality by cutting off unwanted noise due to ambient light and in combination with the lens assists in the reduction of control volume dimensions by cutting off signals from unwanted regions of the control volume. The resulting reduction in control volume dimensions can be quantified as follows:

Consider a pinhole diameter D_{ph} and a light collecting lens magnification M. The diameter of the control volume and the number of fringes that can be viewed by the pinhole is given by:

$$d_{ph} = \frac{D_{ph}}{M} \qquad (3.2.3\text{-}22)$$

$$N_{fr} = \frac{d_{ph}}{\Delta x} \qquad (3.2.3\text{-}22a)$$

and, thus, by careful selection of the parameters D_{ph} and M, the radial extent of the control volume can be controlled. Besides the radial localisation, longitudinal localisation may be achieved by recalling that the depth of field, i.e. the displacement in the object space which results in a degradation of the image, may be controlled by the magnification achieved by the lens. The depth of field, i.e. the control volume length, decreases with increasing magnification and it is preferable to work with high magnifications. However, magnification is limited by lens aberrations and an optimum arrangement must be determined experimentally.

The fact that optimum light detection is achieved with equal scattered light intensities implies that a symmetric light collecting system is advantageous. Because the intensity of scattered light is stronger in the forward direction, it is natural to collect light in this direction. However, both backward and off-axis detection may be employed. Although backward light detection results in poorer Doppler signal quality, it may be of advantage, when the measuring environment imposes the limitation that both the transmitting and receiving optics should lie in the same side. The dimensions of the measuring control volume are calculated from the same equations as for forward detection.

Off-axis detection, on the other hand, may result on a further reduction of the dimensions of the scattering volume. Off-axis detection is discussed later in the experimental results section, together with related theoretical relationships for the estimation of the control volume dimensions. In practice, however, off-axis systems have proved to be difficult to align, especially when the off-axis detection angle is large.

In the case of blood flow measurements, the presence of many particles inside the control volume causes absorption and diffusion of the light. The random passage of red blood cells through the light beams disturbs their wavefront and thus introduces a certain degree of incoherence in either the fringe formation or the detected scattered light. It appears, therefore, that for both *in vitro* and *in vivo* blood flow measurements, the backward detection system offers the potential advantage that the beams do not travel long distances inside the flow. This may result in a better signal quality.

Directional ambiguity

The laser Doppler velocimeters discussed so far will record a Doppler signal from the moving particle without sensing its direction. In laminar flows with recirculation, this directional ambiguity may not present severe problems because the direction of the flow may be deduced from the general flow pattern (Durst, Melling and Whitelaw (1974)). In complicated laminar recirculating flows, however, a direction sensitive LDV may be advantageous and in turbulent flows, directional sensitivity may be essential, for example when negative and positive instantaneous velocities occur at the same location.

To achieve directional sensitivity, it is necessary to frequency-shift one of the light beams relatively to the other so that a frequency bias f_s can be established. Particles moving with positive velocity will then give rise to a total frequency $f = f_s + f_D$, while particles with negative velocity will produce a total frequency $f = f_s - f_D$, where f_D is the frequency corresponding to the Doppler shift of the moving particle.

There are basically four methods of shifting the frequency of light; acousto-optic devices, electro-optic techniques, rotating diffraction gratings and moving mirrors. Bragg cells and Debye-Sears (1932) cells use acoustic waves which interact with light and produce shifted frequencies. They have been used by, for example, Mazumder (1972) and

Durao and Whitelaw (1975). The Kerr and Pockels electro-optic effects have also been used for light frequency shifting. A Kerr cell has been described by Drain and Moss (1972) and used by Baker, Hutchinson and Whitelaw (1974) for measurements in the recirculation zone of a flame. Rotating diffraction gratings have been described by Suzuki and Hioki (1967) and used by Mazumder (1972), and Stevenson (1970); gratings with higher efficiency have been used by Oldengarm (1973) and Wigley (1974).

3.2.4 Doppler Signal Processing

The light scattered by a particle moving inside the control volume, after optical mixing on the photomultiplier, produces an electronic Doppler signal which has the form shown in Figure 3.2.4-1. It consists mainly of a pulse corresponding to the average scattered light intensity which is modulated with a frequency corresponding to the Doppler shift. The width of the pulse depends critically upon the size of the control volume and the velocity of the particle. The Doppler modulation frequency is related to the fringe spacing and the particle velocity via equation (3.2.2-18). This Doppler burst is commonly modulated in a random fashion by optical or electronic noise. The optical noise is due to random noise fluctuations of the laser beams and random vibrations of the optical system. Electronic noise, on the other hand, is produced inside the photodetector and may be either thermal or shot noise. The quality of the signal, therefore, depends on the laser beam used, the transmitting and receiving optics, the scattering properties of the particles and the performance characteristics of the photodetector.

The frequency of the Doppler burst is directly related to the velocity of the moving particle via equation (3.2.2-18), and the purpose of any Doppler signal processing system is to extract this frequency and thus to obtain the velocity information. The good quality of the Doppler signal is important for its processing. The signal-to-noise ratio (SNR) in the output of the photodetector may be calculated as follows (Hauer and Alwang (1973)*):

$$\mathrm{SNR} = \frac{\eta_q}{h\,\nu\,\Delta f}\;\frac{P_{s_I} \cdot P_{s_{II}}}{P_{s_I} + P_{s_{II}} + P_N} \tag{3.2.4-1}$$

where η_q = the quantum efficiency of the photodetector

h = Plank's constant

Δf = the frequency bandwith of the signal processing system

ν = the light frequency

P_{s_I}, $P_{s_{II}}$ = the power incident on the photodetector and scattered from the two incident beams (reference and fringe mode) or scattered and collected in two different directions (Doppler mode)

P_N = the power of background optical noise (light other than that carrying the Doppler frequency information)

For an LDV operating in the reference beam mode, the signal-to-noise ratio becomes:

$$\mathrm{SNR} = \frac{\eta_q}{h\,\nu\,\Delta f} \cdot P_I \tag{3.2.4-2}$$

because the power, P_I, of the reference beam I is much greater than the scattered power, $P_{s_{II}}$, from beam II and the background noise P_N

---

* Signal-to-noise ratio analyses have also been performed by Durst (1972), Lading (1973), and Mazumder and Wankum (1970).

$(P_{s_I} = P_I >> P_{s_{II}}, P_N)$.

For the fringe and Doppler modes, the optimum signal-to-noise ratio is obtained when the two scattered intensities are equal:

$$\text{SNR} = \frac{\eta_q}{h\ \nu\ \Delta f} \cdot \frac{P_s}{2} \tag{3.2.4-3}$$

where: $P_s = P_{s_I} = P_{s_{II}}$

It appears, therefore, that the reference beam mode produces Doppler signals with higher signal-to-noise ratios.

In practice, however, the larger apertures of the light collecting lens used in the fringe mode results in higher scattered power received by the photodetector ($P_s > P_I$) and, thus, the signal-to-noise ratio of this arrangement is higher than the others. This is true in the case of low numbers of scattering particles while reference beam mode results in better quality signals when many particles are present in the scattering optical probe.

There are basically four types of Doppler signal processing; frequency analysis, frequency tracking, frequency counting and photon correlation. In frequency analysis, the spectrum of the Doppler burst is obtained by a frequency spectrum analyser. This spectrum is related to the probability density function of the velocity at a point in the flow. Frequency tracking uses a local oscillator to produce a local frequency of the same order as the received Doppler frequency and by the super-heterodyne method, the Doppler frequency is obtained in the output. A feedback loop is used to shift the local oscillator frequency according to the Doppler frequency and thus an automatic frequency tracking process is created similar to the one for radio receivers. Both these methods use analogue signal techniques.

Frequency counters measure the period of Doppler cycles and, by inversion, yield its frequency. Finally, in photon correlation, an auto-correlation function of the intensity due to photons produced inside the measuring control volume is built by fast digital techniques. The frequency of the auto-correlogram is the Doppler frequency sought.

In general, frequency analysis provides most of the information required. The statistics of the spectrum may, after certain corrections, give the statistics of the velocity at the measuring point, and the only limiting factor is that frequency analysis is a laborious technique.

Frequency tracking appears to be a particularly convenient technique in that it provides an on-line analogue signal proportional to velocity. However, this cannot occur when the Doppler signal is discontinuous and it is then, therefore, that great care must be taken when the drop out of the signal is finite.

In frequency counting, there is no need for a continuous or near-continuous Doppler signal since each burst may be sampled and processed individually. Its limitations seem to be the sample rate of the frequency counter and the additional requirement of a fairly good quality of signal. The former is not of importance since the frequencies obtained in these measurements were low.

Photon correlation offers the advantage of lesser signal quality and laser beam power requirements.

In the present experimental work, frequency analysis and frequency tracking have been used preliminarily. Most of the measurements reported in this thesis have employed a frequency counting method developed by the author (Gosman, Vlachos and Whitelaw (1973)). These signal processing systems are described in later sections where experimental results are presented and discussed.

3.2.5 Doppler Signal Broadening

The velocity probability distribution measured by LDV is subject to broadening from sources which include optical noise, transit time, multiple particle scattering, electronic noise, velocity gradient and particle-concentration gradient. Because the flows considered here are laminar, the broadening of the spectrum may not be of direct interest to the measured velocity profiles. However, the evaluation of the accuracy and precision of the measurements, especially in the small glass capillaries and venules, with a finite optical probe demands an analysis of the sources of error.

Optical noise broadening is associated with the optical components of the LDV. It may be the result of fluctuations of the optical properties of the laser beam, vibrations of the optical benches, refractive index fluctuations, scattered light from walls, etc. Thus, even when a constant velocity is measured and the spectrum is expected to be a Dirac delta function, optical noise may cause a broadening of the spectrum.

Transit time broadening is the result of the finite time the scattering particle travels through the control volume. It is associated with measurements using analogue signal processing methods, such as frequency analysis and frequency tracking, and is not of direct interest here since digital sampling is used.

When more than one particle travels through the control volume, the resulting Doppler signals may be in or out of phase. When they are in phase, the resulting signal is stronger than the individual signals. However, when the individual Doppler signals are out of phase, the resulting signal is weaker. This may cause an additional broadening of the spectrum called multi-particle scatter or phase shift broadening.

Electronic noise of the photomultiplier and the signal processing system, such as shot and thermal noise*, may broaden the Doppler spectrum further.

Velocity gradient broadening of the Doppler spectrum may result when measurements are conducted in flows with spatial velocity variations and a finite size control volume. Finally, when spatial variations of particle concentrations exist in flows with spatial velocity gradients, an additional broadening of the spectrum may result.

Research into the sources of broadening and their effects have been reported, for example, by Edwards et al (1971), Goldstein and Kreid (1967), Greated and Durrani (1971), Adrian (1972), Vlachos and Whitelaw (1974), George and Lumley (1973), McLaughlin and Tiederman (1973), Owen and Rogers (1975), and Melling (1973). The work of Durst, Melling and Whitelaw (1976) also deals with this subject in detail.

In the present measurements, broadening due to velocity and concentration gradients is of importance; the former because of the small size of flow channels, and the latter because of the high particle concentrations when blood flows are measured. The former is of greatest importance and is considered below:

Assuming a velocity profile across the control volume:

$$V = V(x) \qquad (3.2.5\text{-}1)$$

---

* For the theory of noise see, for example, Brown and Glazier (1964).

and a velocity probability distribution of the form:

$$P = P(x) \tag{3.2.5-2}$$

The mean and rms velocities may be calculated as follows, and in accord with Greated and Durrani (1971):

Mean velocity:

$$\overline{V} = \int_{-\infty}^{\infty} V(x)\ P(x)\ dx \tag{3.2.5-3}$$

rms value:

$$\overline{(V - \overline{V})^2} = \int_{-\infty}^{\infty} (V - \overline{V})^2\ P(x)\ dx \tag{3.2.5-4}$$

Thus, for a parabolic velocity profile given by:

$$V = V_o\ (1 - (\frac{r}{R})^2) \tag{3.2.5-5}$$

where V_o is the maximum velocity at $r = 0$, and a Gaussian probability distribution of the velocities, Edwards et al (1971)* evaluated the mean value and the variance of the velocity as follows:

Mean velocity:

$$\overline{V} = V_o\ (1 - (\frac{r}{R})^2 - (\frac{\sigma}{R})^2) \tag{3.2.5-6}$$

---

* Similar analyses have been performed by George and Lumley (1973), and Melling (1973).

Variance:

$$\overline{(V - \overline{V})^2} = 2\, V_o \left(\frac{\sigma}{R}\right)^2 \left[\left(\frac{\sigma}{R}\right)^2 + 2 \left(\frac{r}{R}\right)^2\right] \qquad (3.2.5\text{-}7)$$

where $\sigma = l_m/4$, and l_m the length of the control volume.

Assuming a measuring control volume of length l_m and a normal distribution of light intensity within it, equations (3.2.5-6) and (3.2.5-7) may be employed to evaluate the shift in the mean velocity and rms when measuring in a parabolic velocity profile; corrections may then be applied. It is apparent from equation (3.2.5-6) that the measured velocities will be lower than the expected theoretical ones.

When a computing counter is employed, the continuous sweeping of the filters of the frequency analyser or the frequency tracker are replaced by the sampling of the frequency of individual Doppler bursts. The nature of this signal processing method, therefore, allows a statistical analysis of a sample of discrete measurements to be performed.

Thus, it is assumed that the control volume is centred at a specific measurement point of the given profile and a sample of measured velocities is formed arising from simulated particles crossing the control volume at random. The mean and the rms values of the velocity at the specific point are then obtained by the use of a computer program developed for this purpose*.

When a Gaussian distribution of particle paths was assumed, the results of this procedure were similar to those of Edwards et al (1971). However, there is no specific reason to assume a normal distribution of particle passages and thus a random number sequence is used to simulate the particle paths with any desired probability distribution.

---

* For details of the procedure, see Appendix E.

When a constant concentration exists, particles with higher velocities pass more frequently through the control volume. It appears reasonable, therefore, to weight the probability distribution of the random number sequence with the velocity of the particles (McLaughlin and Tiederman (1973)). When a particle concentration gradient exists in the flow, the above probability should be weighted by the particle concentration. However, the problem is more complex if account is taken of the poly-dispersed particles and the light intensity variation inside the control volume. The analysis presented here makes use of the above simplified observations. These observations have been incorporated into the simulation procedure described in Appendix E. The results of these analyses have been used to correct the measured mean and rms velocity profiles and to determine the size of the control volume as described later.

3.2.6 Closing Remarks

In this section the theoretical relationships for the interpretation of the Doppler signal, the signal quality and the dimension of the control volume have been given.

With the aid of this introductory material, measurements have been conducted in various flow configurations with an LDV operating in fringe mode. These measurements are described in the following sections.

3.3 APPLICATION OF LDV TO FLOWS IN MEDIUM SIZE CHANNELS

3.3.1 Introduction

The purpose of the measurements in medium ($\simeq$ 10 mm) size channels reported in this section may be outlined as follows:

- To acquire the necessary knowledge of the principles of the technique and the function of the associated optical, mechanical and electronic components

- To apply the method to flows not previously investigated, such as the laminar water flow downstream of a bend in a round pipe.

Careful selection of the components of the LDV for these purposes may result in control volumes where the broadening effects are limited, if not negligible, and diffraction effects do not present major difficulties.

The first experimental task was designed to allow knowledge of the method of laser Doppler velocimetry to be acquired. It required the measurement of the velocity profile in laminar air flow at the exit of a long ½" inside diameter copper tube. The experimental apparatus is shown schematically in Figure 3.3.1-1 and photographically in Figure 3.3.1-2. The integrated optical unit developed by Durst and Whitelaw (1971b), shown photographically in Figure 3.3.1-3, was employed for these measurements. A silicone oil atomiser was used to generate droplets with an approximate size of 1 μm with which the air flow was seeded. The signal output of the photomultiplier (EMI 9558B) was monitored by an oscilloscope (Hewlett-Packard 180A) and was processed in the following ways:

- The signal was fed into a spectrum analyser* (Hewlett-Packard 8553B) and the Doppler spectrum was recorded on an X-Y plotter (Bryans 21004).

- Similarly, the Doppler signal was input into a frequency tracker** (DISA 55L 30) and the frequency was read from the tracker's meter.

However, in view of the low Doppler frequencies resulting from very low velocities in blood flows (of the order of 1 mm/sec, see Atherton and Born (1972)), a signal processing system suitable for low frequency ranges was sought. A frequency counting method was then developed based on a computing counter (Hewlett-Packard 5360A) and the above oscilloscope, as described in Appendix F. It was subsequently used for the present measurements with results similar to those obtained with the frequency analyser and the frequency tracker, which were in satisfactory agreement with the expected parabolic profile.

The low rms values (less than 1% of the local mean velocity) measured at the centre of the pipe implied that the high rms values

---

* For details of the Hewlett-Packard spectrum analyser, see Asalor (1973), and for the principle of power spectrum measurements, see, for example, Bendat and Piersol (1971).

** For details of the operation of the DISA frequency tracker, see Deighton and Sayle (1971), and for its principle of superheterodyne reception, see, for example, Lawson and Uhlenbeck (1950).

recorded away from the centre resulted from spatial velocity gradients rather than local velocity fluctuations.

3.3.2 Measurements Downstream of a Bend in a Round Pipe

The purpose of this application was to measure the velocity profiles of the developing laminar water flow downstream of a curved round pipe. Detailed measurements of this kind of flow have not been reported in the literature and, thus, the technique was applied in a flow situation not previously investigated (see Gosman, Vlachos and Whitelaw (1973)). In addition, the present results were used to provide the inlet conditions for the three-dimensional parabolic flow computations of Chapter 2 and confirm its applicability to the present flow situation.

The experimental apparatus is shown schematically in Figure 3.3.2-1. The test section was a 9.5 mm inside diameter glass tube with a 15^{o} bend. It was mounted on a cathetometer which was mounted on a milling machine table and arranged to move along the axis of the LDV and in the normal direction. In addition, the pipe was allowed to slide into the holders of the cathetometer in a vertical manner and to rotate about its axis; a Perspex disc marked in degrees angle and attached on the tube enabled this rotation to be recorded.

The integrated optical unit of the previous subsection was used with approximately $\frac{3}{4}$ of the fringes viewed by the photomultiplier. The beam incidence half angle was of the order of $\phi = 11.3^{o}$ and, combined with the He-Ne laser wavelength, produced a fringe spacing of $\Delta x = 1.615$ μm and a calibration constant of $K \simeq 1.615$ m/sec/MHz.

The axis of the optical system crossed the axis of the pipe at an angle of 90^{o}. The water flowed with a mean velocity of the order of $3.15 cms^{-1}$ measured by a volumetric tube and a stop watch. This corresponded to a Reynolds number of approximately 300, based on the diameter of the tube. The dust particles of the tap water provided the centres of scattered light received on the photocathode. However, in order to speed up the measurements, milk was added in a concentration of approximately 1:10000 parts by volume.

The Hewlett-Packard oscilloscope was used to monitor the Doppler signals and arm the computing counter. The counter was programmed by its keyboard (Hewlett-Packard 5375A) to provide the mean velocities and rms values of the samples of at least 100 individual measurements.

In order to measure the velocity profiles, the tube was first slid to a specific downstream station from the centre of the bend. It was then aligned with the optical axis of the LDV by observing the reflected and transmitted beams on the glass walls to be on the same plane with the tube and the optical axes. Then, a traverse along its diameter was performed with the milling table; the relative movement being recorded on the micrometer.

The initial station was taken to be x/D = 5 diameters downstream of the centre of the bend. Six velocity profiles were measured along diameters 30^0 apart at this station*. Profiles along diameters in the plane of the bend and normal to the bend were measured downstream of the initial station at x/D of 2, 5, 10, 15 and 20. The results of these measurements are plotted in Figures 3.3.2-2, 3.3.2-3 and 3.3.2-4 and comparisons with the computational results have already been described in section 2.6.3.

The measured velocity profiles showed that the flow is

---

* The profiles thus obtained were used as inlet conditions for the numerical flow computations of Chapter 2.

asymmetrical in the plane of the bend and symmetrical in the plane normal to the bend. Fully-developed flow was obtained at about 15 diameters downstream of the initial measuring station, i.e. 20 diameters downstream of the centre of the bend.

Because of the laminar nature of the flow, the rms values of the measured local velocities were expected to be low. The measured rms profiles are also plotted in Figures 3.3.2-3 and 3.3.2-4, and it can be seen that the values are higher in the region of the walls. However, the low rms value in the region of zero velocity gradient (approximately 0.7% of the local mean velocity) implies that the high rms values resulted from velocity gradient broadening.

The pipe diameter, measured with a travelling microscope, was of the order of 9.5 mm and the movement of the milling table from one wall to the other along the pipe diameter corresponded approximately to only 6.85 mm. Thus, a correction was required to account for the refraction through the glass walls (see Figure 3.3.2-5a). From geometrical optics and refraction effects, the following correction formula was derived*:

$$\frac{\Delta x_w}{\Delta x_a} = \frac{\sqrt{\eta_w^2 - \sin^2 \phi_a}}{\sqrt{1 - \sin^2 \phi_a}} \qquad (3.3.2\text{-}1)$$

where Δx_w = displacement of control volume in water

Δx_a = displacement of control volume in air

ϕ_a = half beam incidence angle in air

η_w = water refractive index

The magnitude of the necessary corrections to the measurements for the

* See Appendix G for details on refraction effects.

effect of velocity gradient broadening was also considered. The optical arrangement and the discrimination level of the electronics resulted in a control volume length of the order of 200 μm, i.e. approximately 2% of the tube diameter. Following the procedure documented in Appendix E, the maximum correction to the local mean velocity was evaluated to be less than 0.5% and the correction was subsequently disregarded. The maximum value of the corrected rms profile was of the order of 3% of the local mean velocity and showed that the method of measurement resulted in a good accuracy.

In an attempt to measure the secondary flow, the circumferential velocity component was examined at a number of locations. This was achieved by rotating the optical unit at an angle of 90^0 so that the plane of the beams was rendered normal to the axis of the pipe (see Figure 3.3.2-5b). The control volume was traversed again along a diameter with the fringes remaining parallel to it, so that the system retained its symmetry. The maximum values of the circumferential velocity was of the order of only 10% of the local axial velocity component. It becomes apparent, therefore, that fewer cycles are expected with this arrangement than when the axial component is measured. This is illustrated in Figure 3.3.2-5c where it can be seen that the large axial velocity components force the particle to move out of control volume after having crossed only a few fringes; the number of fringes depends upon the relative magnitude of the tangential and axial velocity components, the number of fringes forming the control volume, and the particle path. For these reasons, but also because of the poor signal quality, these measurements were unreliable and thus disregarded.

3.3.3 Closing Remarks

The results of the experiments reported in this section showed that laser Doppler velocimetry is a reliable measurement method for flow channels of at least 10 mm in size. In addition, its non-invasive character allowed detailed velocity measurements to be carried out in undisturbed flows where other methods have not been successful, if not impossible.

However, the length of the control volume, estimated to be of the order of 200 μm, was far in excess of that required to achieve satisfactory measurement resolution in channels with sizes of the order of 100 μm. Thus, it was necessary to conduct an investigation and determine the features of an LDV design in order to achieve control volume sizes of the order of 10 - 20 μm necessary for capillary flows.

3.4 INVESTIGATION OF SOME LDV DESIGN PARAMETERS

3.4.1 Introduction

The second series of experiments were conducted with the aim of establishing the influence of the various design features of the LDV on its performance, when measuring in small glass capillaries and venules. The study included the following parameters:

-	Half beam incidence angle	ϕ
-	Beam diameter	D
-	Beam wavelength	λ
-	Photomultiplier pinhole diameter	D_{ph}
-	Off-axis detection angle	ϕ_s

The experiments were performed in a fully-developed laminar air flow emerging from either a ½" circular pipe or a 1 × 10 mm plane duct. As a result of this investigation, conclusions were drawn as to the evaluation of the method when applied to small size channel flows.

A method was established for the estimation of the size of the control volume and the subsequent evaluation of the accuracy and precision of the results. Once these investigations were concluded, decisions were taken for the application of the technique to glass capillary water and blood flows.

3.4.2 The Laser Beam Characteristics

The required laser power for a reasonably good Doppler signal critically depends on the particle velocity and signal processing procedure (Durst and Whitelaw (1973)). An approximate figure of 0.40 mW/m/s may serve as a selection criterion for the laser power. In this section, however, the beam properties are reviewed in the context of spatial resolution rather than signal quality.

Thus, from the analysis of section 3.2 regarding the control volume dimensions,it became apparent that larger diameter and shorter wavelength beams may result in smaller control volumes and, subsequently, in a better measurement resolution.

The influence of the beam diameter has been examined by introducing a beam expander before the integrated optical unit. Figure 3.4.2-1 shows the measured mean and rms velocity profiles of the fully-developed laminar pipe flow obtained by an unexpanded and an expanded beam (expansion of the order of 5).

There seems to be no substantial difference in the mean velocity profiles measured. The lower rms values near the flow edges obtained with the expanded beam imply a smaller control volume. However, the less than perfect quality of the beam expander resulted in a distorted control volume. The quality of the fringes was examined either by observing the Doppler pulses on the oscilloscope or projecting the fringes on a screen. In both cases, it was visually determined that the fringe pattern was qualitatively inferior when the beam expander was introduced. This may explain the higher rms values measured at the centre (Hanson (1973)). In an attempt to quantify the fringe distortion, the following experiment was carried out.

The delay time of the delayed sweep pulse of the oscilloscope was varied and measurements at a point in the flow were carried out with different preset delay times. In principle, the delay time controlled the sampled portion of the Doppler signal and, thus, the influence of the fringe pattern on the velocity measurement could be examined by this method.

Figure 3.4.2-2 shows a plot of the results of this examination. Whereas the velocity statistics did not vary substantially across the fringe pattern of the unexpanded beam, a significant variation was observed when the beam expander was introduced. It was then concluded that the beam expander was introducing a statistical bias of the measurements which was difficult to determine. For this reason, but also because good quality beam expanders were too expensive, it was decided to drop it from the rest of the experiments. However, the findings of this investigation, i.e. that a larger beam diameter could, in general, produce smaller control volume, was later substantiated by the use of an Argon laser with a beam diameter twice as large as the present He-Ne laser.

The measurements obtained with the Argon laser (reported in the glass capillary flows section) showed a substantial decrease in the size of the control volume when compared to the measurements obtained with the smaller diameter He-Ne laser beam.

The effect of beam wavelength was difficult to assess, mainly due to the lack of equal diameter laser beams with different wavelengths. Although the Argon laser wavelength was shorter ($\lambda = 0.488\ \mu m$) than the He-Ne laser ($\lambda = 0.6328\ \mu m$), comparison of the two beams with respect to their wavelengths was not straightforward because the diameter of the former was larger than the diameter of the latter. It was difficult, therefore, to decide whether the smaller size control volume observed with the Argon laser was due to the larger diameter of the beam or its shorter wavelength. However, it was suggested that the substantial reduction of the size of the measuring optical probe was a combination of both the larger diameter and the shorter wavelength.

3.4.3 The Transmitting Optics

The transmitting optics of an LDV operating in the fringe mode incorporate beam splitters, mirrors and beam focusing lenses. Durst and Whitelaw (1971a) have shown that the optimum fringe visibility is achieved when the two interferring beams are of equal density. Although they showed that even with intensity ratios of the order of 1:20 a distinguishable fringe pattern could be formed, a careful selection of beam splitters and mirrors for optimum fringe pattern is always desirable.

The focusing lenses should operate with a large F-number in order to avoid aberrations. Spherical aberration and astigmatism are the major problems of the laser Doppler velocimeter incorporated in a microscope, as discussed in section 3.5. The size of the waist of the focused beam is proportional to the focal length of the focusing lens (equation (3.2.3-4)). Because smaller spot sizes result, in general, in smaller control volume sizes, it is always desirable to use short focal length lenses for better measurement resolution.

The theoretical equation (3.2.3-20) for the dimensions of the scattering volume, set by the transmitting optics, imply that a larger incidence angle results in a smaller control volume. It becomes apparent, therefore, that LDV's with larger incidence angles produce, in principle, better measurement resolution.

A verification of the above theoretical derivations was obtained by measuring the velocity profile of the fully developed ½" laminar pipe flow by three different optical arrangements.

While all the other features of the LDV were kept the same, three focusing lenses were used, with focal lengths of 150 mm, 100 mm and 60 mm, respectively. Mounted on the integrated optical unit, they resulted in three different incidence angles of approximately 15.5^{o}, 25.5^{o}

and 41^{o}, respectively. For the same flow conditions, the recorded frequency and number of fringes were higher for larger incidence angles; the effective control volume diameter was kept constant during these measurements by use of the same pinhole and the same magnification of the receiving optics. The measured mean velocity and rms profiles are plotted in Figure 3.4.3-1. It can readily be seen that the larger angle of incidence produced lower rms values and, thus, a smaller control volume, the flow being laminar and with the same Reynolds number in all cases.

The values of the length of the scattering volume, calculated from equation (3.2.3-20), were approximately 1400 μm, 600 μm and 200 μm, respectively. Applying the simulation procedure outlined in Appendix E, the rms profiles due to velocity gradient broadening were calculated. The effective length of the control volume set by the electronic discrimination level was assumed to be 80% of that set by the transmitting optics. The theoretical rms profiles thus obtained are also plotted in Figure 3.4.3-1 for comparison. The good agreement between theoretical and experimental rms values supports both the theoretical evaluation of the size of the control volume and the simulation procedure for the calculation of velocity gradient broadening.

3.4.4 The Receiving Optics

In general, the receiving optics of an LDV comprise a light collecting lens and a pinhole in front of the photomultiplier; the lens is used to collect scattered light from particles travelling through the control volume, and the pinhole to mask unwanted light from entering the photomultiplier. Because the pinhole serves as a field stop of the receiving optical system, it may be used to control the part of the control volume viewed by the photomultiplier (equation (3.2.3-22)).

When aligning the receiving optics, it was always sought to allow the photomultiplier to view the centre of the optical probe, thus resulting in the best signal quality.

When the transmitting optics set a control volume of a smaller size, the receiving optics had to be adjusted accordingly. This was achieved by either changing the magnification or the pinhole diameter. Thus, a series of pinholes was constructed from ebonite with diameters of 0.008", 0.012", 0.016", 0.02" and 0.025". With fixed magnifications, there is a range of pinhole diameters producing the optimum quality of signals; outside this range, the signal deteriorates rapidly.

It was of interest, when setting the LDV for any kind of flow, to select the appropriate size of pinhole for best signal quality. Experience has shown that it was always best to choose the pinhole to view between 50 - 80% of the fringes.

3.4.5 Off-Axis Detection

Another series of experiments was conducted with the purpose of establishing the effect of off-axis detection on the size of the control volume with the objective of reducing its size. The term "off-axis detection" implies that the axis of the receiving optics no longer coincides with that of the transmitting optics (see Figure 3.4.5-1a). The angle formed by the two axes is the off-axis detection angle denoted by ϕ_s in the figure.

From the optical arrangement shown in Figure 3.4.5-1a where the control volume is assumed to be an ellipsoidal (Adrian and Goldstein (1971)), one may derive relevant formulae for the size of the control volume. Two off-axis detection cases are considered; one, when the receiving optics are rotated in the beam symmetry plane, and the other when they are rotated in the plane of the beams.

(a) Detection in the symmetry plane of the beams

From the geometry of Figure 3.4.5-1c, the following formulae may be derived:

Control volume diameter:

$$d_s = \frac{D_{ph}}{M} \quad , \quad \text{if} \quad \frac{D_{ph}}{M} \le \frac{d}{\cos \phi}$$

or:

$$d_s = \frac{d}{\cos \phi} \quad , \quad \text{if} \quad \frac{D_{ph}}{M} > \frac{d}{\cos \phi} \qquad (3.4.5\text{-}1)$$

Control volume length:

$$l_s = \frac{d}{\sin \phi} \quad , \quad \text{if} \quad \frac{D_{ph}}{M \sin \phi_s} \ge \frac{d}{\sin \phi}$$

or:

$$l_s = \frac{D_{ph}}{M} \cdot \frac{\dfrac{\tan \phi_s}{\cos \phi_s} + \sqrt{(\dfrac{M\, d}{D_{ph}})^2 \, (\tan^2 \phi + \tan^2 \phi_s) - \dfrac{\tan^2 \phi}{\cos^2 \phi_s}}}{\tan^2 \phi + \tan^2 \phi_s}$$

$$\text{if} \quad \frac{D_{ph}}{M \sin \phi_s} < \frac{d}{\sin \phi} \qquad (3.4.5\text{-}2)$$

(b) Detection in the plane of the beams

From the geometry of Figure 3.4.5-1b, the following formulae may be derived:

Control volume diameter:

$$d_s = \frac{d}{\cos\phi} \quad , \quad \text{if} \quad \frac{D_{ph}}{M\cos\phi_s} \geq \frac{d}{\cos\phi}$$

or:

$$d_s = \frac{D_{ph}}{M} \cdot \frac{\dfrac{c\tan\phi_s}{\sin\phi_s} + \sqrt{(\dfrac{M\,d}{D_{ph}})^2 \dfrac{(c\tan^2\phi + c\tan^2\phi_s)}{\sin^2\phi} - \dfrac{c\tan^2\phi}{\sin^2\phi_s}}}{c\tan^2\phi + c\tan^2\phi_s}$$

$$\text{if} \quad \frac{D_{ph}}{M\cos\phi_s} < \frac{d}{\cos\phi} \qquad (3.4.5\text{-}3)$$

Control volume length:

$$l_s = \frac{d}{\sin\phi} \quad , \quad \text{if} \quad \frac{D_{ph}}{M\sin\phi_s} \geq \frac{d}{\sin\phi}$$

or:

$$l_s = \frac{D_{ph}}{M} \cdot \frac{\dfrac{\tan\phi_s}{\cos\phi_s} + \sqrt{(\dfrac{M\,d}{D_{ph}})^2 \dfrac{(\tan^2\phi + \tan^2\phi_s)}{\cos^2\phi} - \dfrac{\tan^2\phi}{\cos^2\phi_s}}}{\tan^2\phi + \tan^2\phi_s}$$

$$\text{if} \quad \frac{D_{ph}}{M\sin\phi_s} < \frac{d}{\sin\phi} \qquad (3.4.5\text{-}4)$$

An analysis was then performed, based on the above theoretical derivations, of the Durst and Whitelaw integrated optical unit and of an arrangement employing loose optical components similar to those used for the capillary flows. The analysis involved an He-Ne laser light source, various beam expansion ratios, different transmitting and receiving lenses, different pinholes, and off-axis detection.

Table 3.4.5-1 shows the effects of beam expansion and incidence angle on the major dimensions of the ellipsoidal forming the fringe pattern. It can readily be seen that a smaller fringe pattern may be formed when expanded beams or larger beam incidence angles are used. Then, assuming an unexpanded beam and various angles of incidence, the effect of the pinhole diameter and off-axis detection angle was examined. Tables 3.4.5-2 and 3.4.5-3 present the results of this examination. It can be concluded that larger angles of detection and smaller sizes of pinholes (or magnifications) produce smaller control volumes.

An experimental verification of these derivations may be seen in Figure 3.4.5-2, where the results of measurements in the fully-developed ½" pipe flow for two different arrangements of off-axis detection are plotted. It can readily be deduced that the larger angle of off-axis detection produced better measurement resolution, observed from the lower rms levels. Predicted rms due to velocity gradient are also plotted.

However, during these series of measurements, it was observed that the signal quality was dropping with increasing angle of detection. This was attributed mainly to the reduced intensity of scattered light. This may be seen from the results of Figure 3.4.5-3 where the mean velocity and rms values measured at the same location in the flow with different detection angles are plotted. The rms values dropped substantially up to an off-axis detection angle of around 60^0 and then, because of a drop in the intensity of the scattered light, the rms values rose again.

In the meantime, the effect of the pinhole size was investigated. The conclusion was that smaller pinhole diameters resulted in better resolution (lower rms values) as long as the pinhole size did not limit the signal quality received by the photomultiplier.

Similar experiments in a fully-developed laminar air flow emerging from a 1 × 10 mm^2 channel produced results which led to the same conclusions. During these experiments, it was realised that off-axis detection presented difficulties with the alignment of the optical system, although the measurements were conducted in unconfined flows. The situation was expected to be worse for confined glass capillary or venous blood flows because of the associated refraction effects*. It was then decided to seek to reduce the size of the control volume selecting proper transmitting optics and to use in-axis detection with appropriate pinhole sizes. In addition, a further means of reducing the effective size of the control volume was offered by the signal processing system itself; this is described in the following section.

3.4.6 The Photomultiplier and the Electronic Trigger

The Gaussian light intensity distribution of the interference pattern forming the control volume implied that the scattered light intensity was critically dependent upon the position of the particle within the interference pattern. For optimum signal quality, it was always desirable to arrange the photomultiplier to view the central part of the control volume. The high voltage of the power supply (Hewlett-Packard 6110A) to the photomultiplier had to be selected according to the receiving optics arrangement and the size and concentration of the scattering particles for optimum results; for example, the optimum voltage was different for different blood concentrations.

In addition, the pseudo-Gaussian shape of the Doppler burst

---

* For refraction effects in LDV, see Appendix G.

indicated that, by arranging a higher trigger level of the electronic signal processing system, information was allowed to be recorded from only the central part of the control volume, thus effectively reducing its size further and improving the measurement resolution.

An experiment was then conducted to assess the above theoretical speculations as follows:

For the same measuring location of the fully-developed pipe flow, the trigger level of the oscilloscope was altered and the mean velocity and rms values were recorded. The results of this test are plotted in Figure 3.4.6-1. It can readily be seen that higher trigger levels resulted in lower rms values, thus improving the measurement resolution by reducing the effective size of the control volume.

However, there are two reasons opposing the application of these theoretical and experimental observations. Firstly, in most flow situations the scattering particles are not mono-dispersed and thus the scattered intensity is not only a function of the incident light intensity but it strongly depends upon the size of the particle. Secondly, by raising the trigger level, the number of Doppler bursts admitted for measurement is reduced critically. Thus, very high trigger levels may result in prolonged times of measurement, which are not practically desirable.

3.4.7 Closing Remarks

The theoretical analysis and experimental results presented in this section revealed that the theoretical predictions of the control volume size agree, in general, with the experiments. It was concluded that larger beam diameters, shorter wavelengths, larger angles of beam incidence, shorter focal lengths of transmitting and receiving lenses, smaller pinholes, and off-axis detection would produce, in principle, smaller control volume sizes.

In order to construct a Doppler velocimeter with a control volume size of the order of $10 \times 10\ \mu m^2$, a loose lens system should be preferred to the available integrated optical arrangement. The main reason for this is that such a system would allow the use of short focal length lenses and large incidence angles, necessary for small control volumes, without the introduction of severe lens aberrations.

This arrangement was then used to investigate the flow of water and blood in small glass capillaries reported in the following sections. Prior to its application to the capillary flows, test measurements were performed to assess its performance.

The comparison, in terms of measurement resolution, between the two systems, i.e. the integrated optics and the loose lens optics, was in favour of the latter. However, the major disadvantage of the system to be described in the following sections was that it demanded considerable care and skill for its alignment, and it was more sensitive to mechanical vibrations than the integrated optical unit.

3.5 APPLICATION OF LDV IN GLASS CAPILLARY FLOWS

3.5.1 Introduction

The present series of *in vitro* blood flow measurements form a major part of the experimental investigation. The main purpose was to assess problems associated with the applicability of laser Doppler velocimetry to blood flows in venules of the living animal. The following tasks were, therefore, undertaken:

- To determine and implement a convenient and precise means of manipulating flows in miniature size ducts;
- To assess the performance of laser optics in small size channels, and to determine a preferred arrangement;
- To develop an electronic signal processing system for the required low velocity ranges; and
- To obtain and measure Doppler signals in flows with high particle concentrations, such as blood.

The resulting system was then to be applied to the living animal to determine velocity profiles in the small venules. A longer term purpose is to use the resulting system to measure local velocities in the vicinity of white bodies (platelet thrombi) formed by the iontophoresis method (Begent and Born (1970)).

Two LDV arrangements have been employed for the measurements. While all other characteristics were kept similar, one LDV was operated with an He-Ne laser beam and the other with an Argon laser beam; the main function of this difference was to allow an assessment of the influence of beam diameter and wavelength on the performance and measurement resolution of the system.

3.5.2 Measurements with an He-Ne LDV

The optical arrangement used for the present measurements is shown schematically in Figure 3.5.2-1a and photographically in Figure 3.5.2-1b. A 5 mW He-Ne laser beam (Spectra-Physics, Model 120) was divided into two equal intensity beams by a beam splitter. Mirrors were used to render the beams normal to each other (90^{0} beam incidence angle). The beams were focused by two equal focal length (f_t = 50 mm) lenses before intersection.

The laser and the transmission optics were mounted on optical benches and each component could be adjusted in three orthogonal planes with microscopic screws. The optical components could also be rotated about two orthogonal axes, one horizontal and the other vertical. The photograph also shows the microscope which was used to observe the two beams and to ensure that they crossed at their waists. It was also used during the measurements to observe the flow through the capillary, Figure 3.5.2-2

An integrated receiving optical unit (see Figure 3.5.2-3) was used. It consisted of a light collecting lens with a short focal length (f_r = 25 mm) and a photomultiplier pinhole with a small diameter (D_{ph} = 0.500mm). A series of lens-holding tubes with different lengths was constructed to allow a wide range of magnifications to be selected. A camera diaphragm was placed in front of the light collecting lens in order to adjust the solid angle of detection, see Figure 3.5.2-2. The receiving optics were mounted on an adjustable camera tripod and, thus, detection could be performed either on-axis or off-axis with a wide range of angles. Forward on-axis detection was easier to align and the resulting Doppler signals were of superior quality. Satisfactory signal quality could, however, be obtained from red blood cells even when the light was collected at an angle of 90^{0} to the plane of the beams. It was also observed that the diameter of the camera aperture, which was placed in front of the light collecting lens, had an influence on the quality of the Doppler signals from highly concentrated or whole blood; it improved with smaller aperture diameters. This is in accordance with the theoretical derivations of section 3.2 which indicate that coherent detection should be applied for multi-particle scattering. However, this requirement is in contradiction with that for high scattered light energy which demanded large aperture diameters. It was also observed that scattered light energy from whole blood was stronger than from water impurities, due to the presence of many scattering centres and, as a consequence, optimum signal quality corresponded to a lower photomultiplier supply voltage.

The flow configurations consisted of glass capillaries which were made by drawing small bore glass tubing while rotating it with the axis in the vertical plane and heating with a low temperature natural gas Bunsen burner. The inside diameter of the capillaries ranged from 50 to 300 μm, measured with a travelling microscope*, and maintained these diameters within ± 10% over a distance of at least 50 diameters. Variations of this order of magnitude had no significant effects on the flow at Reynolds numbers between 1 to 100. These Reynolds numbers are characteristic of the flows in these experiments and also in small venules. The wall thickness of the capillaries measured with the travelling microscope was of the order of 20% of the inside diameter. Thus, the present glass capillaries had considerably thicker walls than venules where the thickness is of the order of 1 - 5%. Prior to their use, the capillaries were perfused with cleansing fluids consisting of carbon

---

* A correction was applied to the measured capillary diameter to account for refraction (see Appendix G).

tetrachloride, water and saline. A holder with two micrometric orthogonal adjustments (see Figure 3.5.2-4) was used to mount the capillaries. It was designed to allow the capillaries to be viewed by the velocimeter and the microscope, and to minimise the possibility of vibrations and breakage. The flow was controlled by a constant head tank which allowed water, saline and blood in different concentrations to flow with velocities in the range of interest.

Blood was handled with care* in order to avoid cell damage, coagulation and to ensure that its rheological properties were kept as close to *in vivo* blood as possible. It was 1 - 2 weeks old and heparinised to prevent coagulation. Its haematocrit level was of the order of 40%; the red cell concentration was about 3.5×10^6 cells/mm^3 with an average cell volume of 90 μm^3. Blood was kept in a refrigerator at 4 - 6^{0}C temperature and, prior to the experiments, was left at room temperature ($\simeq$ 15^{0}C) for at least two hours.

Flexible surgical tubing was used to connect the constant head tank with the glass capillaries. Stagnation points were avoided wherever possible in order to prevent thrombus formation. A syringe was used to initiate the flow through the capillary and was allowed to settle for several minutes prior to any measurements.

The signal processing system was arranged as follows: the optical signal was transformed to an electronic Doppler burst via a photomultiplier (EMI 9558B). An adjustable amplifier (Harwell 95/2151) was used to amplify the signal to levels higher than the trigger level limitations of the electronics. However, saturation of the amplifier was carefully avoided. A variable bandwidth filter (Krohn-Hite 3502) removed

---

* See Appendix H for blood handling and preparation.

the low frequency of the Doppler burst before it was input into the oscilloscope (Hewlett-Packard 180A) and the computing counter (Hewlett-Packard 5360A).

Because all the investigated flows were laminar, the measurement of the frequency of a single cycle of the Doppler burst should provide, in principle, sufficient information to determine the local fluid velocity. However, in practice, at least 100 measurements of individual Doppler bursts were recorded and the average and rms values of the frequency, and thus the local velocity, were obtained*.

Prior to the present series of measurements, the possibility of obtaining good quality Doppler signals from scattering particles with high diameter-to-fringe spacing ratios, such as red blood cells, was investigated. Thus, a 10 μm diameter wire was placed on a disc rotating in the plane normal to the fringes. The transmission optics were arranged with a 60^o beam incidence angle, which produced a fringe spacing of the order of Δx = 0.633 μm. The rotating wire then served as a scattering cylinder with a diameter-to-fringe spacing ratio of the order of 16. The quality of the signals obtained from this arrangement was only slightly worse than the signals obtained from 1 μm particles with a ratio of about 1.5. This supported the expectation that good quality Doppler signals could be obtained from red blood cells. The latter was then confirmed by observing the quality of the signals obtained from the flow of blood diluted in saline at a level of 1:100. The transmitting optics in this case were arranged with a 90^o beam incidence angle, corresponding to a fringe spacing of approximately Δx = 0.445 μm. Typical Doppler signals

---

* The Doppler signal processing by the computing counter is described in Appendix F.

are shown in Figure 3.5.2-5 where their good quality and deep modulation may be readily seen, although the ratio of particle size-to-fringe spacing was as high as 12. The figure also presents signals from water and plasma flows.

It was concluded from the above tests that the high ratio of cell size-to-fringe spacing was unlikely to cause problems for blood flow measurements by laser Doppler velocimetry.

The attenuation of laser light by blood seemed to be a more serious problem. With the aid of the microscope, the control volume was observed to be distorted. Figure 3.5.2-6 shows the two beams passing through the whole thickness of blood in 250 μm and 125 μm diameter capillaries. The diffusion of the beams can easily be noticed and the control volume can no longer be identified. The diffusion of the beams increased with increasing red cell concentration and blood depth. It was almost impossible to obtain a Doppler burst from whole blood flow in capillaries with diameters larger than of the order of 300 μm.

The absorption of laser light by red blood cells is not fully understood and there are no established theoretical analyses of the diffusion of coherent beams passing through whole blood.

Theoretical and experimental work* by McRae et al (1961) showed that, assuming that the red cell haemoglobin obeys the Lambert-Beer transmission law, the transmittance, absorption and scattering of light by red blood cells depends on the light wavelength and the thickness of the blood layer through which light is passing. Anderson and Sekelj (1967a,b) applied a theory, developed by Twerskey (1960) to describe multiple scattering of waves by random distributions of particles, to the prediction

---

* Relevant work has also been presented by Kramer et al (1951), Lothian and Lewis (1956), and Zdrojkowski and Longini (1969).

of red blood cell absorption, scattering, reflection, and transmittance. However, much remains to be done for the implementation of these analyses to blood flow measurements by laser Doppler velocimetry. The work of Kreid and Goldstein (1971) and DiGiovanni and Einav (1974) showed that measurements are possible with blood, from which the red cell haemoglobin content has been removed by the method described by Goldsmith (1967), in channels of depths as large as 2.3 mm and 4 mm.

However, there is no evidence that ghost red cells may represent, rheologically, whole blood and thus the need for *in vitro* and *in vivo* whole blood flow measurements still remains.

Figure 3.5.2-7 presents a series of photographs which indicate signals obtained with the optical system described above close to the centre of a 125 μm inside diameter glass capillary. The velocity of the flow was approximately 10 mm/sec and the concentration of blood-to-saline ranged from 1:100 to whole blood. It is evident that the signal quality decreases with increasing blood concentration. The presence of phase shifts due to multiple scattering is obvious in the Doppler signal from whole blood, where it is impossible to identify all the fringes of the control volume (approximately 50). The signal obtained from the centre of a 250 μm glass capillary with whole blood flow is also shown in the figure and indicates that the signal quality is now worse and that phase shifts are still present.

Attempts to measure the velocity profiles in whole blood were partly successful. It was possible to obtain measurable signals from all radial locations in the 125 μm capillary but, in the case of the 250 μm capillary, measurable signals could be obtained from only the central 100 μm of the blood depth. The high diffusion of laser light transmitted through more than 150 μm of whole blood resulted in a distortion of the fringe pattern forming the control volume. Melling and Whitelaw (1976), in a recent extension of the present work, obtained photographs of the fringe pattern with different concentrations of blood in saline flowing in a 300 μm diameter glass capillary. From the records of the fringes thus obtained, it could be concluded that the fringe pattern is highly distorted for whole blood.

The above observations suggest that the collection of scattered light forming a Doppler burst on the photomultiplier is not possible when the capillary diameter is more than approximately 200 μm for whole blood. However, it is expected that the thinner venule walls will allow a better quality of Doppler signals.

The extent to which localisation of measurements could be achieved in the small glass capillaries may be assessed with the aid of the plotted velocity profiles shown in Figures 3.5.2-8abcde and 3.5.2-9abc The dimensions of the beam intersection region of the present LDV (see Table 3.5.2-1) were approximately 87.7μm in length and 50 μm in diameter calculated from equations 3.2.3-20 and 3.2.3-22. The table shows also the dimensions of the interference pattern in water and blood. Due to refraction effects, the control volume is larger in water and blood. A scanning of a 2 μm rotating wire along the fringe pattern and a finite electronic discrimination level of the detected Doppler signal suggested a control volume length of the order of 30 μm and a corresponding diameter of 20 μm in air. Assuming these dimensions to be correct, the measured rms values may be attributed to velocity gradient broadening and thus corrections according to the procedure outlined in Appendix E are applied to both the mean and rms velocity values. From the corrected profiles, plotted also in Figures 3.5.2-8abcde and 3.5.2-9abc, it may readily be seen that, with the exception of whole blood flow, all measured profiles are parabolic within experimental uncertainty.

The maximum deviation of the measured velocities in saline, plasma and diluted blood from a parabolic profile is of the order of 5% and is mainly due to velocity gradient broadening which may be corrected. Thus, provided that a correction for velocity gradient is applied, the above results demonstrate that local velocity measurements can be obtained in the laminar flow in small glass capillaries with satisfactory resolution.

The measured velocity profiles in whole blood flowing in the 125 μm glass capillary are subject to greater uncertainties indicated by the measured higher rms values. Further work was, therefore, necessary to determine the sources of these high rms values.

In contrast to measurements in water flow, those in blood are subject to a significant concentration gradient broadening in addition to the velocity gradient broadening. Merill et al (1963) and Goldsmith (1967) have shown that there is a significant radial variation of haematocrit in small venules. The equation:

$$H = H_m \left(1 - \left(\frac{r}{R}\right)^2\right) \qquad (3.5.2\text{-}1)$$

where H = the haematocrit

r = radial distance

R = radius of tube

H_m = maximum haematocrit

is a convenient approximation to their derivations. The above relationship has been used to allow corrections to the measurements of Figure 3.5.2-9c. Thus, the figure shows velocity values which correspond to the measured values corrected for both velocity and concentration gradients.

The profile obtained from whole blood flow is considerably flatter than parabolic. This may stem from the reported non-Newtonian behaviour of blood flowing in small diameter ducts. The high rms values, even at the centre line of the uncorrected profiles, suggest that the velocity profiles of whole blood flow are measured with significant uncertainty. This may be attributed to a distorted fringe pattern due to beam diffusion through blood, loss of light coherence because of wavefront disturbances along the blood path, and signal processing inefficiency. Experience with the present system suggested that the first two sources of error are predominant and need to be carefully investigated and corrected.

No particular difficulties were experienced in processing the Doppler signals by the computing counter when flows of water, saline, plasma and diluted blood were considered. The LDV control volume could be well observed and identified through the attached travelling microscope and the fringes were of good visibility when projected on a screen. However, the signals obtained from whole blood did not reveal the usual Doppler burst shapes and phase shifts were present due to multiple particle scattering. The latter may be the cause of inaccurate measurements, although visual attempts were made during the course of a measurement to discard bad quality signals.

3.5.3 Measurements with an Argon LDV

In a further attempt to reduce the control volume size and determine its effect on the measured high rms values in whole blood flow, the He-Ne laser beam was substituted by an Argon laser beam.* The diameter of the beam was of the order of D = 1.5 mm at the e^{-2} intensity level and its blue light corresponded to a wavelength of λ = 0.488 μm. The laser power could be adjusted manually from approximately 10 to 1000 mW.

Following the derivations of section 3.4, it was expected that

---

* Spectra-Physics Model 164.

the larger diameter and the shorter wavelength of the Argon beam would give rise to a smaller control volume. The beam was operated at low power to avoid damage to blood cells*. It was observed during the experiments that, when the flow of blood through capillaries with diameters of 100 μm to 200 μm was stopped, with laser powers in excess of approximately 40 mW, a thrombus started to form. When blood was allowed to flow with velocities of approximately 10 mm/sec and the laser power was increased to approximately 100 mW, thrombi formed rapidly. With laser powers in excess of approximately 500 mW, a total burn-out of the capillaries occurred.

These tests established the maximum allowed laser power and were prompted by the work of Kochen and Baez (1964) and Arfors et al (1968), which indicated that laser pulses could be used to initiate microvascular thrombosis. The work of Bendick (1974) showed that laser induced coagulations could not allow useful LDV measurements.

The dimensions of the interference pattern and the control volume of the present LDV are given in Table 3.5.3-1. Comparison with the dimensions corresponding to the He-Ne laser (Table 3.5.2-1) revealed that the intersection volume was reduced both in diameter and length from 87.7 μm to 29.3 μm in air. The dimensions of the scattering volume observed by the photomultiplier and those resulting from the electronic trigger level are also shown in the table. The receiving optics (M = 10) and the pinhole (D_{ph} = 200 μm) reduced the diameter of the control volume to 20 μm. The effective control volume dimensions were further reduced to 15 μm in diameter and 20 μm in length by the high discrimination level of the signal processing system, which were confirmed with a rotating 2 μm wire.

---

* For laser hazards, see Appendix I.

The alignment of the optical components required considerable skill and care because of the small dimension of the measuring optical probe. The crossing region of the beams was again observed by the travelling microscope at a magnification of 75. The Doppler signals showed modulations up to 35 db for water, saline and plasma, and up to 20 db for whole blood flows, although the ratio of particle size-to-fringe spacing was of the order of 20. Typical Doppler signals obtained by the present LDV arrangement are shown in Figure 3.5.3-1.

The filtering of the Doppler bursts was more critical for blood than for water flows; typical settings were 1 kHz and 100 kHz for a signal centred at about 20 kHz. The number of fringes observed, corresponding to the number of cycles of a single burst, was of the order of 40. With blood flow, this number was smaller for an individual burst, due mainly to interference of light scattered by more than one particle within the control volume. The average number of red blood cells present in the measuring volume was around 20.

Local mean and rms profiles measured in 550 μm, 125 μm and 80 μm inside diameter glass capillaries with water flowing at average velocities of 210 mm/sec, 55 mm/sec and 9 mm/sec, respectively, are shown in Figure 3.5.3-2abc; the corresponding Reynolds numbers were approximately 115, 7 and 0.7. The velocity profile measured in the large capillary is in accord with the expected parabola. The maximum deviation of any measured point from the parabola is of the order of less than 3%. The rms values normalised by the mean velocity value varied from approximately 0.5% on the axis of the capillary and increased towards the walls.

Since the flow was laminar and connected to a constant head tank, the measured rms values at the centre line resulted from optical broadening, light scattered from the walls of the capillaries, electronic noise, and velocity gradient broadening. The higher rms values near the walls were mainly due to the increase of velocity gradient broadening with increased velocity gradients. The measured higher rms values with the narrower capillary confirmed the greater magnitude of velocity gradient broadening resulting from larger velocity gradients and the same control volume dimensions.

Application of the approximate method for the estimation of the control volume length, described in Appendix E, resulted in a length of the order of 20 ± 5 μm. The length of the intersection region was measured to be approximately 20 μm, with the aid of the travelling microscope, for the same optical arrangement in air.

Refraction effects through the glass walls and the water resulted in a smaller incidence angle which increased the intersection length to approximately 46.7 μm. However, the estimated value of 20 μm for the effective control volume suggests that the photomultiplier pinhole and the discrimination level of the electronic signal processing reduced the intersection length by more than 50%; this result assists the estimation of the length of the control volume in whole blood flow.

The mean velocity and rms profiles of blood flowing in the 125 μm capillary at a maximum velocity of 6.5 mm/sec are also presented in Figure 3.5.3-3. Two series of measurements were made using light collecting lenses with F-numbers of 16 and 2.8 (the latter was also used for the measurements with water). The centre line rms values were 3.5% for F-number of 16 and 2% for 2.8, respectively. The larger F-number (smaller diaphragm diameter) resulted in a better signal quality. This is mainly due to the detection of scattered light with smaller solid angles (coherent detection).

However, the effects of gradient broadening were greater with the larger F-number, mainly due to an increased effective control volume length. When the aperture of the light collecting lens was reduced, the voltage supplied to the photomultiplier had to be increased so that an equally strong signal could be obtained.

Reliable measurements could not be obtained near the walls of the capillary due to optical noise from the walls themselves and the poor quality of the Doppler signals.

The effects of velocity and concentration gradient broadening were also considered and corrections were applied to the measured profiles of Figure 3.5.3-3. To allow these corrections to be applied, the length of the control volume was required. The calculated length was 29.3 μm in air and 46.7 μm in water. The estimated value, allowing for the discrimination level of the signal processing system, was approximately 20 μm. Microscopic measurements in the blood flow indicated that, due to dispersion of light by the red cells, the control volume dimensions were more than 1.5 times those in water. Thus, a control volume length of 30 μm was used to evaluate the corrections for velocity and haematocrit gradient broadening.

The corrected measurements are also shown in Figure 3.5.3-3 and suggest that at low shear rates, the velocity profile of fully-developed capillary blood flow is not parabolic. This conclusion is in accordance with the results of blood flow measurements in glass capillary tubes of Bugliarello and Hayden (1962) and of Einav et al (1975a, b) and Mishina et al (1974, 1975).

The effect of differences in control volume dimensions due to different laser beams may be assessed by comparison of the present results with those obtained with the He-Ne laser in the same 125 μm capillary.

Thus, from Figure 3.5.3-4ab, it may be seen that the rms values measured with the Argon laser were lower than those with the He-Ne laser. The rms value, normalised by the local mean velocity, at the centre line was of the order of 15.5% for the He-Ne LDV and only 2.5% for the Argon LDV. The Argon laser with its larger diameter and shorter wavelength gave rise to smaller control volume dimensions, thus resulting in reduced velocity and concentration broadening.

However, it was more difficult to obtain measurements near the walls with the Argon laser due, probably, to the higher angle of convergence and divergence of the focused Argon beams.

3.5.4 Closing Remarks

It is apparent from the measurements of the previous sections that Doppler signals can be obtained from laser light scattered by red blood cells, from which the haemoglobin content has not been removed. In the case of whole blood, the Doppler signals were obtained provided that the size of the flow channel did not exceed approximately 200 μm. A signal processing system based on a computer counter allowed the profiles of water velocity to be measured satisfactorily in glass capillaries as small as 80 μm. In the case of whole blood, the use of a larger diameter and shorter wavelength Argon beam produced improved measurement resolution but the inability to measure closer to the walls with this beam suggested that an expanded He-Ne laser beam should be employed for optimum results. Also, even with the Argon laser, the effective control volume dimensions were approximately 30 μm in length and 15 μm in diameter.

It is also suggested that the capillary wall thickness contributed to the uncertainty of the measurements because the light scattered from the walls increased further the measured rms values. Thus, it is anticipated that thinner capillary walls, such as the walls of the venules, will result in an improved signal quality.

3.6 ON THE VISCOSITY OF BLOOD

The rheological equation of state for blood was necessary in the numerical procedures of Chapter 2 in order to complete the required information. A power law was then selected and a justification is outlined in this section.

Blood plasma has been reported to be a Newtonian fluid (Charm and Kurland (1962); Merill et al (1964)) but certain investigators, for example Copley (1971), found a slightly non-Newtonian behaviour. However, it is generally accepted that experimental errors in the viscometers are the main cause of the latter observations.

The particulate nature of whole blood renders it a non-Newtonian fluid under certain flow conditions and there are various viscosity laws reported in the literature. At low haematocrit levels ($H < 5\%$), blood may be considered Newtonian with a viscosity given by Einstein's relationship for suspensions (see Charm and Kurland (1974)):

$$\mu_s = \mu_p \frac{1}{1 - a H} \tag{3.6-1}$$

where μ_s = suspension viscosity

μ_p = plasma viscosity

H = haematocrit

a = particle shape factor

Cokelet (1963) proposed the following relationship for red blood cell suspensions:

$$\mu_s = \mu_p \frac{1}{(1 - H)^{2\cdot5}} \tag{3.6-2}$$

Reiner and Scott-Blair (1959) suggested the following viscosity law:

$$\sqrt{|\tau|} = \sqrt{\mu}\sqrt{|\gamma|} + \sqrt{\tau_y} \tag{3.6-3}$$

where τ = blood local shear stress

γ = blood local shear rate

τ_y = blood yield stress

μ = blood viscosity

This equation, derived by Casson (1959) for printing inks, is based on the behaviour of mutually attracted particles subjected to disruptive forces such that particle group size is a function of shear rate. In addition, the yield stress of the suspension must be exceeded before the structure can be broken and flow initiated. Scott-Blair (1959) and Charm and Kurland (1962,1965) showed that this relation may be applied to blood flows of a wide range of haematocrits and shear rates (1 - 100,000 sec^{-1}). Merill et al (1964) have applied it to shear rates of 0.1 to 20 sec^{-1}.

Scott-Blair (1967) has also proposed the following expression:

$$\tau = m\,\gamma^{n} + \tau_y \tag{3.6-4}$$

where m and n are functions of temperature and pressure.

The presence of yield stress of blood has been disputed by some investigators, and Charm and Kurland (1962) have suggested a power law expression as a more convenient means of characterising blood viscosity:

i.e. $$\tau = m\,\gamma^{n} \tag{3.6-5}$$

The power law (with the appropriate index, n, matching the experimental data of section 3.5) has been preferred in the present calculations, largely because of numerical convenience. Casson's law can also be used to fit the present experimental data. The Casson and power laws are now examined in greater detail.

Casson's Law

Integration of equation (3.6-3) for a fully-developed capillary flow yields:

$$\frac{u}{\bar{u}} = \frac{\frac{N}{16}\left(1 - (\frac{r}{R})^2\right) - \frac{N^{\frac{1}{2}}}{3}\left(1 - (\frac{r}{R})^{3/2}\right) + \frac{1}{2}\left(1 - \frac{r}{R}\right)}{\frac{N}{32} - \frac{N^{\frac{1}{2}}}{7} - \frac{8}{21N^3} + \frac{1}{6}}$$

$$\text{if} \quad r_p < r < R$$

and: $$\frac{u}{\bar{u}} = \text{constant} \quad , \quad \text{if} \quad 0 < r < r_p \qquad (3.6\text{-}6)$$

where: $r_p = \frac{2\tau_y}{(dp/dx)}$ = the radius of the plug flow

and: $N = \frac{(dp/dx)}{\tau_y/2R}$ = a non-dimensional parameter

where R the capillary radius and dp/dx the pressure gradient.

From equation (3.6-6), it becomes apparent that:

$$\lim_{N\to\infty} \frac{u}{\bar{u}} = 2\left(1 - (\frac{r}{R})^2\right) \qquad (3.6\text{-}7)$$

This is consistent with the results of Munter and Stein (1973) that under high shear rates, i.e. large N, the velocity profile of blood becomes parabolic.

Equation (3.6-6) has been plotted in Figure 3.6-1 with N as a parameter; from its definition, this parameter is related to the ratio of normal-to-shear stresses exerted on the flowing blood elements. It is derived that Casson's law suggests a plug flow for low shear rate (small N) and a parabolic profile for high shearing (large N). This conforms with the reported behaviour of blood flowing in small capillaries and venules.

Power Law

A similar analysis based on power law for the viscosity of blood yields the following velocity distribution when equation (3.6-5) is integrated for the fully-developed capillary flow:

$$\frac{u}{\bar{u}} = \frac{3n + 1}{n + 1} \left(1 - \left(\frac{r}{R}\right)^{(n+1)/n}\right) \qquad (3.6\text{-}8)$$

where n is the power index.

The profiles suggested by equation (3.6-8) have been plotted in Figure 3.6-2 with the power index n as a parameter. It becomes apparent from these plots that power law for the viscosity of blood suggests a plug flow for power index near zero and parabolic flow for power index near unity.

However, because blood viscosity is reported to depend upon haematocrit and temperature, so must the constants of equations (3.6-3) and (3.6-5). The results of Merill et al (1963) suggest the following relationships for the constants of Casson's law:

$$\mu = A \exp (-E/RT)$$

and:

$$\tau_y = \tau_m (H - H_c)^3 \qquad (3.6\text{-}9)$$

where A is a function of shear rate and of the morphology of the suspended particles; E is an activation energy similar to that of Arrhenius for chemical reaction; R is the gas constant; τ_m is a characteristic value of yield stress; and H_c is a critical haematocrit below which there is no yield stress, and which has a value of between 1.3% and 6.5%.

It appears, therefore, that Casson's relationship for stress and strain of flowing blood varies with temperature and haematocrit*. In the circulation, the concentration of red cells tends to be highest in the centre of the blood vessel and decreases sharply near the walls. Such local differences in haematocrit give rise to large differences in the constants of Casson's equation.

If it is assumed, for simplicity, that the blood haematocrit and yield stress are given by the following relationships:

$$H = H_m \left(1 - \left(\frac{r}{R}\right)^2\right) \tag{3.6-10}$$

$$\tau_y = \tau_m \cdot H^2 \tag{3.6-11}$$

where H_m and τ_m are characteristic values.

Then, from equation (3.6-3), the velocity distribution may be derived as follows:

$$\frac{u}{\bar{u}} = \frac{R^2}{4\mu}\left|\frac{dp}{dx}\right|\left(1 - \left(\frac{r}{R}\right)^2\right) - \frac{\sqrt{\tau_m \cdot H_m^{\ 2}}}{21\mu}\sqrt{2R\left|\frac{dp}{dx}\right|}\left(8 - 14\left(\frac{r}{R}\right)^{3/2} + 6\left(\frac{r}{R}\right)^{7/2}\right)$$
$$+ \frac{\tau_m \cdot H_m^{\ 2}}{15\mu}\left(8 - 15\frac{r}{R} + 10\left(\frac{r}{R}\right)^3 - 3\left(\frac{r}{R}\right)^5\right) \tag{3.6-12}$$

---

* It also varies with the health of the human, Harkness (1971).

This equation is plotted in Figure 3.6-3 with the constants having the following values:

$$\mu = 0.0279 \text{ gr/cms} \quad , \quad H_m = 0.80 \quad , \quad \tau_m = 7 \times 10^{-5} \; dyn/cm^2$$

and a pressure gradient of dp/dx = 1000 dyn/cm^3. If a yield stress value of τ_y = 0.1 dyn/cm^2 is assumed which conforms with the range of values found by Charm and Kurland (1965) and Merill et al (1964), then a parameter N of the order of 125 is calculated (from the definition of N and a capillary diameter of 125 μm) and the corresponding velocity profile (equation (3.6-6)) is plotted in the same graph. Comparison of the two profiles show that the variation of yield stress with haematocrit suggests a further blunting of the profile.

Similarly, the constants m and n of the power law model may vary with radial location which may affect the velocity profile. However, there is no relevant work reported in the literature on this dependence.

A comparison of the results of the above analyses with the present experiments may be carried out with the aid of Figure 3.6-3 where the velocity profiles of Casson's law with constant yield stress (equation (3.6-6)), Casson's law with variable yield stress (equation (3.6-12)), power law (equation (3.6-8)), and experimental data obtained by laser Doppler velocimetry are shown. This comparison suggests that power law may be selected to represent the viscosity of blood with an index of the order of $n \approx 0.4$ or Casson's law with a constant N of 20. The power law has been used in the non-Newtonian numerical flow computations described in Chapter 2. For economic reasons (the convergence of the iterative procedures is slower for lower indices n), a power index of n = 2/3 has been selected to demonstrate the applicability of computational schemes to non-Newtonian blood flows.

3.7 LASER DOPPLER MICROSCOPE: A PROPOSAL

The skill and care required for the alignment of the loose lens arrangement used in the present *in vitro* measurements suggested that an integrated system should be constructed for the planned *in vivo* experiments. It was known in advance (Born (1974)) that the possibility of visually observing the region where the measurements were carried out was highly desirable. Thus, it was decided to use a microscope to serve both purposes and the essentials of the optical system were incorporated into a Leitz microscope (Orthoplan), as shown schematically in Figure 3.7-1, and photographically in Figure 3.7-2. As indicated in Figure 3.7-1, the two parallel beams, after reflection on the annular mirror, were focused by the annular microscope condenser to an intersection region inside the glass capillary. Velocity measurements were made with both forward and backward on-axis detection; the photograph of Figure 3.7-2 shows the system operating with forward detection. The Doppler signals obtained from back-scattered light were of a considerably poorer quality than those obtained with forward detection. The possibility of obtaining back-scatter Doppler signals from small capillary flows with a similar system was also demonstrated by Mishina, Koyama and Asakura (1975), and Melling and Whitelaw (1976). An arrangement with backward detection offers the potential advantage of shorter light paths through blood and, for measurements close to the wall, would result in less diffusion of the beams, and thus a smaller and more precisely defined control volume. In addition, back-scatter detection requires instrumentation on only one side of the flow and when the LDV is applied to real flow situations, such as those of blood flows in the living animal, this is a particular convenience.

Measurements with the LDV employing the commercially available and unmodified microscope shown in Figures 3.7-1 and 3.7-2 were found not to be sufficiently precise for the present small glass capillary flows. The imprecision stemmed mainly from the large optical aberrations caused by the annular lens. Two Leitz Ultropack lenses were used; U06.5 with focal length 25 mm and diameter around 21.5 mm, and U011 with a combined focal length of 16 mm. Both arrangements gave rise to unacceptable aberrations which were greater in the case of the lens combination of U011. The annular lenses were designed only for illuminating purposes and, thus, they were not corrected for spherical aberration and astigmatism. The effect of spherical aberration and astigmatism on the control volume are demonstrated, schematically, in Figure 3.7-3. Whereas spherical aberration caused the parts of the beams closer to the optical axis to be focused further from the lens, astigmatism resulted in a distortion of the shape of the circular beam cross-section; this is demonstrated by the photograph of Figure 3.7-4, where the fringe pattern is compared to that of earlier LDVs. Observations of the crossing region of the two beams with the travelling microscope showed that the two beams were no longer focused at their crossing point; this is demonstrated in Figure 3.7-5. An annular lens, free of these aberrations, could not readily be obtained and, acting on a suggestion of Wellford (1974), negative (diverging) or positive (converging) lenses were introduced to make the beam waists coincide with their crossing. The implication of these suggestions is demonstrated in Figure 3.7-6 where the correcting action of these elements may be seen. To interpret the diagrams of the figure, it should be borne in mind that the laser beam itself is slightly diverging with its waist originating from the laser cavity (Ross (1966)). In addition, the two waists formed on the two sides of the lens are complex conjugates of each other (Meyer-Arendt (1972)); that is, when one waist moves close to the lens, the other moves away and vice versa. However, in practice, this correction proved to be inadequate and the beams still crossed away from their waists.

Melling (1975b) applied this microscope LDV arrangement, together with positive correcting lenses, and obtained the velocity profile in a 1.18 mm glass capillary with a control volume length of 110 μm. The magnitude of the length of the control volume suggested that no useful Doppler signals could be obtained from capillaries of the order of 100 μm.

A separate lens system, replacing the annular lens, seemed to be the best solution. However, the construction and alignment of such a design would have presented difficulties and Melling and Whitelaw (1976) chose to modify the present system in accordance with the design of Mishina et al (1975) and Einav et al (1975a). Thus, a microscope objective, rather than the annular condenser, was used to focus the two laser beams to form the measuring control volume with predicted dimensions of the order of 10 μm in diameter and 18 μm in length, see Figure 3.7-7.

3.8 *IN VIVO* BLOOD FLOW MEASUREMENTS

The possibility of *in vivo* blood flow measurements with laser Doppler velocimetry was demonstrated by Durst (1972). He obtained a series of Doppler-like pulses which ceased to appear on the monitoring oscilloscope when the control volume was traversed across the venules of the mesentery of the hamster. The pulses also disappeared as soon as the animal was killed by an overdose of barbiturate. The present experimental work was carried out to demonstrate the extent to which localisation of velocity measurements in similar flow situations could be obtained. In addition, the possibility of *in vivo* blood velocity profile measurements with highly localised LDV arrangements was to be demonstrated and measurements in a mouse mesentery to be carried out.

In the course of the present investigation, attempts were made to obtain the velocity profile of blood flowing in venules of the order of 100 μm. At an early stage, the optical unit of Durst and Whitelaw (1971b) resulted in signals similar to those obtained by Durst (1972). It was almost impossible to distinguish whether the signals were the result of scattering from moving cells inside the venules or from lipoids of the surrounding tissues. However, the fact that the Doppler signals ceased to appear on the oscilloscope when the LDV was scanned across the venules suggested that the signal was the result of light scattered from the moving cells.

In a later stage, when the loose lens system was constructed and tested with *in vitro* flows of diluted and whole blood, attempts to measure the flow of blood *in vivo* were repeated. The experimental apparatus, shown in Figure 3.8-1, consisted of the He-Ne LDV used for the *in vitro* measurements described in section 3.5.4. The mouse was anaesthetised with a dose of barbiturate and was placed in a specially designed Perspex holder allowing easy access with the LDV and the travelling microscope, also shown in the figure. The holder was attached to an optical bench and could be traversed in 1 μm intervals by a micrometer screw. A constant supply of saline was used to superfuse the mesentery preparation which was stretched on the Perspex plate. The plate had a bore of 10 mm diameter in the centre to allow the free passage of the scattered and transmitted laser light through the mesentery and the air pipe flow used to align the LDV before the *in vivo* measurements.

During the test measurements, the travelling microscope was aligned to view the centre of the control volume and the mouse mesentery was scanned until a proper size venule was selected ($\sim$ 100 μm); illumination of the preparation was supplied by the laser beams. Micro-adjustments of the stage were then made and the Doppler signal was observed on the monitoring oscilloscope. Figure 3.8-2 shows unfiltered and filtered Doppler signals thus obtained. The mean frequency measured by the counter was of the order of 1.15 kHz corresponding to a blood velocity of 2.58 mm/sec and the rms value recorded was of the order of 26% of the mean local velocity. The poor quality of the signal did not allow any substantial measurements of the velocity profile across the venule diameter to be made. Apart from the reasons described in connection with the *in vitro* blood flow measurements, additional sources of distorted control volume may include the optical and geometrical imperfection of the venules and the periodic contraction and expansion of the mesentery.

As a consequence of the above tests, difficulties associated with the application of LDV to the flow of blood in venules have been identified and, in some cases, quantified. It is clear that, with whole blood, local measurements cannot be obtained in vessels, either venules or glass capillaries, greater than 200 μm in diameter and it is likely that, even with smaller vessels, precise measurements will not be obtained in whole blood. It is probably wise for future related research to concentrate on blood with haematocrit less than 0.45. The work of Mishina et al (1975) and Einav et al (1975 b) suggest that measurements of *in vivo* blood flow are possible but their results are not, at present, supporting an accurate method.

3.9 CLOSURE

The application of integrated LDV optical units for the measurement of velocity profiles in air and water flows has been demonstrated in this chapter. A Doppler signal processing method based on a frequency computing counter has been successfully applied throughout the present series of experiments.

The parametric study reported here revealed the effects of the LDV design features on the control volume dimensions and the measurement precision and accuracy.

Subsequently, a loose lens LDV system was designed and tested successfully in glass capillary flows. The resulting Doppler signal quality and the measurement resolution was satifactory for blood diluted in saline up to 1:10.

In the case of whole blood, the signal quality and the measurement resolution was of poor quality, mainly due to dispersion and loss of coherence of the beams caused by the moving red blood cells, and phase shifts of the Doppler signal caused by multiple scattering.

The estimated measurement localisation achieved was of the order of 15 - 20 μm in air, 20 - 25 μm in water and diluted blood, and 30 - 40 μm in whole blood.

The aberrations of the annular lens of the microscope when combined with the LDV did not allow a satisfactory measurement localisation to be achieved with the present system. However, this design seemed to offer advantages if the microscope objective is used instead of the bad quality annual condenser.

The optical imperfections of the venules, the periodic contraction and expansion of the mouse mesentery combined with the previously stated *in vitro* whole blood flow problems should be further investigated for satisfactory measurements of blood velocity *in vivo*.

CHAPTER 4

GENERAL CONCLUSIONS AND RECOMMENDATIONS

4.1 CONCLUSIONS

The purpose of this section is to briefly review the achievements of the applied experimental and numerical methods and to point out the merits of the successful applications and the limitations of the methods when applied to blood flows.

4.1.1 Contributions in Numerical Computations

The contributions of the computational work reported in Chapter 2 may be outlined as follows:

1. The extension and successful application of an existing numerical procedure to allow the representation of a three-dimensional developing laminar water flow downstream of a bend in a round pipe was demonstrated in sections 2.2, 2.3 and 3.6. The initial velocity profiles necessary for the present computations were measured by laser Doppler velocimetry as described in Chapter 3. The agreement between the experimental and computational results demonstrated the appropriateness of both the experimental and computational methods for this kind of flow. The possibility of extending the numerical method to include non-Newtonian blood flows was also described and the effects of high and low shear stress regions in the outer and inner walls of the bend, respectively, on the cell break-down and atherosclerotic

plaque formation pointed out.

2. An existing numerical procedure* was modified and applied for the prediction of the laminar water flow in the vicinity of an axisymmetric constriction in a pipe, as described in sections 2.2, 2.4 and 2.6 of Chapter 2. The procedure was extended to include non-Newtonian blood flow in the vicinity of an aortic stenosis. The effects of the local flow characteristics on the break-down of blood cells, the growth of the stenosis and the formation of emboli were also discussed.

3. A numerical procedure*, similar to that of item 2 above but covering also the third dimension, was developed and applied to the prediction of the laminar water flow in the vicinity of an asymmetric blockage in a pipe, as described in sections 2.2, 2.5 and 2.6 of Chapter 2. The procedure was also extended to include the non-Newtonian blood flow in the vicinity of a thrombus in a venule. The effects of the local flow characteristics on the break-down of blood cells, the growth of the thrombus, and embolus formation were also outlined.

4. Computer routines* were developed and applied to produce graphical presentations of vector fields, velocity profiles, shear stress contours, and streamlines (in the case of the axisymmetric flows), thus reducing the time required for the interpretation of the computational results.

---

* Listings of the computer programmes of these procedures may be obtained from the author on request.

4.1.2 Contributions in Laser Doppler Velocimetry

The experimental work presented in Chapter 3 has contributed to the understanding, improvement and application of laser Doppler velocimetry as follows:

1. A Doppler signal processing system was devised to allow the measurement of the Doppler frequency statistics and, thus, of the velocity. As discussed in section 3.3 of Chapter 3, this was achieved by combining a digital frequency computing counter and an oscilloscope. By presetting various time constants of the system, control of the measured part of the Doppler burst was achieved. The method was tested with known signals from a generator and subsequently proved to be very reliable for the laminar flows considered. Careful filtering of the Doppler signal input to the oscilloscope and the computing counter may allow the extension of the method to the measurement of flow turbulent quantities (Baker (1973); Durao (1976)).

2. An integrated optical unit developed by Durst and Whitelaw (1971b) has been successfully applied for the measurement of the velocity profiles of the laminar water flow downstream of a 15^{o} bend in a round pipe, as described in section 3.3.2 of Chapter 3. The resolution was sufficient for the measurements to be considered reliable. The results were used as inlet information and to allow an existing numerical procedure to be

extended to represent this flow configuration.

3. In view of the requirement for a minute control volume necessary to achieve adequate measurement resolution of flows in glass capillaries and in venules with size of the order of 100 μm, a parametric study was conducted to determine the effect of the various LDV design features on the size of the control volume. This study, reported in section 3.4 of Chapter 3, was based on the available theoretical formulae and was supported by a series of experiments; in almost all cases, the experimental results verified the theoretical derivations.

4. Guided by the above investigation, a loose lens LDV arrangement was developed and applied for the measurement of the velocity profile of water, plasma, diluted and whole blood flows in glass capillaries of inside diameter of the order of 100 μm. These measurements, reported in section 3.5 of Chapter 3, showed that, for all fluids but whole blood, the measurement resolution was satisfactory and the profiles conformed to the expected parabolic form for fully-developed laminar Newtonian flows. In the case of whole blood, although corrections for velocity and haematocrit gradient broadening were applied, the velocity profiles were far from parabolic, thus revealing the non-Newtonian behaviour of blood flow in small capillaries and low rates of shear.

5. The associated optical, electronic and flow problems in the glass capillaries were discussed and in many cases cured by careful selection and control of the apparatus involved. An Argon laser beam substituting the He-Ne laser beam of the previous experiments resulted in an improved measurement resolution by a factor of 2, as reported in section 3.5 of Chapter 3. In the case of water, plasma and diluted blood (up to 5% haematocrit), the control volume of the LDV could be well defined when observed through a travelling microscope and the Doppler signals were of a satisfactory and measurable quality. The latter proved that Doppler signals of good quality could be obtained from scattering red blood cells from which the haemoglobin content was not removed although the particle size-to-fringe spacing ratio was as high as 20. In the case of whole blood, however, measurable signals could be obtained from blood depths only of the order of 200 μm. Dispersion of the beams by the red blood cells resulted in a distortion of the control volume which was not easily defined when observed by the travelling microscope. In addition, loss of coherence of the beam due to wavefront disturbance from the moving blood cells and multiple scattering resulted in a bad quality of Doppler signal.

6. A correction procedure, to allow for velocity and concentration gradient broadening, was described in section 3.3 of Chapter 3. It was subsequently used to

either correct the biased mean velocity and rms profiles or to estimate the dimensions of the measuring control volume.

7. A constitutive equation for blood was derived in section 3.6 of Chapter 3 and subsequently used for the numerical computations of blood flows. The derivation was based on a survey of the existing blood viscosity laws available in the literature. Casson's law and power law matched the experimental results of glass capillary flow and the power law with a power index of $n = 2/3$ was finally selected for demonstrative purposes.

8. A laser Doppler velocimeter incorporated in a microscope was proposed for miniature flows, in section 3.7 of Chapter 3. Design aspects and optical problems were discussed and it was pointed out that lens aberrations resulted in a distorted control volume when the beams were focused by an annular condenser. Introduction of correcting lenses could, in principle, improve the shape and size of the control volume. However, it was argued that a better system could be obtained by focusing the beams through the microscope objective. This system, which requires further development, may be suitable for thrombosis research by the physiologist.

9. The application of laser Doppler velocimetry to *in vivo* blood flows was partly successful with the LDV's developed

for *in vitro* experiments, as described in section 3.8 of Chapter 3. Doppler-like bursts could be obtained while scanning with the LDV through the venules of the mouse mesentery, but problems similar to those discussed in item 5 above and, in addition, optical and geometrical imperfections of the venules combined with a periodic contraction and expansion of the mesentery did not allow detailed *in vivo* measurements.

Mishina et al (1975) and Einav et al (1975a,b) demonstrated that *in vivo* measurements may be obtained with systems similar to those of item 8 above but the locality and precision of their results is unspecified and requires careful evaluation.

4.2 RECOMMENDATIONS

The computational work reported in this thesis is far from completing the long term objectives of the present investigation. In addition, the experimental work left a number of problems unsolved and, in some circumstances, the specific objectives set *a priori* obviated the extension of the research to other potential paths. Some of these examples are listed below and may be considered as recommendations for future work.

4.2.1 Recommendations for Computational Work

Work is recommended in the following directions:

1. To extend the numerical procedures to predict the flow through bends, bifurcations, and axisymmetric and asymmetric blockages of streamline shapes, i.e. similar to *in vivo* situations.

2. To apply Casson's law of viscosity for blood flows, which is most generally accepted to be valid for blood.

3. To extend the procedures to cover turbulent blood flows, which occur in parts of the vascular system and may alter the mass and heat transfer characteristics of the flow. A turbulence model based on Prandtl's mixing length hypothesis (Schlichting (1968)) or the k-ε turbulence model (Launder and Spalding (1972)) could be used for this purpose.

4. To extend the procedures to cover the pulsatile nature of

blood flow in the more central parts of the vascular bed.

5. To examine the possibility of incorporating into the present numerical procedures the particulate nature of blood, and study its influence on the local characteristics of blood flow; the initiation and growth of atheromatic and thrombotic lesions could then be studied in more detail.

4.2.2 Recommendations for Laser Doppler Velocimetry

The author's general experience with LDV and the shortcomings and successes of the specific objectives of the present investigation support the following recommendations:

1. The effect of beam expanders on the measurement resolution should be investigated carefully by employing good quality expanders.

2. The velocity and concentration gradient broadening correction procedure should be extended to include and quantify the effect of fringe spacing gradient in accordance with the suggestions of Hanson (1973).

3. Backward scatter systems should be extensively investigated in view of the advantages they offer when applied to *in vivo* blood flows.

4. The lens effects encountered with the glass capillaries

suggest that parallel plane channels should be used for future blood flow investigations. In order to avoid the diffusion and attenuation of the beams when passing through whole blood, the haemoglobin content of the red cells should be removed. Capillary sizes of less than 100 μm should be used to avoid severe beam diffusion and absorption when whole blood is measured.

5. The signal phase shifts resulting from multiple particle scattering suggests that the reference beam mode should be examined. It is claimed, for example by Drain (1972), to be the proper LDV mode of operation when many particles are present in the control volume, and Kreid and Goldstein (1971) used it successfully for ghost blood cell flows.

6. The whole LDV system for measurements in small diameter ducts should be designed in an integrated form to minimise alignment and vibration problems. A proposal was outlined in section 3.8 of Chapter 3 where a microscope was used. However, the optical problems of lens aberrations should be carefully overcome for a useful application.

7. In view of the low frequency and poor quality, the Doppler signals obtained in blood flows should be recorded on magnetic tape-recorders and carefully examined. The possibility of recording analogue signals of frequencies up to 20 kHz on magnetic tapes and analysing them by a

laboratory digital computer has been demonstrated by, among others, Vlachos (1972).

8. Finally, integrated LDV measurement units seemed to be the natural extension of the present state of art of laser Doppler velocimetry. Such a unit is shown in Figure 4.2.2-1 and consists of the optical components, the test section, the electronic conditioning of the Doppler signals, the extraction of the velocity information by different signal processing methods, and finally a central processing unit to collect the data, process them and take decisions accordingly. In a fully automatic stage, the LDV unit, through its central processor which could be any digital mini-computer programmed accordingly, could work in a closed-loop mode whereby information is input, processed, rejected or accepted, and feedback signals are sent for either the measurements to continue at the same or another location by moving the test section or the optics with the aid of servo-mechanisms controlled by the central processor.

REFERENCES

ADRIAN, R. J. 1972 Statistics of laser Doppler velocimeter signals: frequency measurement, J. Phys. E: Sci. Instrum. 5, 91 - 95

ADRIAN, R. J. and GOLDSTEIN, R. J. 1971 Analysis of a laser Doppler anemometer, J. Phys. E: Sci. Instrum. 4, 505 - 511

AMES, W. F. 1969 Numerical methods for partial differential equations, Nelson

ANDERSON, N. M. and SEKELJ, P. 1967a Light-absorbing and scattering properties of non-haemolysed blood, Phys. Med. Biol., 12, 2, 173 - 184

ANDERSON, N. M. and SEKELJ, P. 1967b Reflection and transmission of light by this films of non-haemolysed blood, Phys. Med. Biol., 12, 2, 185 - 192

ARFORS, K. E., DHALL, D. P., ENGESET, J., HINT, H., MATHESON, N. A., and TANGEN, O. 1968 Biolaser endothelial trauma as a means of quantifying platelet activity in-vivo, Nature, 218, 887 - 888

AROESTY, J. and GROSS, J. F. 1972 Pulsatile flow in small blood vessels - I. Casson theory, Biorheology, 9, 33 - 43

ASALOR, J. 1973 An examination of spectrum analysis for the processing of laser anemometer signals, Imperial College, Mech. Eng. Dept. Report, HTS/73/46

ATHERTON, A. and BORN, G. V. R. 1972 Quantitative investigations of the adhesiveness of circulating polymorphonuclear leukocytes to blood vessels wall, J. Phys., 222, 447 - 474

ATHERTON, A. and BORN, G. V. R. 1973 Relationship between the velocity of rolling granulocytes and that of the blood flow in venules, J. Phys., 233, 157 - 165

AUSTON, D. H. 1968 Traverse mode locking, IEEE, J. Quantum Electronics, QE-4, 6, 420 - 422

BAKER, R. J. 1973 A Filter bank signal processer for laser anemometry AERE-R7652

BAKER, R. J., HUTCHINSON, P. and WHITELAW, J. H. 1974 Velocity measurements in the recirculation region of an industrial burner flame by laser Anemometry with light frequency shifting, Combustion and flame, 23, 57 - 71

BEAVERS, G. S., SPARROW, E. M. and MAGNUSON, R. A. 1970 Experiments on hydrodynamically developing flow in rectangular ducts of arbitrary aspect ratio, Int. J. of Heat Mass Transfer, 13, 689 - 702

BEDI, P. S. and THEW, M. T. 1973 Localised velocity and turbulence measurement in turbulent swirling flows using laser Doppler anemometry, Opto-electronics, 5, 1, 9 - 25

BEGENT, N. and BORN, G. V. R. 1970 Growth rate in-vivo of platelet thrombi, produced by iontophoresis of ADP, as a function of mean blood flow velocity, Nature, 227, 926 - 930

BENDAT, J. S. and PIERSOL, A. G. 1971 Random data: Analysis and measurement procedures, Wiley - Interscience

BENDICK, P. 1974 Discussion on the paper: "The measurement of blood velocity by laser Doppler anemometry" by VLACHOS, N. S. and WHITELAW, J. H., 2nd Int. Workshop on laser velocimetry, Purdue University, 1, 521 - 544

BENNET, L. 1968 Blood flow: velocity profile continuity near a wall, Biorheology, 5, 253 - 262

BERMAN, H. J. and FUHRO, R. L. 1969 Effect of rate of shear on the shape of the velocity profile and orientation of red cells in arterioles, Bibl. Anat., 10, 32 - 37

BERMAN, N. S. 1972 Fluid particle considerations in the laser Doppler velocimeter, Technical Report, ERC-R-73017, Arizona State University - in DURST, F., MELLING, A. and WHITELAW, J. H. 1976, Principles and practice of laser Doppler anemometry, Academic Press

BERMAN, N. S. 1973 Particle fluid interaction corrections for flow measurements with a laser Doppler flow meter, NASA Report-CR-124254 - in DURST, F., MELLING, A. and WHITELAW, J. H. 1976, Principles and practice of laser Doppler anemometry, Academic Press

BERMAN, N. S. and DUNNING, J. W. 1973 Pipe flow measurements of turbulence and ambiguity using laser Doppler velocimetry, J. Fluid Mech., 61, 289 - 299

BIRD, R. B., LIGHTFOOT, E. N. and STEWART, W. E. 1960 Transport phenomena, Wiley

BLACKSHEAR, P. L. 1972 Mechanical haemolysis in flowing blood, in: Biomechanics - its foundations and objectives, FUNG, Y. C., PERRONE, N. and ANLIKER, M. (Eds.), 501 - 528

BLAKE, K. A. and JESPERSEN, K. I. 1972 The NEL laser velocimeter, NEL Report 510

BROWN, J. and GLAZIER, E. V. D. 1964 Telecommunications, Chapman and Hall/ London

BORN, G. V. R. 1974 Private communications, Cambridge University

BORN, G. V. R., VLACHOS, N. S. and WHITELAW, J. H. 1975 Measurements of blood velocity and their implications for non-Newtonian viscosity laws, Imperial College, Mech. Eng. Dept. Report

BORN, M. and WOLF, E. 1964 Principles of optics; electromagnetic theory of propagation, interference and diffraction of light, Pergamon Press

BRAYTON, D. B., KALB, H. T. and CROSSWY, F. L. 1973 Two-component, dual-scatter laser Doppler velocimeter with frequency burst signal readout, Appl. Optics, 12, 6, 1145 - 1156

BRITISH STANDARD 1042 1964 Methods for the measurement of fluid flow in pipes, Part 1: Orifice plates, nozzles and venturi tubes

BUGLIARELLO, G. and HAYDEN, J. W. 1962 High speed microcinephotographic studies of blood flow in-vitro, Science, 138, 981 - 983

BUGLIARELLO, G. and SEVILLA, J. 1970 Velocity distribution and other characteristics of steady and pulsatile blood flow in fine glass tubes, Biorheology, 7, 85 - 107

BURGRAFF, O. 1966 Analytical and numerical studies of the structure of steady separated flows, J. Fluid Mech., 24, 1, 113 - 151

CARO, C. G., FITZ-GERALD, J. M. and SCHROTER, R. C. 1971 Atheroma and arterial wall shear: Observation, correlation and proposal of a shear dependent mass transfer mechanism for atherogenesis, Proc. Royal Soc., London, B177, 109 - 159

CASSON, N. 1959 A flow equation for pigment-oil suspensions of the printing ink type, Chapter 5 - in Rheology of disperse systems, Mill, C. C. (Ed.), Pergamon Press

CHAMPION, J. V., NORTH, P. F., COAKLEY, W. T. and WILLIAMS, A. R. 1971 Shear fragility of human orythrocytes, Biorheology, 8, 23 - 29

CHARM, S. and KURLAND, G. S. 1962 Tube flow behaviour and shear stress-shear rate characteristics of canine blood, Amer. J. of Physiology, 203, 417 - 421

CHARM, S. E. and KURLAND, G. S. 1965 Viscometry of human blood for shear rates of 0-100000 sec^{-1}, Nature, 206, 617 - 618

CHARM, S. E. and KURLAND, G. S. 1974 Blood flow and microcirculation, Wiley

CHORIN, A. J. 1968 Numerical solution of the Navier-Stokes equations, Math. of Computations, 22, 104, 745 - 762

CHRISTIANSEN, E. B., KELSEY, S. J. and CARTER, T. R. 1972 Laminar tube flow through an abrupt contraction, AIChE J., 18, 2, 372 - 380

COKELET, G. R. 1963 The rheology of human blood - in Biomechanics, its foundations and objectives, FUNG, Y. C., PERRONE, N. and ANLIKER, M. (Eds.), Prentice-Hall, 63 - 103

COLLIER, R. J., BURCKHARDT, C. B. and LIN, L. H. 1971 Optical holography, Academic Press

CONSTANTINIDES, P. 1965 Experimental atherosclerosis, Elsevier

COPLEY, A. L. 1971 Non-Newtonian behaviour of surface layers of human plasma protein systems and a new concept of the initiation of thrombosis, Biorheology, 8, 79 - 84

CORCORAN, V. J. 1965 Directional characteristics in optical heterodyne detection processes, J. Appl. Phys., 36, 6, 1819 - 1825

CURR, R. M., SHARMA, D. and TATCHELL, D. G. 1972 Numerical predictions of some three-dimensional boundary layers in ducts, Comp. Math. in Appl. Mech. Eng., 1, 143 - 158

DEBYE, P. and SEARS, F. W. 1932 On the scattering of light by supersonic waves, Proc. Nat. Acad. Science, 18, 6, 409 - 414

DEIGHTON, M. O. and SAYLE, E. A. 1971 An electronic tracker for the continuous measurement of Doppler frequency from a laser anemometer, DISA Information, 12, 5 - 10

DENISON, E. B. and STEVENSON, W. H. 1970 Oscillatory flow measurements with a directionally sensitive laser anemometer, Rev. Scient. Instrum. 41, 1475 - 1478

DETRA, R. W. 1953 The secondary flow in curved pipes, Mit. Inst. Aerodynamic E.T.H., Zurich, Nr. 20

DICKE, R. H. 1958 Molecular amplification and generation systems and methods, cited in KOGELNIK, H. and LI, T. 1966 Laser beams and resonators, Proc. IEEE, 54, 10, 1312 - 1329

DiGIOVANI, P. R. and EINAV, S. 1974 Hemodynamics of coronary artery-saphenous vein bypass using laser Doppler anemometry, Proc. 2nd Int. Workshop on laser velocimetry, Purdue University, 1, 545 - 565

DRAIN, L. E. 1972 Coherent and non-coherent methods in Doppler optical beat velocity measurement, J. Phys. D: Appl. Phys. 5, 481 - 495

DRAIN, L. E. and MOSS, B. C. 1972 The frequency shifting of laser light by electro-optic techniques, Opto-electronics, 4, 429 - 439

DURAO, D. F. G. 1976 The application of laser Anemometry to free jets and flames with and without recirculation, Ph.D. Thesis, London University

DURAO, D. F. G. and WHITELAW, J. H. 1974a Instantaneous velocity and temperature measurements in oscillating diffusion flames, Proc. Royal Soc., London, A338, 479 - 501

DURAO, D. F. G. and WHITELAW, J. H. 1974b Performance characteristics of two frequency tracking demodulators and a counting system, Proc. 2nd Int. Workshop on laser velocimetry, Purdue University, 1, 170 - 203

DURAO, D. F. G. and WHITELAW, J. H. 1975 The performance of acousto-optic cells for laser Doppler anemometers, J. Phys. E: Scient. Instrum. 8, 9, 776 - 780

DURRANI, T. S. and GREATED, C. A. 1973 Statistical analysis and computer simulation of laser Doppler velocimeter systems, Trans. IEEE, IM-22, 1, 23 - 34

DURRANI, T. S. and GREATED, C. 1974a Theory of LDV tracking systems, IEEE. Trans., AES-10, 4, 418 - 428

DURRANI, T. S. and GREATED, C. 1974b Statistical analysis of velocity measuring systems employing the photon correlation technique, IEEE. Trans., AES-10, 1, 17 - 24

DURRANI, T. S., GREATED, C. and WILMSHURST, T. H. 1973 An analysis of simulators and tracking systems for laser Doppler velocimeters, Opto-electronics, 5, 1, 71 - 89

DURST, F. 1972 Development and application of optical anemometers, Ph.D. Thesis, London University

DURST, F., MELLING, A. and WHITELAW, J. H. 1974 Low Reynolds number flow over a sudden plane symmetrical sudden expansion, J. Fluid. Mech., 64, 1, 111 - 128

DURST, F., MELLING, A. and WHITELAW, J. H. 1976 Principles and practice of Laser Doppler Anemometry, Academic Press

DURST, F. and WHITELAW, J. H. 1971a Optimization of optical anemometers, Proc. Royal Soc., London, A324, 157 - 181

DURST, F. and WHITELAW, J. H. 1971b Integrated optical units for laser anemometry, J. Phys. E: Scient. Instrum., 4, 804 - 808

DURST, F. and WHITELAW, J. H. 1973 Light source and geometrical requirements for the optimisation of optical anemometry signals, Opto-electronics, 5, 137 - 151

EDWARDS, R. V., ANGUS, J. C., FRENCH, M. J. and DUNNING, J. W. 1971 Spectral analysis of the signal from the Laser Doppler Flowmeter: Time-Independent systems, J. Appl. Phys., 42, 2, 837 - 850

EINAV, S., BERMAN, H. J., FUHRO, R. L., DiGIOVANNI, P. R., FRIDMAN, J. D. and FINE, S. 1975a Measurement of blood flow in-vivo by Laser Doppler Anemometry through a microscope, Biorheology, 12, 203 - 205

EINAV, S., BERMAN, H. J., FUHRO, R. L., DiGIOVANNI, P. R., FINE, S. and FRIDMAN, J. D. 1975b Measurement of velocity profiles of red blood cells in the microcirculation by Laser Doppler Anemometry, Biorheology, 12, 207 - 210

ELECCION, M. 1973 Laser hazards, IEEE, Spectrum, Aug. 32 - 38

FAHRAEUS, R. and LINDQVIST, T. 1931 The viscosity of human blood in narrow capillary tubes, Amer. J. Physiology, 96, 562 - 568

FENDER, B. H. 1964 Control mechanisms of the eye, Scientific American, 211, 1, 24 - 34

FORRESTER, A. T. 1956 On coherence properties of light waves, Amer. J. Physics, 24, 192 - 196

FORRESTER, A. T. 1961 Photoelectric mixing as a spectroscopic tool, J. Optical Soc. America, 51, 3, 253 - 259

FORRESTER, A. T., GUDMUNDSEN, R. A. and JOHNSON, P. O. 1955 Photoelectric mixing of incoherent light, Physical Rev., 99, 6, 1691 - 1700

FORSYTHE, G. W. and WASOW, W. R. 1960 Finite difference methods for partial differential equations, Wiley

FOWLES, G. R. 1968 Introduction to modern optics, Holt, Rinehart and Winston

FRY, D. L. 1968 Circulation Research, 22, 165, cited in: MUNTER, W. A. and STEIN, P. D. 1973 Newtonian behavior of blood at high rates of shear, Biorheology, 10, 501 - 508

GEORGE, W. K. and LUMLEY, J. L. 1973 The laser-Doppler velocimeter and its application to the measurement of turbulence, J. Fluid Mech., 60, 2, 321 - 362

GOLDSMITH, H. L. 1967 Microscopic flow properties of red cells, Proc. Fed. Amer. Soc. Exp. Biol., 26, 6, 1813 - 1820

GOLDSTEIN, R. J. and ADRIAN, R. J. 1971 Measurement of fluid velocity gradients using Laser-Doppler techniques, Rev. Scient. Instrum., 42, 9, 1317 - 1320

GOLDSTEIN, R. J. and HAGEN, W. F. 1967 Turbulent flow measurements utilizing the Doppler shift of scattered laser radiation, Physics of Fluids, 10, 1349 - 1352

GOLDSTEIN, R. J. and KREID, D. K. 1967 Measurement of laminar flow development in a square duct using a Laser-Doppler flowmeter, Trans. ASME, J. Appl. Mech., 34, 813 - 818

GOSMAN, A. D., LOCKWOOD, F. C. and SYED, S. A. 1976 Predictions of a horizontal turbulent diffusion flame, 16th Int. Symp. Comb., Publ. by Combustion Institute

GOSMAN, A. D. and PUN, W. M. 1974 Lecture notes for a course entitled: "Calculation of recirculating flows", Imperial College, Mech. Eng. Dept. Report HTS/74/2

GOSMAN, A. D., PUN, W. M., RUNCHAL, A. K., SPALDING, D. B. and WOLFSHTEIN, M. 1969 Heat and Mass transfer in recirculating flows, Academic Press

GOSMAN, A. D., VLACHOS, N. S. and WHITELAW, J. H. 1973 Laminar pipe flow downstream of a 15^{0} bend, Imperial College, Mech. Eng. Dept. Report HTS/73/4 also in: Measurement and calculation of laminar flow downstream of a bend in a round pipe and the prognosis for similar investigations of blood flow in venules, ASME, Symposium on Biomechanics, Troy, N.Y., 1975

GREATED, C. 1970a Measurements of turbulence statistics with a laser velocimeter, J. Phys. E: Scient. Instrum., 3, 158 - 160

GREATED, C. 1970b Measurement of Reynolds stresses using an improved laser flowmeter, J. Phys. E: Scient. Instrum., 3, 753 - 756

GREATED, C. 1971 Resolution and back-scattering optical geometry of laser-Doppler systems, J. Phys. E: Sci. Instrum., 4, 585 - 588

GREATED, C. and DURRANI, T. S. 1971 Signal analysis for laser velocimeter measurements, J. Phys. E: Sci. Instrum., 4, 24 - 26

GREEN, J. H. 1968 An introduction to human physiology, Oxford

GREENSPAN, D. 1967 Numerical studies of two-dimensional steady state Navier-Stokes equations for arbitrary Reynolds numbers, Univ. Wisconsin, Comp. Science Dept., Techn. Report 9

GREENSPAN, D. 1973 Numerical studies of viscous, incompressible flow through an orifice for arbitrary Reynolds numbers, Int. J. Num. Methods Eng., 6, 489 - 496

HALMOS, A. L., BOGER, D. V. and CABELLI, A. 1975 The behaviour of a power-law fluid flowing through a sudden expansion, Parts I and II, AIChE J., 21, 3, 540 - 553

HAN, L. S. 1960 Hydrodynamic entrance lengths for incompressible laminar flow in rectangular ducts, Trans. ASME, J. Appl. Mech., 403 - 409

HANSON, S. 1973 Broadening of the measured frequency spectrum in a differential laser anemometer due to interference plane gradients, J. Phys. D: Appl. Phys., 6, 164 - 171

HARKNESS, J. 1971 The viscosity of human blood plasma; its measurement in health and disease, Biorheology, 8, 171 - 193

HAUER, A. and ALWANG, W. G. 1973 Design of a laser velocimeter for use in turbomachinery. Electro-optics systems Design Conf., N.Y.

HELMHOLTZ, Von H. 1962 Physiological optics, Southall, J. P., (Ed.), Dover

HOERNER, S. F. 1965 Fluid-dynamic drag, The Author

HUFFAKER, R. M., FULLER, C. E. and LAWRENCE, T. R. 1969 Application of laser-Doppler velocity instrumentation to the measurement of jet turbulence, SAE Conference, Detroit

HULST, Van de, H. C. 1957 Light scattering by small particles, Wiley

IVANOFF, A. 1956 About the spherical aberration of the eye, J. Optical Soc. America, 46, 10, 901 - 903

JACKSON, D. A. and PAUL, D. M. 1971 Measurement of supersonic velocity and turbulence by laser anemometry, J. Phys. E: Scient. Instrum., 4, 173 - 177

JENSON, V. G. 1959 Viscous flow round a sphere at low Reynolds numbers (<40), Proc. Royal Soc., A249, 346 - 366

JOHANSEN, F. C. 1930 Flow through pipe orifices at low Reynolds numbers, Proc. Royal Soc., A126, 231 - 245

KAWATA, M., KURASE, K., YOSHIDA, K. and UTSUMI, H. 1971 Laminar flow and pressure drop in a capillary tube, 1st Symp. Flow, its measurement and control in Science and Industry, Pittsburgh, Penn., 17 - 26

KERKER, M. 1969 The scattering of light and other electromagnetic radiation, Academic Press

KNISELY, M. H. 1965 Intravascular erythrocyte aggregation (blood sludge), Handbook of Physiology - Circulation III, Ch. 63, 2249 - 2292

KOCHEN, J. A. and BAEZ, S. 1964 Laser induced microvascular thrombosis. Embolization and recanalization in the rat, Annals of N.Y. Academy Science, 122, 2, 728 - 737

KOGELNIK, H. 1965 Imaging of optical modes-resonators with internal lenses, Bell System Techn. J., 44, 455 - 494

KOGELNIK, H. and LI, T. 1966 Laser beams and resonators, Proc. IEEE, 54, 10, 1312 - 1329

KRAMER K., ELAM, O., SAXTON, G. and ELAM, W. N. 1951 Influence of oxygen saturation, erythrocyte concentration and optical depth upon the red and near-infrared light transmittance of whole blood, Amer. J. Phys., 165, 229 - 245

KREID, D. K. 1974 Laser-Doppler velocimeter measurements in nonuniform flow: Error Estimates, Appl. Optics, 13, 8, 1872 - 1881

KREID, D. K. and GOLDSTEIN, R. J. 1971 Measurements of velocity profiles in simulated blood by the laser-Doppler technique, Proc. ISA Symp. on Flow - Its measurement and Control in Science and Industry, Paper 4-2-95, Pittsburgh

LADING, L. 1971 Differential Doppler heterodyning technique, Appl. Optics, 10, 8, 1943 - 1949

LADING, L. 1973 Analysis of signal-to-noise ratio of the laser Doppler velocimeter, Opto-electronics, 5, 175 - 187

LAMB, W. E. 1964 Theory of an optical Maser, Phys. Rev., 134, 6A, A1429 - A1450

LAUNDER, B. and SPALDING, D. B. 1972 Mathematical models of turbulence, Academic Press

LEE, Y. W. 1960 Statistical theory of communication, Wiley

LOTHIAN, G. F. and LEWIS, P. C. 1956 Spectrophotometry of granulated materials, with particular reference to blood corpuscles, Nature, 178, 1342 - 1343

LAWSON, J. L. and UHLENBECK, G. E. 1950 Threshold signals heterodyning reception and noise, McGraw-Hill

LYNN, N. S., FOX, V. G. and ROSS, L. W. 1972 Computation of fluid-dynamical contribution to atherosclerosis at arterial bifurcations, Biorheology, 9, 61 - 66

McGUIRK, J. J. 1975 Prediction of turbulent buoyant jets in co-flowing streams, Ph.D. Thesis, London University

McLAUGHLIN, D. K. and TIEDERMAN, W. G. 1973 Biasing correction for individual realisation of Laser Anemometer measurements in turbulent flows, Phys. Fluids, 16, 12, 2082 - 2091

McRAE, R. A., McCLURE, J. A. and LATIMER, P. 1961 Spectral transmission and scattering properties of red blood cells, J. Optical Soc. America, 51, 12, 1366 - 1372

MACAGNO, E. O. and HUNG, T. K. 1967 Computational and experimental study of a captive annular eddy, J. Fluid Mech., 28, 1, 43 - 64

MASON-GUEST, M. 1965 Circulatory effects of blood clotting, fibrinolysis, and related hemostatic processes, Handbook of Physiology, Circulation III, Chapter 62, 2209 - 2248

MAYDAN, D. 1971 Micromachining and image recording in thin films by laser beams, Bell Syst. J., 50, 6, 1761 - 1789

MAZUMDER, M. K. 1972 A symmetrical laser Doppler velocity meter and its application to turbulence characterization, NASA CR-2031

MAZUMDER, M. K. and WANKUM, D. L. 1970 SNR and spectral broadening in turbulence structure measurement using a CW laser, Appl. Optics, 9, 3, 633 - 637

MELLING, A. 1971 Scattering particles for laser anemometry in air: selection criteria and their realisation, Imperial College, Mech. Eng. Dept. Report HTS/71/1

MELLING, A. 1973 The influence of velocity gradient broadening on mean and rms velocity measured by laser anemometry, Imperial College, Mech. Eng. Dept., HTS/73/33

MELLING, A. 1975a Investigation of flow in non-circular ducts and other configurations by Laser Doppler Anemometry, Ph.D. Thesis, London University

MELLING, A. 1975b Application of laser Doppler anemometry to velocity measurements in capillary blood flow, Report to British Heart Foundation

MELLING, A. and WHITELAW, J. H. 1976 Laser Doppler Microscope for blood velocity measurements, Report to British Heart Foundation

MERRILL, E. W., COKELET, G., BRITTEN, A. and WELLS, R. E. 1964 Rheology of human blood and the red cell plasma membrane, Bibl. Anatomica, 4, 51 - 57

MERRILL, E. W., GILLILAND, E. R., COKELET, G. SHIN, H., BRITTEN, A. and WELLS, R. E. 1963 Rheology of human blood, near and at zero flow: Effects of temperature and hematocrit level, Biophys. J., 3, 199 - 213

MEYER-ARENDT, J. 1972 Introduction to classical and modern optics, Prentice-Hall

MILLS, R. D. 1968 Numerical solutions of viscous flow through a pipe orifice at low Reynolds numbers, J. Mech. Eng. Science, 10, 2, 133 - 140

MISHINA, H., ASAKURA, T. and NAGAI, S. 1974 A laser Doppler microscope, Optics Commun., 11, 99

MISHINA, H., KOYAMA, T. and ASAKURA, T. 1975 Velocity measurements of blood flow in the capillary and vein using a Laser Doppler microscope, Appl. Optics, 14, 10, 2326 - 2327

MONRO, P. A. G. 1964 Visual particle velocity measurement for fast particles and blood cells in-vivo and in-vitro, Bibl. Anat., 4, 34 - 45

MUNTER, W. A. and STEIN, P. D. 1973 Newtonian behaviour of blood at high rates of shear, Biorheology, 10, 501 - 508

OLDENGARM, J. 1973 Instruction manual for rotating grating system type PS21, Technish Physische Dienst, Delft

OWEN, J. M. and ROGERS, R. H. 1975 Velocity biasing in laser Doppler anemometer, Proc. LDA-Symposium, Copenhagen, 89 - 114

PATANKAR, S. V., PRATAP, V. S. and SPALDING, D. B. 1974 Prediction of laminar flow and heat transfer in helically coiled pipes, J. Fluid Mech., 62, 3, 539 - 551

PATANKAR, S. V. and SPALDING, D. B. 1972 A calculation procedure for heat, mass and momentum transfer in three-dimensional parabolic flows, Int. J. Heat and Mass Transfer, 15, 1787 - 1806

PEACEMAN, D. W. and RACHFORD, H. H. 1955 The numerical solution of parabolic and elliptic differential equations, J. Soc. Ind. Appl. Maths., 3, 28 - 41

PFEIFER, H. J. and VOM STEIN, H. D. 1973 Application of the laser velocimeter in supersonic wind tunnel, Opto-electronics, 5, 1, 53 - 58

PIKE, E. R. 1972 The application of photon correlation spectroscopy to laser Doppler measurements, J. Phys. D: Appl. Phys., 5, L23 - 25

PROKHOROV, A. M. 1958 Molecular amplifier and generator for submillimeter waves, JETP (USSR), 34, 1658 - 1659, cited in KOGELNIK, H. and LI, T. 1966 Proc. IEEE, 54, 1312 - 1329

REINER, M. and SCOTT-BLAIR, G. 1959 The flow of blood through narrow tubes, Nature, 184, 354 - 355

RICHTMYER, R. D. 1957 Difference methods for initial value problems, Interscience

RIVA, C., ROSS, B. and BENEDEK, G. B. 1972 Laser Doppler measurements of blood flow in capillary tubes and retinal arteries, Invest. Ophthal., 11, 11, 936 - 944

RODKIEWICZ, C. M. 1975 Localisation of early atherosclerotic lesions in the aortic arch in the light of fluid flow, J. Biomechanics, 8, 149 - 156

RODKIEWICZ, C. M. and ROUSSEL, C. L. 1973 Fluid mechanics in a large arterial bifurcation, Trans. ASME., J. Fluid Eng., 95, 108 - 112

ROSS, M. 1966 Laser receivers: devices, techniques, systems, Wiley

ROWE, M. 1970 Measurements and computations of flow in pipe bends of constant cross-section, J. Fluid Mechanics, 43, 771 - 780

RUDD, M. J. 1972 Velocity measurements made with a laser dopplermeter on the turbulent pipe flow of a dilute polymer solution, J. Fluid Mech., 51, 4, 573 - 685

RUNCHAL, A. K. 1969 Transfer processes in steady two dimensional separated flows, Ph.D. Thesis, London University

RUNCHAL, A. K. 1972 Convergence and accuracy of three finite difference schemes for a two-dimensional conduction and convection problem, Int. J. Num. Meth. Eng., 4, 541 - 550

RUNCHAL, A. K. and WOLFSTEIN, M. 1969 A finite difference procedure for the investigation of the Navier-Stokes equations, J. Mech. Eng. Sciences, 11, 445 - 453

SACKS, A. H. and TICKNER, E. G. 1968 The compressibility of blood, Biorheology, 5, 271 - 274

SCHAWLOW, A. L. and TOWNES, C. H. 1958 Infrared and optical Masers, Phys. Rev. 112, 1940 - 1949

SCHLICHTING, H. 1968 Boundary-layer theory, McGraw-Hill

SCOTT-BLAIR, G. W. 1959 An equation for the flow of blood, plasma and serum through glass capillaries, Nature, 183, 613 - 614

SCOTT-BLAIR, G. W. 1967 A model to describe the flow curves of concentrated suspensions of spherical particles, Rheologica Acta, 6, 201 - 202

SEGRÉ, G. and SILBERBERG, A. 1962 Behaviour of macroscopic rigid spheres in Poiseuille flow, Parts 1 and 2, J. Fluid Mech., 14, 115 - 157

SHAH, V. L. 1975 Private communications, University of Wisconsin, Mech. Eng. Dept.

SHAPIRO, A. H., SIEGEL, R. and KLINE, S. J. 1954 Friction factor in the laminar artery region of a smooth tube, Proc. 2nd U.S. Congr. Appl. Mech., 733 - 741

SLINEY, D. H. and PALMISANO, W. A. 1968 The evaluation of laser hazards, Amer. Industry Hyg. Assoc. J., 29, 425

SMITH, G. D. 1965 Numerical solution of partial differential equations, Oxford

SMITH, P. W. 1970 Mode-locking of lasers, Proc. IEEE, 58, 1342 - 1357

SPAIN, D. M. 1966 Atherosclerosis, Scient. American, 215, 49 - 56

SPALDING, D. B. 1972 A novel finite difference formulation for differential expressions involving both first and second derivatives, Int. Num. Mech. Eng., 4, 551 - 559

SPALDING, D. B. 1974 Numerical computations of steady boundary layers - A survey, Imperial College, Mech. Eng. Dept. Report HTS/74/27

STEVENSON, W. H. 1970 Optical frequency shifting by means of a rotating diffraction grating, Appl. Optics, 9, 649 - 652

SUTERA, S. P. and MEHRJANDI, M. H. 1975 Deformation and frangmentation of human red blood cells in turbulent shear flows, Bioph. J., 15, 1 - 10

SUZUKI, T. and HIOKI, R. 1967 Translation of light frequency by a moving grating, J. Opt. Soc. America, 57, 12, 1551

THOM, A. 1932 An arithmetical solution of certain problems in steady viscous flows, Rep. Memo. Aeronaut. Res. Comm., 1475

THOM, A. 1933 The flow past circular cylinders and low speeds, Proc. Royal Soc., London, A141, 651 - 669

TUVE, G. L. and SPRENKLE, R. E. 1933 Orifice discharge coefficients for viscous liquids, Instruments, 6, 201 - 206

TWERSKEY, V. 1964 Proc. Symp. Appl. Math., 16, 84

VARGA, R. S. 1962 Matrix iterative analysis, Prentice-Hall

VAVRA, M. H. 1960 Aero and aerio thermodynamics and flow in turbomachinery, Wiley

VLACHOPOULOS, J. and STOURNARAS, C. 1975 Laminar two-dimensional non-Newtonian jets, AIChE J., 21, 2, 385 - 388

VLACHOS, N. S. 1972 A Statistical analysis of cyclic variations in internal combustion engines, M.Sc. Thesis, London University

VLACHOS, N. S. and LEKKAS, T. D. 1977 Surface blocking of granular water filters, Imperial College, Civil Eng. Dept. Report, In preparation

VLACHOS, N. S. and WHITELAW, J. H. 1974 The measurement of blood velocity with Laser Doppler Anemometry, Proc. 2nd Int. Workshop on Laser Velocimetry, Purdue University, 1, 521 - 544

WANG, C. P. 1972 A unified analysis on laser Doppler velocimeters, J. Phys. E: Scient. Instr. 5, 763 - 766

WANG, C. P. 1973 Effect of Doppler ambiguity on the measurement of turbulence spectra by laser Doppler velocimeter, Appl. Phys. Lett., 22, 4, 154 - 156

WANG, C. P. and SNYDER, D. 1974 Laser Doppler velocimetry: Experimental study, Appl. Optics, 13, 1, 98 - 103

WARD-SMITH, A. J. 1963 The flow and pressure losses in smooth pipe bends of constant cross-section, J. Royal Aero. Soc., 67, 437 - 447

WELFORD, W. T. 1974 Private communication, Imperial College, Physics Dept.

WESOLOWSKI, S. A., FRIES, C. C., SABINI, A. M. and SAWYER, P. N. 1962 The significance of turbulence in hemic systems and in the distribution of the atherosclerotic lesions, Surgery, 57, 155 - 162

WESTLAKE, J. R. 1968 Numerical matrix inversion and solution of linear equations, Wiley

WHITELAW, J. H. 1975 Developments in Laser Doppler Anemometry, article in: Studies in convection: Theory, measurement and applications, B. E. Launder (Ed.), Academic Press

WIGINTON, C. L. and DALTON, C. 1970 Incompressible laminar flow in the entrance region of a rectangular duct, J. Appl. Mech. (ASME), 37, 854 - 856

WIGLEY, G. 1974 The application of radial diffraction gratings to laser anemometry, AERE-R 7886

WILMSHURST, T. H., GREATED, C. A. and MANNING, R. 1971 A laser fluid-flow velocimeter of wide dynamic range, J. Phys. E: Scient. Instrum., 4, 81 - 85

YANTA, W. J., GATES, D. F. and BROWN, F. W. 1971 The use of a laser-Doppler velocimeter in supersonic flow, AIAA paper 71 - 287

YEH, Y. and CUMMINS, H. Z. 1964 Localised fluid flow measurements with an He-Ne laser spectrometer, Appl. Phys. Lett., 4, 10, 176 - 178

YOUNG, D. F. and TSAI, F. Y. 1973 Flow characteristics in models of arterial stenoses - I. steady flow, J. Biomech., 6, 395 - 410

ZDROJKOWSKI, R. J. and LONGINI, R. L. 1969 Optical transmission through whole blood illuminated with highly collimated light, J. Optical Soc. Amer., 59, 8, 1, 898 - 903

APPENDIX A

THE TRI-DIAGONAL MATRIX ALGORITHM (TDMA)

The solution of the resulting finite difference flow equations of Chapter 2 may be outlined as follows:

Consider the set of linear equations:

$$x_i = a_i\, x_{i+1} + b_i\, x_{i-1} + c_i \quad , \quad i = 1, N \tag{A.1}$$

valid in a region bound by a close curve S, as shown in the Figure below.

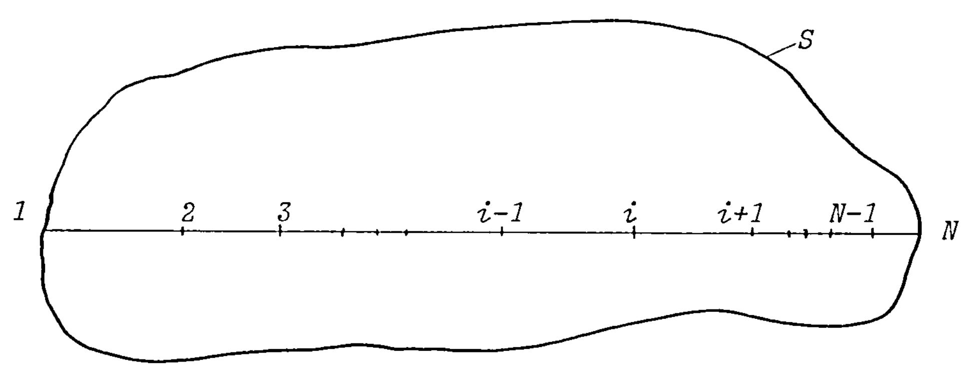

Figure A.1: The TDMA domain

The boundary conditions are:

$$a_N = 0 \quad , \quad b_1 = 0 \quad , \quad x_1, x_N = known \tag{A.2}$$

Since x_1 is known, x_2 can be expressed as:

$$x_2 = a_2'\, x_3 + c_2' \tag{A.3}$$

where: $\quad a_2' = a_2 \quad$ and $\quad c_2' = b_2\, x_1 + c_2 \quad$ (A.4)

Then:

$$x_3 = a_3' x_4 + c_3' \qquad (A.5)$$

where: $$a_3' = \frac{a_3}{1 - b_3 a_2'} \quad \text{and} \quad c_3' = \frac{b_3 c_2' + c_3}{1 - b_3 a_2'} \qquad (A.6)$$

Thus, the general recurrence formula may be written as follows:

$$x_i = a_i' x_{i+1} + c_i' \qquad (A.7)$$

where: $$a_i' = \frac{a_i}{1 - b_i a_{i-1}'} \quad \text{and} \quad c_i' = \frac{b_i c_{i-1}' + c_i}{1 - b_i a_{i-1}'} \qquad (A.8)$$

This formula is used by the TDMA to obtain the solution of the set of equations (A.1) in the bound region prescribed by the boundary conditions (A.2). Thus, the coefficients of the recurrence formula (equation (A.7)) are calculated from equations (A.8). Then, the values of the variable x_i are obtained by substitution into equation (A.7).

The direction of the TDMA may be reversed. In this case, the formulae, corresponding to equations (A.7) and (A.8), are as follows:

$$x_i = a_i' x_{i-1} + c_i' \qquad (A.9)$$

where: $$a_i' = \frac{b_i}{1 - a_i b_{i+1}'} \quad \text{and} \quad c_i' = \frac{a_i c_{i+1}' + c_i}{1 - a_i b_{i+1}'} \qquad (A.10)$$

APPENDIX B

DERIVATION OF THE FINITE-DIFFERENCE EQUATIONS FOR THREE-DIMENSIONAL PARABOLIC FLOWS

In this Appendix, the derivation of the finite-difference equations of the three-dimensional parabolic flows is described. Only the u-momentum and the pressure-correction equations are dealt with, the others being similar.

(a) u-momentum equation

By integration over the control volume shown in Figure 2.3.2-2, equation (2.2.2-7) becomes:

$$\left[(\rho uuA)_P - (\rho uuA)_U\right] + \left[(\rho vuA)_n - (\rho vuA)_s\right] + \left[(\rho wuA)_e - (\rho wuA)_w\right]$$

$$- \left[((\eta \frac{\partial u}{\partial y})\ A)_n - ((\eta \frac{\partial u}{\partial y})\ A)_s + ((\eta \frac{\partial u}{\partial z})\ A)_e - ((\eta \frac{\partial u}{\partial z})\ A)_w\right]$$

$$= (\frac{d\bar{p}}{dx}\ A)_P + f_x\ (cell\ volume) \qquad (B.1)$$

where the A's represent areas of the cell surfaces and f_x is the generation term (source term).

With the aid of the assumptions of section 2.2.5 for the variation of the variables over the cell, and the geometrical quantities of Figure 2.3.2-2, equation (B.1) transforms to the following form:

$$\left[\left\{(\rho u^*A)_U - ((\rho v^*A)_n - (\rho v^*A)_s) - ((\rho w^*A)_e - (\rho w^*A)_w)\right\} u_P\right.$$

$$\left. - (\rho u^*A)_U\, u_U^*\right] + \left[(\rho v^*A)_n \left(\frac{u_N + u_P}{2}\right) - (\rho v^*A)_s\left(\frac{u_P + u_S}{2}\right)\right]$$

$$+ \left[(\rho w^*A)_e \left(\frac{u_E + u_P}{2}\right) - (\rho w^*A)_w \left(\frac{u_P + u_W}{2}\right)\right]$$

$$- \left[\left(\frac{\eta A}{\delta y}\right)_n (u_N - u_P) - \left(\frac{\eta A}{\delta y}\right)_s (u_P - u_S)\right]$$

$$- \left[\left(\frac{\eta A}{\delta z}\right)_e (u_E - u_P) - \left(\frac{\eta A}{\delta z}\right)_w (u_P - u_W)\right]$$

$$= \left(A \frac{d\bar{p}}{dx}\right)_P + f_x \text{ (cell volume)} \tag{B.2}$$

where the * represents upstream or guessed values. Rearranging the terms, the finite-difference equation is derived in its final form as follows:

$$A_P^u\, u_P = A_N^u\, u_N + A_S^u\, u_S + A_E^u\, u_E + A_W^u\, u_W + S^u \tag{B.3}$$

where the coefficients are a combination of convective and diffusive terms, and they are given by:

$$S^u = S_p \cdot u_P + S_u$$

$$A_P^u = A_N^u + A_S^u + A_E^u + A_W^u$$

$$\begin{aligned} A_N^u &= D_n - C_n/2 \\ A_S^u &= D_s + C_s/2 \\ A_E^u &= D_e - C_e/2 \\ A_W^u &= D_w + C_w/2 \end{aligned} \tag{B.4}$$

$$S_u = F_U\, u_U^* + f_x\,(\Delta x\ \Delta y\ \Delta z)\ ,\quad S_p = -F_U$$

The convective parts of these coefficients are as follows:

$$\begin{aligned} C_n &= (\rho\ v^*\ \Delta x\ \Delta z)_n \\ C_s &= (\rho\ v^*\ \Delta x\ \Delta z)_s \\ C_e &= (\rho\ w^*\ \Delta x\ \Delta y)_e \\ C_w &= (\rho\ w^*\ \Delta x\ \Delta y)_w \end{aligned} \tag{B.5}$$

The diffusive parts are:

$$\begin{aligned} D_n &= \left(\frac{\eta\ \Delta x\ \Delta z}{\delta y}\right)_n \\ D_s &= \left(\frac{\eta\ \Delta x\ \Delta z}{\delta y}\right)_s \\ D_e &= \left(\frac{\eta\ \Delta x\ \Delta y}{\delta z}\right)_e \\ D_w &= \left(\frac{\eta\ \Delta x\ \Delta y}{\delta z}\right)_w \end{aligned} \tag{B.6}$$

and the term F_U is calculated from the relationship:

$$F_U = (\rho\ u^*\ \Delta y\ \Delta z)_U \tag{B.7}$$

The "hybrid scheme" mentioned in section 2.2.5 to account for high lateral fluxes is implemented by substituting the D's with the D^*'s evaluated from the formula:

$$D^* = \tfrac{1}{2}\left|D + \left|\frac{C}{2}\right| + \left|D - \left|\frac{C}{2}\right|\right|\right| \tag{B.8}$$

(b) Pressure-correction equation

To obtain the velocity components v and w, a cross-stream pressure field p^* is guessed. Then, the velocities v^* and w^* are obtained by solving the momentum equations:

$$
\begin{aligned}
A_P^v \, v_P^* &= \Sigma \, A_i^v \, v_i^* + S^v + D^v \, (p_S^* - p_P^*) \\
A_P^w \, w_P^* &= \Sigma \, A_i^w \, w_i^* + S^w + D^w \, (p_W^* - p_P^*)
\end{aligned}
\qquad (B.9)
$$

The starred velocities do not, in general, satisfy local mass continuity (equation (2.2.2-6)) which, by integration over the control volume of Figure 2.3.2-2, may become as follows:

$$(\rho uA)_P - (\rho uA)_U + (\rho vA)_n - (\rho vA)_s + (\rho wA)_e - (\rho wA)_w = 0 \qquad (B.10)$$

The aim now is to correct the cross-stream velocities by correction of the pressure field so that continuity is satisfied. Assuming that the necessary pressure-corrections are p_P', p_N', p_S', p_E', p_W' for each point P, the following formulae may be derived from the momentum equations (B.9)*:

$$
\begin{aligned}
v_P &= v_P^* + v_P' = v_P^* + D^v \, (p_S' - p_P') \\
w_P &= w_P^* + w_P' = w_P^* + D^w \, (p_W' - p_P')
\end{aligned}
\qquad (B.11)
$$

where v_P' and w_P' are the velocity corrections. Substitution into the continuity equation (B.10) yields the finite-difference form of the pressure-correction equation:

$$A_P^p \, p_P' = A_N^p \, p_N' + A_S^p \, p_S' + A_E^p \, p_E' + A_W^p \, p_W' + S^p \qquad (B.12)$$

---

* Higher order tems are neglected for this derivation.

where the coefficients are given by:

$$S^p = S_p p'_P + S_u$$

$$A_P^p = A_N^p + A_S^p + A_E^p + A_W^p$$

$$A_N^p = (\rho\ D^v\ \Delta x\ \Delta z)_n$$

$$A_S^p = (\rho\ D^v\ \Delta x\ \Delta z)_s$$

$$A_E^p = (\rho\ D^w\ \Delta x\ \Delta y)_e \qquad \text{(B.13)}$$

$$A_W^p = (\rho\ D^w\ \Delta x\ \Delta y)_w$$

$$S_p = 0$$

$$S_u = (\rho\ u^*\ \Delta y\ \Delta z)_P - (\rho\ u^*\ \Delta y\ \Delta z)_U + C_n - C_s + C_e - C_w$$

The values of the convective terms C are calculated in the same manner as for the momentum equations, and the D coefficients as follows:

$$D_n^v = \left(\frac{\Delta x\ \Delta z}{A_P}\right)_n$$

$$D_s^v = \left(\frac{\Delta x\ \Delta z}{A_P}\right)_s$$

$$D_e^w = \left(\frac{\Delta x\ \Delta y}{A_P}\right)_e \qquad \text{(B.14)}$$

$$D_w^w = \left(\frac{\Delta x\ \Delta y}{A_P}\right)_w$$

where the A_P's are those defined in the corresponding momentum equations.

APPENDIX C

DERIVATION OF THE FINITE-DIFFERENCE EQUATIONS FOR TWO-DIMENSIONAL ELLIPTIC FLOWS

The finite-difference form of the two-dimensional elliptic flow equations given in section 2.2.2 are now derived. Because of the similarity of the equations, only the u-momentum and the pressure-correction equations are derived.

(a) u-momentum equation

Integration of equation (2.2.2-12) over the finite control volume of Figure 2.4.2-2 yields:

$$\left[(\rho uuA)_e - (\rho uuA)_w + (\rho vuA)_n - (\rho vuA)_s\right]$$

$$- \left[((\eta \frac{\partial u}{\partial x}) A)_e - ((\eta \frac{\partial u}{\partial x}) A)_w + ((\eta \frac{\partial u}{\partial y}) A)_n - ((\eta \frac{\partial u}{\partial y}) A)_s\right]$$

$$= (pA)_w - (pA)_e + f_x \text{ (cell volume)} \tag{C.1}$$

where the A's represent the areas of the cell surfaces, and f_x is the generation term (source term).

With the aid of the assumptions of section 2.2.5 for the variation of the variables and substitution of the geometrical quantities of Figure 2.4.2-2, equation (C.1) becomes:

$$\left[((\rho u^* r\Delta y)_e \, (u_P f_e^{\S} + u_E (1 - f_e)) - ((\rho u^* r\Delta y)_w \, (u_P f_w^{\S} + u_W (1 - f_w)) \right.$$

$$\left. + (\rho v^* r\Delta x)_n \left(\frac{u_N + u_P}{2}\right) - (\rho v^* r\Delta x)_s \left(\frac{u_S + u_P}{2}\right) \right]$$

$$- \left[\left(\frac{\eta\, r\, \Delta y}{\delta x}\right)_e (u_E - u_P) - \left(\frac{\eta\, r\, \Delta y}{\delta x}\right)_w (u_P - u_W) \right.$$

$$\left. + \left(\frac{\eta\, r\, \Delta x}{\delta y}\right)_n (u_N - u_P) - \left(\frac{\eta\, r\, \Delta x}{\delta y}\right)_s (u_P - u_S) \right]$$

$$= p_W^* \, (r\, \Delta y)_w - p_P^* \, (r\, \Delta y)_e + f_x \, (cell\ volume) \qquad (C.2)$$

where the * denotes guessed or newly calculated values. Rearranging the terms of equation (C.2), the final form is derived:

$$A_P^u \, u_P = A_E^u \, u_E + A_W^u \, u_W + A_N^u \, u_N + A_S^u \, u_S + S^u \qquad (C.3)$$

where the coefficients are a combination of convective and diffusive parts as follows:

$$\begin{aligned} S^u &= S_p u_P + S_u \\ A_E^u &= D_e - (1 - f_e)\, C_e \\ A_W^u &= D_w + (1 - f_w)\, C_w \\ A_N^u &= D_n - C_n/2 \\ A_S^u &= D_s + C_s/2 \\ S_p &= C_e - C_w + C_n - C_s \\ S_u &= f_x \cdot (r\Delta x\Delta y) + \left[p_W^* \, (r\, \Delta y)_w - p_P^* \, (r\, \Delta y)_e \right] \end{aligned} \qquad (C.4)$$

§ The coefficients f_e and f_w are the weighting factors used to obtain the velocities at the cell surfaces.

The convective terms are given by:

$$
\begin{aligned}
C_e &= (\rho\ u^*\ r\ \Delta y)_e \\
C_w &= (\rho\ u^*\ r\ \Delta y)_w \\
C_n &= (\rho\ v^*\ r\ \Delta x)_n \\
C_s &= (\rho\ v^*\ r\ \Delta x)_s
\end{aligned}
\tag{C.5}
$$

and the diffusive parts by the following formulae:

$$
\begin{aligned}
D_e &= \left(\frac{\eta\ r\ \Delta y}{\delta x}\right)_e \\
D_w &= \left(\frac{\eta\ r\ \Delta y}{\delta x}\right)_w \\
D_n &= \left(\frac{\eta\ r\ \Delta x}{\delta y}\right)_n \\
D_s &= \left(\frac{\eta\ r\ \Delta x}{\delta y}\right)_s
\end{aligned}
\tag{C.6}
$$

(b) Pressure-correction equation

Integration of the mass conservation equation (2.2.2-11) over the control volume shown in Figure 2.4.2-2 yields:

$$(\rho uA)_e - (\rho uA)_w + (\rho vA)_n - (\rho vA)_s = 0 \tag{C.7}$$

The solution of momentum equations of the form:

$$A_P^u \, u_P^* = \Sigma \, A_i^u \, u_i^* + S^u + D^u \, (p_W^* - p_P^*)$$

and

$$A_P^v \, v_P^* = \Sigma \, A_i^v \, v_i^* + S^v + D^v \, (p_S^* - p_P^*) \qquad \text{(C.8)}$$

produces velocities u^* and v^* which do not, in general, satisfy local mass continuity.

Thus, pressure corrections are applied at each point P in order to satisfy local mass balance. If p_E', p_W', p_N', p_S' and p_P' are the necessary corrections at P, the following relationships may be derived from equation (C.8), neglecting higher order terms:

$$u_P = u_P^* + u_P' = u_P^* + D^u \, (p_W' - p_P')$$

$$v_P = v_P^* + v_P' = v_P^* + D^v \, (p_S' - p_P') \qquad \text{(C.9)}$$

$$p_P = p_P^* + p_P'$$

where u_P' and v_P' are the velocity corrections. Substitution of the latter relationships into equation (C.7) yields the pressure-correction equation in its final form:

$$A_P^p \, p_P' = A_E^p \, p_E' + A_W^p \, p_W' + A_N^p \, p_N' + A_S^p \, p_S' + S^p \qquad \text{(C.10)}$$

where the coefficients are defined as follows:

$$S^p = S_p \cdot p'_P + S_u$$

$$A_P^p = A_E^p + A_W^p + A_N^p + A_S^p$$

$$\begin{aligned}
A_E^p &= (\rho\ D^u\ r\ \Delta y)_e \\
A_W^p &= (\rho\ D^u\ r\ \Delta y)_w \\
A_N^p &= (\rho\ D^v\ r\ \Delta x)_n \\
A_S^p &= (\rho\ D^v\ r\ \Delta x)_s
\end{aligned} \qquad \text{(C.11)}$$

$$S_p = 0$$

$$S_u = C_e - C_w + C_n - C_s$$

The convective terms C_e, C_w, C_n, C_s are defined in the same manner as for the u-momentum equation and the D^u's and D^v's as follows:

$$\begin{aligned}
D_e^u &= \left(\frac{r\ \Delta y}{A_P}\right)_e \\
D_w^u &= \left(\frac{r\ \Delta y}{A_P}\right)_w \\
D_n^v &= \left(\frac{r\ \Delta x}{A_P}\right)_n \\
D_s^v &= \left(\frac{r\ \Delta x}{A_P}\right)_s
\end{aligned} \qquad \text{(C.12)}$$

where the A_P's are those defined in the corresponding momentum equations.

There are two modifications applied to these coefficients. The first is called mass stability modification and is used to avoid rising of the residual mass source at the beginning of the iteration procedure when the guessed variable fields are not satisfactory.

The second, called high flux modification, implements the "hybrid scheme" referred to in section 2.2.5.

Both these modifications are dealt with in the following Appendix D, where the complete three-dimensional flows are considered.

APPENDIX D

DERIVATION OF THE FINITE-DIFFERENCE EQUATIONS FOR THREE-DIMENSIONAL ELLIPTIC FLOWS

The finite-difference form of the three-dimensional elliptic flow equations are derived. Only the u-momentum and the pressure-correction equations are dealt with, the others being derived in the same manner.

(a) u-momentum equation

Integration of equation (2.2.2-16) over the finite control volume of Figure 2.5.2-2 yields:

$$\Big[(\rho uuA)_e - (\rho uuA)_w + (\rho vuA)_n - (\rho vuA)_s + (\rho wuA)_d - (\rho wuA)_u\Big]$$

$$- \Big[((\eta \frac{\partial u}{r\partial x}) A)_e - ((\eta \frac{\partial u}{r\partial x}) A)_w + ((\eta \frac{\partial u}{\partial y}) A)_n - ((\eta \frac{\partial u}{\partial y}) A)_s$$

$$+ ((\eta \frac{\partial u}{\partial z}) A)_d - ((\eta \frac{\partial u}{\partial z}) A)_u\Big] \qquad \Big[(pA)_w - (pA)_e\Big] + f_x \textit{ (cell volume)}$$

$$+ \left(\frac{2\eta}{r^2}\frac{\partial v}{\partial x} - \frac{\eta u}{r^2} - \frac{\rho vu}{r}\right) \times \textit{cell volume} \qquad \text{(D.1)}$$

where the A's represent the areas of the cell surfaces, and f_x is the generation term (source term).

Considering the assumptions of section 2.2.5 for the variation of the variables and substituting the geometrical quantities of Figure 2.5.2-2, equation (D.1) becomes:

$$\Big[(\rho u^*\Delta y\Delta z)_e\ (u_P\, f_e^{\S} + u_E\ (1 - f_e)) - (\rho u^*\Delta y\Delta z)_w\ (u_P\, f_w^{\S} + u_W\ (1 - f_w))$$

$$+ (\rho v^* r\Delta x\Delta z)_n\ (\frac{u_P + u_N}{2}) - (\rho v^* r\Delta x\Delta z)_s\ (\frac{u_P + u_S}{2})$$

$$+ (\rho w^* r\Delta x\Delta y)_d\ (\frac{u_P + u_D}{2}) - (\rho w^* r\Delta x\Delta y)_u\ (\frac{u_P + u_U}{2})\Big]$$

$$- \Big[(\frac{\eta\ \Delta y\ \Delta z}{r\delta x})_e\ (u_E - u_P) - (\frac{\eta\ \Delta y\ \Delta z}{r\delta x})_w\ (u_P - u_W)$$

$$+ (\frac{\eta\ r\ \Delta x\ \Delta z}{\delta y})_n\ (u_N - u_P) - (\frac{\eta\ r\ \Delta x\ \Delta z}{\delta y})_s\ (u_P - u_S)$$

$$+ (\frac{\eta\ r\ \Delta x\ \Delta y}{\delta z})_d\ (u_D - u_P) - (\frac{\eta\ r\ \Delta x\ \Delta y}{\delta z})_u\ (u_P - u_U)\Big]$$

$$= p_W^*\ (\Delta y\Delta z)_w - p_E^*\ (\Delta y\Delta z)_e + f_x\ (r\Delta x\Delta y\Delta z) + \Big[\frac{2\eta}{r^2}\ (\frac{\partial v}{\partial x})^*\ (r\Delta x\Delta y\Delta z)\Big]_P$$

$$- \Big[(\frac{\eta}{r^2}\ (r\ \Delta x\ \Delta y\ \Delta z))_P + (\frac{\rho v^*}{r}\ (r\ \Delta x\ \Delta y\ \Delta z))_P\Big]\ u_P \qquad (D.2)$$

where the * denotes guessed or newly calculated values.

Rearranging the terms of equation (D.2), the final form is derived:

$$A_P^u\, u_P = A_E^u\, u_E + A_W^u\, u_W + A_N^u\, u_N + A_S^u\, u_S + A_D^u\, u_D + A_U^u\, u_U + S^u \qquad (D.3)$$

where the coefficients are a combination of convective and diffusive parts:

---

§ The coefficient f_e and f_w are the weighting factors used to obtain the velocities at the cell surfaces.

$$S^u = S_p u_P + S_u$$

$$A_P^u = A_E^u + A_W^u + A_N^u + A_S^u + A_D^u + A_U^u$$

$$A_E^u = D - (1 - f_e)\ C$$

$$A_W^u = D + (1 - f_w)\ C$$

$$A_N^u = D - C\ /2$$

$$A_S^u = D + C\ /2 \tag{D.4}$$

$$A_D^u = D_D - C_D/2$$

$$A_U^u = D + C\ /2$$

$$S_p = -(C - C + C - C + C - C) + S_{P_1} + S_{P_2}$$

$$S_u = f_x \cdot (r\,\Delta x\,\Delta y\,\Delta z) + S_{U_1} + \left[p_W^* (\Delta y\ \Delta z)_w - p_P^* (\Delta y\ \Delta z)_e\right]$$

The convective terms are:

$$C = (\rho\ u^*\ \Delta y\ \Delta z)_e$$

$$C = (\rho\ u^*\ \Delta y\ \Delta z)_w$$

$$C = (\rho\ v^*\ \Delta x\ \Delta z)_n$$

$$C = (\rho\ v^*\ \Delta x\ \Delta z)_s \tag{D.5}$$

$$C = (\rho\ w^*\ \Delta x\ \Delta y)_d$$

$$C = (\rho\ w^*\ \Delta x\ \Delta y)_u$$

and the diffusive terms are defined as follows:

$$
\begin{aligned}
D_e &= \left(\frac{\eta\ \Delta y\ \Delta z}{r\delta x}\right)_e \\
D_w &= \left(\frac{\eta\ \Delta y\ \Delta z}{r\delta x}\right)_w \\
D_n &= \left(\frac{\eta\ r\ \Delta x\ \Delta z}{\delta y}\right)_n \\
D_s &= \left(\frac{\eta\ r\ \Delta x\ \Delta z}{\delta y}\right)_s \\
D_d &= \left(\frac{\eta\ r\ \Delta x\ \Delta y}{\delta z}\right)_d \\
D_u &= \left(\frac{\eta\ r\ \Delta x\ \Delta y}{\delta z}\right)_u
\end{aligned}
\qquad (D.6)
$$

The extra cylindrical terms are:

$$
\begin{aligned}
S_{P_1} &= \left(\frac{\eta}{r^2}\ (r\ \Delta x\ \Delta y\ \Delta z)\right)_P \\
S_{P_2} &= \left(\frac{\rho v^*}{r}\ (r\ \Delta x\ \Delta y\ \Delta z)\right)_P \\
S_{U_1} &= \left(\frac{2\eta}{r^2}\ \left(\frac{\partial v}{\partial x}\right)^*\ (r\ \Delta x\ \Delta y\ \Delta z)\right)_P
\end{aligned}
\qquad (D.7)
$$

(b) Pressure-correction equation

From mass continuity (equation (2.2.2-15)) over the control volume of Figure 2.5.2-2 it is derived:

$$
(\rho uA)_e - (\rho uA)_w + (\rho vA)_n - (\rho vA)_s + (\rho wA)_d - (\rho wA)_u = 0 \qquad (D.8)
$$

The solution of momentum equations of the form:

$$A_P^u\, u_P^* = \Sigma\, A_i^u\, u_i^* + S^u + D^u\, (p_W^* - p_P^*)$$

$$A_P^v\, v_P^* = \Sigma\, A_i^v\, v_i^* + S^v + D^v\, (p_S^* - p_P^*) \qquad \text{(D.9)}$$

and

$$A_P^w\, w_P^* = \Sigma\, A_i^w\, w_i^* + S^w + D^w\, (p_U^* - p_P^*)$$

produces velocities u^*, v^* and w^* which satisfy the momentum equations but do not, in general, satisfy local mass continuity.

It is then assumed that pressure corrections can be applied at each point P in order to satisfy this condition.

Thus, if p_E', p_W', p_N', p_S', p_D', p_U' and p_P' are the necessary corrections at P for satisfaction of mass conservation, the following formulae may be derived from equation (D.9), neglecting higher order terms:

$$u_P = u_P^* + u_P' = u_P^* + D^u\, (p_W' - p_P')$$

$$v_P = v_P^* + v_P' = v_P^* + D^v\, (p_S' - p_P')$$

$$w_P = w_P^* + w_P' = w_P^* + D^w\, (p_U' - p_P') \qquad \text{(D.10)}$$

$$p_P = p_P^* + p_P'$$

where u_P', v_P' and w_P' are the velocity corrections. Substituting into equation (D.8), the final finite-difference form of the pressure-correction equation is derived:

$$A_P^p\, p_P' = A_E^p\, p_E' + A_W^p\, p_W' + A_N^p\, p_N' + A_S^p\, p_S' + A_D^p\, p_D' + A_U^p\, p_U' + S^p \qquad \text{(D.11)}$$

where the coefficients are defined as follows:

$$S^p = S_p \cdot p'_P + S_u$$

$$A_P^p = A_E^p + A_W^p + A_N^p + A_S^p + A_D^p + A_U^p$$

$$
\begin{aligned}
A_E^p &= (\rho\, D^u\, \Delta y\, \Delta z)_e \\
A_W^p &= (\rho\, D^u\, \Delta y\, \Delta z)_w \\
A_N^p &= (\rho\, D^v\, r\, \Delta x\, \Delta z)_n \\
A_S^p &= (\rho\, D^v\, r\, \Delta x\, \Delta z)_s \\
A_D^p &= (\rho\, D^w\, r\, \Delta x\, \Delta y)_d \\
A_U^p &= (\rho\, D^w\, r\, \Delta x\, \Delta y)_u \\
S_p &= 0
\end{aligned}
\qquad (D.12)
$$

$$S_u = C_e - C_w + C_n - C_s + C_d - C_u$$

The convective terms C_E, C_W, C_N, etc., are defined in the same manner as in the u-momentum equation, and the D^u's, etc., as follows:

$$
\begin{aligned}
D_e^u &= \left(\frac{\Delta y\ \Delta z}{A_P}\right)_e \\
D_w^u &= \left(\frac{\Delta y\ \Delta z}{A_P}\right)_w \\
D_n^v &= \left(\frac{r\ \Delta x\ \Delta z}{A_P}\right)_n \\
D_s^v &= \left(\frac{r\ \Delta x\ \Delta z}{A_P}\right)_s \\
D_d^w &= \left(\frac{r\ \Delta x\ \Delta y}{A_P}\right)_d \\
D_u^w &= \left(\frac{r\ \Delta x\ \Delta y}{A_P}\right)_u
\end{aligned}
\qquad (D.13)
$$

where the A_P's are those defined in the corresponding momentum equations.

(c) Mass stability modification

The coefficients A_P of the u, v, w-momentum equations include a sum:

$$sum \; = \; C_e - C_w + C_n - C_s + C_d - C_u$$

which is the residual mass source. If this sum becomes negative, it appears that a mass is supplied to the cell. This may cause instability in the solution by raising the calculated values to unlimited levels.

A remedy to this instability problem has been incorporated by setting sum to zero, if negative, and including an extra source term in S_u. Thus:

$$C_P \; = \; |(0, sum)|$$

$$S_p \; = \; other\ terms \; - \; C_P$$

$$S_u \; = \; other\ terms \; + \; C_P \, u_P^*$$

where $|(a,b)|$ denotes the maximum of the arguments.

(d) The high flux modification

The "hybrid scheme" referred to in section 2.2.5 is implemented in the manner shown below. The same practice applies for the three momentum equations and, thus, only the u-momentum equation is referred to here. For this reason, the coefficients A_i of the finite difference equations are modified as follows:

$$A_E^u \; = \; \left|\left(0 \; , \; D_e - (1 - f_e) \, C_e \; , \; - C_e\right)\right|$$

$$A_W^u \; = \; \left|\left(0 \; , \; D_w + (1 - f_w) \, C_w \; , \; C_w\right)\right|$$

$$A_N^u = \left|\left(0\ ,\ D_n - C_n/2\ ,\ -\ C_n\right)\right|$$

$$A_S^u = \left|\left(0\ ,\ D_s + C_s/2\ ,\ C_s\right)\right|$$

$$A_D^u = \left|\left(0\ ,\ D_d - C_d/2\ ,\ -\ C_d\right)\right|$$

$$A_U^u = \left|\left(0\ ,\ D_u + C_u/2\ ,\ C_u\right)\right|$$

where $\left|\left(a,b,c\right)\right|$ denotes the maximum of the arguments.

APPENDIX E

A STATISTICAL ANALYSIS OF ERROR IN LASER DOPPLER MEASUREMENTS DUE TO VELOCITY AND CONCENTRATION GRADIENTS

In laser Doppler velocimetry, the finite dimensions of the control volume may lead to an error in the measured mean and rms velocity values, when velocity and concentration gradients are present. A simulation procedure to compute these errors pertinent to Doppler signal processing by a computing counter has been developed for the present experimental investigation and may be outlined as follows:

Consider a measuring location, x_o, in a flow with a finite velocity gradient as shown in Figure E.1. Assuming a finite control volume length, l_m, it becomes apparent that particles passing at different locations have different velocities. The photocathode, therefore, will observe a range of velocities which stem from variations in space rather than in time. The computing counter then measures the frequency of the Doppler signals arising from particles passing through the control volume and evaluates the statistics (mean velocity and rms values) of a set of Doppler bursts.

With the aid of the foregoing material, the simulation procedure may now be outlined in terms of the operations required to compute the statistics of the Doppler signals arising from particles passing at random through the control volume of the LDV. These operations (forming a computer program)*are listed below:

(a) The control volume length, l_m, and the velocity profile ($V = V(x)$) is fed as initial information. The latter may be

---

* Obtainable from the author on request.

represented by an analytical function or by a two-dimensional array.

(b) A set of random numbers (r_i, $i = 1,N$) is generated by the computer's random function generator ranging from 0 to R. This set of numbers simulates the locations of the particle paths within the control volume of length, l_m. The probability distribution of the random numbers is even.

(c) For a given location, x_o, the corresponding random location of the particle path is evaluated from the formula:

$$x_i = x_o + l_m \left(\frac{r_i}{R} - 0.5\right) \tag{E.1}$$

(d) The velocity V_i at the location x_i is then obtained either by the available analytical expression or by interpolation of the given velocity profile of step (a).

(e) The mean velocity and the rms value normalised by the mean velocity are calculated accordingly.

(f) Finally, another location, x_o, is considered and the operations are repeated from step (c).

The procedure, therefore, evaluates the mean local velocity and normalised rms profiles which include the effect of velocity gradients. Application of this analysis to a laminar flow with a parabolic velocity profile produced the results given in Table E.1 for different control volume lengths, l_m, as shown in the table. It may be readily seen that there exists a shift of the mean velocity profile towards lower values* which was pronounced in the region of steep velocity gradients, while the rms values increased in this region. This is in contradiction with the experiments, where a shift towards higher values is measured. It was then realised that in a real measurement situation, particles with higher velocities had a higher probability to cross the control volume, assuming that there are no concentration gradients. The probability distribution of the random particle paths, therefore, should be weighted by the local velocity**. Thus, the velocities obtained at step (d) above were weighted by the velocity profile. Results of this analysis are given in Table E.2 for the same lengths of control volume as in Table E.1. The mean velocities are now shifted towards higher values in the region of steeper velocity gradients and the rms values are lower than those of Table E.1 corresponding to the same length of control volume. These may be explained by the fact that the weighting of the probability distribution of the particle paths by the velocity profile causes a shift of the population of the sample towards higher velocities (lower gradients).

When concentration gradients are present in the flow, the random velocities calculated at step (d) should be weighted by the concentration profile. Thus, Table E.3 has been prepared assuming parabolic velocity and concentration profiles and corresponding to the same control volume

---

* Similar results may be obtained following the analyses of Edwards et al (1971), and Melling (1973).

** This is in agreement with the derivations of McLaughlin and Tiederman (1973), and Owen and Rogers (1975).

lengths as the results of Tables E.1 and E.2. The mean velocity values show a greater shift towards higher values and the rms values are lower in the steeper velocity (and concentration) gradient region for the same reasons as explained before.

With the aid of the above theoretical derivations, the control volume length may be estimated as follows:

Suppose that the mean velocity and rms profiles have been measured in a laminar fully-developed pipe flow where velocity fluctuations are not present. For a constant concentration flow, the results of Table E.2 - and similarly produced for other control volume lengths - may be used to match the theoretical and experimental profiles and extract an estimate of the length of the control volume. This is illustrated graphically in Figure E.2. Corrections to the rms and mean velocity profiles may then be applied accordingly.

Similarly, for a parabolic concentration profile the results of Table E.3 may be used to obtain an estimate of the length of the control volume.

APPENDIX F

DOPPLER SIGNAL PROCESSING WITH A COMPUTING COUNTER

In this Appendix, the principles of a method for Doppler signal processing developed during the present experimental investigation is described. The method, involving a digital computing counter in combination with an analogue oscilloscope, is shown schematically in Figure F.1a and photographically in Figure F.1b, and may be outlined as follows:

Consider a Doppler burst, as shown in Figure F.2a, which is band-pass filtered (Figure F.2b) before entering the oscilloscope (Hewlett-Packard 180A) and the computing counter (Hewlett-Packard 5360A). If the triggering level of the oscilloscope is V_t, the signal displayed on the screen of the oscilloscope will be of the form shown in Figure F.2c. The oscilloscope produces a delayed sweep pulse with a saw-tooth form, shown in Figure F.2d, where the delay time Δt is controlled by a switch on the oscilloscope. The delayed sweep output is then used to arm the counter externally. By setting an appropriate measurement time, ΔT_o, on the switches of the counter, a pulse is produced internally, as shown in Figure F.2e.

Once the signal display has been triggered (c) and the delayed sweep pulse (d) has armed the counter, measurement of the signal starts over a time period determined by the measurement pulse (e). The counter starts measuring the time elapsing between the first positive going zero crossing of the Doppler burst, after the measurement pulse (e) has been produced, until the first positive going zero crossing, after the measurement pulse (e) has been removed (see Figure F.2f). Interpolators are used at the start and the end of the measurement to stretch the counter's clock pulses

(10MHz) 1000 times; thus, to obtain a higher accuracy of measurement of the two time intervals δT_1 and δT_2 (see Figure F.2g).

The counter then determines the following:

(a) the number of Doppler cycles, N;

(b) the measurement time, $\Delta T_N = \delta T_1 + \Delta T + \delta T_2$;

(c) the average period of the Doppler cycle, $T = \Delta T_N/N$; and

(d) the Doppler frequency, $f = 1/T$.

Thus, the average period of the Doppler cycle is firstly computed and then, by inversion, the frequency. Period measurements, therefore, are slightly faster than frequency measurements. The minimum time required by the above measuring process is of the order of 3 msec, and thus approximately 300 measurements per second may be obtained.

The principle of the measurement process allows control of the position of the start of the measurement, by adjusting the delay time Δt, and its extent, by selecting a desired measurement time, ΔT_o.

The counter may be programmed by a keyboard (Hewlett-Packard 5375A) to compute the mean frequency and rms values of a sample of measurements. The population of the sample may be set to 1, 10, 100, 1000, or 10000 via a switch on the keyboard. Alternatively, it may measure the frequency spectrum of the Doppler signals. Thus, the lower and upper limits of the frequency spectrum, the frequency bandwidth, and the population of the analysed samples must be determined in advance.

The necessary keyboard commands for the above analyses are listed below, together with comments:

(a) Mean and rms frequency

Command		Comments
CLEAR x		
$b \rightleftarrows x$	:	Clear register b
CLEAR x		
X-FER PROGRAM	:	Transfer control to subprogram
$a \rightleftarrows x$		
MODULE A (or B)	:	Frequency f_i measured from input A or B
$\overrightarrow{xy}$		
X		
$\overrightarrow{bxy}$		
+	:	Compute Σf_i^2
$b \rightleftarrows x$		
$z \rightleftarrows x$		
$\overrightarrow{axy}$		
+	:	Compute Σf_i
REPEAT	:	Set sample number, N (N is set by the DO LOOP switch of the keyboard)
$\overrightarrow{Nxy}$		
÷	:	Compute mean frequency, $\overline{f}$
PAUSE	:	Display mean frequency
X-FER PROGRAM	:	Transfer control to main program
$\overrightarrow{xy}$		
X		
$a \rightleftarrows x$		
$\overrightarrow{bxy}$		
$\overrightarrow{Nxy}$		
÷		

Command		Comments
$\overrightarrow{axy}$		
-	:	Compute sample variance, s_f^2
$\overrightarrow{axy}$		
÷		
$\sqrt{x}$		
PAUSE	:	Display normalised rms, $s_f / \bar{f}$

(b) Frequency spectrum

Command		Comments
CLEAR x		
X-FER PROGRAM	:	Transfer control to subprogram
$c \leftrightarrows x$		
MODULE A (or B)	:	Frequency f_i measured from input A or B
$z \leftrightarrows x$		
$\overrightarrow{1xy}$		
$z \leftrightarrows x$		
IF x > a	:	Reject measurement if greater than a (a is the preset upper frequency limit)
CLEAR xyz		
IF x < b	:	Reject measurement if less than b (b is the preset lower frequency limit)
CLEAR xyz		
$\overrightarrow{1xy}$		
$\overrightarrow{cxy}$		
+		
REPEAT	:	Set sample number N (N is set by the DO LOOP switch of the keyboard)

Command		Comments
PAUSE	:	Display number of measurements within bandwidth
X-FER PROGRAM	:	Transfer control to main program
$a\overrightarrow{xy}$		
$b\overrightarrow{xy}$		
-	:	Calculate bandwidth, Δf = a - b
$z\rightleftarrows x$		
$z\overrightarrow{xy}$		
$a\overrightarrow{xy}$		
+		
$a\rightleftarrows x$	:	Increase upper frequency limit by Δf
$b\overrightarrow{xy}$		
$z\overrightarrow{xy}$		
+		
$b\leftrightarrows x$	:	Increase lower frequency limit by Δf
REPEAT	:	Repeat procedure for new bandwidth (b,a)

The present arrangement of the method is suitable for laminar flow measurements where the velocity fluctuations, which correspond to frequency variations, are limited. It is possible then to preset Δt and ΔT_o so that the central part of the Doppler burst is always measured. In addition, the use of high trigger levels on the oscilloscope allows only bursts from the high light intensity (central region of the fringe pattern) to be admitted for measurement. These two facilities imply that an additional reduction of the measuring control volume may be achieved.

Although the counter has a wide range of frequency response (two inputs are provided ranging from 0 to 10 MHz and 1 kHz to 320 MHz, respectively), the arrangement described above may result in erroneous measurements when the frequency of the Doppler bursts is largely varying. Thus, for high spatial velocity gradients when measuring close to walls, or for high temporal fluctuations when measuring in turbulent flows, the Doppler frequencies vary accordingly and the preset values of Δt and ΔT_o may result in a frequency counting of that part of the input signal where noise is predominant or no Doppler signal exists, as demonstrated in Figure F.3a. A simple remedy to this is to select the minimum Δt and ΔT_o available. However, for signals with frequencies higher than approximately 10 MHz, selection of even the minimum measurement time ($\simeq$ 1 μs) of the counter may result in inaccurate measurements, when the Doppler burst does not contain more than 10 cycles.

This may be overcome by determining the measurement pulse with the Doppler burst itself. Thus, as shown in Figure F.3b, the envelope of the Doppler burst may be used to construct a square pulse, whose width determines the measurement time, ΔT_o.

Problems related to inaccurate measurements with a computing counter have been reported, for example, by Brayton, Kalb and Crosswy (1973), and Durao (1976). However, for the laminar flows investigated here, these problems are not of direct interest and, thus, are not dealt with in detail.

The counter itself requires a triggering level to be satisfied before any measurement is initiated. The triggering level may be controlled by a switch on the counter or may be selected automatically. It is apparent, therefore, that the Doppler signal strength should be higher than this level. Thus, an experiment has been carried out to determine the minimum triggering level required for an accurate measurement as follows:

The rms velocity values at a location in the laminar fully-developed pipe flow have been recorded for different peak-to-peak strengths of the incoming Doppler bursts. The results of this test showed that a minimum peak-to-peak signal strength of the order of 300 mV is required to avoid inaccurate measurements.

When a Doppler signal is modulated by noise (Figure F.3c), there exists a possibility that a false measurement may result if the noise amplitude is large enough to register an erroneous zero crossing. It is desirable, therefore, to make sure that the Doppler signal is of good quality before admitted for measurement by the computing counter.

The present arrangement of the frequency counting system has been used for the mean and rms velocity measurements reported in this thesis. The ability of the system to measure the frequency spectrum of the recorded velocities is demonstrated in Figure F.4, where the frequency histogram of the velocities at the centre-line of the fully developed pipe flow is shown.

APPENDIX G

OPTICAL REFRACTION IN LASER DOPPLER VELOCIMETRY

There are several optical refraction effects occurring when measuring with an LDV which should be taken into account in the interpretation of the results. This Appendix describes the refraction effects on the location of the control volume, the alignment of the receiving optics for off-axis detection and the error in the measurement of the inside diameter of a capillary.

(a) Location of the Control Volume

When the two laser beams pass through the glass walls to form the control volume inside the water flow, refraction effects cause the displacement of the control volume in air to be different from that in water.

Assuming that the glass wall is formed by two plane surfaces (Figure G.1), one may derive from geometrical optics and the laws of refraction the following formula:

$$\frac{\Delta x_w}{\Delta x_a} = \sqrt{\frac{\eta_w^2 - \sin^2 \phi_a}{1 - \sin^2 \phi_a}} \qquad \text{(G.1)}$$

where η_w = water refractive index

Δx_a = control volume displacement in air

Δx_w = control volume displacement in water

ϕ_a = beam incidence angle in air

For example, if $\phi_a = 11.3^\circ$ and $\eta_w = 1.33$, then $\phi_w = 8.5^\circ$ and $\Delta x_w/\Delta x_a = 1.37$.

(b) Alignment for Off-Axis Detection

When off-axis detection is employed, the relationship between the displacement of the receiving optics in air and the displacement of their focus inside the water flow (see Figure G.2) may serve as a guide for the alignment of the optics. Two cases, for given off-axis detection angles in air or in water, are considered. The following formulae may be derived then, with the aid of Figure G.2:

1. ϕ_a given:

$$\frac{\Delta x_w}{d_a} = \frac{1}{\sin \phi_a} \sqrt{\frac{n_w^2 - \sin^2 \phi_a}{1 - \sin^2 \phi_a}} \tag{G.2}$$

where n_w = water refractive index

d_a = displacement of optical axis in air

Δx_w = displacement of focus in water

ϕ_a = off-axis detection angle in air

For example, if $\phi_a = 30^o$ and $n_w = 1.33$, then $\phi_w = 22^o$ and $\Delta x_w/d_a = 2.74$

2. ϕ_w given:

$$\frac{\Delta x_w}{d_a} = \frac{1}{\sin \phi_w} \sqrt{\frac{1 - \sin^2 \phi_w}{1 - n_w^2 \sin^2 \phi_w}} \tag{G.3}$$

For example, if $\phi_w = 30^o$ and $n_w = 1.33$, then $\phi_a = 41.7^o$ and $\Delta x_w/d_a = 2.32$.

(c) Glass Capillary Diameter Measurement

When the inside diameter of a glass capillary is required, the apparent diameter may be measured with a travelling microscope (see Figure

G.3). Then, the inside diameter may be calculated from the following formula, which can be derived with the aid of geometrical optics and refractions laws:

$$\frac{R_i}{R_a} = \frac{1}{\sqrt{\left[1 - \left(\frac{R_a}{R_o}\right)^2\right]\left[\eta_g^{\,2} - \left(\frac{R_a}{R_o}\right)^2\right] + \left(\frac{R_a}{R_o}\right)^2}} \tag{G.4}$$

where R_i = inside diameter of glass capillary

R_a = apparent diameter of glass capillary

R_o = outside diameter of glass capillary

η_g = glass refractive index

For example, if η_g = 1.45 and R_a/R_o = 0.80, then R_i/R_a = 0.73.

APPENDIX H

BLOOD HANDLING FOR *IN VITRO* CAPILLARY FLOWS

It is important to ensure that the blood or its components used for *in vitro* blood flow experiments is rheologically similar to that which flows in the blood vessels.

Certain hints are given here for laboratory blood preparation and handling:

1. The blood used in the experiments should be as fresh as possible.

2. The capillaries should be heparinised in order to avoid clotting.

3. There are biological processes occurring in the plasma proteins which can be speeded up by contact with the atmosphere and thus this should be avoided if possible.

4. Because the plasma proteins play an important rôle in the blood viscosity (see, for example, Charm and Kurland (1974)), blood should be sterilised and kept at 0-4^{o}C.

5. Anticoagulants are necessary in fresh blood to avoid clotting. Such coagulant agents are:

   (a) 3.8% solution of tri-sodium citrate

   (b) Acid-citrate-dextrose solution. Its formula is:

0.8 (0.94)*	gr	citric acid
2.2 (2.50)*	gr	sodium citrate
2.4	gr	dextrose (D-glucose)

Make up to 100 ml with distilled water, and adjust to pH 5.0. Mix 1 volume of anticoagulant with 6 volumes of blood.

6. The procedures of plasma, platelet and red blood cell preparation are as follows:

(a) Platelet rich plasma (PRP)

In order to obtain PRP from whole blood, proceed as follows:

- Spin whole blood at 250 g for 10 minutes
- Remove PRP from the top. This contains some white blood cells

(b) Platelet poor plasma (PPP)

- Respin blood from which PRP has been removed at 2000 g for 10-20 minutes
- Remove PPP from the top

(c) Platelet free plasma (PFP)

- Respin PPP at 9000-10000 g for 20-30 minutes

---

* Weights in parentheses apply to the case of hydrates.

- Separate PFP from small pellet at the bottom of the test tube

(d) Washed red blood cells (RBC)

- Remove "buffy coat" from the top of the packed red cells obtained in procedure (b)
- Resuspend in saline or Ringer's solution
- Spin at 2000 g for 10-20 minutes
- Resuspend in saline of Ringer's solution
- Spin at 2000 g for 10-20 minutes
- Remove the top to obtain packed washed RBCs

7. Saline (isotonic; 0.9%) referred to in this text corresponds to full strength Ringer's solution. Each tablet (BDH Chemicals Limited, Poole, Dorset, England) contains:

$NaCl$	1.125 gm
KCl	0.0525 gm
$CaCl_2$	0.0300 gm
$NaHCO_3$	0.0250 gm

One tablet makes up to 125 ml for full strength.

APPENDIX I

LASER HAZARDS

Since the invention of lasers, investigators have been concerned with the hazards from the use of highly intense, coherent radiation. It is difficult, at present, to develop standards for the evaluation of laser hazards because of few instances of injuries on humans (Eleccion (1973)). Animal experiments have been used so far for most of the evaluation and thus the application to humans is more a matter of subjective judgement.

The results of biological damage due to laser radiation may include photochemical, thermal and pressure effects. It is believed that there are no long term effects, such as those of X-rays or nuclear radiation, caused by laser beams. The release of thermal energy by highly concentrated laser beams seems to be the main cause of the damages, which are commonly occular or dermal. Their mechanism is the same in both coherent and non-coherent radiation. However, the spatial and temporal coherence of laser beams, which result in their focusing to small spots, allows the generation of higher energy densities. Although this property of the laser beams is advantageous in many applications, for example, material cutting, micromachining and image recording (see Maydan (1971)), it may cause hazardous occular or dermal effects. Hazards to the skin are less significant to those of the eye. The latter is more sensitive to light and the focusing effect of its lens may result in higher energy densities on the retina. It becomes apparent, therefore, that the primary region of irreversible damage is the retina. However, for higher power beams, damage to the cornea and the skin may also occur.

When a light beam is focused on the retina, the cornea or the skin, the absorbed energy is released to the surrounding tissues as thermal energy. The temperature rise of the tissues depends critically on the light energy, the size of the spot of the focused beam and the duration of the radiation.

Assuming that the eye lens is a perfect optical instrument and that a beam spot size of the order of 10 μm can be achieved, Sliney and Palmisano (1968) concluded that the power threshold for laser retinal damage is of the order of 1 mW. However, if the aberrations of the eye lens are considered (Ivanoff (1956)), and the motions of the eyeball and the head are taken into account (Von Helmoltz (1962) and Fender (1964)), the minimum laser power for observable lesions may be of the order of 10 mW.

During the present glass capillary experiments, it has been observed that Argon laser powers higher than approximately 40 mW resulted in blood coagulation. Laser powers in excess of approximately 500 mW resulted in a total burn-out of the blood and the glass capillary.

It is strongly recommended, therefore, that direct observation of laser radiation or strongly scattered laser light, should be avoided when working with laser beams. In addition, the power of the laser beams for blood flow experiments should be controlled to avoid coagulation (less than approximately 20 mW).

TABLE 2.6.4-1

Geometries and flow rates studied for Newtonian flows in a round pipe with an axisymmetric constriction

Re_D	d/D	l/D	Figure Numbers of Results
100	0.80	0.40	Figure 2.6.4-3
100	0.60	0.20	Figure 2.6.4-4
100	0.60	0.40	Figure 2.6.4-5
100	0.60	0.60	Figure 2.6.4-6
100	0.40	0.40	Figure 2.6.4-7
10	0.40	0.40	Figure 2.6.4-8
1	0.40	0.40	Figure 2.6.4-9

TABLE 2.6.4-2

Computational results of Newtonian flow in a round pipe with an axisymmetric constriction

Re	d/D	l/D	l_r/DRe	τ_{max}/τ_w	C_p	C_x	L/DRe	C_d	C_d Johansen (1930)	C_d Mills (1968)	C_{D_p}	C_{D_τ}	C_D	F/τ_w
100	0.80	0.40	0.0024	5.16	0.8	0.165	0.076	0.712	0.800	-	2.87	4.11	6.98	12.33
100	0.60	0.20	0.0145	15.5	5.3	0.563	0.146	-	-	-	11.42	2.75	14.17	44.51
100	0.60	0.40	0.0149	13.8	6.5	0.660	0.154	0.714	0.745	-	13.03	4.54	17.57	55.19
100	0.60	0.60	0.0158	13.1	7.7	0.767	0.157	-	-	-	14.58	6.22	20.80	65.31
100	0.40	0.40	0.0604	39.6	52.1	2.95	0.276	0.724	0.705	-	71.70	7.48	79.18	326.5
10	0.40	0.40	0.0740	26.4	170.1	7.36	0.36	0.543	0.555	0.600	194.75	48.17	242.92	100.2
1	0.40	0.40	0.1600	21.1	1336	9.97	2.09	0.163	0.180	0.190	1436	436	1872	77.19

TABLE 2.6.5-1

Geometries and flow rates studied for non-Newtonian blood flows in an aortic stenosis

Re_D	d/D	l/D	Figure Numbers of Results
100	0.80	0.40	Figure 2.6.5-1
100	0.60	0.20	Figure 2.6.5-2
100	0.60	0.40	Figure 2.6.5-3
100	0.60	0.60	Figure 2.6.5-4
100	0.40	0.40	Figure 2.6.5-5
10	0.40	0.40	Figure 2.6.5-6
1	0.40	0.40	Figure 2.6.5-7

TABLE 2.6.5-2

Computational results of non-Newtonian blood flow in an aortic stenosis

Re_N	d/D	l/D	l_r/DRe_N	l_r/DRe'_N	τ_{max}/τ_w	C_p	C_x	L/DRe_N	C_d	C_{D_p}	C_{D_τ}	C_D	F/τ_w
100	0.80	0.40	0.0028	0.0015	1.86	0.36	0.075	0.14	0.894	1.79	1.75	3.54	11.58
100	0.60	0.20	0.0212	0.0115	3.53	3.07	0.295	0.30	-	8.25	0.77	9.02	52.33
100	0.60	0.40	0.0212	0.0115	3.45	3.33	0.309	0.31	0.873	8.64	1.46	10.10	58.54
100	0.60	0.60	0.0217	0.0118	3.39	3.75	0.337	0.32	-	9.30	2.10	11.4	66.05
100	0.40	0.40	0.117	0.063	6.33	31.4	1.297	0.72	0.876	48.8	1.4	50.2	382.8
10	0.40	0.40	0.142	0.077	5.65	63	1.70	1.11	0.667	85.0	11.7	96.7	73.69
1	0.40	0.40	0.160	0.086	4.47	319	2.55	4.01	0.332	368	94	462	35.22

TABLE 2.6.6-1

Geometries and flow rates studied for Newtonian flows

in a round pipe with an asymmetric obstacle

Re	d/D	l/D	α^{o}	Figure Numbers of Results
100	0.40	0.40	72^{o}	-
1	0.40	0.40	72^{o}	-
10	0.40	0.40	54^{o}	-
10	0.40	0.40	72^{o}	Figures 2.6.6-4 to 2.6.6-11
10	0.40	0.40	90^{o}	-

TABLE 2.6.6-2

Computational results of Newtonian flow in a pipe with an asymmetric obstacle

Re	d/D	l/D	α^{o}	l_r/DRe	τ_{max}/τ_w	C_p	C_x	L/DRe	C_{D_p}	$C_{D_{\tau_I}}$	$C_{D_{\tau_{II}}}$	C_D	F/τ_w
100	0.40	0.40	72^{o}	0.007	7.78	1.6	0.325	0.076	4.54	1.17	0.50	6.21	43.89
1	0.40	0.40	72^{o}	0.010	4.81	73.5	0.595	1.93	158.5	75.9	44.3	278.7	2.3
10	0.40	0.40	54^{o}	0.014	4.62	5.2	0.392	0.207	14.4	7.3	5.2	26.9	1.66
10	0.40	0.40	72^{o}	0.017	5.18	7.8	0.434	0.281	17.3	7.7	4.6	29.6	2.44
10	0.40	0.40	90^{o}	0.022	5.97	11.50	0.496	0.361	21.4	8.7	4.4	34.5	3.55

TABLE 2.6.7-1

Geometry and flow rate studied for non-Newtonian blood flow in a venule with an asymmetric thrombus

Re	d/D	l/D	α°	Figure Numbers of Results
10	0.40	0.40	72°	Figures 2.6.7-1 to 2.6.7-8

TABLE 2.6.7-2

Computational results of non-Newtonian blood flow in a venule with an asymmetric thrombus

Re	d/D	l/D	α^{o}	l_r/DRe_N	l_r/DRe'_N	τ_{max}/τ_w	C_p	C_x	L/DRe	C_{D_p}	$C_{D_{\tau_I}}$	$C_{D_{\tau_{II}}}$	C_D	F/τ_w
10	0.40	0.40	72^{o}	0.023	0.012	3.32	3.3	0.205	0.465	9.3	3.2	1.6	14.10	2.15

TABLE 3.4.5-1

Influence of beam incidence angle and diameter on dimensions of interference pattern

ϕ	D = 0.65 mm d = 124 µm				D = 1.30 mm d = 62 µm			
	Length (µm)	Diameter (µm)	Δx (µm)	N_{fr}	Length (µm)	Diameter (µm)	Δx (µm)	N_{fr}
11.3°	633	126	1.615	78	316	63	1.615	39
22.5°	324	134	0.827	162	162	67	0.827	81
30.0°	248	143	0.633	226	124	71	0.633	113
45.0°	175	175	0.447	391	87	87	0.447	195
60.0°	143	248	0.365	678	71	124	0.365	339

N.B. He-Ne laser beam wavelength: λ = 0.6328 µm

Focal length of beam focusing lens: f = 100 mm

TABLE 3.4.5-2

Influence of off-axis detection on dimensions of control volume viewed by receiving optics (detection in the beam symmetry plane)

ϕ	ϕ_s	M = 10 and D_{ph} = 0.5 mm				M = 10 and D_{ph} = 1 mm			
		Length (μm)	Diameter (μm)	Δx (μm)	N_{fr}	Length (μm)	Diameter (μm)	Δx (μm)	N_{fr}
11.3^o	0^o	633	50	1.615	31	633	100	1.615	62
	30^o	290	50	1.615	31	372	100	1.615	62
	60^o	126	50	1.615	31	184	100	1.615	62
22.5^o	0^o	324	50	0.827	60	324	100	0.827	121
	30^o	234	50	0.827	60	279	100	0.827	121
	60^o	137	50	0.827	60	174	100	0.827	121
30.0^o	0^o	248	50	0.633	79	248	100	0.633	158
	30^o	193	50	0.633	79	215	100	0.633	158
	60^o	123	50	0.633	79	162	100	0.633	158
45.0^o	0^o	175	50	0.447	112	175	100	0.447	224
	30^o	114	50	0.447	112	124	100	0.447	224
	60^o	100	50	0.447	112	123	100	0.447	224

N.B. He-Ne laser beam wavelength: λ = 0.6328 μm, diameter D = 0.65 mm

Focal length of beam focusing lens: f = 100 mm

Beam waist diameter: d = 124 μm

TABLE 3.4.5-3

Influence of off-axis detection on dimensions of control volume viewed by receiving optics (detection in the beam plane)

ϕ	ϕ_s	M = 10 and D_{ph} = 0.5 mm				M = 10 and D_{ph} = 1 mm			
		Length (μm)	Diameter (μm)	Δx (μm)	N_{fr}	Length (μm)	Diameter (μm)	Δx (μm)	N_{fr}
11.3^o	0^o	633	50	1.615	31	633	100	1.615	62
	30^o	294	124	1.615	77	376	126	1.615	78
	60^o	129	126	1.615	78	185	126	1.615	78
22.5^o	0^o	324	50	0.827	60	324	100	0.827	121
	30^o	249	125	0.827	151	295	134	0.827	162
	60^o	129	134	0.827	160	180	134	0.827	162
30.0^o	0^o	248	50	0.633	79	248	100	0.633	158
	30^o	218	126	0.633	199	244	141	0.633	223
	60^o	128	142	0.633	224	174	143	0.633	226
45.0^o	0^o	175	50	0.447	112	175	100	0.447	224
	30^o	171	127	0.447	284	175	159	0.447	356
	60^o	127	171	0.447	382	159	175	0.447	391

N.B. He-Ne laser beam wavelength: λ = 0.6328 μm, diameter D = 0.65 mm

Focal length of beam focusing lens: f = 100 mm

Beam waist diameter: d = 124 μm

TABLE 3.5.2-1: Dimensions of interference pattern and control volume in air, water and whole blood for the He-Ne LDV

Fluid	Calculated intersection region (transmitting optics)		Calculated control volume (receiving optics)		Measured control volume (trigger level)	
	Length (μm)	Diameter (μm)	Length (μm)	Diameter (μm)	Length (μm)	Diameter (μm)
In air : $\phi = 45^{\circ}$ $\Delta x = 0.447$ μm $d = 62$ μm N_{fr}* = 196	87.7	87.7	87.7	50	≃ 30	≃ 20
In water: $n_w = 1.33$ $\phi = 32.1^{\circ}$ $\Delta x = 0.447$ μm $d = 74.3$ μm $N_{fr} = 196$	139.8	87.7	139.8	50		
In blood: $n_b = 1.41$ $\phi = 30.1^{\circ}$ $\Delta x = 0.447$ μm $d = 75.6$ μm $N_{fr} = 196$	150.7	87.7	150.7	50		

* Number of fringes observed in water flow approximately 40 - 60.

N.B. He-Ne laser beam wavelength: $\lambda = 0.6328$ μm, diameter $D = 0.65$ mm

Pinhole diameter $D_{ph} = 0.500$ mm, lens magnification $M = 10$

TABLE 3.5.3-1: Dimensions of interference pattern and control volume in air, water and whole blood for the Argon LDV

Fluid	Calculated intersection region (transmitting optics)		Calculated control volume (receiving optics)		Measured control volume (trigger level)	
	Length (μm)	Diameter (μm)	Length (μm)	Diameter (μm)	Length (μm)	Diameter (μm)
In air : ϕ = 45^o Δx = 0.345 μm d = 20.7 μm N_{fr}* = 85	29.3	29.3	29.3	20	≃ 20	≃ 15
In water: n_w = 1.33 ϕ = 32.1^o Δx = 0.345 μm d = 24.8 μm N_{fr} = 85	46.7	29.3	46.7	20		
In blood: n_b = 1.41 ϕ = 30.1^o Δx = 0.345 μm d = 25.3 μm N_{fr} = 85	50.4	29.3	50.4	20		

* Number of fringes observed in water flow approximately 30 - 50.

N.B. Argon laser beam wavelength: λ = 0.488 μm, diameter D = 1.5 mm

Pinhole diameter D_{ph} = 0.200 mm, lens magnification M = 10

TABLE E.1: Mean and rms velocity profiles for random particle paths (even probability distribution of particle paths)

r/R	V_{th}	$l_m = 0.05D$		$l_m = 0.10D$		$l_m = 0.15D$		$l_m = 0.20D$		$l_m = 0.25D$		$l_m = 0.30D$		$l_m = 0.35D$		$l_m = 0.40D$	
		$\overline{V}$	$rms/\overline{V}$	$\overline{V}$	$rms/\overline{V}$	$\overline{V}$	$rms/\overline{V}$	$\overline{V}$	$rms/\overline{V}$	$\overline{V}$	$rms/\overline{V}$	$\overline{V}$	$rms/\overline{V}$	$\overline{V}$	$rms/\overline{V}$	$\overline{V}$	$rms/\overline{V}$
0.00	2.000	1.998	0.001	1.993	0.003	1.985	0.007	1.973	0.012	1.957	0.020	1.938	0.029	1.916	0.039	1.891	0.052
0.08	1.987	1.985	0.005	1.980	0.010	1.971	0.016	1.959	0.023	1.943	0.032	1.924	0.042	1.902	0.053	1.876	0.067
0.16	1.949	1.947	0.010	1.941	0.020	1.932	0.030	1.919	0.042	1.904	0.054	1.884	0.067	1.862	0.083	1.835	0.099
0.24	1.885	1.882	0.015	1.877	0.030	1.867	0.046	1.855	0.063	1.838	0.080	1.819	0.099	1.796	0.119	1.769	0.141
0.32	1.795	1.793	0.021	1.786	0.042	1.777	0.064	1.764	0.087	1.748	0.110	1.728	0.135	1.704	0.162	1.678	0.190
0.40	1.680	1.677	0.028	1.671	0.056	1.661	0.085	1.648	0.115	1.631	0.146	1.611	0.179	1.588	0.214	1.561	0.250
0.48	1.539	1.536	0.037	1.529	0.074	1.519	0.112	1.506	0.151	1.489	0.191	1.469	0.234	1.445	0.279	1.418	0.327
0.56	1.373	1.369	0.048	1.363	0.096	1.352	0.146	1.339	0.197	1.321	0.251	1.301	0.307	1.277	0.366	1.249	0.430
0.64	1.181	1.177	0.064	1.170	0.128	1.160	0.195	1.146	0.263	1.128	0.335	1.107	0.411	1.083	0.492	1.118	0.502
0.72	0.963	0.959	0.088	0.952	0.177	0.941	0.269	0.927	0.365	0.909	0.467	0.922	0.528	0.980	0.521	1.036	0.514
0.80	0.720	0.716	0.131	0.708	0.265	0.697	0.404	0.683	0.551	0.753	0.545	0.821	0.538	0.885	0.532	0.945	0.525
0.88	0.451	0.447	0.231	0.439	0.470	0.484	0.566	0.563	0.560	0.639	0.554	0.711	0.548	0.781	0.542	0.847	0.536
0.96	0.157	0.172	0.585	0.263	0.580	0.351	0.575	0.435	0.569	0.516	0.564	0.594	0.558	0.668	0.552	0.740	0.546
1.00	0.0	0.097	0.589	0.190	0.584	0.281	0.579	0.368	0.574	0.451	0.568	0.532	0.563	0.609	0.557	0.683	0.551

N.B. V_{th} and $\overline{V}$ are non-dimensionalised by the average flow velocity

TABLE E.2: Mean and rms velocity profiles for random particle paths

(probability distribution of particle paths weighted by velocity profile)

r/R	V_{th}	$l_m = 0.05D$		$l_m = 0.10D$		$l_m = 0.15D$		$l_m = 0.20D$		$l_m = 0.25D$		$l_m = 0.30D$		$l_m = 0.35D$		$l_m = 0.40D$	
		$\overline{V}$	$rms/\overline{V}$	$\overline{V}$	$rms/\overline{V}$	$\overline{V}$	$rms/\overline{V}$	$\overline{V}$	$rms/\overline{V}$	$\overline{V}$	$rms/\overline{V}$	$\overline{V}$	$rms/\overline{V}$	$\overline{V}$	$rms/\overline{V}$	$\overline{V}$	$rms/\overline{V}$
0.00	2.000	1.998	0.001	1.993	0.003	1.985	0.007	1.973	0.012	1.958	0.020	1.940	0.028	1.919	0.039	1.896	0.051
0.08	1.987	1.985	0.005	1.980	0.010	1.972	0.016	1.960	0.023	1.945	0.031	1.928	0.041	1.907	0.052	1.884	0.064
0.16	1.949	1.947	0.010	1.942	0.020	1.934	0.030	1.923	0.041	1.909	0.052	1.893	0.065	1.874	0.078	1.853	0.093
0.24	1.885	1.883	0.015	1.878	0.030	1.871	0.045	1.862	0.061	1.850	0.077	1.836	0.093	1.821	0.110	1.804	0.127
0.32	1.795	1.793	0.021	1.790	0.042	1.784	0.063	1.777	0.084	1.769	0.105	1.759	0.126	1.749	0.147	1.738	0.167
0.40	1.680	1.678	0.028	1.676	0.056	1.673	0.083	1.670	0.111	1.666	0.137	1.663	0.163	1.660	0.187	1.658	0.209
0.48	1.539	1.538	0.036	1.538	0.073	1.538	0.108	1.540	0.143	1.544	0.175	1.549	0.205	1.557	0.230	1.569	0.251
0.56	1.373	1.373	0.048	1.375	0.095	1.381	0.140	1.391	0.182	1.404	0.219	1.423	0.251	1.448	0.274	1.480	0.286
0.64	1.181	1.182	0.063	1.189	0.124	1.203	0.181	1.225	0.231	1.255	0.270	1.294	0.295	1.345	0.303	1.400	0.297
0.72	0.963	0.967	0.087	0.982	0.168	1.010	0.237	1.051	0.289	1.107	0.316	1.178	0.315	1.247	0.310	1.310	0.306
0.80	0.720	0.728	0.127	0.758	0.236	0.811	0.309	0.890	0.330	0.977	0.326	1.059	0.322	1.135	0.318	1.206	0.313
0.88	0.451	0.471	0.212	0.536	0.333	0.639	0.340	0.740	0.336	0.835	0.332	0.925	0.329	1.010	0.325	1.090	0.320
0.96	0.157	0.231	0.351	0.351	0.348	0.466	0.345	0.576	0.342	0.680	0.338	0.779	0.335	0.872	0.331	0.960	0.327
1.00	0.0	0.130	0.353	0.255	0.350	0.375	0.347	0.489	0.344	0.597	0.341	0.700	0.337	0.798	0.334	0.890	0.330

N.B. V_{th} and $\overline{V}$ are non-dimensionalised by the average flow velocity

TABLE E.3: Mean and rms velocity profiles for random particle paths

(probability distribution of particle paths weighted by velocity and concentration profiles)

r/R	V_{th}	$l_m = 0.05D$		$l_m = 0.10D$		$l_m = 0.15D$		$l_m = 0.20D$		$l_m = 0.25D$		$l_m = 0.30D$		$l_m = 0.35D$		$l_m = 0.40D$	
		$\overline{V}$	$rms/\overline{V}$	$\overline{V}$	$rms/\overline{V}$	$\overline{V}$	$rms/\overline{V}$	$\overline{V}$	$rms/\overline{V}$	$\overline{V}$	$rms/\overline{V}$	$\overline{V}$	$rms/\overline{V}$	$\overline{V}$	$rms/\overline{V}$	$\overline{V}$	$rms/\overline{V}$
0.00	2.000	1.998	0.001	1.993	0.003	1.985	0.007	1.973	0.012	1.959	0.019	1.942	0.028	1.922	0.038	1.901	0.050
0.08	1.987	1.985	0.005	1.980	0.010	1.972	0.016	1.961	0.023	1.947	0.031	1.931	0.040	1.912	0.050	1.892	0.062
0.16	1.949	1.947	0.010	1.943	0.019	1.935	0.030	1.926	0.040	1.914	0.051	1.901	0.062	1.886	0.074	1.869	0.086
0.24	1.885	1.883	0.015	1.880	0.030	1.875	0.045	1.869	0.060	1.861	0.074	1.853	0.088	1.843	0.102	1.834	0.115
0.32	1.795	1.794	0.021	1.793	0.042	1.791	0.062	1.790	0.081	1.788	0.100	1.787	0.117	1.787	0.132	1.787	0.145
0.40	1.680	1.680	0.028	1.681	0.055	1.685	0.081	1.690	0.106	1.697	0.128	1.707	0.147	1.718	0.162	1.731	0.173
0.48	1.539	1.540	0.036	1.546	0.072	1.556	0.104	1.571	0.134	1.591	0.158	1.614	0.177	1.640	0.189	1.668	0.195
0.56	1.373	1.376	0.047	1.388	0.092	1.408	0.132	1.437	0.165	1.472	0.189	1.513	0.204	1.557	0.210	1.601	0.208
0.64	1.181	1.187	0.063	1.208	0.120	1.243	0.166	1.290	0.199	1.346	0.217	1.407	0.223	1.468	0.220	1.524	0.215
0.72	0.963	0.974	0.085	1.010	0.157	1.066	0.205	1.139	0.229	1.218	0.233	1.295	0.229	1.367	0.226	1.432	0.222
0.80	0.720	0.740	0.123	0.800	0.207	0.888	0.240	0.987	0.241	1.081	0.238	1.168	0.235	1.250	0.232	1.325	0.228
0.88	0.451	0.492	0.192	0.595	0.250	0.713	0.248	0.823	0.246	0.928	0.243	1.025	0.240	1.117	0.237	1.202	0.234
0.96	0.157	0.259	0.256	0.394	0.254	0.522	0.252	0.643	0.250	0.758	0.247	0.866	0.245	0.967	0.242	1.063	0.239
1.00	0.0	0.147	0.258	0.287	0.256	0.420	0.254	0.546	0.252	0.666	0.249	0.780	0.247	0.887	0.244	0.987	0.241

N.B. V_{th} and $\overline{V}$ are non-dimensionalised by the average flow velocity

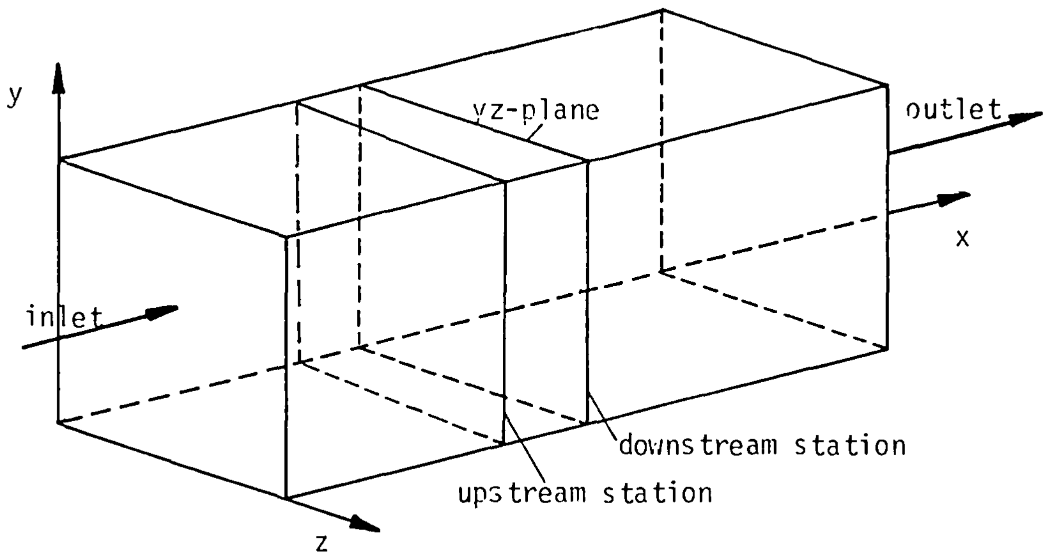

(a) Square duct geometry

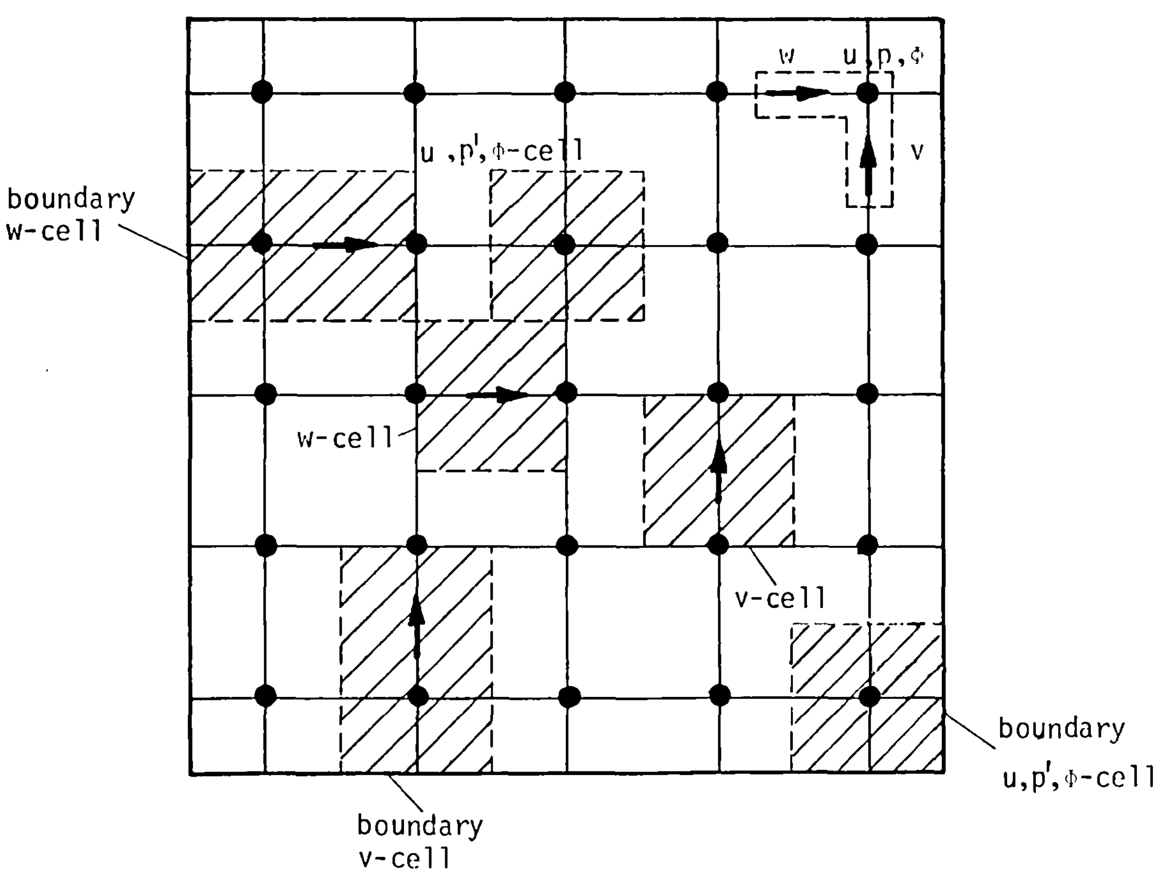

(b) Grid disposition in yz-plane

Fig. 2.3.2-1 Square duct and grid geometry for 3-D parabolic flows

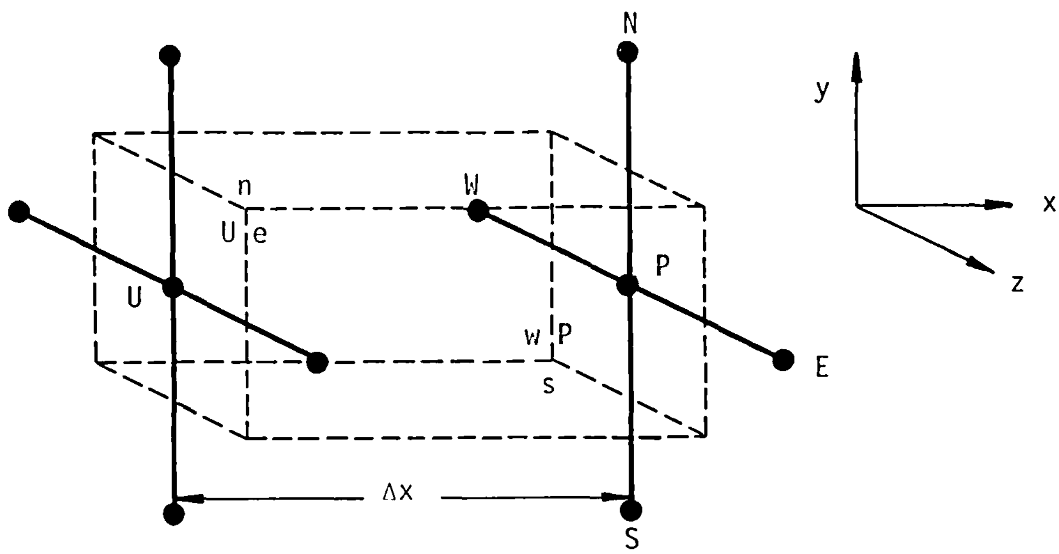

(a) The computational cell

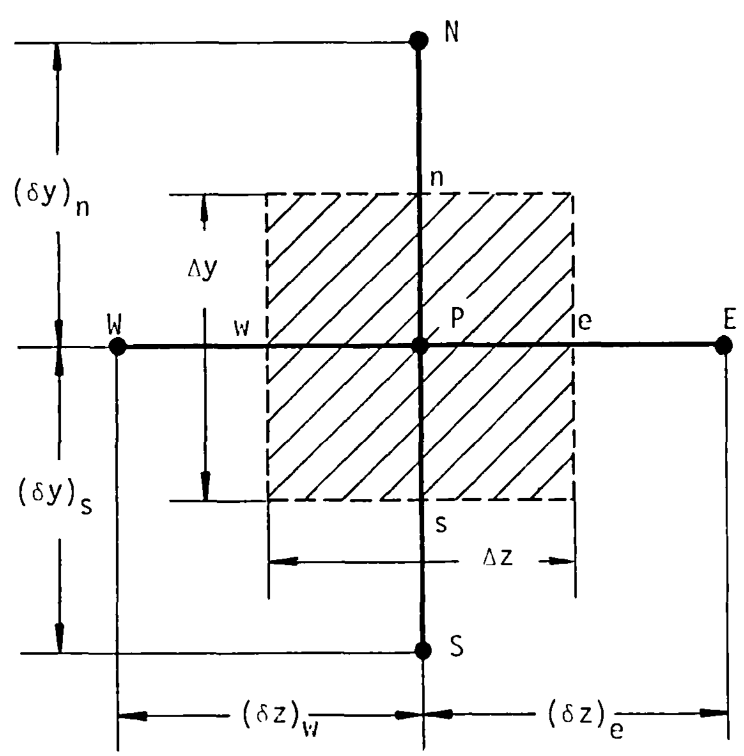

(b) yz-cell face

Fig. 2.3.2-2 The control volume for the 3-D parabolic flows

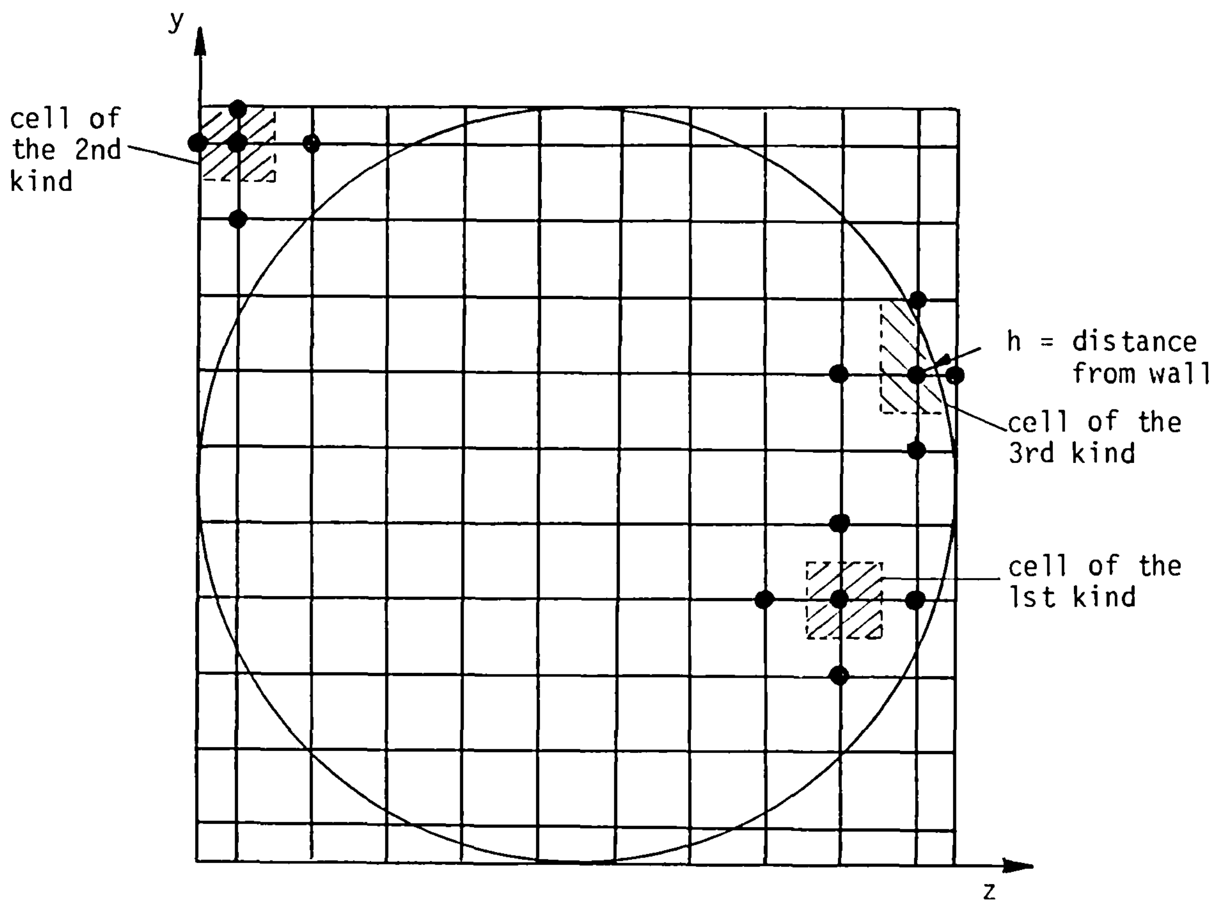

Fig. 2.3.5-1 Cartesian grid with curved boundary for 3-D parabolic flows

$$f_w = \frac{\delta w}{(\delta x)_w} \quad , \quad f_e = \frac{\delta e}{(\delta x)_e}$$

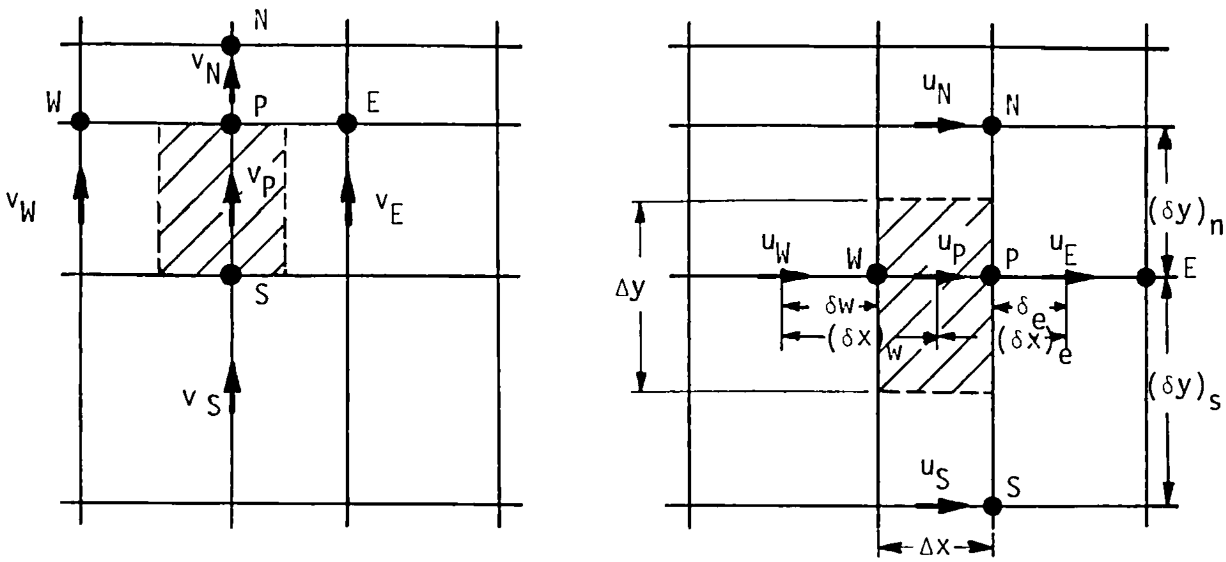

(a) The v-cell

(b) The u-cell and the weighting factors f_w and f_e

Fig. 2.4.2-2 The control volumes for the 2-D elliptic flows

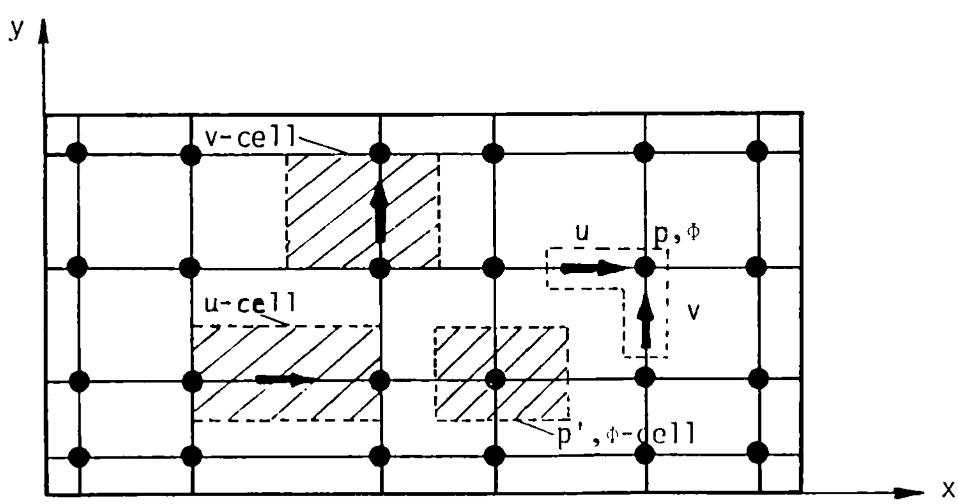

(c) The grid disposition

Fig. 2.4.2-1 The grid geometry for the 2-D elliptic flows

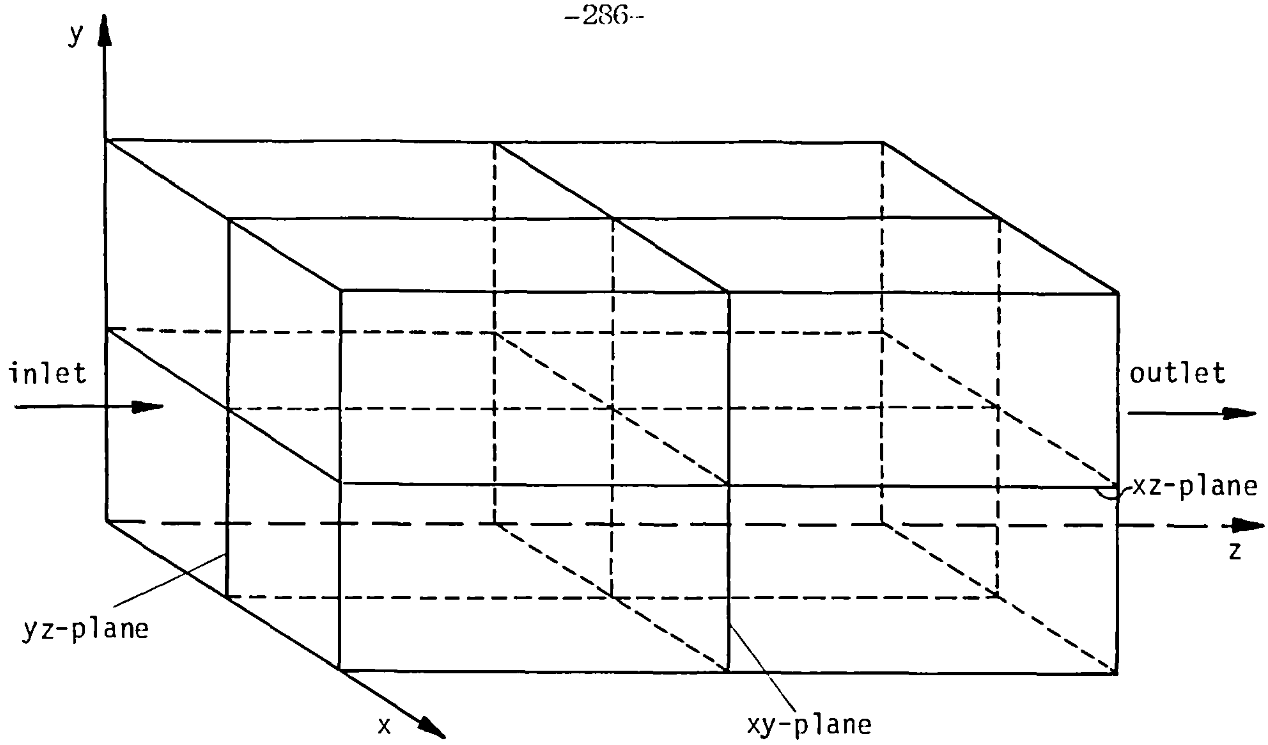

(a) Square duct geometry

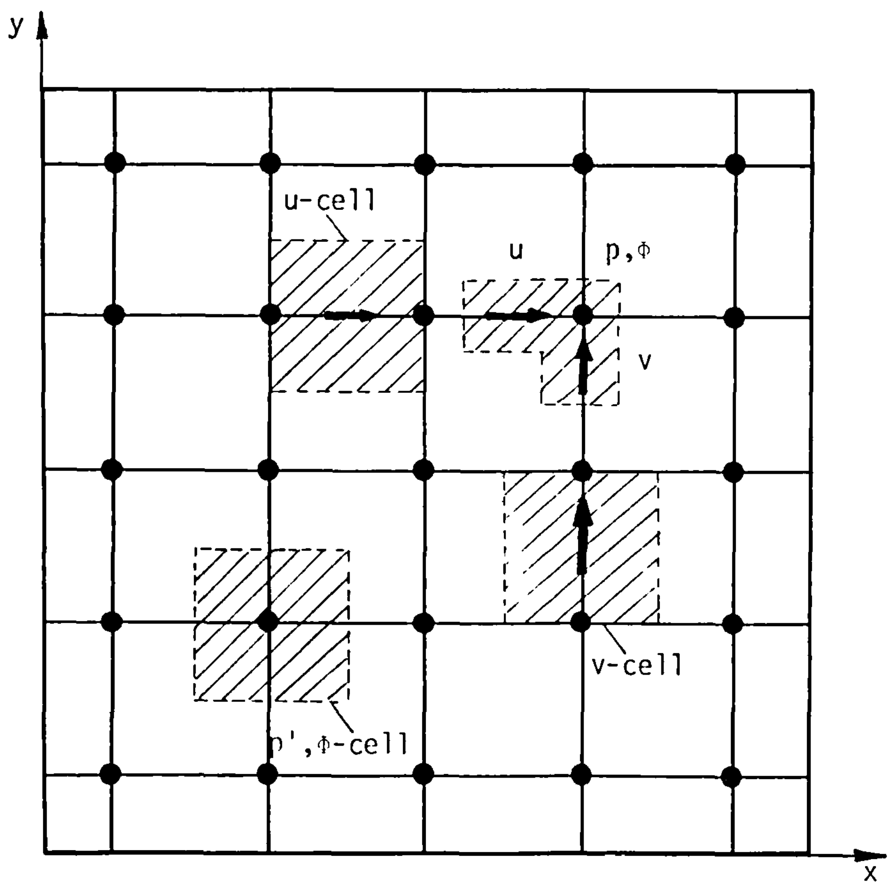

(b) Grid disposition in xy-plane

Fig. 2.5.2-1 The square duct and grid geometry for 3-D elliptic flows

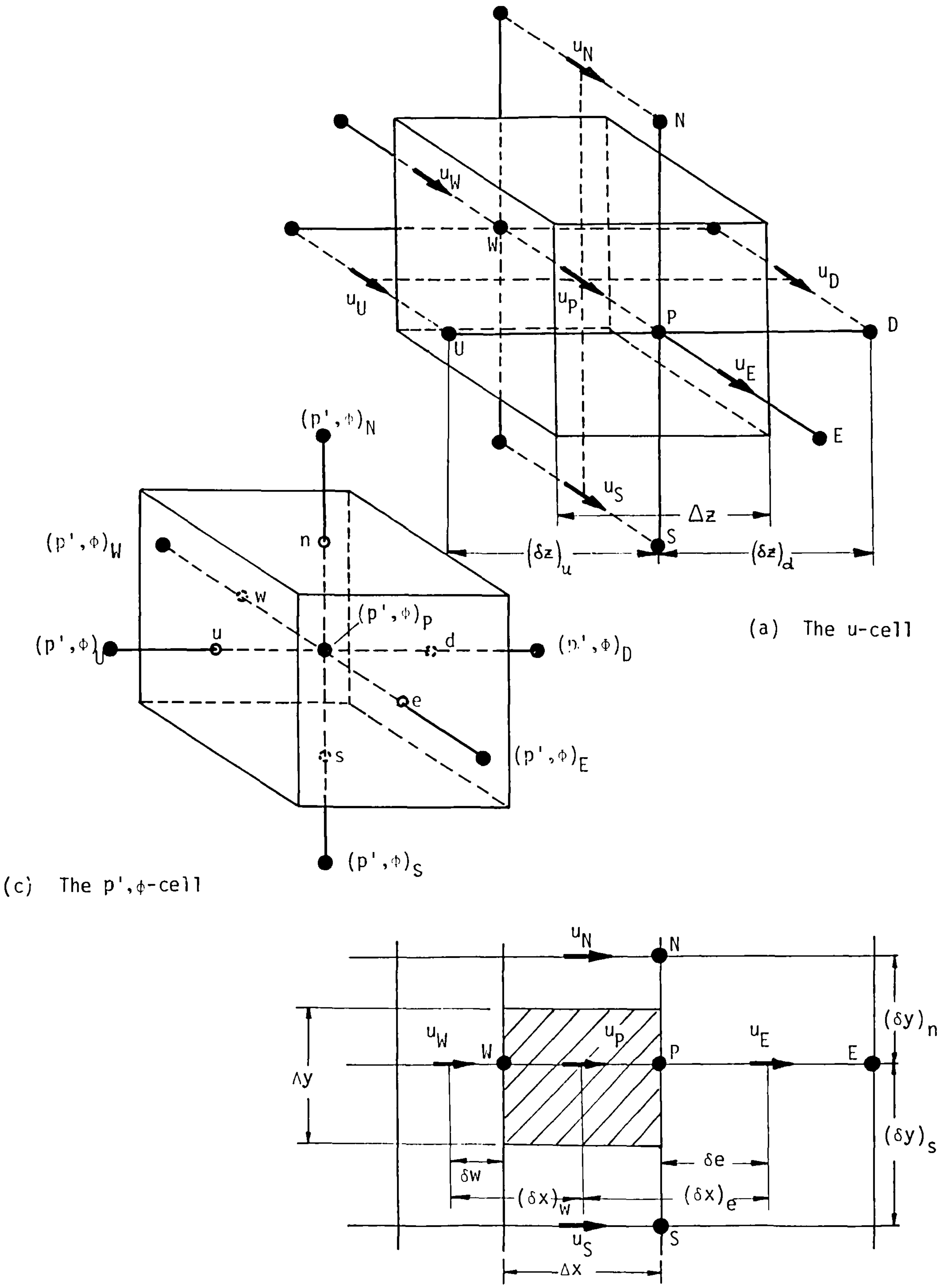

Fig. 2.5.2-2 The control volumes for 3-D elliptic flows

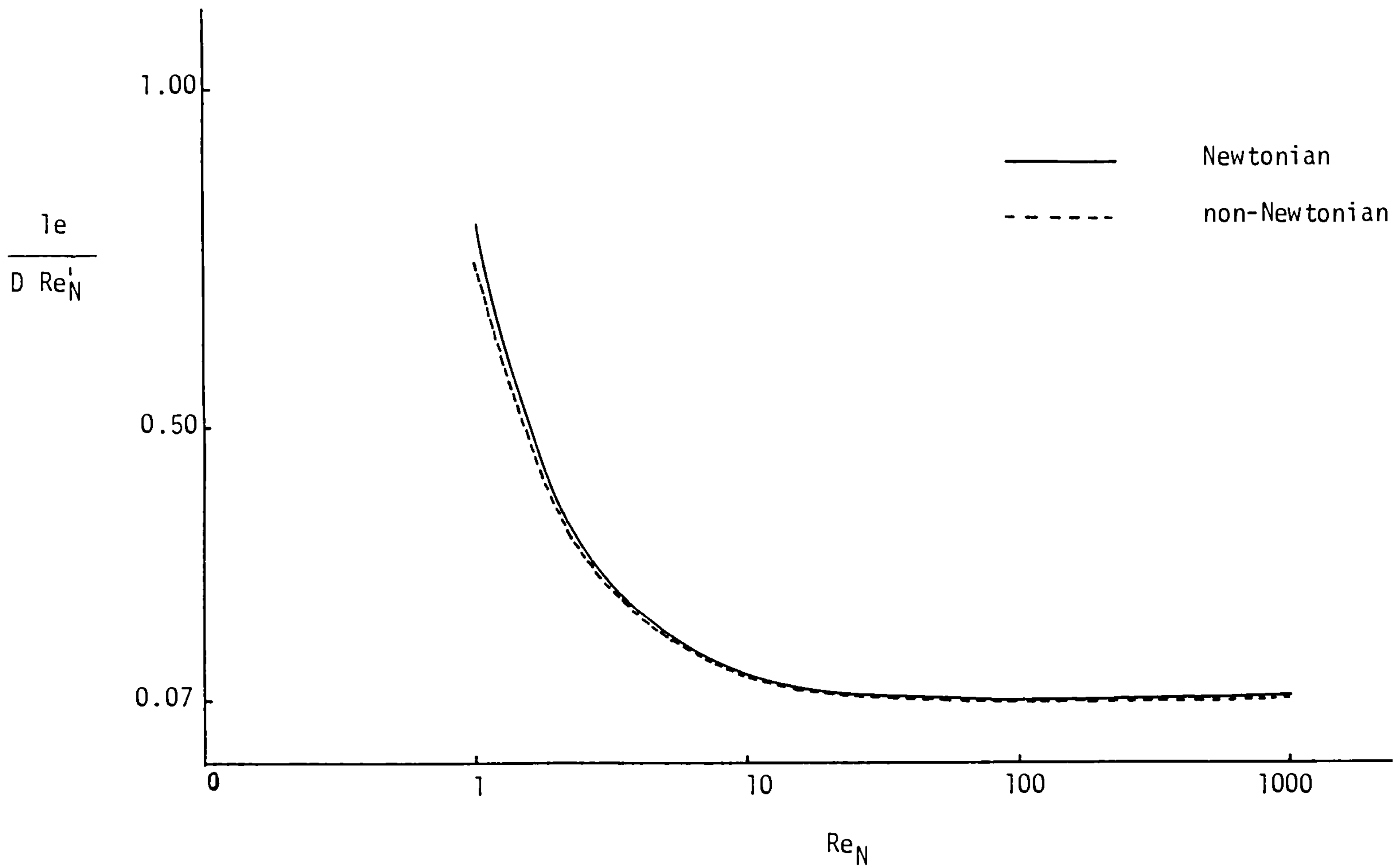

Fig. 2.6.2-1 Entrance lengths for Newtonian and non-Newtonian pipe flow

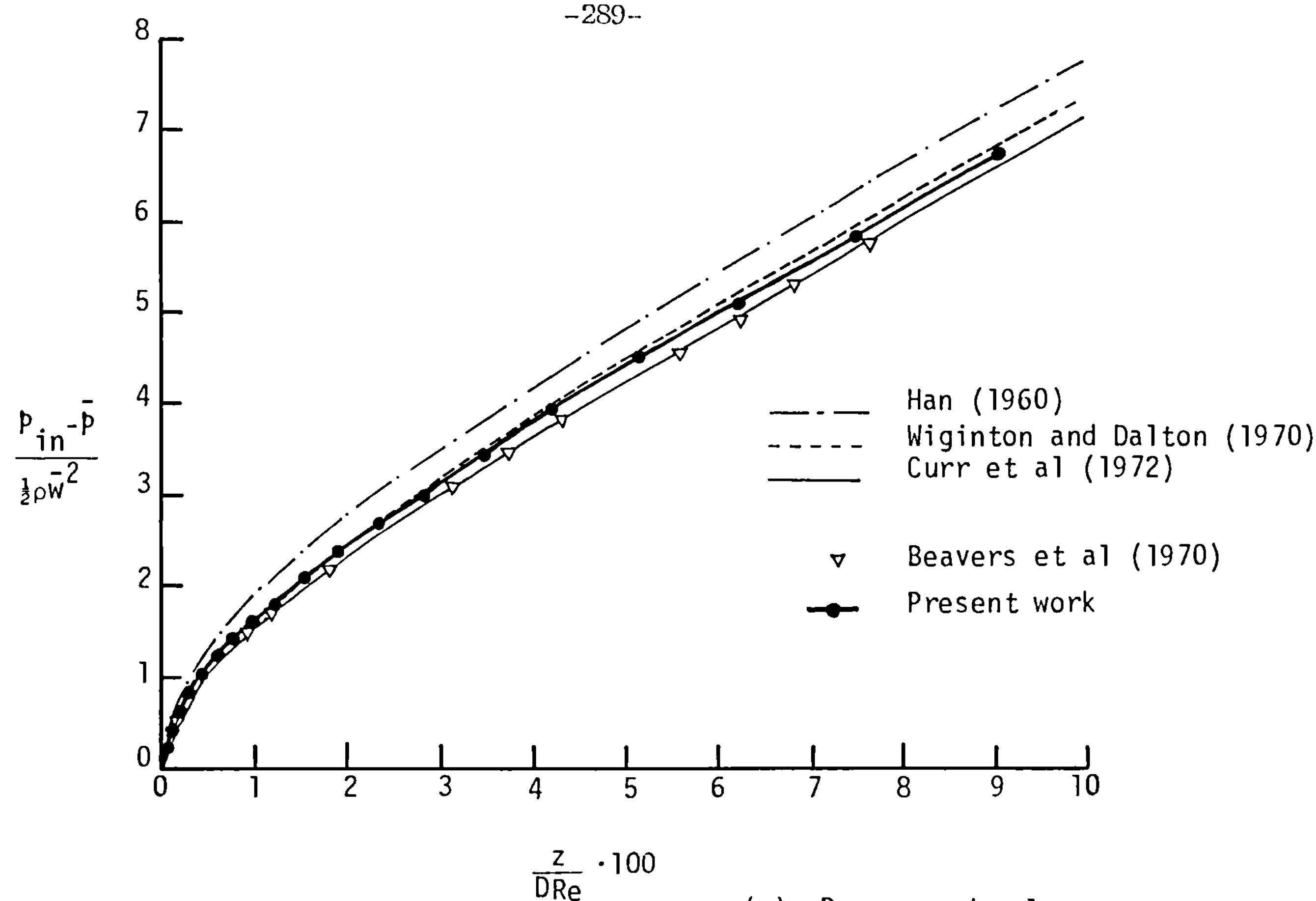

(a) Pressure development

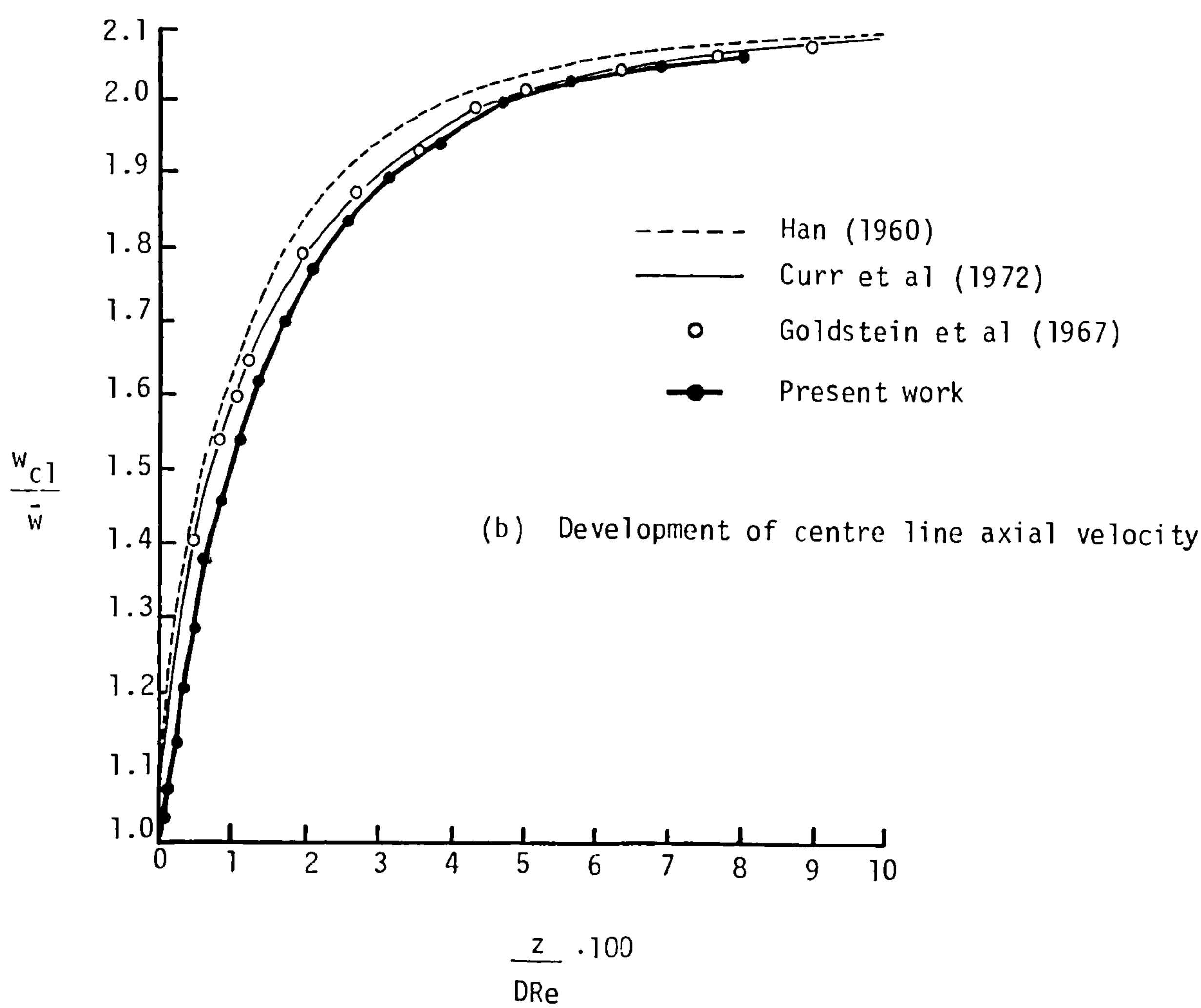

(b) Development of centre line axial velocity

Fig. 2.6.2 -2 Developing laminar square duct flow

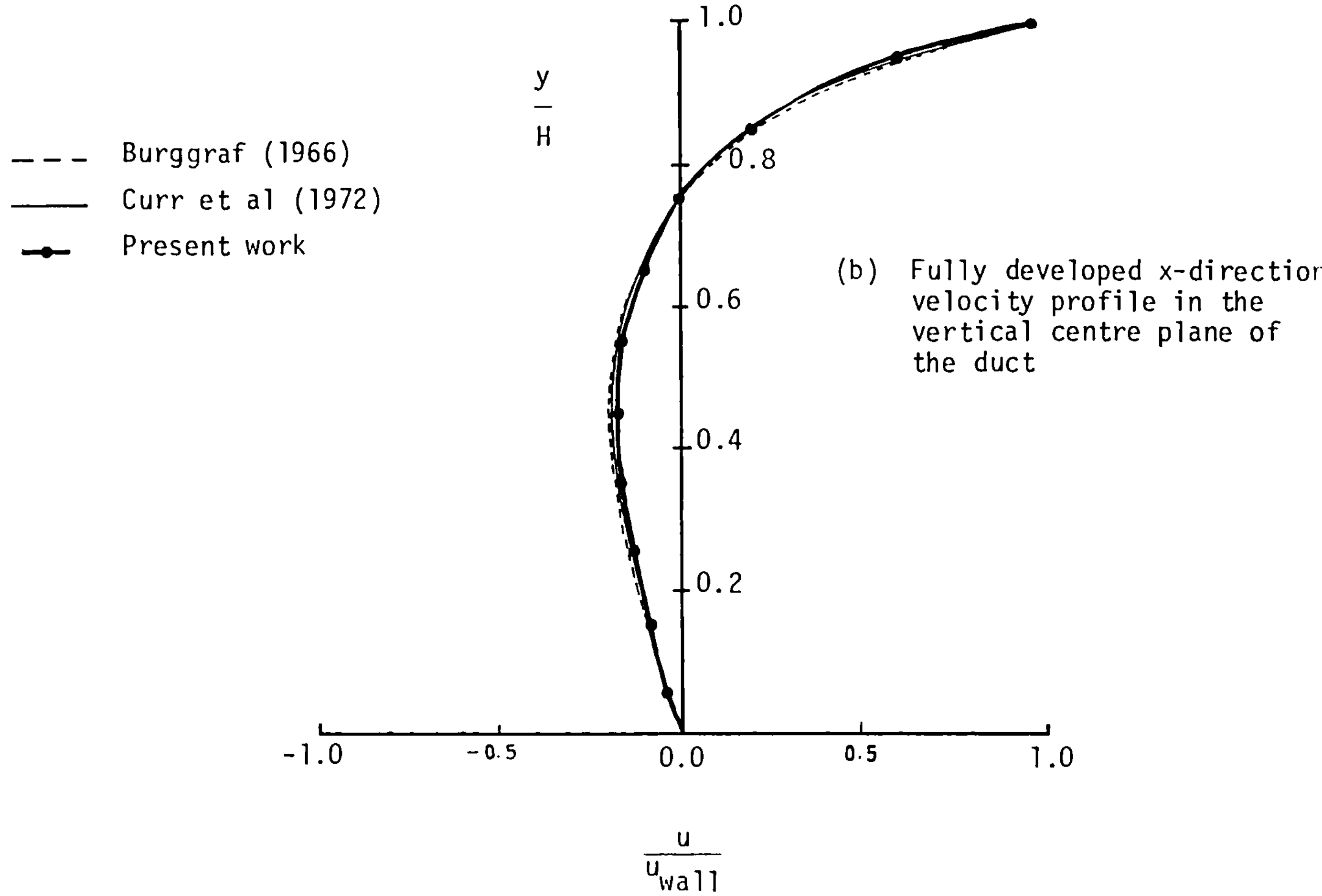

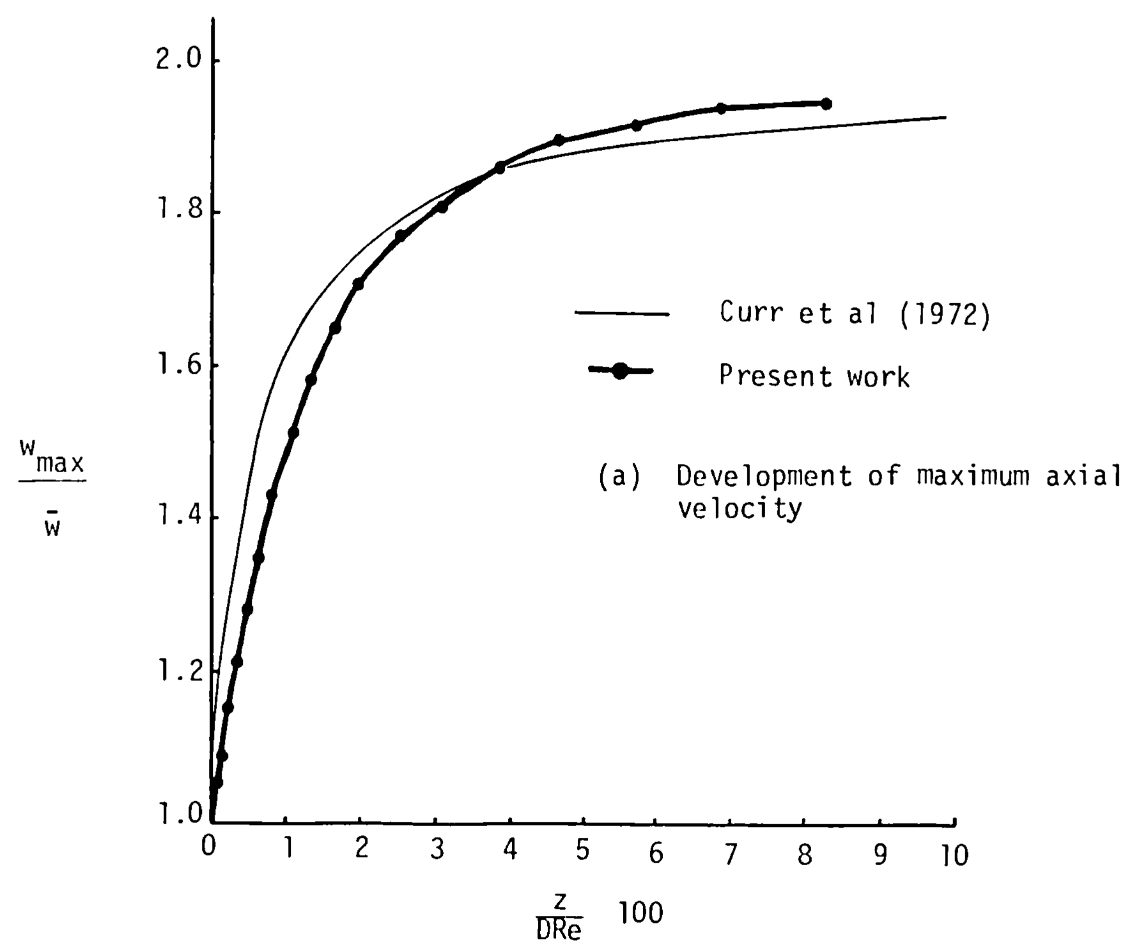

Fig. 2.6.2-3 Developing laminar square duct flow with a moving wall

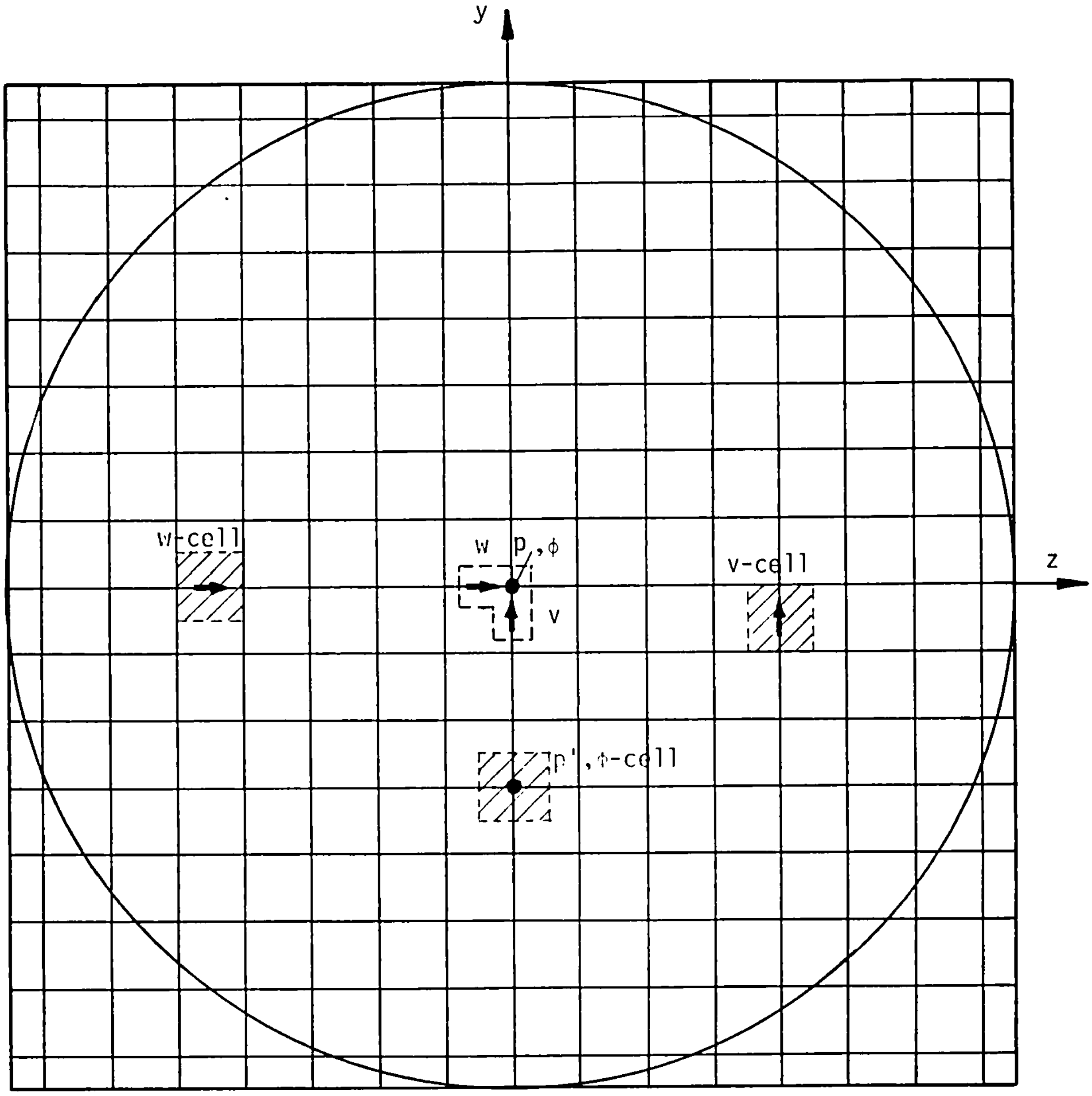

Fig. 2.6.3-1 The 17 x 17 grid for the flow downstream of a 15^0 bend in a round pipe

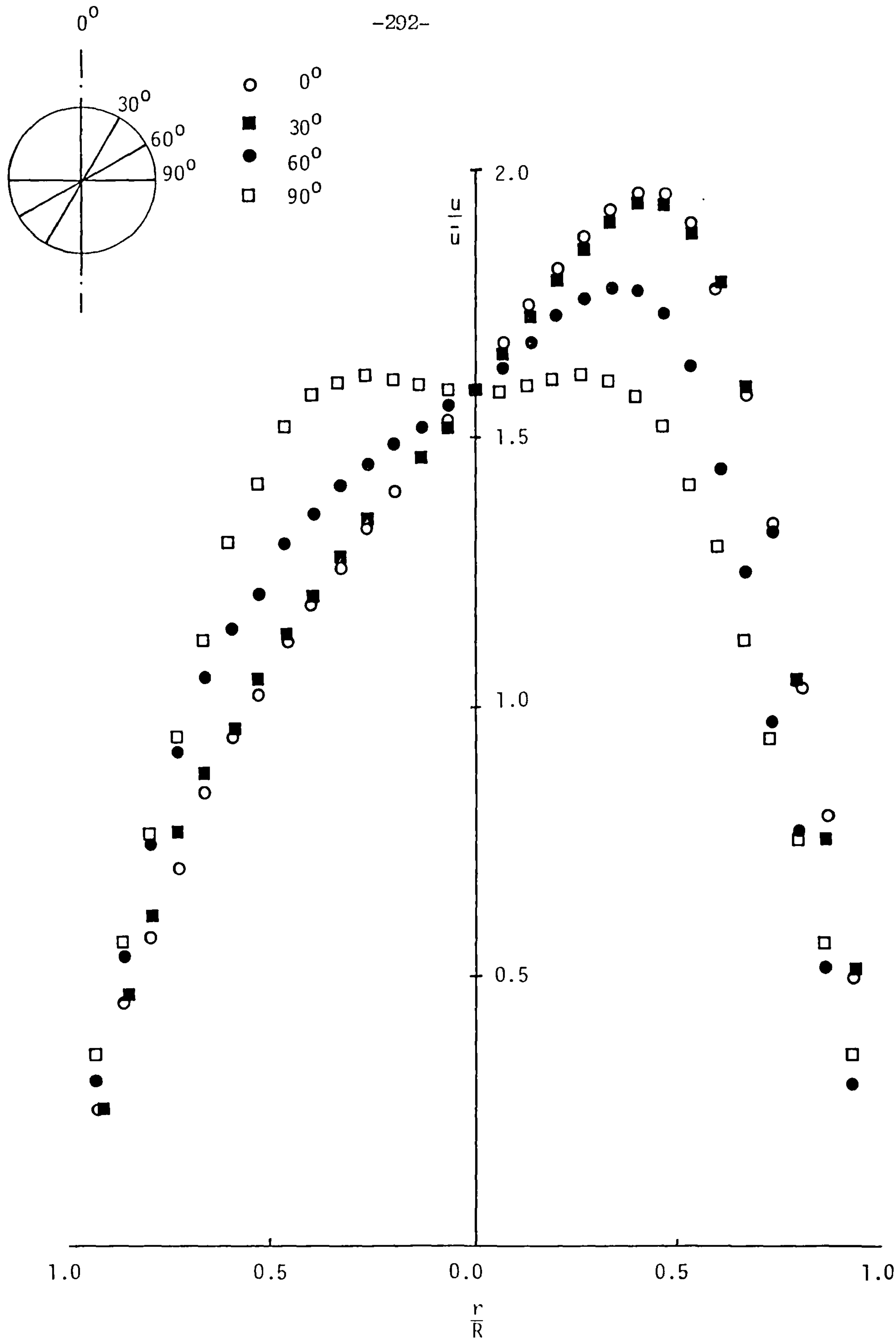

Fig. 2.6.3-2 The inlet profile for the flow downstream of a 15^0 bend in a round pipe

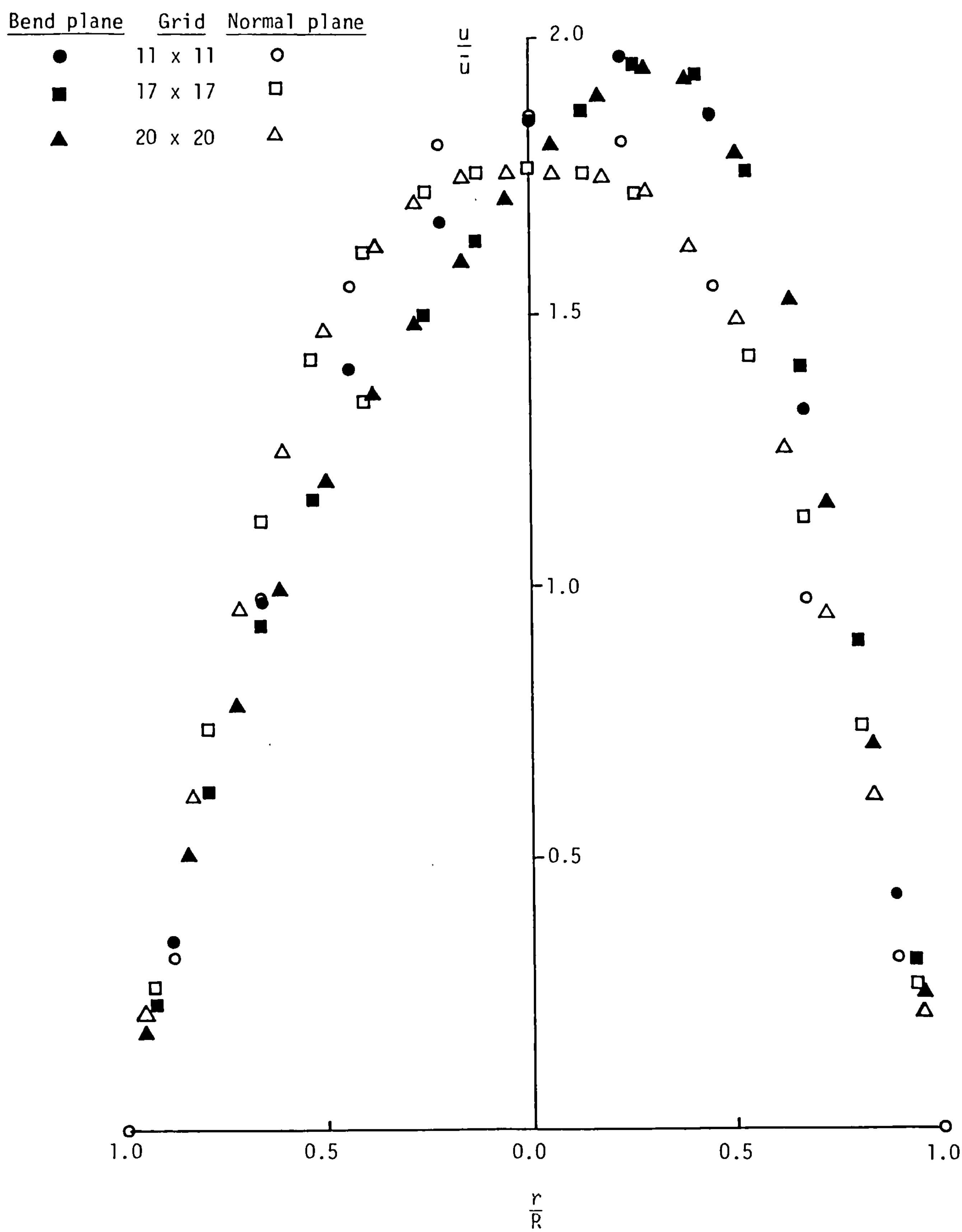

Fig. 2.6.3-3 Grid independence test for the flow downstream of a bend in a round pipe.

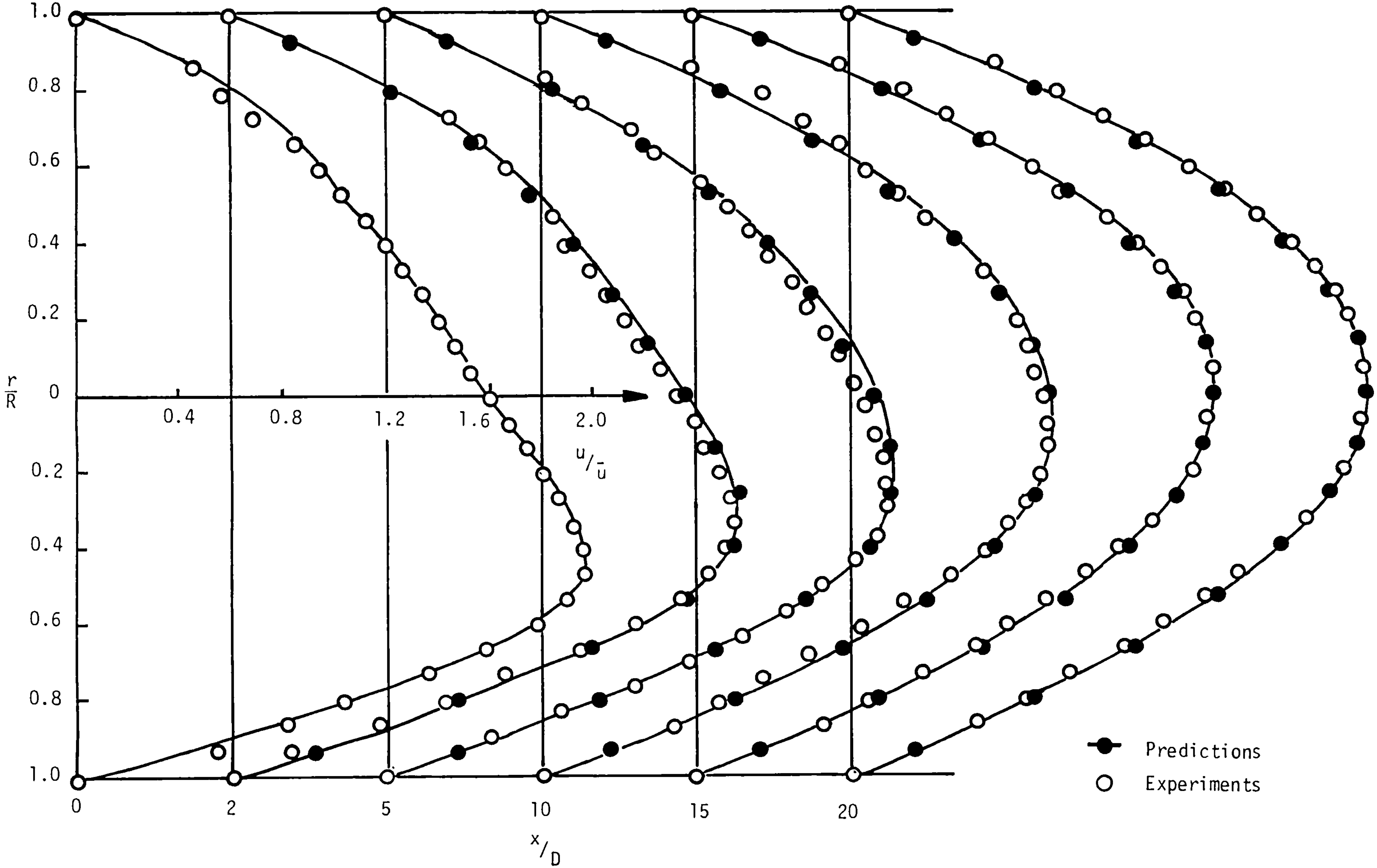

Fig. 2.6.3-4 Development of axial velocity profile in the plane of the bend

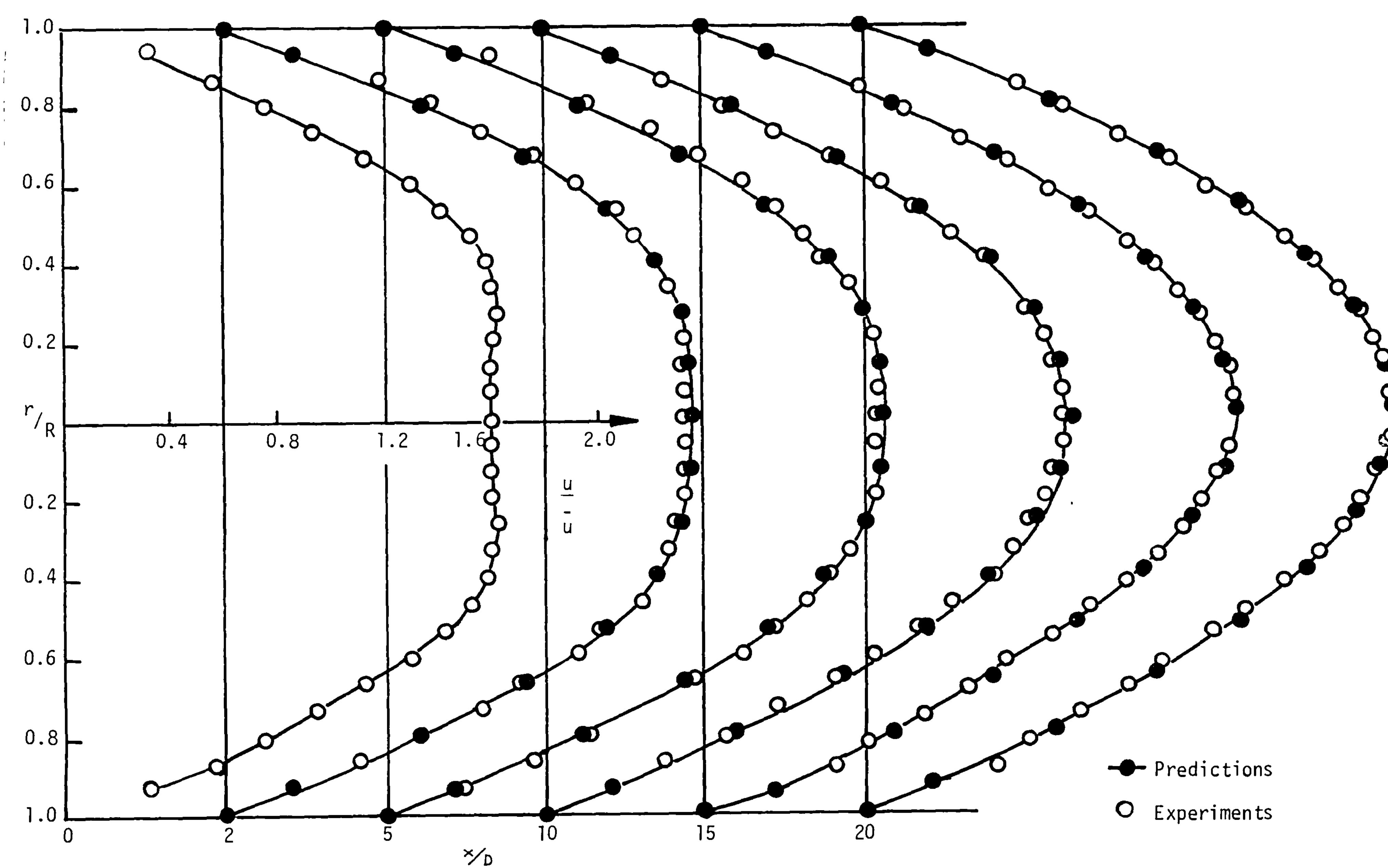

Fig. 2.6.3-5 Development of axial velocity profile in the plane normal to the bend

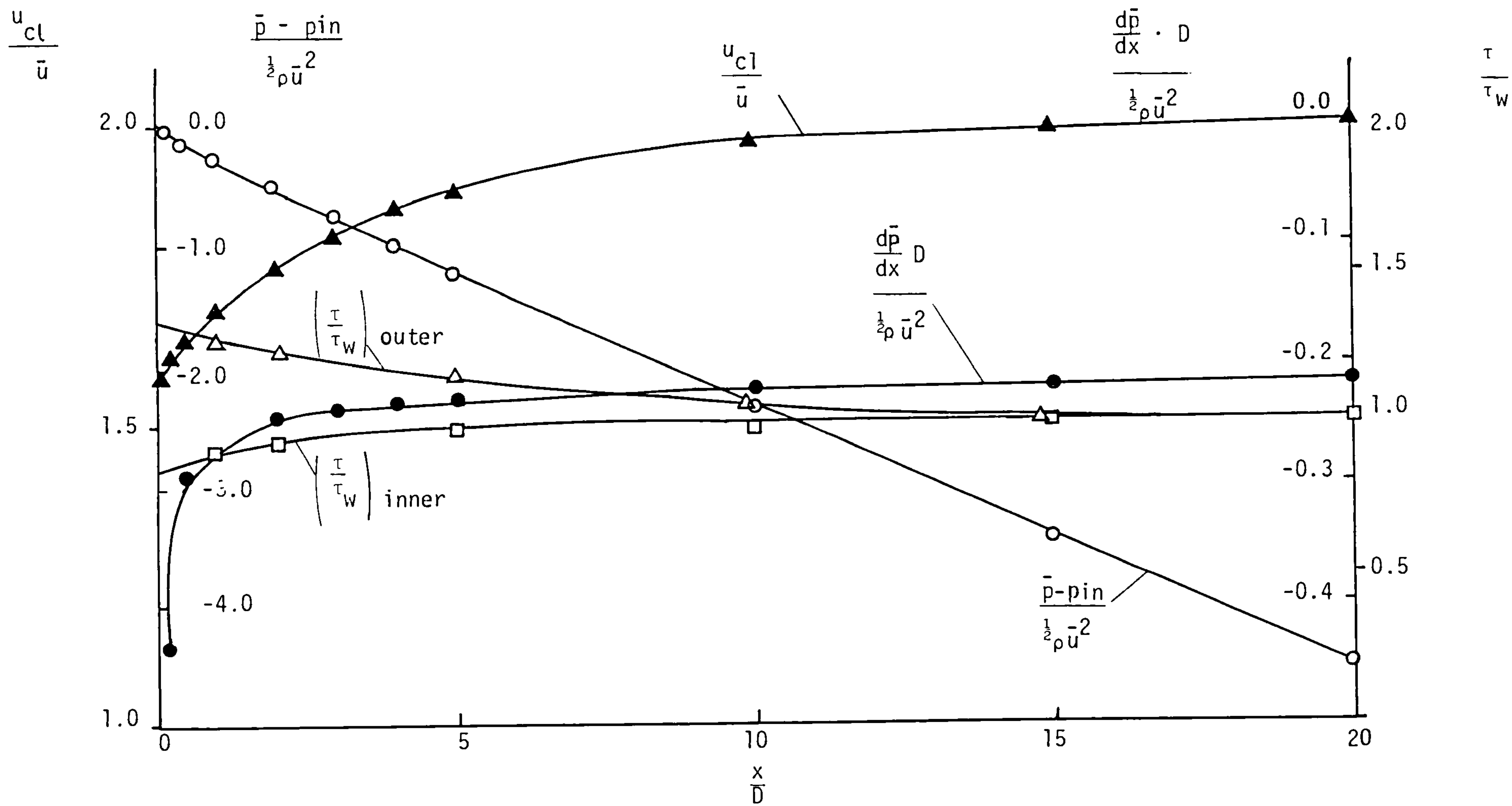

Fig. 2.6.3-6 Flow development downstream of a 15° bend in a round pipe

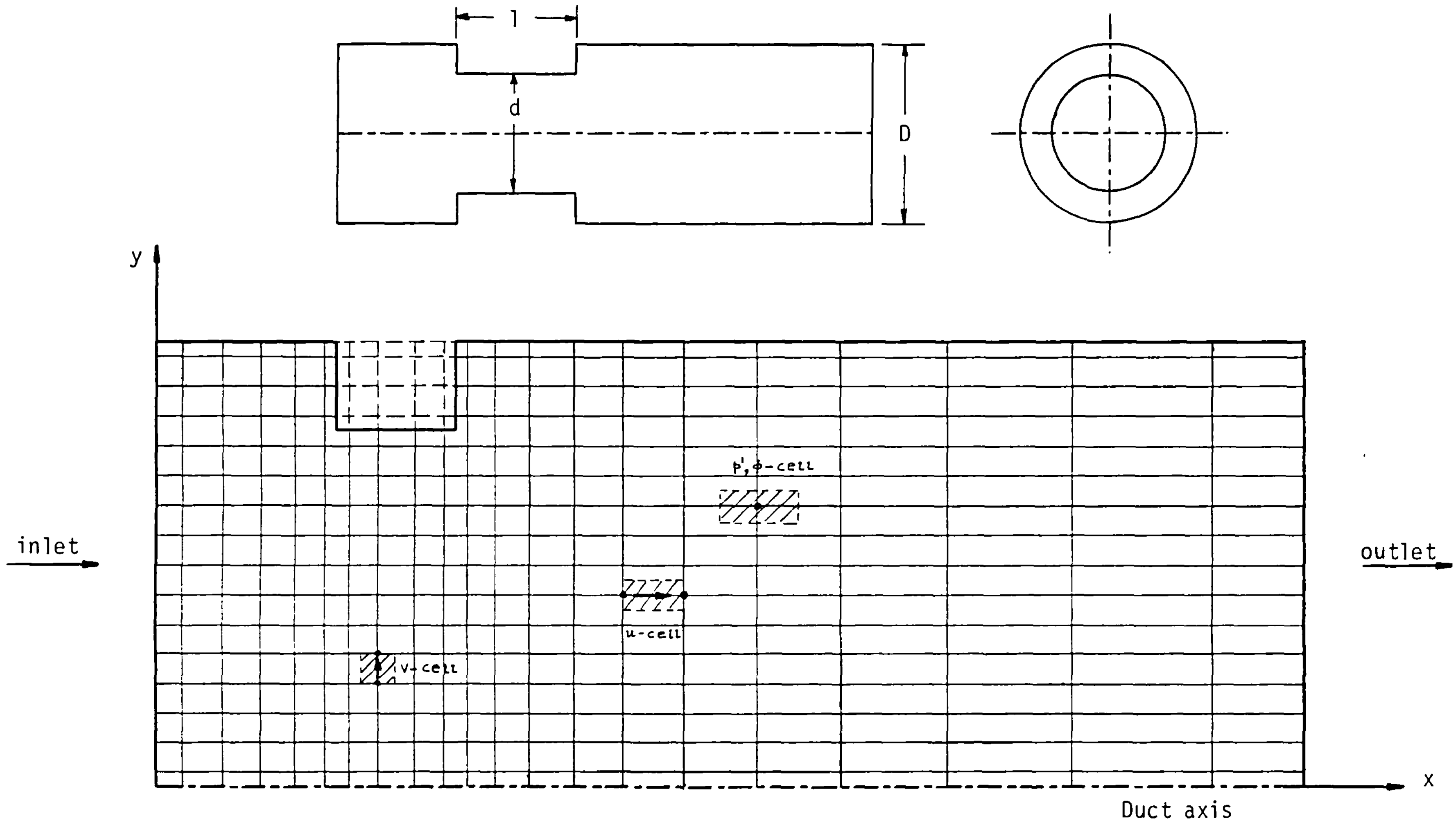

Fig. 2.6.4-1 The 22 x 17 grid for the flow around an axisymmetric constriction

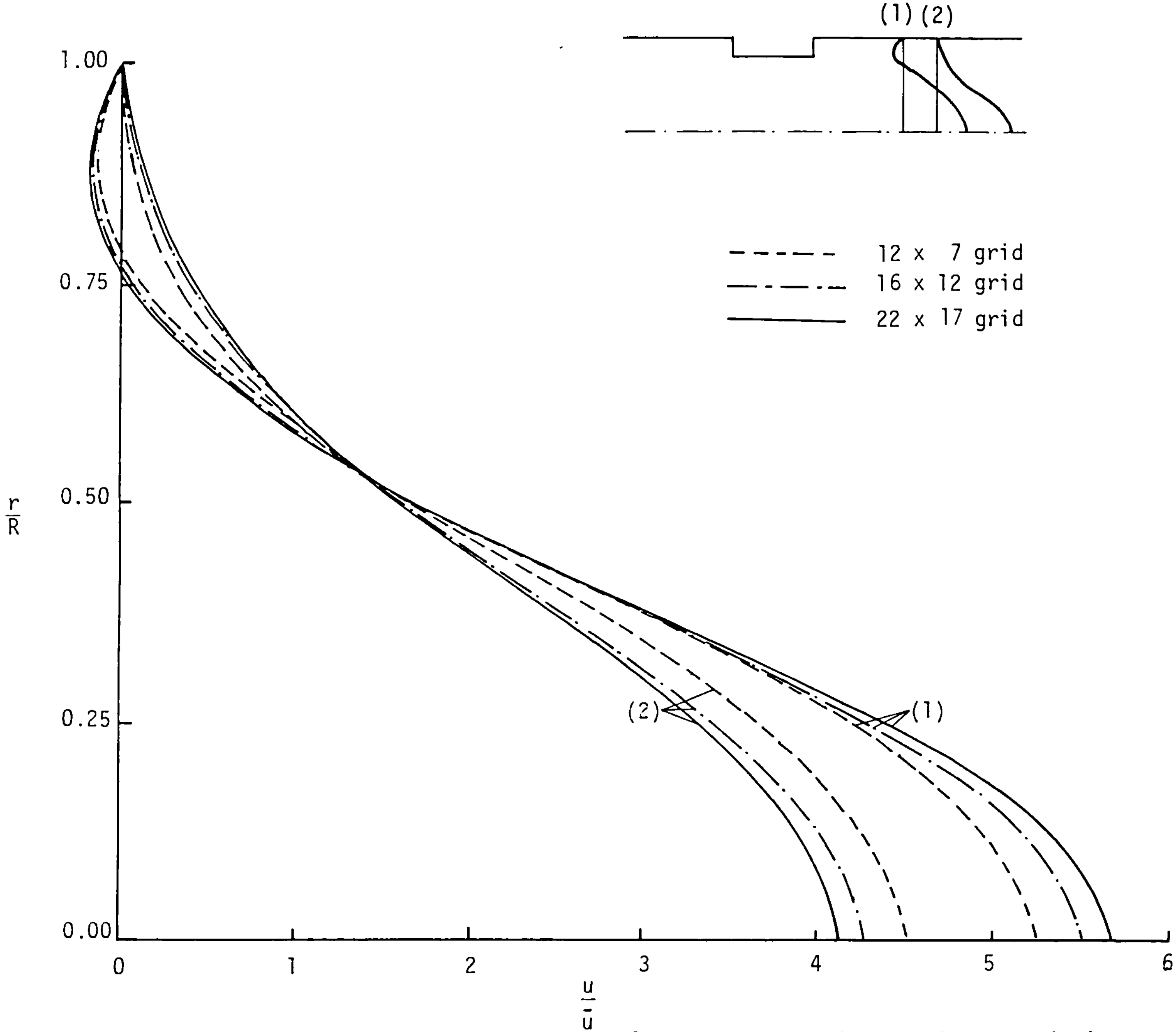

Fig. 2.6.4-2 Grid independence test for the flow around an axisymmetric constriction

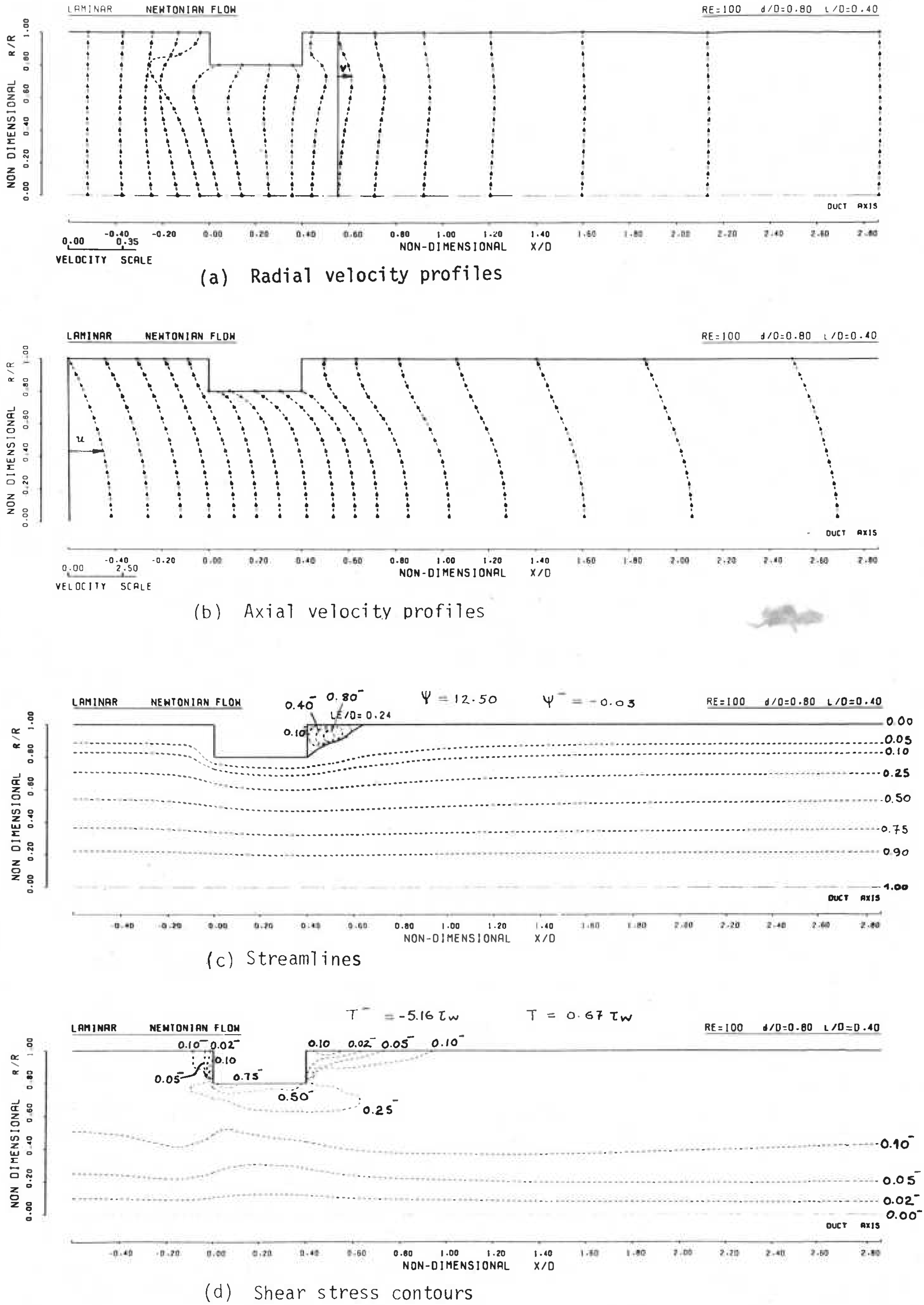

Fig. 2.6.4-3 Laminar Newtonian flow around an axisymmetric constriction (Re = 100, d/D = 0.80, l/D = 0.40)

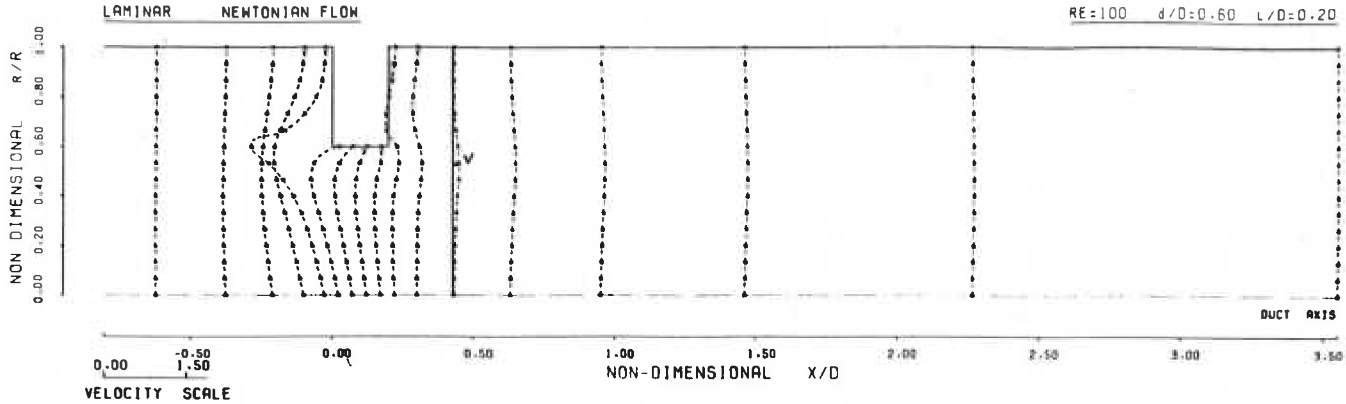

(a) Radial velocity profiles

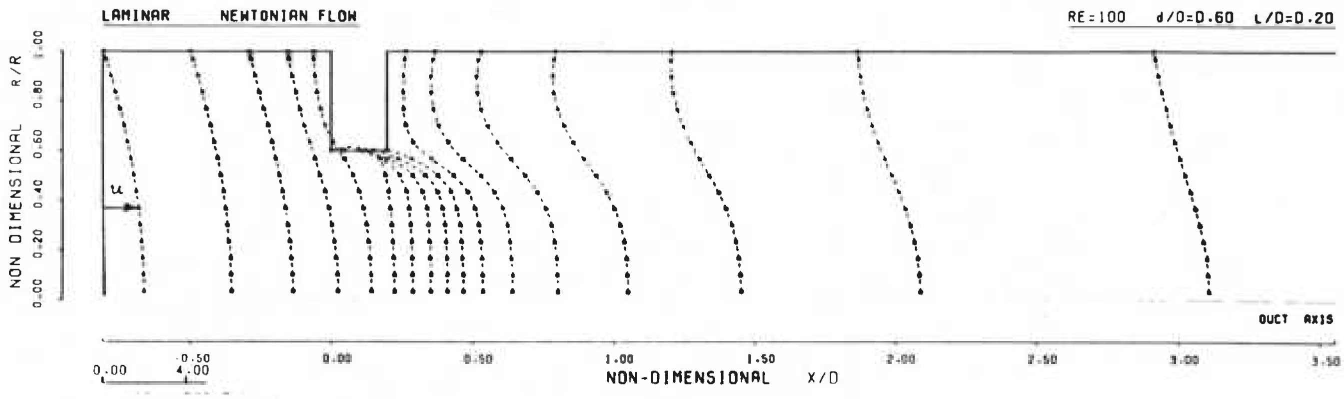

(b) Axial velocity profiles

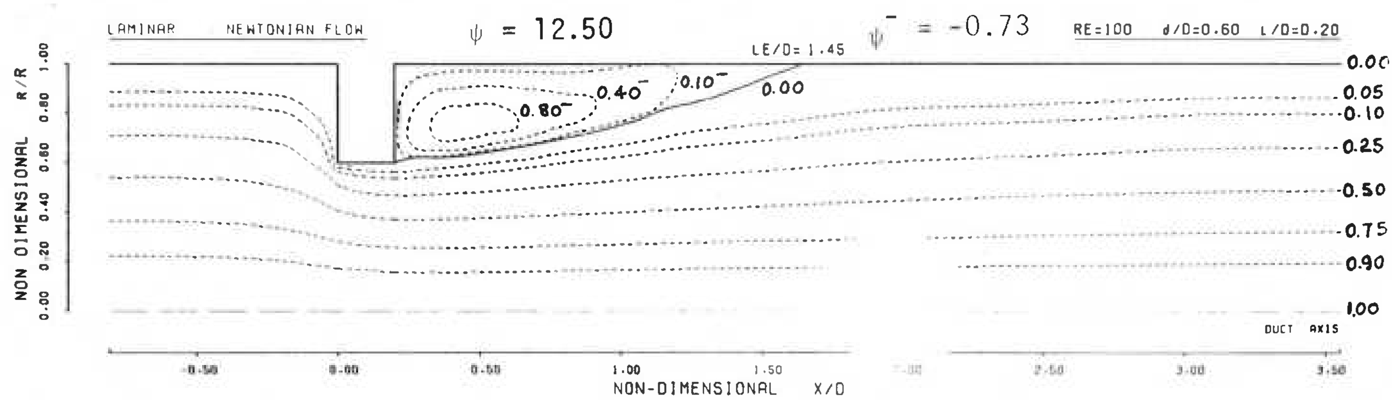

(c) Streamlines

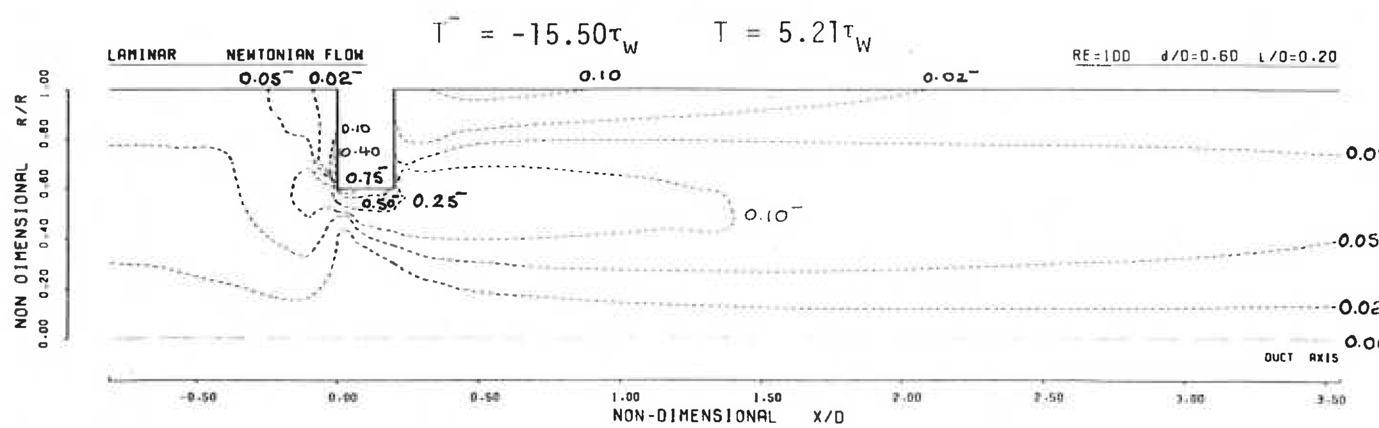

(d) Shear stress contours

Fig. 2.6.4-4 Laminar Newtonian flow around an axisymmetric constriction (Re = 100, d/D = 0.60, l/D = 0.20)

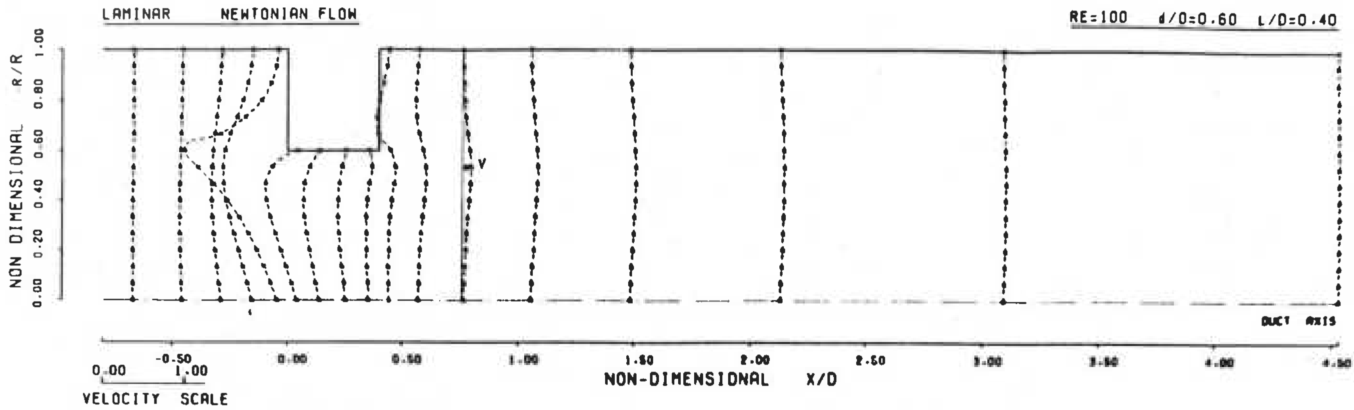

(a) Radial velocity profiles

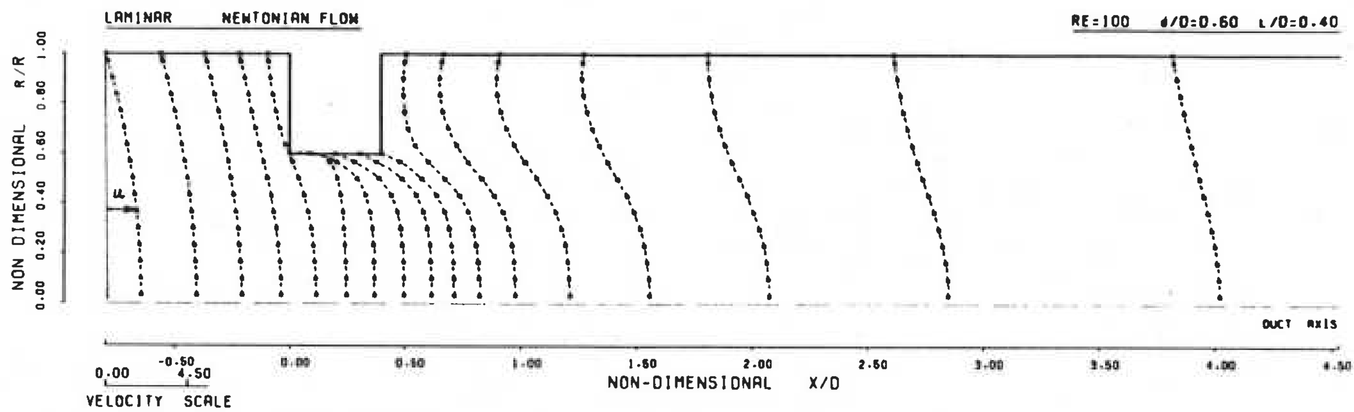

(b) Axial velocity profiles

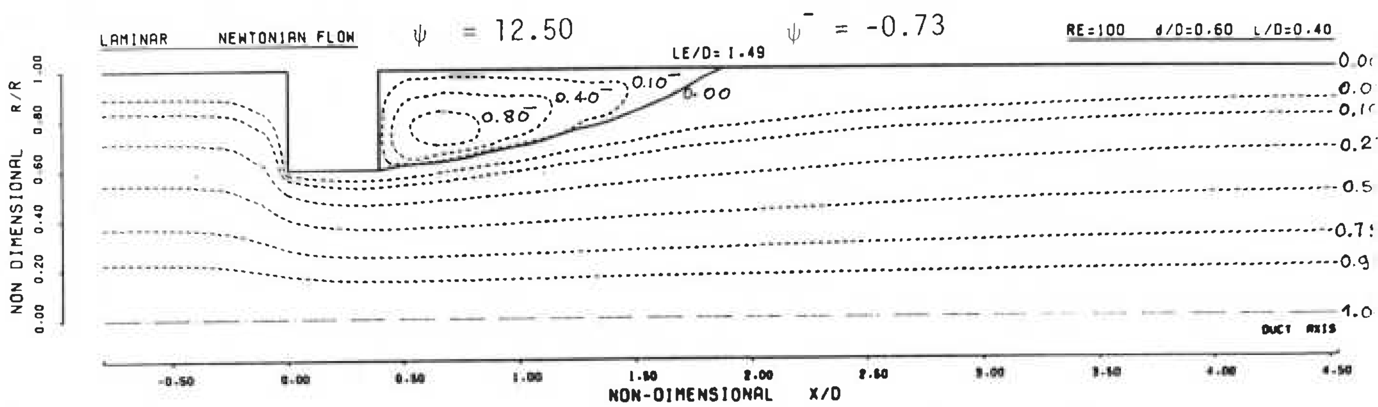

(c) Streamlines

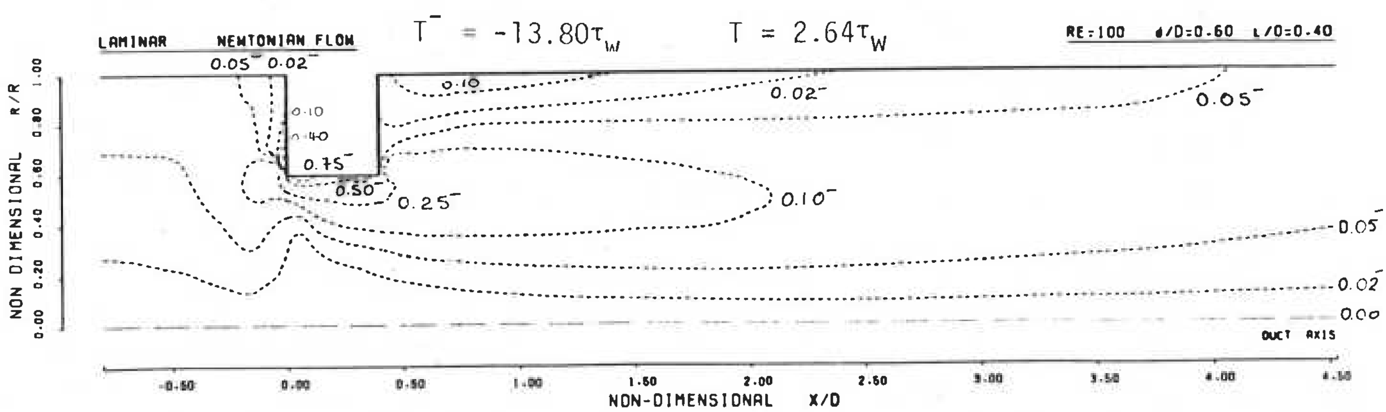

(d) Shear stress contours

Fig. 2.6.4-5 Laminar Newtonian flow around an axisymmetric constriction (Re = 100, d/D = 0.60, l/D = 0.40)

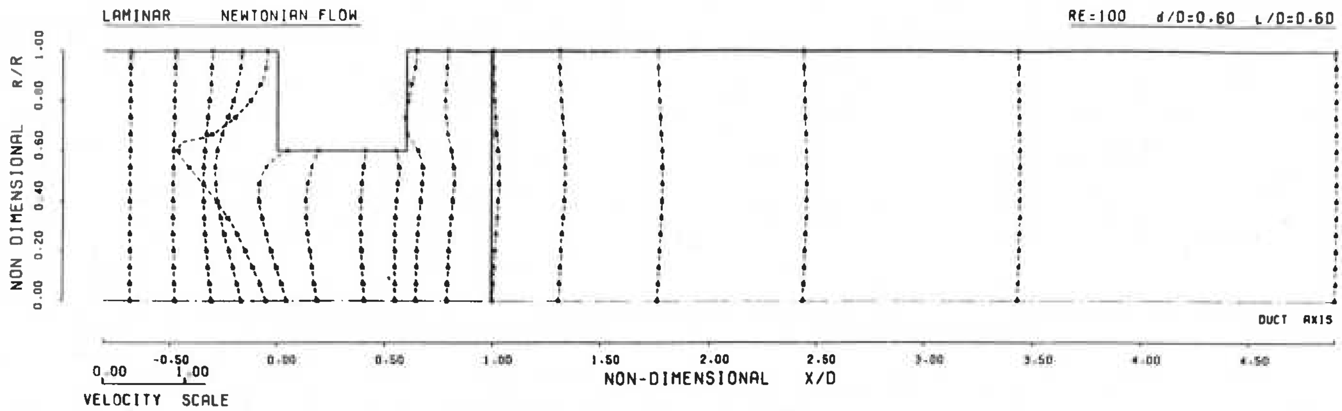

(a) Radial velocity profiles

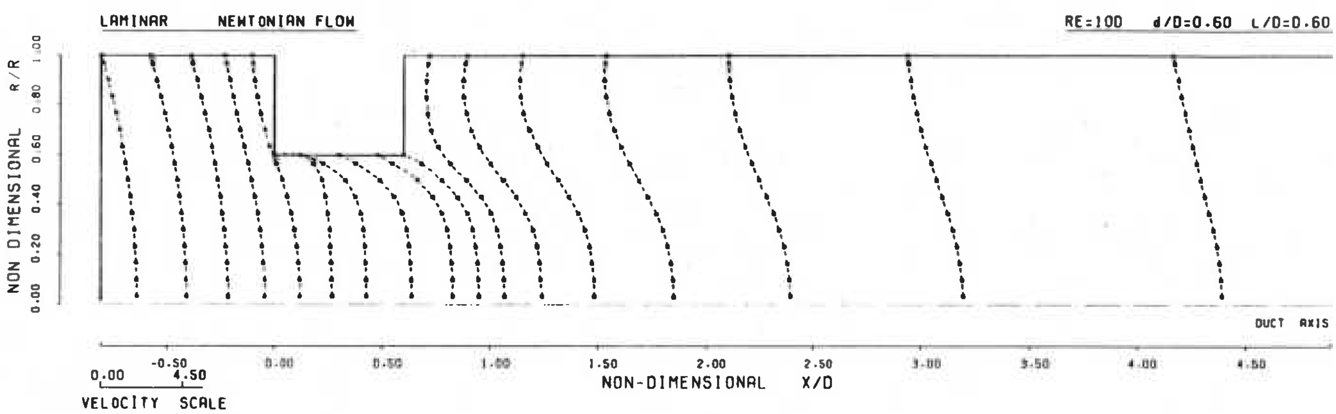

(b) Axial velocity profiles

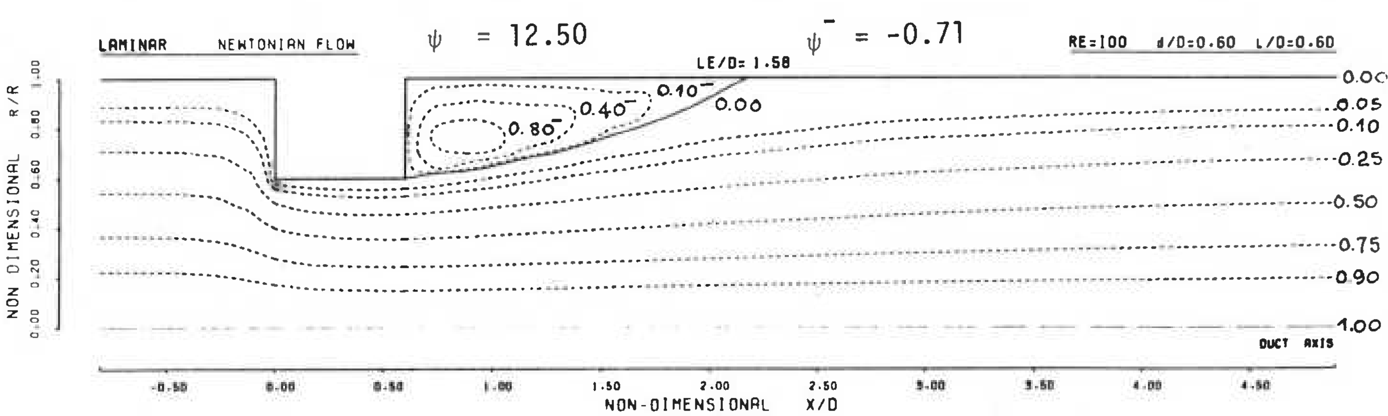

(c) Streamlines

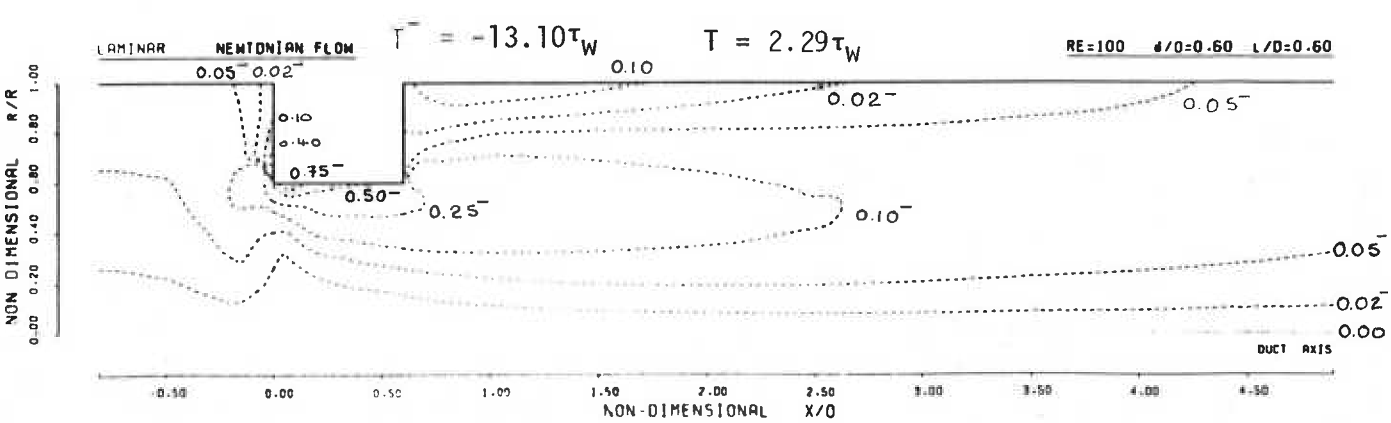

(d) Shear stress contours

Fig. 2.6.4-6 Laminar Newtonian flow around an axisymmetric constriction
(Re = 100, d/D = 0.60, l/D = 0.60)

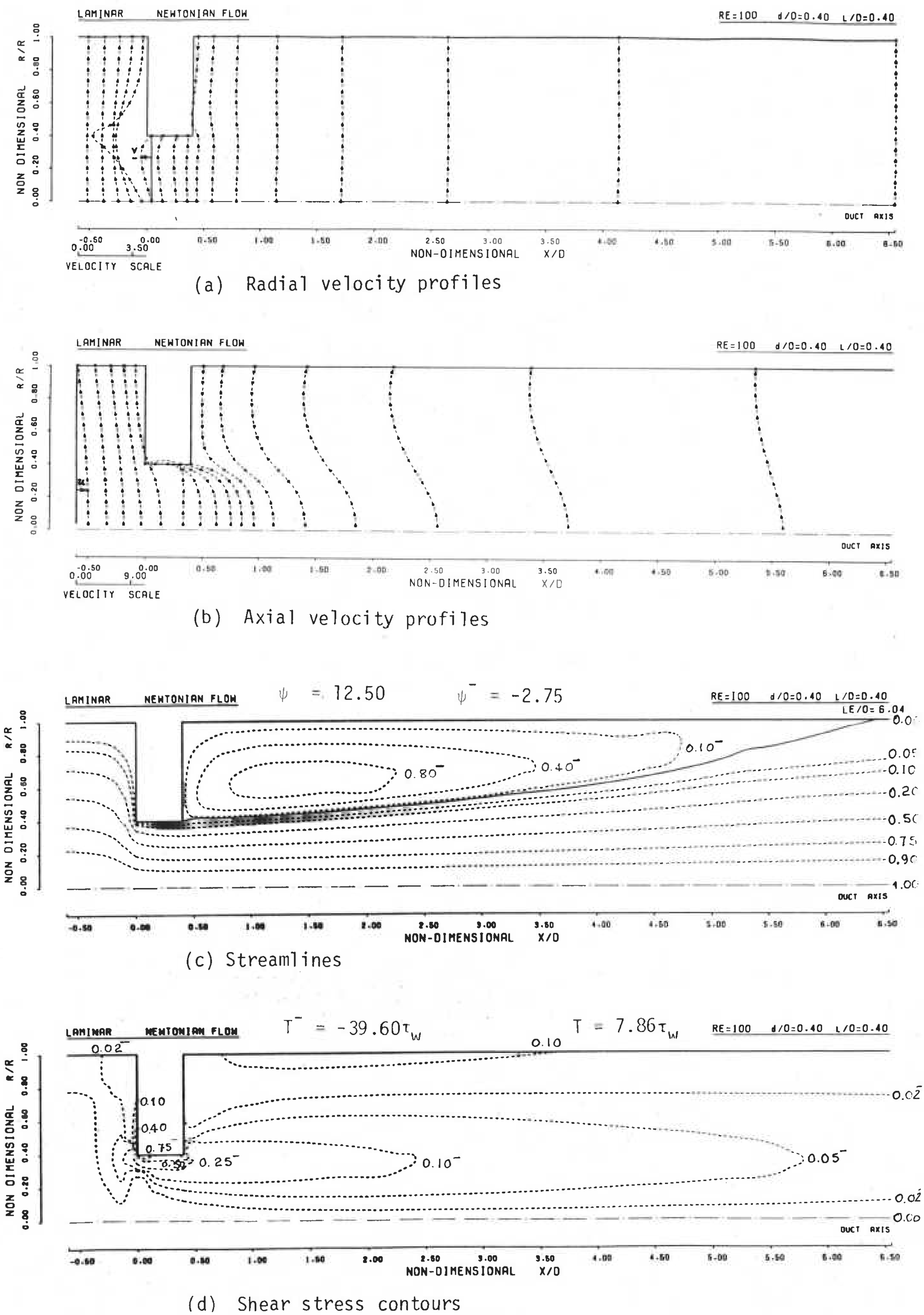

Fig. 2.6.4-7 Laminar Newtonian flow around an axisymmetric constriction (Re = 100, d/D = 0.40, l/D = 0.40)

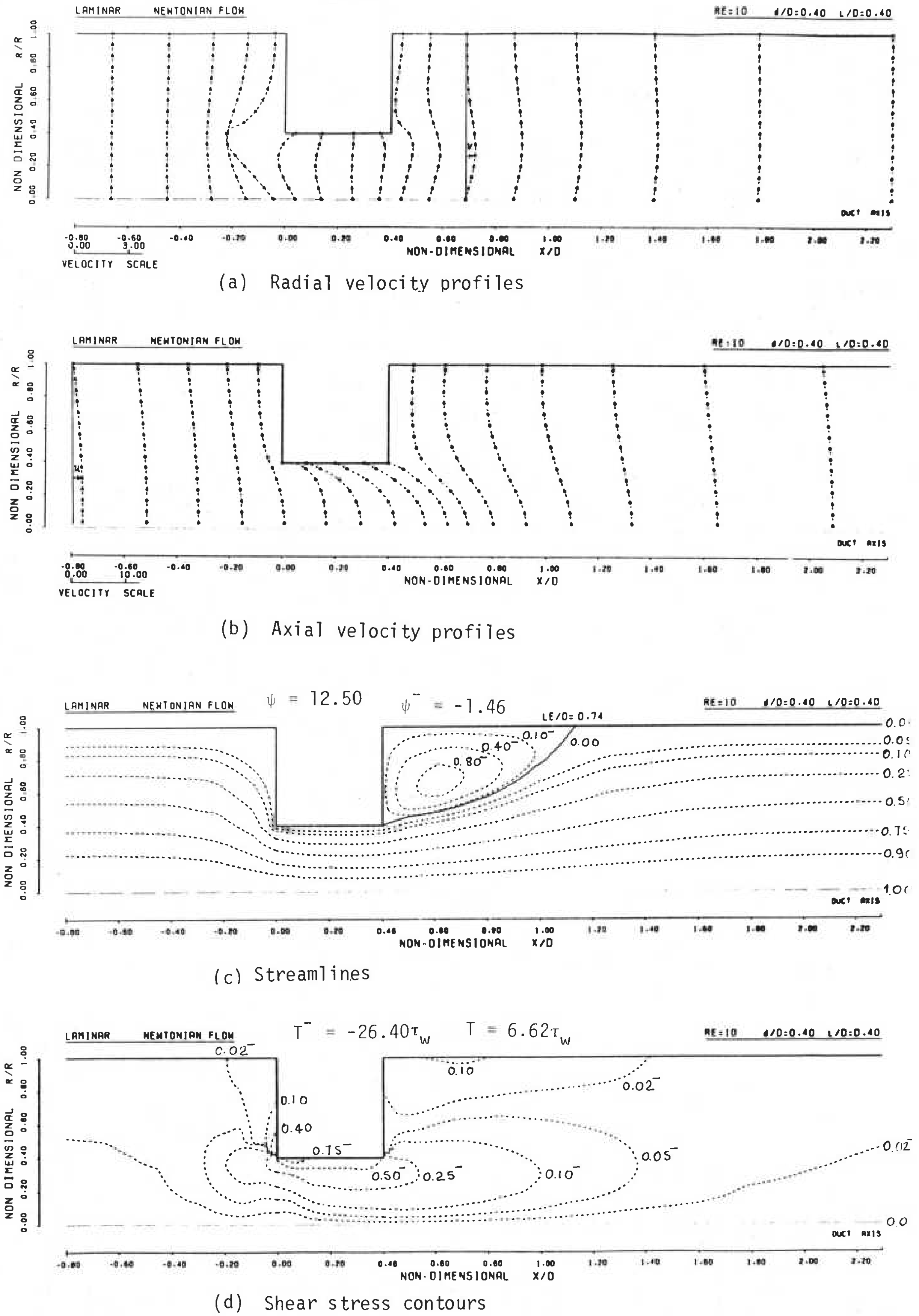

(a) Radial velocity profiles

(b) Axial velocity profiles

$\psi = 12.50$ $\psi^{-} = -1.46$

(c) Streamlines

$T^{-} = -26.40\tau_w$ $T = 6.62\tau_w$

(d) Shear stress contours

Fig. 2.6.4-8 Laminar Newtonian flow around an axisymmetric constriction (Re = 10, d/D = 0.40, l/D = 0.40)

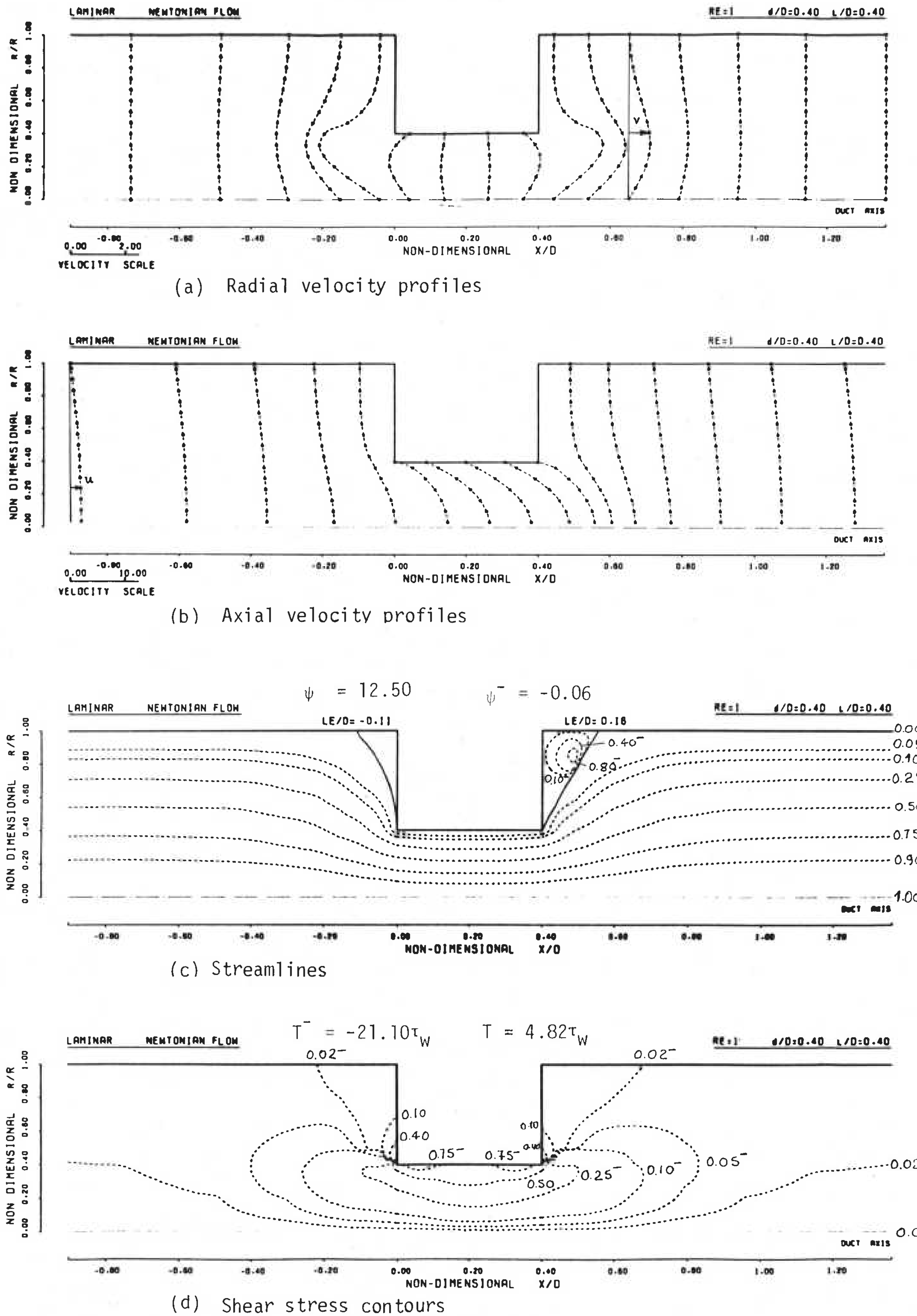

Fig. 2.6.4-9 Laminar Newtonian flow around an axisymmetric constriction (Re = 1, d/D = 0.40, l/D = 0.40)

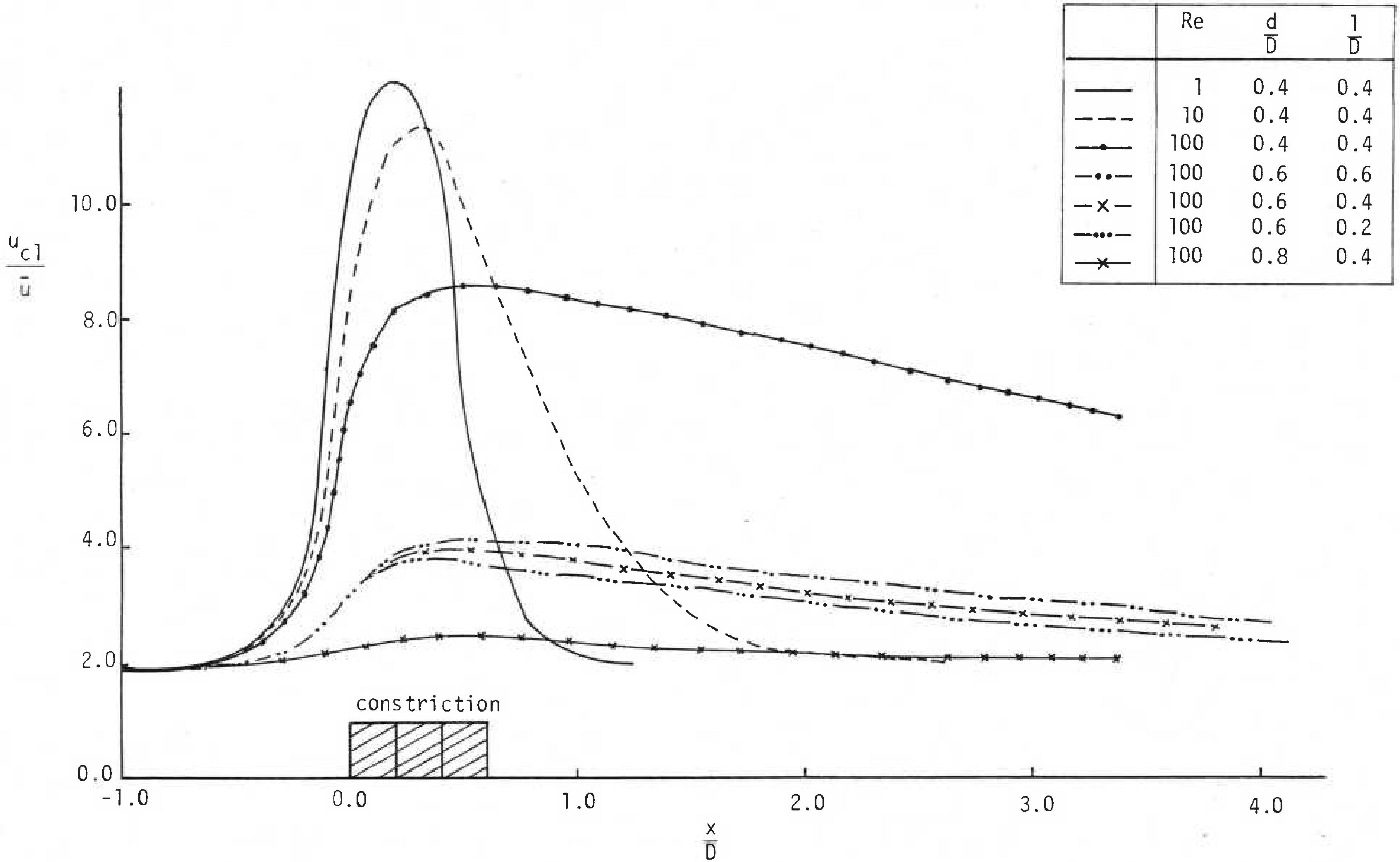

Fig. 2.6.4-10 Development of centre-line axial velocity for Newtonian flow around an axisymmetric constriction

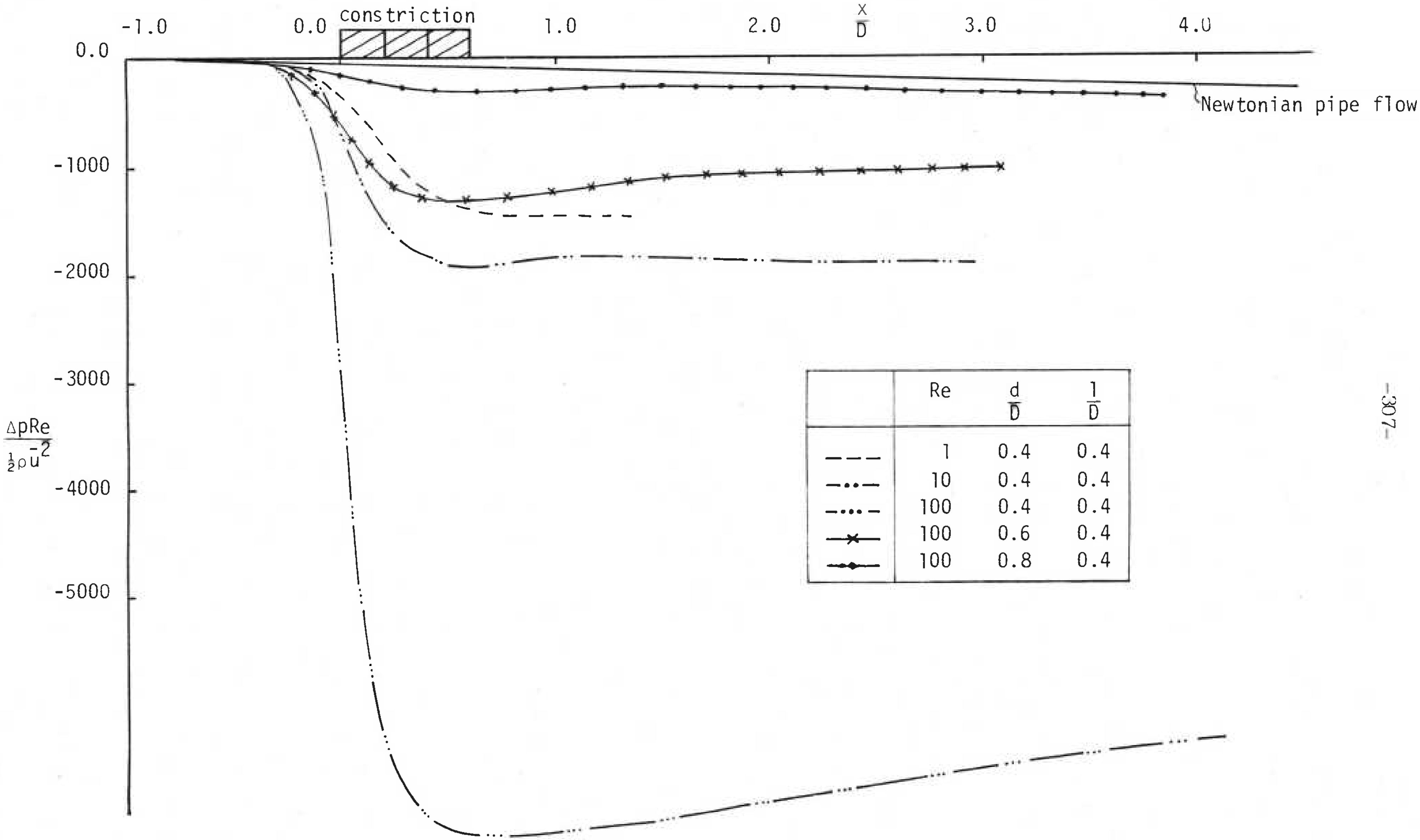

Fig. 2.6.4-11 Development of centre-line pressure for Newtonian flow around an axisymmetric constriction

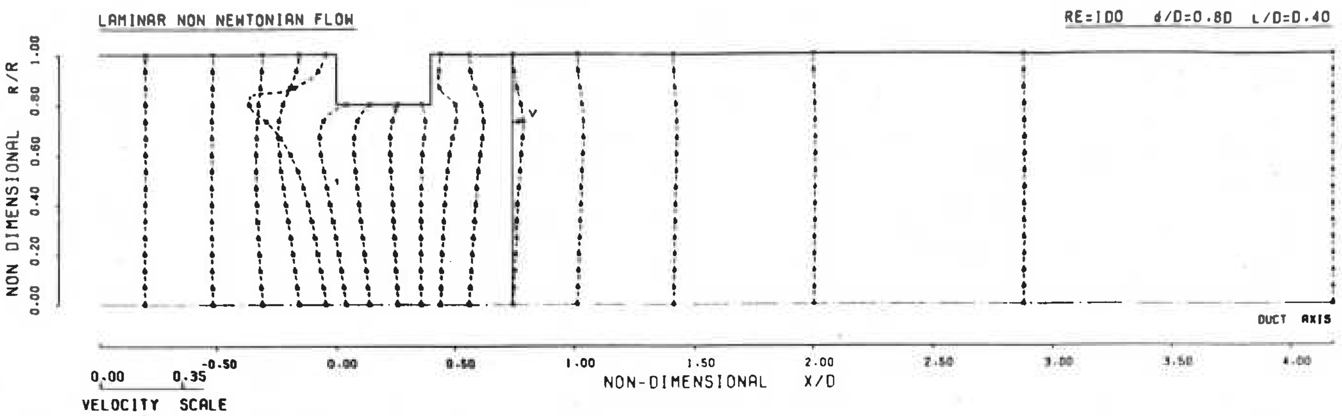

(a) Radial velocity profiles

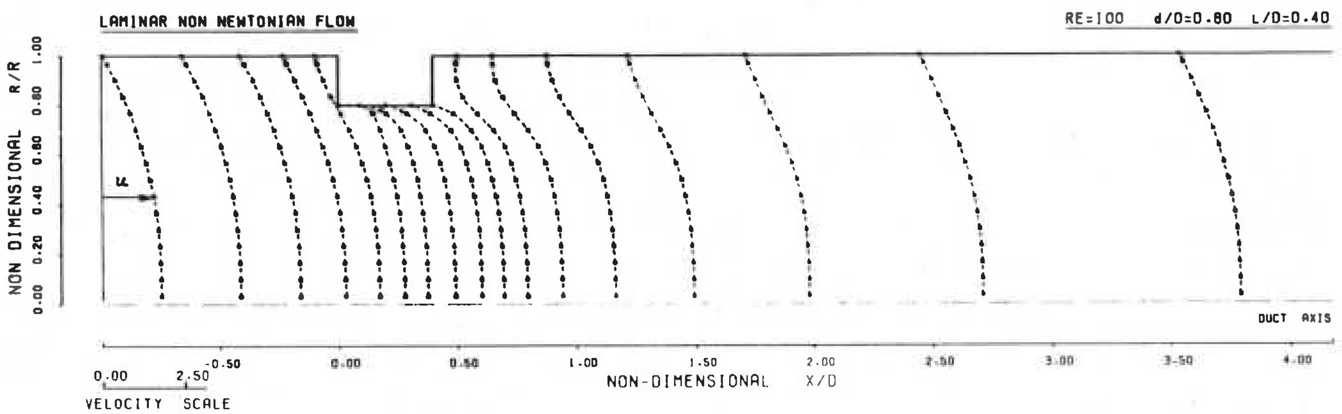

(b) Axial velocity profiles

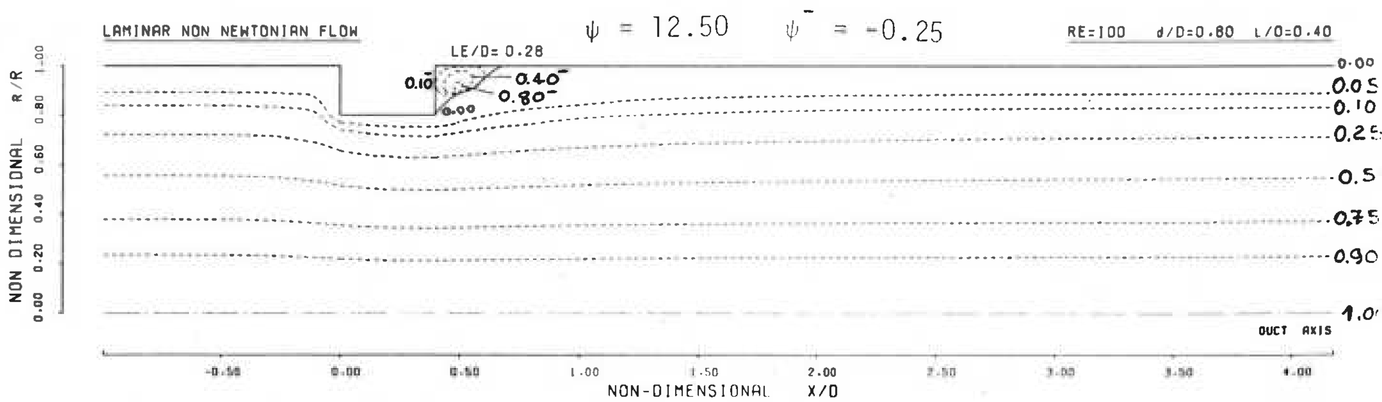

(c) Streamlines

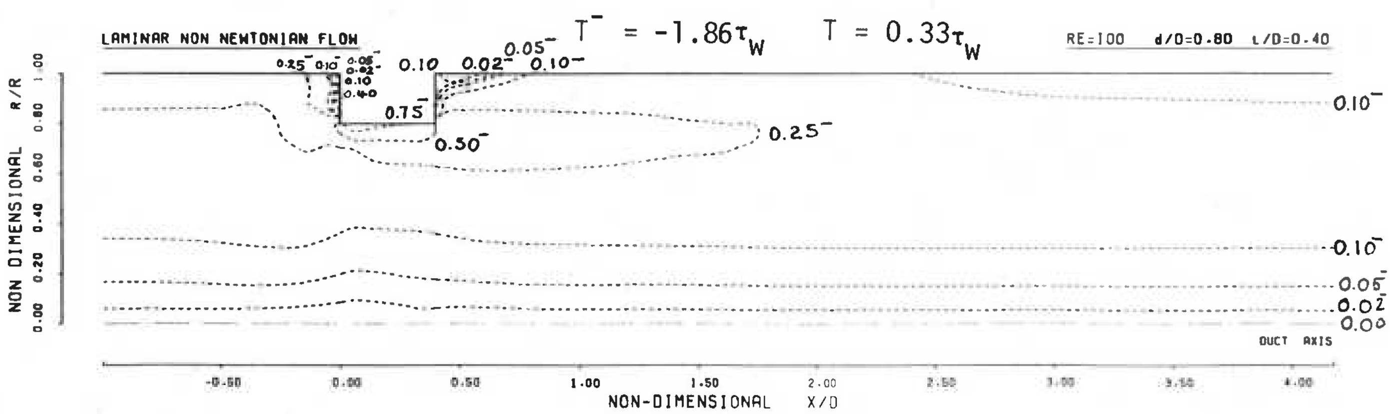

(d) Shear stress contours

Fig. 2.6.5-1 Laminar non-Newtonian blood flow around an aortic stenosis (Re = 100, d/D = 0.80, l/D = 0.40)

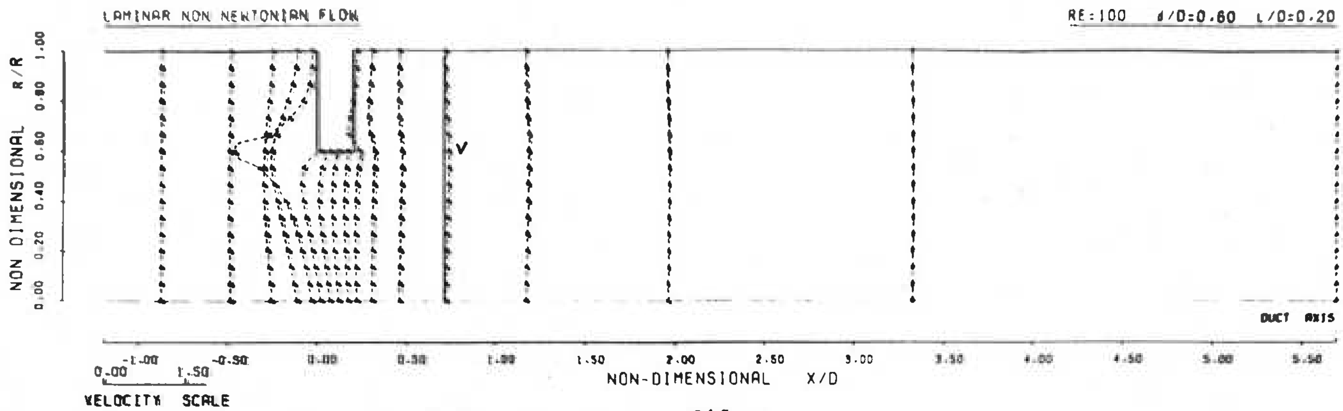

(a) Radial velocity profiles

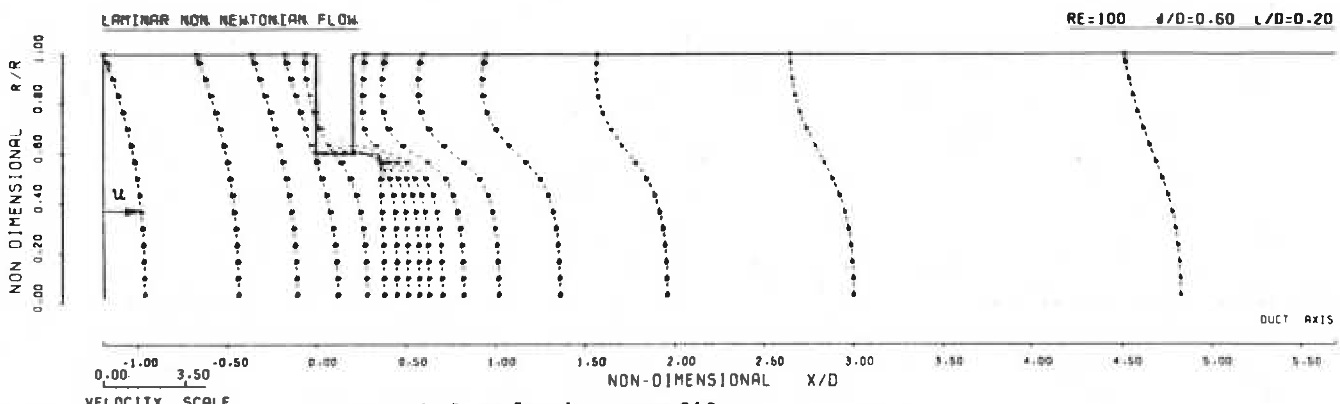

(b) Axial velocity profiles

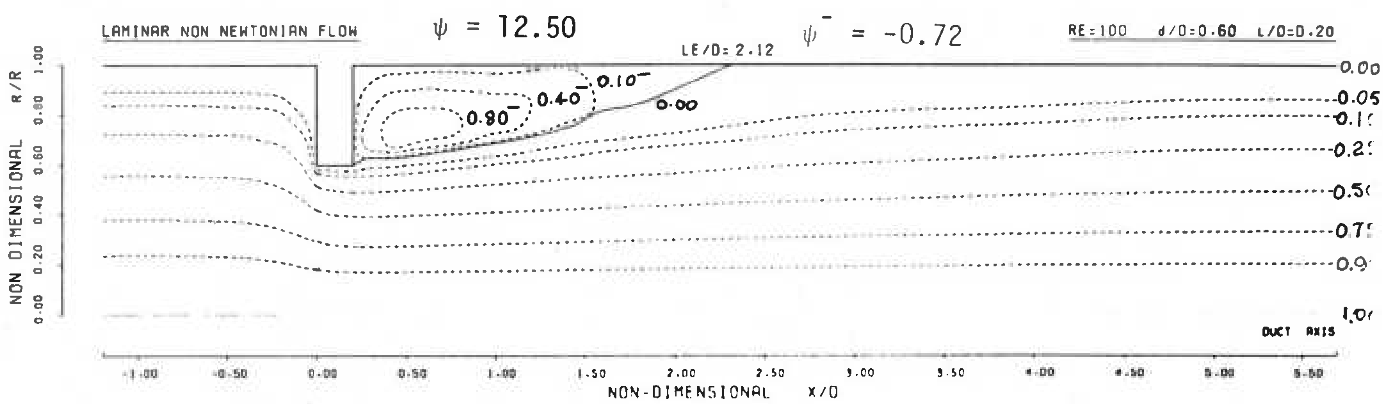

(c) Streamlines

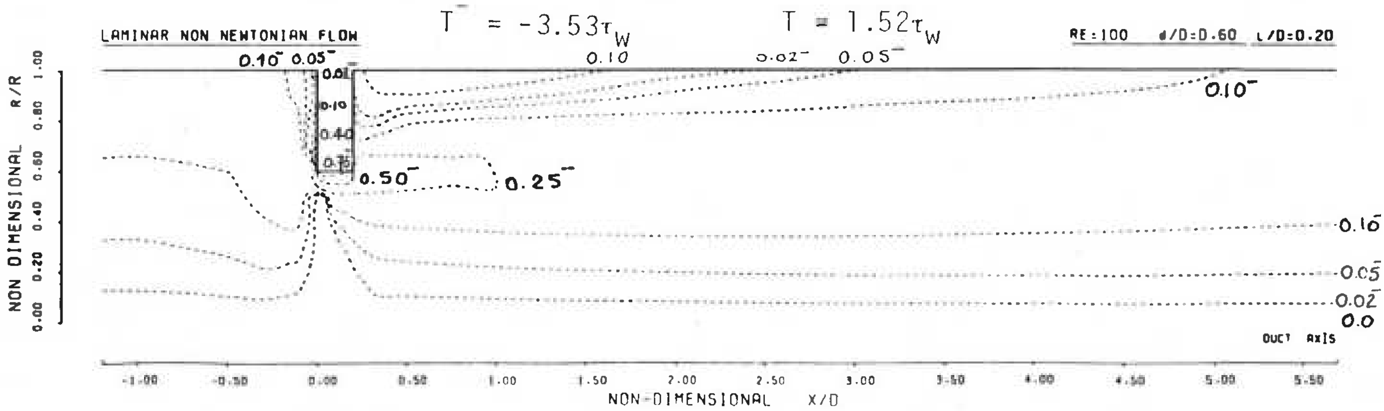

(d) Shear stress contours

Fig. 2.6.5-2 Laminar non-Newtonian blood flow around an aortic stenosis
(Re = 100, d/D = 0.60, l/D = 0.20)

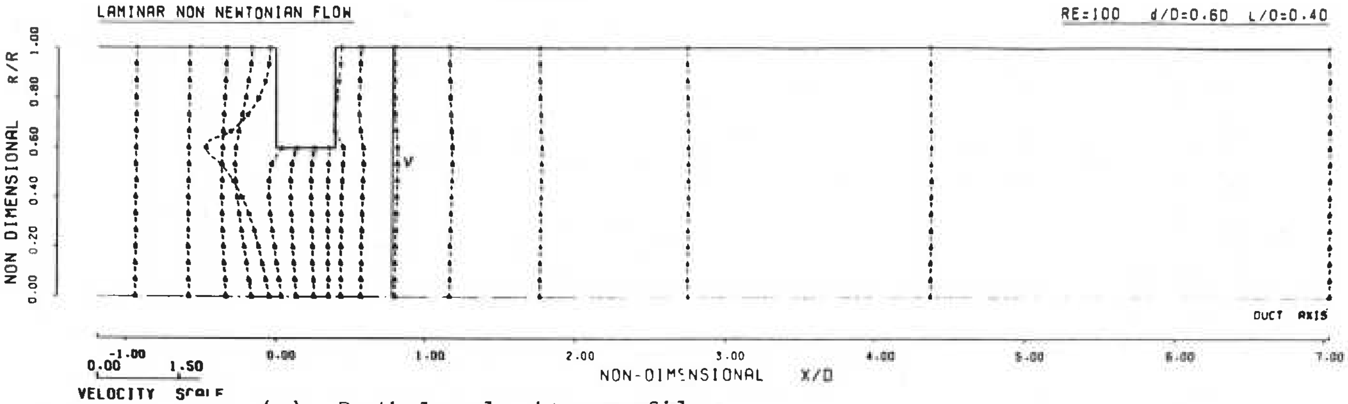

(a) Radial velocity profiles

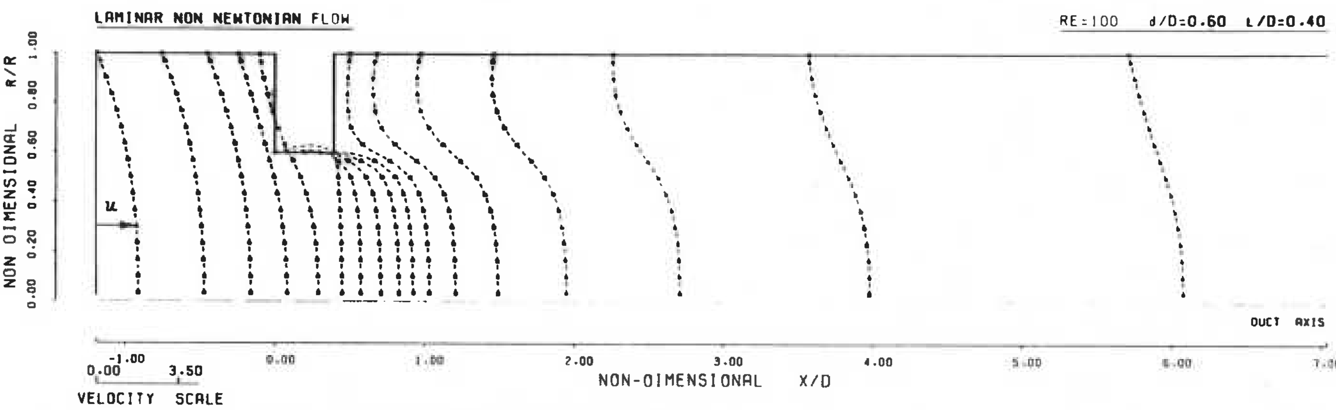

(b) Axial velocity profiles

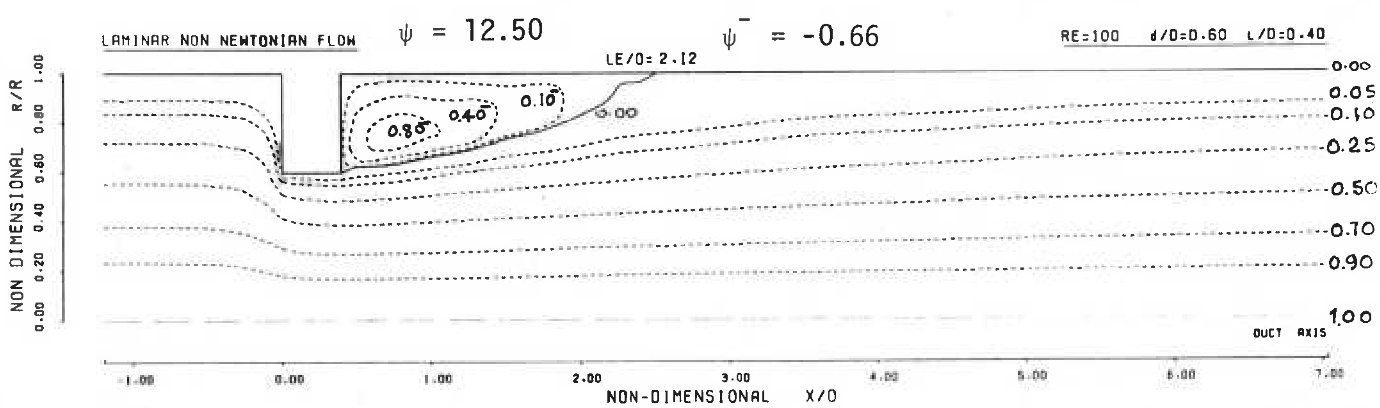

(c) Streamlines

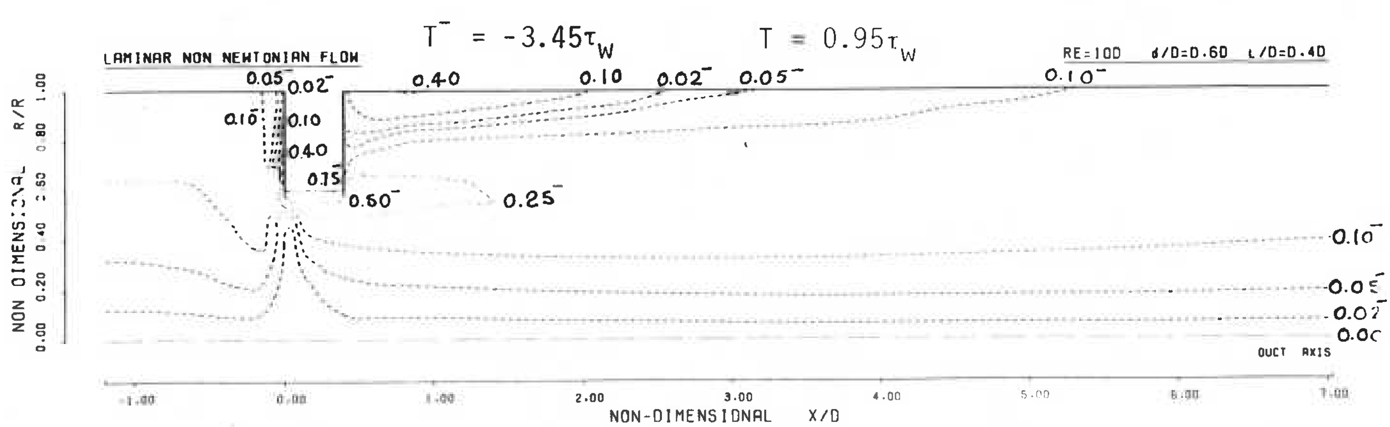

(d) Shear stress contours

Fig. 2.6.5-3 Laminar non-Newtonian blood flow around an aortic stenosis
($Re = 100$, $d/D = 0.60$, $l/D = 0.40$)

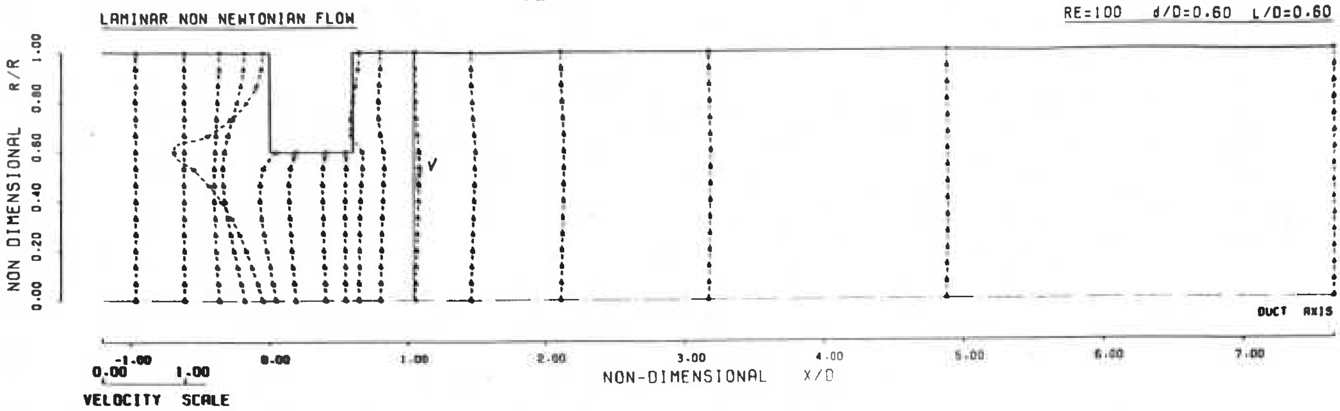

(a) Radial velocity profiles

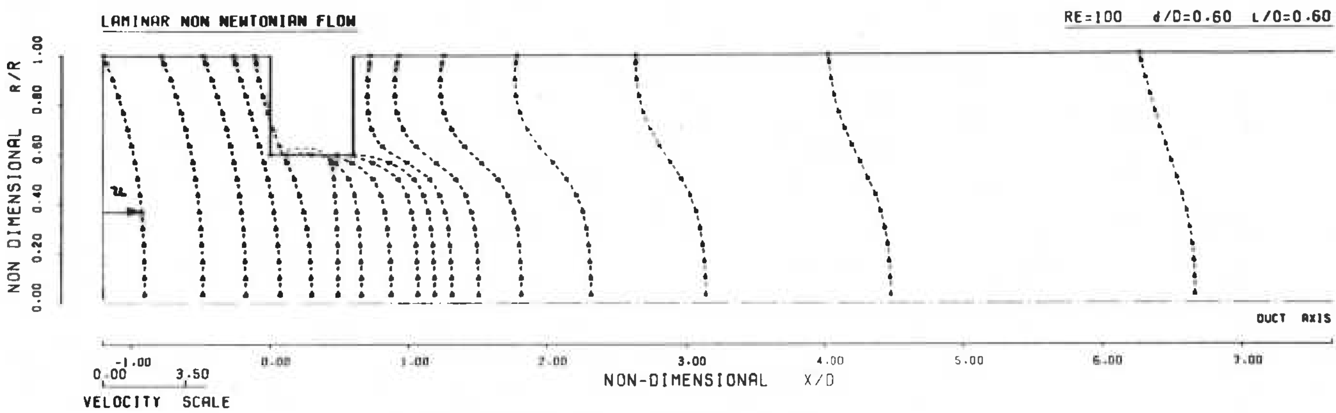

(b) Axial velocity profiles

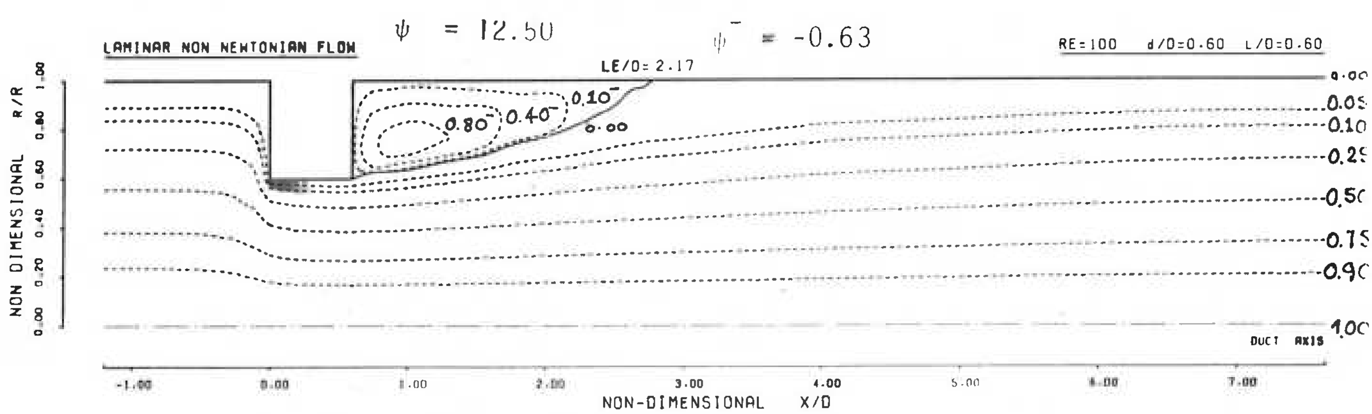

(c) Streamlines

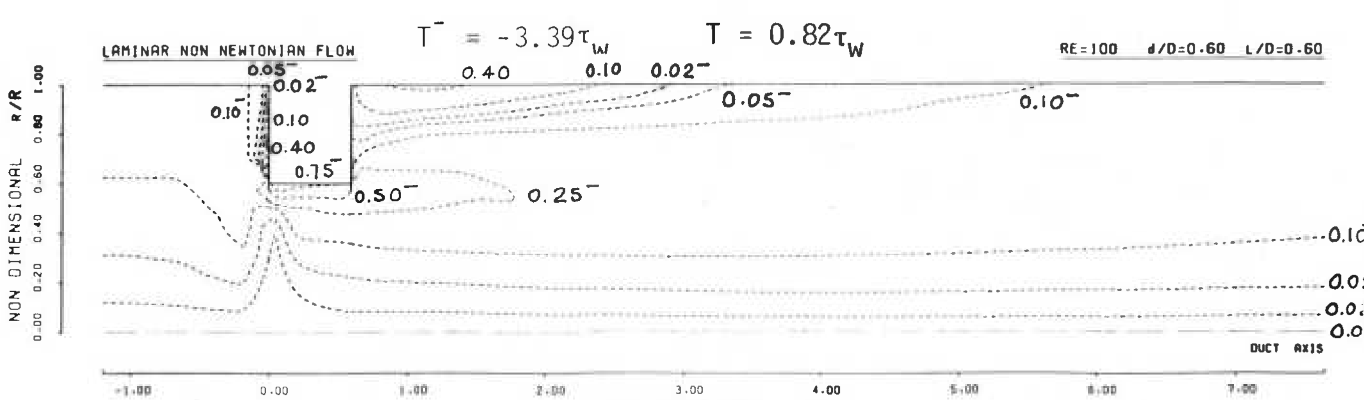

(d) Shear stress contours

Fig. 2.6.5-4 Laminar non-Newtonian blood flow around an aortic stenosis
(Re = 100, d/D = 0.60, l/D = 0.60)

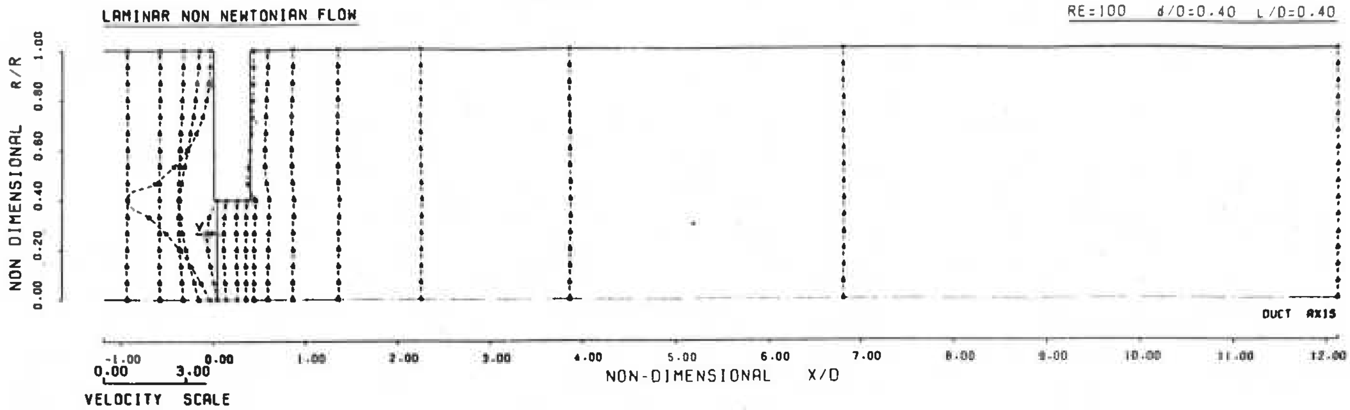

(a) Radial velocity profiles

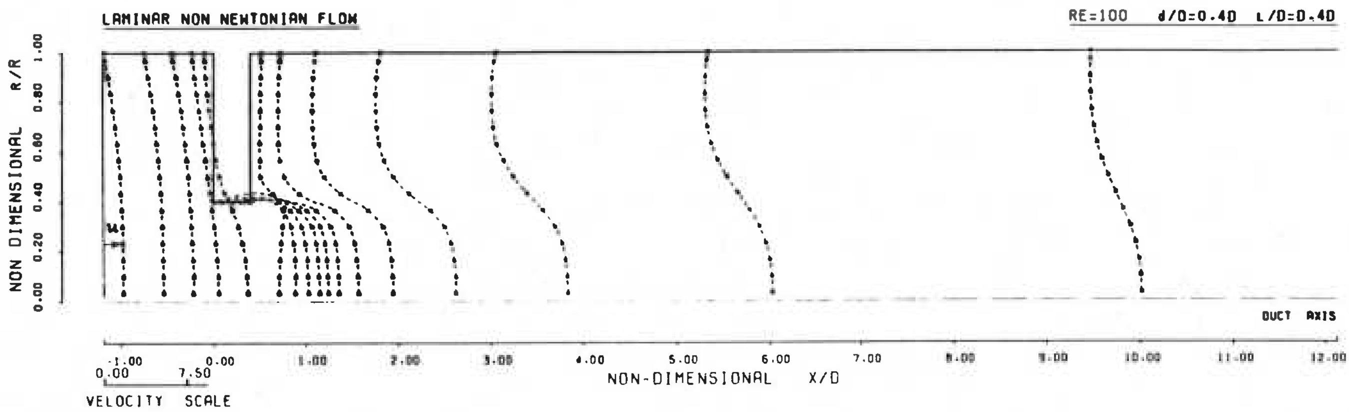

(b) Axial velocity profiles

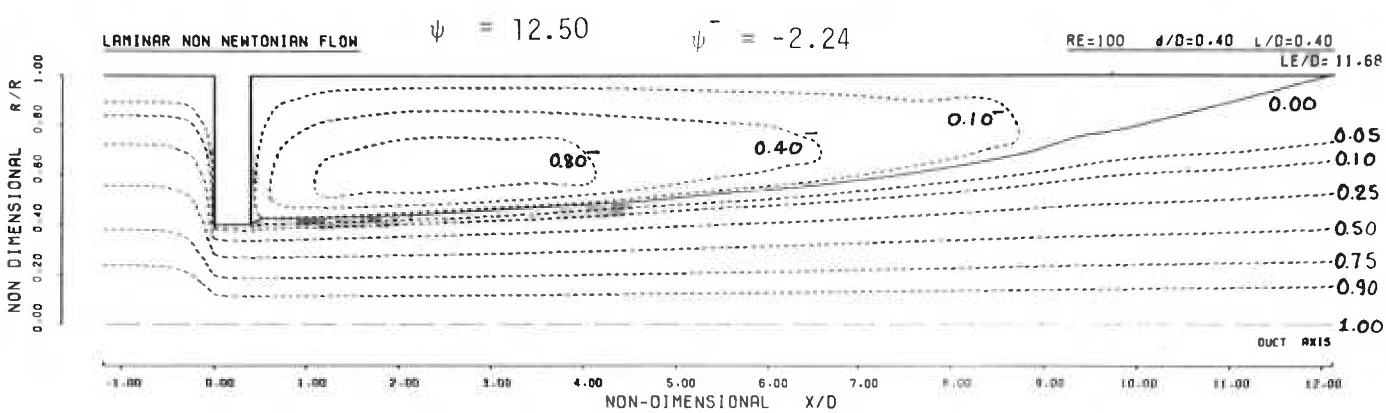

(c) Streamlines

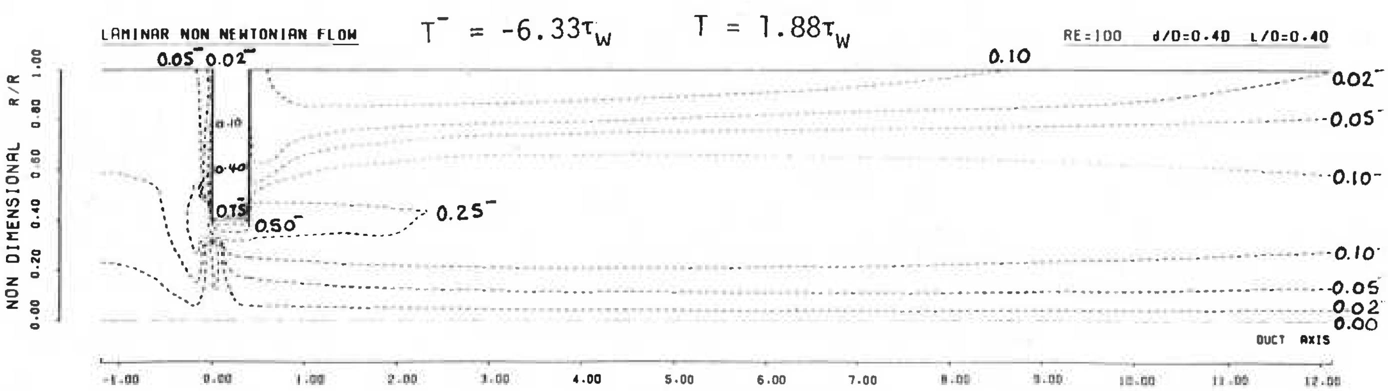

(d) Shear stress contours

Fig. 2.6.5-5 Laminar non-Newtonian blood flow around an aortic stenosis (Re = 100, d/D = 0.40, l/D = 0.40)

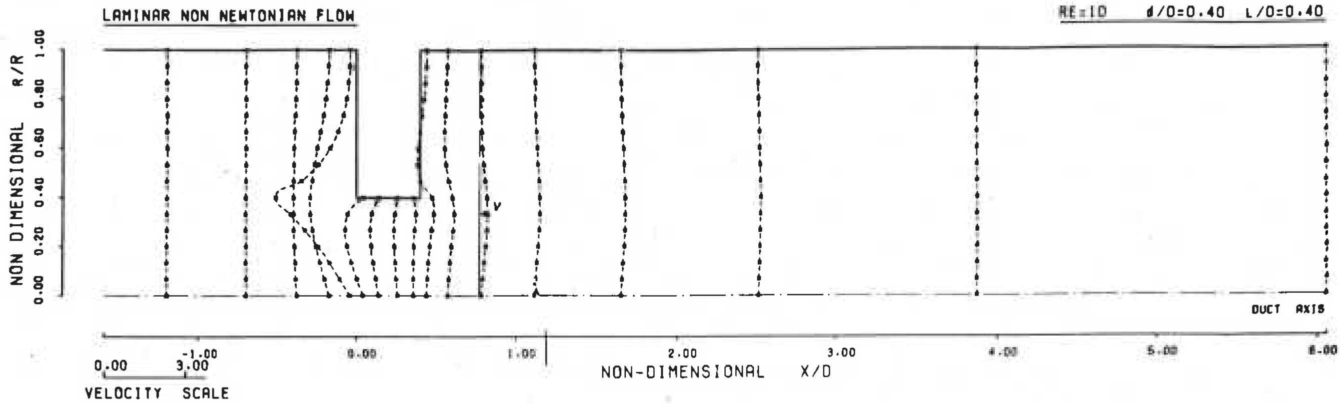

(a) Radial velocity profiles

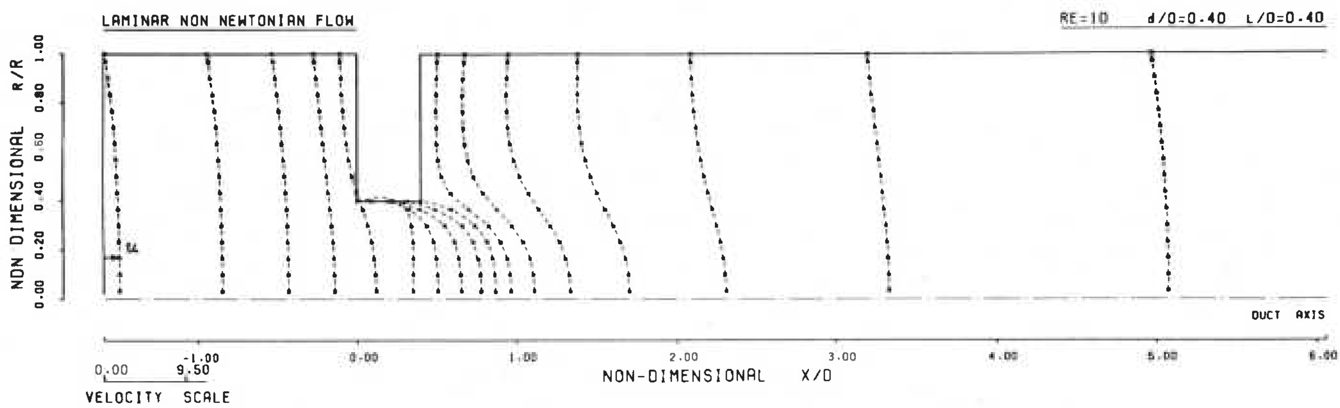

(b) Axial velocity profiles

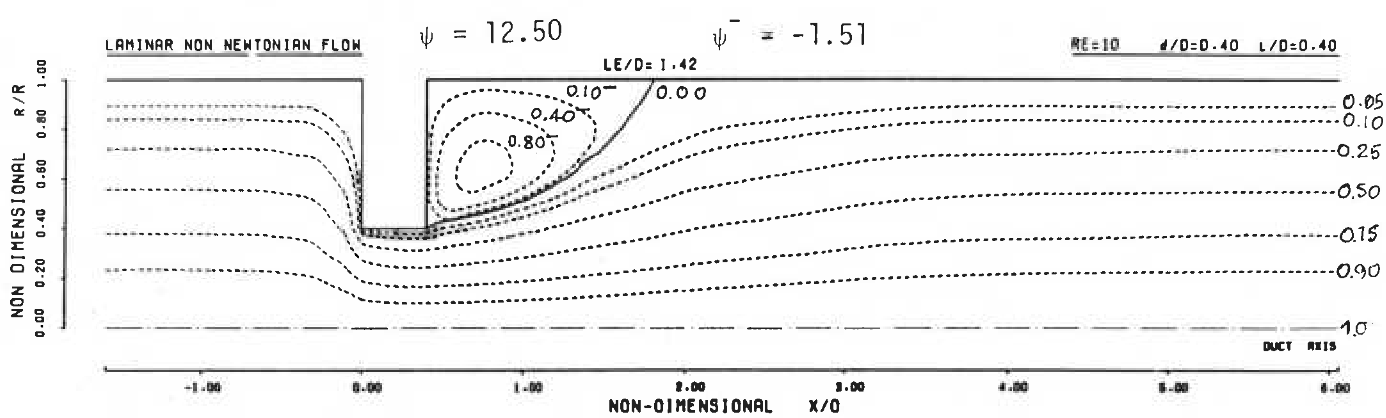

(c) Streamlines

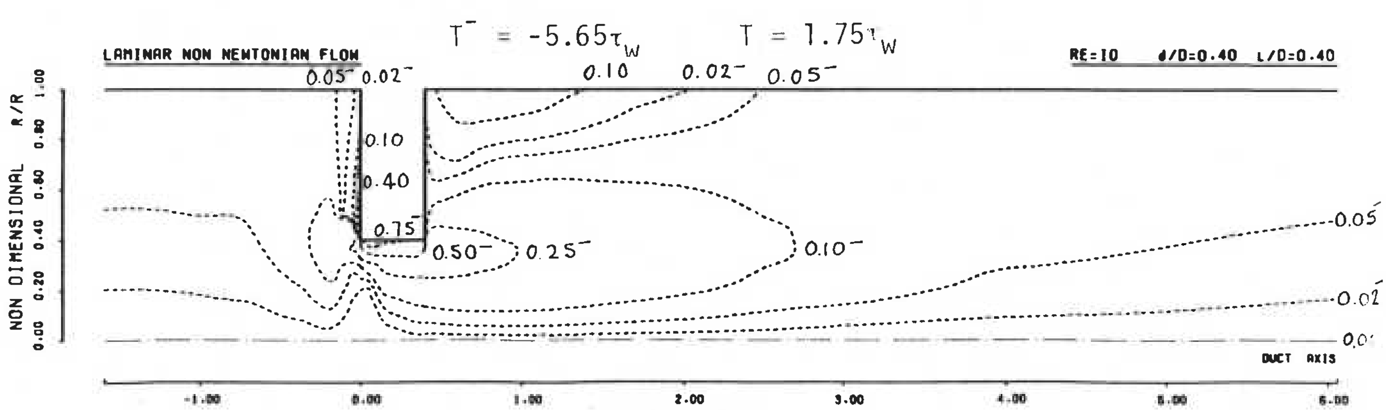

(d) Shear stress contours

Fig. 2.6.5-6 Laminar non-Newtonian blood flow around an aortic stenosis (Re = 10, d/D = 0.40, l/D = 0.40)

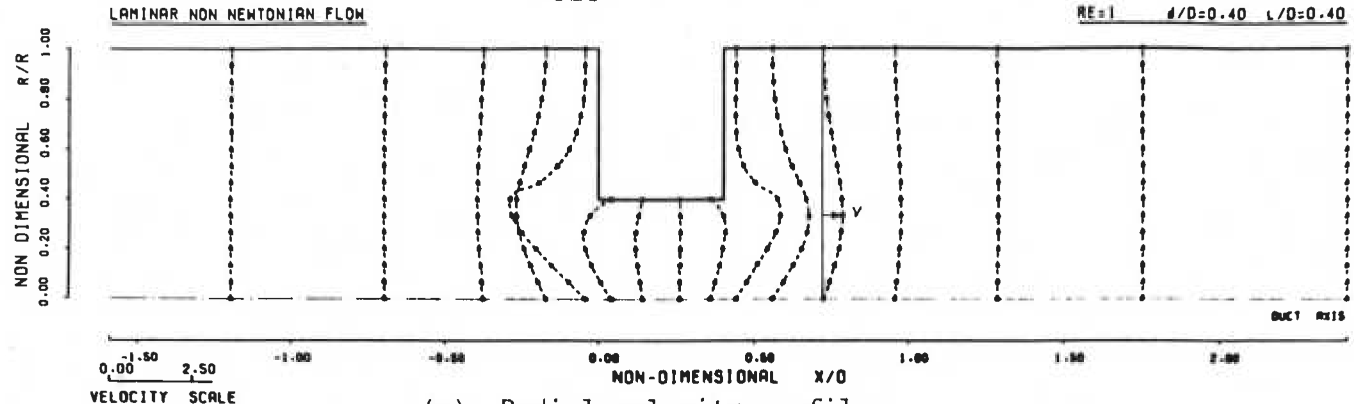

(a) Radial velocity profiles

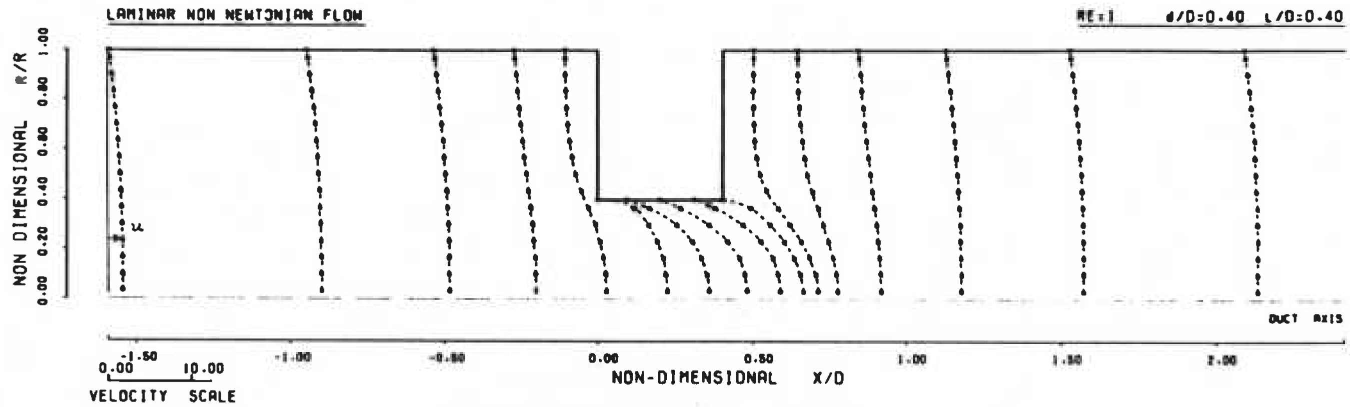

(b) Axial velocity profiles

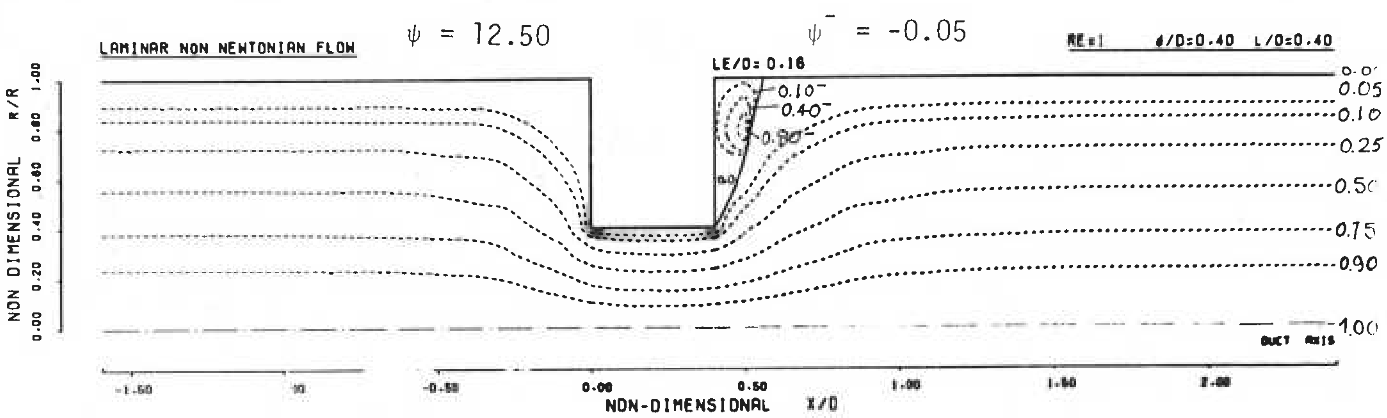

(c) Streamlines

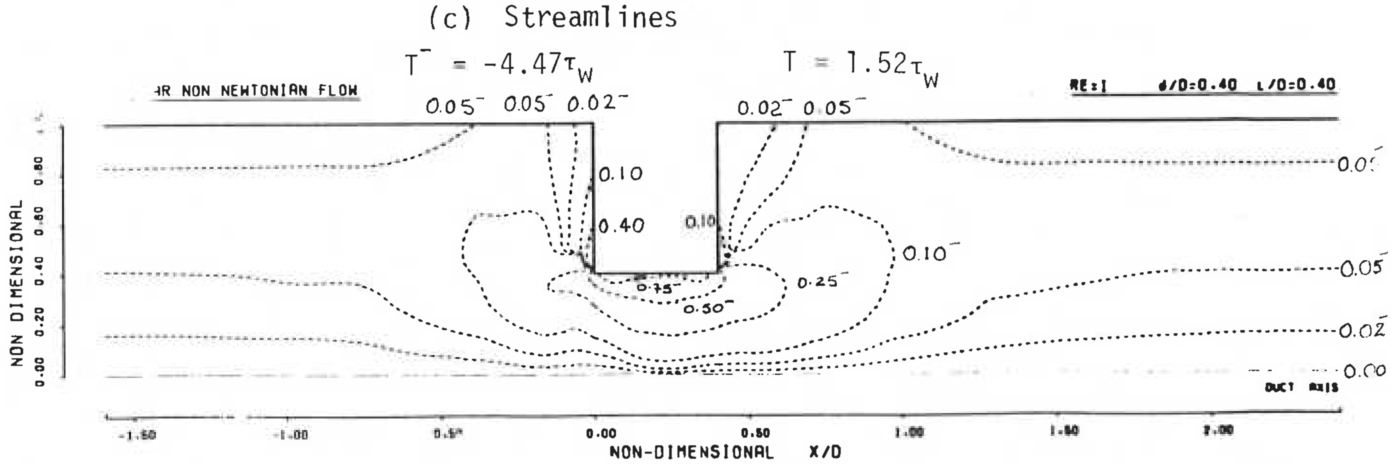

(d) Shear stress contours

Fig. 2.6.5-7 Laminar non-Newtonian blood flow around an aortic stenosis
(Re = 1, d/D = 0.40, l/D = 0.40)

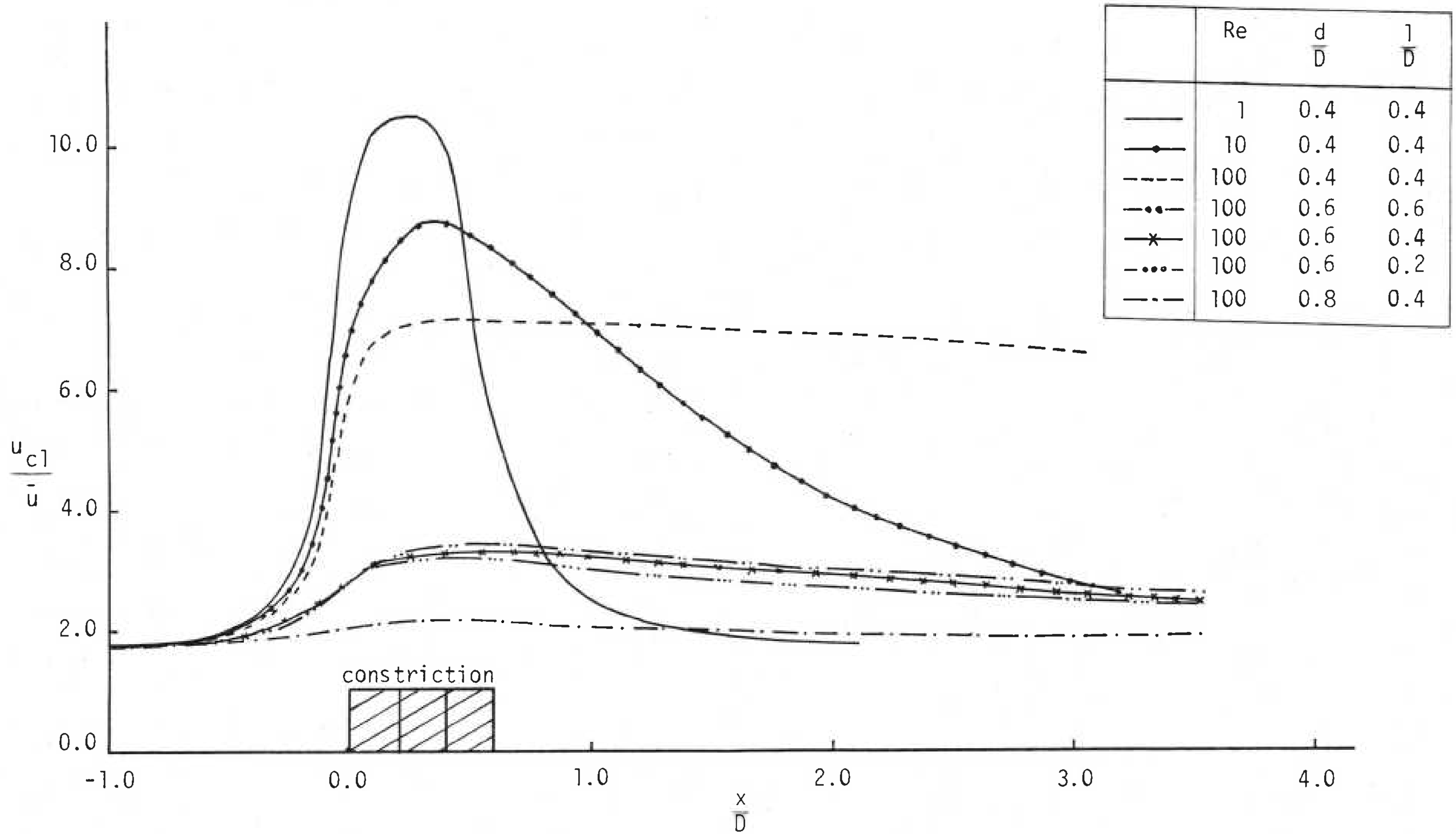

Fig. 2.6.5-8 Development of centre-line axial velocity for non-Newtonian blood flow around an aortic stenosis

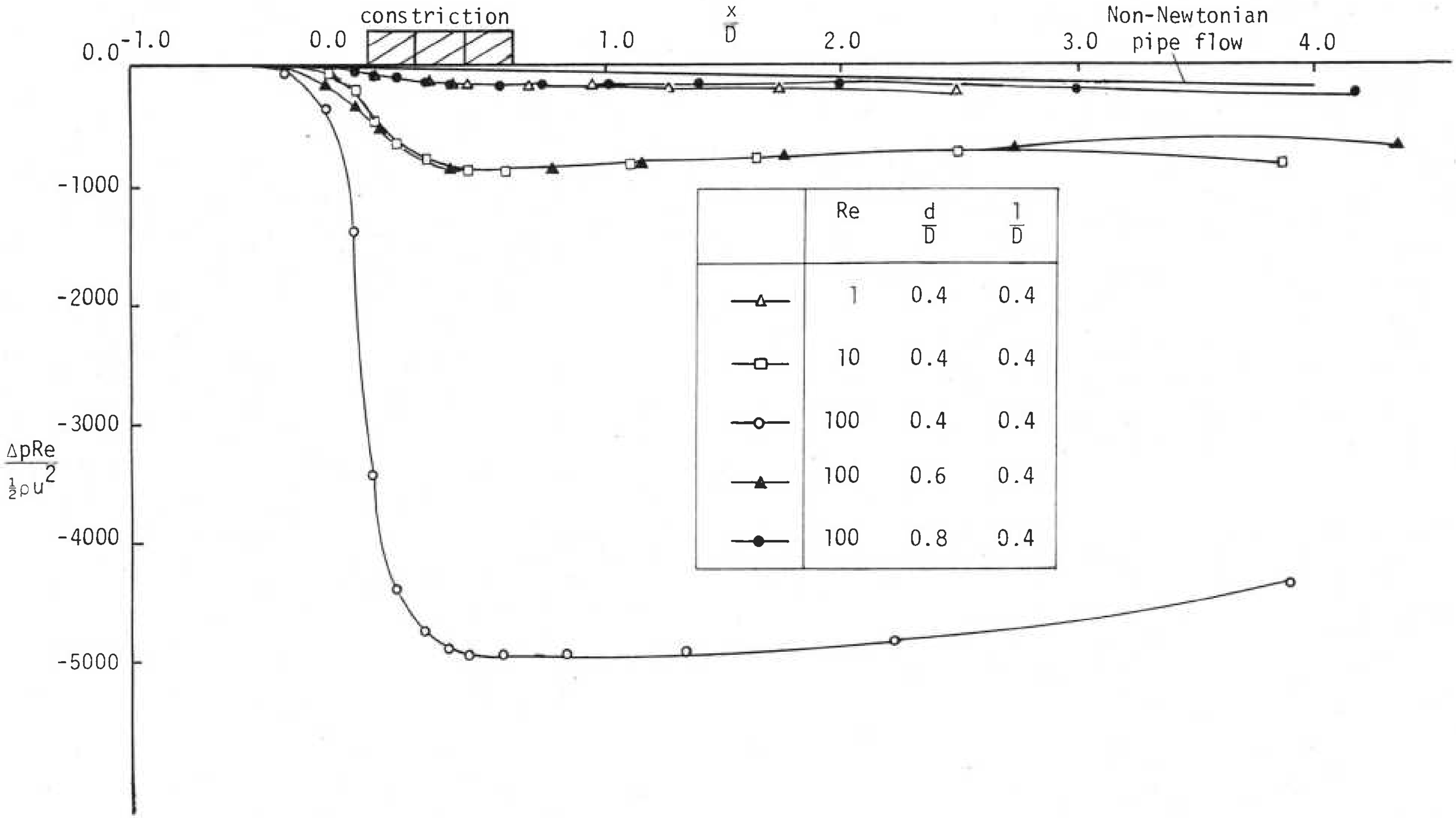

Fig. 2.6.5-9 Development of centre-line pressure for non-Newtonian blood flow around an aortic stenosis

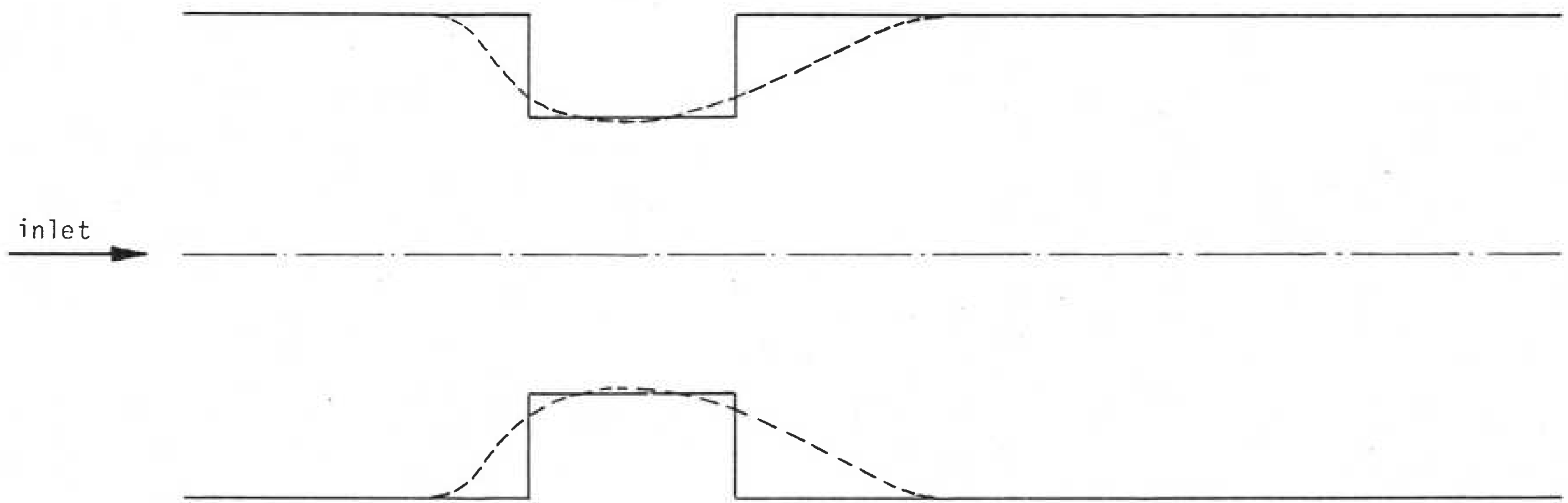

Fig. 2.6.5-10 Possible deformation of aortic stenosis due to shear forces

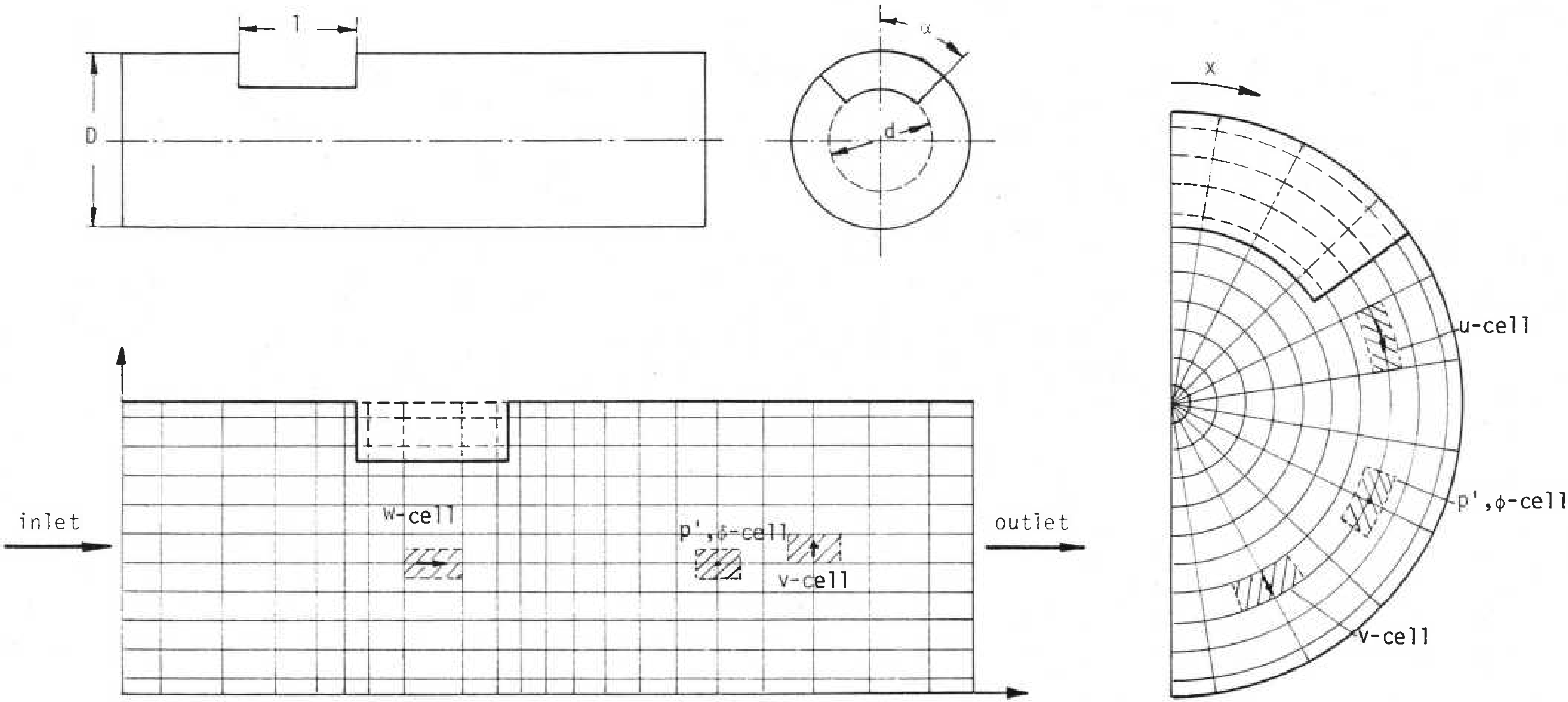

Fig. 2.6.6-1 The 12 x 12 x 22 grid for the flow around an asymmetric obstacle

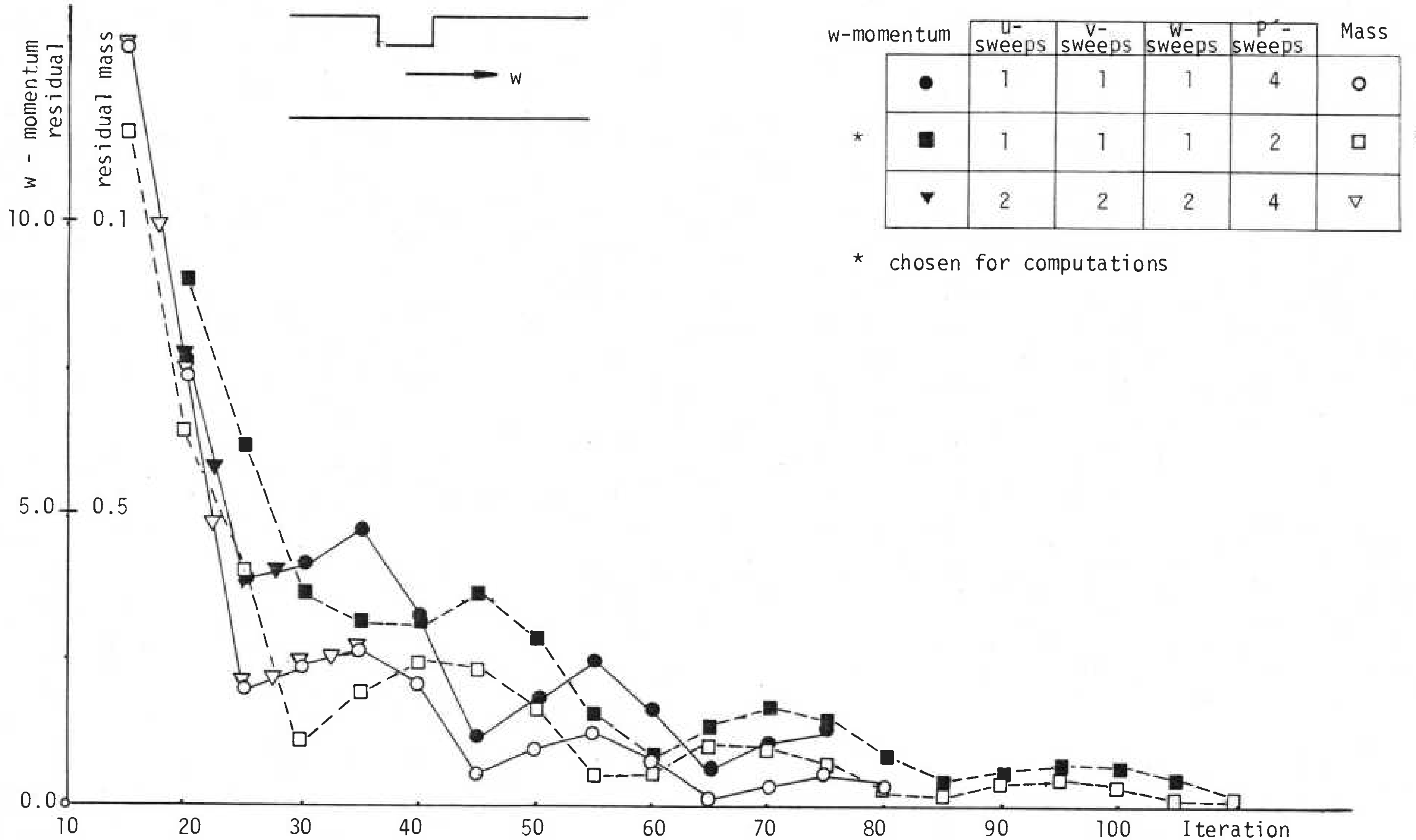

Fig. 2.6.6-2 Rate of convergence for 3-D elliptic flows (Grid 12 x 12 x 22, Newtonian flow, Re = 10, $\frac{d}{D}$ = 0.4, $\frac{l}{D}$ = 0.4, α = 72^{o} - residual sources v.number of iterations)

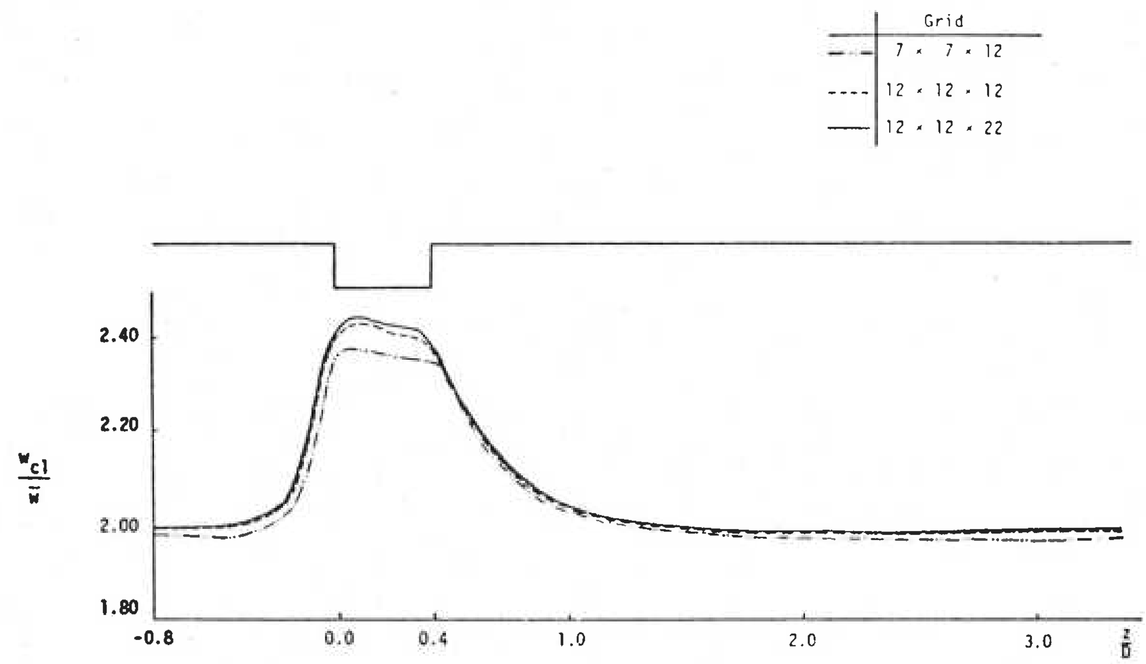

(a) Centre line axial velocity development

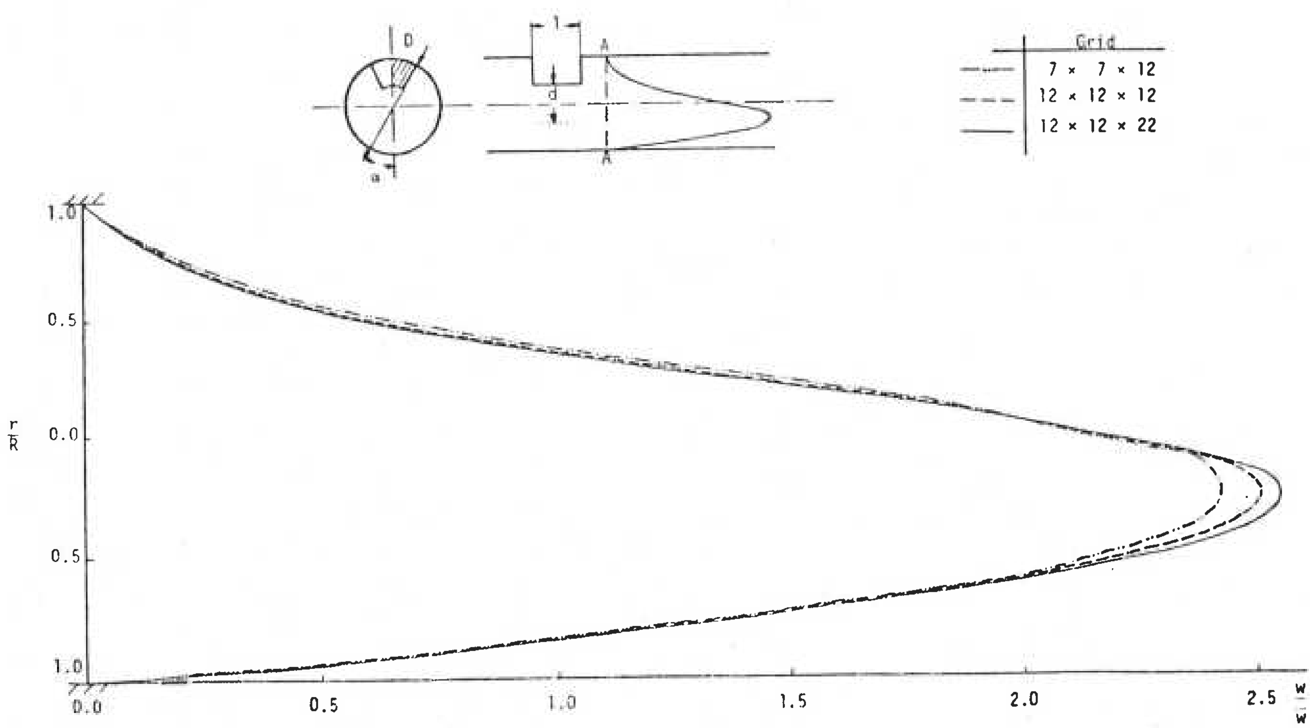

(b) Axial velocity profile at A-A

Fig. 2.6.6-3 Grid independence test for the flow around an asymmetric obstacle

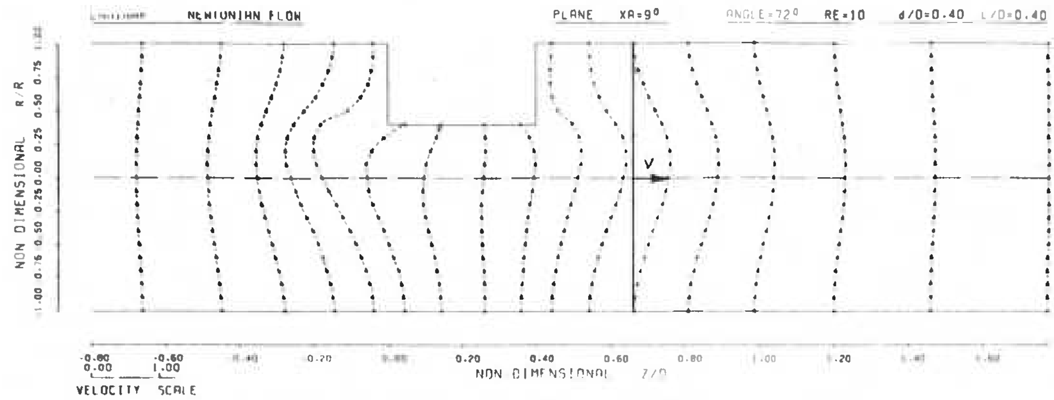

(a) Radial velocity profiles

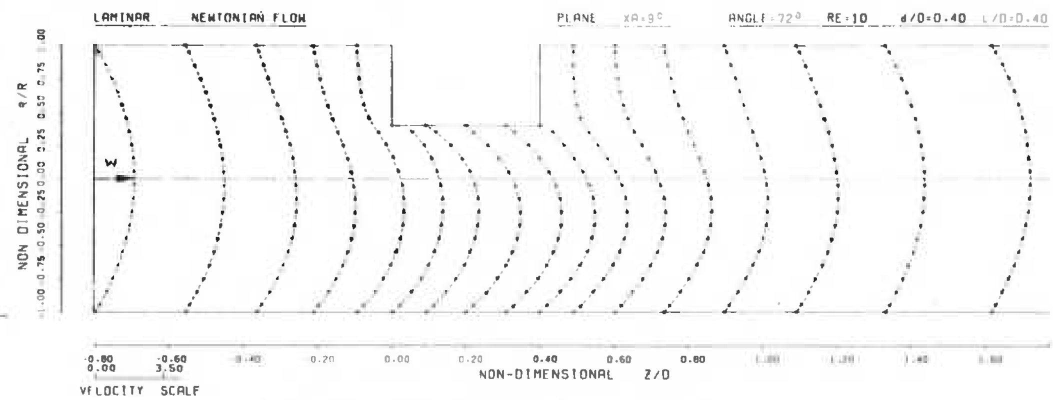

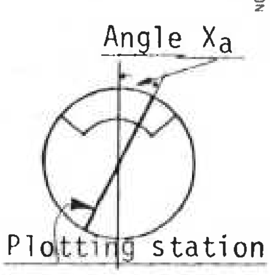

(b) Axial velocity profiles

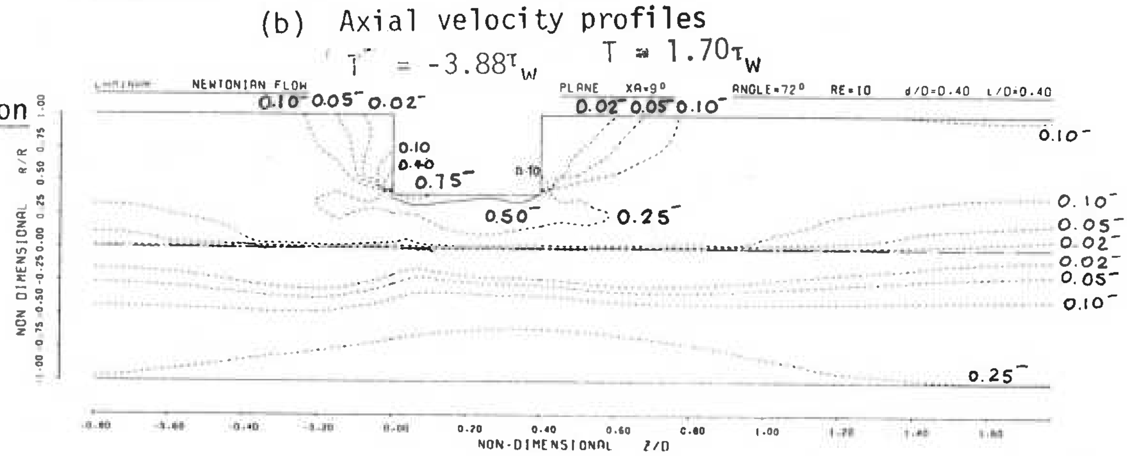

(c) Shear stress contours

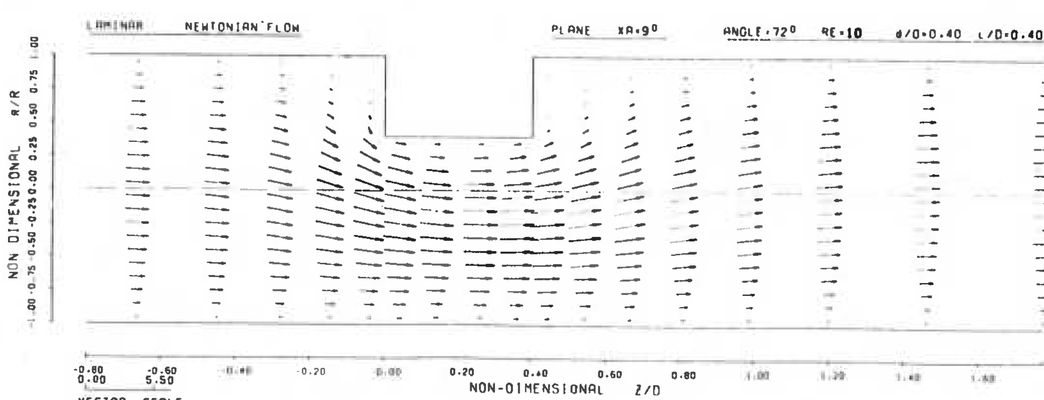

(d) Velocity vector field

Fig. 2.6.6-4 Laminar Newtonian flow around an asymmetric obstacle (Re = 10, d/D = 0.40, l/D = 0.40) - Plane XA = 9°

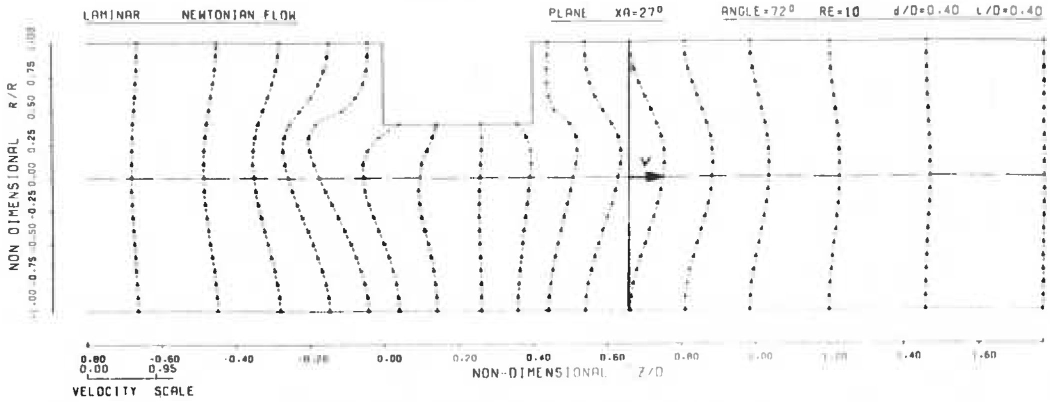

(a) Radial velocity profiles

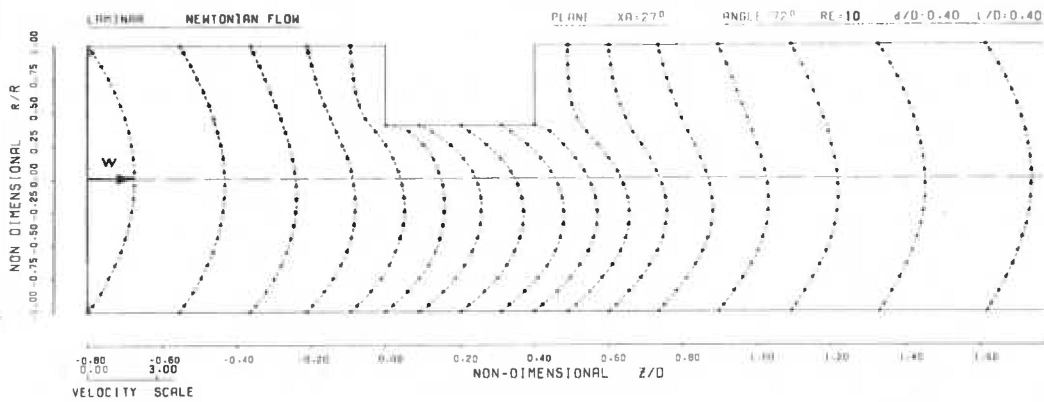

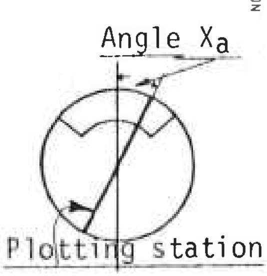

(b) Axial velocity profiles

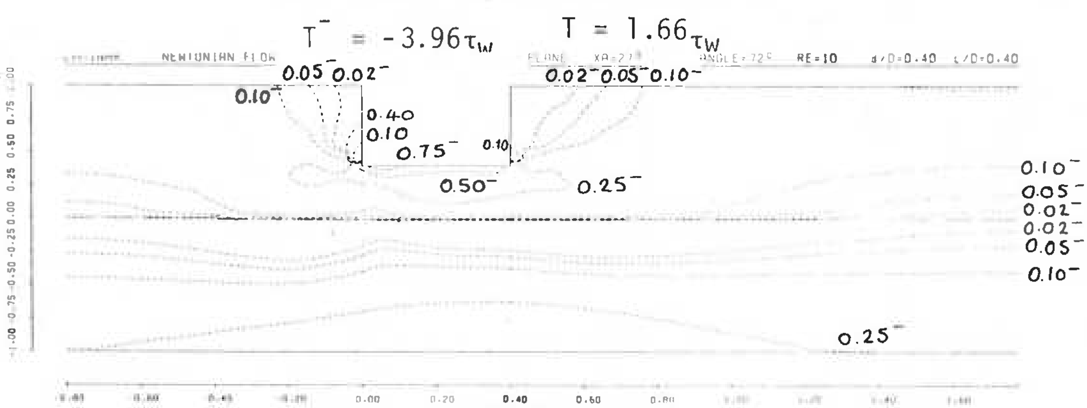

(c) Shear stress contours

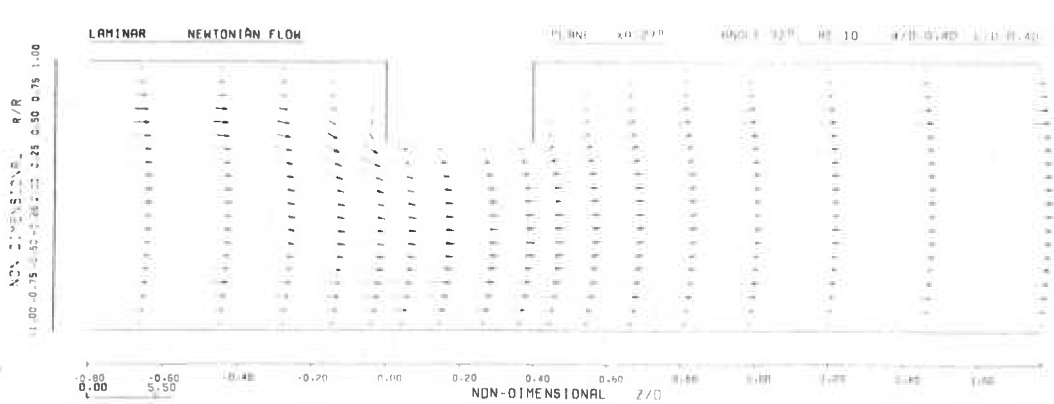

(d) Velocity vector field

Fig. 2.6.6-5 Laminar Newtonian flow around an asymmetric obstacle (Re = 10, d/D = 0.40, 1/D = 0.40) - Plane XA = 270

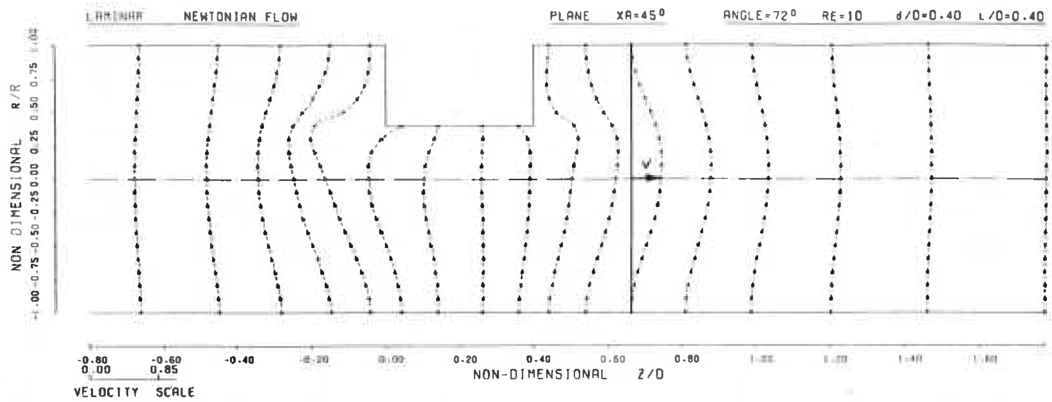

(a) Radial velocity profiles

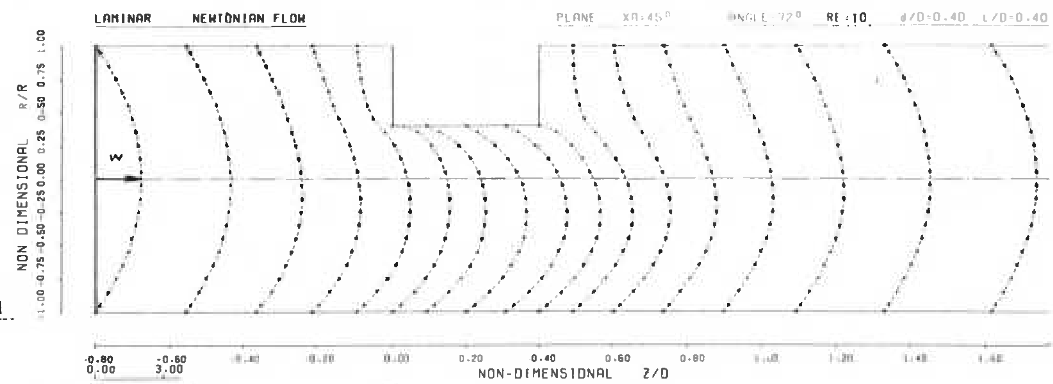

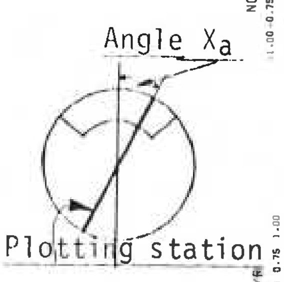

(b) Axial velocity profiles

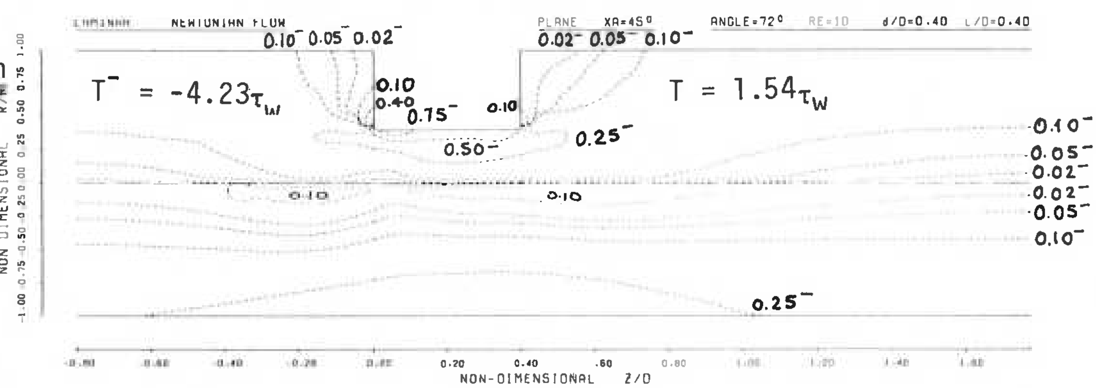

(c) Shear stress contours

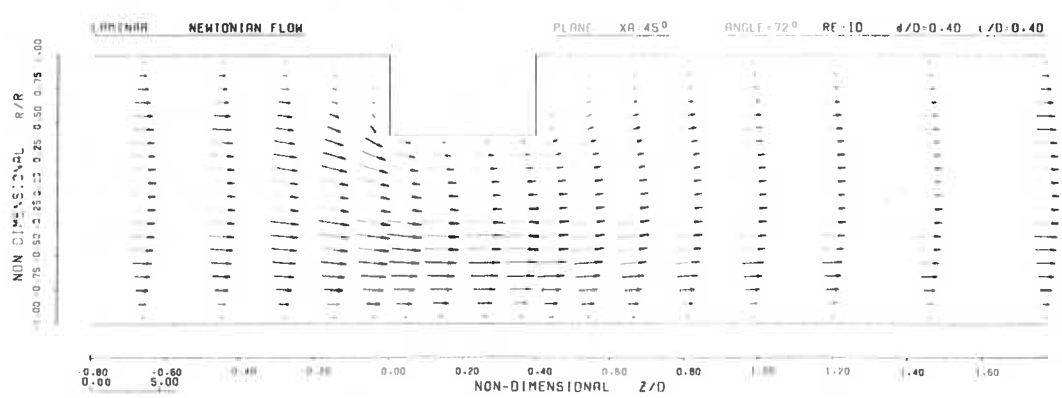

(d) Velocity vector field

Fig. 2.6.6-6 Laminar Newtonian flow around an asymmetric obstacle (Re = 10, d/D = 0.40, l/D = 0.40) - Plane XA = 45°

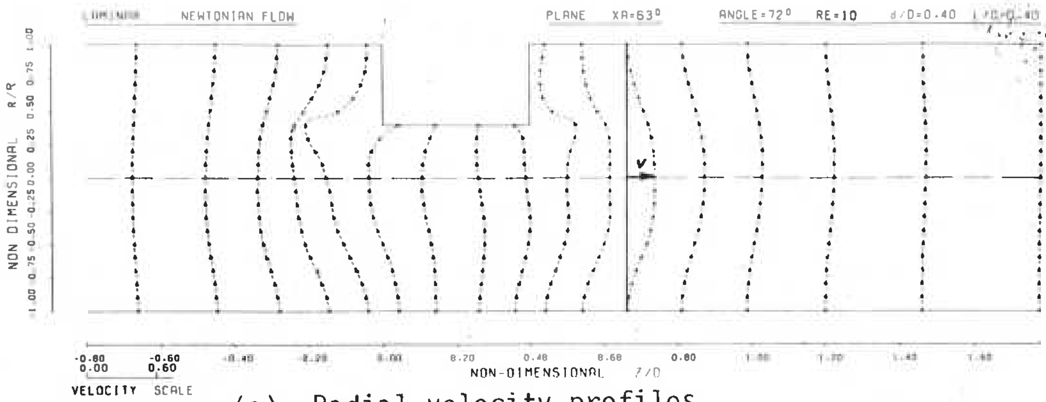

(a) Radial velocity profiles

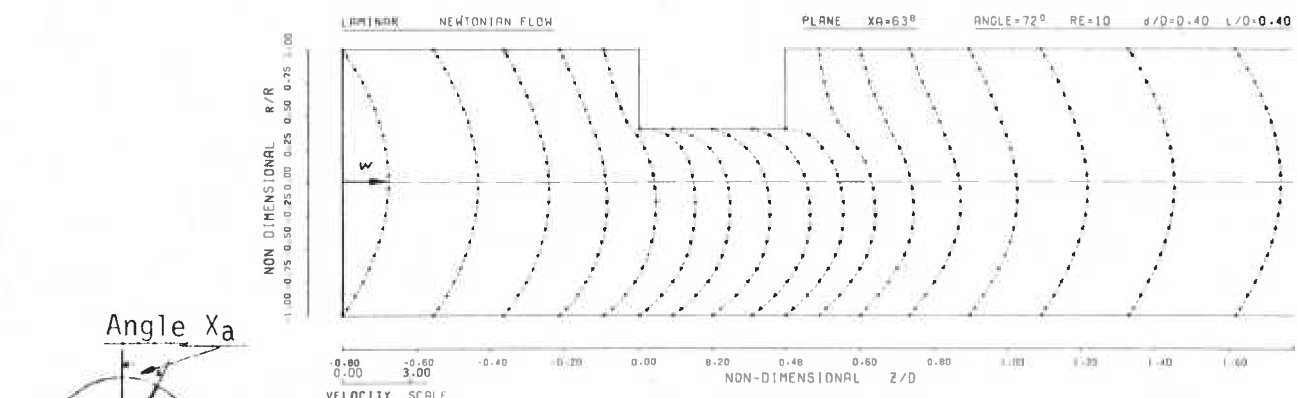

(b) Axial velocity profiles

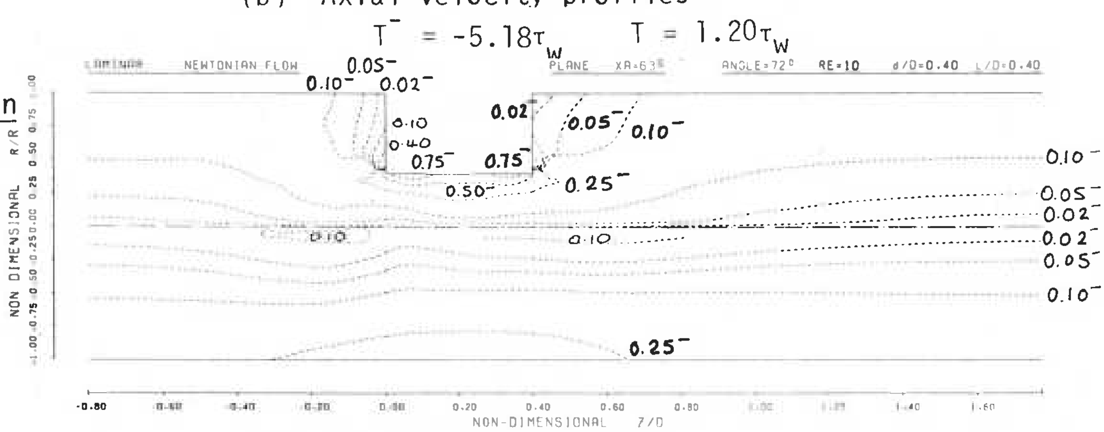

(c) Shear stress contours

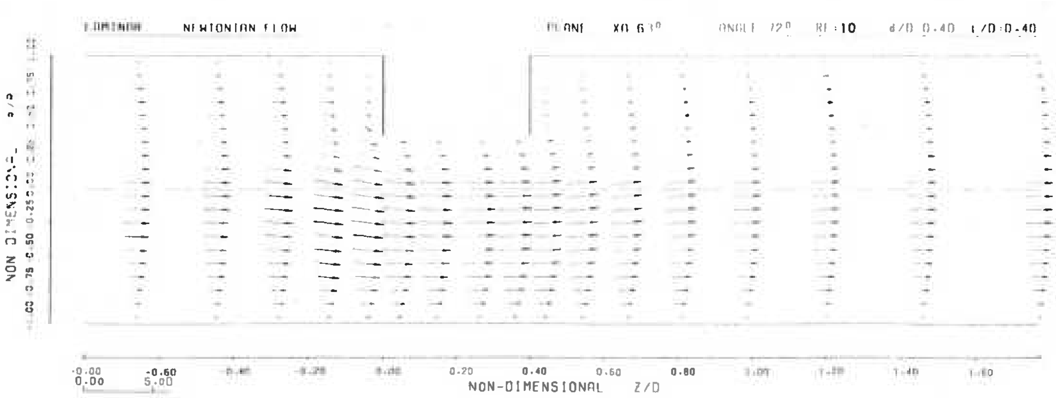

(d) Velocity vector field

Fig. 2.6.6-7 Laminar Newtonian flow around an asymmetric obstacle (Re = 10, d/D = 0.40, l/D = 0.40) - Plane XA = 63°

$T^{-} = -1.07\tau_w$ $T = 0.36\tau_w$

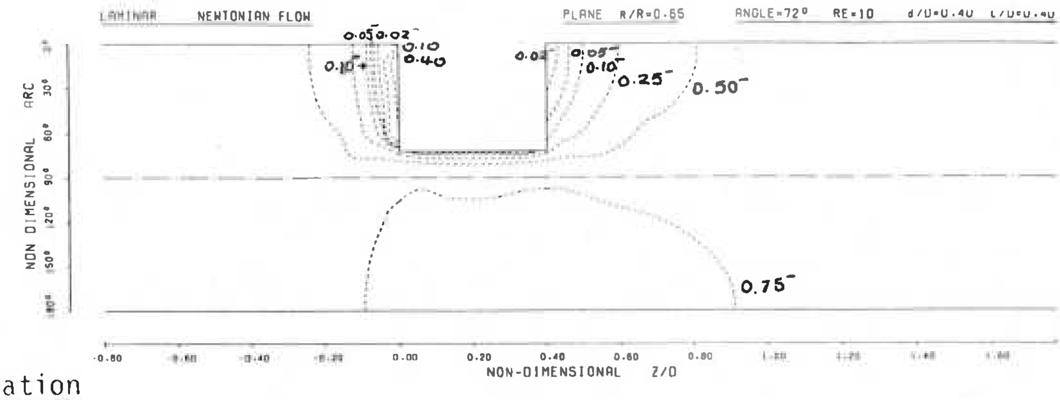

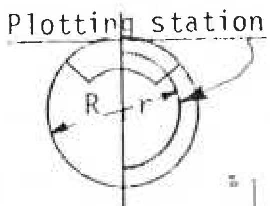

(a) Shear stress contours

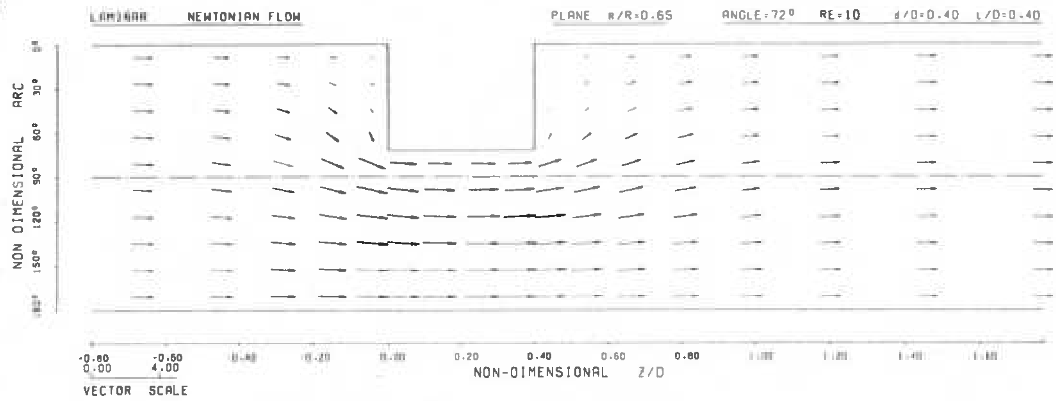

(b) Velocity vector field

$T^{-} = -1.30\tau_w$ $T = 0.13\tau_w$

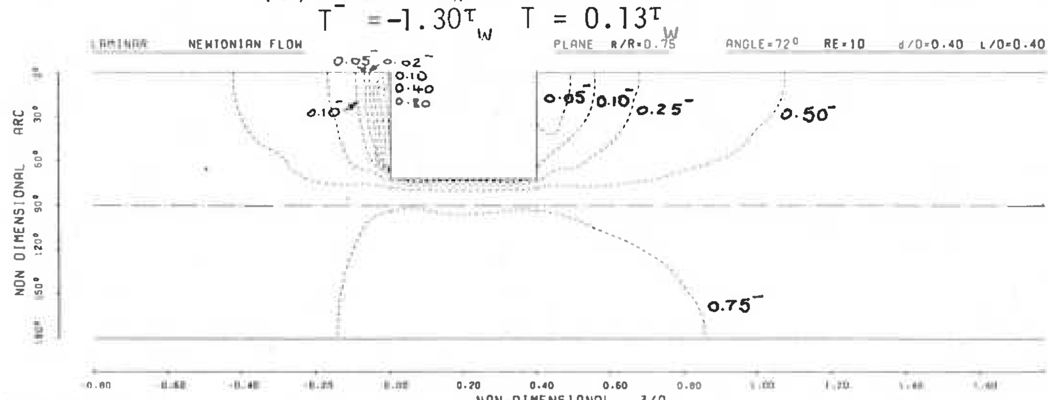

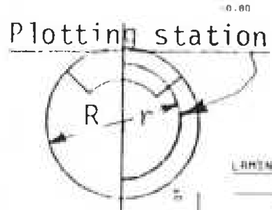

(a) Shear stress contours

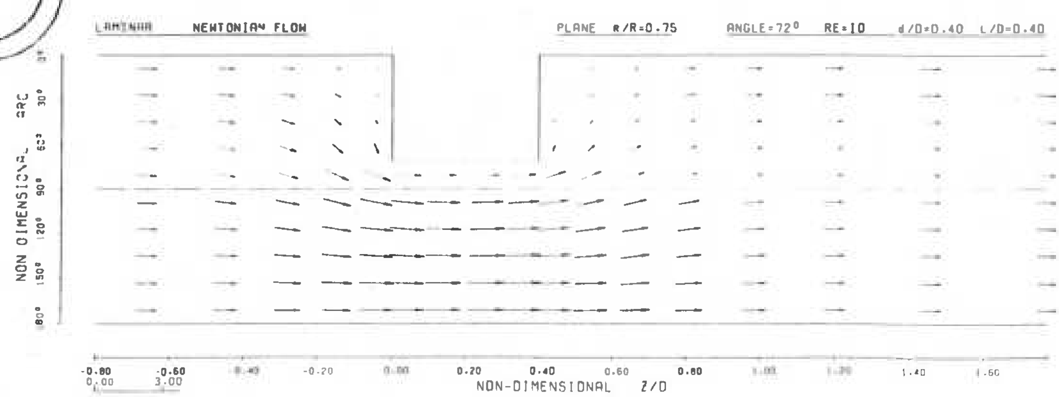

(b) Velocity vector field

Fig. 2.6.6-8 Laminar Newtonian flow around an asymmetric obstacle (Re = 10, d/D = 0.40, l/D = 0.40) - Planes r/R = 0.65, 0.75

$T^{-} = -1.55\tau_W$ $T = 0.025\tau_W$

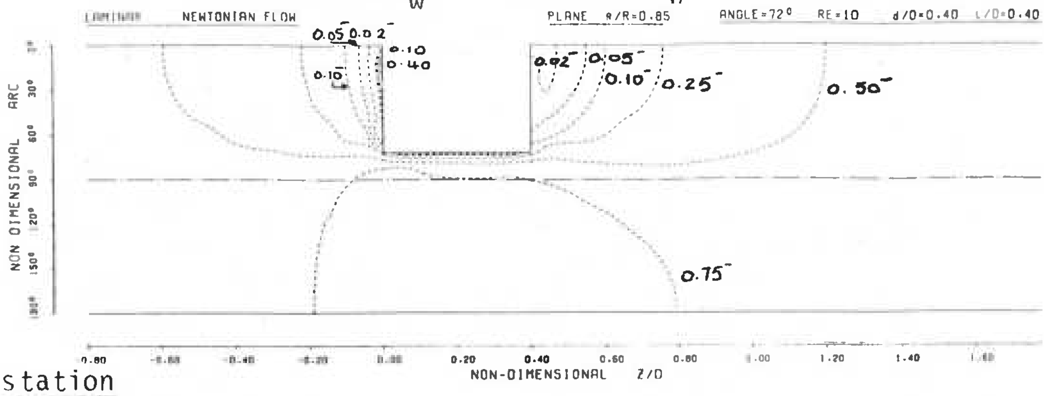

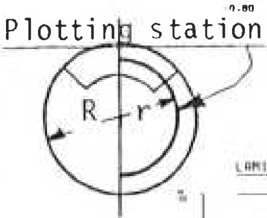

(a) Shear stress contours

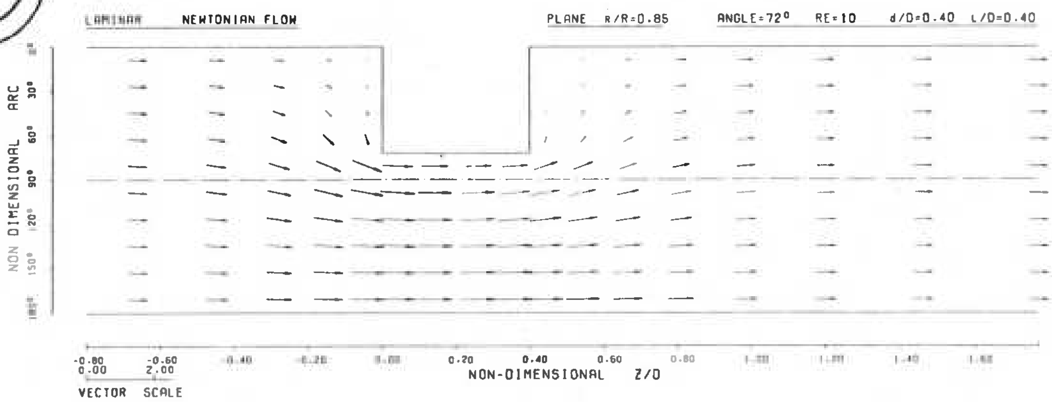

(b) Velocity vector field

$T^{-} = -1.83\tau_W$ $T = 0.013\tau_W$

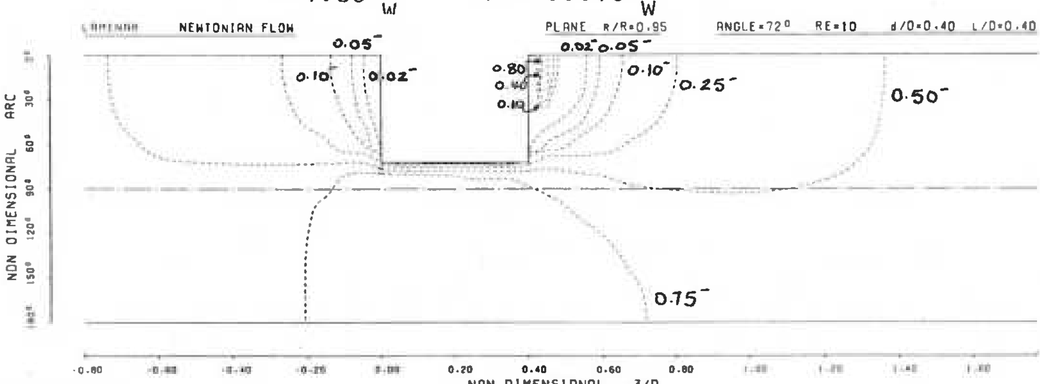

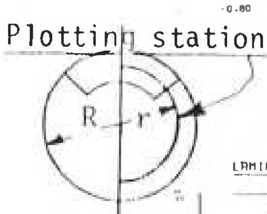

(a) Shear stress contours

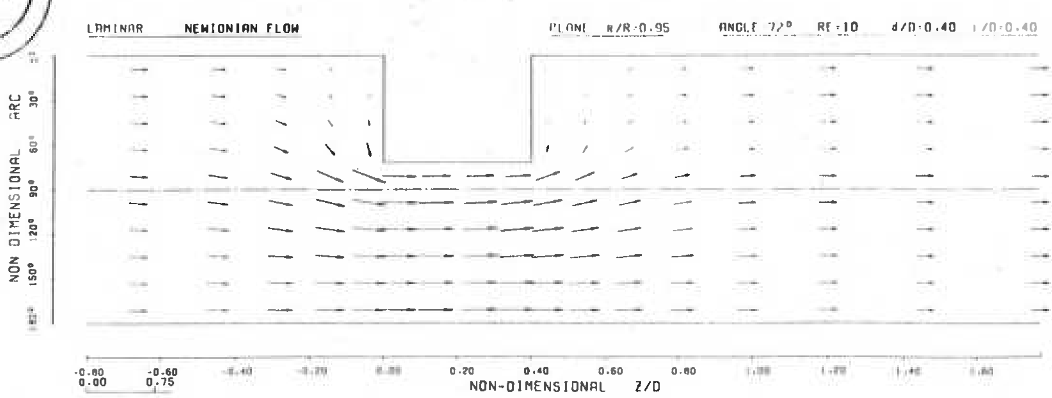

(b) Velocity vector field

Fig. 2.6.6-9 Laminar Newtonian flow around an asymmetric obstacle (Re = 10, d/D = 0.40, l/D = 0.40) - Planes r/R = 0.85,0.95

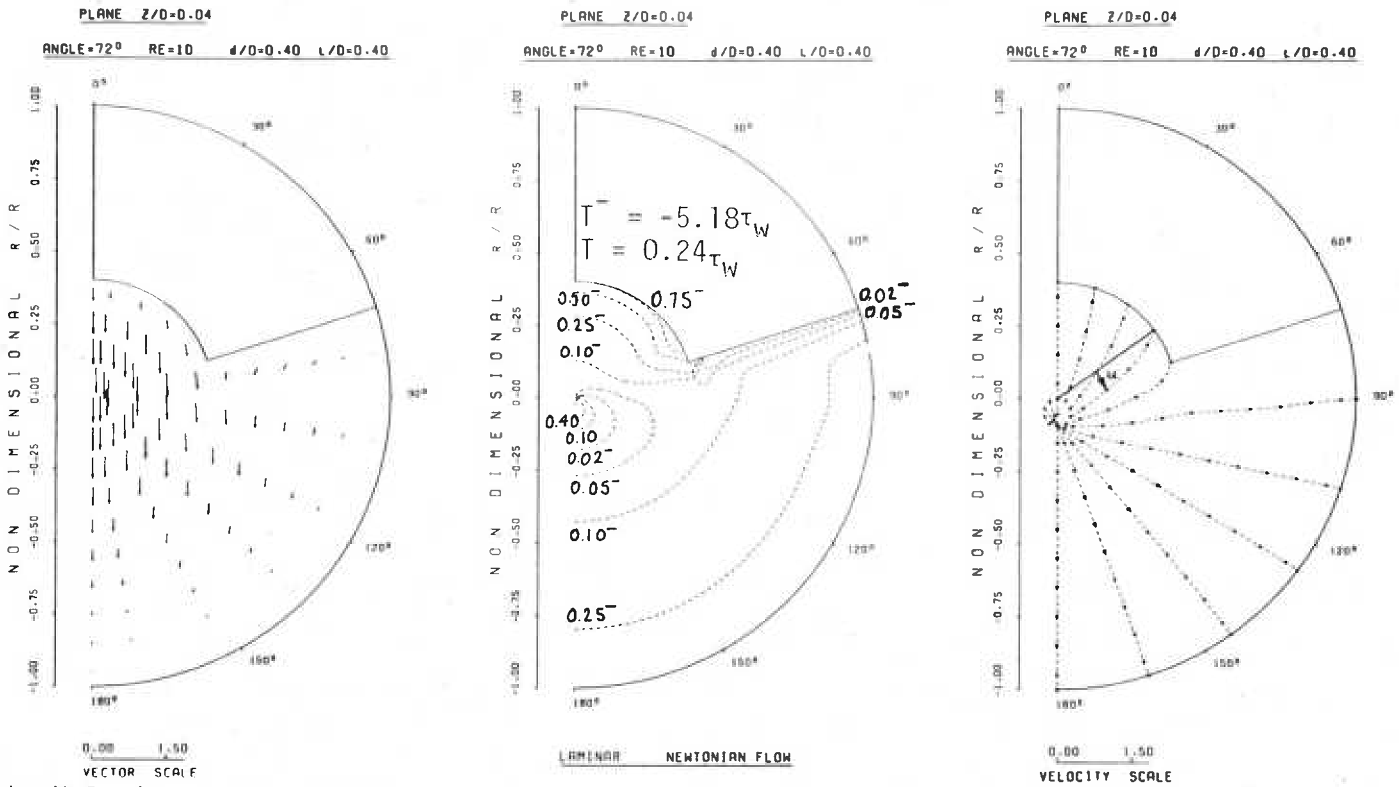

(a) Velocity vector field

(b) Shear stress contours

(c) Circumferential velocity profile

Plotting station

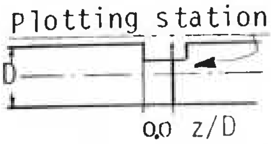

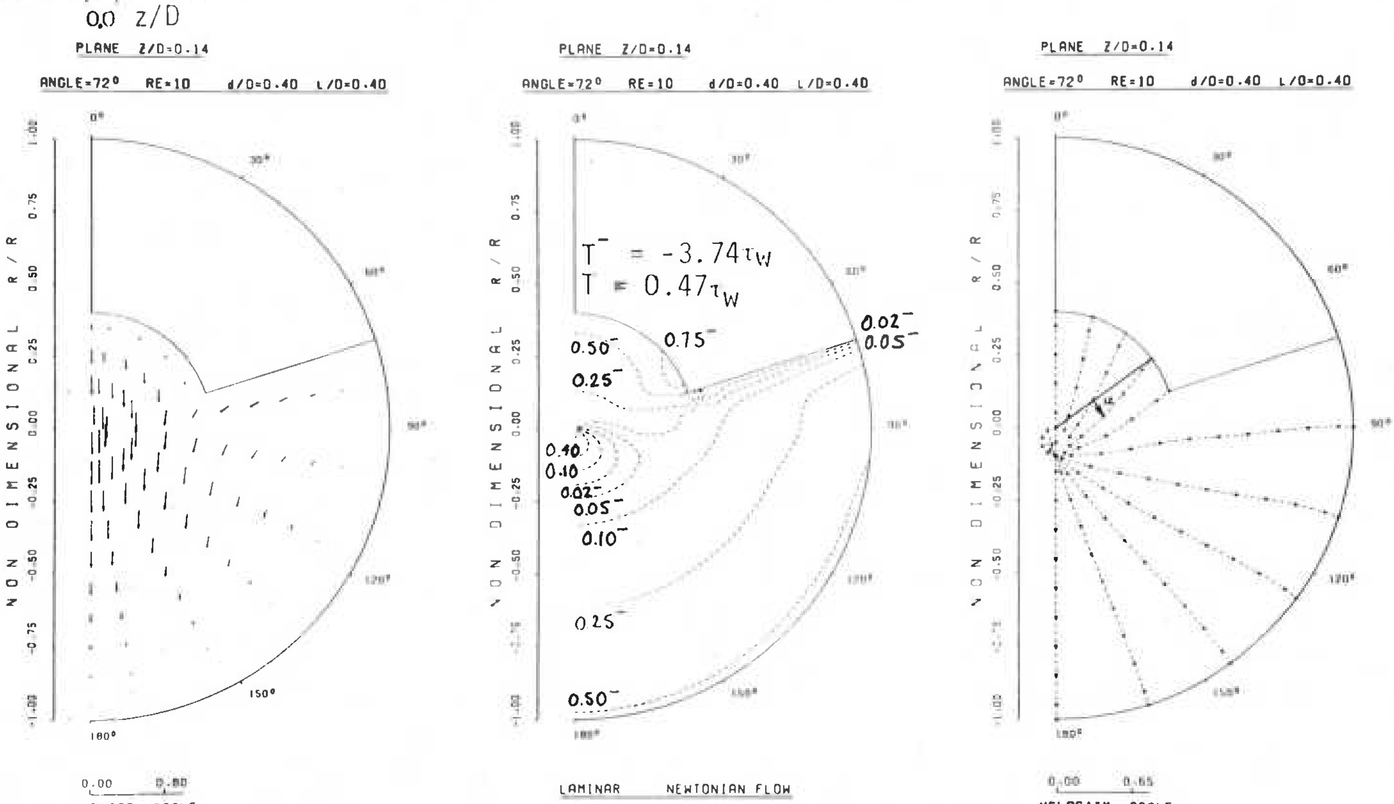

(a) Velocity vector field

(b) Shear stress contours

(c) Circumferential velocity profiles

Fig. 2.6.6-10 Laminar Newtonian flow around an asymmetric obstacle (Re = 10, d/D = 0.40, l/D = 0.40) - Planes z/D = 0.04,0.14

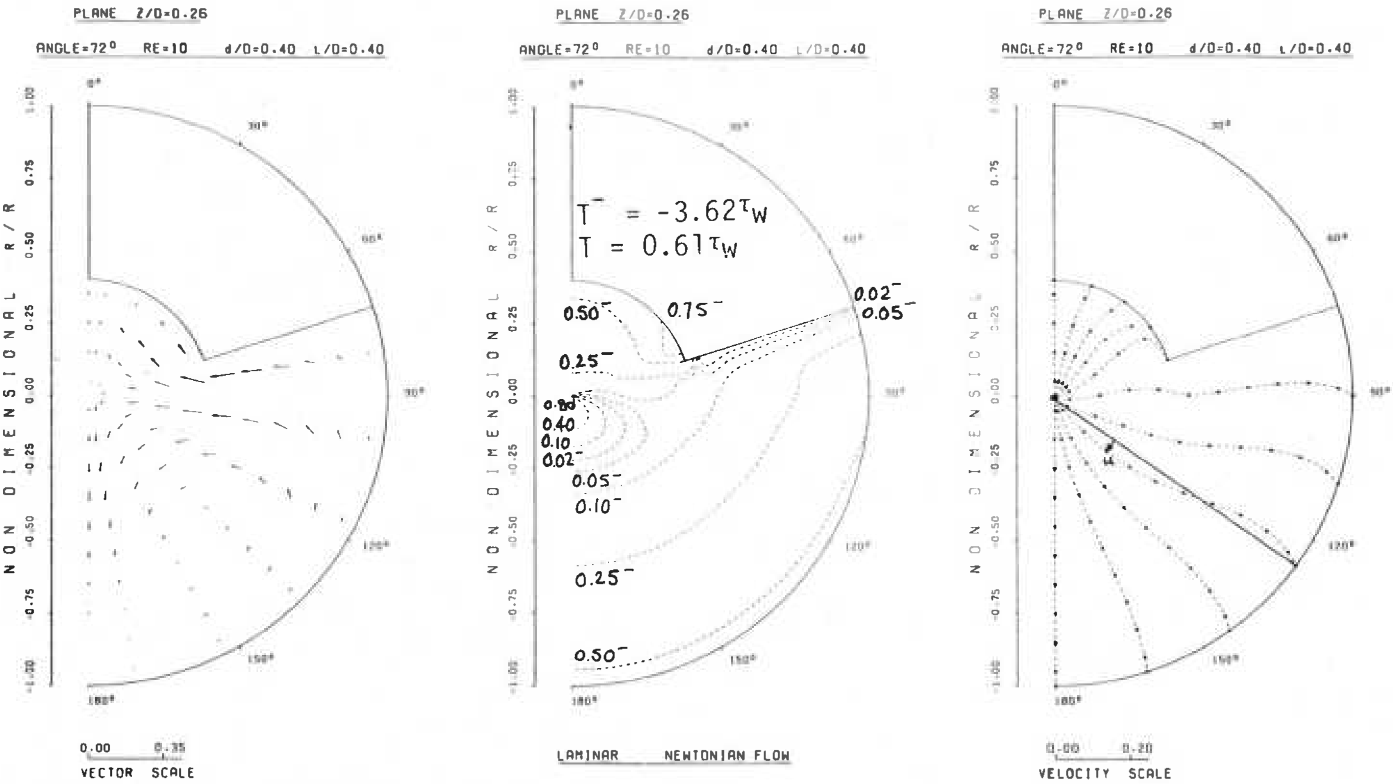

(a) Velocity vector field

Plotting station

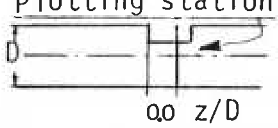

(b) Shear stress contours

(c) Circumferential velocity profiles

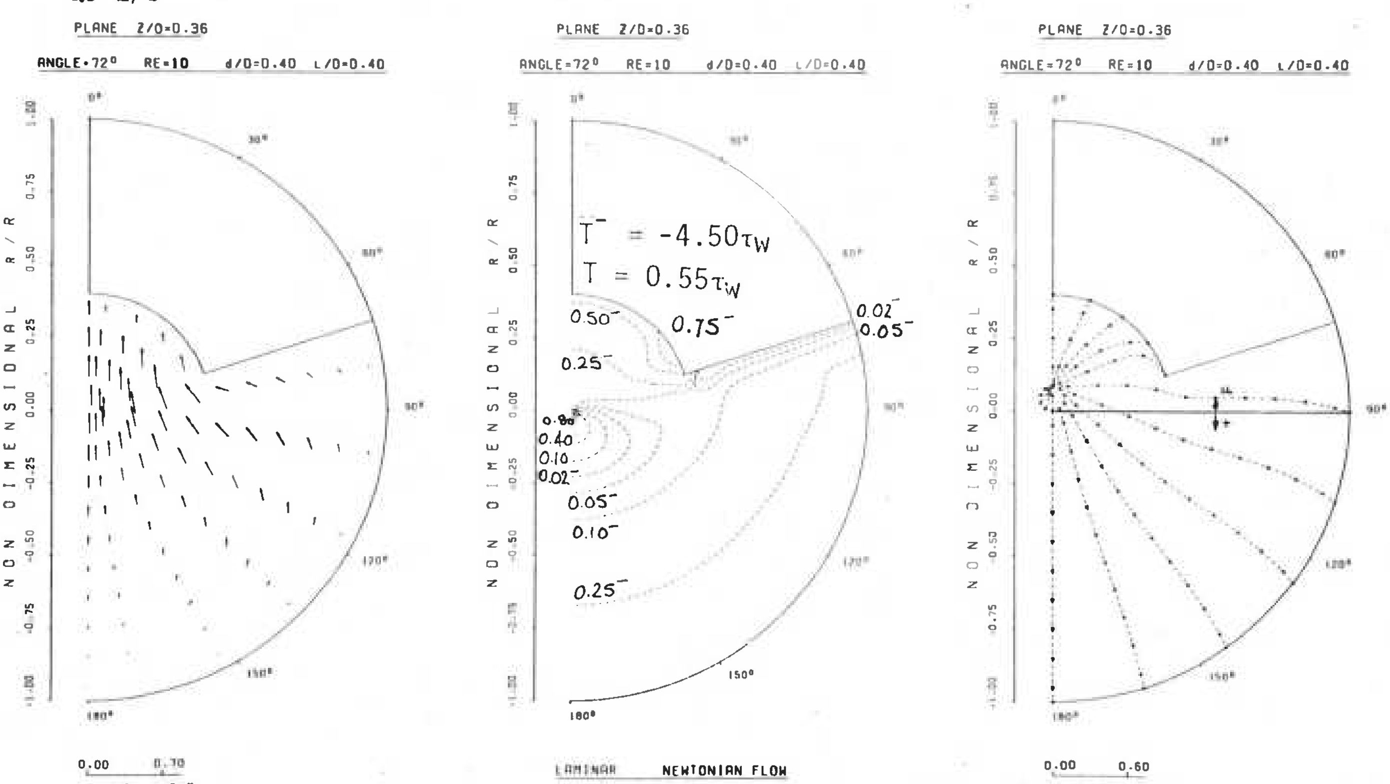

(a) Velocity vector field

(b) Velocity vector field

(c) Circumferential velocity profiles

Fig. 2.6.6-11 Laminar Newtonian flow around an asymmetric obstacle (Re = 10, d/D = 0.40, l/D = 0.40) - Planes z/D = 0.26, 0.36

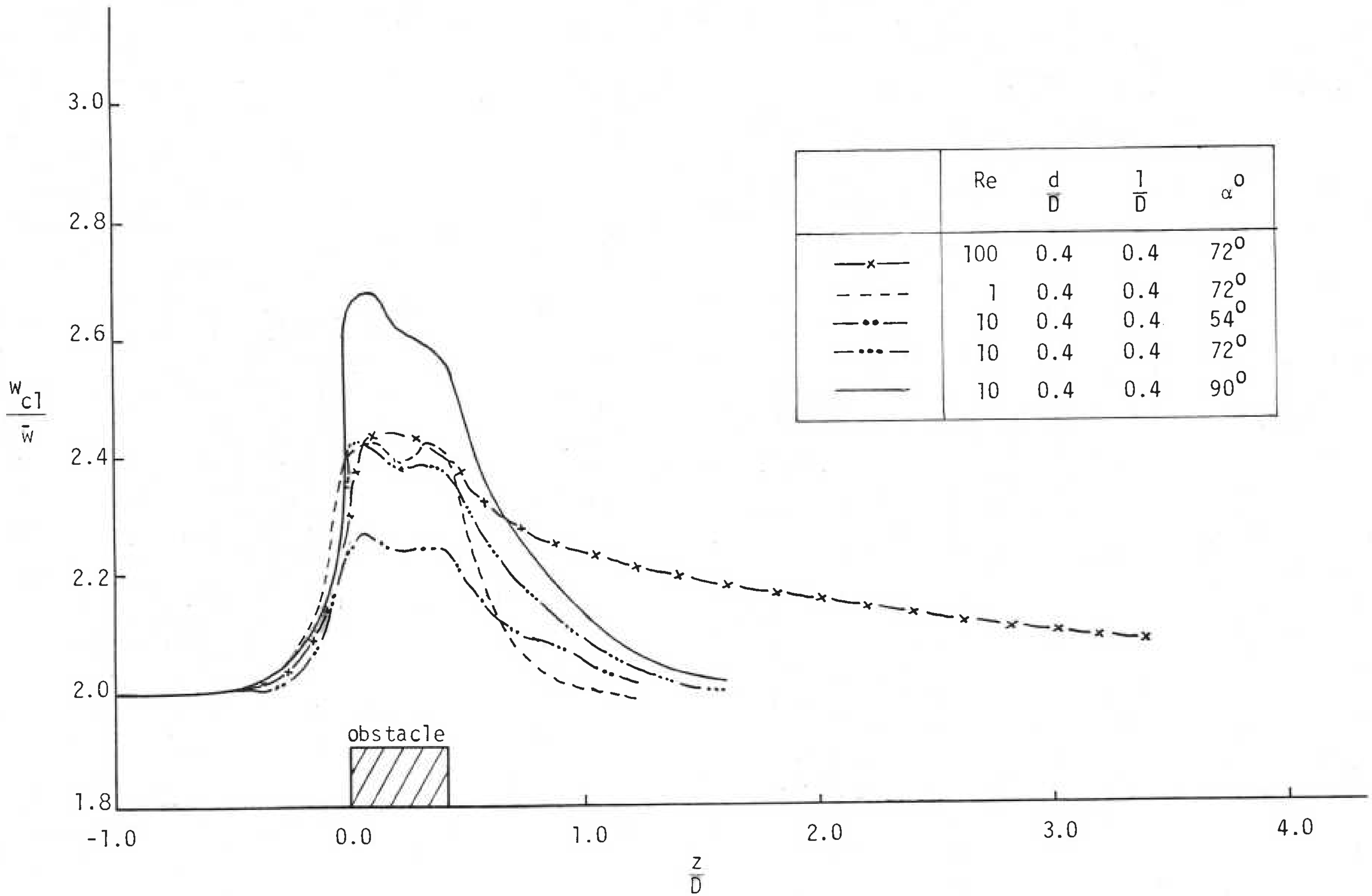

Fig. 2.6.6-12 Development of centre-line axial velocity of Newtonian flows around an asymmetric obstacle

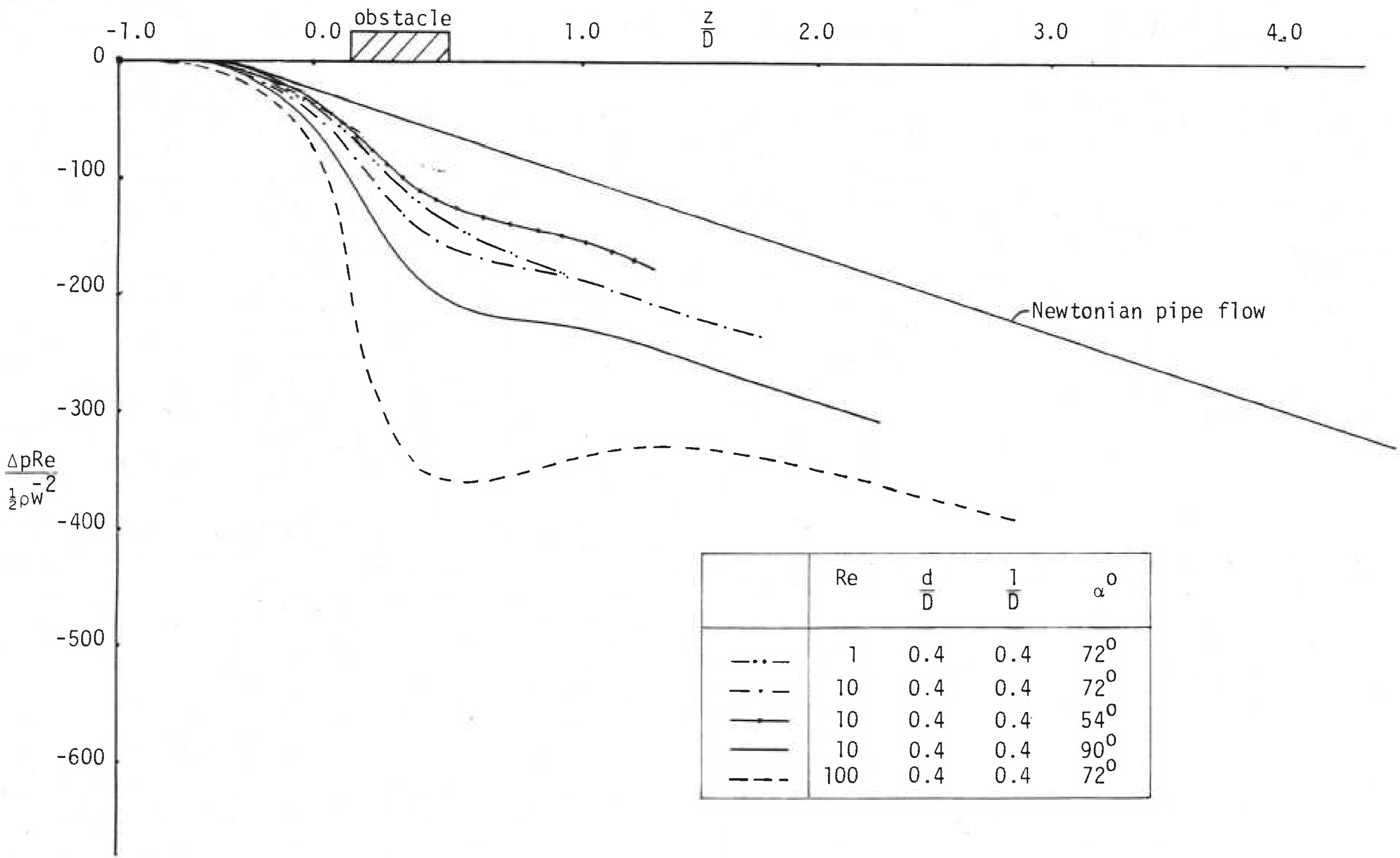

Fig. 2.6.6-13 Development of centre-line pressure for Newtonian flow around an asymmetric obstacle

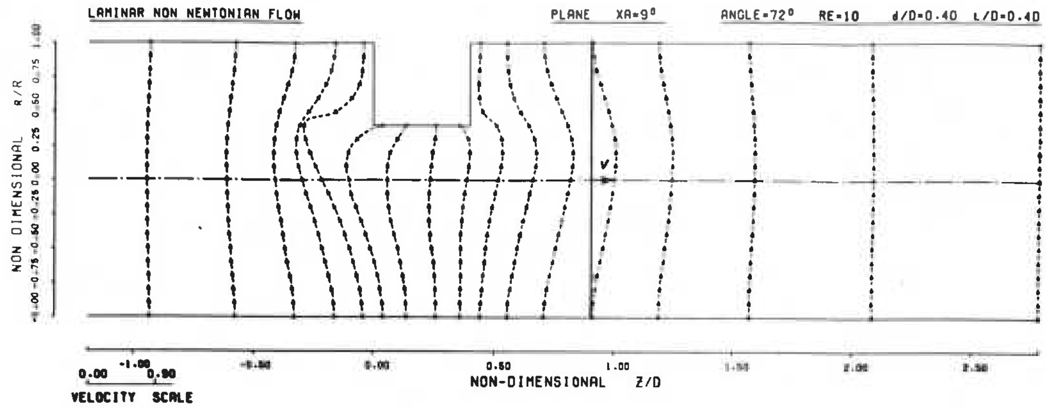

(a) Radial velocity profiles

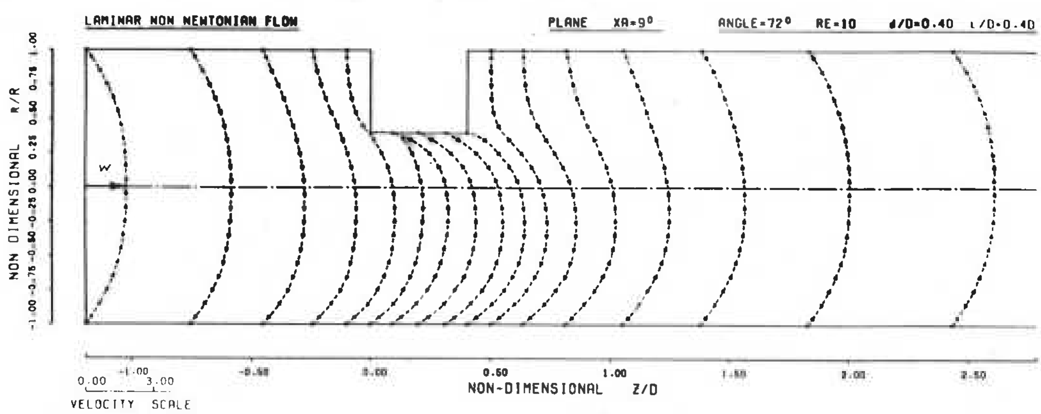

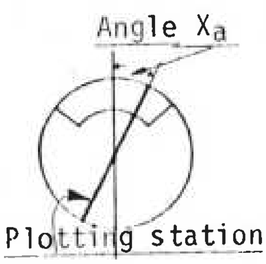

(b) Axial velocity profiles

$T^{-} = -2.91\tau_W \quad T = 1.26\tau_W$

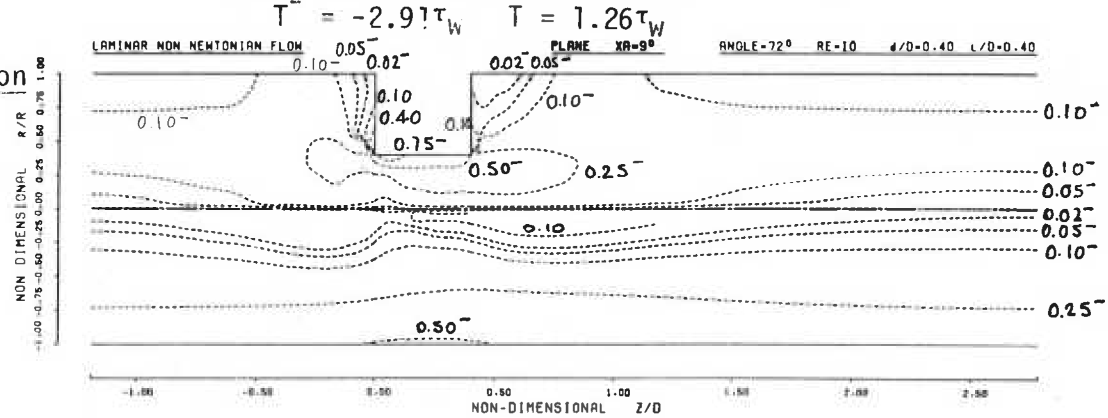

(c) Shear stress contours

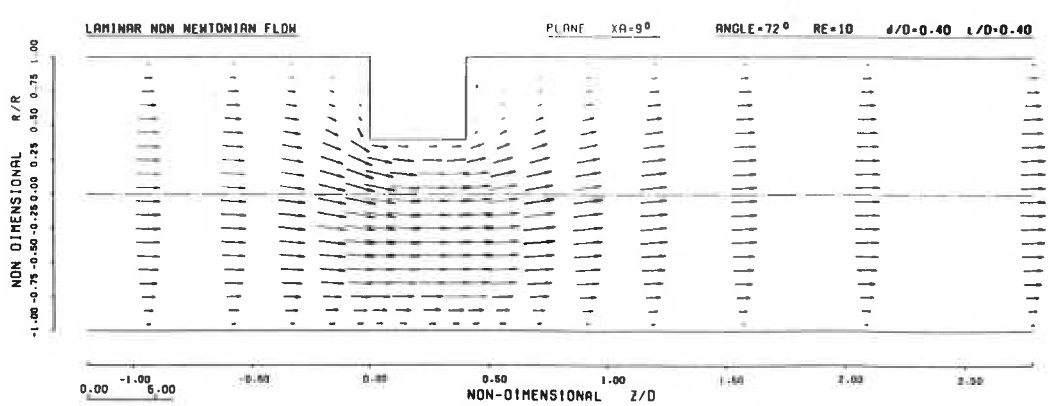

(d) Velocity vector field

Fig. 2.6.7-1 Laminar non-Newtonian blood flow around an asymmetric thrombus (Re = 10, d/D = 0.40, l/D = 0.40) - Plane XA = 90

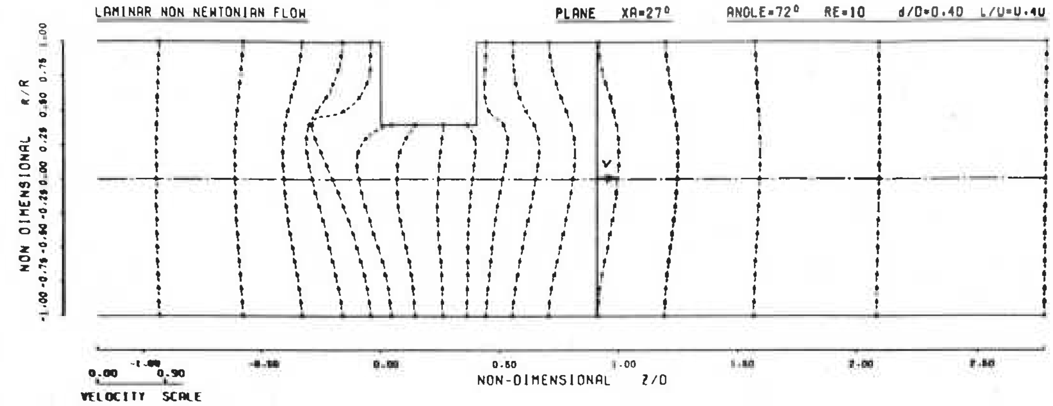

(a) Radial velocity profiles

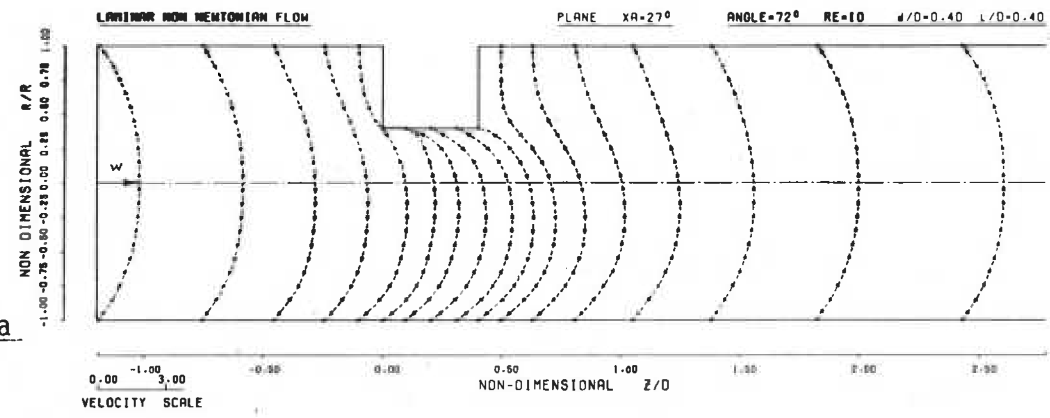

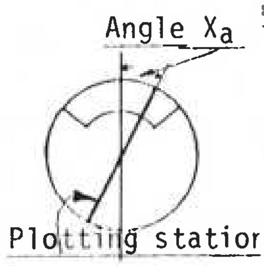

(b) Axial velocity profiles

$T^{-} = -2.95\tau_W$ $T = 1.22\tau_W$

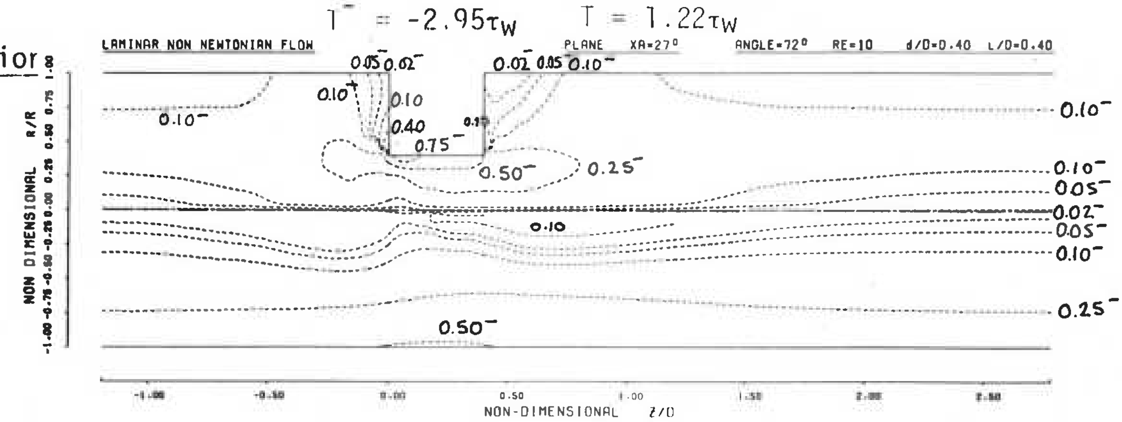

(c) Shear stress contours

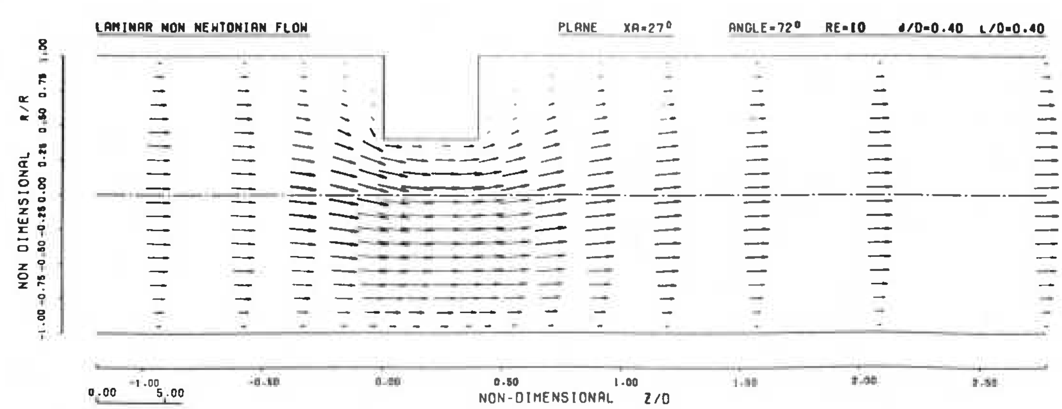

(d) Velocity vector field

Fig. 2.6.7-2 Laminar non-Newtonian blood flow around an asymmetric thrombus (Re = 10, d/D = 0.40, l/D = 0.40) - Plane XA = 27°

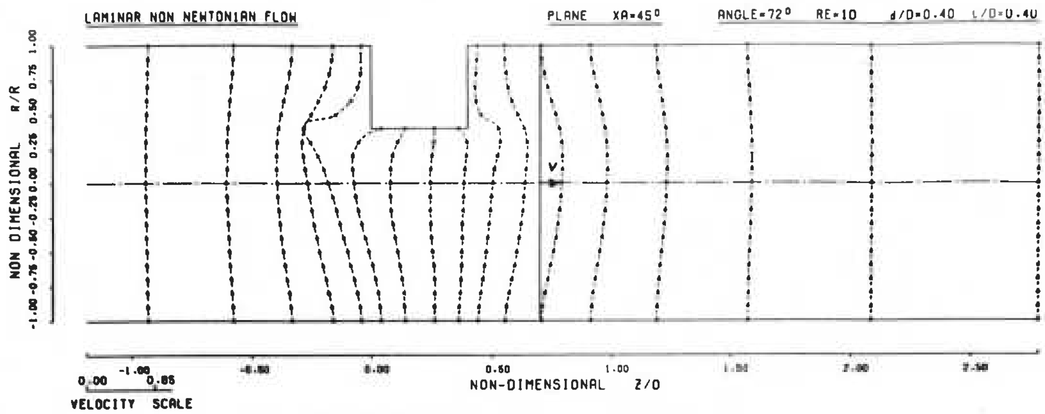

(a) Radial velocity profiles

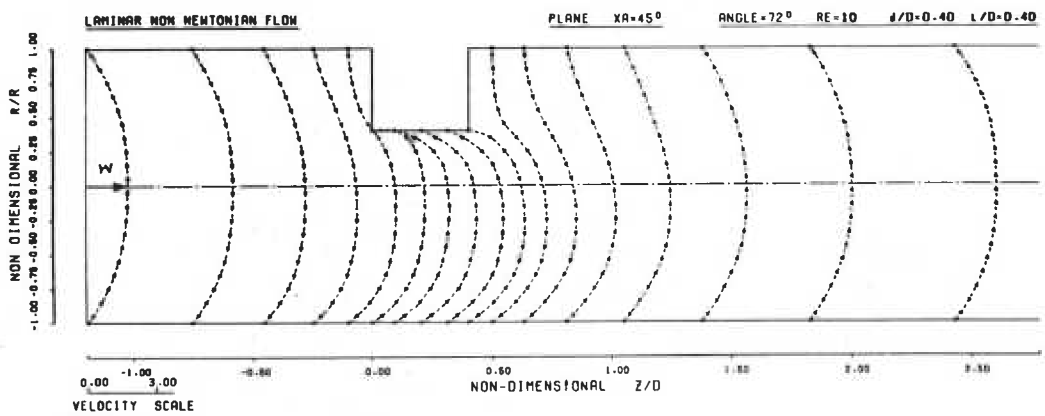

(b) Axial velocity profiles

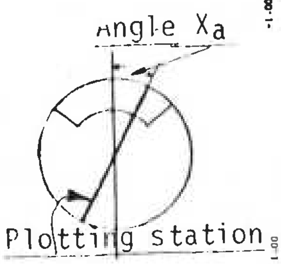

$T^{-} = -3.04\tau_W \qquad T = 1.09\tau_W$

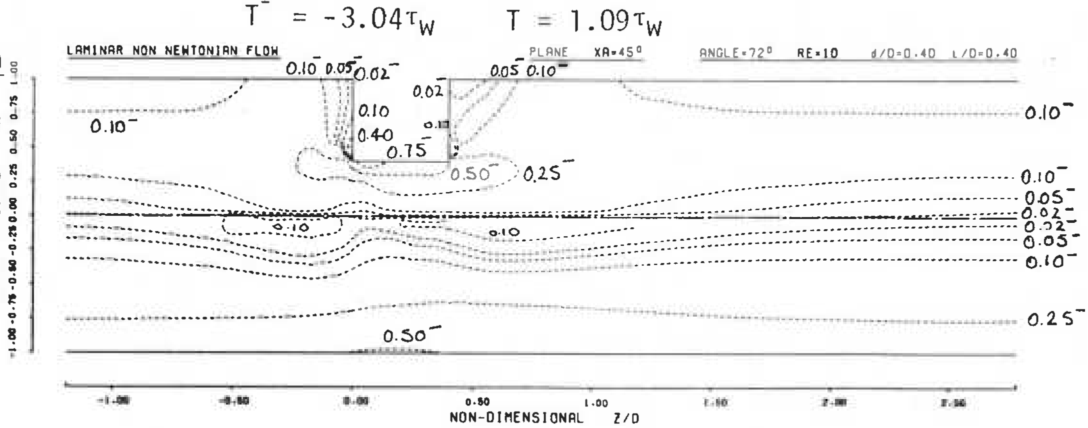

(c) Shear stress contours

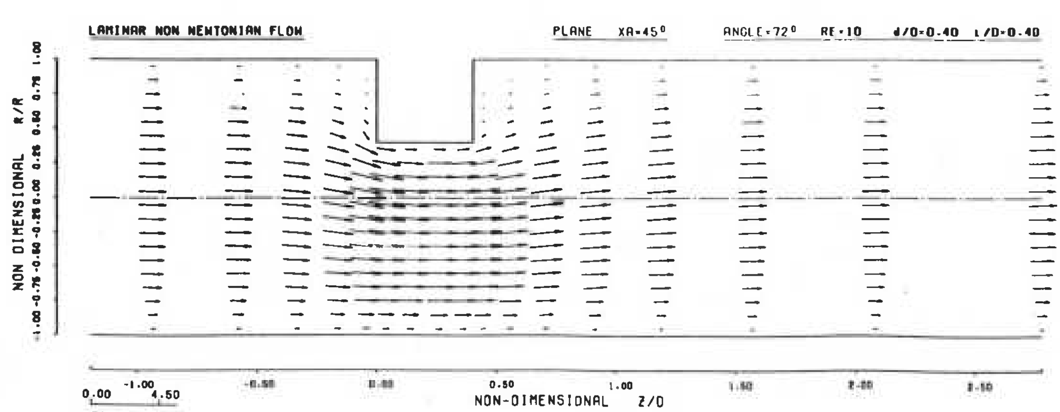

(d) Velocity vector field

Fig. 2.6.7-3 Laminar non-Newtonian blood flow around an asymmetric thrombus (Re = 10, d/D = 0.40, l/D = 0.40) - Plane XA = 45°

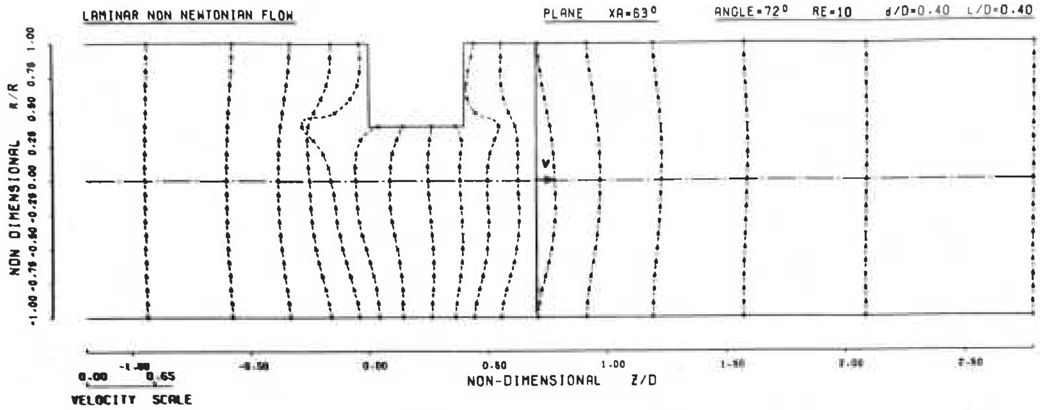

(a) Radial velocity profiles

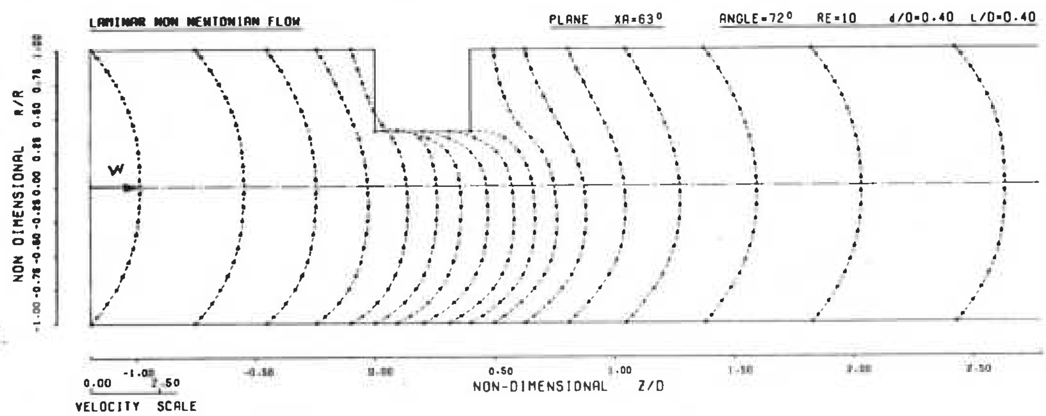

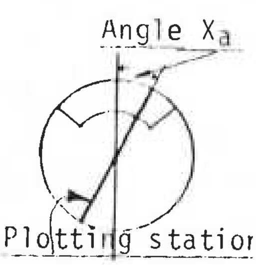

(b) Axial velocity profiles

$T^{-} = -3.32\tau_w$ $T = 0.75\tau_w$

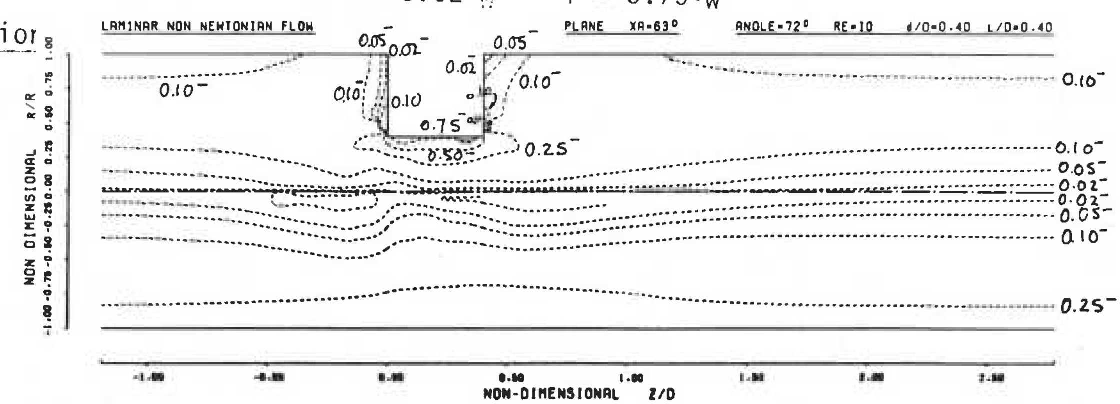

(c) Shear stress contours

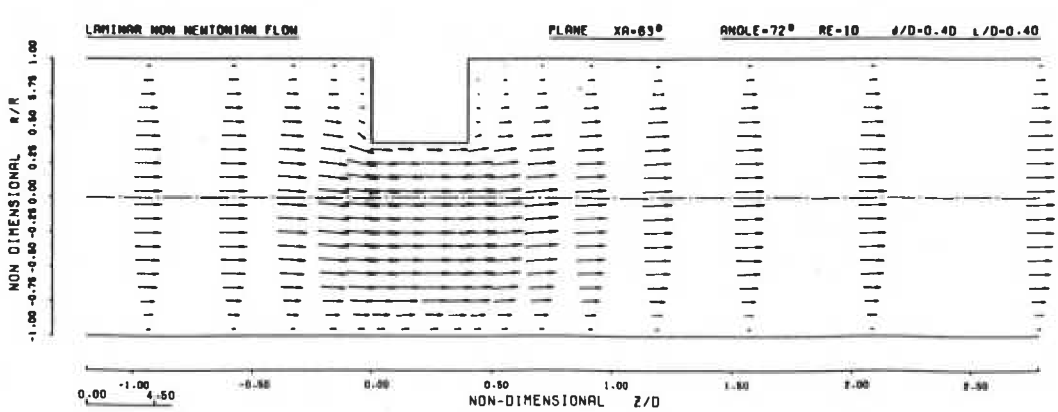

(d) Velocity vector field

Fig. 2.6.7-4 Laminar non-Newtonian blood flow around an asymmetric thrombus (Re = 10, d/D = 0.40, l/D = 0.40) - Plane XA = 63°

$T^{-} = -0.82\tau_W \quad T = 0.37\tau_W$

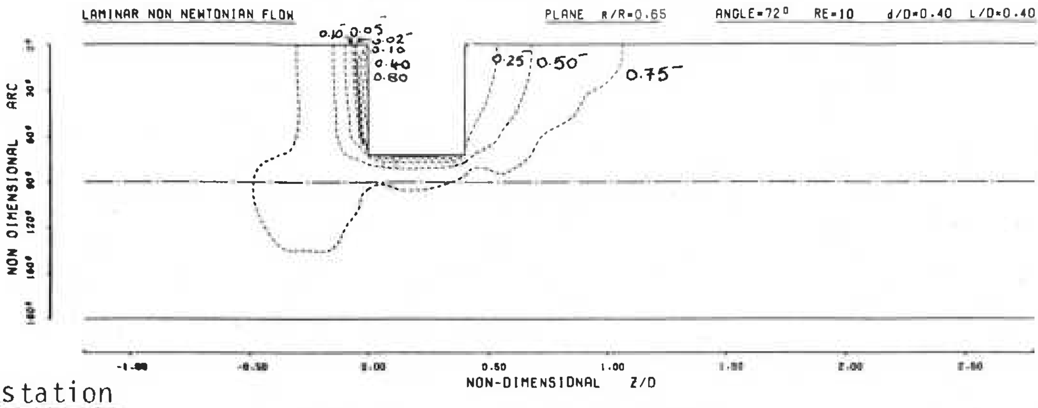

Plotting station

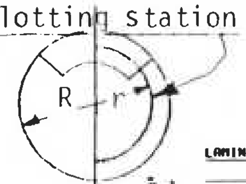

(a) Shear stress contours

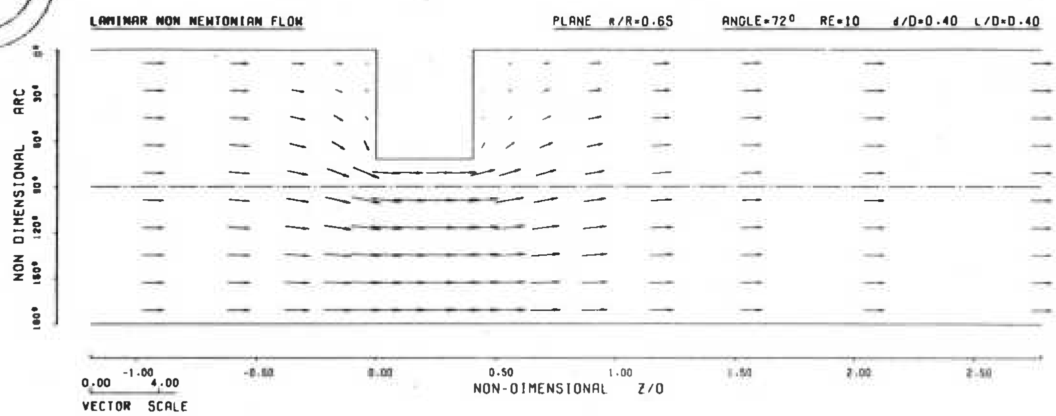

(b) Velocity vector field

$T^{-} = -1.01\tau_W \quad T = 0.16\tau_W$

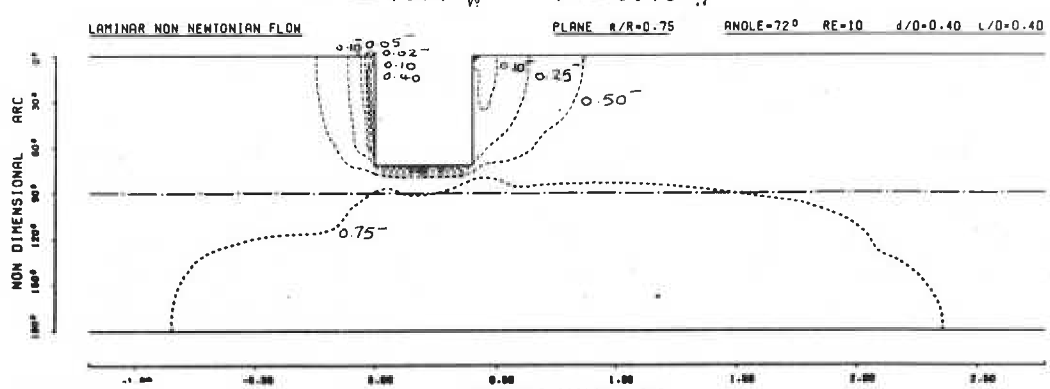

Plotting station

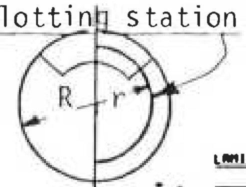

(a) Shear stress contours

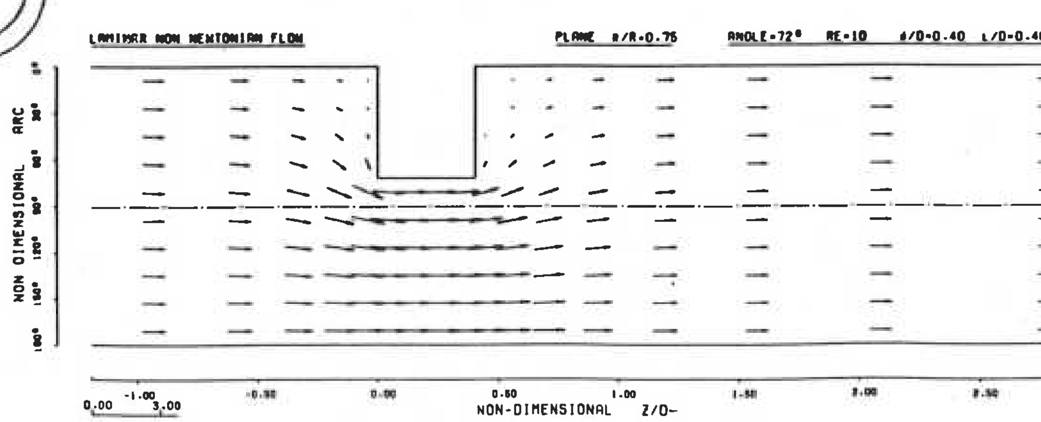

(b) Velocity vector field

Fig. 2.6.7-5 Laminar non-Newtonian blood flow around an asymmetric thrombus (Re = 10, d/D = 0.40, l/D = 0.40) - Planes r/R = 0.65, 0.75

$T^{-} = -1.22\tau_W$ $T = 0.04\tau_W$

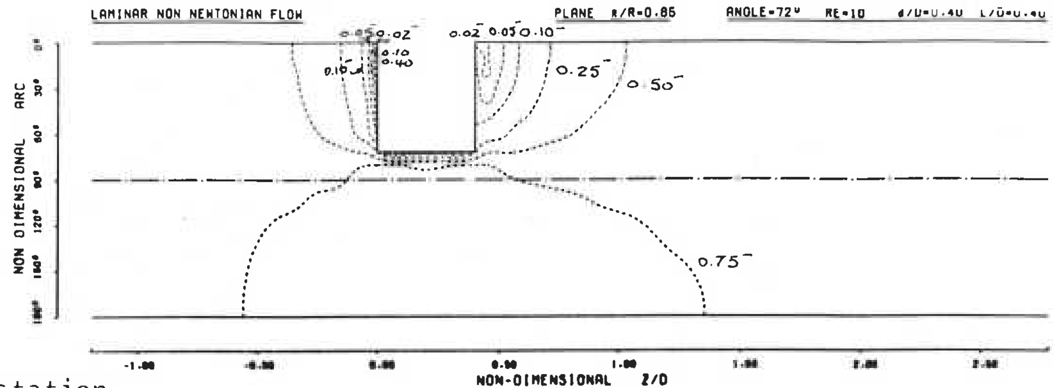

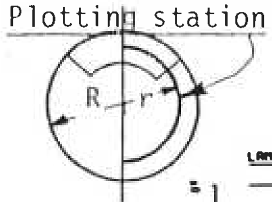

(a) Shear stress contours

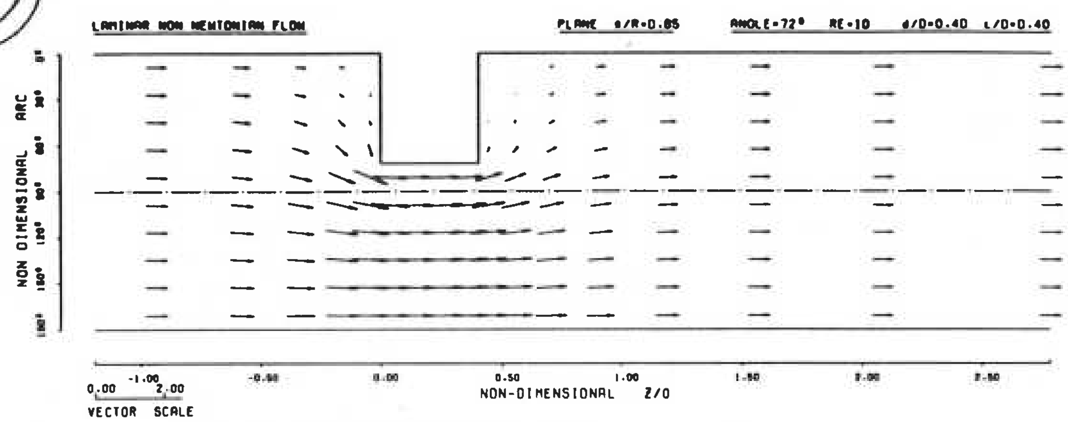

(b) Velocity vector field

$T^{-} = -1.47\tau_W$ $T = 0.34\tau_W$

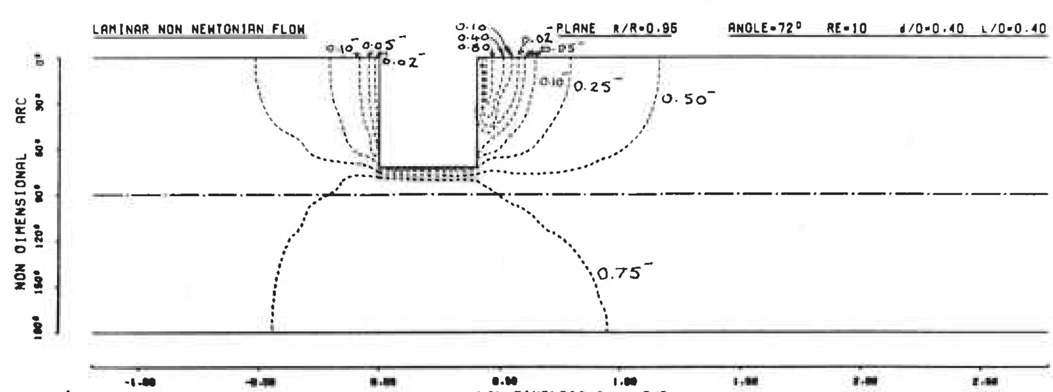

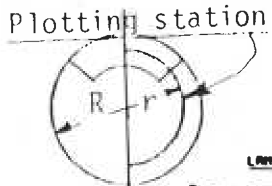

(a) Shear stress contours

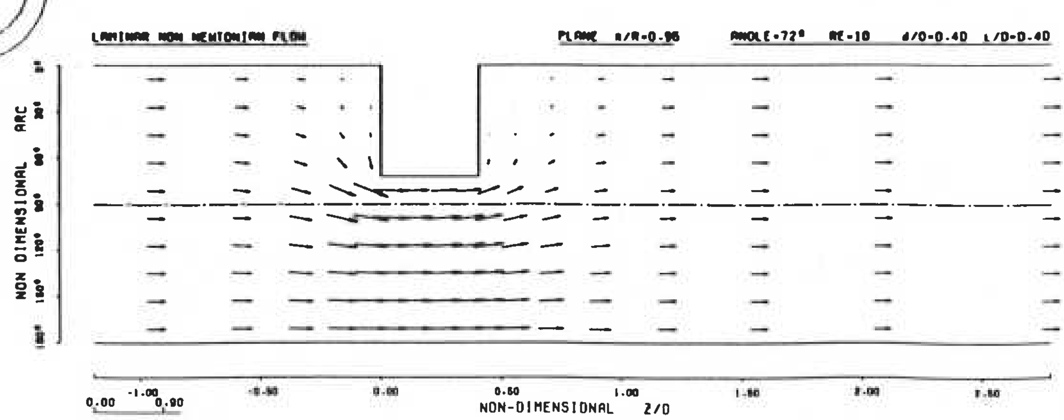

(b) Velocity vector field

Fig. 2.6.7-6 Laminar non-Newtonian blood flow around an asymmetric thrombus (Re = 10, d/D = 0.40, l/D = 0.40). Planes r/R = 0.85, 0.95

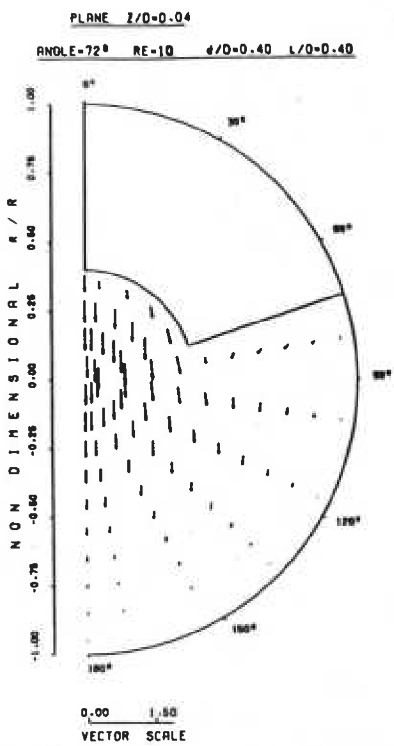

(a) Velocity vector field

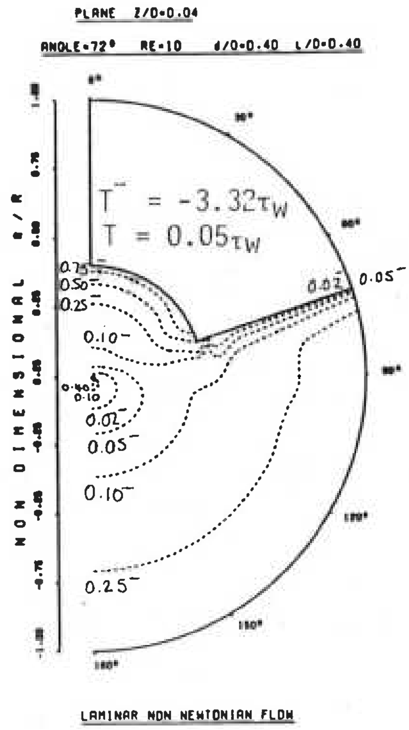

(b) Shear stress contours

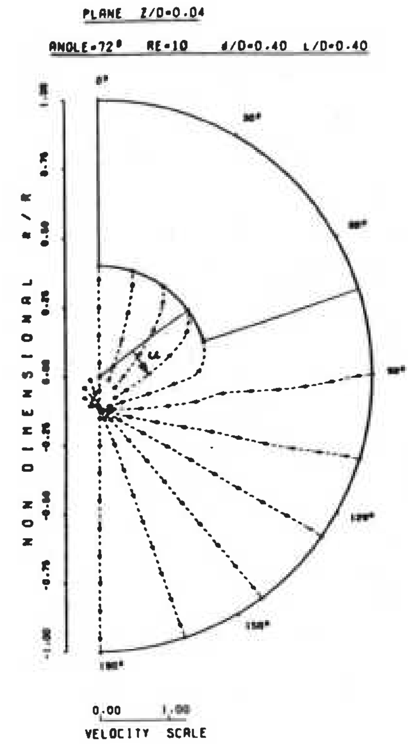

(c) Circumferential velocity profile

Plotting station

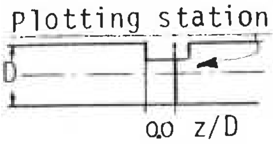

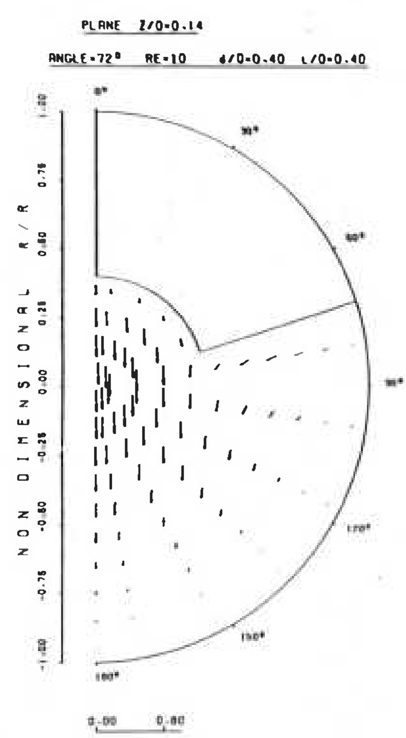

(a) Velocity vector field

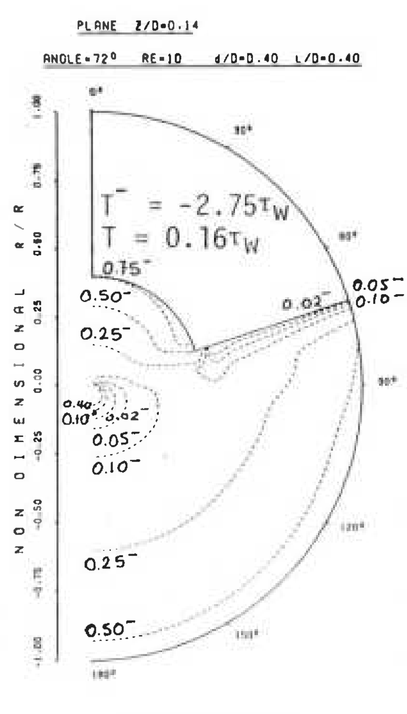

(b) Shear stress contours

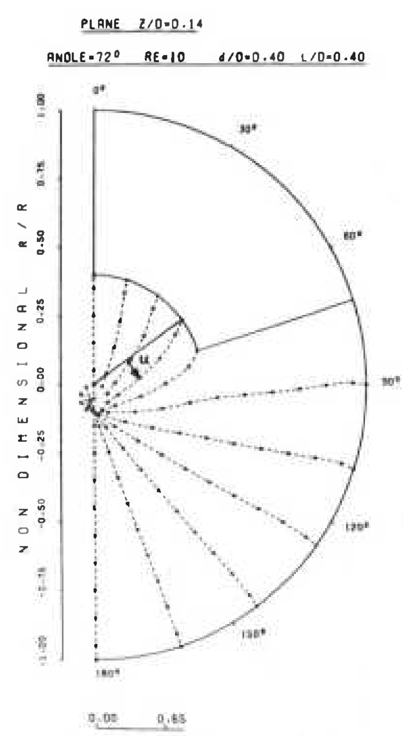

(c) Circumferential velocity profile

Fig. 2.6.7-7 Laminar non-Newtonian blood flow around an asymmetric thrombus (Re = 10, d/D = 0.40, 1/D = 0.40) - Planes z/D = 0.04, 0.14

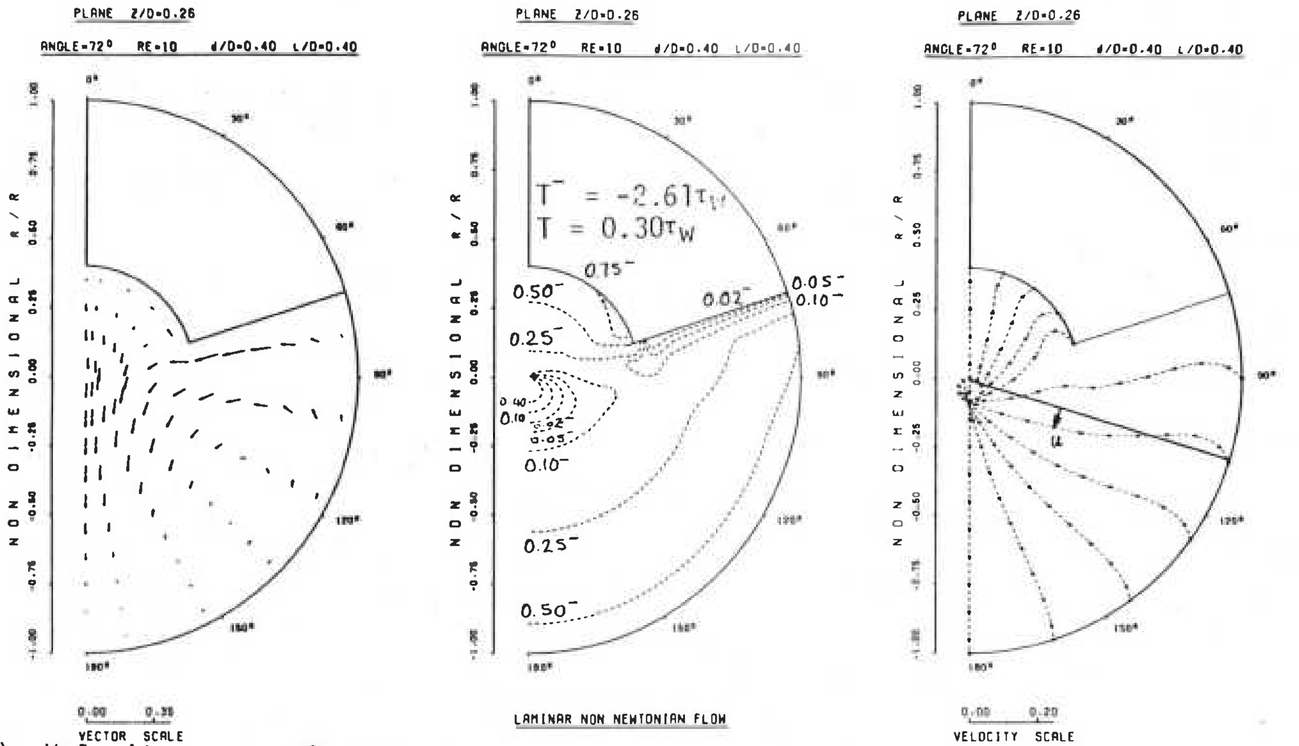

(a) Velocity vector field

(b) Shear stress contours

(c) Circumferential velocity profiles

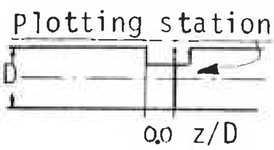

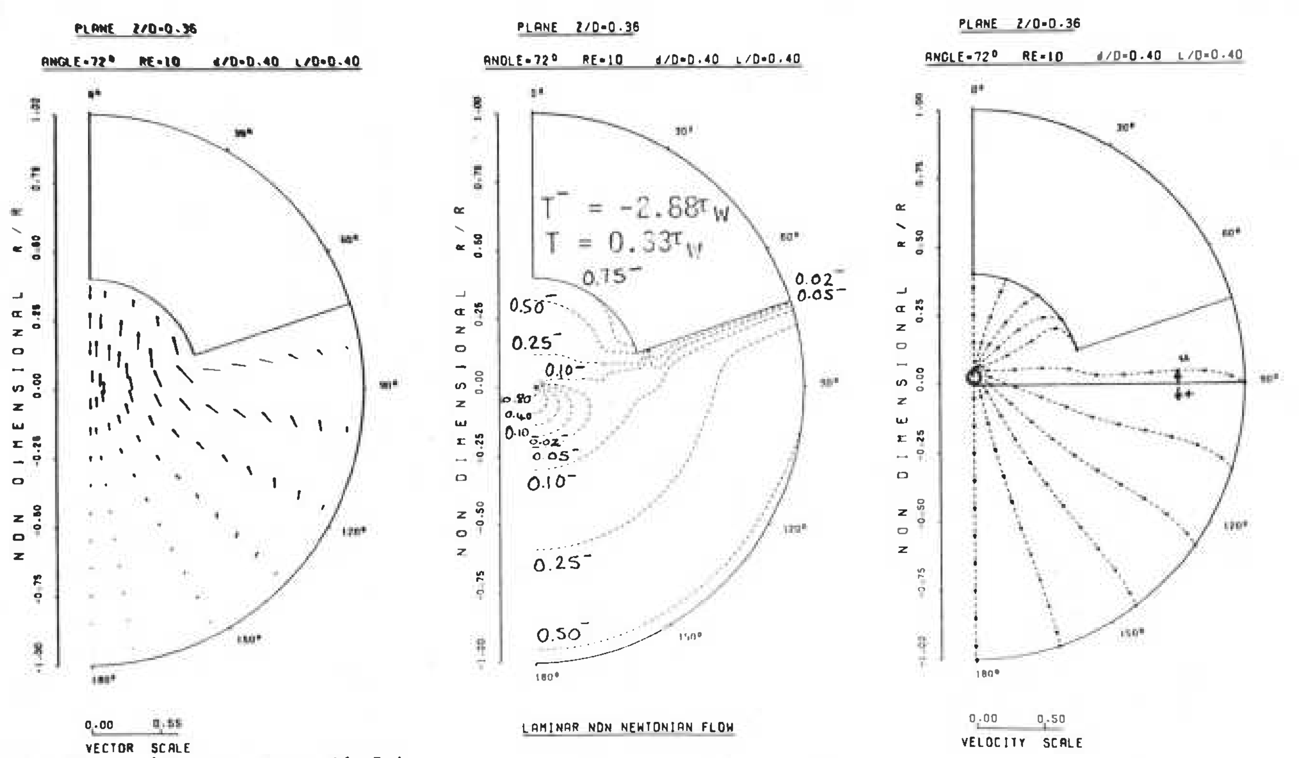

(a) Velocity vector field

(b) Shear stress contours

(c) Circumferential velocity profiles

Fig. 2.6.7-8 Laminar non-Newtonian blood flow around an asymmetric thrombus (Re = 10, d/D = 0.40, l/D = 0.40) - Planes z/D = 0.26, 0.36

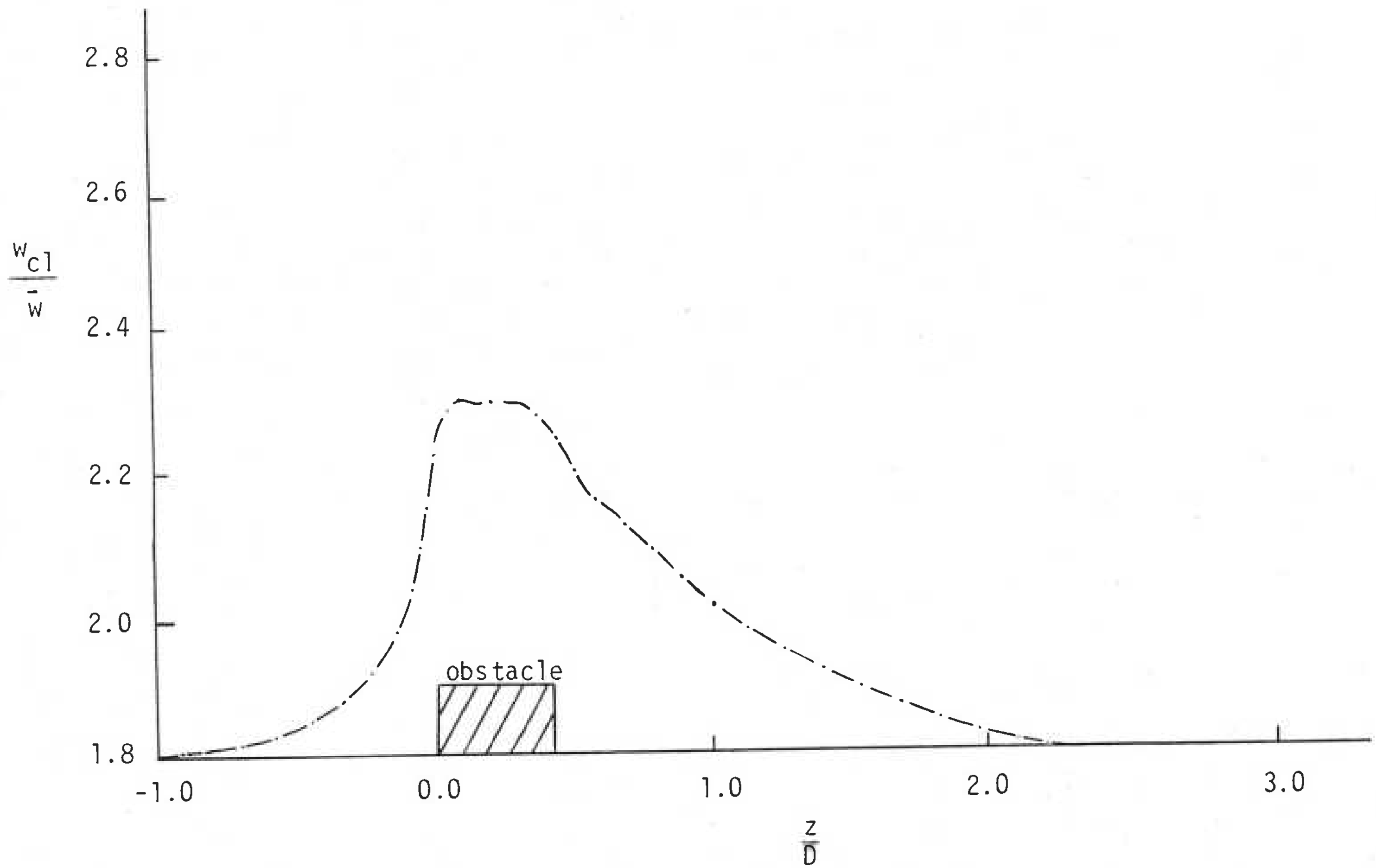

Fig. 2.6.7-9 Development of centre-line axial velocity of non-Newtonian blood flow around an asymmetric thrombus

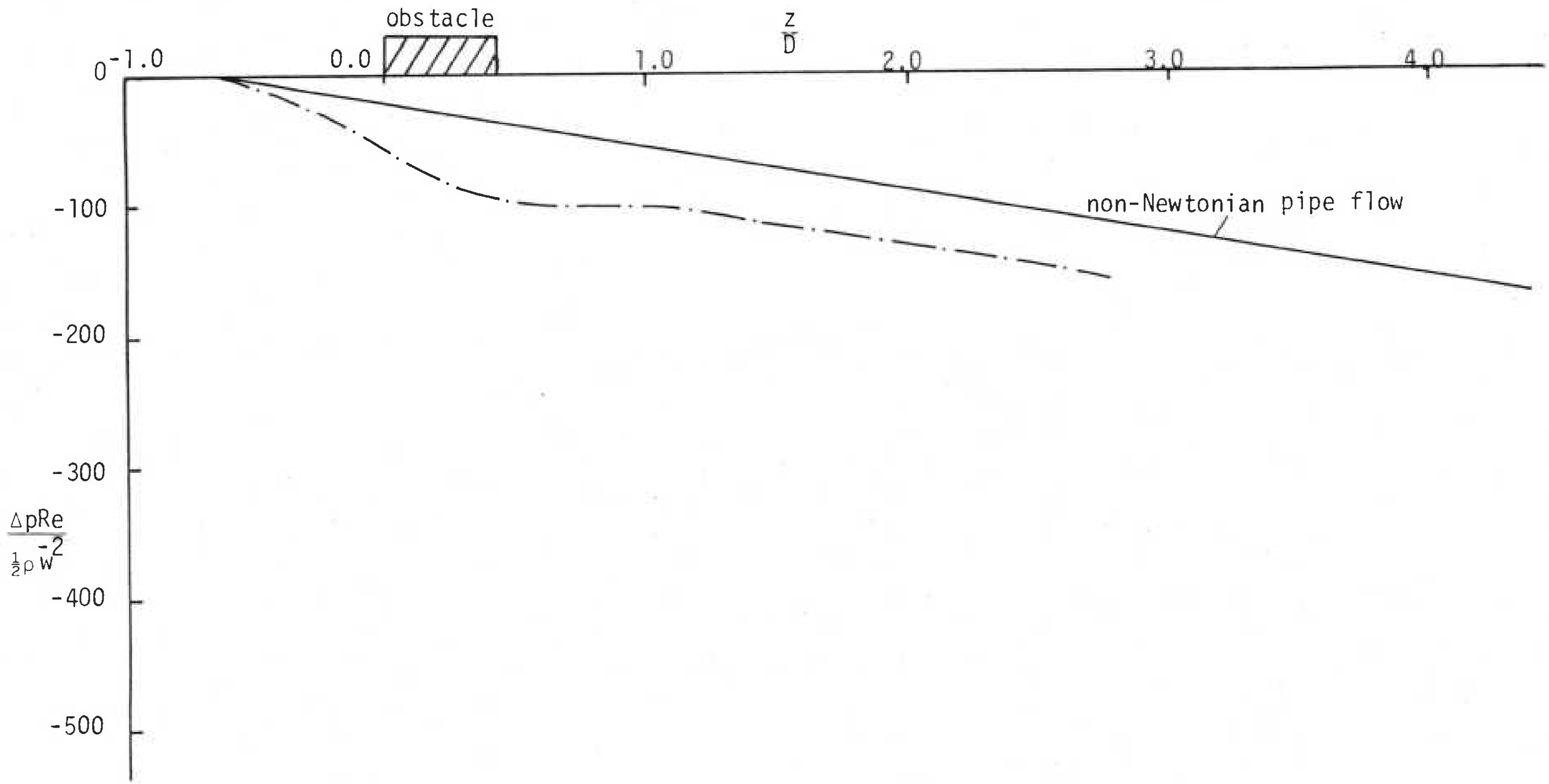

Fig. 2.6.7-10 Development of centre-line pressure for non-Newtonian blood flow around an asymmetric thrombus

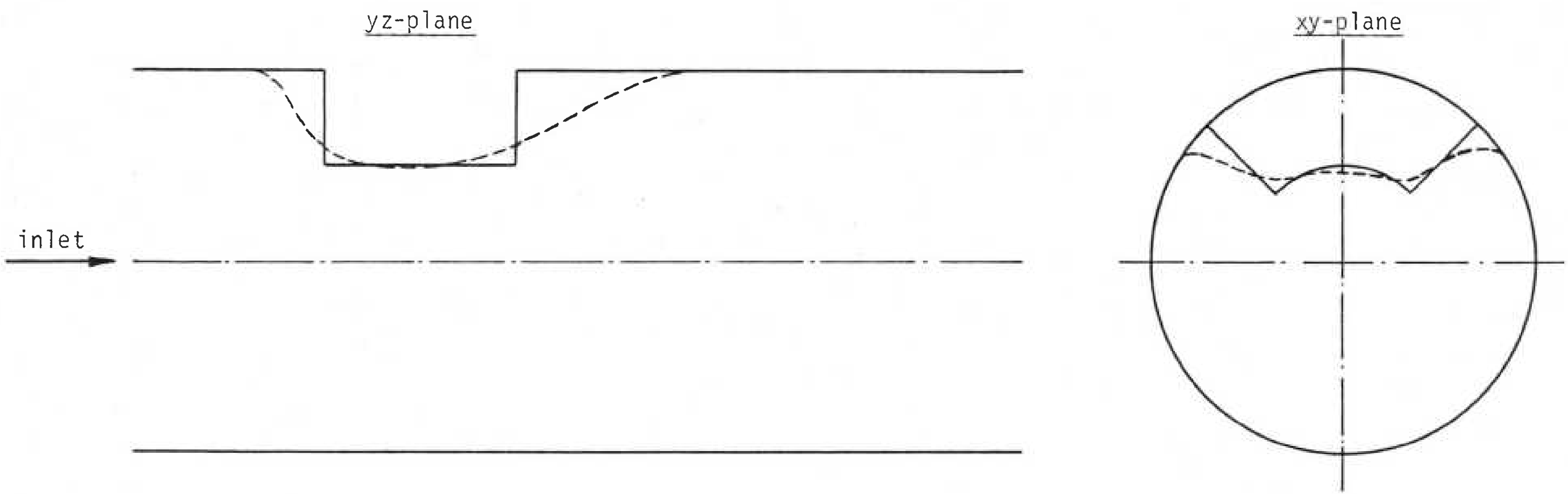

Fig. 2.6.7-11 Possible shape of thrombus deformed under the influence of the haemodynamic forces

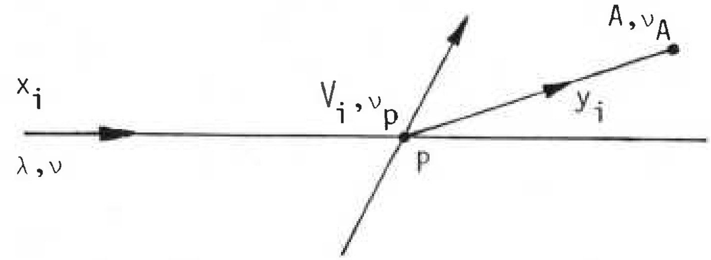

(a) The Doppler frequency shift

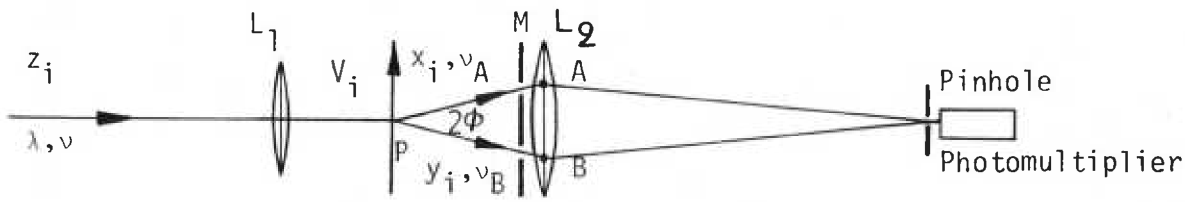

(b) The Doppler mode

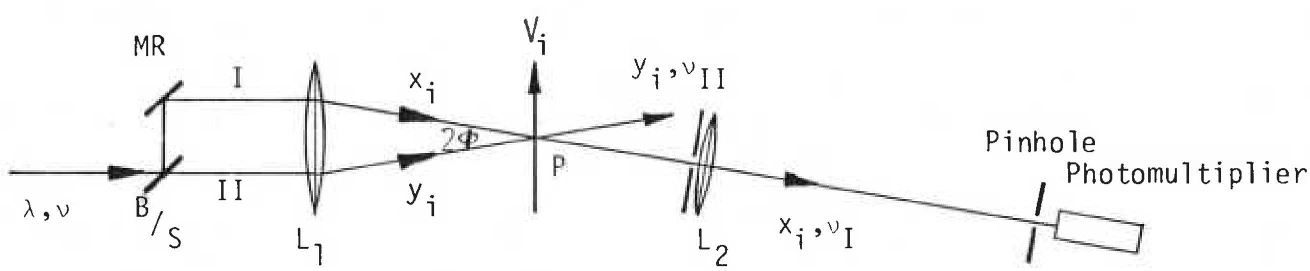

(c) The reference beam mode

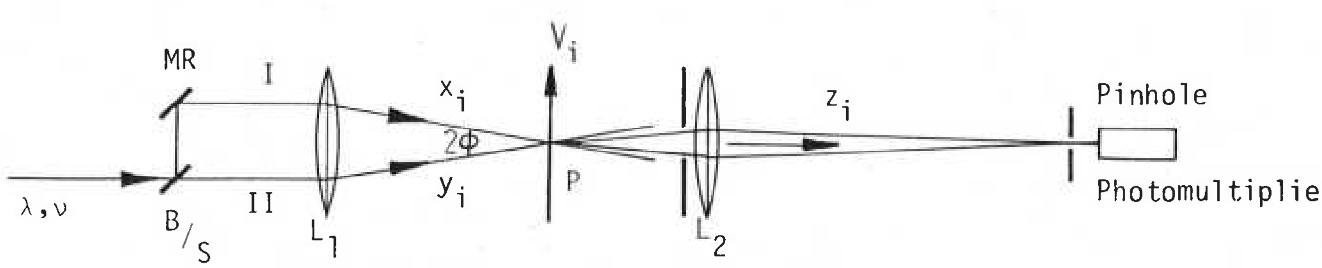

(d) The fringe mode

Fig. 3.2.2-1 Doppler frequency shift and LDV modes

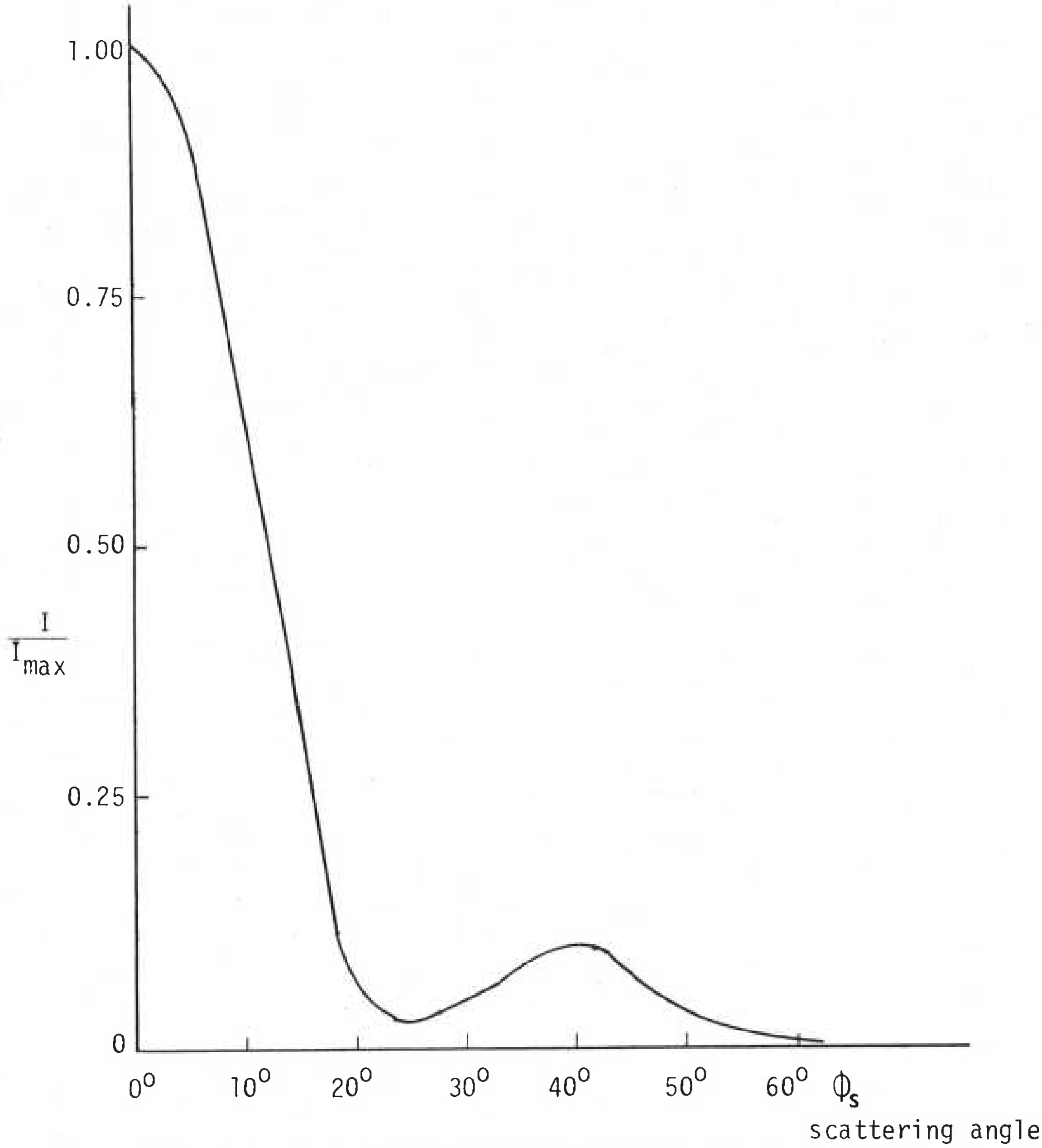

(a) Azimuthal distribution of scattered intensity

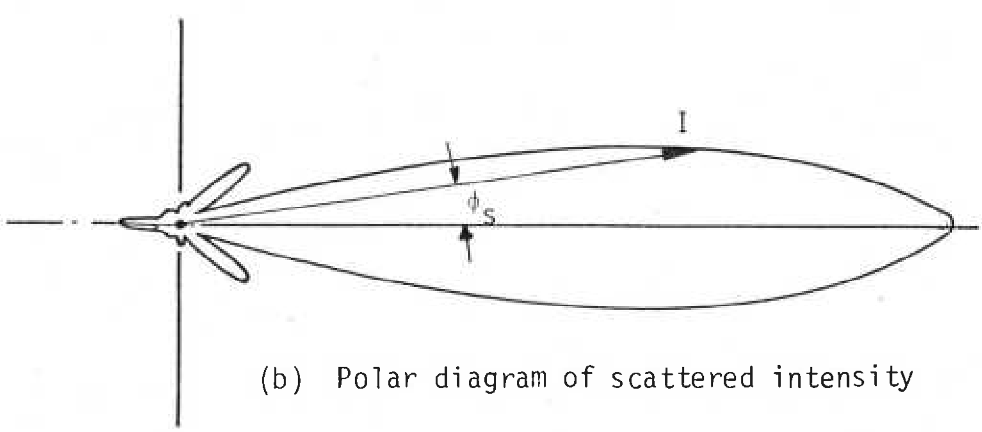

(b) Polar diagram of scattered intensity

Fig. 3.2.2-2 Light scattering by a small particle

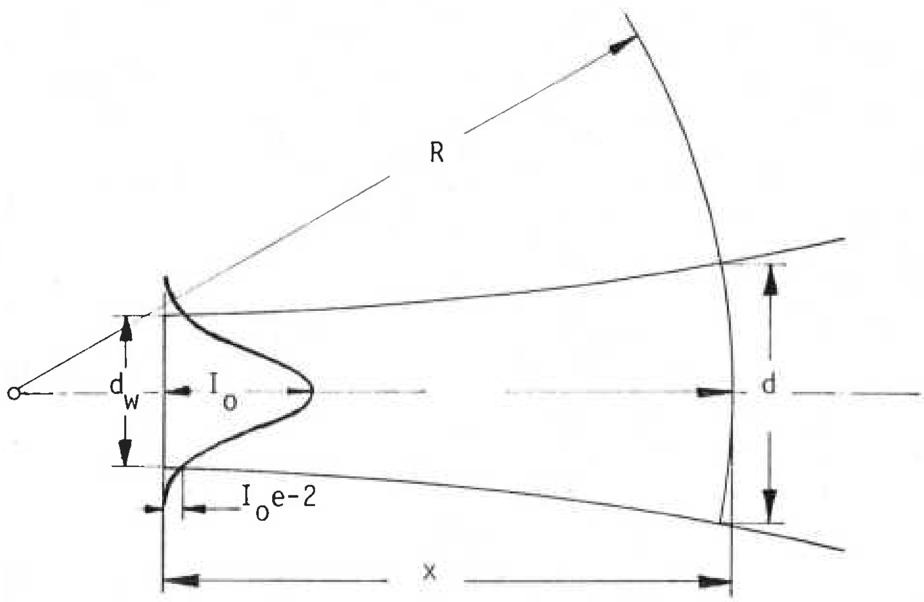

(a) Gaussian beam expansion

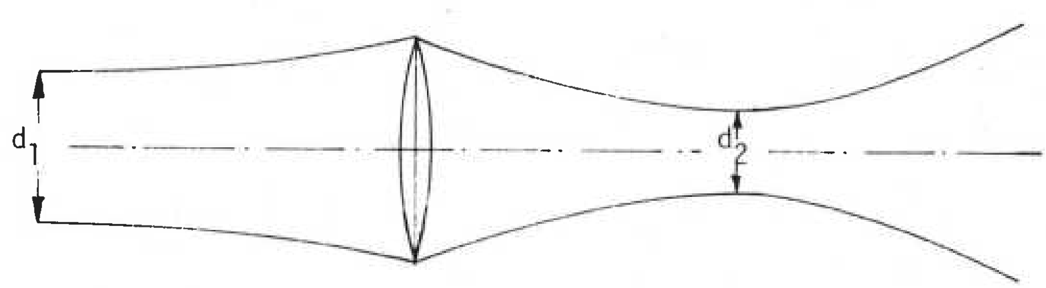

(b) Gaussian beam focused by a lens

Fig. 3.2.3-1 Gaussian beam propagation

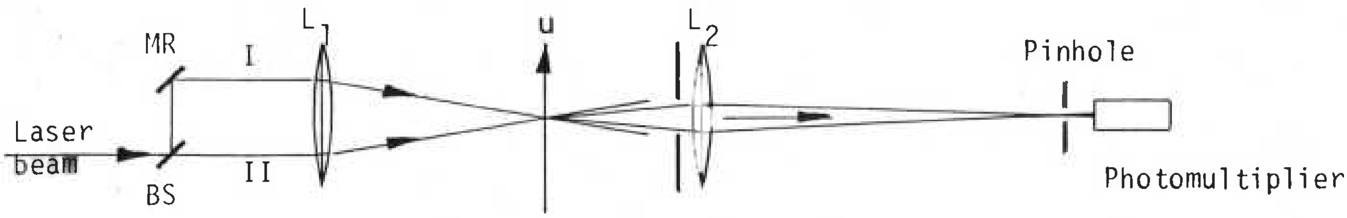

(a) The LDV operating in fringe mode

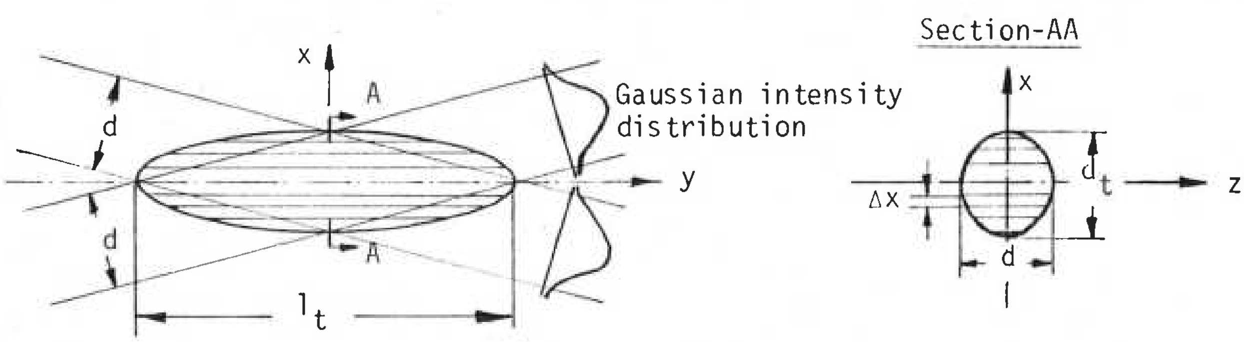

(b) The fringe pattern

Fig. 3.2.3-2 The LDV control volume

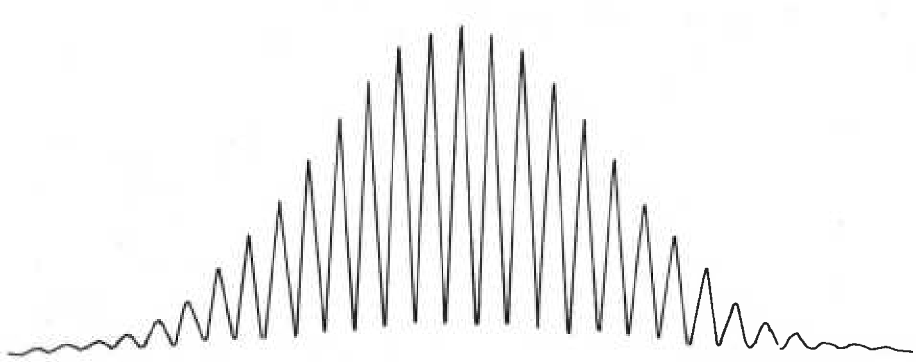

Fig. 3.2.4-1 The Doppler signal

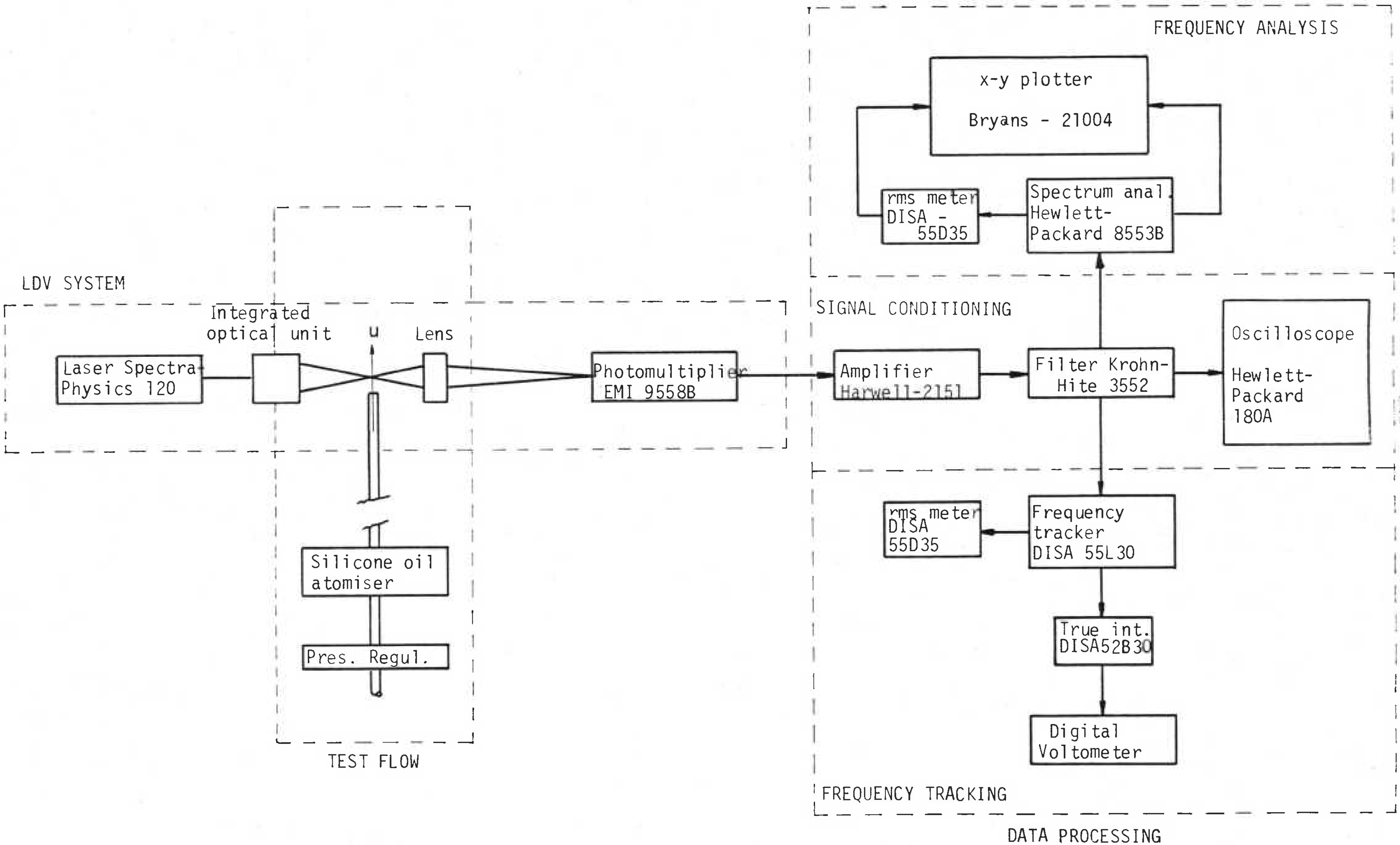

Fig. 3.3.1-1 Schematic diagram of experimental apparatus for pipe flow

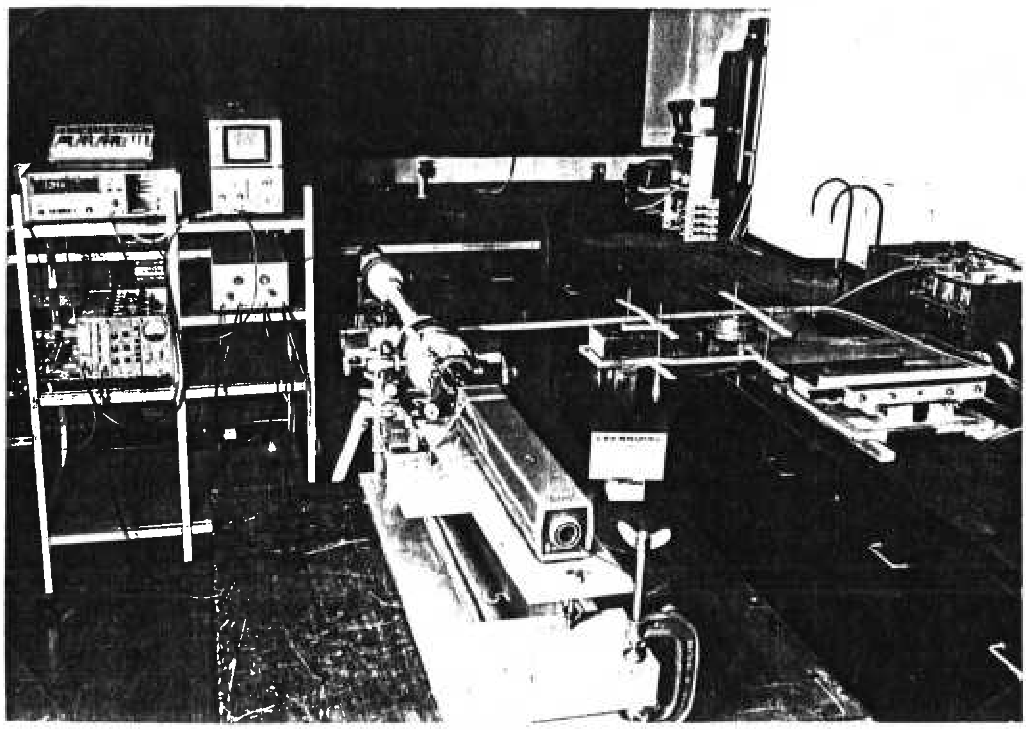

Fig. 3.3.1-2 Experimental set-up for pipe flow

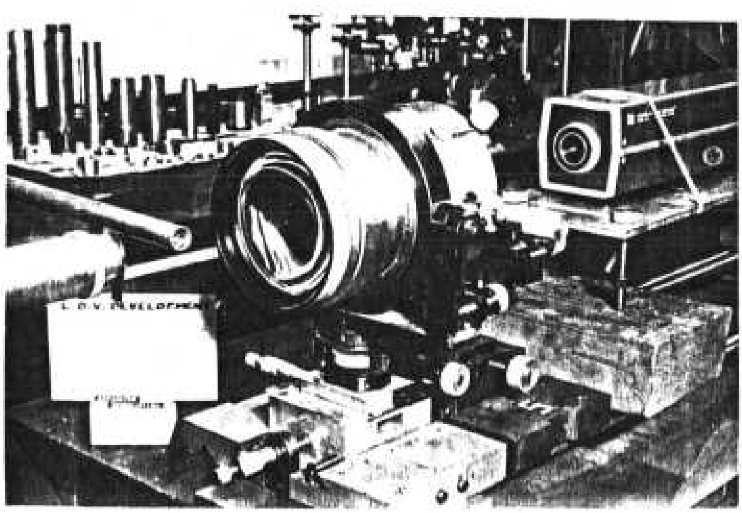

Fig. 3.3.1-3 The Durst and Whitelaw optical unit

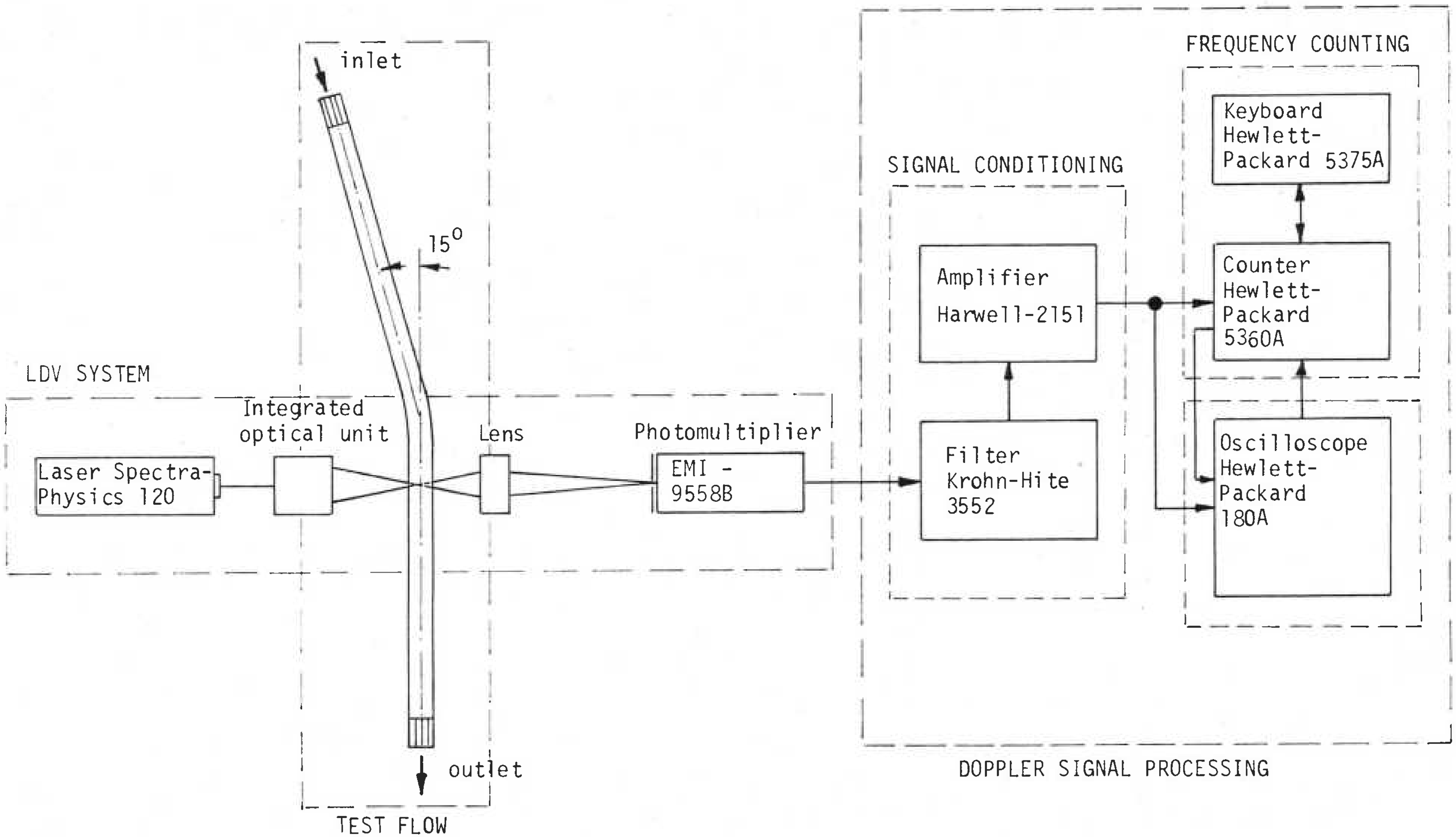

Fig. 3.3.2-1 Schematic diagram of the experimental aparatus for the flow downstream of a bend in a round pipe

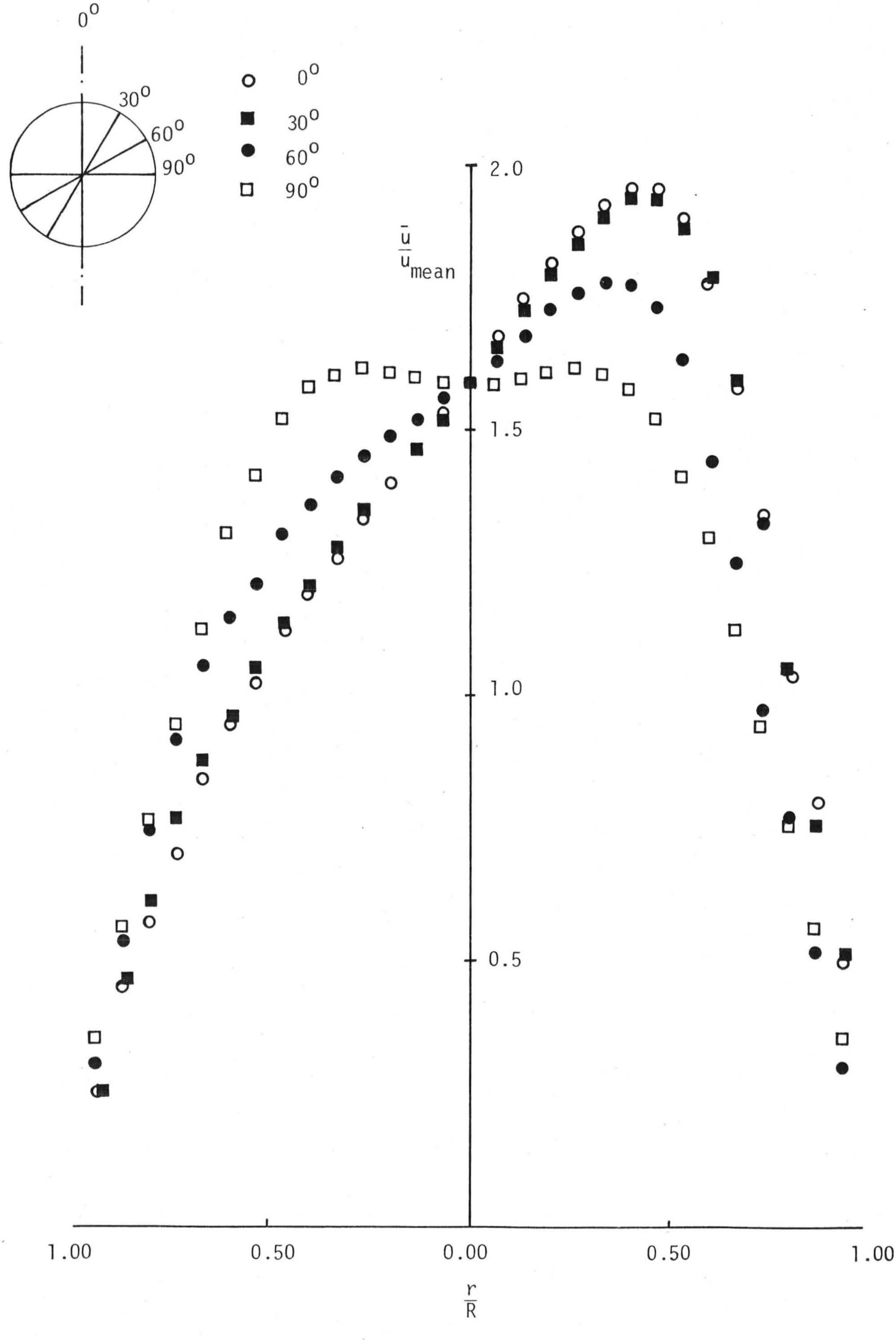

Fig. 3.3.2-2 Measured velocity profiles five diameters downstream the bend

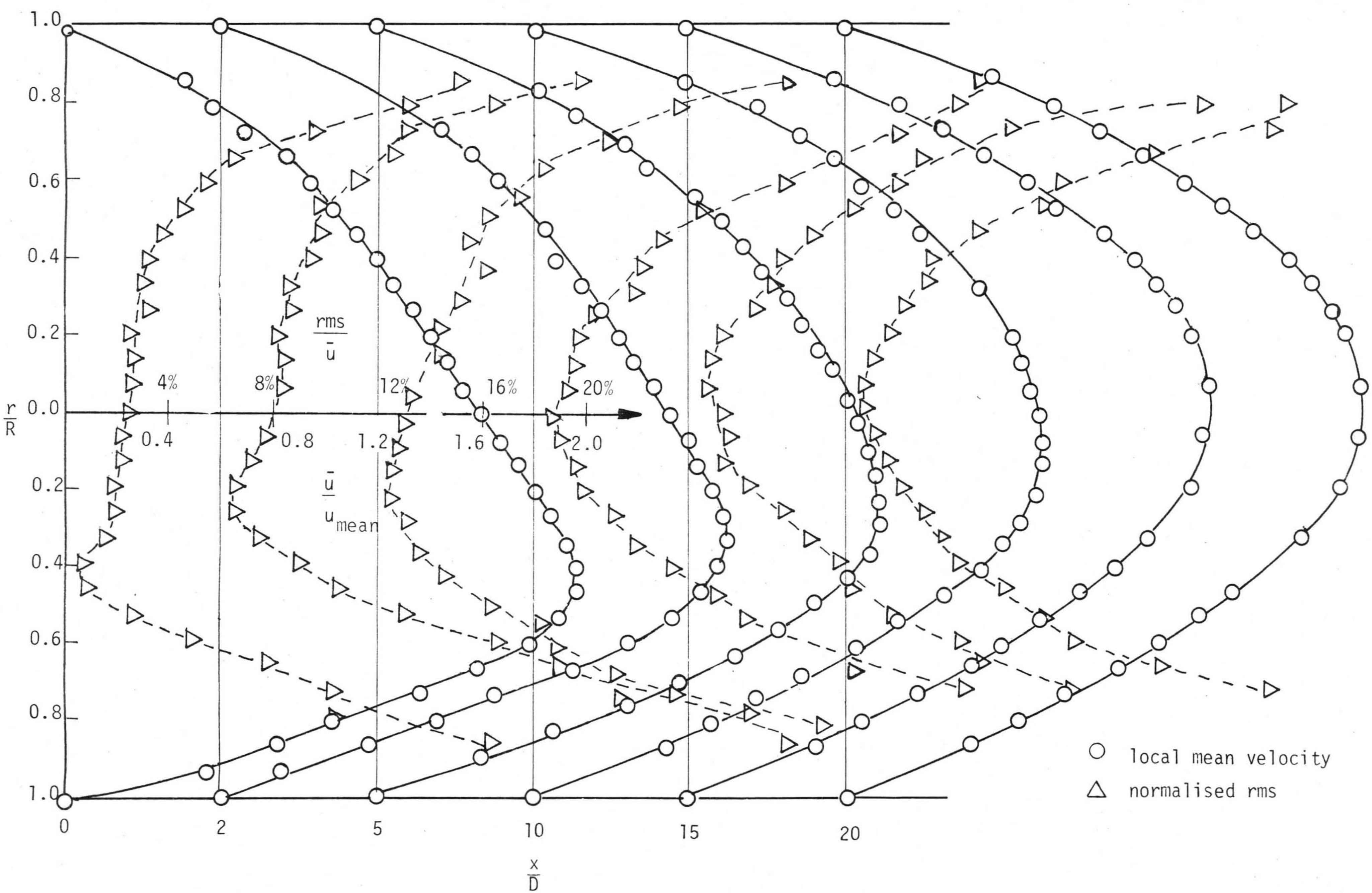

Fig. 3.3.2-3 Measured mean and rms velocity profiles downstream the bend in a round pipe (in the bend plane)

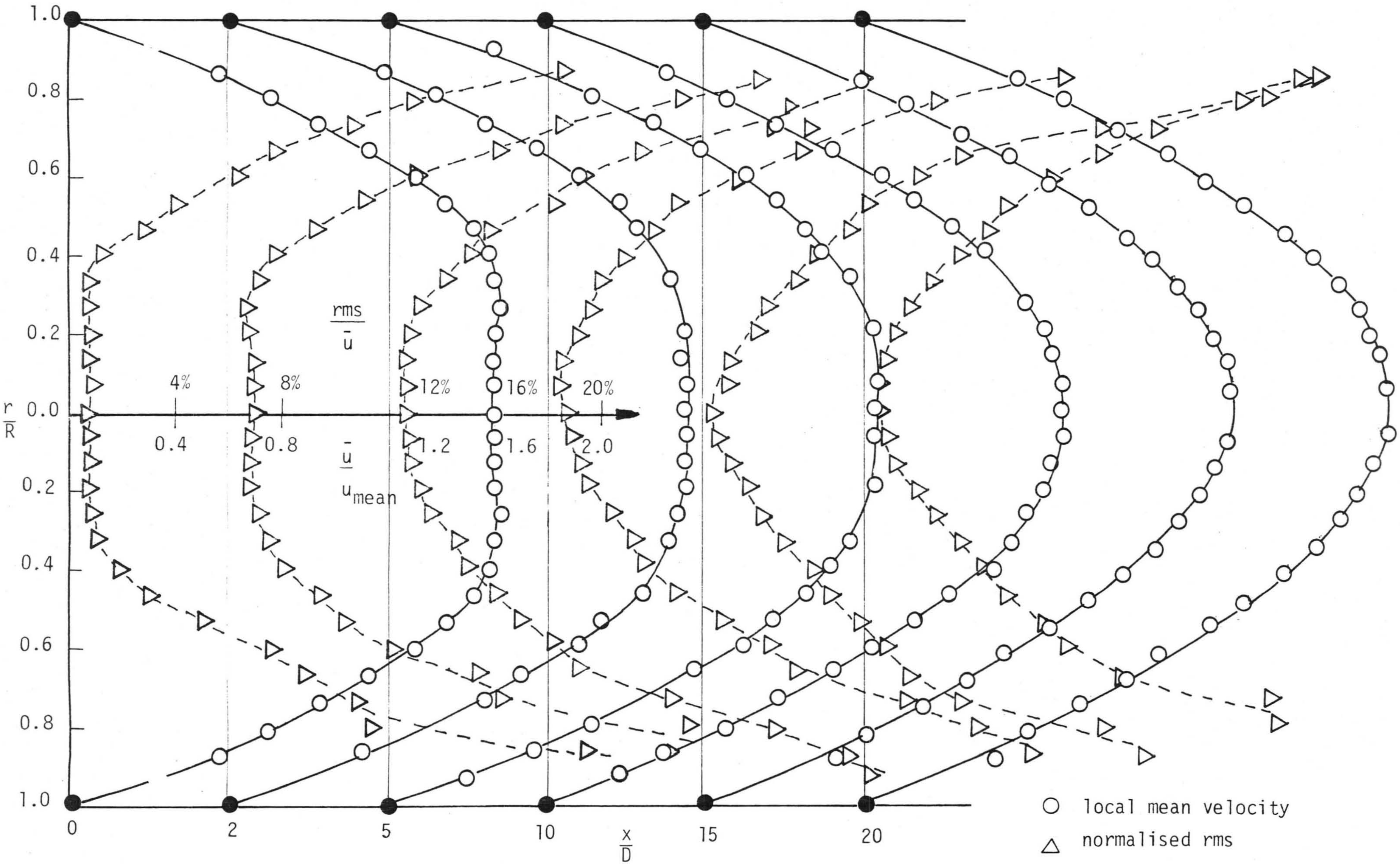

Fig. 3.3.2-4 Measured mean and rms velocity profiles downstream the bend in a round pipe (normal to the bend)

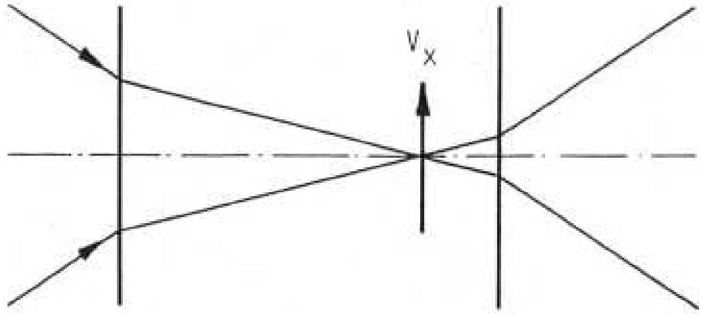

(a) Measurement of the axial velocity

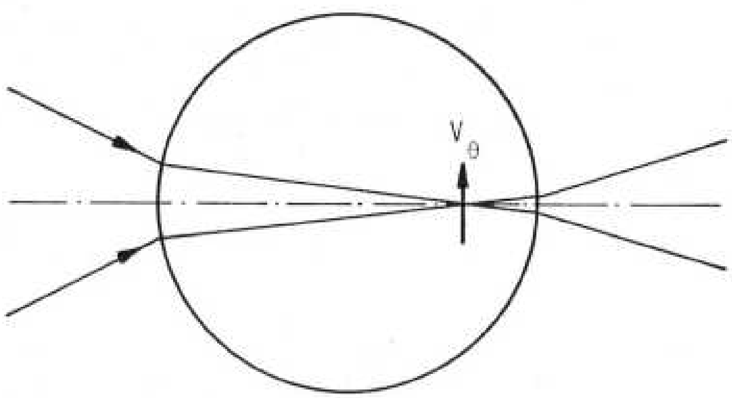

(b) Measurement of the circumferential velocity

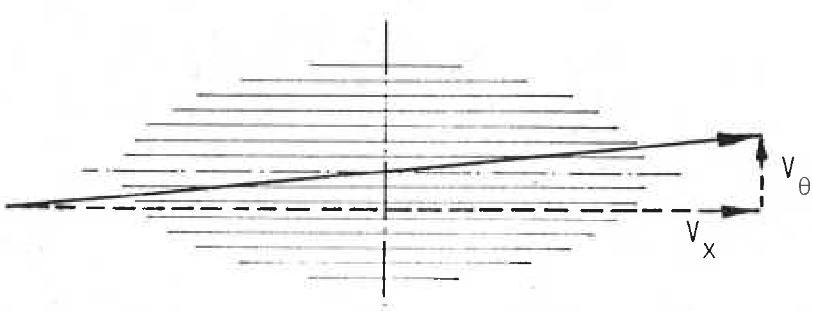

(c) Velocity measurement in the presence of a high lateral velocity component

Fig. 3.3.2-5 Velocity measurements in a round pipe

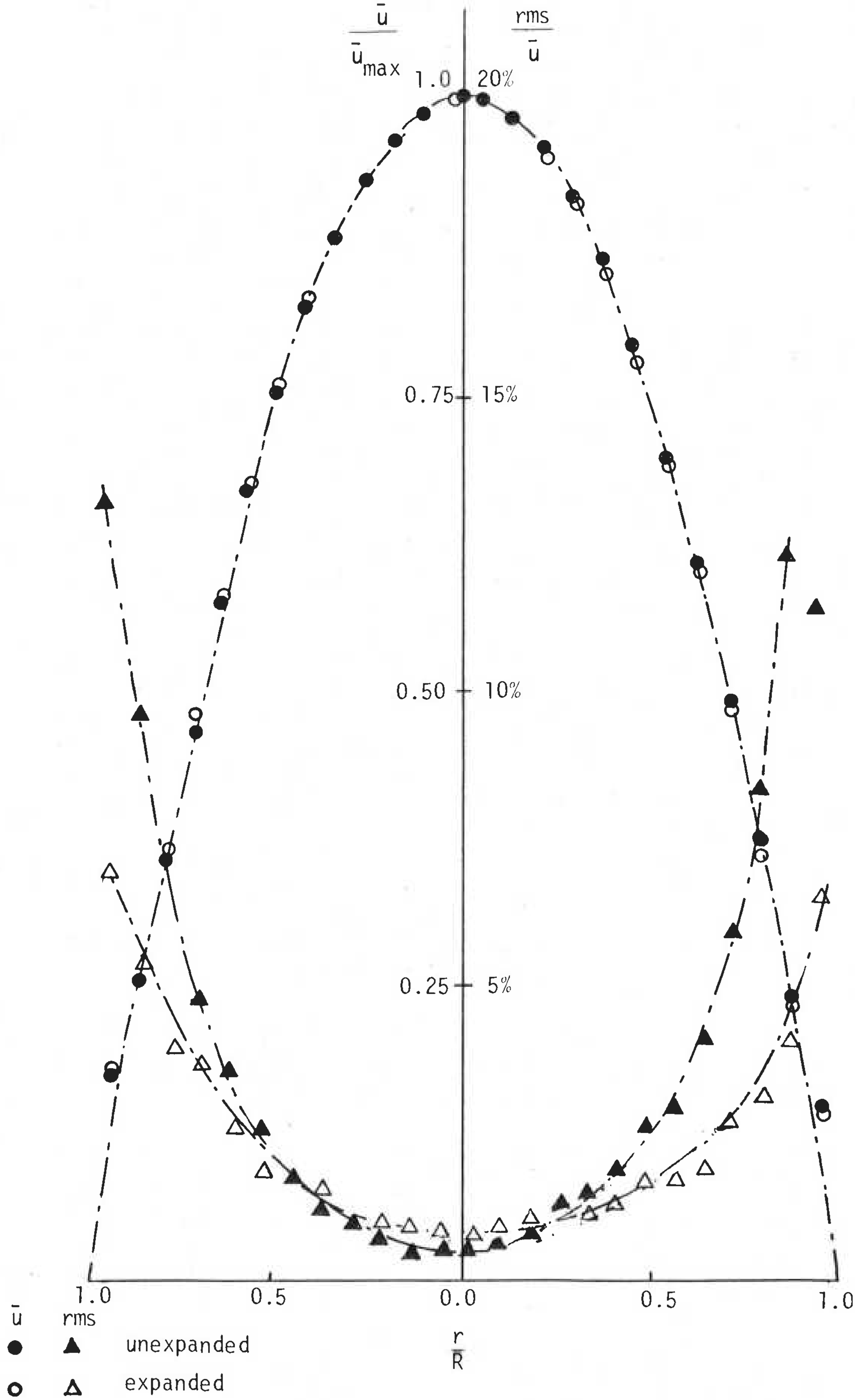

Fig. 3.4.2-1 Influence of beam expansion on the measured mean and rms velocities

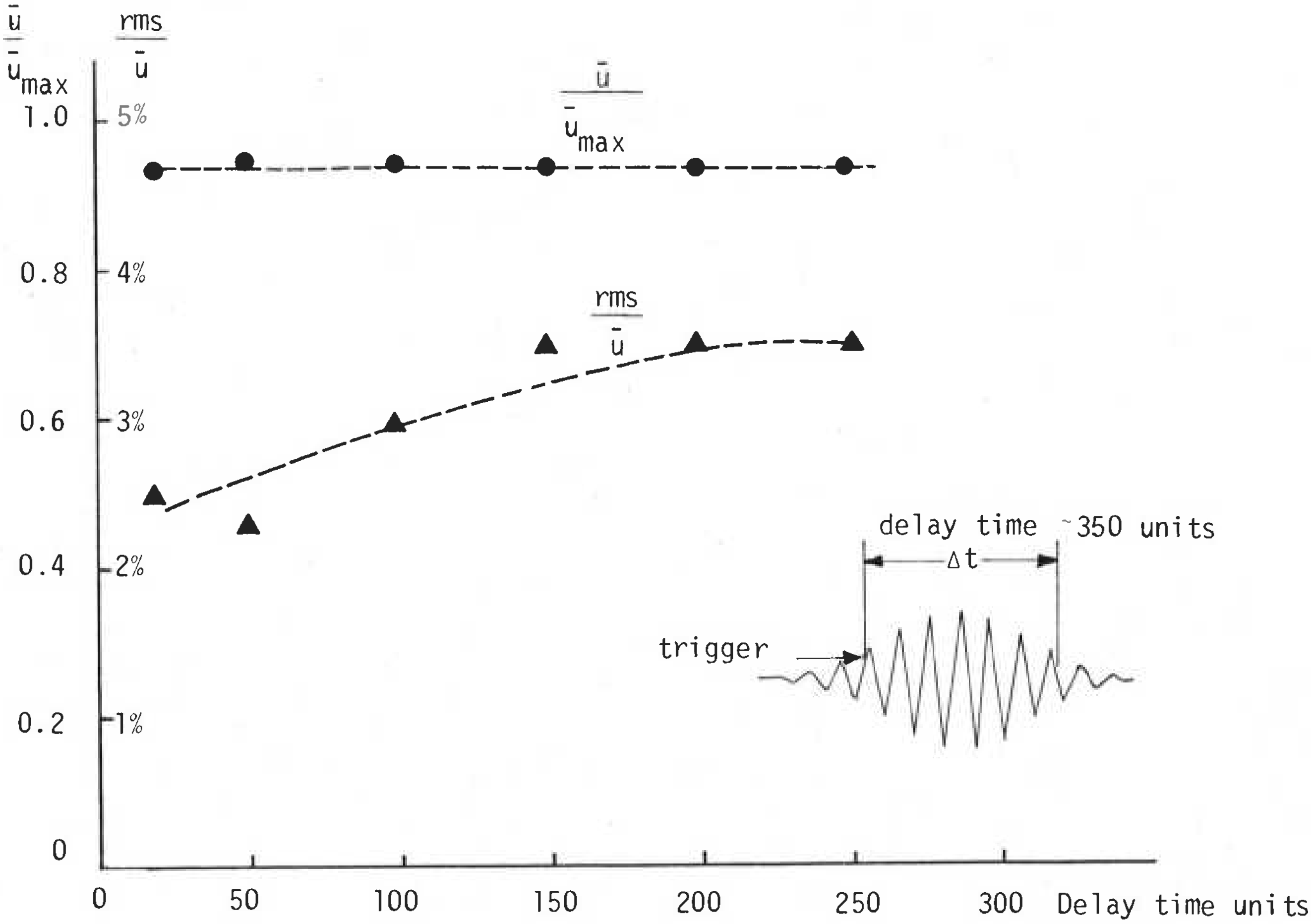

(a) Expanded beam

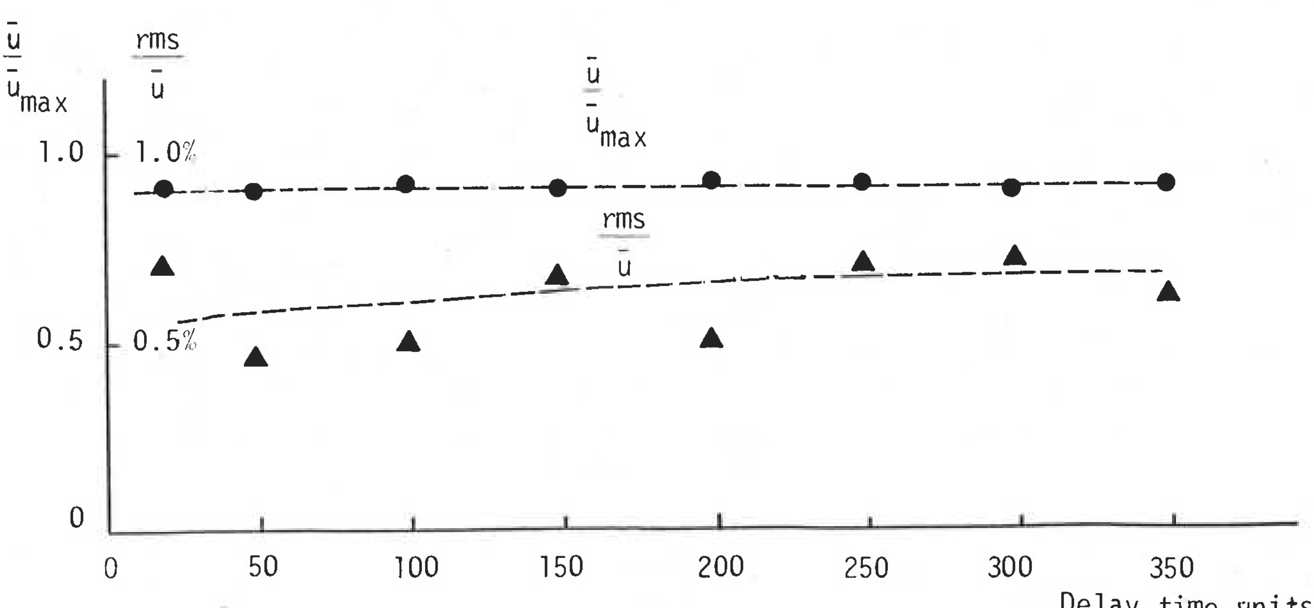

(b) Unexpanded beam

Fig. 3.4.2-2 Influence of measured part of Doppler burst on the measured mean and rms velocities

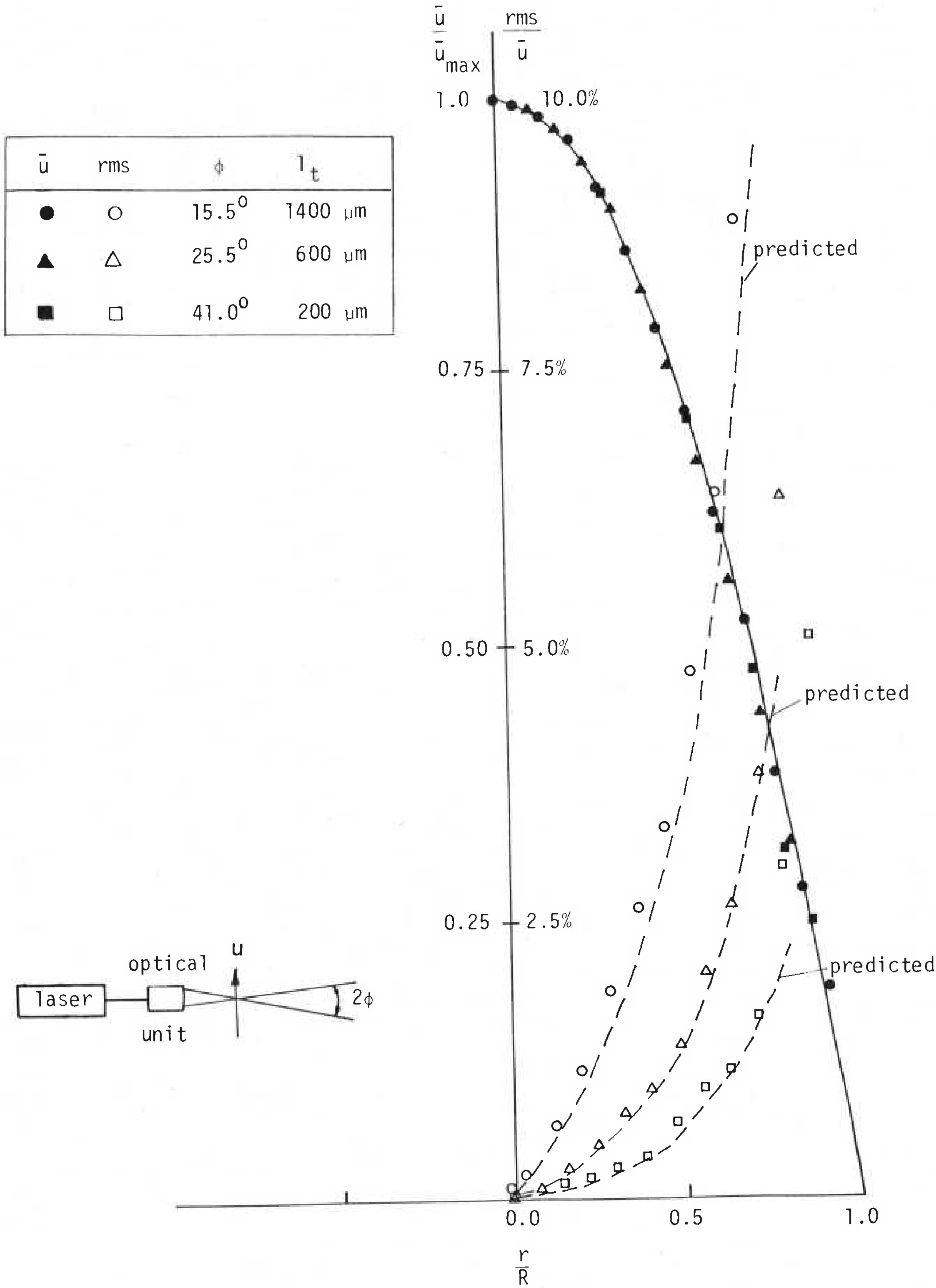

Fig. 3.4.3-1 Influence of beam incidence angle on the measured mean and rms velocities

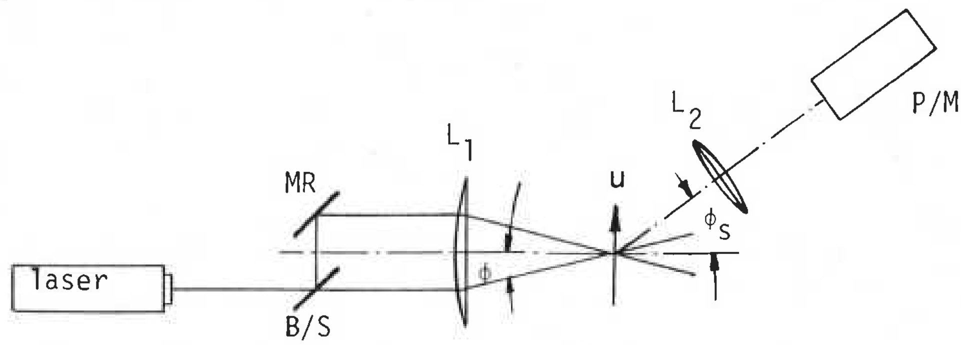

(a) LDV operating in off-axis detection

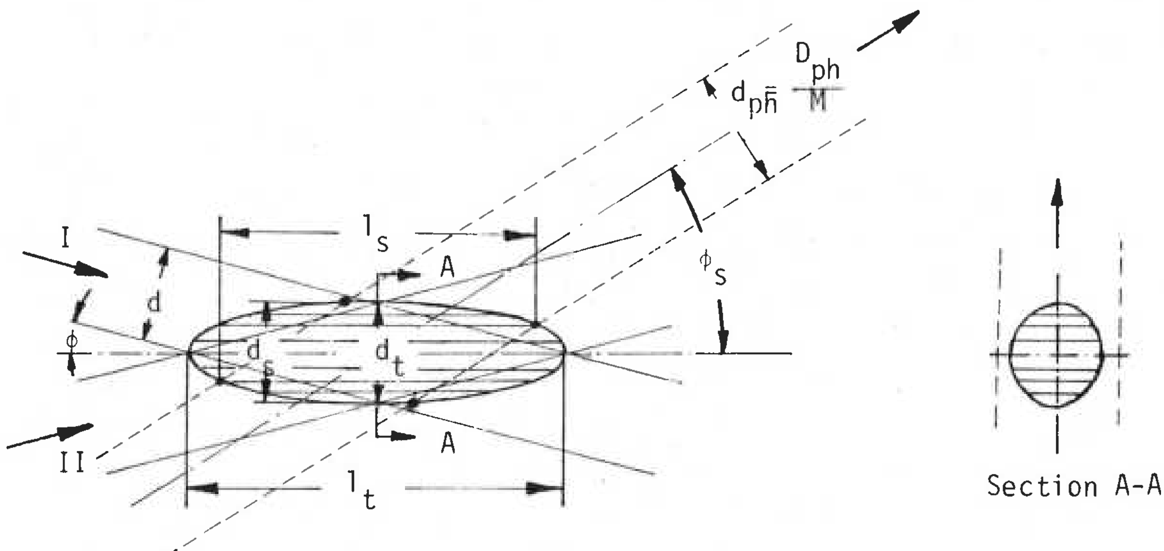

(b) Off-axis detection in the beam plane

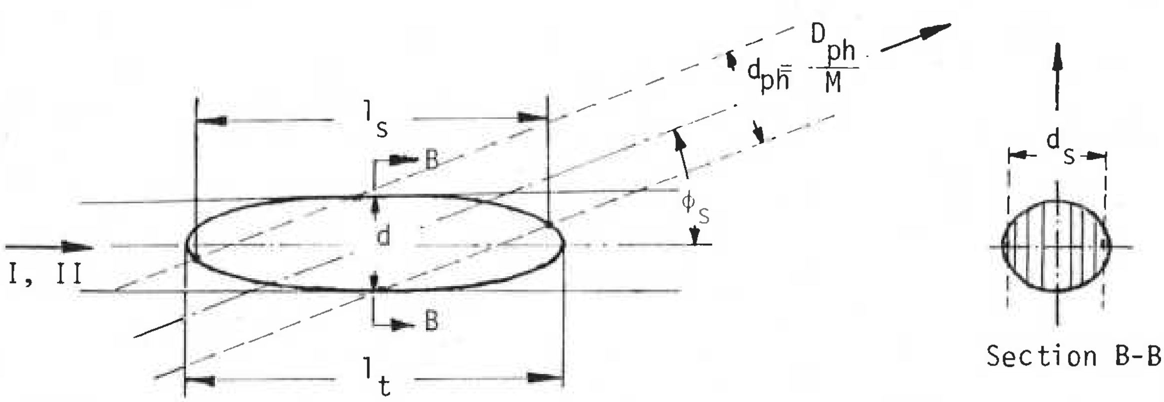

(c) Off-axis detection in the beam symmetry plane

Fig. 3.4.5-1 Off-axis detection

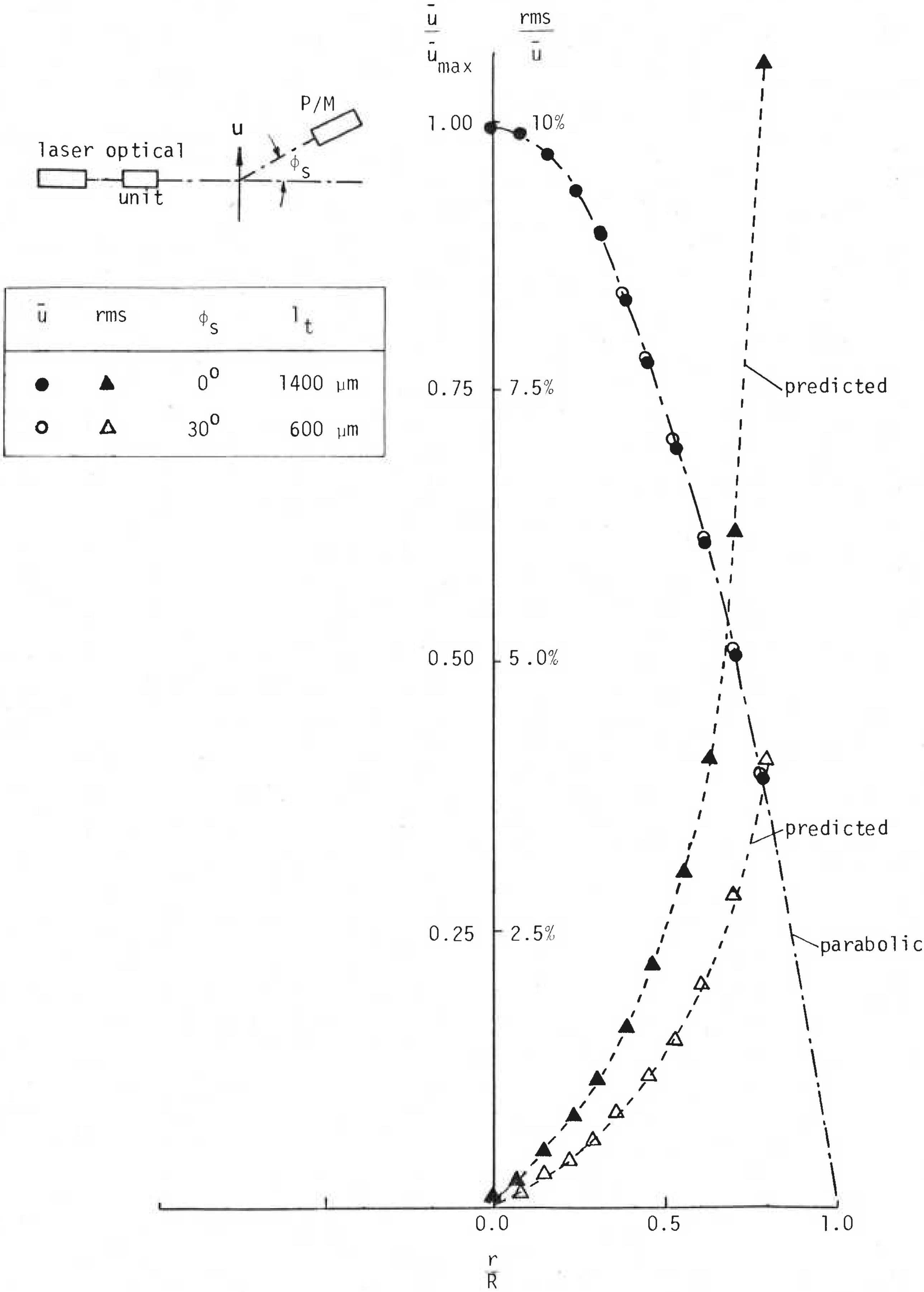

Fig. 3.4.5-2 Influence of off-axis detection on the measured mean and rms velocities

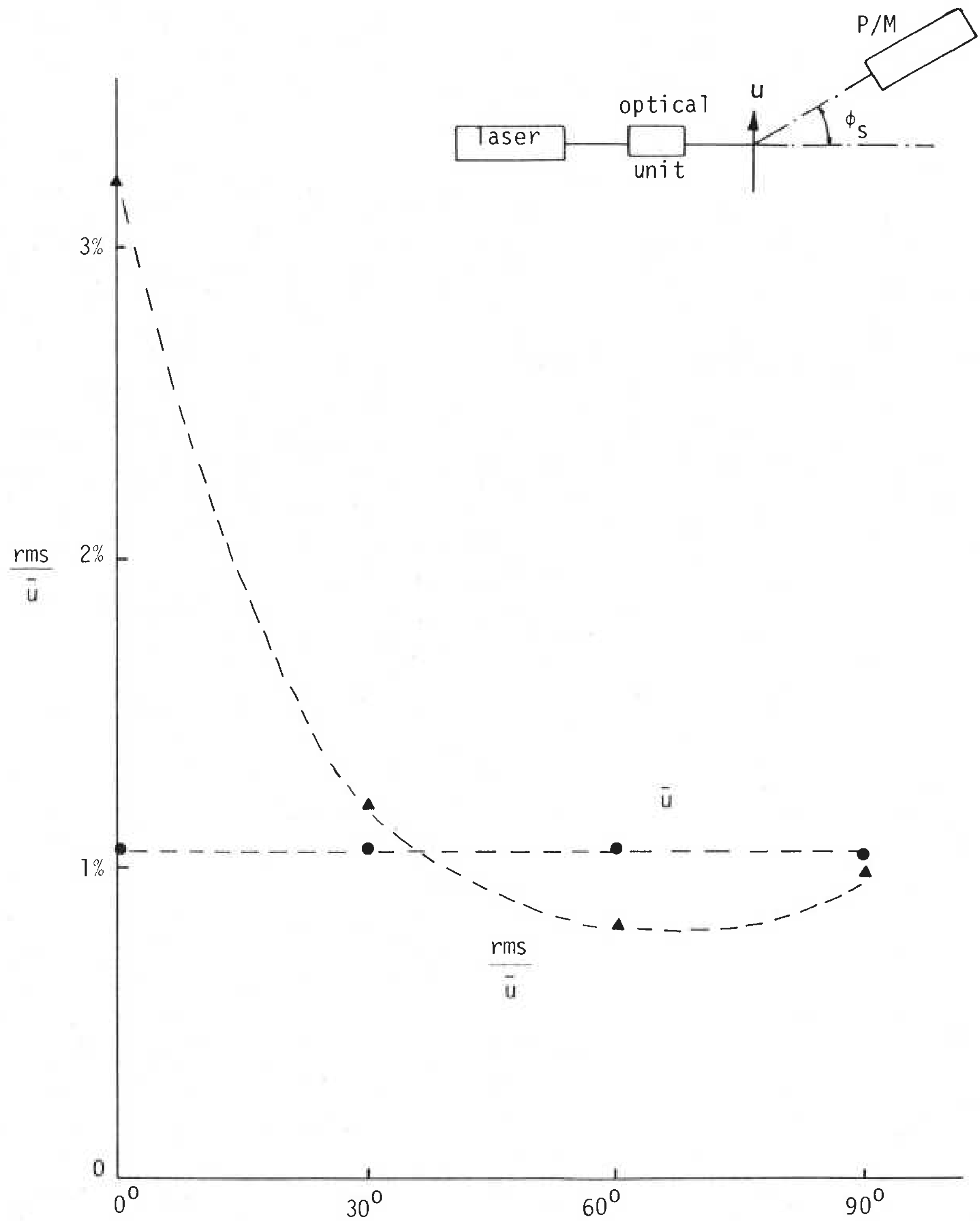

Fig. 3.4.5-3 Influence of off-axis detection on the measured mean and rms velocities

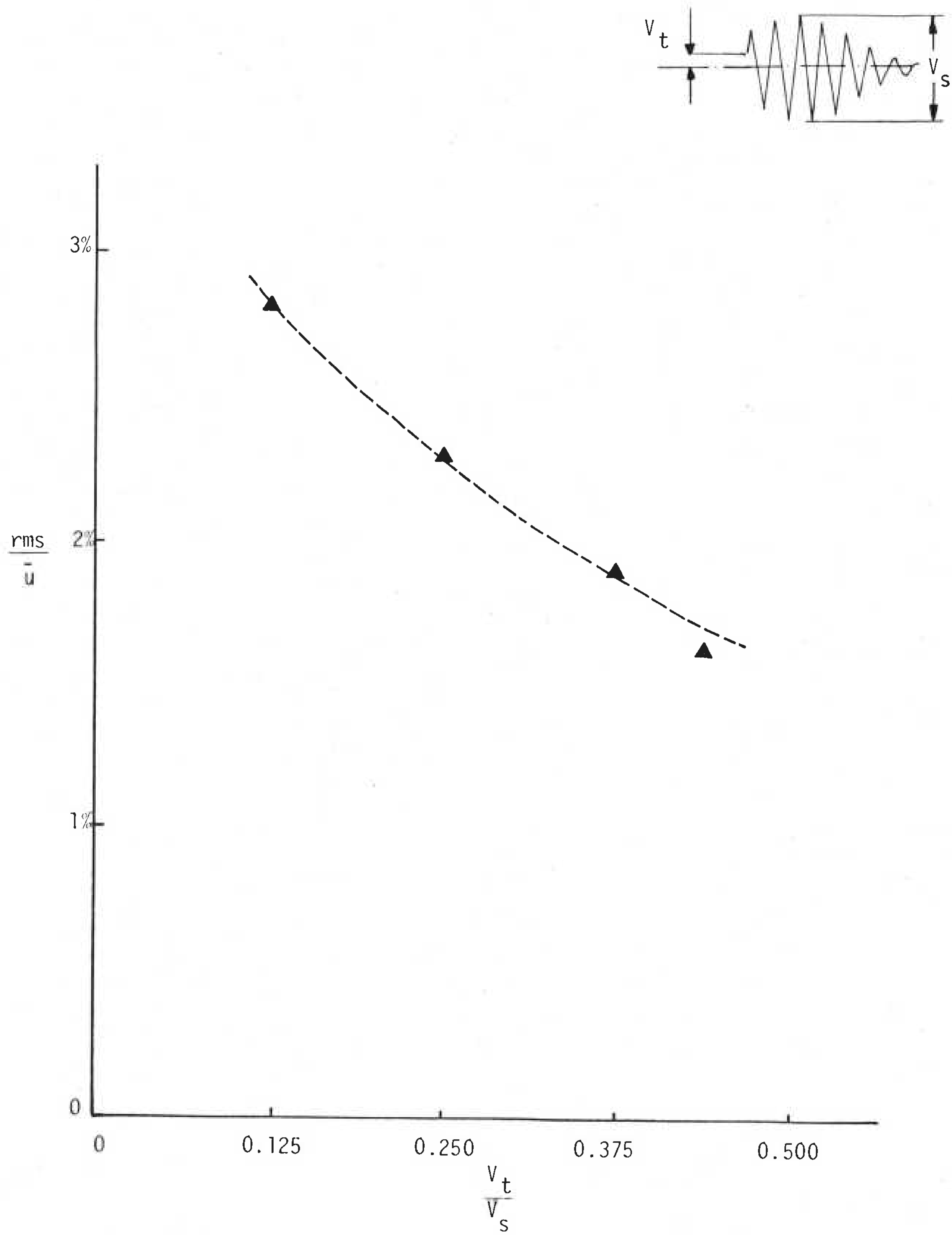

Fig. 3.4.6-1 Effect of triggering level on the measured rms velocities

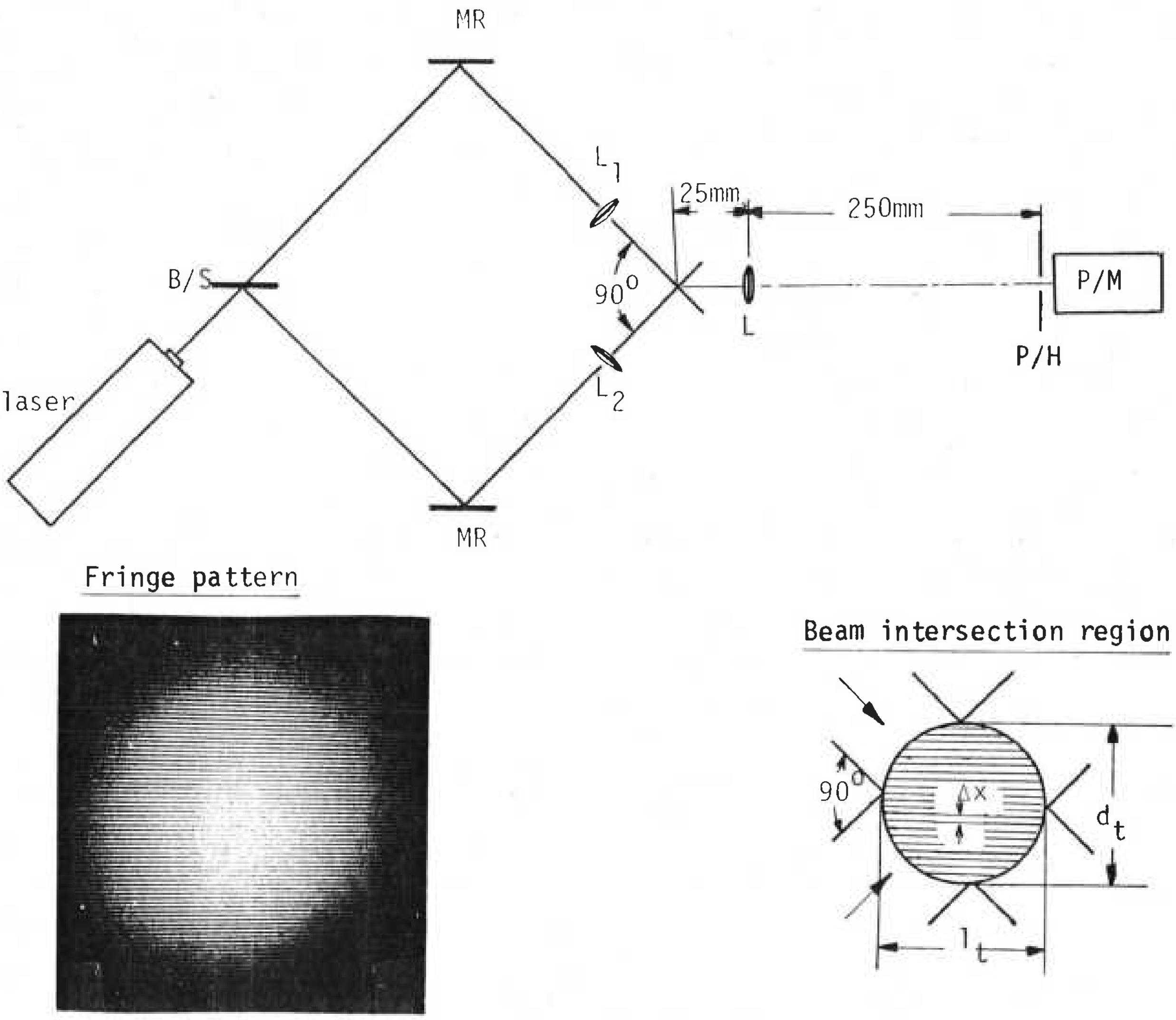

(a) Schematic diagram

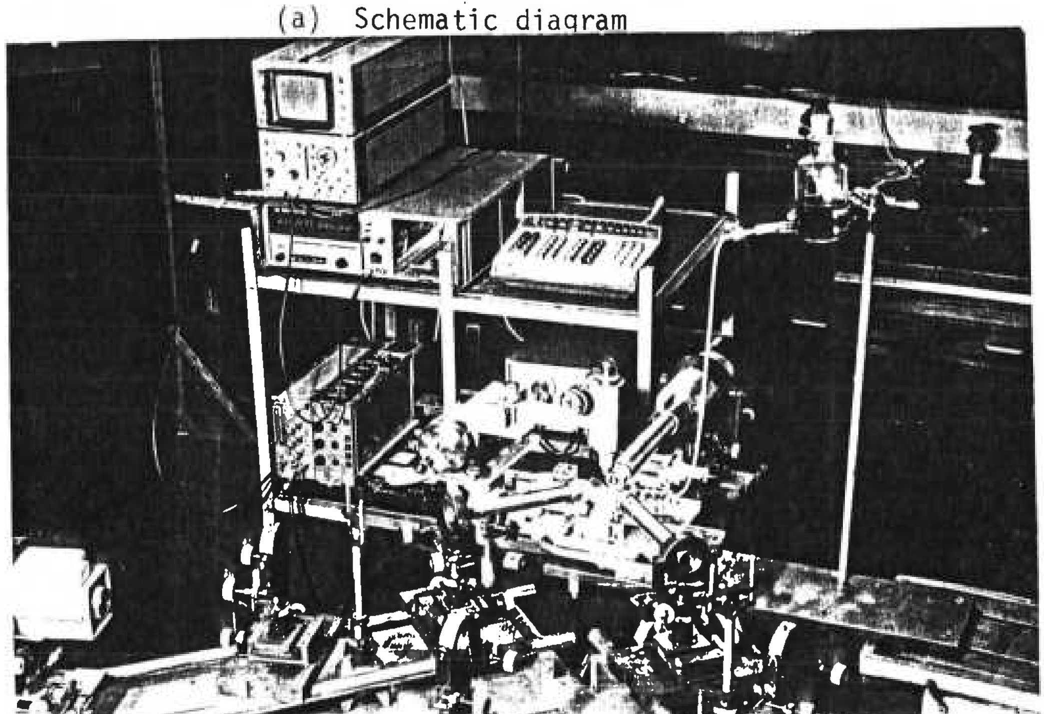

(b) Photographic view

Fig. 3.5.2-1 The loose lens LDV

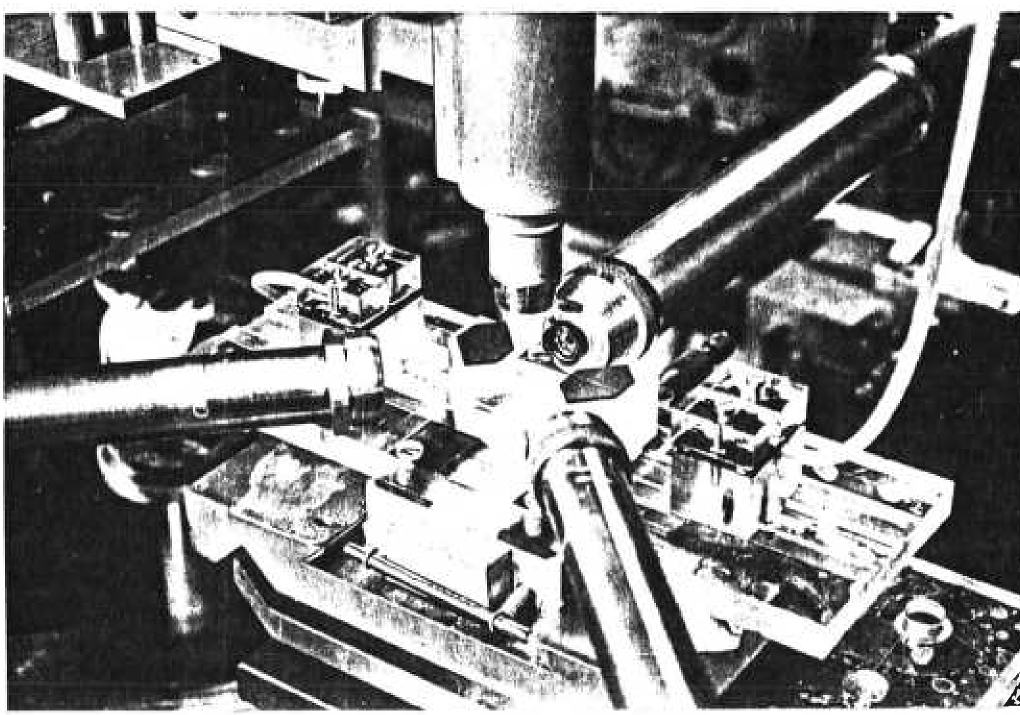

Fig. 3.5.2-2 Close view of the measuring region

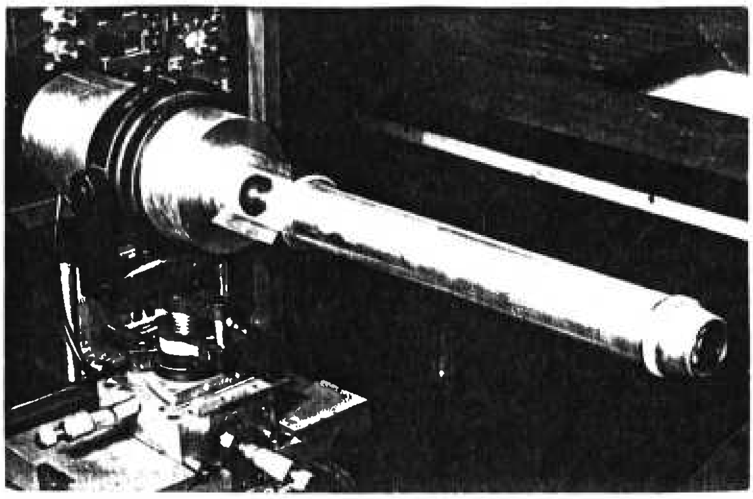

Fig. 3.5.2-3 The integrated receiving optics

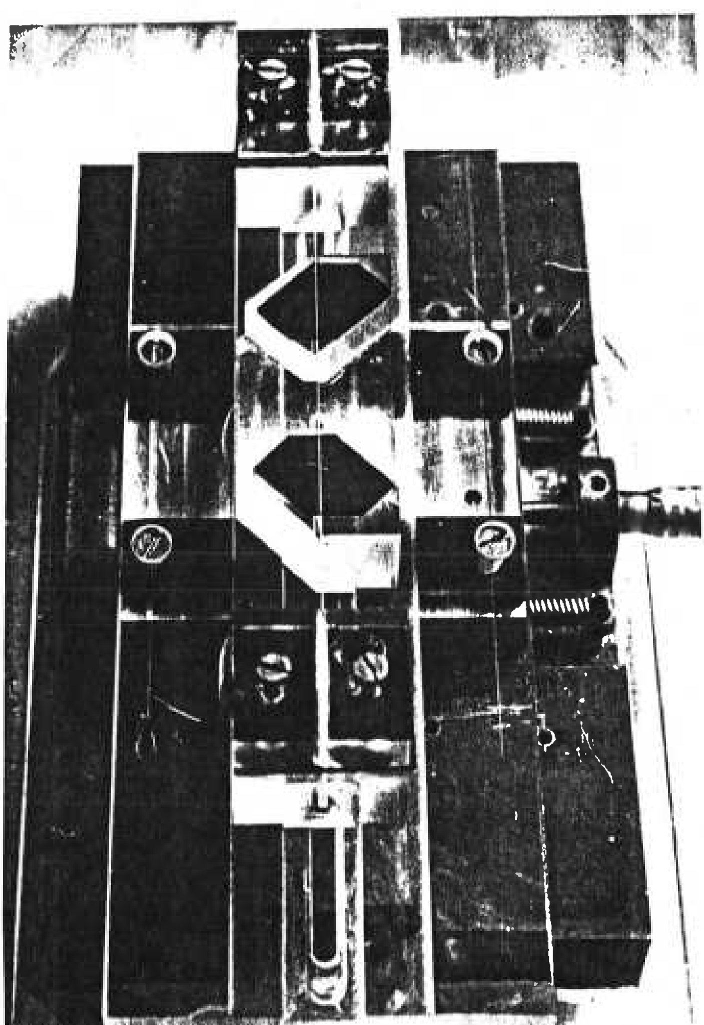

Fig. 3.5.2-4 The capillary holder

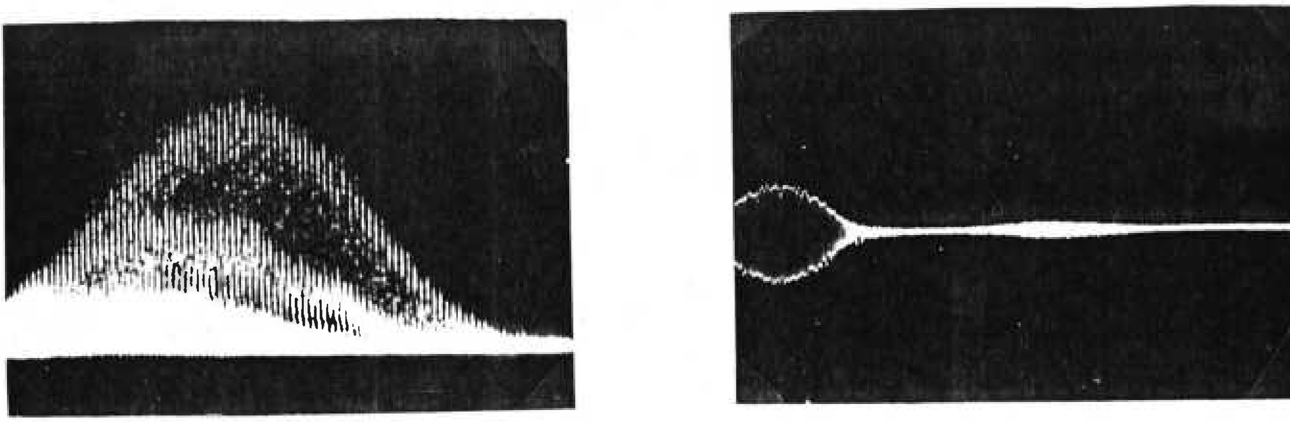

Unfiltered Filtered

(a) Water (D = 250 μm)

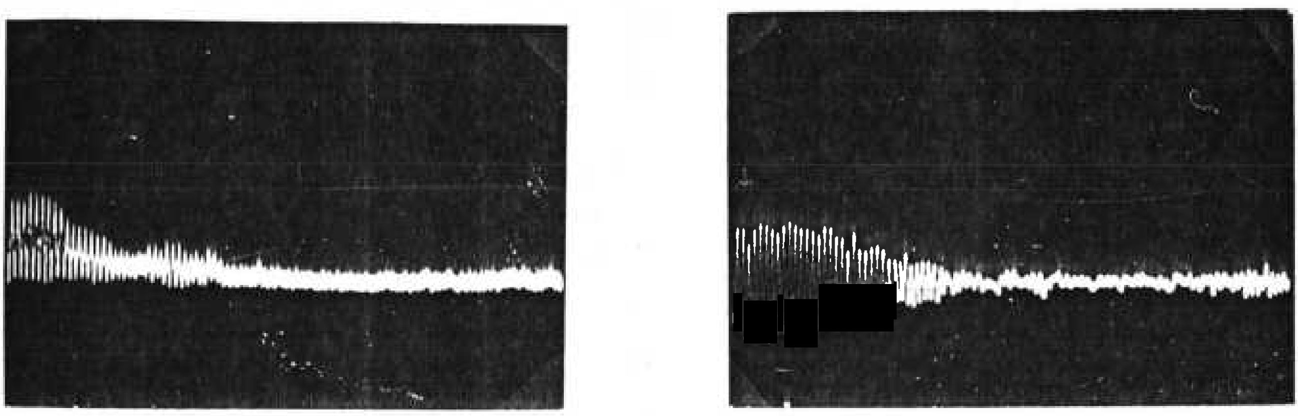

Unfiltered Filtered

(b) Plasma (D = 250 μm)

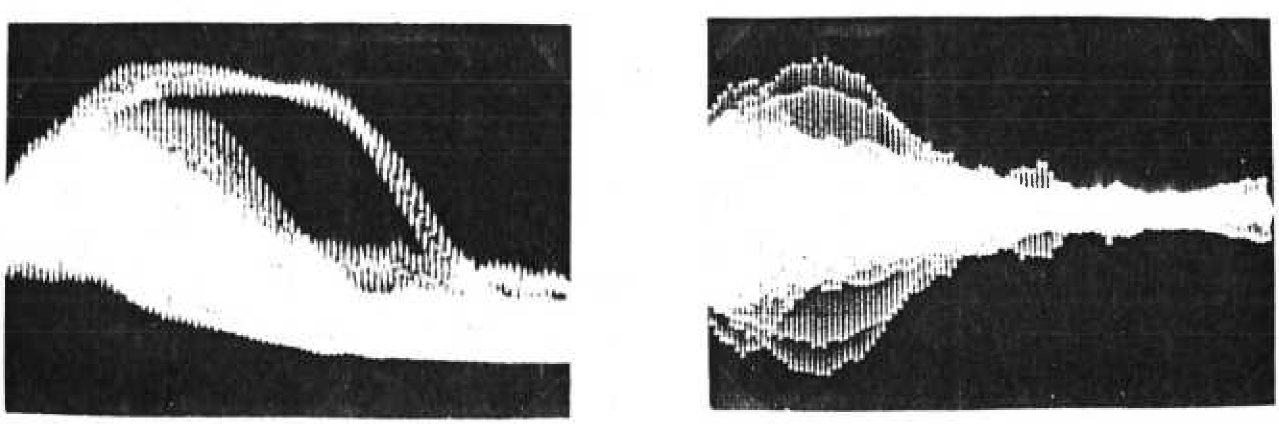

Unfiltered Filtered

(c) 100:1 diluted blood (D = 250 μm)

Fig. 3.5.2-5 Doppler signals with He-Ne LDV in glass capillary flows

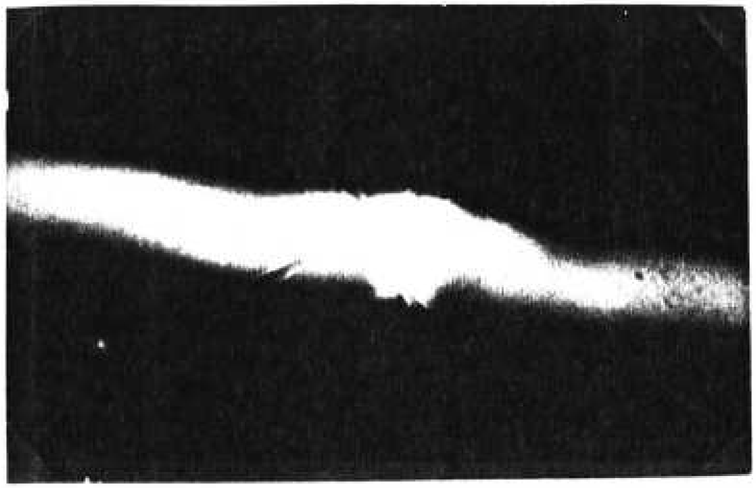

(a) Glass capillary (D = 125 μm)

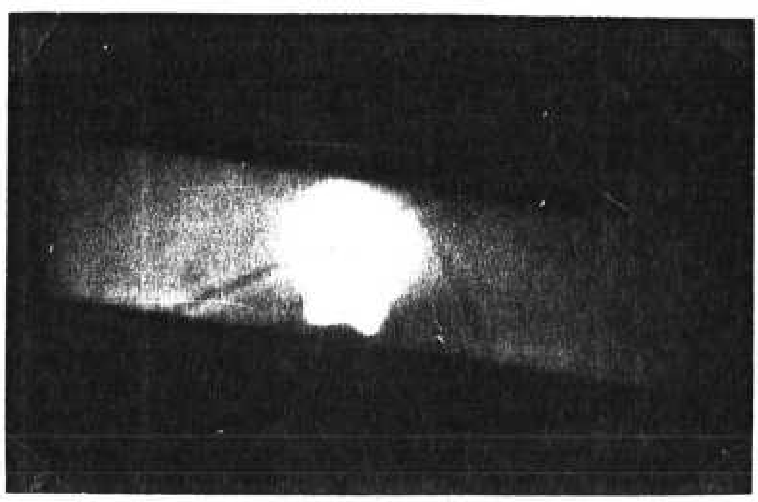

(b) Glass capillary (D = 250 μm)

Fig. 3.5.2-6 Diffusion of the laser beams in whole blood

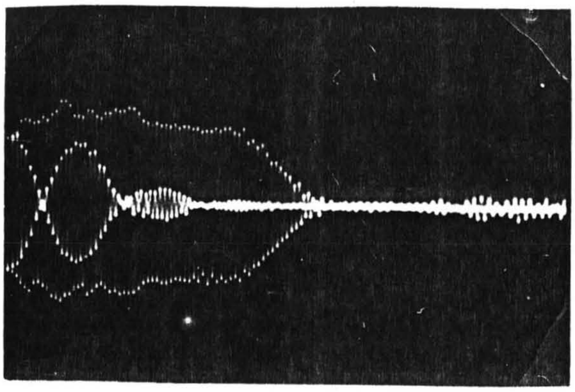

(a) 100:1 Diluted blood (D = 125 μm)

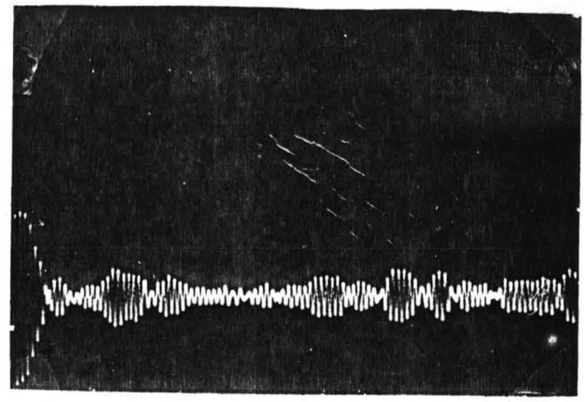

(b) 10:1 Diluted blood (D = 125 μm)

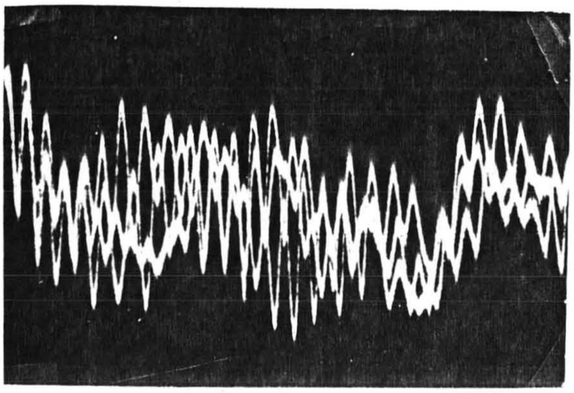

Unfiltered

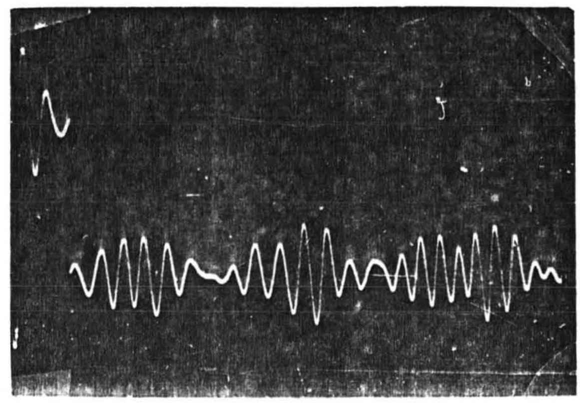

Filtered and processed

(c) Whole blood (D = 125 μm)

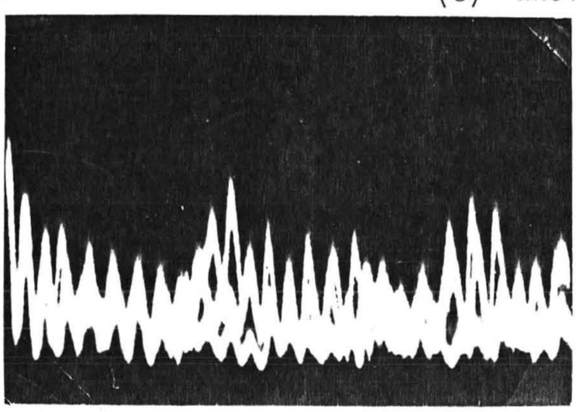

Unfiltered

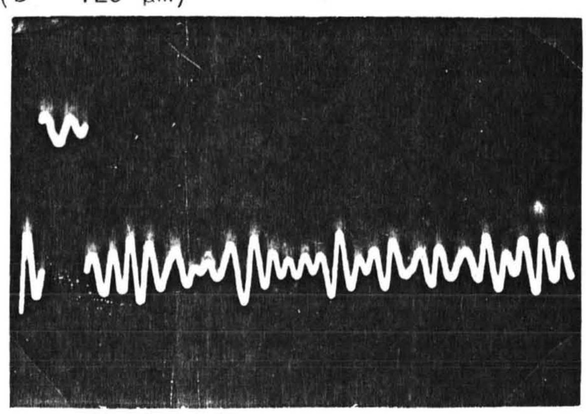

Filtered and processed

(d) Whole blood (D = 250 μm)

Fig. 3.5.2-7 Doppler signals with He-Ne LDV in glass capillary flows

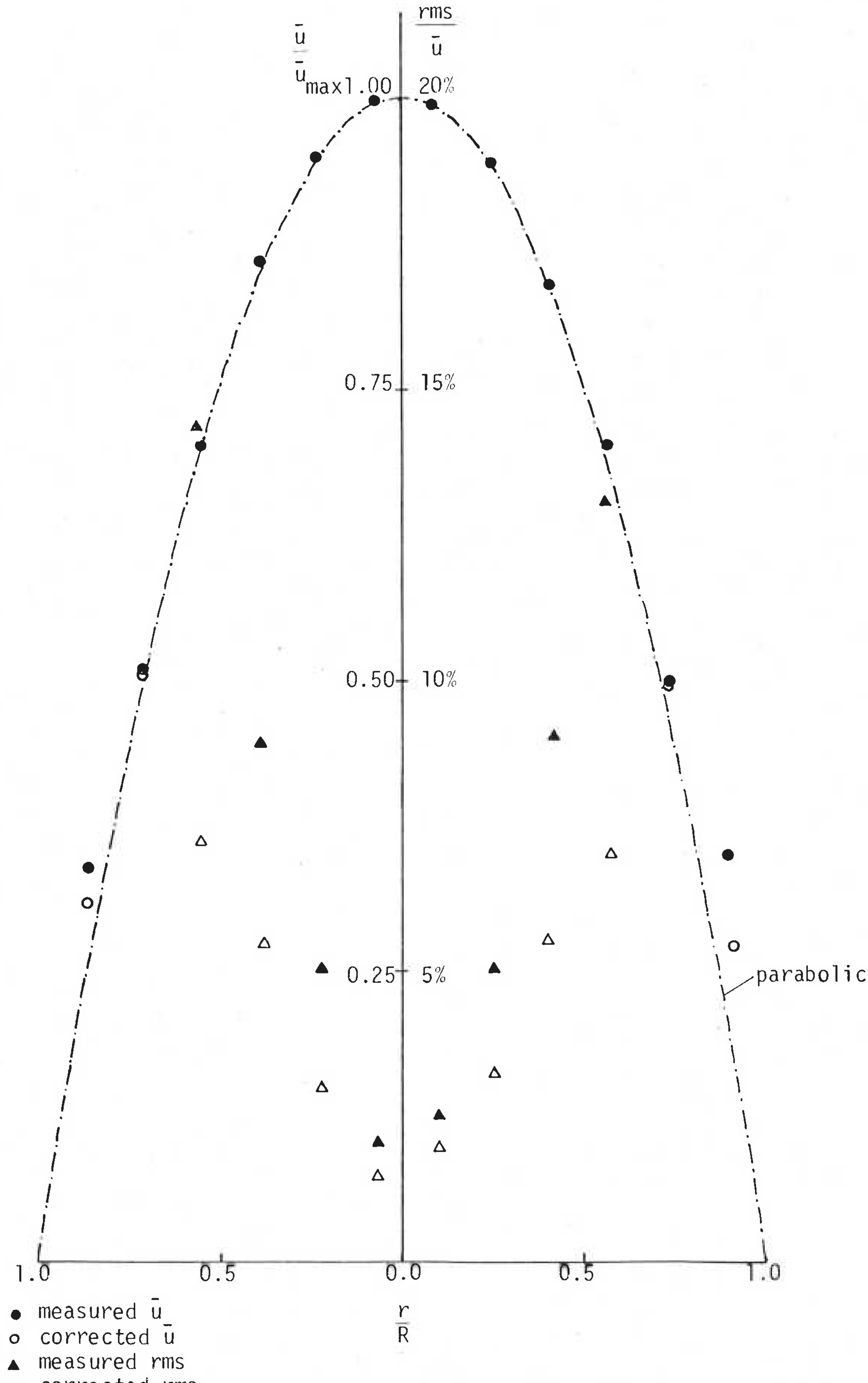

Fig. 3.5.2-8a Measured mean and rms velocity profiles
Saline (H = 0, D = 250 μm)

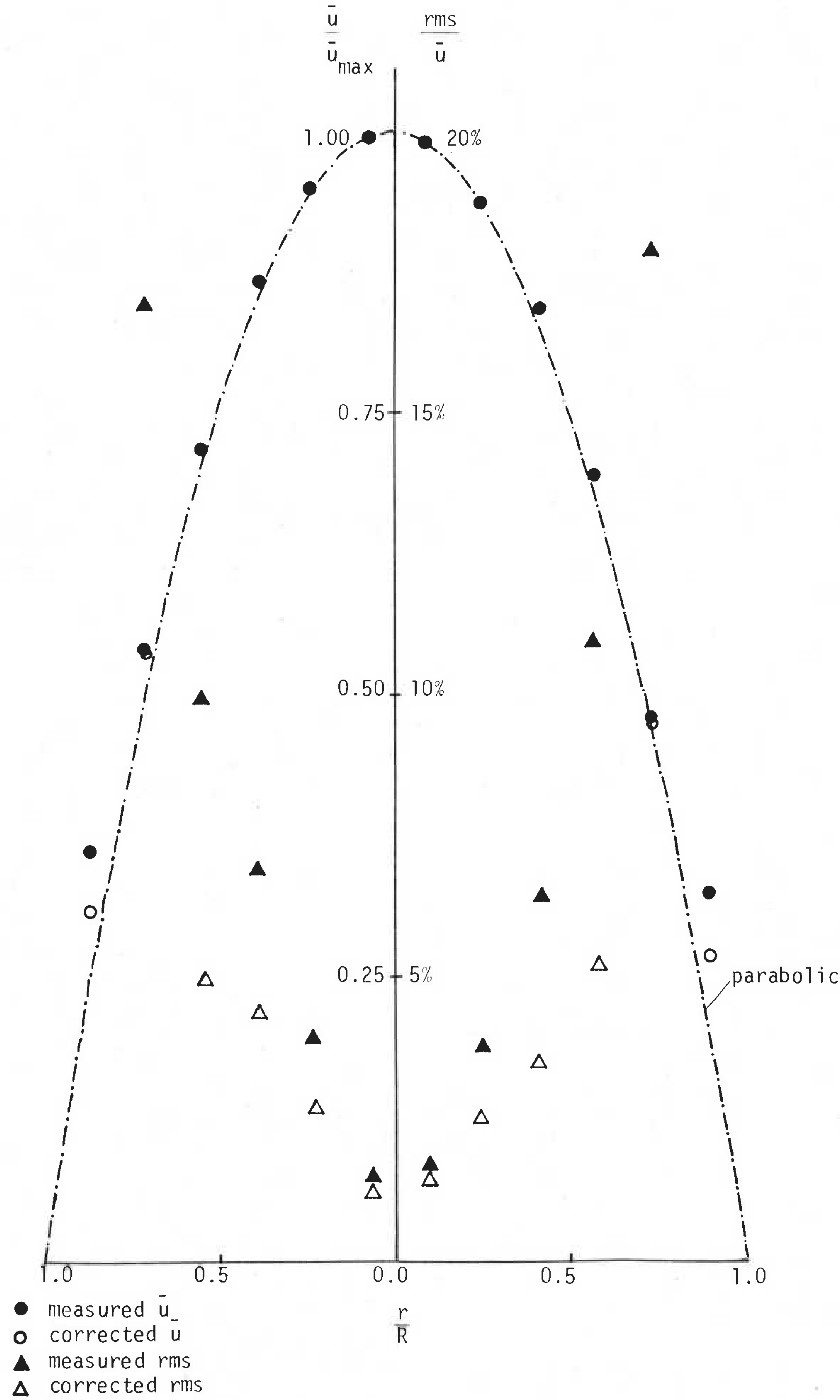

Fig. 3.5.2-8b Measured mean and rms velocity profiles
100:1 Diluted blood (H = 0.5%, D = 250 μm)

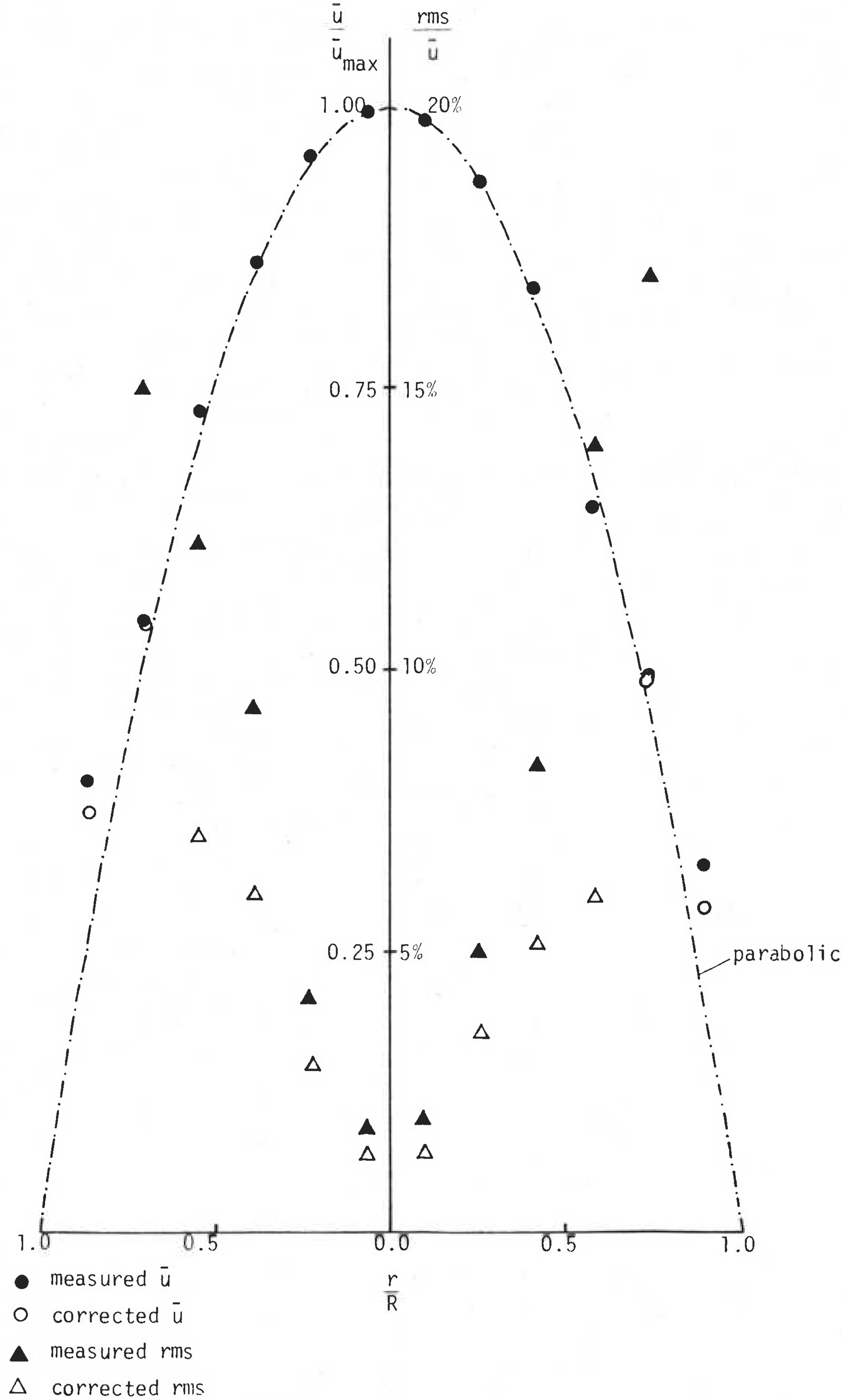

Fig. 3.5.2-8c Measured mean and rms velocity profiles
50:1 Diluted blood (H = 1%, D = 250 μm)

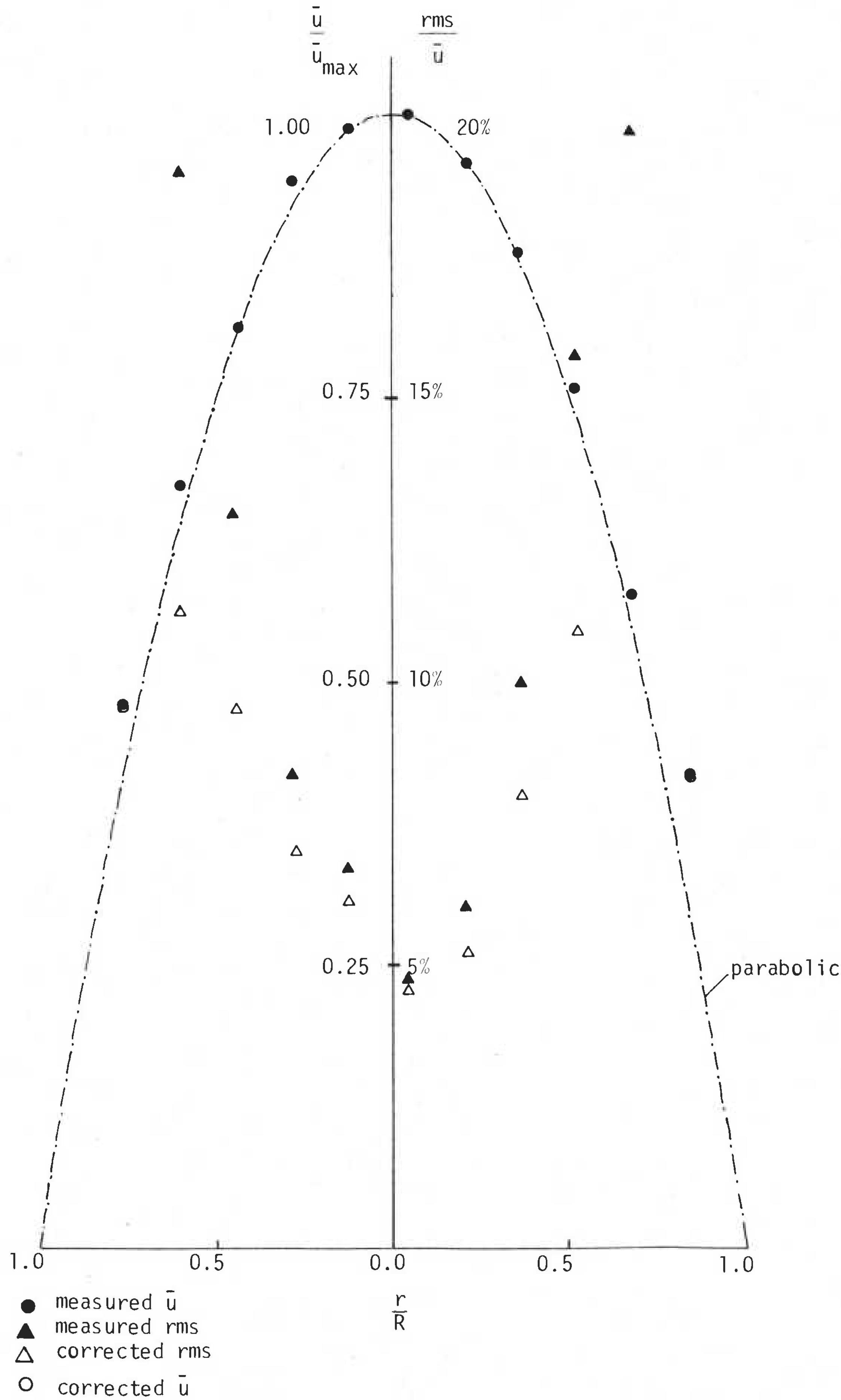

Fig. 3.5.2-8d Measured mean and rms velocity profiles
20:1 Diluted blood (H = 2.5%, D = 250 μm)

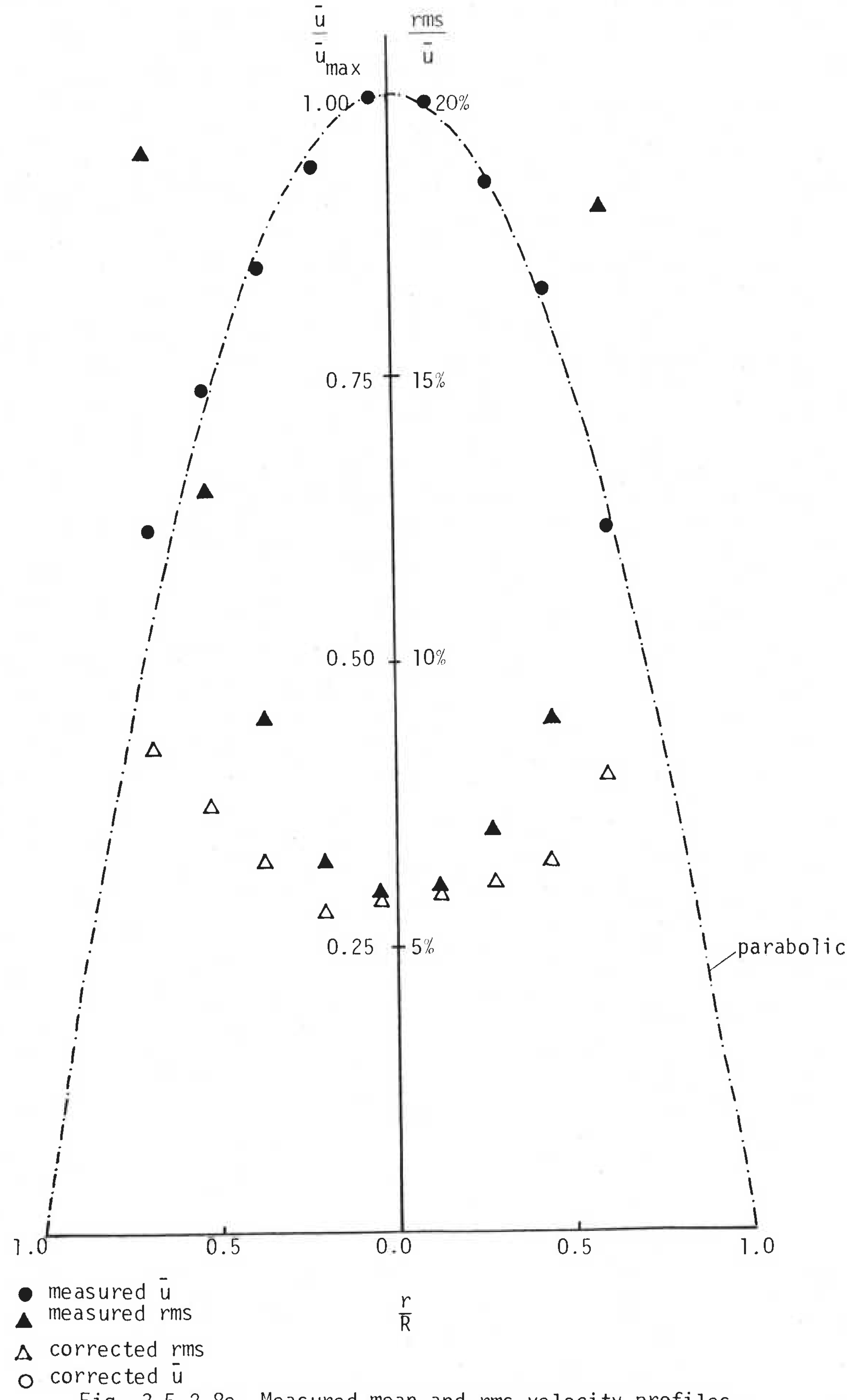

Fig. 3.5.2-8e Measured mean and rms velocity profiles
10:1 Diluted blood (H = 4.5%, D = 250 μm)

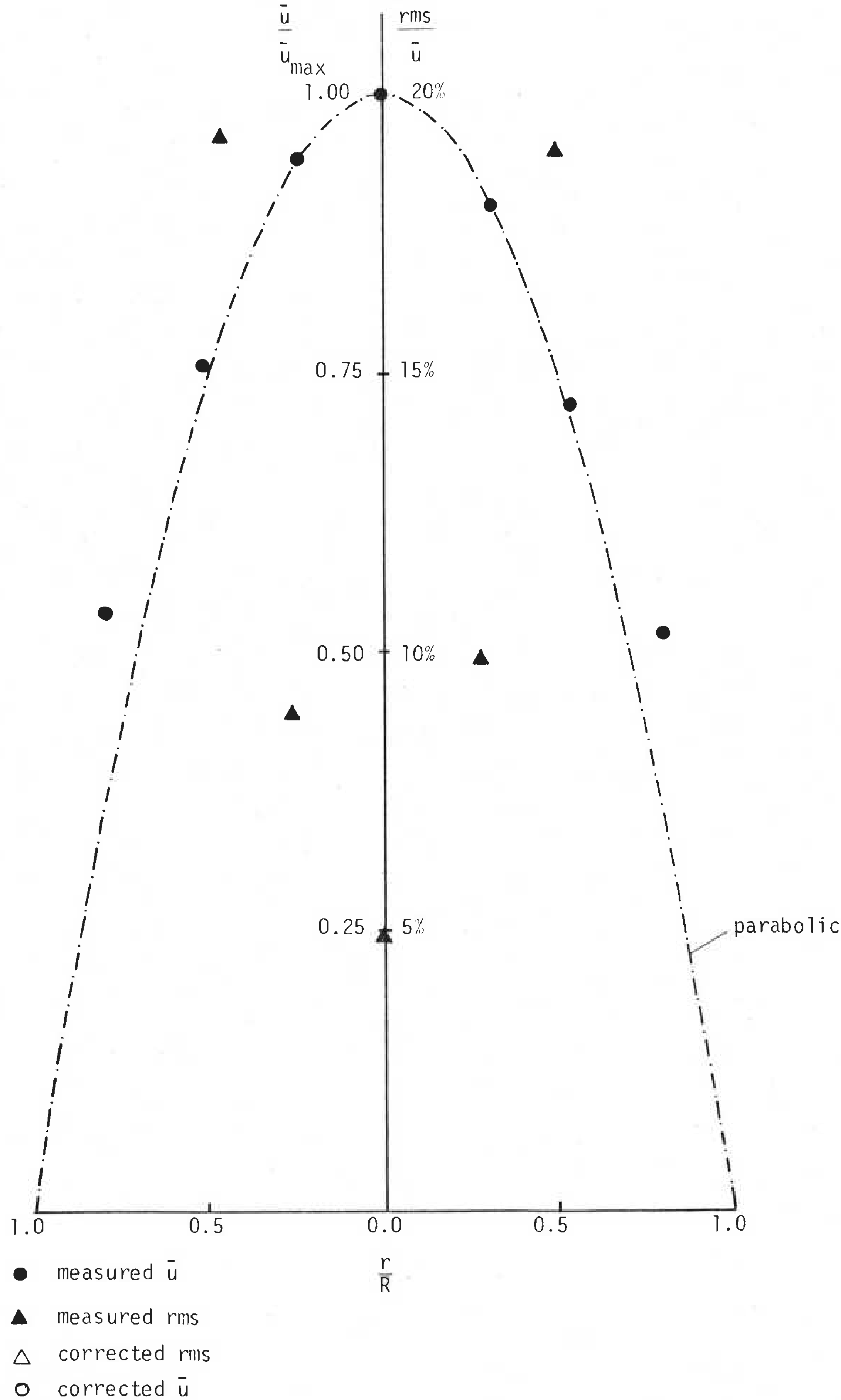

Fig. 3.5.2-9a Measured mean and rms velocity profiles
Water flow (D = 125 μm)

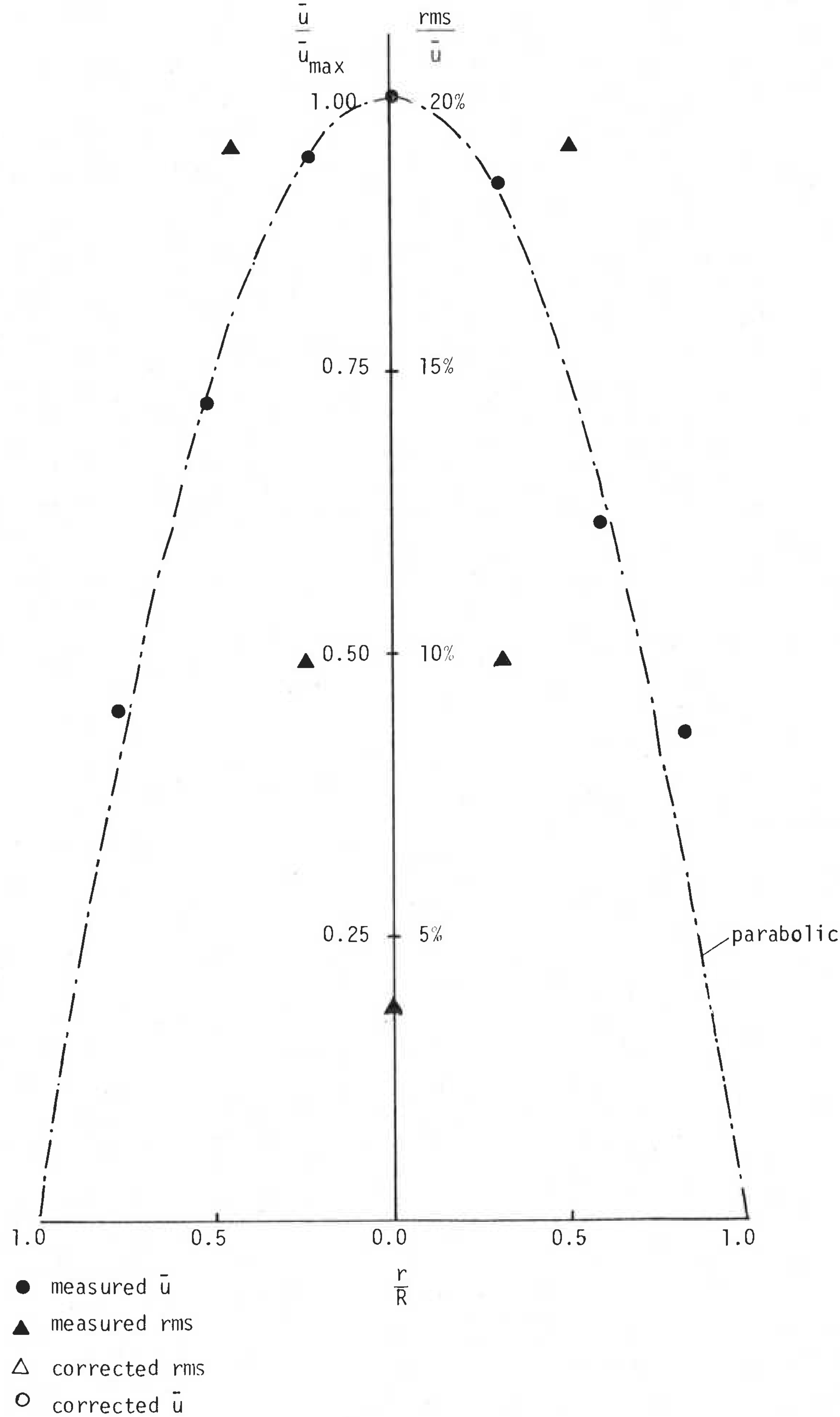

Fig. 3.5.2-9b Measured mean and rms velocity profiles
Plasma flow (D = 125 μm)

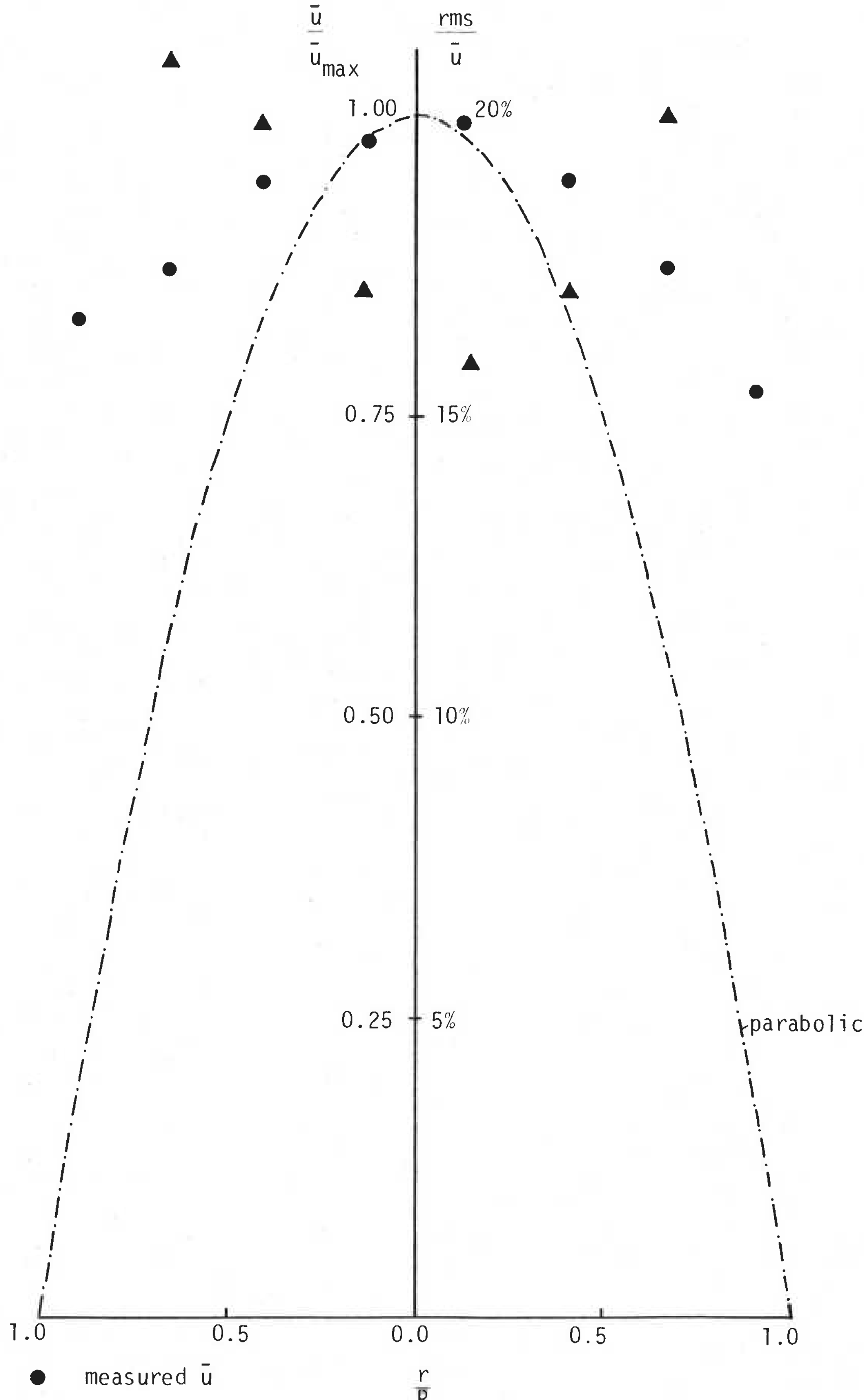

● measured $\bar{u}$

▲ measured rms

△ corrected rms

○ corrected $\bar{u}$

Fig. 3.5.2-9c Measured mean and rms velocity profiles
Whole blood (H = 40%, D = 125 μm)

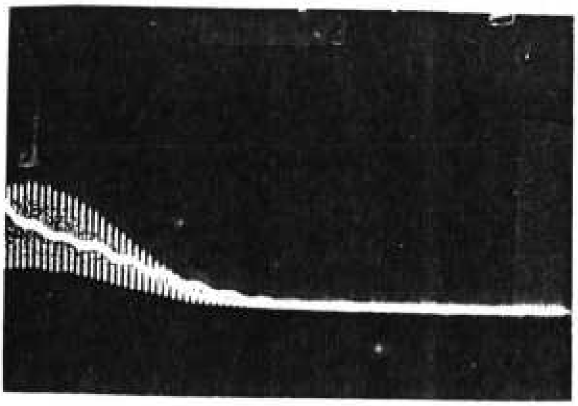

Unfiltered

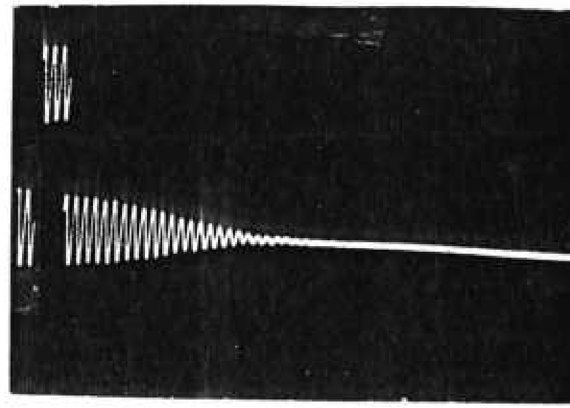

Filtered and processed

(a) Water (D = 125 μm)

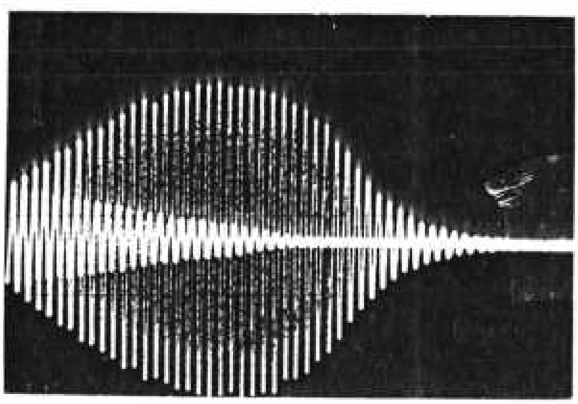

Filtered

(b) Water (D = 125 μm)

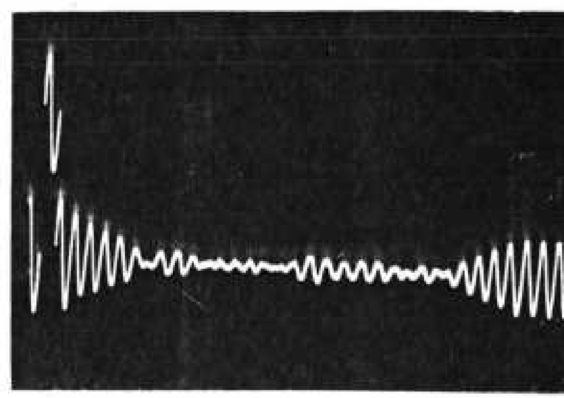

Filtered and processed

(c) Whole blood (D = 125 μm)

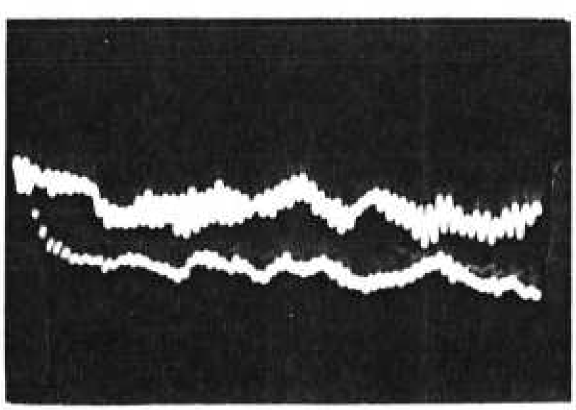

Unfiltered

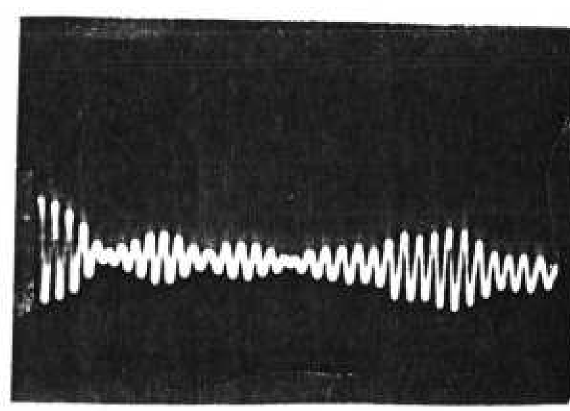

Filtered

(d) Whole blood (D = 125 μm)

Fig. 3.5.3-1 Doppler signals with the Argon LDV in glass capillary flows

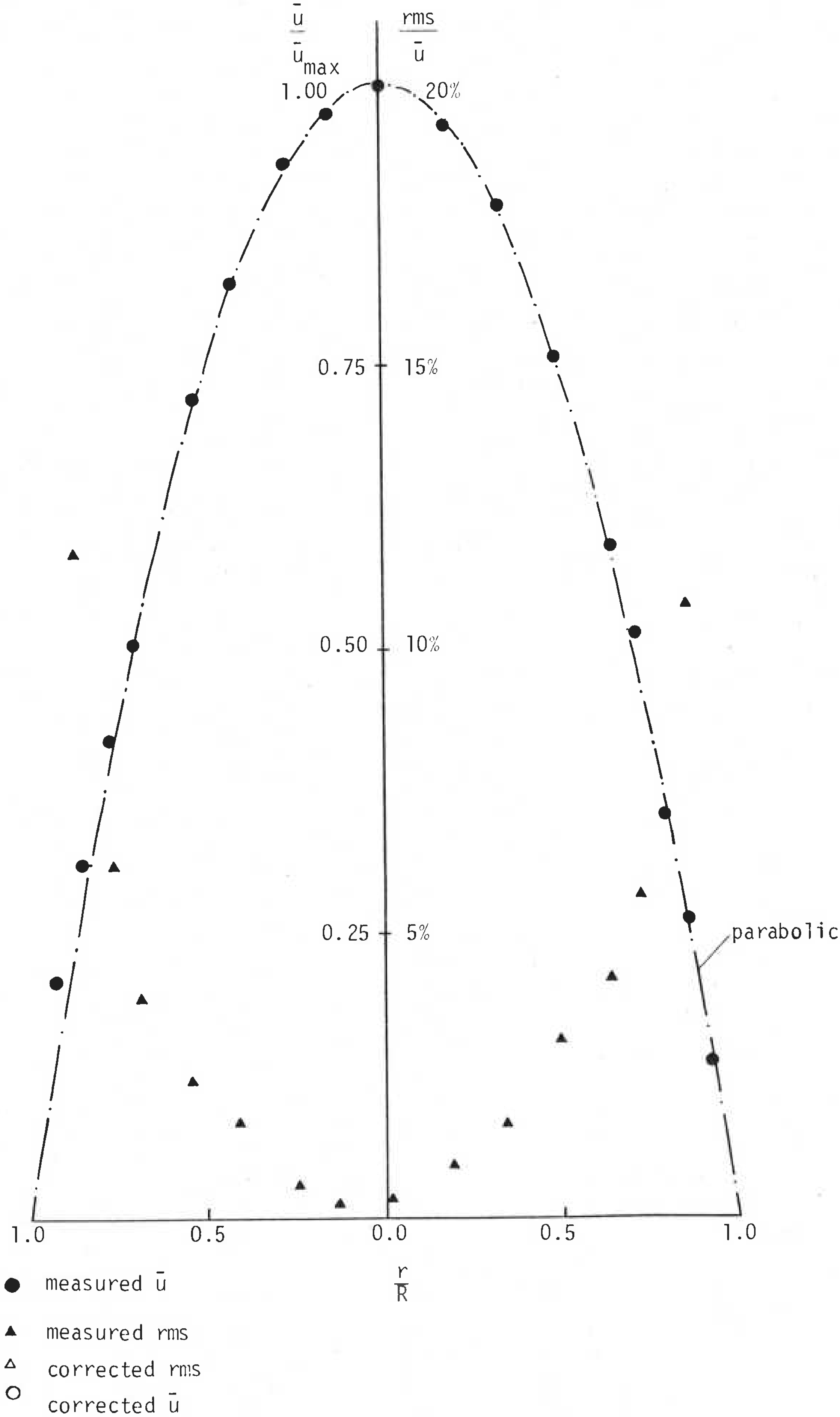

Fig. 3.5.3-2a Measured mean and rms velocity profiles
Water flow (D = 550 μm)

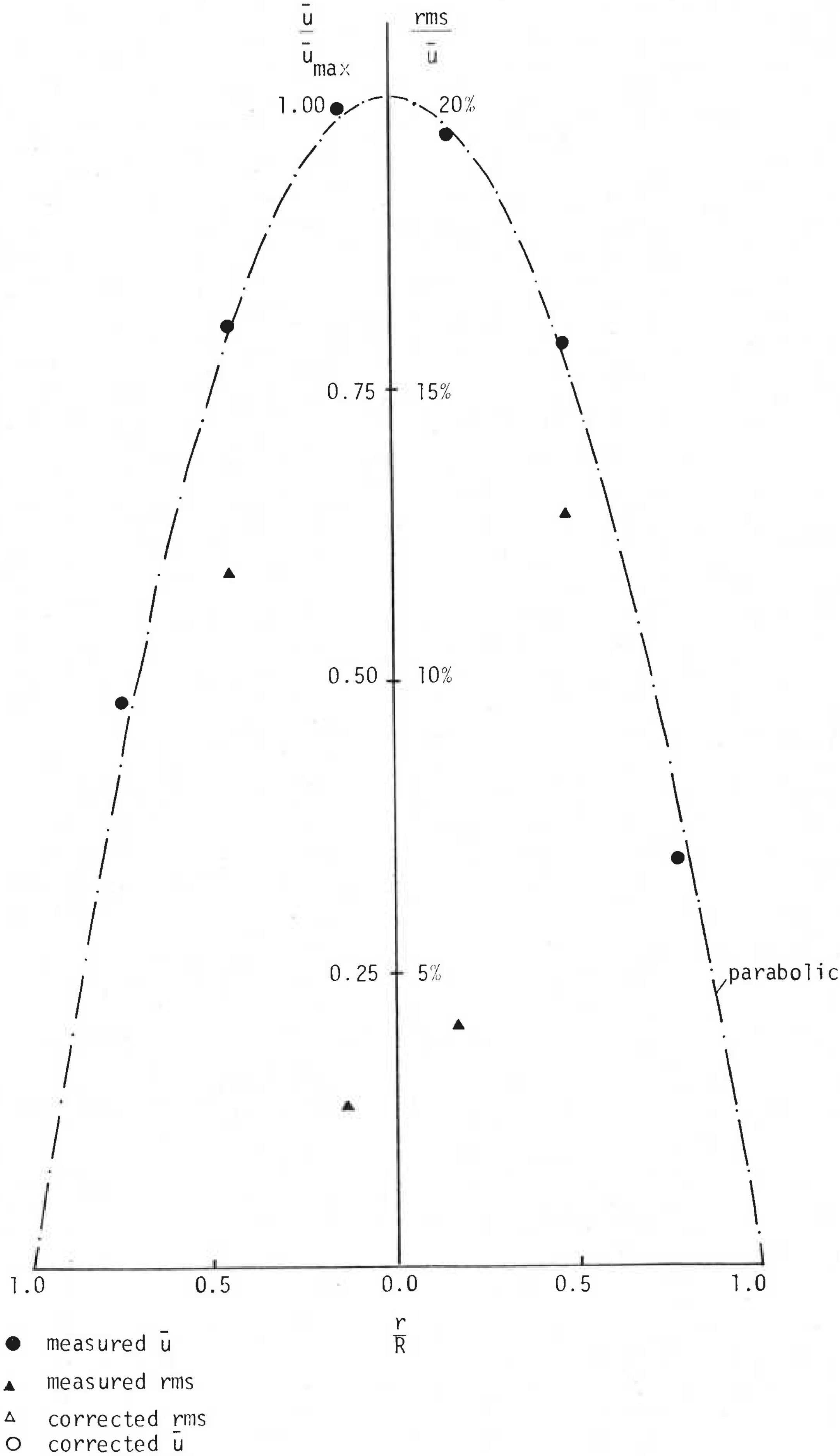

Fig. 3.5.3-2b Measured mean and rms velocity profiles
Water flow (D = 125 μm)

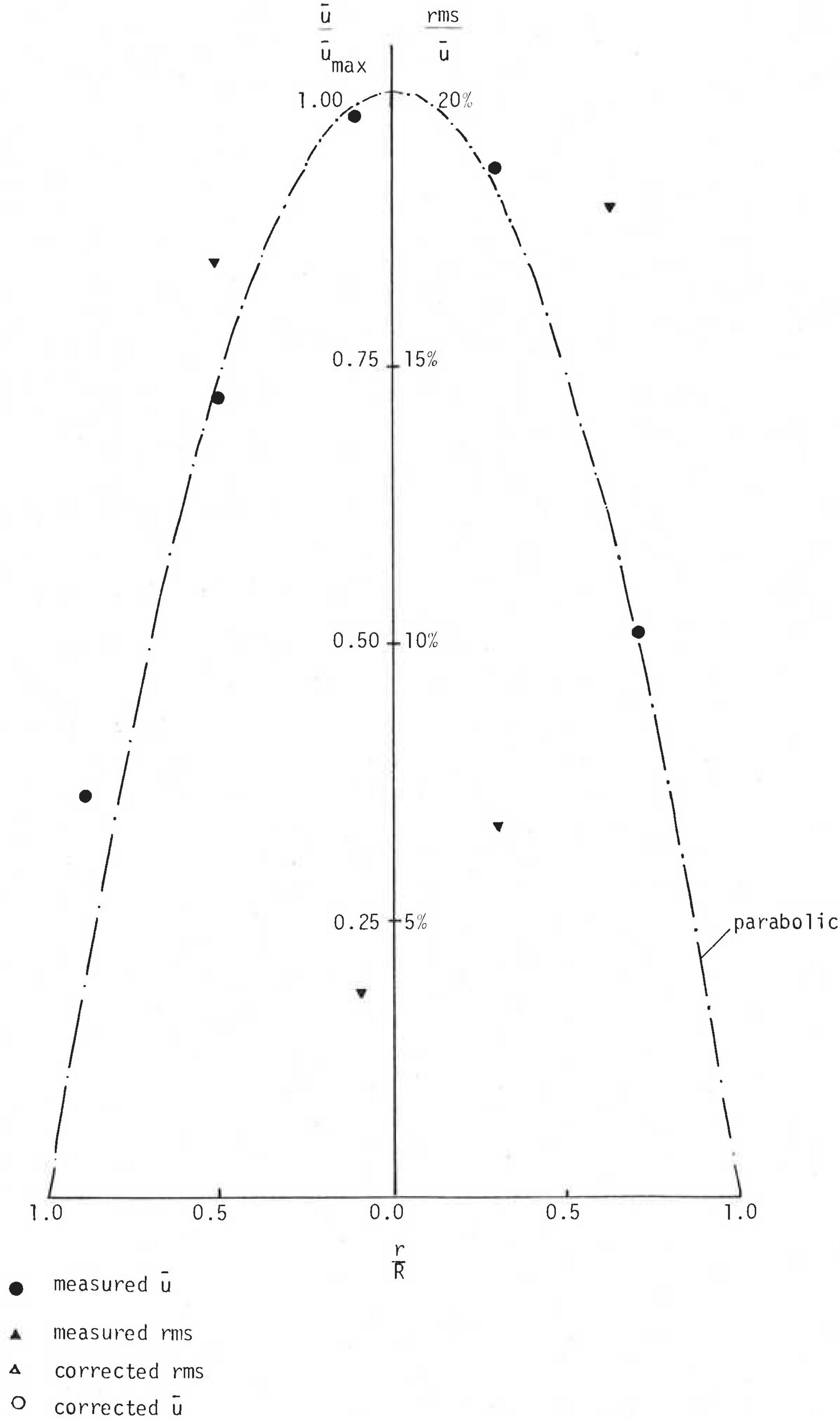

Fig. 3.5.3-2c Measured mean and rms velocity profiles
Water flow (D = 80 μm)

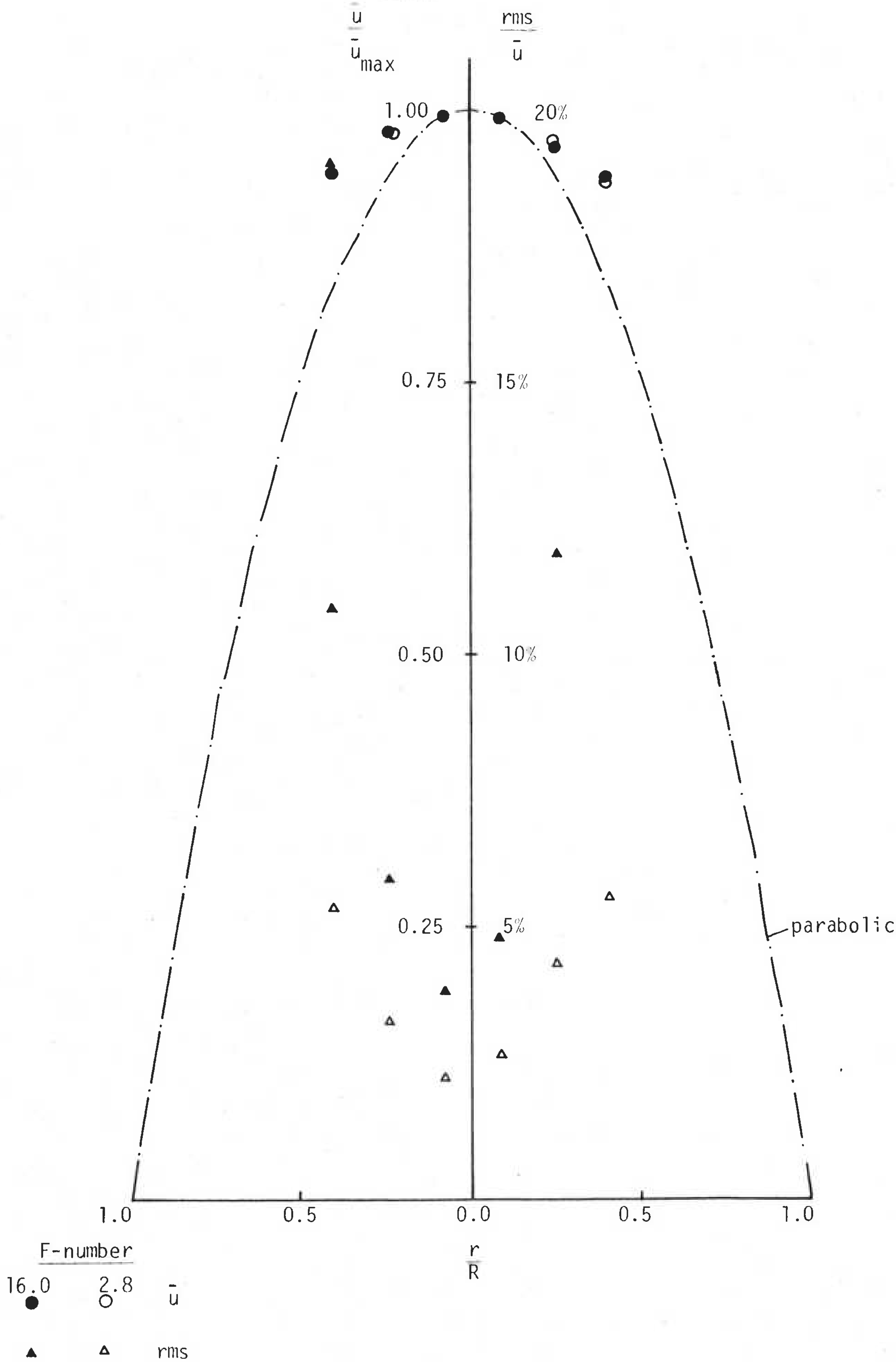

Fig. 3.5.3-3 Measured mean and rms velocity profiles
Blood flow (D = 125 μm)

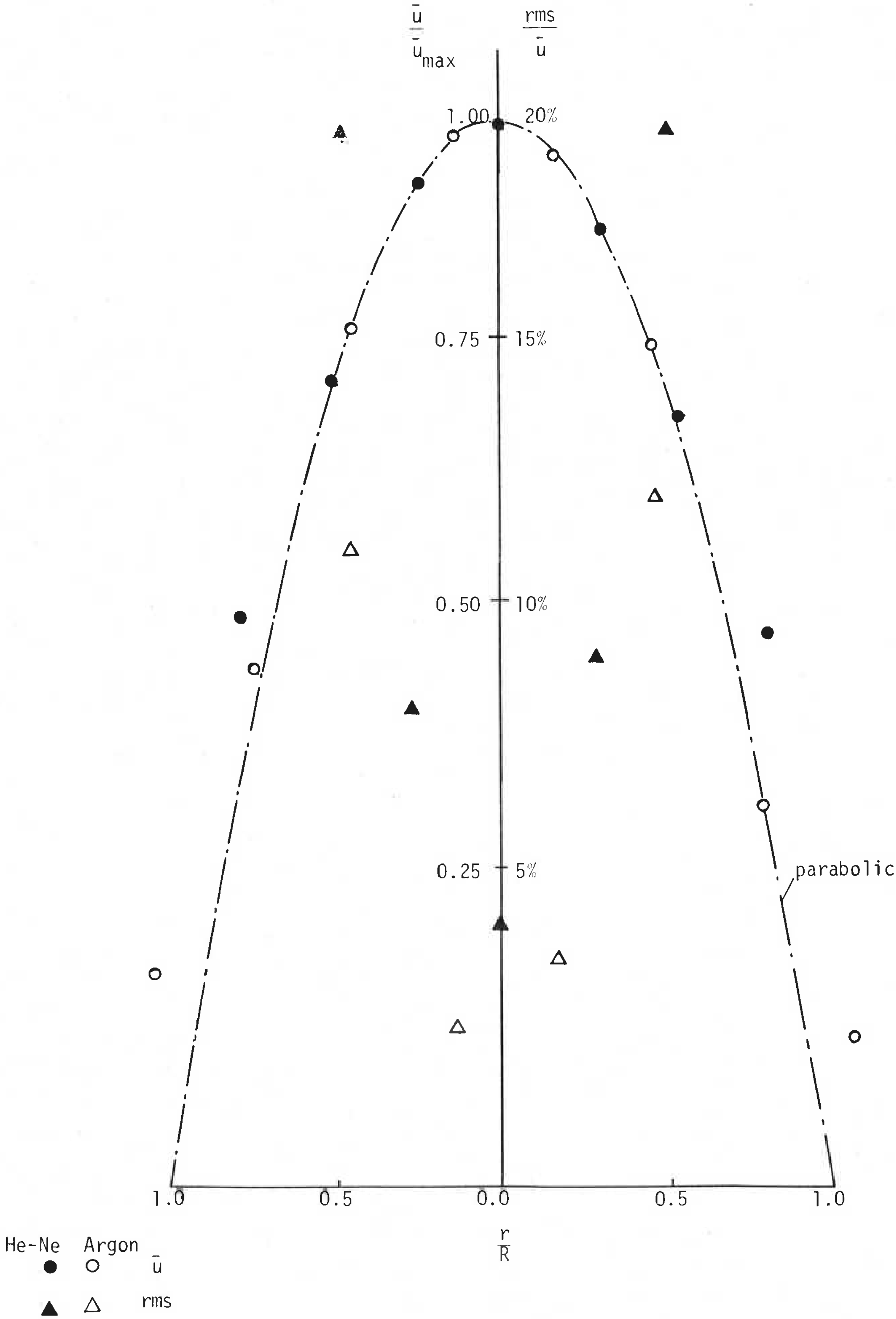

Fig. 3.5.3-4a Comparison of the He-Ne and Argon LDVs
Water flow (D = 125 μm)

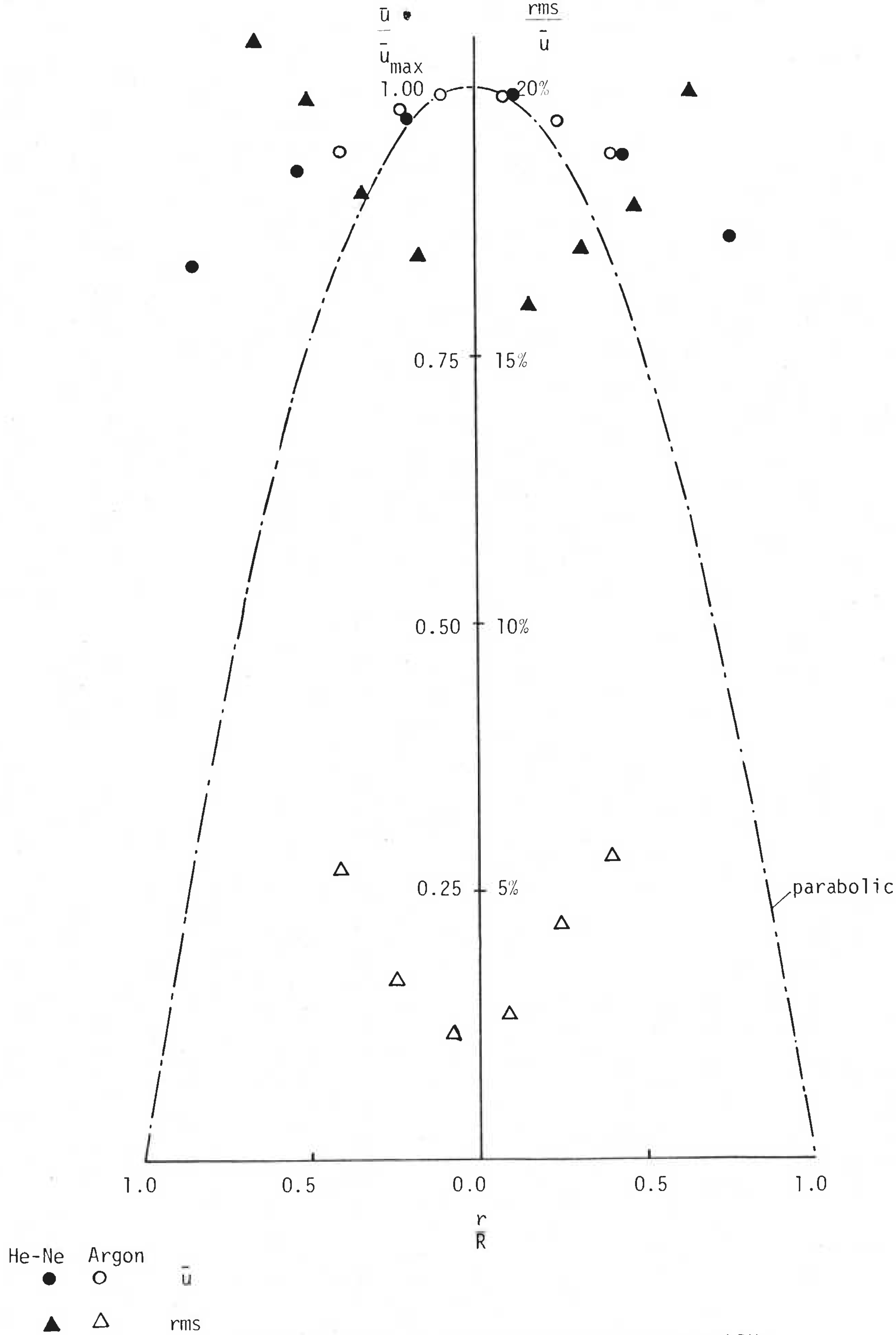

Fig. 3.5.3-4b Comparison of the He-Ne and Argon LDVs
Blood flow (D = 125 μm)

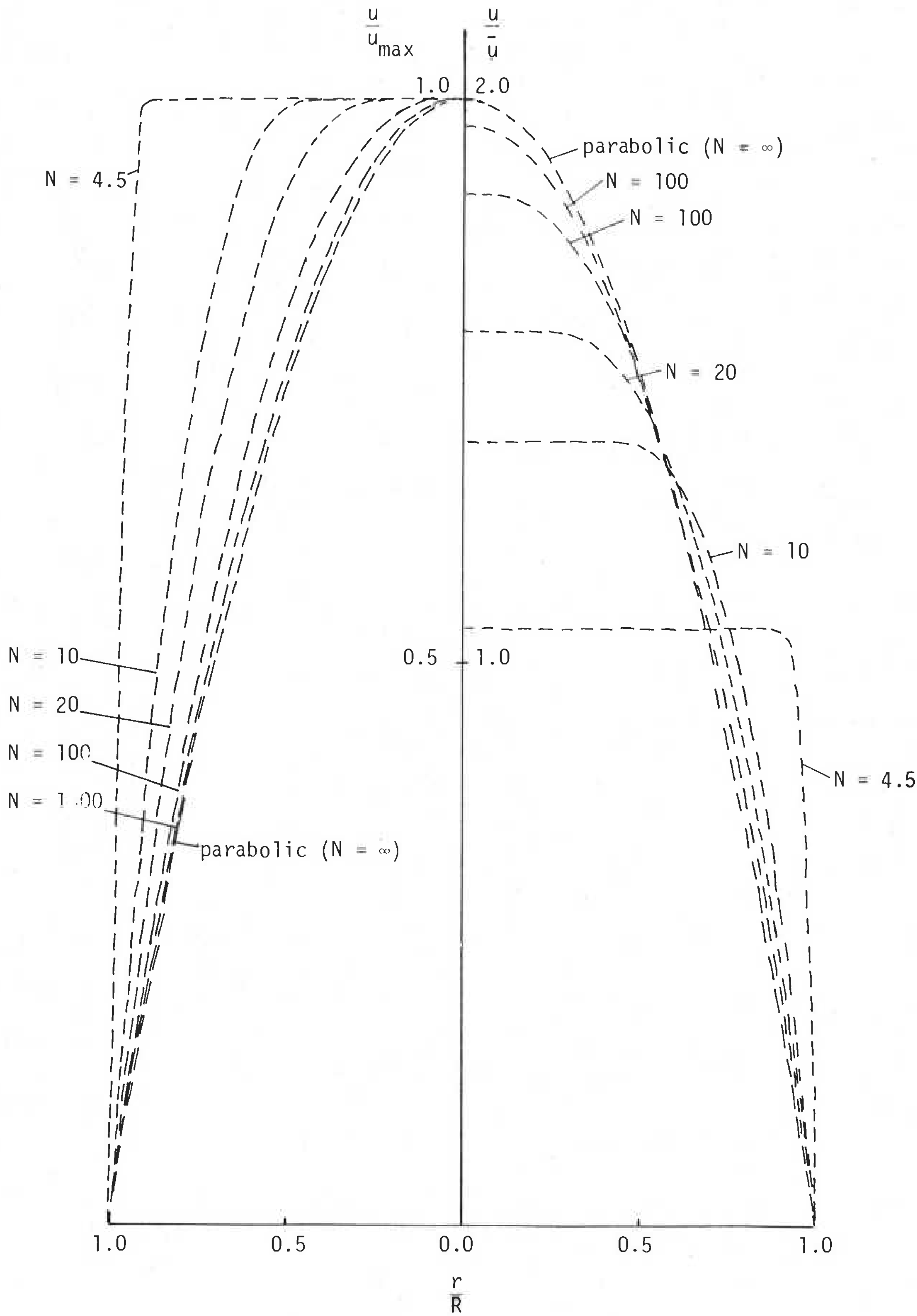

Fig. 3.6-1 Velocity profiles for fully developed blood flow in a glass capillary (Casson's law)

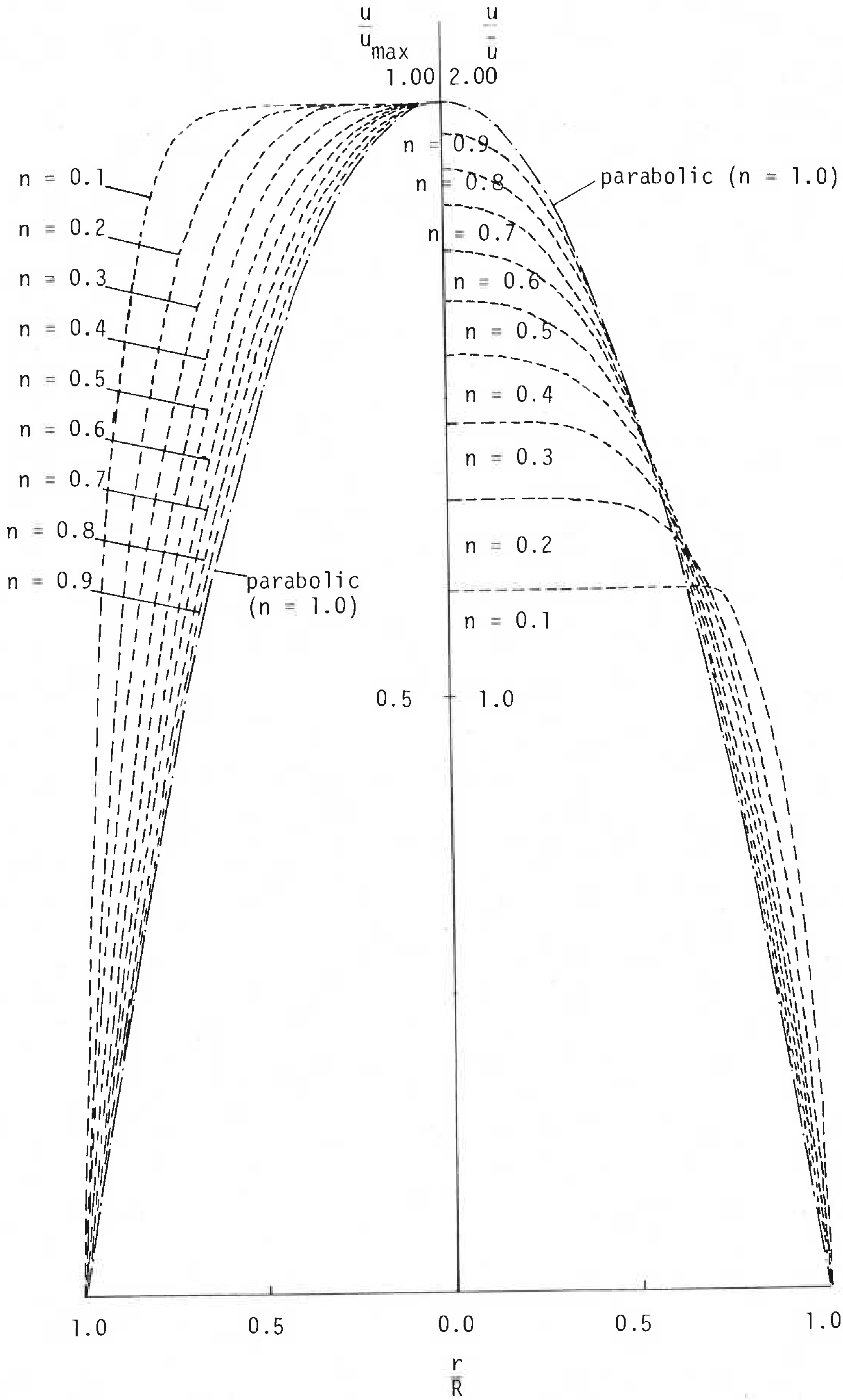

Fig. 3.6-2 Velocity profiles of fully developed blood flow in a glass capillary (Power law)

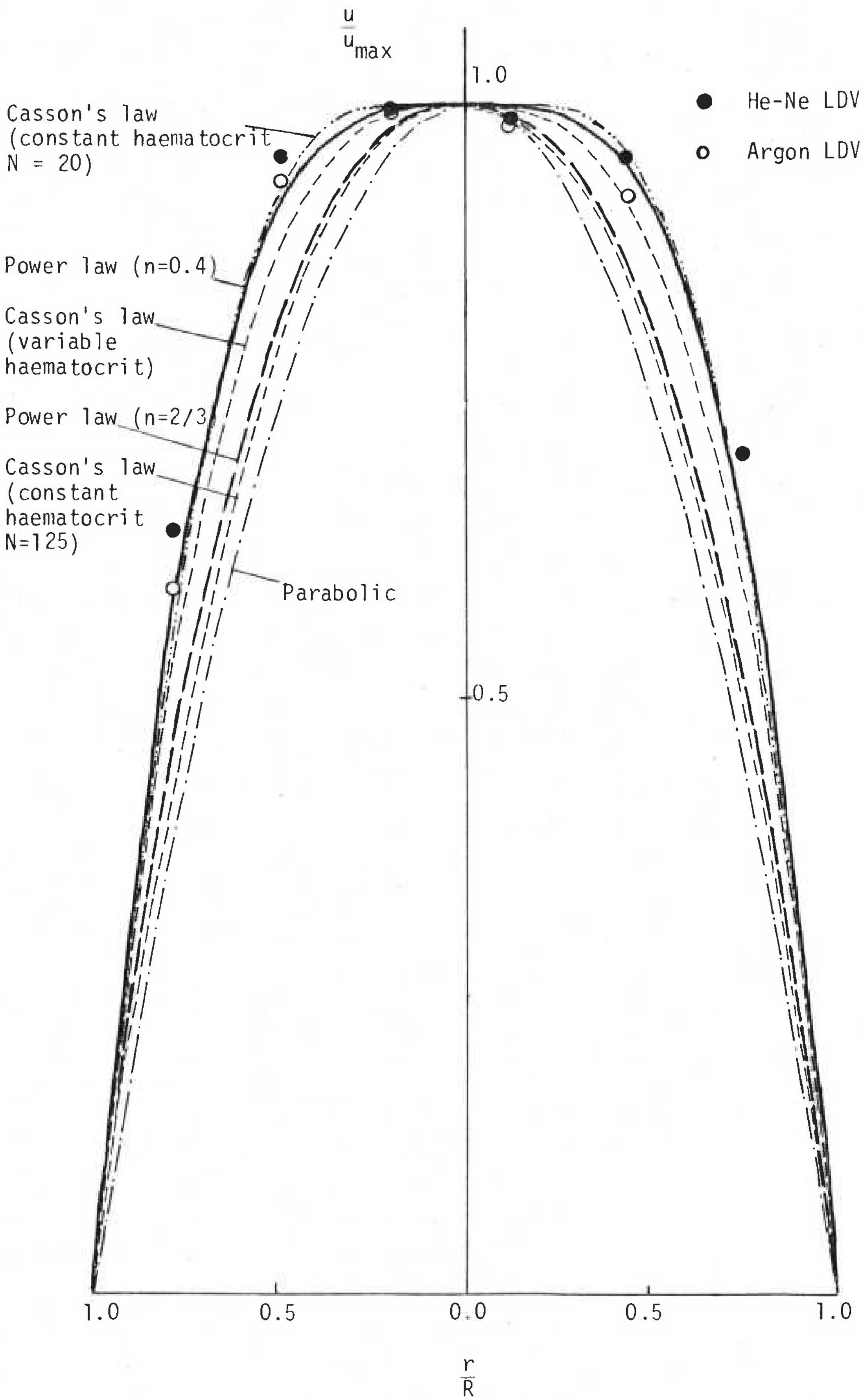

Fig. 3.6-3 Selection of blood viscosity law

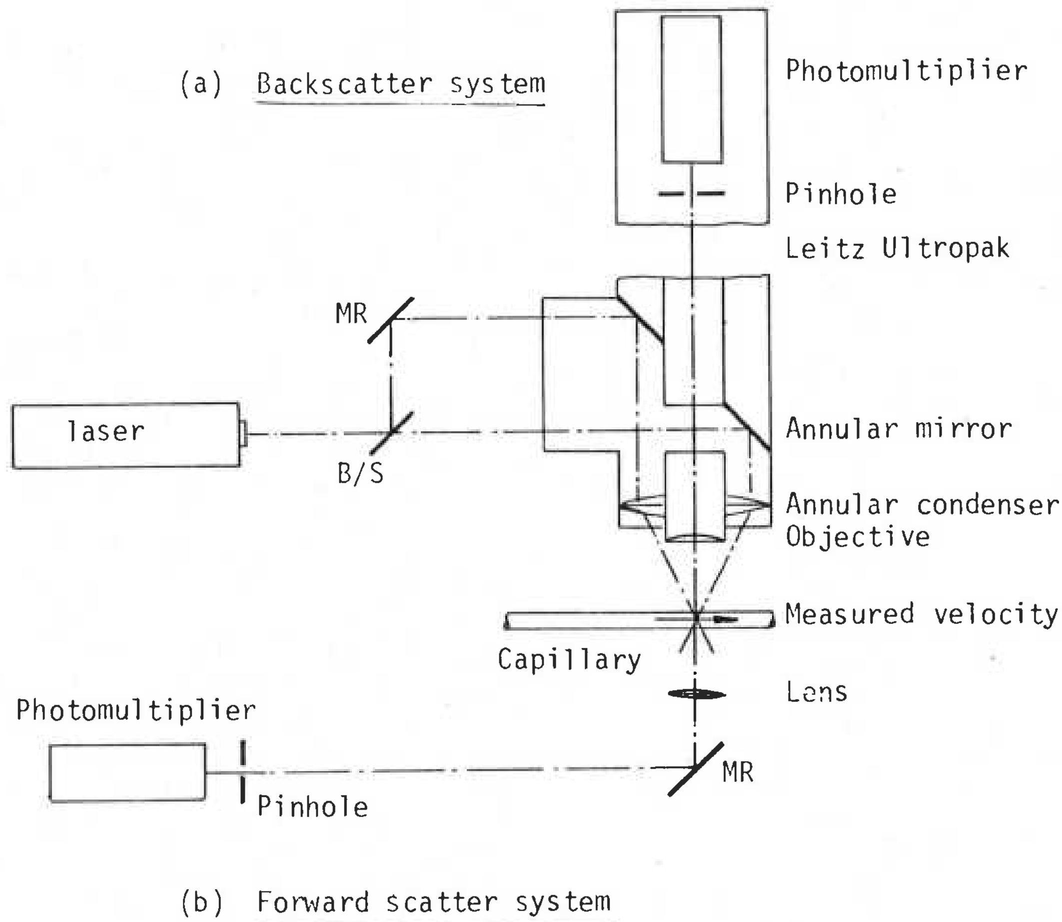

Fig. 3.7-1 Schematic diagram of laser Doppler microscope

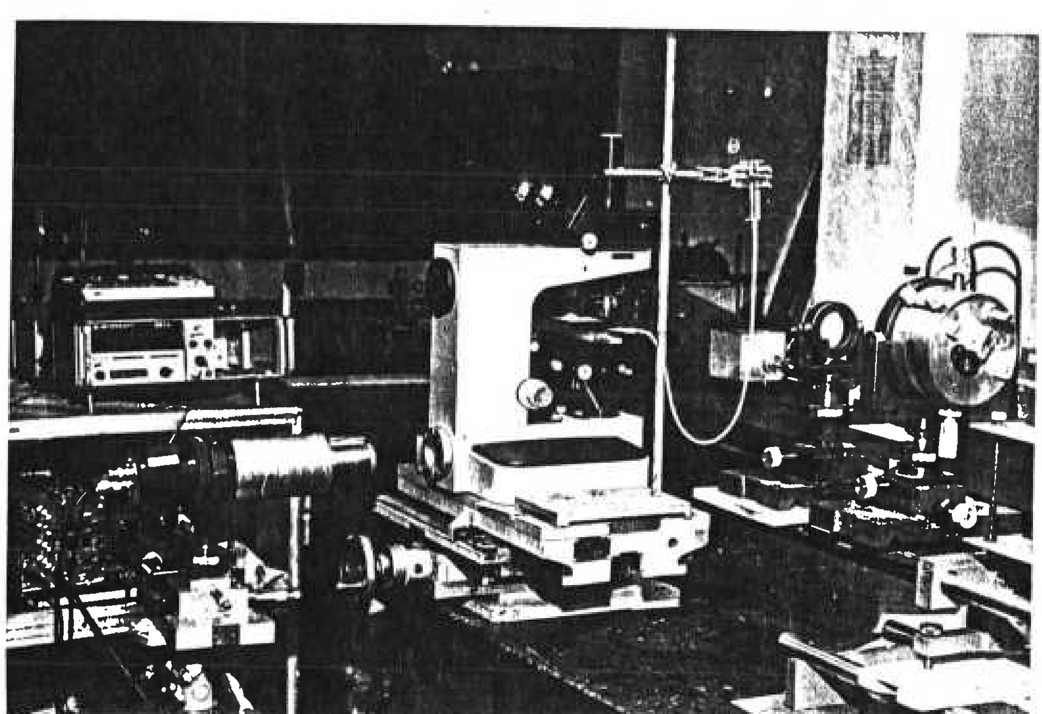

Fig. 3.7-2 Photographic view of the laser Doppler microscope

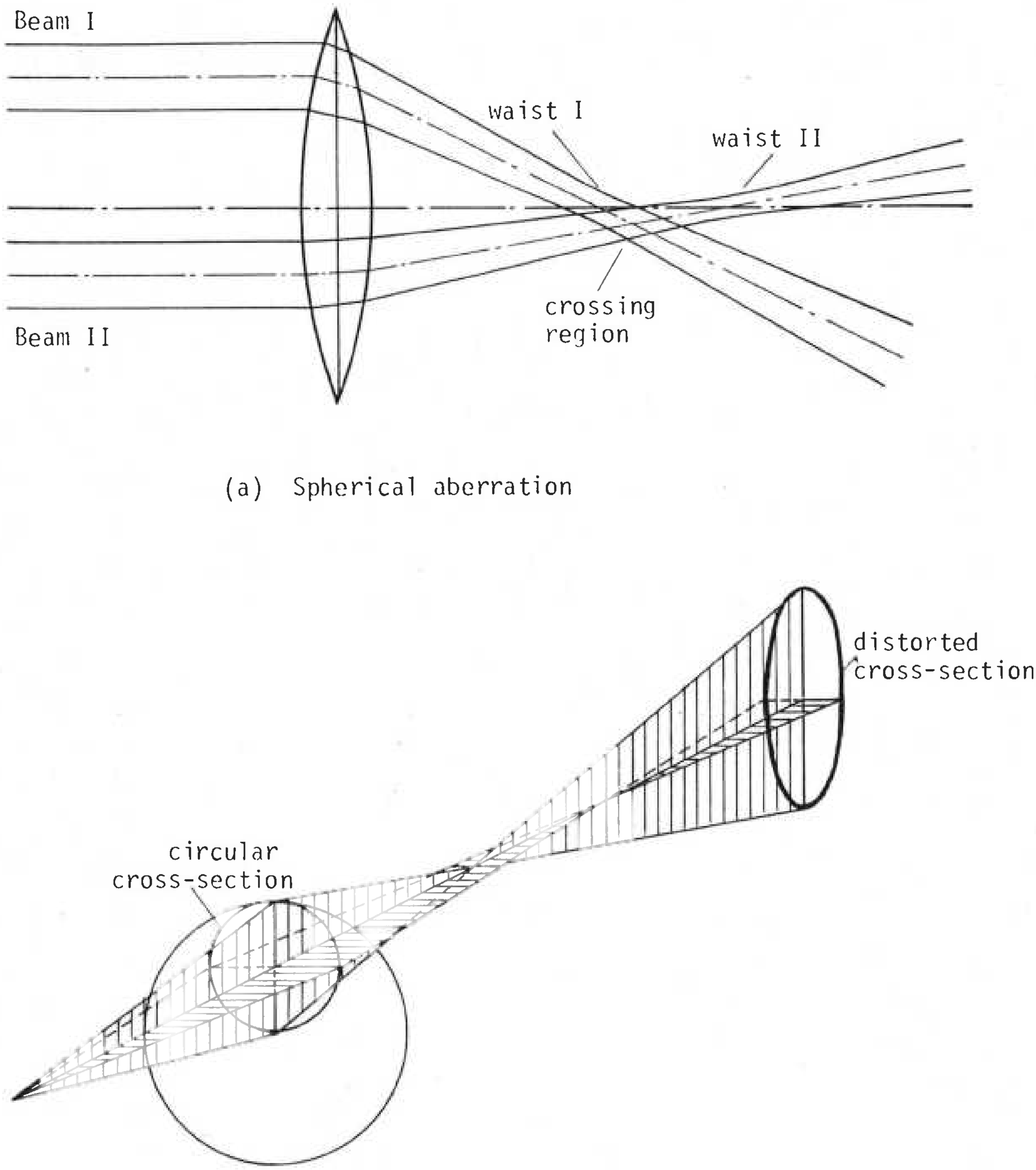

(a) Spherical aberration

(b) Astigmatism

Fig. 3.7-3 Lens aberrations

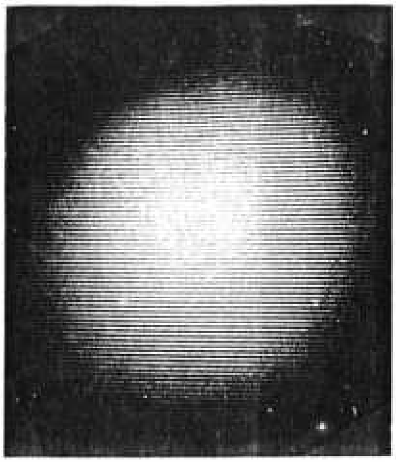

(a) Ordinary LDV

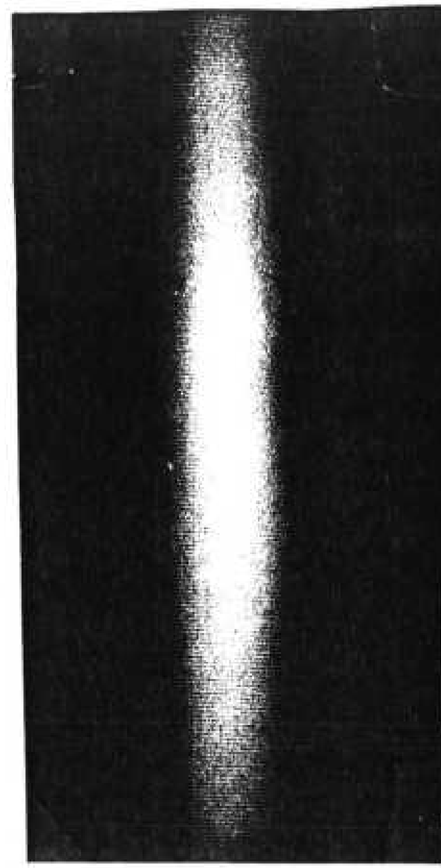

(b) Laser Doppler microscope

Fig. 3.7-4 Effect of lens aberrations on the fringe pattern

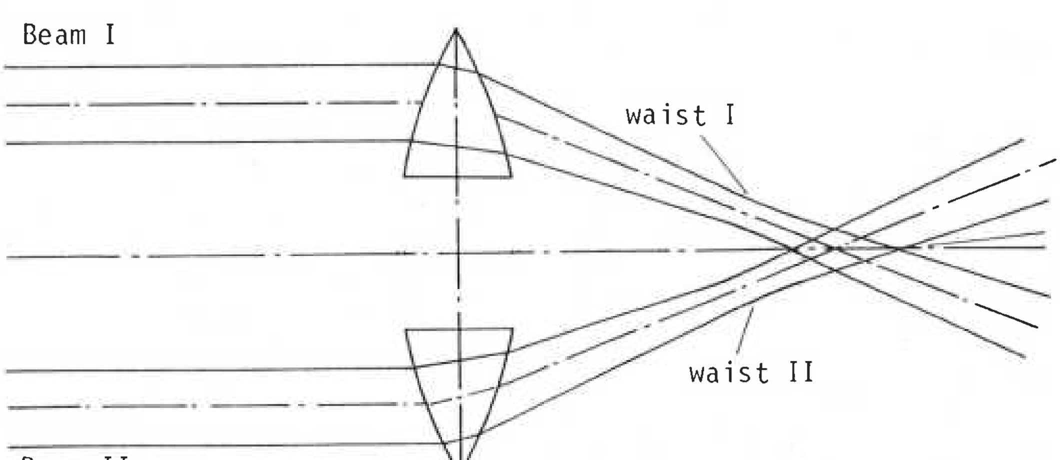

Fig. 3.7-5 Effect of lens aberrations on the beam intersection region

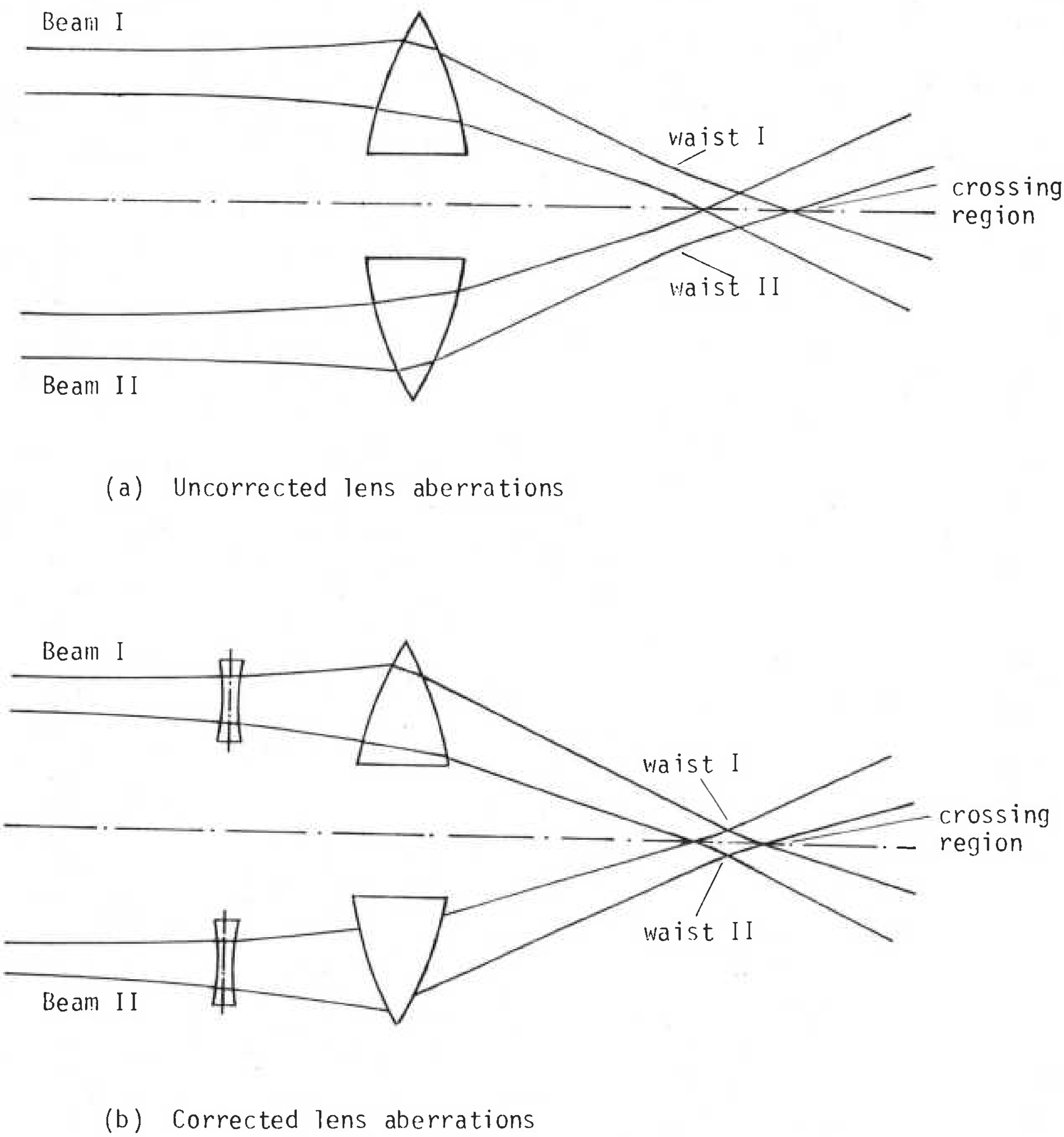

Fig. 3.7-6 Correction of lens aberrations by negative lenses

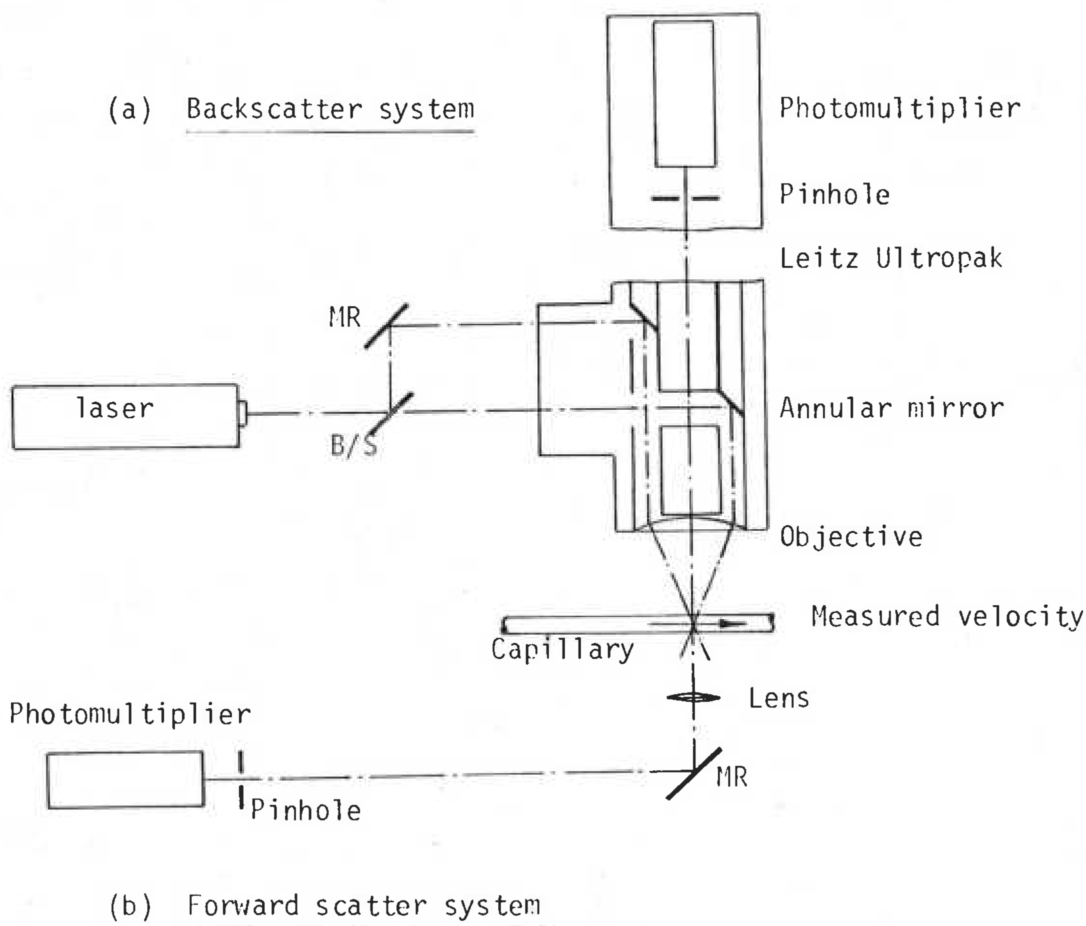

Fig. 3.7-7 A laser Doppler microscope using the objective

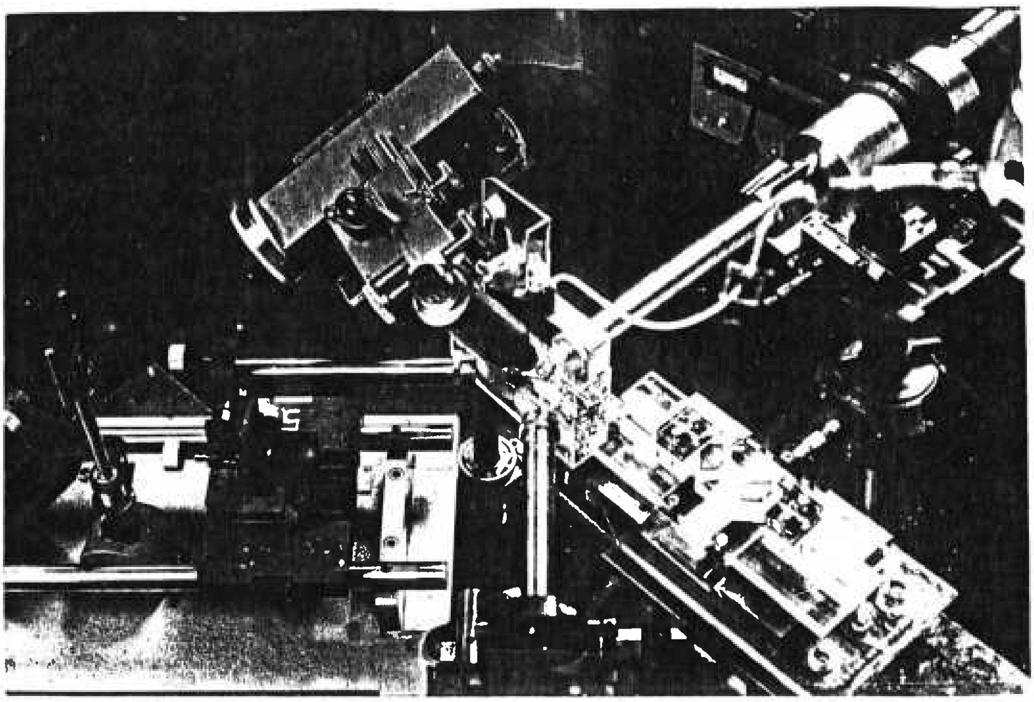

(a) Photographic view

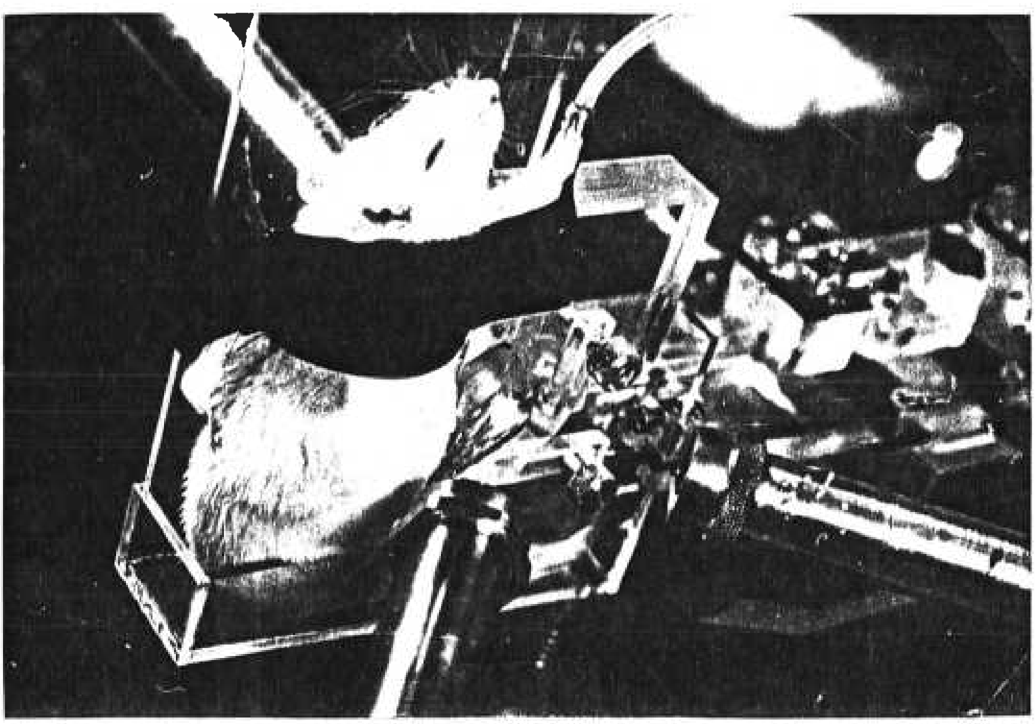

(b) Close view of the hamster starring - Mickey Mouse

Fig. 3.8-1 The experimental apparatus for in-vivo blood flow measurements

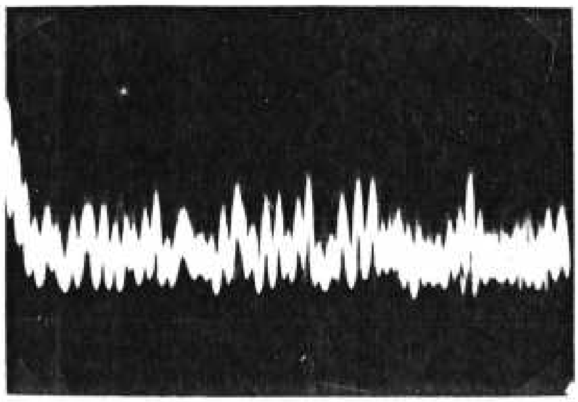

(a) Unfiltered

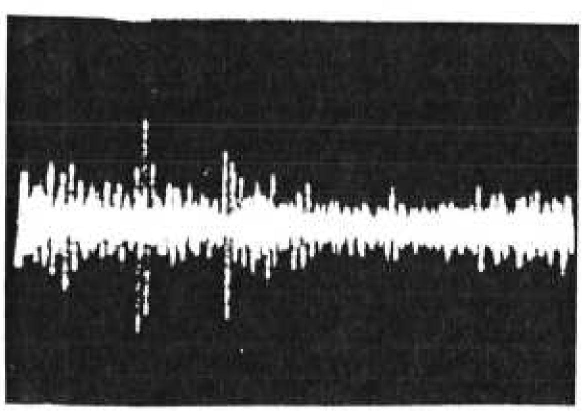

(b) Filtered

Fig. 3.8-2 Doppler signals from in-vivo blood flow

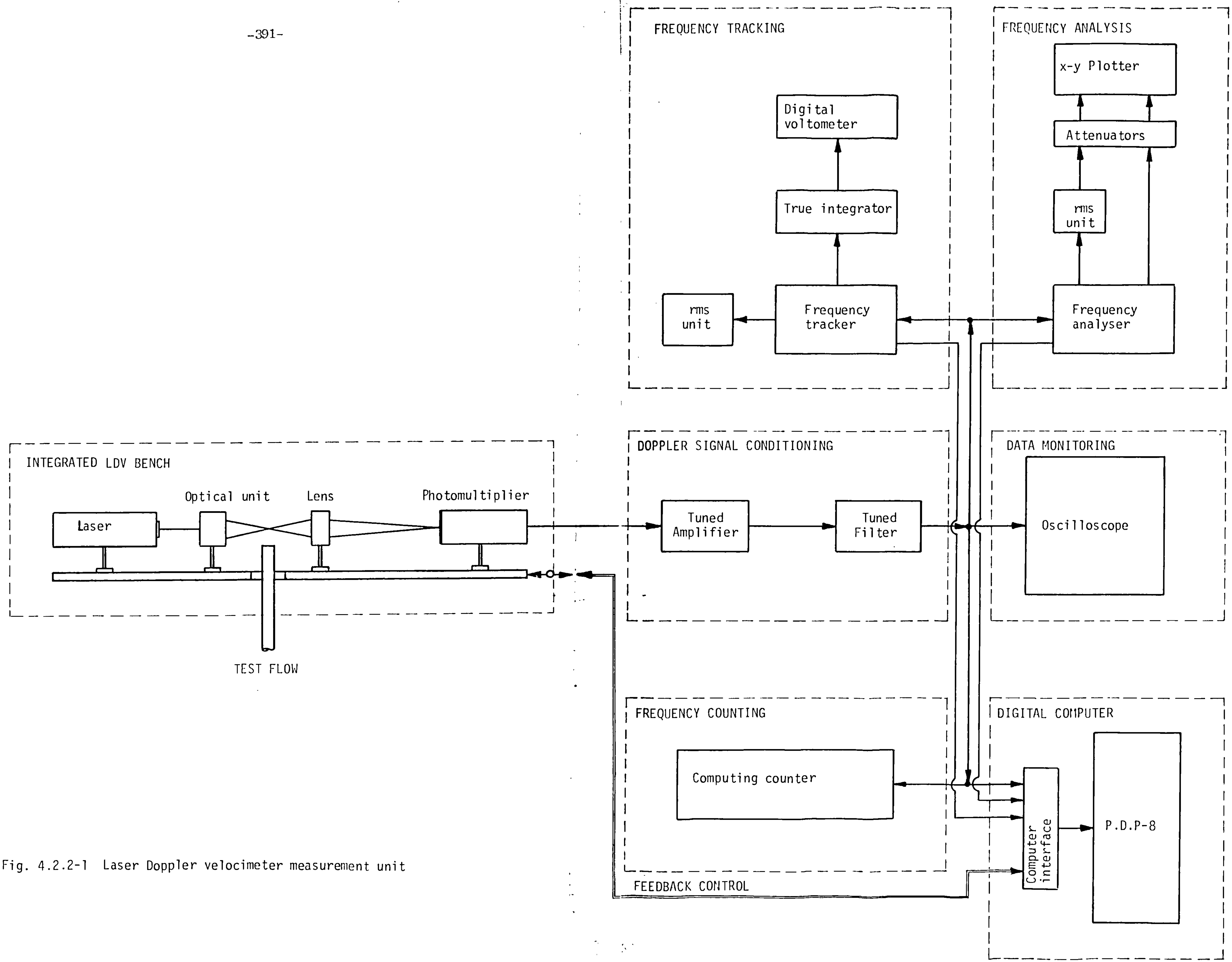

Fig. 4.2.2-1 Laser Doppler velocimeter measurement unit

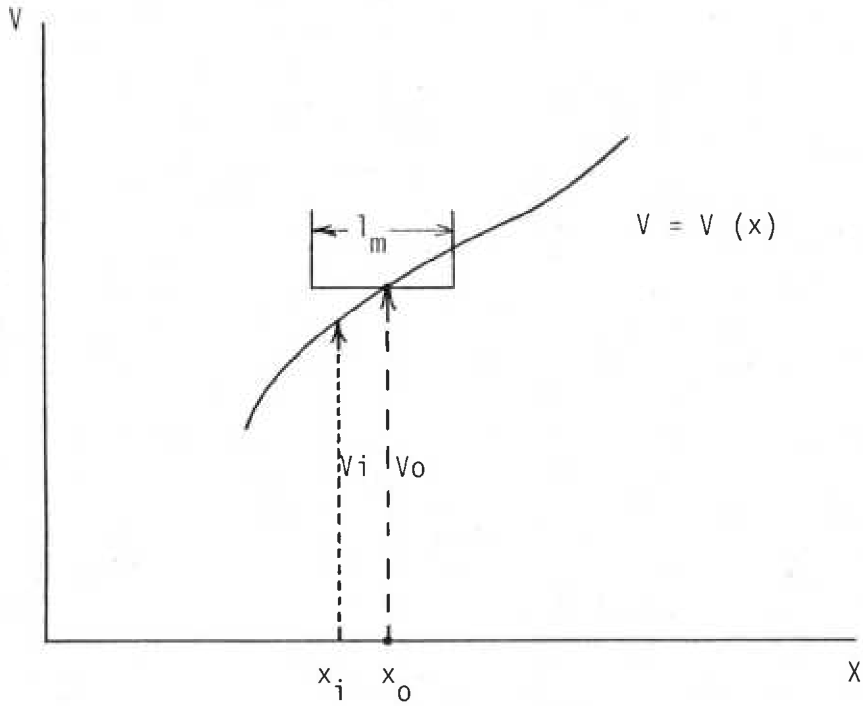

Fig. E.1 Velocity gradient broadening

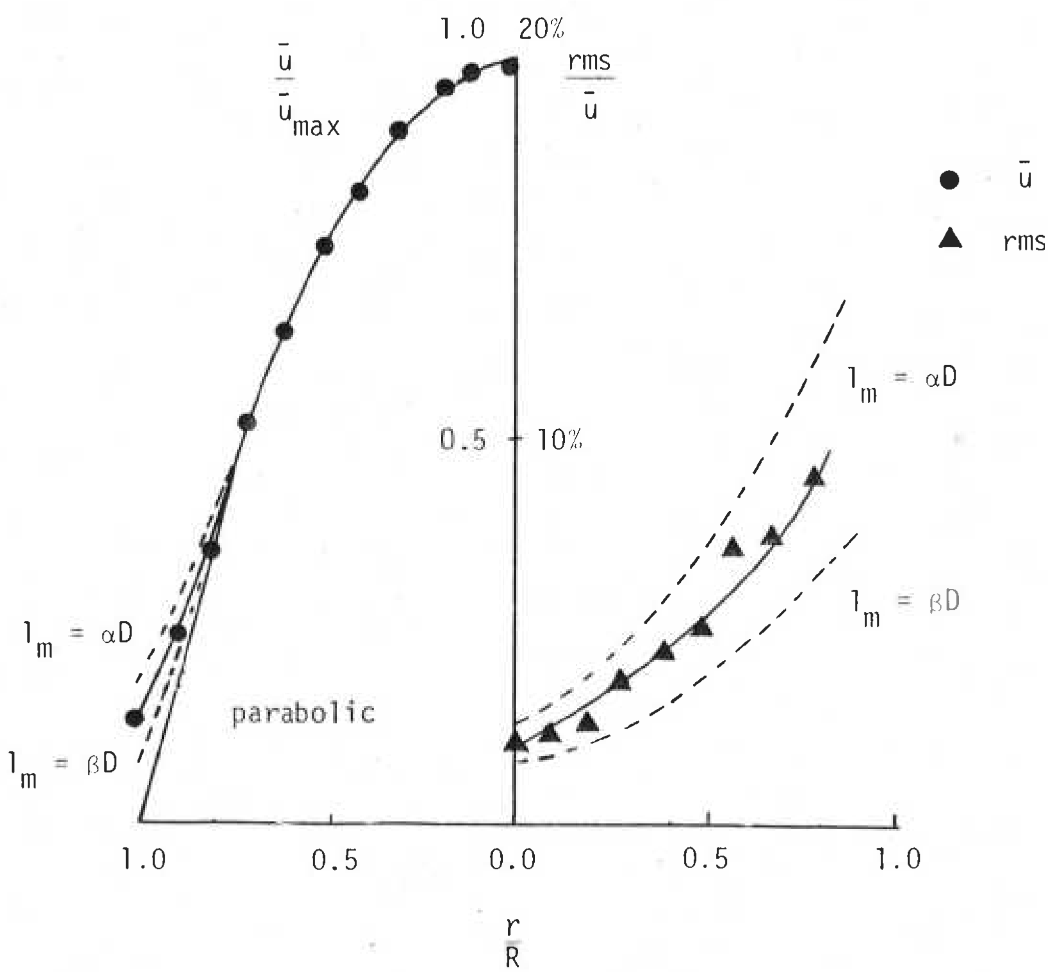

Fig. E.2 Estimation of control volume length

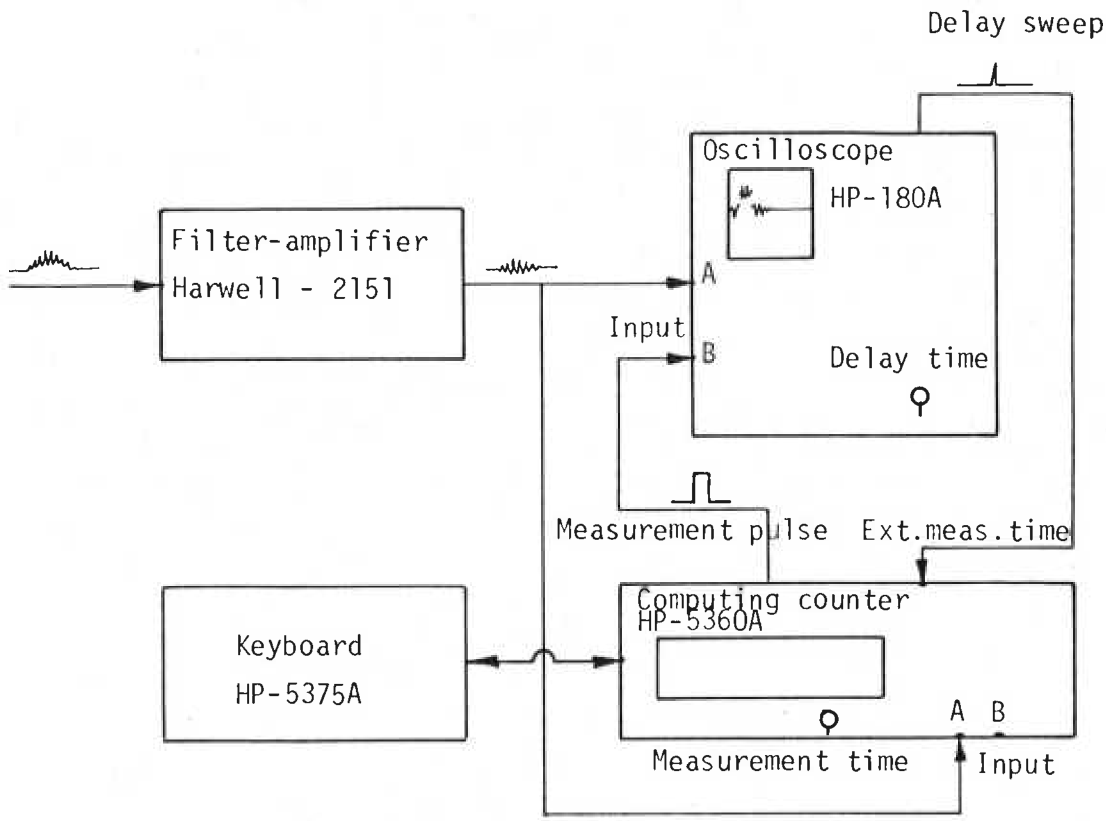

(a) Block diagram

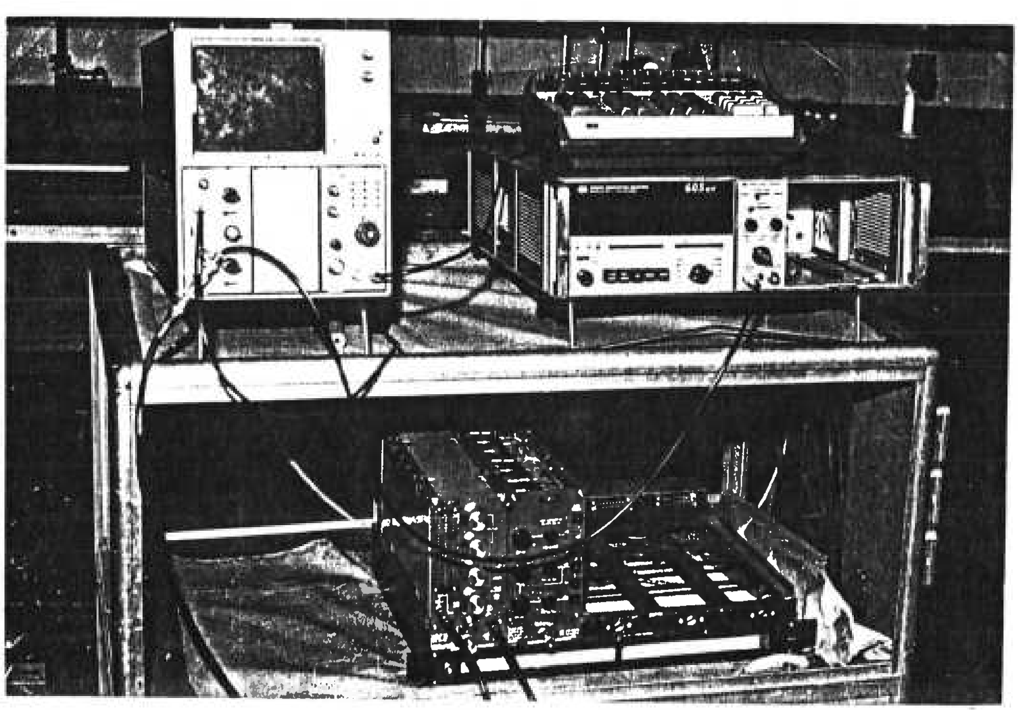

(b) Photographic view

Fig. F.1 The Doppler frequency counting system

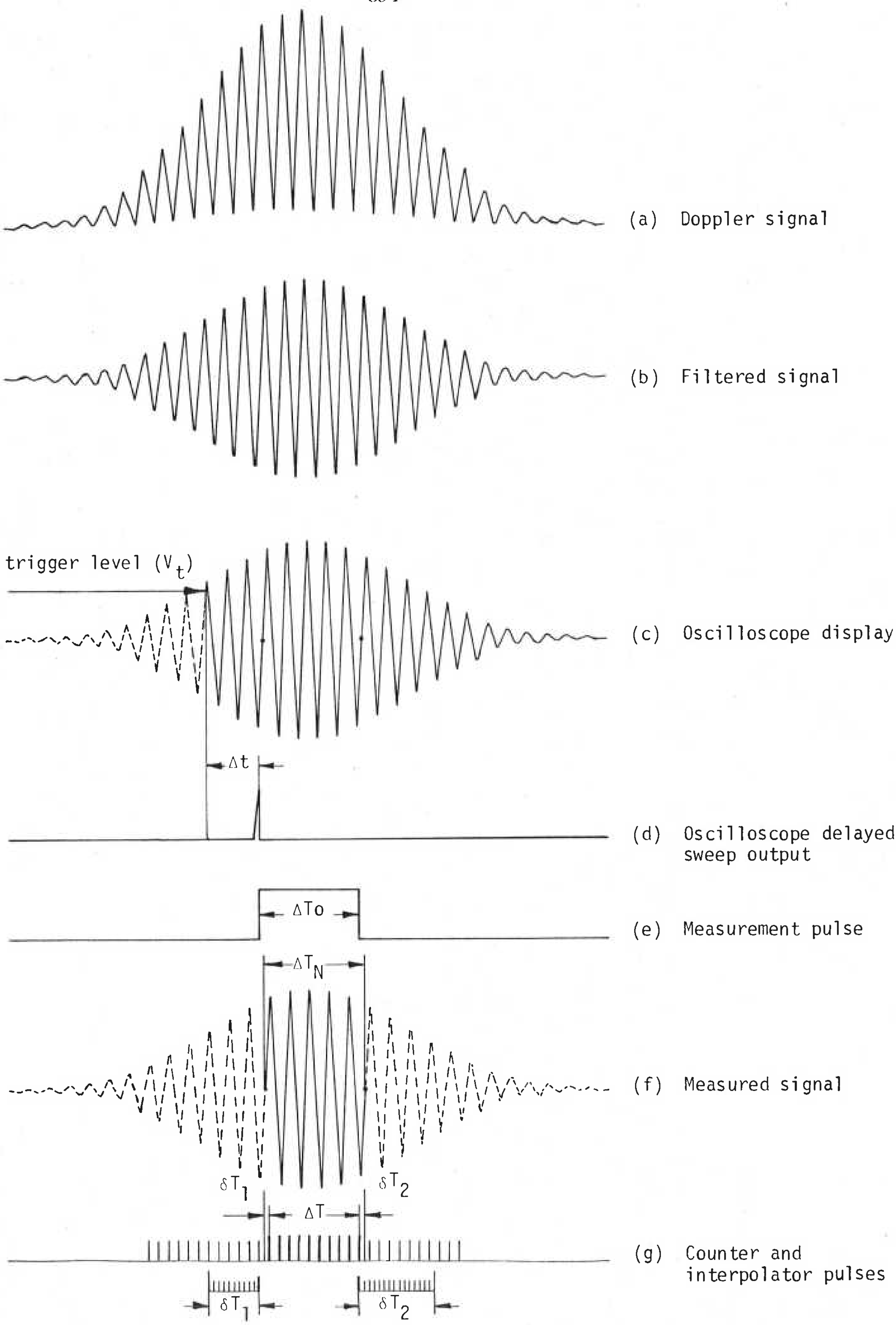

Fig. F.2 The frequency counting principle

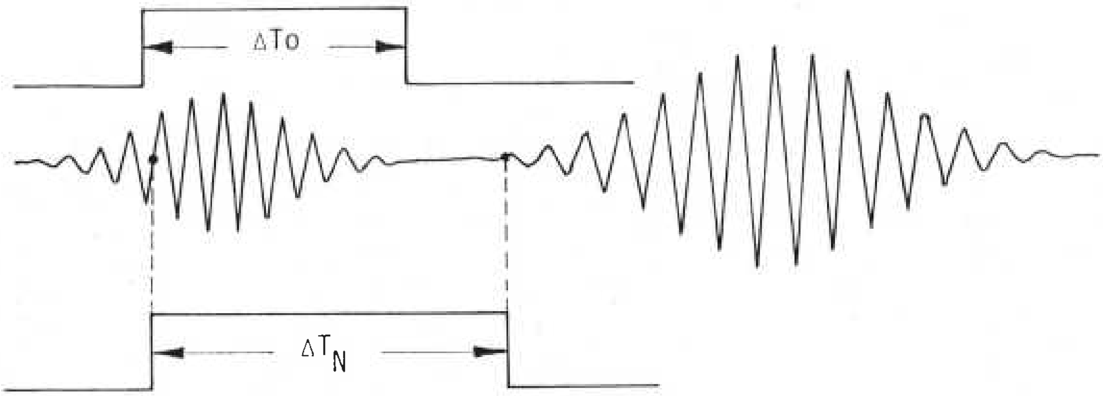

(a) False Doppler frequency measurement

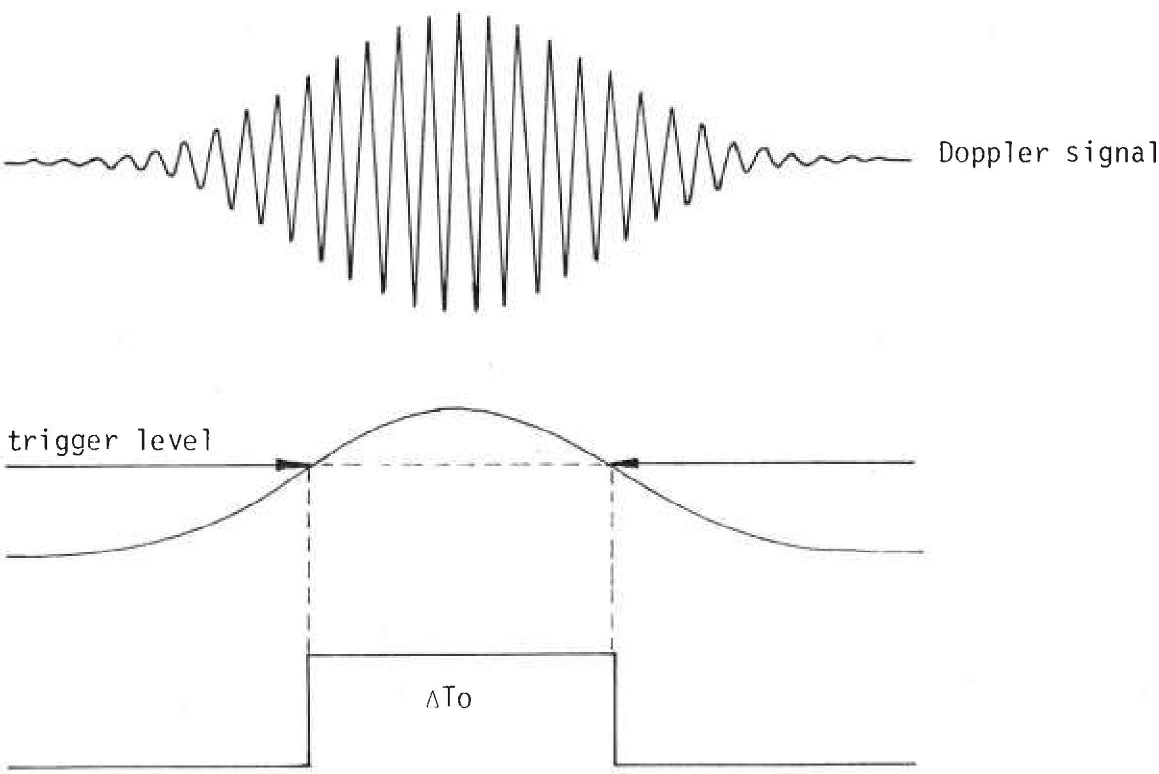

(b) The controlled square pulse for the measurement time

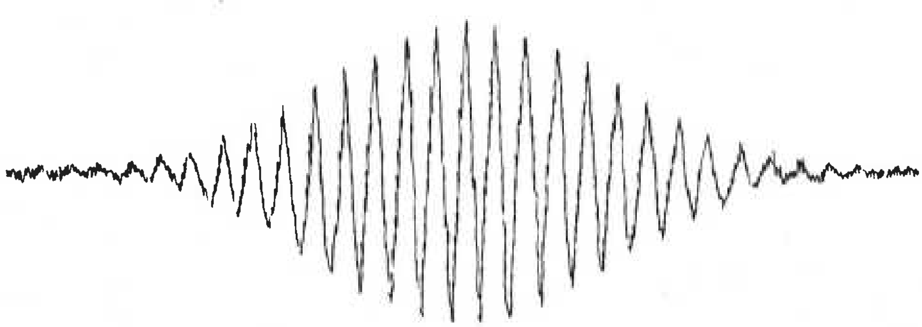

(c) Doppler signal modulated by noise

Fig. F.3 False measurement and controlled measurement time

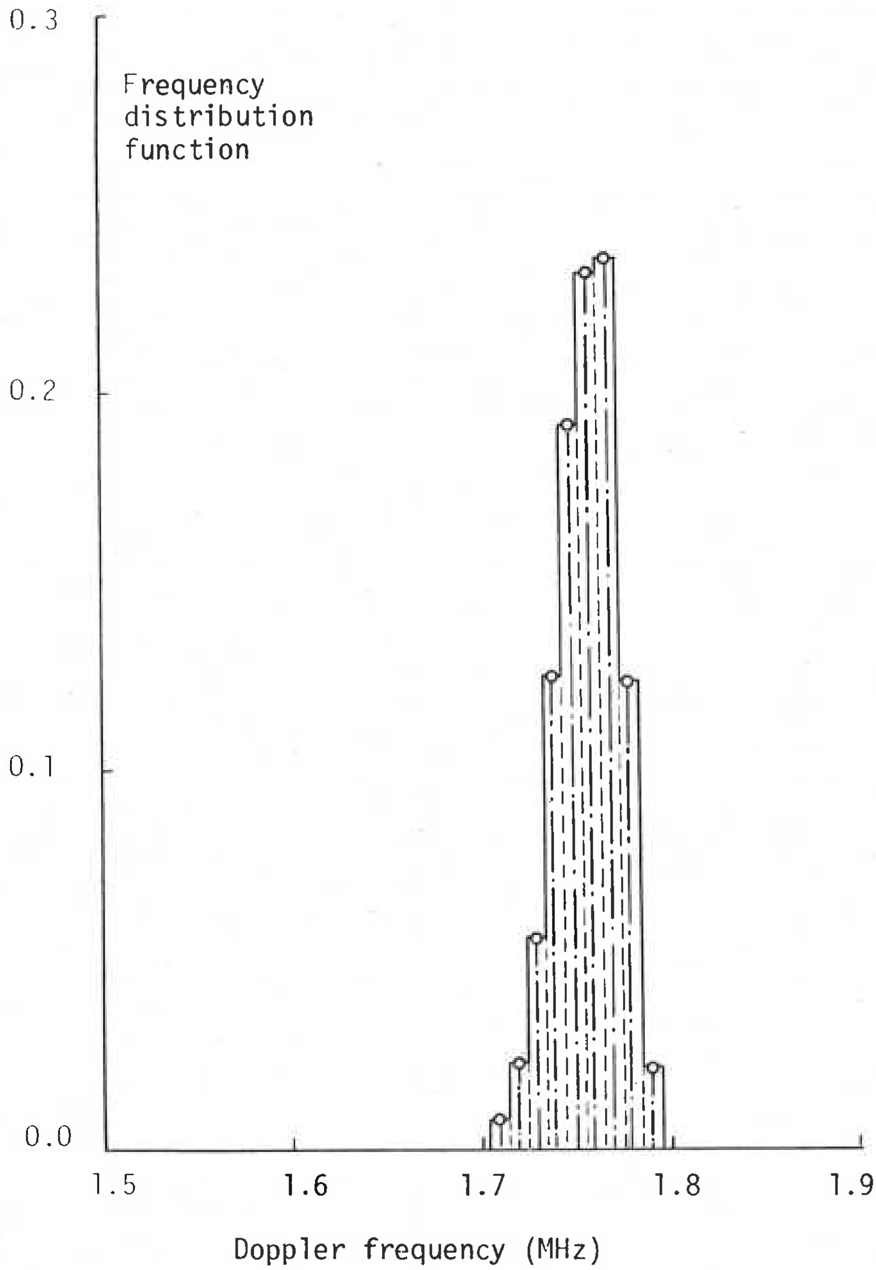

Fig. F.4 Doppler frequency histogram measured by the computing counter in a laminar pipe flow

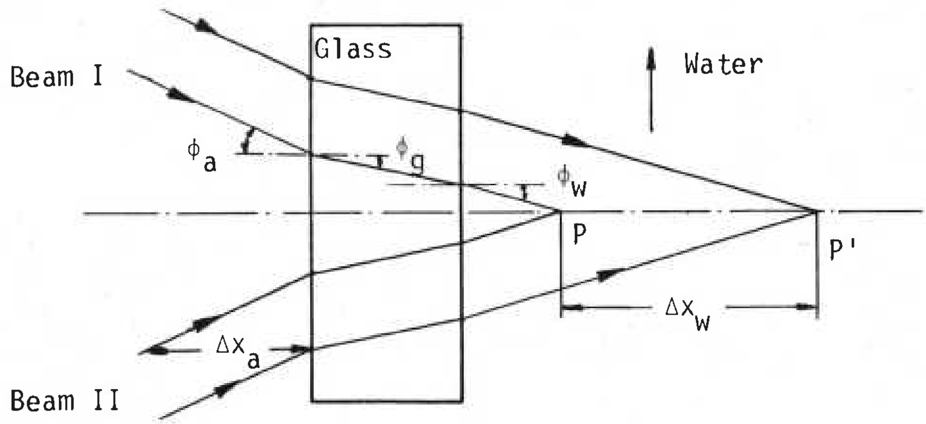

Fig. G.1 Refraction of control volume

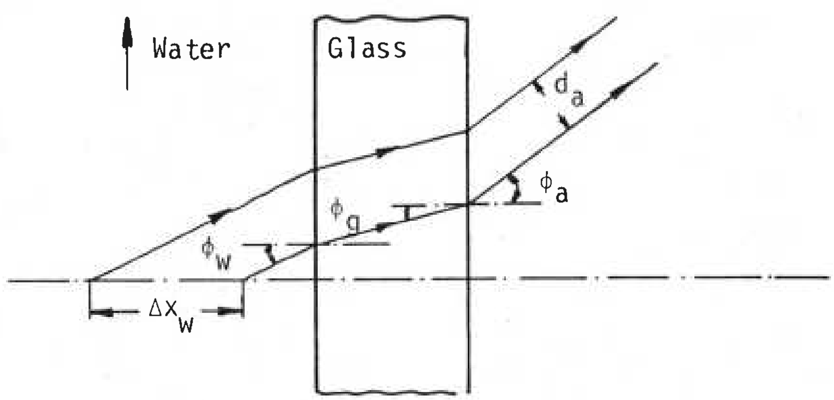

Fig. G.2 Refraction in off-axis detection

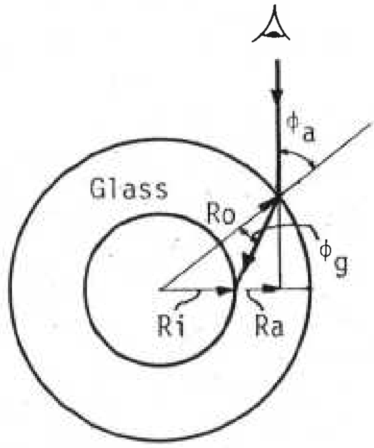

Fig. G.3 Refraction error in capillary diameter